Cinétique de la purification par plasma de silicium pour cellules photovoltaïques : étude expérimentale par spectrométrie Kinetics of the plasma refining process of silicon for solar cells

Jochen Altenberend

UNIVERSITÉ DE GRENOBLE

THÈSE

Pour obtenir le grade de

DOCTEUR DE L'UNIVERSITÉ DE GRENOBLE

Spécialité : **Mécanique des Fluides, Procédés, Energétique**

Arrêté ministériel : 7 août 2006

Présentée par

Jochen ALTENBEREND

Thèse dirigée par **Yves DELANNOY** et
codirigée par **Guy CHICHIGNOUD**

préparée au sein du **Laboratoire SIMAP**
dans **l'École Doctorale** : **Ingénierie – Matériaux Mécanique Environnement Energétique Procédés Production (I-MEP^2)**

Kinetics of the plasma refining process of silicon for solar cells: experimental study with spectroscopy

Thèse soutenue publiquement le **11 décembre 2012**
devant le jury composé de :

M. Jochen SCHEIN Professeur, UniBW Munich, Allemagne	Rapporteur
Mme. Gabriella TRANELL Professeur associé, NTNU Trondheim, Norvège	Rapporteur
M. Yves DELANNOY Professeur, Grenoble INP	Membre
M. Guy CHICHIGNOUD Chercheur, SIMaP/CNRS, Grenoble	Membre
M. Malek BENMANSOUR Ingénieur Chercheur, CEA-INES, Chambery	President
M. Michel VARDELLE Professeur, ENSIL, Limoges	Membre
Mme. Caroline ROSSET Ingénieur, FerroPem, Chambery	Invité

Acknowledgments

I am very grateful to my two directors for giving me the possibility to work on this exciting subject. Prof. Yves Delannoy was always open for scientific discussion and taught me a lot about fluid dynamics. Dr. Guy Chichignoud helped me and supervised the experiments.

I want to thank all the other members who worked in our Group on the plasma process. Bachir Saadi worked on the development of the new plasma setup Susi that was used for the spectroscopic measurements. Jonas Meyer studied the coupling of the torch. Mickael Majchrzak developed the computational fluid dynamic model. Simon Nosari run the computational fluid dynamic model so that I could compare the results to the measurements.

Special thanks go to Christian Trassy for all the helpful discussions on plasma physics and plasma spectroscopy. With his great knowledge he introduced me into the subject of my project.

I want thank the technical team at SIMAP/EPM for their great support. They solved all technical problems rapidly and thus made the experiments possible. Gabriel Fournier, Christian Garnier, Patrick Petitpas, Ghatfan Hasan, and Denis Bon helped a lot.

I want to thank our partners from the CEA and Ferropem for their helpful collaboration. Ferropem financed some purification experiments.

I would like to express my gratitude to all the EPM-Team who provided a very supportive and friendly atmosphere during this work.

Content

I. Introduction

The present study has the objective to better understand the plasma refining process for the purification of silicon. Before presenting the process itself the "standard" technologies used for the production of solar cells are presented. We present all steps from the reduction of the quartz to the assembling of the modules. Although there are many different technologies, most solar cells are produced with the technologies that are presented here. The "standard" technology for the purification of silicon is the Siemens process. We present several technologies that may replace the Siemens process at lower costs. The plasma refining process can remove boron that can hardly be removed by other processes. At the end of this chapter we introduce to the need for a fundamental understanding of the plasma refining process.

I.1. From silica to solar cells (the "standard" technology)

I.1.1. Production of metallurgical silicon

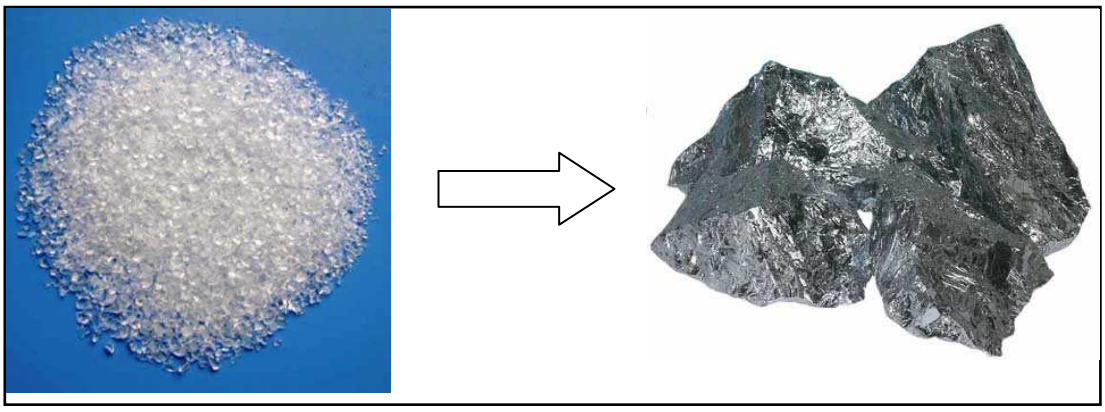

Figure I-1 Silica stones and silicon

The raw materials for the production of silicon are quartz and different reductants (coal, coke, wood). Quartz is a chemical compound consisting of the two most abundant elements on earth, Oxygen and Silicon. Most sands contain a high quantity of quartz but for silicon production pure silica stones are used. The silica stones are reduced by coal in an electric arc furnace (Figure I-2). The energy furnished by the furnace is used to melt the quartz so that it can react with the reducing agents.

For the production of 1 ton of silicon one needs [Dub90]:

- 2.5 tons quartz
- 0.8 tons charcoal
- 0.2 tons coke
- 1.2 tons wood
- 0.1 tons graphite electrodes
- 11000 kWh electricity

The global reaction that takes place in the reduction furnace is $SiO_2 + 2C \rightarrow Si + 2CO$. This global reaction is the sum of different elementary reactions that take place at different zones of the reduction furnace. A detailed description can be found in [STT98]

The silicon flows into a ladle with air bubbling (oxidizing refining). The oxygen of the air reacts with the elements that are more reactive than silicon such as aluminum and calcium. The oxides form a layer on the silicon and can thus be removed. The silicon produced by the

furnace has a high concentration of impurities which come from the quartz and the reductants. Baluais [BCD09] measured the concentration of several impurities in the silicon from an electric arc furnace (Table I-1). The impurity contents vary with the raw materials and a compromise has to be found considering their purity, cost and availability. Especially the boron and phosphors content of the raw material is very important because the removal of these elements from the silicon is expensive. By choosing well the quartz and the reductants the concentration of boron can be reduced down to 7 ppm and the concentration of phosphorus can be reduced down to 10 ppm. [Deg08]. The impurities must be removed in order to obtain solar grade silicon. This is typically done with the Siemens process

Fe	Ca	Al	Ti	B	P	C
2400 ppm	98 ppm	245 ppm	240 ppm	32 ppm	19 ppm	100 ppm

Table I-1 Impurity concentration of metallurgical silicon [BCD09]

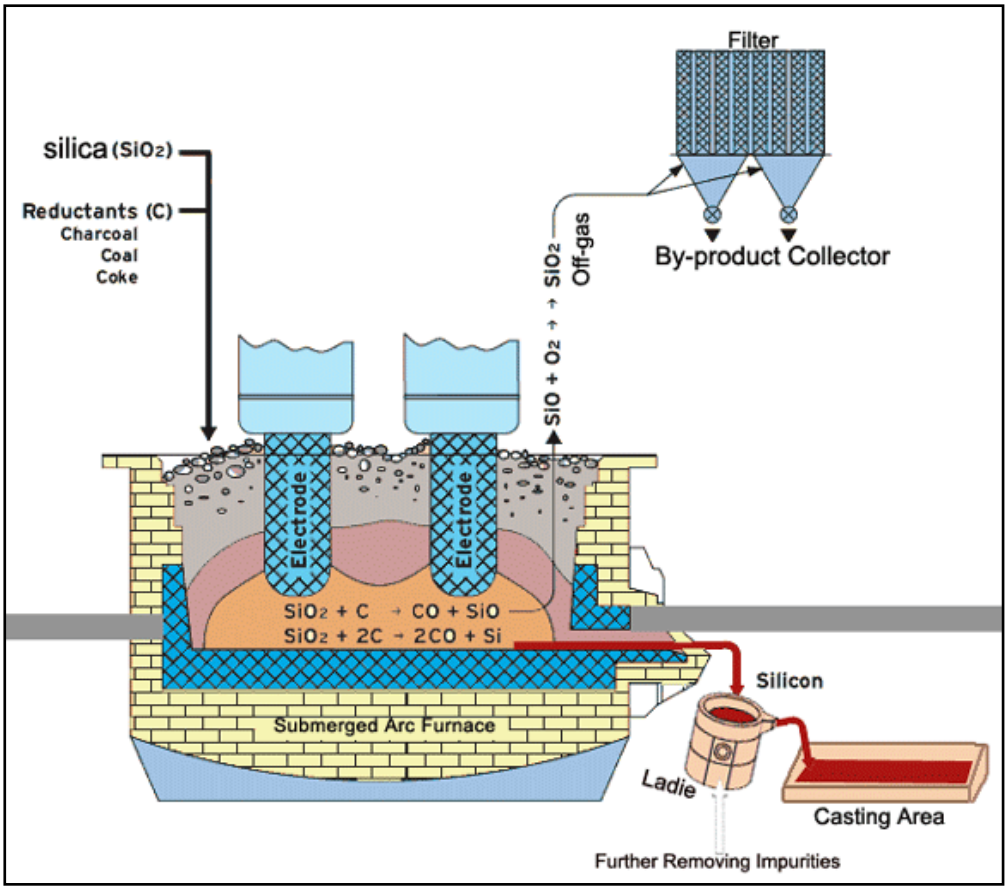

Figure I-2 Electric arc furnace for silicon reduction

I.1.2. The Siemens process

In the Siemens process the metallurgical silicon reacts with hydrogen chloride producing the gas trichlorosilane.

$$Si + 3HCl \rightarrow SiHCl_3 + H_2$$

This gas, having already a higher purity than the metallurgical silicon, is then distilled. The distillation separates the trichlorosilane from the impurities. The high purity trichlorosilane is then reduced in a CVD reactor (chemical vapor deposition) to silicon.

$$SiHCl_3 + H_2 \rightarrow Si + 3HCl$$

For the purification of 1 kg of silicon the energy consumption of the Siemens process is [AW07] 110 kWh of electricity and 51 kWh of heat. This is 30 % of the total primary energy input for the production of a solar cell and therefore new processes are being developed to replace this process. The production costs for solar silicon from the Siemens process is about 50 €/kg [SSC10]. The silicon from the Siemens process has only ~0.02 ppm of impurities. A dopant can be added to the silicon to increase the conductivity (doping). Boron may be used to obtain p-type silicon and phosphorus for n-type silicon.

I.1.3. Crystallization

The silicon is crystallized either into a single crystal or to a multicrystalline ingot. The Czochralski method is used for the growth of a silicon crystal. For this a small seed crystal is dipped in a silicon melt at the melting point. The rotating crystal is then pulled up and grows. The pulling speed needs to be controlled precisely in order to maintain the diameter of the crystal constant. Multicrystalline ingots are crystallized in furnaces in silica crucibles. The heat is extracted at the bottom of the crucible and the silicon melt crystallizes from the bottom to the top. For the crystallization of multicrystalline silicon the growth speed is typically 0.5-1.5 cm/h [MGS06]. The mass of the ingots is about 400 kg [ITR11].

Recently Lan et al. [LLY12] showed that the efficiency of multicrystalline solar cells can be significantly improved by reducing the growth of dislocations during solidification. Even though recombinations at the grain boundary reduce the efficiency of the solar cell it is better to have small columnar grains and thus a lower dislocation density.

Currently research is going on to use the furnaces for multicrystalline silicon for crystallization of monocrystalline silicon with seed crystals. This technology may combine the higher efficiency of monocrystalline silicon and the higher throughput of directional solidification furnaces. However there are still some issues that need to be resolved. For example the high dislocation density and the multicrystalline parts [PFC12].

I.1.4. Cutting

The crystallized silicon ingot is then cut into bricks at the size of the wafer (156x156 mm^2) and then by a wire saw into wafers with a thickness of about 180 µm [ITR11]. As the wire of the saw has a diameter of about 130 µm [Mey12] the wafer slicing process has a loss of about 50% of the silicon. Today the wire sawing process uses typically a smooth steel wire with a slurry of SiC abrasive.

The lost silicon becomes unusable because it is mixed with the abrasive and small particles of the wire. The project ReSicle in the laboratory SIMaP/EPM tried to develop a process for the recycling of this waste. The project was not continued due to high economic costs particularly due to the technical difficulties to separate the abrasive SiC from Si which have similar properties. Tai et al. [TL10] patented a method of separation of Si and SiC using the different surface properites of the oxidized silicon surface and the SiC surface. While the oxidized silicon surface is hydrophilic the SiC surface is hydrophobic. Wang et al. [WLT08] found that Si and SiC can be separated due to their different melting temperature. At high temperature the liquid Si forms clusters. After cooling the Si clusters can be separated from the SiC by water cleaning.

A new emerging technology is the diamond plated wire saw technology which has the advantage of a higher productivity and an easier recycling of the cooling liquid [BWK09]. While in the process with slurry the small silicon debris have to removed from the slurry with SiC, all particles can be removed from the cooling liquid in the diamond saw process. An inconvenience of the diamond plated wire is the high price of the wire.

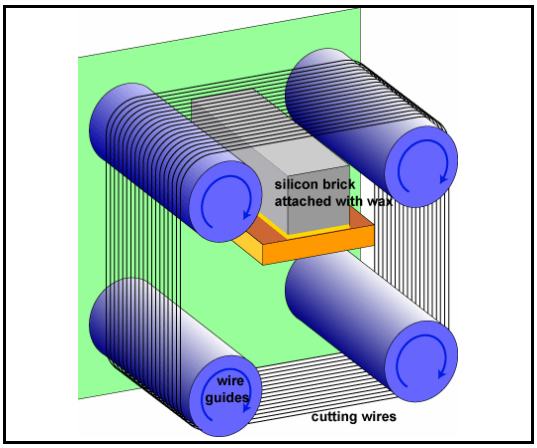

Figure I-3 Sawing the bricks to wafers

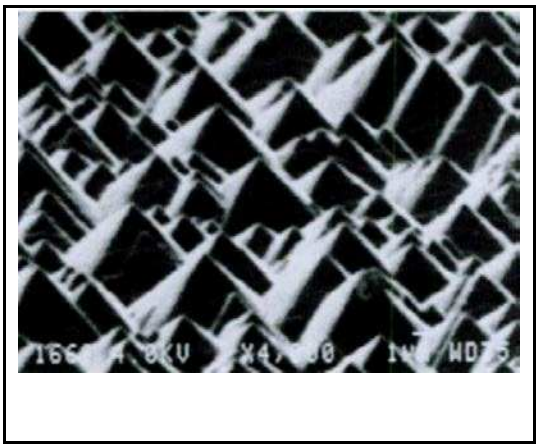

Figure I-4 Texturized silicon surface

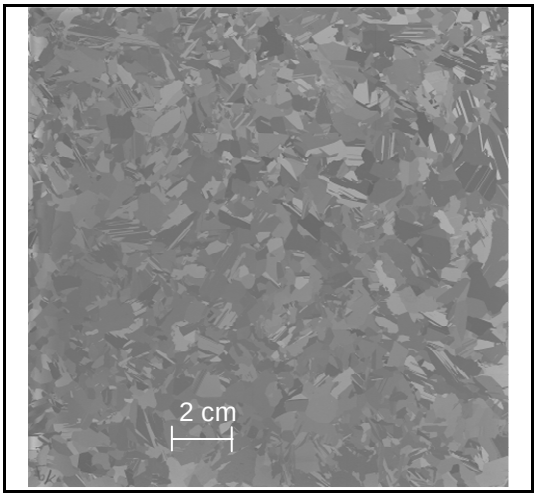

Figure I-5 A multicrystalline Si wafer

Figure I-6 The solar cell

I.1.5. Texturization

Monocrystalline wafers are edged with a solution of NaOH or KOH mixed with isopropyl alcohol [Car08]. This creates pyramidal structures (Figure I-4) that give the surface a low reflectivity and enhance thus the light trapping. The reflectivity of a polished silicon surface is 34% and the reflectivity after texturization is only 11%. The described edging process is not efficient for multicrystalline wafers due the random grain orientations. Several texturization processes for multicrystalline silicon are under development but have not reached mass production. Monocrystalline solar cells have thus a better light trapping which is one of the reasons for their higher efficiency.

I.1.6. Doping

For the charge separation a p-n junction is necessary. Typically the bulk of the silicon is doped with boron (p-type) and one surface of the wafers is doped with phosphorous (n-type). A phosphorous containing coating is applied to one surface and then the wafer is sent into an oven where the phosphorous diffuses into the silicon. After the diffusion the coating is removed.

For mono-crystalline silicon a transition to the use of n-type silicon is forecast [ITR11]. Boron is used instead of phosphorus to dope the front-side of an n-type wafer. N-type solar cells do not suffer from light induced efficiency degradation [LF10] as it often happens in p-type solar cells.

I.1.7. Antireflection coating

On the front side a silicon nitride film is deposited by chemical vapor deposition giving the solar cell its characteristic blue color. The antireflection coating reduces the reflections and improves so the absorption of the light.

I.1.8. Contacts

The electrical contacts are printed onto the wafer. On the rear side the whole surface is covered with aluminum while on the front side thin contacts are printed with silver paste.

Copper may replace the silver contacts because it is cheaper [JPV12]. For the use of copper a chemical barrier is necessary to avoid the diffusion of copper into the silicon. The reliability of these chemical barriers is one of the issues that need to be controlled for the use of this technology.

After the printing of the metal contacts, the solar cell is heated up in a furnace. First the solvents are evaporated at low temperatures. Then the silver and aluminium paste are sintered and create a contact with the silicon.

The solar cell is now finished and can be assembled in modules.

I.2. Overview of alternative purification technologies

The Siemens process for the purification procedure requires a lot of energy and is expensive. It was developed to supply high purity silicon for the semiconductor industry. The solar industry needs a lower purity but a larger quantity and therefore cheaper silicon is desired. Alternative purification processes have the potential to reduce the cost of solar silicon. We present here some technologies that can purify silicon and that can be adapted for industry. All technologies are based on these three physical phenomena:

- Segregation
- Evacuation of impurities or reaction products due to higher solubility
- Evacuation of volatile impurities or reaction products

I.2.1. Segregation

When a silicon crystal is growing it costs less energy to add a silicon atom to the crystal lattice than to add an impurity atom. This microscopic effect leads to a lower macroscopic concentration of the impurity in the solid than in the liquid due to a higher solubility of the impurity in the liquid. At equilibrium the ratio between the concentrations of an impurity in solid and liquid is given by the thermodynamic segregation coefficient. Table I-2 shows the thermodynamic segregation coefficient for different elements. When the solidification is slow enough, so that the transport in the liquid silicon homogenizes the impurity concentration in the liquid efficiently, the effective segregation coefficient is close to the thermodynamic segregation coefficient. The solidification can thus be used to purify the silicon

Segregation works well for elements with small segregation coefficients, while it is not very efficient for the elements phosphorous and boron with segregation coefficients close to one. There are three silicon refining techniques that use the principle of segregation

Impurities	Al	B	C	Ca	Cu	Fe	P	Ti
Equilibrium segregation coefficient	2.10^{-3}	0.8	0.07	0.05	4.10^{-4}	8.10^{-6}	0.35	10^{-6}

Table I-2 Equilibrium segregation coefficients for different impurities in silicon

Directional solidification

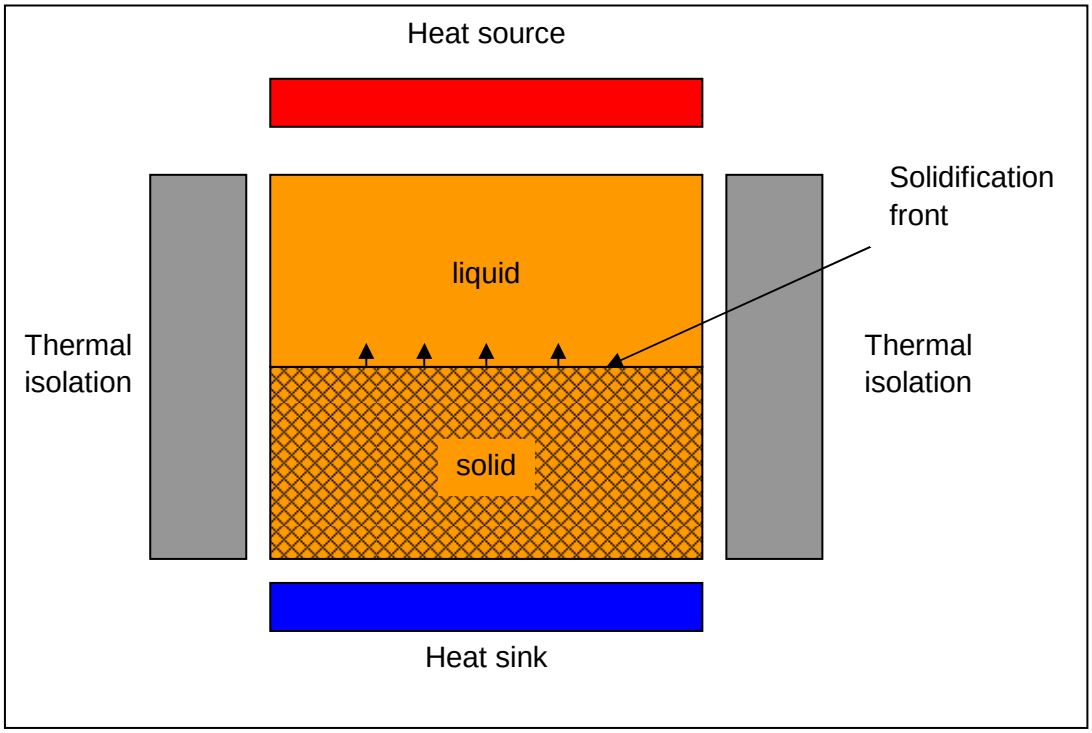

Figure I-7 Scheme for a furnace for directional solidification

During directional solidification the silicon is cooled on one side and solidifies into one direction as shown in Figure I-7. The solidification speed is limited by the transport of the impurities at the solid-liquid interface towards the liquid bulk. When diffusion is the only transport mechanism the solidification should be slow in order to avoid a higher impurity concentration above the solid-liquid interface. Air bubbling [And04], electromagnetic stirring [LDZ12] and mechanical stirring can be used to homogenize the impurity concentration in the liquid silicon by convection. So a higher solidification speed can be used because the concentration at the solid-liquid interface remains low. The choice of the crucible is very important as crucibles that do not pollute the silicon (typically made of silica) are very expensive and can not be reused.

If several successive solidifications are necessary the first solidifications may be done in a crucible that pollutes the silicon only with elements that are efficiently removed in the last solidification or during the crystallization. It is important to avoid pollution with elements that segregate little, especially phosphorus.

After the solidification most of the impurities are concentrated in the last solidified ingot end. This end is cut off in order to obtain an ingot with a mean concentration that is much lower than the initial concentration. Otherwise the silicon melt may be partially solidified so that the impurities are concentrated in the last liquid that is poured out.

In ideal conditions the concentration profile after complete solidification can be calculated with the Scheil equation (I-1) [KF86], where k is the equilibrium segregation coefficient, C_0 is the concentration before segregation, x is the position in the ingot and L is the length of

the ingot. Figure I-8 shows the result of the Scheil equation for phosphorus and boron with different initial concentrations.

$$C(x) = kC_0\left(1-\frac{x}{L}\right)^{k-1} \qquad \textbf{(I-1)}$$

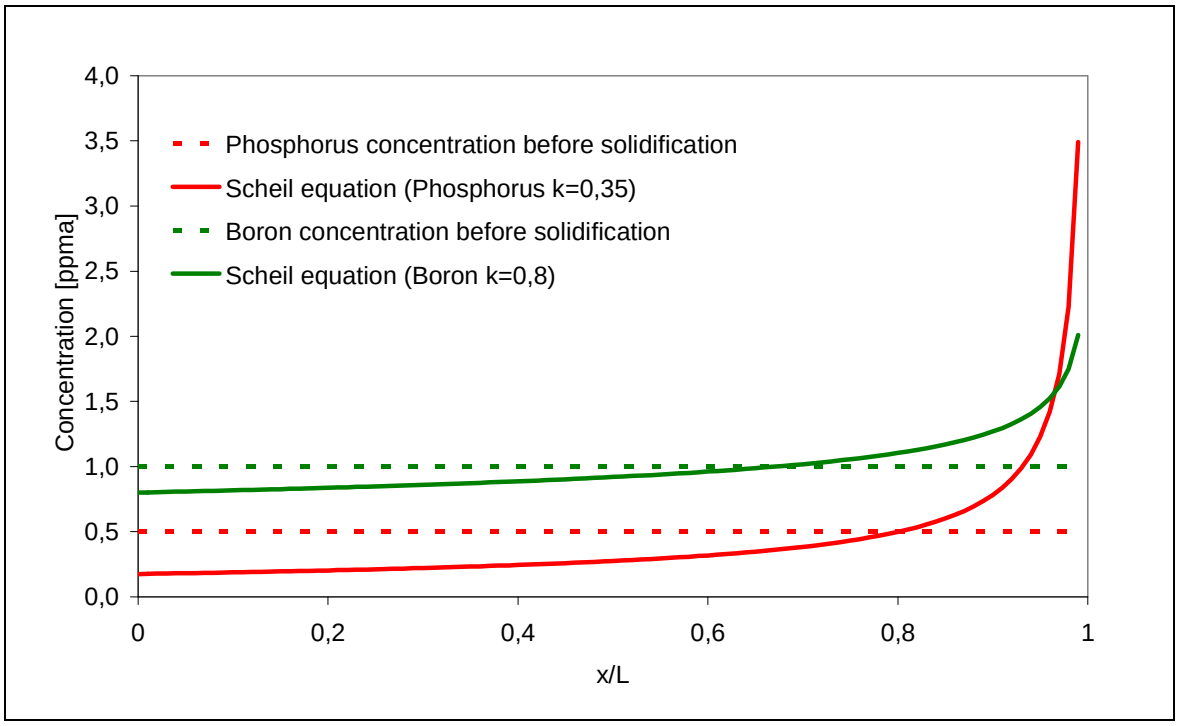

Figure I-8 Concentration profile of phosphorus and boron before and after directional solidification

Acid leaching

When the silicon is solidified fast, small grains are growing and the impurities segregate to the liquid part. In the liquid part the concentration of the metallic impurities increase above the solulibility so that they precipitate in separate phases. These separate phases dissolve well in acids and can be removed this way after cooling. As fractures occur mainly at grain boundaries, grinding can be used to make the separate phases accessible to the acid. Voos [Voo61] patented a process for treating pulverized silicon with aqua regia, H_2SO_4, HF etc. with yield silicon suitable for the application in microwave diodes. Santos [SGS90] reported that using hydrochloric acid (16%, 5 h, 80℃) and s ilico n with a relatively coarse fraction (116 µm) it is possible to remove 85% of the impurities. In the acid leaching process the addition of calcium can help to remove phosphorus which would otherwise segregate only little. Shimpo [SYM04] reports that the phosphorous content in the silicon was decreased by 80.4% when adding 5.17 at % calcium.

Solvent refining

The solvent refining method was developed to remove also the elements boron and phosphorus that have thermodynamic segregation coefficient close to one. A solvent is added to the liquid silicon. The solvent is miscible with liquid silicon but not with solid silicon. The solvent is chosen so that the segregation coefficient of boron and phosphorus is reduced. This can be obtained by an eutectic that reduces the melting temperature. Yoshikawa [YM09] showed that the thermodynamic segregation coefficients of phosphorus

and boron are reduced to respectively 0.08 and 0.2 in an Si-Al eutectic at 1273 K. Yoshikawa [YAM05] reports that the boron content in the silicon was decreased by about 99% when adding 60% aluminum and about 600 ppma titanium due to the formation of TiB_2. Normal segregation in equilibrium would result in a decrease of less than 20%.

After the solidification of silicon flakes, the remaining liquid aluminum melt can be poured out. The remaining aluminum can be removed by acid leaching and directional solidification. The company Silicor Materials applies this method. The economic efficiency of the company depends also on the sale of the byproducts.

I.2.2. Evacuation of reaction products due to higher solubility

Slag Refining

Silica sand (SiO_2) and lime/limestone ($CaO/CaCO_3$) are added to the liquid silicon. These additives oxidize impurities and form a slag. The oxidized impurities have a higher solubility in the slag than in the silicon so that they can be removed together with the slag. The alkaline earth metals Ca, Al and Mg can be efficiently removed by slag refining due to their high reactivity [TST09]. The process is less efficient for boron and phosphorus. Johnston [JB10] measured a 9 times higher phosphorus concentration in an Al_2O_3-CaO-MgO-SiO_2 slag in equilibrium with silicon. Teixeira et al. [TTY09] measured a five times higher boron concentration in a SiO_2-CaO slag in equilibrium with silicon. Johnston et al. [JB10] calculated the quantity of slag that is needed to reduce the Boron concentration from 15 ppm to 1.5 ppm and the Phosphorus concentration from 30 ppm to 1 ppm. For a 9%Al_2O_3-24%CaO-33%MgO-34%SiO_2 slag the phosphorus concentration is 8.8 higher in the slag than in the silicon and the boron concentration is 1.8 times higher. They find thus a slag mass that is 5.5 times that of silicon.

I.2.3. Evacuation of volatile impurities and reaction products

Vacuum refining

Dissolved phosphorous has a volatility about 10000 times higher than that of silicon at 1823 K [MMS96]. Thus, during evaporation the phosphorous content in the melt decreases. The evaporation is very slow and it costs a lot of energy to keep the silicon at a high temperature. In order to increase the evaporation rate the pressure is reduced and some techniques use high power electron beams [YAH01].

Moist gas blowing

Theuerer [The56] blew yet in the 50's hydrogen with water vapor onto liquid silicon and reduced thus the boron content. The water in the gas reacts with boron and forms volatile products which are then evacuated by the gas flow. Khattak et al [KJS02] injected moist gas in molten silicon. The boron content of a charge of 50 kg silicon was reduced by a factor of two in two hours. Nordstrand et al. [NT12] showed that it is possible to purify a 200g silicon melt by blowing 3 l/min of hydrogen with water vapor onto the surface of a silicon melt.

Thermal plasma treatment

This method is similar to moist gas blowing. A thermal plasma with argon, hydrogen and oxygen (or water vapor) is applied to the molten silicon. The hydrogen and oxygen react with the boron and form volatile products that are evacuated by the gas flow.

The method was first applied by Morvan et al [MAC83]. They used a small 12 kW inductively coupled plasma torch for the zone melting of the silicon. The gas flow contained

Ar with 1% of hydrogen and up to 0.2% of oxygen. Since then the process has been continuously improved. One improvement is the use of electromagnetic stirring of the silicon melt so that the boron is better transported to the surface of the melt [ATP02]. Another improvement is the use of high power plasma torches up to 1.2 MW [NBS04] with high gas flows. Fast purification of large quantities of silicon has thus been made possible.

It could be shown that purification is possible on an industrial scale but the chemical reactions of the processes are still poorly understood. Studies of Khattak [KJS02] and Degoulange [Deg08] showed that at thermodynamic equilibrium purification with hydrogen and oxygen should not be possible because thermodynamic equilibrium calculations give a B/Si ratio in the gas phase that is similar to the B/Si ratio in the silicon melt.

In this study we want to find a better understanding of this process with the objective to improve the process.

I.3. Target Purity

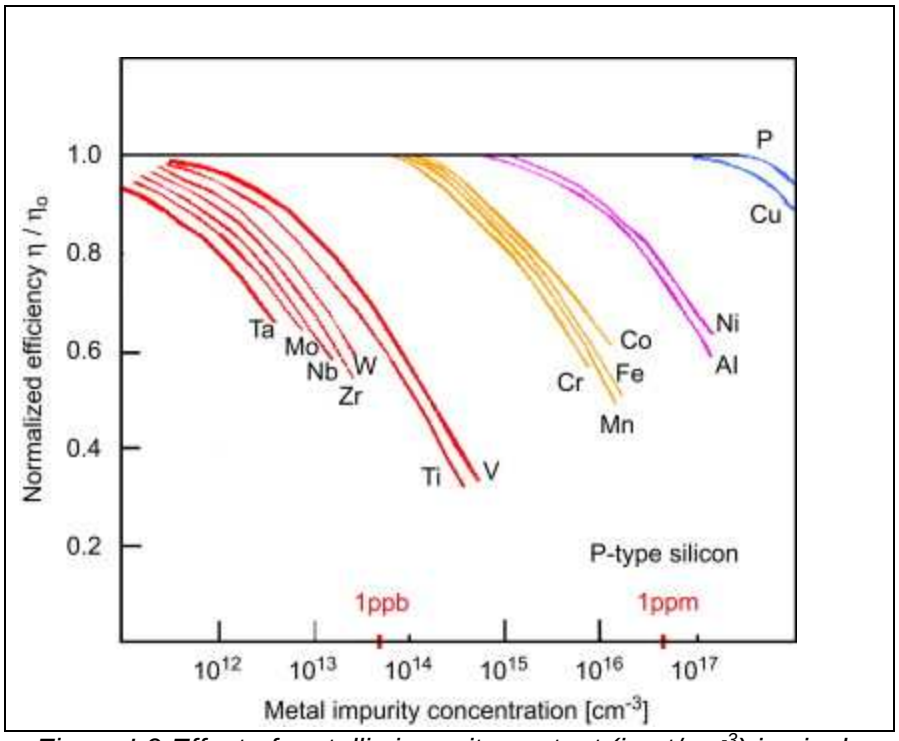

Figure I-9 Effect of metallic impurity content (in at/cm^{-3}) in single crystal silicon on the normalized efficiency of solar cells [Piz10],[DRH80]

Impurities can reduce the efficiency of a solar cell. Below a maximum concentration the effect of the impurity is negligible but above this concentration it degrades the efficiency of the solar cells with increasing concentration. Studies on doped single crystal showed that the maximum acceptable concentration is very different for different elements (Figure I-9). The effect of fast diffusing elements can be reduced by gettering during the cell fabrication process so that higher concentration than in indicated by Figure I-9 can be acceptable. During the gettering the elements diffuse to locations where they are electrically inactive and have therefore no influence on the cell efficiency.

The cost of the silicon purification by the metallurgical route increases strongly with the desired purity level. Therefore it is possible to obtain a lower price for the electricity ($/W$_p$ Dollar per Watt peak) with a solar cell that has a sligthly lower efficiency and at the same time a lower price due to less pure silicon. In order to optimize the purity level with the lowest

price for the electricity one has to analyze the cost of the complete module. Powell et al [PWC12] estimated a cost of 0.23\$/W_p for the silicon feedstock and 1.29\$/W_p for the total module. Using a lower quality feedstock with half the price and giving a 9% (relative) lower efficiency of the solar cell one obtains thus the same \$/W_p for the solar cell. This gives an idea about the reduction of efficiency that can be accepted to reduce the cost of the silicon feedstock.

For the metallurgical silicon the concentration of boron and phosphorus is very important because they are hard to remove. Delannoy [Del11] reports a maximum accepted concentration of 0.5 ppmw of boron and 1.5 ppmw of phosphorus. Elkem [Elk12] announced concentrations of less than 0.2 ppmw for boron and 0.62 ppmw for phosphorus. In the two specifications the atomic concentrations are similar. When the donor concentration is similar to the acceptor concentration they compensate each other and increase the resistivity of the silicon. Such a silicon is called compensated silicon. Xiao et al. [XYX12] found that the efficiency of a solar cell with compensated silicon with less than 5 ppmw of boron is similar to the efficiency of conventional doped silicon. However the formation of boron-oxygen complexes can significantly reduce the efficiency at high boron concentrations. This effect occurs during the exposure of the solar cell to light and is therefore called light induced degradation. [GKR11]

During the crystalization the phosphorus segregates much more than boron so that one obtains a higher P/B ratio at the upper part of the silicon ingot than at the lower part. With 0.4 ppm of boron and 1.0 ppm of phosphorus as initial concentration 88% of the ingot is p-type after solidification and can be used for the solar cell production. Also the resistivity of the lingot changes with the phosphorus concentration. With the co-doping of gallium one can increase the resistivity and the yield of p-type silicon [KWH10]

I.4. Economic aspects of alternative purification technology

The research on the purification processes of silicon for solar cells has the objective to reduce the cost of solar energy. As this study aims to understand and improve such a process it is important to know the economic aspects that define the cost of the process.

I.4.1. Scale up of a plasma treatment facility

An important step towards an economic process is the scale-up. The scale-up helps to increase cost effectiveness as operational costs and capital investment do not increase linearly with scale.

A lot of experiments have been done on boron removal of silicon (see Table I-3). Nakamura showed that it is possible to scale-up the process. He increased at the same time the mass of the silicon charge, the plasma power and the gas flow and obtained so a high productivity. During the process the concentration of boron decreases exponentially. A good parameter for the productivity of a purification installation is the half-life time divided by the mass of the silicon charge $T_{0,5}$/m. The smaller this factor is the higher is the throughput rate of the installation. That means more silicon is purified per unit time.

	m [kg]	$T_{0,5}$ [min]	$T_{0,5}$/m [min/kg]	Plasma Power [kW]	Ar [m3/h]	H_2 [m3/h]	H_2O [m3/h]	O_2 [m3/h]	H_2O Fraction	H_2+H_2O Fraction
[FKM06]	0.003	30	**10000**		0.06	0	?	0	?	?
[SKS92]	0.006	4	**730**	10	0.4	0	0.005	0	1.2%	1.2%
[NT12]	0.2	17	**85**	0	0	0.18	0.0059	0	3.2%	100%
[IM96]	0.04	3	**75**	30	0.9	0	0.012	0.023	1.3%	1.3%
[KJS02]	2	120	**60**	0	?	0	?	0	?	?
This study	2.9	89	**31**	38	7.3	0.3	0	0.06	1.6%	3.9%
[NBS04]	2.4	69	**29**	30	0.9	0	0.09	0	9.5%	9.5%
[FNP04]	3	67	**22**	30	4.5	0.15	0	0.038	1.6%	3.2%
[NBS04]	7	40	**5.7**	100	13	0	1.2	0	8.5%	8.5%
[NBS04]	300	80	**0.27**	650	130	122	12	0	4.6%	50%

Table I-3 Purification rate and experimental parameters

I.4.2. Throughput rate

The throughput rate depends on the one hand on the productivity of the installation which is given by $T_{0,5}$/m and on the other hand on the target boron concentration $[B]_{target}$ and the raw material boron concentration $[B]_{start}$. With equation (I-4), which has been derived from the exponential decrease (Equation (I-2)), we can calculate the throughput rate using the three parameter $T_{0,5}$/m, $[B]_{start}$ and $[B]_{target}$.

$$[B]_{target} = [B]_{start} \times \exp\left(\frac{-T \cdot \ln(2)}{T_{0.5}}\right) \quad \textbf{(I-2)}$$

$$T = \frac{\ln([B]_{start}) - \ln([B]_{target})}{\ln(2)} T_{0.5} \quad \textbf{(I-3)}$$

$$\frac{m}{T} = \frac{\ln(2)}{\ln([B]_{start}) - \ln([B]_{target})} \left(\frac{T_{0.5}}{m}\right)^{-1} \quad \textbf{(I-4)}$$

Using $[B]_{target}$=0.4 ppm and $[B]_{start}$=8 ppm we can calculate the throughput rate of the 300 kg installation of Nakamura [NBS04] with $T_{0,5}$/m=0.27 min/kg

$$\frac{m}{T} = 0.86 kg/min = 1.2 t/24 h \quad \textbf{(I-5)}$$

The installation of Nakamura can produce roughly 1.2 tons of silicon per day with a boron content of $[B]_{target}$=0.4 ppm when using silicon with a boron concentration of $[B]_{start}$=8 ppm as raw material.

I.4.3. Operational cost

The operational costs of a purification process depend a lot on the concentration of the input material and on the desired purity degree. In our estimation for the operational cost we use the target concentration of 0.4 ppm for boron and 1.0 ppm for phosphorus as announced by Elkem [Elk09]. For the concentration of the raw material we use 8 ppm for boron and 16 ppm for phosphorus which is slightly above the concentrations that can be achieved for the raw silicon.

We do not regard the concentration of other impurities because they segregate much better than phosphorus so that their concentration should not be a problem. In industrial application the pollution of the silicon by other impurities during processing may be a problem.

Boron removal by plasma treatment

Large scale installations have smaller labor costs per purified ton of silicon than small scale installations. But the energy and gas consumption per ton of purified silicon are similar because they increase linearly with the scale as we can see in Table I-3. The energy consumption of the plasma torch in the 300 kg installation of Nakamura is 650 kW [NBS04] and we assume that the energy consumption of the crucible is negligible. By multiplying the energy consumption with a typical electricity cost of 0.10 €/kWh we can calculate the energy cost of the installation to 65 €/h. We divide the energy cost by the throughput rate and obtain an energy cost of 0.90 € per kg of purified silicon. Table I-4 shows the main operational costs of the purification installation. It costs about 4.60 € to reduce the boron content by a factor 20 which correspond to the reduction from 8 ppm to 0.4 ppm. These costs do not include the labor costs and the cost of capital investment which are probably also important.

	Consumption	Price per Unit	Costs per h	Costs per kg
Electricity	650 kW	0.10 €/kWh	65 €/h	1.30 €/kg
Argon	130 m^3/h	1 €/m^3	130 €/h	2.50 €/kg
Hydrogen	122 m^3/h	1 €/m^3	122 €/h	2.40 €/kg
Total			317 €/h	6.10 €/kg

Table I-4 Cost for gas and electricity for the 300 kg installation of Nakamura [NBS04] (the costs per kg were calculated for the reduction of the boron concentration from 8 ppm to 0.4 ppm)

Phosphorus purification by directional solidification

The major costs of the directional solidification are the costs of energy. The minimum energy consumption to heat the silicon up to 1410 °C is 0.27 kWh/kg (Heat capacity 19.8 J/mol/K) and 0.50 kWh/kg are needed for the fusion enthalpy (50.2 kJ/mol). Typically an industrial furnace consumes 1.8 kWh/kg [Apo12] for the fusion of silicon. When the segregation is ideal one can solidify two third of the silicon melt to obtain a mean phosphorus concentration that is half of the initial concentration (equation (I-6)) and the liquid rest has thus twice the initial concentration (equation (I-7))

$$\frac{3}{1L}\int_{2L/3}^{L} C(x)dx = \frac{3}{1L}\int_{2L/3}^{L} 0.35 \times C_0\left(1-\frac{x}{L}\right)^{0.35-1} dx = \frac{3}{2L}\left[C_0\left(1-\frac{x}{L}\right)^{0.35}\right]_{2L/3}^{L} = 2.04 \times C_0 \qquad \textbf{(I-6)}$$

$$\frac{3}{2L}\int_{0}^{2L/3} C(x)dx = \frac{3}{2L}\int_{0}^{2L/3} 0.35 \times C_0\left(1-\frac{x}{L}\right)^{0.35-1} dx = \frac{3}{2L}\left[C_0\left(1-\frac{x}{L}\right)^{0.35}\right]_{0}^{2L/3} = 0.48 \times C_0 \qquad \textbf{(I-7)}$$

In order to reduce the phosphorus content by a factor 16 one would need four successive directional solidifications. A factor 16 corresponds to a reduction from 16.0 ppm to 1.0 ppm. The last solidified third of the solidification can be recycled in the precedent solidification as shown in Figure I-10. In order to calculate the masses, we first calculate the mass of the 4. and the 3. solidification. We multiply the target 1 kg by 1.5 and 1.5^2 because only two third of the silicon continues to the next step. For the 2. solidification we have to subtract the recycled part of the 4. solidification (0.5 kg) from the mass of the 3. solidification (2.25 kg) and multiply than by 1.5 and obtain thus 2.63 kg. The calculation of the mass of the 1. solidification is similar. We present all masses in Table I-5.

We can so sum over the masses of all solidification steps and find that we need to melt 9.2 kg of silicon to obtain 1 kg of silicon with a phosphorus concentration that is 16 times lower than that of the raw material. We multiply the 9.2 kg/kg with the energy cost of the fusion 1.8 kWh/kg and obtain a total energy cost of 16.6 kWh/kg (1.66 €/kg) for the process with four segregations.

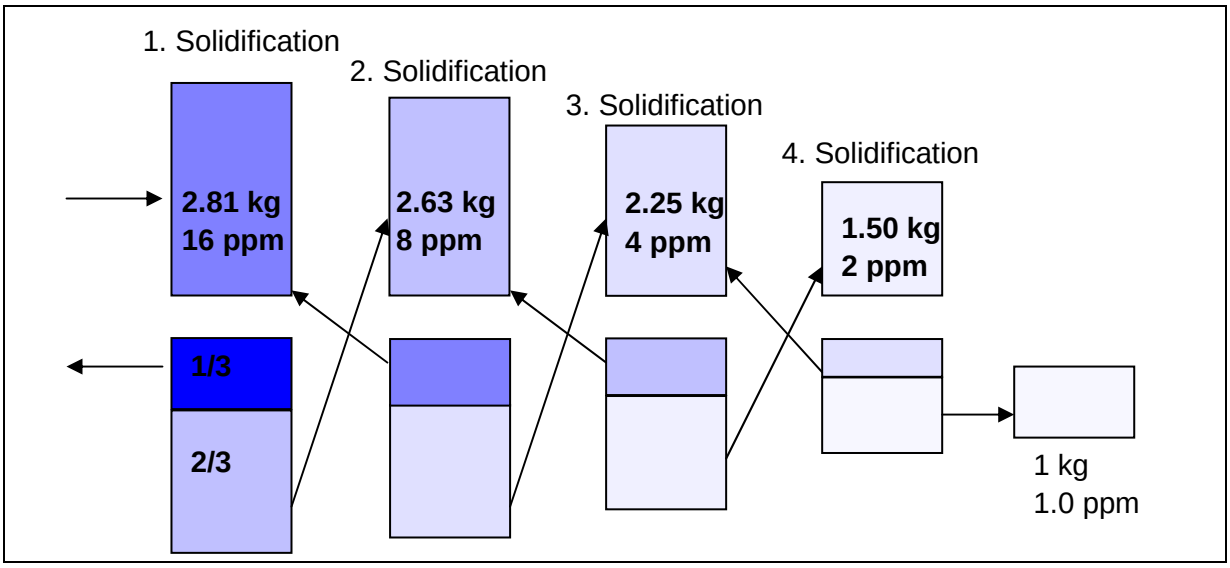

Figure I-10 Schematic for a for purification process with four purifications (2/3 of the charge is solidified and has half of the initial phosphorus concentration, the liquid 1/3 has twice the initial concentration and is recycled in the solidifcation before)

No	Input ppm	Output ppm	Input [kg]	Output [kg]	
				Solid	Liquid
4	2.0	1.0	1.50	1.00	0.50
3	4.0	2.0	2.25	1.50	0.75
2	8.0	4.0	2.63	1.75	0.88
1	16.0	8.0	2.81	1.88	0.94
Sum :			9.2 kg		

Table I-5 Mass of each solidification for a continuous flow with four solidifications

We repeat the calculation for different numbers of solidification and present the results in Table I-6. The total mass of silicon melted and thus the energy consumption increase only slowly when increasing the number of solidification. Each supplementary solidification decreases the final phosphorus concentration by a factor two.

Such a process is very sensible to the effective segregation coefficient that can be obtained. Liquid inclusions between grains and insufficient stirring can lead to a higher phosphorus concentration in the solid silicon. The higher concentration can be approximately described with a Scheil law with a higher effective segregation coefficient. In Table I-7 we show the calculated energy and raw silicon consumption for different effective segregation coefficients and different number of solidification. The segregated ratio was calculated so that the final phosphorus concentration is 16 times lower than that of the raw silicon. The remaining silicon is recycled in the solidification before (similar to Figure I-10). In the calculation we took into account the mixing of pure and less pure silicon. For an effective segregation coefficient of 0.45 the energy and raw silicon consumption is much lower when using five instead of four solidifications. However for an effective segregation coefficient of 0.45 the consumption (energy and silicon) is still significantly higher than for an effective segregation coefficient of 0.35.

Number of Solidifications	6	5	4	3	2	1
Input concentration / Output concentration	64	32	16	8	4	2
Total mass of Si melted [kg]	15.0	12.1	9.2	6.4	3.8	1.5
Energy Consumption [kWh]	27.0	21.8	16.6	11.5	6.8	2.7

Table I-6 Energy consumption to obtain 1 kg of pure silicon and removal ratio in dependency of the number of solidifications

Number of Solidifications	4	4	4	5	5	5
Effective segregation coefficient	0,35	0,4	0,45	0,35	0,4	0,45
Segregated ratio	70%	60%	46%	78%	71%	64%
Total mass of Si melted [kg]	8,2	12	26	8,2	10	14
Energy consumption [kWh]	15	22	47	15	18,5	24
Raw silicon consumption [kg]	1.7	2.6	7.1	1.4	1.7	2.2

Table I-7 Consumptions to obtain 1 kg of silicon with 16 times lower phosphorus concentration in dependency of the effective segregation coefficient and the number of solidifications

Conclusion on operational costs

Even though cost estimations given here are very rough they still show that this technology can be competitive to the Siemens process with costs that are around 50 €/kg [SSC10]. However at the redaction of this study, on August 2012, the average price of solar silicon at the market was 17.70 $/kg [Pvi12]. At this price a combination of plasma refining and segregation can hardly be economically viable.

An approach that may significantly reduce the energy consumption is that of Khattak [KJS02] and Nordstrand [NT12] who do not use plasma torches. Khattak injects the argon and steam at the bottom of a crucible while Nordstrand blows argon, hydrogen and steam on the surface of the silicon melt. Nordstrand does not use a plasma torch and his gas consumption per kg of purified silicon is similar to that of Nakamura. By up scaling it may be possible to reduce operational costs compared to those of Nakamura. Khattak gives no information about the gas consumption.

I.5. Conclusion

We have presented the current technology that is typically used for the production of solar cells. Then we presented several technologies that have the potential to produce silicon with lower purity at lower costs than the siemens process. We discussed the purity necessary for the production of solar cells. Then we estimated qualitatively the costs of a purification process using the combination of directional solidification and plasma refining. We identified the parameters energy consumption and gas consumption as important costs of the purification process. We also discussed that up-scaling can reduce the costs of the process.

When a new setup is implemented (up-scaling) it is important to adapt different parameters in order to achieve the highest possible deboronization rate. One should optimize the temperature, concentration and velocity profile of the plasma. The parameters that can be modified are the power, the gas flows and the geometry of the plasma torch. So far the process is poorly understood so that improvements could only be obtained by empirical studies. With a better understanding it would be easier to optimize a setup and to up-scale the process.

The objective of this study is to obtain a better understanding of the mass transfer and the reactions that play a role in the process. For this we first analyze and improve a basic mass transfer system in order to identify the steps that are likely to be rate limiting (chapter

II). A computational fluid dynamics model was elaborated at SIMaP by Mickael Majchrzak. This model simulates the plasma and can thus calculate the mass transfer to the silicon surface. The validation of this model by spectroscopy is the most important point of this study. In chapter III we present the theory that is necessary for the understanding of the spectroscopic method. In chapter IV we present the experimental facilities for the implementation of the method. In chapter V the results of the spectroscopic measurements are shown and compared to the model. In chapter VI we present tests of the method for the velocity measurement and the measurements of the coupling of the inductively coupled plasma torch. In Chapter VII we present parametric tests of the purification efficiency.

II. Boron removal by gas blowing

In chapter I we have presented an overview on the purification technologies for silicon for solar cells. Now we want to focus on the plasma refining process. We also include the gas blowing process without plasma because it is very similar. First we present a simplified mass transfer model and the parameters that are generally used for the characterization of the efficiency of such a process. We then analyse the empirical relations between the removal rate and the experimental parameters using data from literature. A new point presented in this chapter is that we compare different results from literature to chemical equilibrium calculation. We show that the reactions at the silicon surface are probably at chemical equilibrium. This indicates that the reactions at the surface are not the rate limiting step, which is in contradiction with most papers in literature. Then we analyze the literature about the oxidation of silicon because this reaction plays an important role in the process. On the one hand the formation of a silica layer at the surface hinders the purification. On the other hand the formation of a silica aerosol may have a significant influence on the efficiency of the process.

II.1. The simplified mass transfer model

To our knowledge literature agrees that the boron reacts with species consisting of H and O (H_2O, H_2, H, O) from the gas flow to form volatile compounds. The mass transfer (transport and/or reaction kinetics) is therefore a priori the key point to optimize this gas blowing purification process (plasma refining process and cold gas blowing process).

Figure II.1 shows a simplified mass transfer system for the gas blowing process. The transport mechanisms are convection (1 and 5) and diffusion (2, 4 and 6). The reaction (3) takes place at the interface between the silicon and the gas phase. The concentrations in the bulk gas are equal to the concentrations in the injected gas flow and the concentrations in the bulk liquid are equal to the concentrations in the silicon melt. In the two boundary layers the diffusion flux can be calculated with Fick's law (Equation (II-1)). J (mol/m^2/s) is the calculated diffusion flux, D (m^2/s) is the diffusion coefficient, $\Delta\phi$ (mol/m^3) is the concentration difference between the surface and the bulk and Δx (m) is the thickness of the boundary layer which in turn depends on the convection steps (1 and 5). At the interface, the global reactions taking place are given by (II-2) and (II-3). These global reactions can be deduced from the reactants involved in the process and from the products present at chemical equilibrium. In the plasma process the reactions with the radicals O and H have to be added.

$$J = -D\frac{\Delta\phi}{\Delta x} \qquad \textbf{(II-1)}$$

$$Si + H_2O \rightarrow SiO + H_2 \qquad \textbf{(II-2)}$$

$$B + H_2O \rightarrow HBO + 0.5H_2 \qquad \textbf{(II-3)}$$

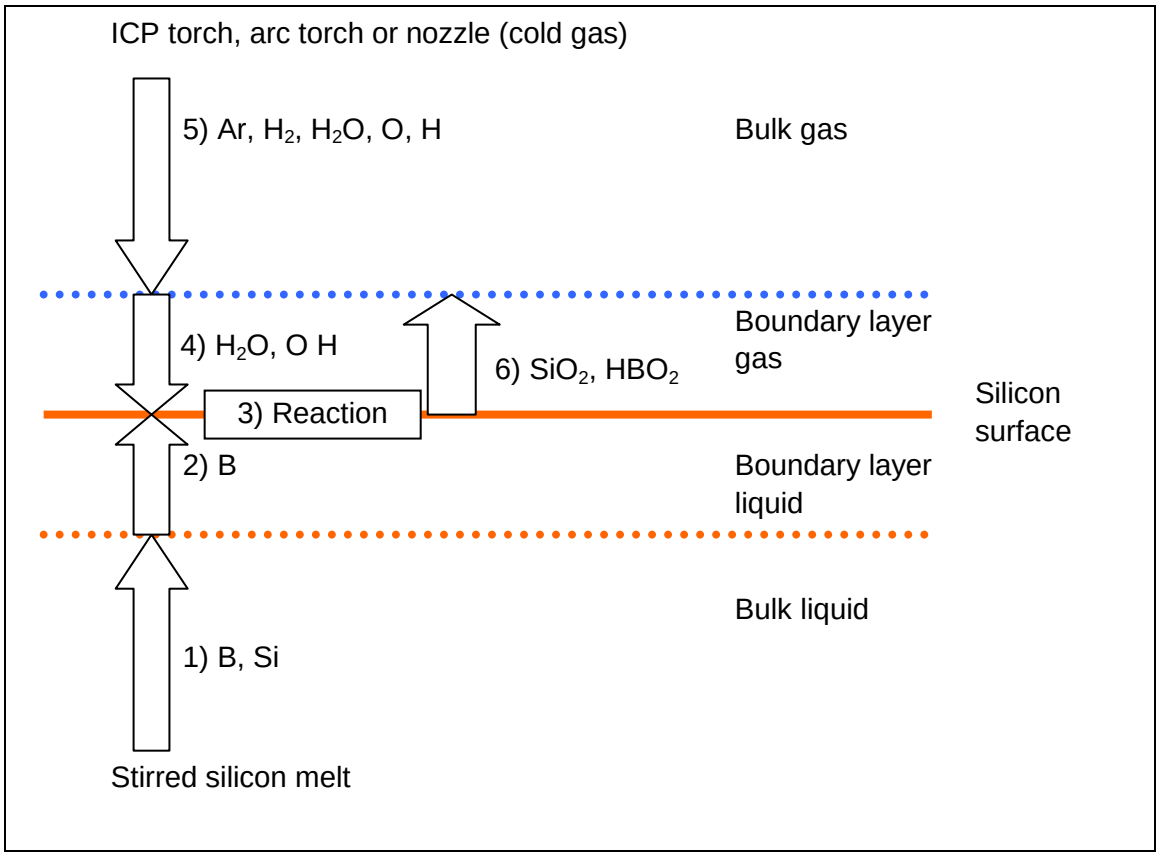

Figure II.1 Mass transfer model of the gas blowing purification process
1) Convection of silicon and boron
2) Diffusion of boron across the liquid boundary layer
3) Reaction of boron and silicon with water vapour
4) Diffusion of water vapour across the gaseous boundary layer
5) Convection of argon, hydrogen and water vapour
6) Slow diffusion of SiO_2 aerosol and fast diffusion of gaseous HBO_2

Literature suggests that the reaction rate of the reaction at the surface (3) is rate limiting. However, we show in II.6 that these reactions are probably very fast. Probably the mass transfer in the gas phase (4, 5 and 6) is rate limiting.

The boron concentration follows a first order law, which has been verified by many studies [NBS04], [FNP04], [NT12]. Thus, the flow of boron across the surface is proportional to the the boron concentration in the bulk silicon. This can be explained by diffusion as rate limiting step but also by chemical reactions (with a first order reaction of B) as rate limiting step.

Equation (II-4) gives the differential equation of a first order law, where [B] (kg/m^3) is the boron concentration in the melt and the decay rate K (s^{-1}) is the proportionality constant between the concentration and its time derivative. The boron concentration decreases thus exponentially (II-5). The proportionality constant K or the half-life of the boron concentration $T_{0.5}$ (II-6) can be used for the comparison of different experiments with the same silicon melt. For the comparison of different silicon melts, with different surface area and different volumes it is convenient to define the constant k (m/s) given by equation (II-7). V (m^3) is the volume of the melt and A (m^2) is the surface area of the melt. The constant k can be seen as the flow velocity of the boron atoms towards the surface. This constant is often used in literature and gives the efficiency of the process per surface area.

$$d[B]/dt = -K[B] \quad \textbf{(II-4)}$$

$$[B] = [B]_{t=0} \times \exp(-Kt) \quad \textbf{(II-5)}$$

$$T_{0.5} = \frac{\ln 2}{K} \quad \textbf{(II-6)}$$

$$k = \frac{K \cdot V}{A} \quad \textbf{(II-7)}$$

Multiplying k with the boron concentration [B] and the surface area A gives the total mass flow of boron J_B (kg/s) that quits the silicon melt. This mass flow is independent of the volume of the silicon melt (Equation (II-8)).

$$J_B = k \cdot A \cdot [B] \quad \textbf{(II-8)}$$

When using k one has to keep in mind, that this is the mean value of the mass flow per unit area which is probably not uniform because of the non uniform gas flow above the surface.

The boron flux across the silicon surface is independent of the mass of the silicon melt. In order to quantify the productivity of an installation we can divide the half-life time $T_{0.5}$ by the mass of the crucible m: $T_{0.5}$/m. Two installations with the same $T_{0.5}$/m can purify the same quantity of silicon per unit time.

In this mass transfer model (Figure II.1) there are some uncertainties that are treated in this study. When the study was started we believed that the chemical reactions (3) are the limiting step. Therefore the radicals of the plasma should have an important role. For this reason we developed a method to characterize the plasma and to test a computational fluid dynamic (CFD) model. The CFD model was developed by M. Majchrzak and S. Nosaris. The CFD model can then simulate the mass flux of the radicals arriving at the surface. Therefore, the characterization of the plasma is the main part of the present study.

During the study we obtained results showing that the radicals have not such an important role. We analyzed the chemical equilibrium at the surface and found that the chemical reactions are probably not a rate limiting step (chapter II.5). When the chemical reactions are fast the transport of reactants to the surface and the evacuation of reaction products remain as rate limiting steps. For the evacuation of the reaction products the reactions in the gas phase need to be included. A calculation of the chemical equilibrium in the gas phase shows that probably a SiO_2 aerosol gets formed. The formation of the aerosol may explain why the evacuated B/Si flux ratio is higher than the [B]/[Si] concentration ratio at the surface of the silicon melt.

II.1.1. The limits of a mass transfer model with separation of convection and diffusion

The mass tansfer system that separates convection and diffusion is however a simplification, that is often used in literature devoted to process engineering. The separation of convection and diffusion allows to study easily the interaction of chemical reactions and diffusion. The application of Fick's law across the whole boundary layer is however misleading as we want to show here.

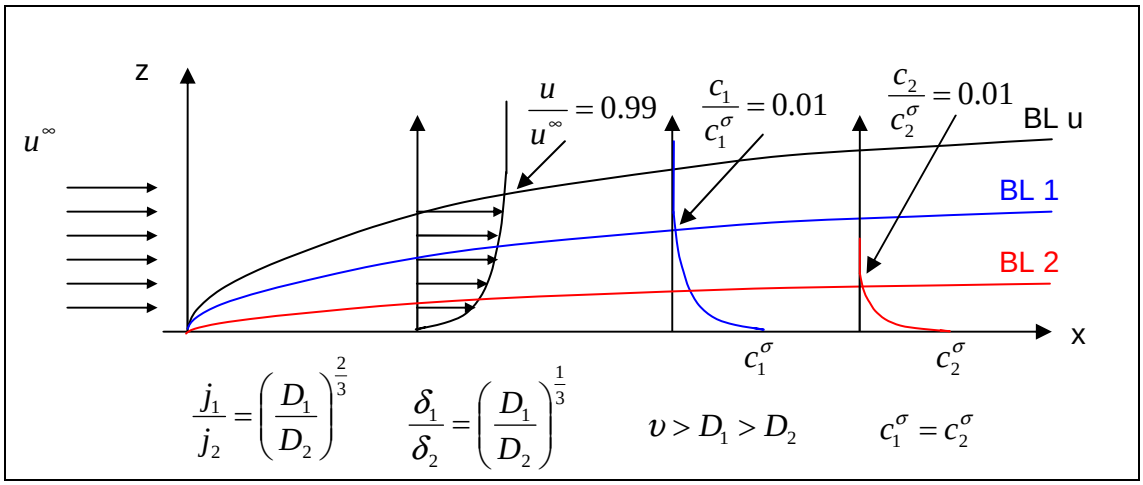

Figure II.2 Schema of the laminar boundary layer of a flat plane with two species with different diffusion coefficients. BL u is the dynamic boundary layer, BL 1 and BL 2 are the concentration boundary layers of the species 1 and 2
The graph shows that the diffusion is not uniform and not proportional to the diffusion coefficient

In a real boundary layer the limit between diffusive transport and convective transport is gradual. In the zone next to the surface the transport is mainly diffusive whereas far away the transport is mainly convective. Figure II.2 shows the velocity boundary layer and concentration boundary layer of two species with different diffusion coefficients in the boundary layer of a flat plane. The thickness of the dynamic boundary layer (velocity) can be defined by the height, where the velocity u is 99% of the velocity u_∞ (reached far from the plate at the scale of the boundary layer). For diffusion towards a non polluted gas ($c_\infty = 0$), the thickness of the boundary layer for the concentrations can be defined by the height, where the concentration is 1% of the concentration at the surface c^σ.

We can see in Figure II.2 that the thickness of the three boundary layers (BL u, BL 1 BL 2) increases in the direction of the gas flow. Thus for a uniform concentration at the surface c^σ, the diffusion flux density is not uniform, as it is suggested by the simplified mass transfer model. Mass transfer correlations can be used to quantify the effective thickness as a function of the flow regime (turbulent or laminar) and the Schmidt number (II-9)

$$Sc = \frac{\upsilon}{D} \qquad \textbf{(II-9)}$$

(υ (m^2/s) kinematic viscosity, D (m^2/s) diffusion coefficient).

From these correlations one can deduce that a species 1 with a higher diffusion coefficient than a species 2 ($D_1 > D_2$), also has a thicker boundary layer ($\delta_1 > \delta_2$). The diffusion flux at the wall (proportional to the diffusion coefficient and to the inverse of the thickness) is still higher. The diffusion flux is thus not proportional to the diffusion coefficient as it seems from the simplified mass transfer model used with a constant boundary layer thickness.

Cussler [Cus97] gives equation (II-10) for the relation between the thickness of the boundary layer and equation (II-11) for the relation between the diffusion fluxes of two species with different diffusion coefficients.

$$\frac{\delta_1}{\delta_2} = \left(\frac{D_1}{D_2}\right)^{\frac{1}{3}} \text{ for } Sc > 0.6 \qquad \textbf{(II-10)}$$

$$\frac{j_1}{j_2} = \left(\frac{D_1}{D_2}\right)^{\frac{2}{3}} \text{ for } c_1^{\sigma} = c_2^{\sigma} \text{ and } Sc > 0.6 \qquad \textbf{(II-11)}$$

The higher the diffusivity or the fluid flow velocity, the thinner is the boundary layer. A thinner boundary layer has a higher concentration gradient at the surface and thus a higher net transport. The strong variation of the gas temperature from the surface to the hot gas (if a plasma is used) or to the cold gas (without plasma) further complexify the situation because of temperature dependant gas-phase reactions or density variations.

II.2. Empirical relations from literature

Several papers deal with the purification of silicon by gas blowing. On the following pages we present the empirical relations that have been collected in the literature. Most data are from the papers of Alemany et al [ALD03], Nakamura et al. [NBS04] (Figure II-4) and Nordstrand et al. [NT12] (Figure II-3). They blew an Ar-H_2-H_2O mixture onto the surface of the liquid silicon that is held in a crucible. [ALD03] and [NBS04] used a plasma torch to heat up the gases to several thousands of degrees Celsius whereas [NT12] heat the gases just a little to avoid condensation of the water vapor. [ALD03] had a similar setup as [NBS04], but with a cold crucible, which maintains the silicon temperature at its melting temperature and a inductively coupled plasma torch instead of an arc torch. [ALD03] injected Ar, O_2 and H_2 into the plasma but as the molecules get dissociated in the plasma this is equivalent to the injection of H_2 and H_2O.

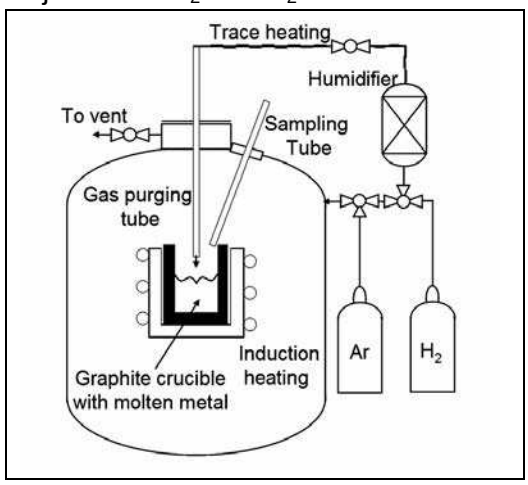

Figure II-3 Schematic of the setup of Nordstrand et al. [NT12]

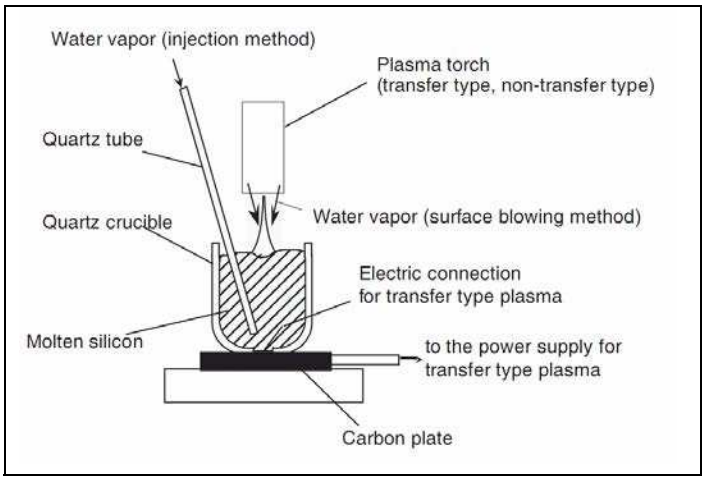

Figure II-4 Schematic of the setup of Nakamura et al. [NBS04]

II.2.1. The role of water vapour

The boron removal rate increases with the oxygen or water vapor concentration until a silica layer gets formed. This has been observed by different studies.

Previously in our group, Alemany et al. [ALD03] observed that the boron removal rate increases linearly with the oxygen concentration up to a total oxygen concentration of 0.8% (Figure II-5). At this concentration a silica layer was formed on the surface of the silicon and the boron removal rate decreased significantly. Nakamura et al. [NBS04] (Figure II-6) observed this linear increase up to a water vapor concentration of 8.5% without the formation of a silica layer. This corresponds to an oxygen concentration of 4.2%. Several differences may explain the higher oxygen concentration of [NBS04]:

a) [ALD03] used an inductively coupled plasma torch while [NBS04] used an arc torch.

b) The silicon temperature in the experiments of [ALD03] was lower than in the experiment of [NBS04].

The formation of the silica layer explains the use of oxygen contents lower than 4.2% in previous experiments. At higher oxygen concentration silica layer gets formed and the reaction between the gas and the liquid phase is blocked.

Rousseau et al. [RBM07] observed the emission of the boron lines in the plasma above the silicon surface. The intensity of the boron lines increased linearly with the concentration of oxygen in the plasma. This corresponds to the increase of the boron removal rate with the oxygen concentration.

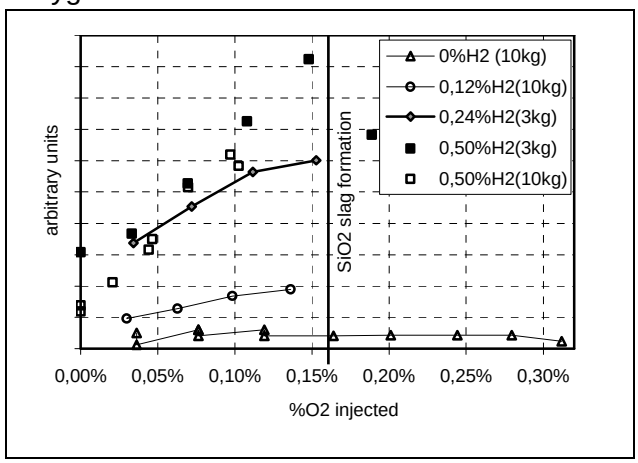

Figure II-5 Dependance of the boron concentration in the exhaust gases on the reactive gas content [ALD03]
T_{Si}=1687 K

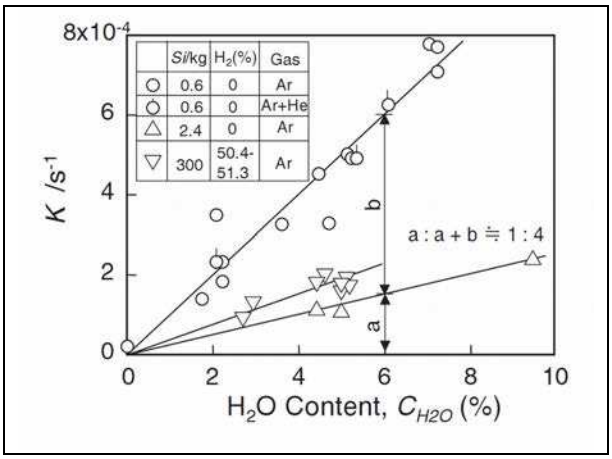

Figure II-6 Relation between H_2O content, the silicon mass and deboronization rate [NBS04]
T_{Si}=1823-1973 K

II.2.2. The role of hydrogen

The boron removal rate increases with the concentration of hydrogen. This has been observed by different studies. [ALD03] (Figure II-5) observed a strong increase of the deboronization rate from 0% to 0.5% of hydrogen. They also observed a very small deboronization rate when no hydrogen is injected. This indicates the importance of the reaction products $H_xB_yO_z$. Nakamura et al. [NBS04] blew an Ar-H_2-H_2O mixture heated by a plasma arc torch onto the silicon surface. Figure II-8 shows the result of [NBS04]. They observed only a small increase between 0% and 30% of hydrogen but a strong increase between 30% and 50%. Figure II-7 shows the results of Nordstrand et al. [NT12]. They blew an Ar-H_2-H_2O mixture onto the surface of the silicon. The deboronization rate increased with increasing hydrogen concentration up to 50% of hydrogen and then saturation occurs. From another figure in the same paper we can deduce that the points at 50% and 75% have been swapped in this figure, so that the real increase is close to a square root curve and agrees with chemical equilibrium, as we will show later.

While [ALD03] and [NT12] observed a strong increase at low hydrogen concentrations this is not the case in [NBS04]. Both, [NBS04] and [NT12], observed that the deboronization rate at 50% hydrogen is about four times higher than the deboronization rate with 0 % hydrogen besides the water vapor.

Suzuki et al. [SKS92] observed that, when they added O_2 or CO_2 to the Ar of the arc torch, a silica layer was formed. When they added H_2O instead, this silica layer did not occur. They attributed this effect to the thermal equilibrium between SiO_2 and Si(l) at the surface, which is shiftet towards Si(l) by the addition of hydrogen. The high thermal conductivity of hydrogen

may also reduce the formation of the silica layer by increasing the temperature of the gaseous and liquid boundary layer.

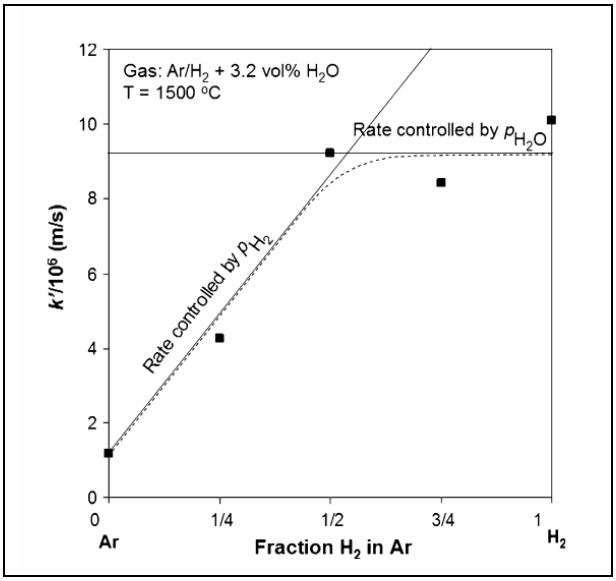

Figure II-7 Relation between H_2 content and deboronization rate in the setup of Nordstrand without plasma [NT12]

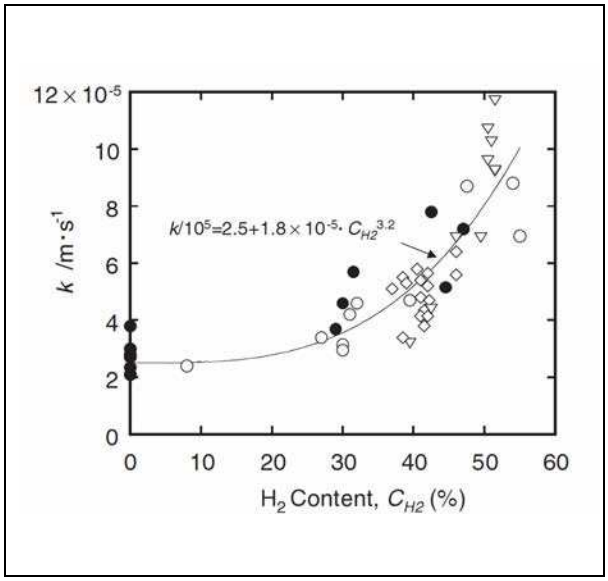

Figure II-8 Relation between H_2 content and deboronization rate in the setup of Nakamura with plasma [NBS04]

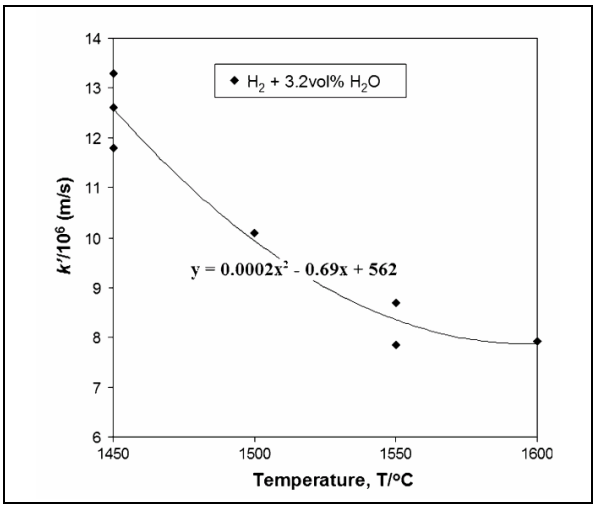

Figure II-9 Relation between silicon temperature and deboronization rate [NT12]

II.2.3. The role of the silicon temperature

During previous studies in our group, Degoulange [Deg08] could show qualitatively that the deboronization rate decreases when the temperature increases. However he could not measure the temperature of the silicon melt because the plasma disturbed both thermocouples and pyrometers. Fourmond et al. [FNP04], previously in our group, found that, when they increased the silicon temperature by 150 K, they could inject twice the concentration of oxygen without forming the silica layer. They measured the purification rate with 0.8% oxygen and at a 150 K higher temperature with 1.6% oxygen. They used two different crucible sizes and obtained a similar purification rate of 26 min/kg ($T_{0.5}$/m)[Del09]. The higher oxygen concentration compensates thus the effect of the silicon temperature.

[NT12] (Figure II-9) measured quantitatively the influence of the temperature on the deboronization rate. They observed that the deboronization rate decreased by a factor 0.7 when the silicon temperature was increased from 1723 K to 1873 K. This factor agrees with chemical equilibrium as we will show later.

II.2.4. The role of the gas velocity and gas temperature

Most of the purification studies have been done with plasma torches. In plasma torches it is difficult to modify the gas velocity without modifying the gas temperature. Furthermore the gas velocity and temperature depend on the position at the silicon surface. So far no study has measured the influence of gas velocity and gas temperature separately.

Nakamura et al. [NBS04] observed that, when they blew the gases without the plasma heating onto the silicon surface, a silica layer was formed on the silicon. Nordstrand et al. [NT12] calculated that the boron removal rate per surface area with plasma torches is 6 times faster than without plasma torches. They blew the gases without plasma heating onto the surface and did not observe a silica layer. The higher boron removal rate with plasma can be attributed to the higher gas temperature, the higher flow velocity, the higher oxygen concentration (the molar fraction of [H_2O] was 4.6% for [NBS04] and 3.2% for [NT12] see Table I-3) or another characteristic of the gas flow.

[NBS04] observed that the deboronization rate does not directly depend on the plasma gas flow rate. It is not clear how the plasma gas flow rate influences the gas velocity and temperature at the silicon surface. [NBS04] observed that plasma torches with a high gas flow and a high power lead to a higher purification rate.

In our group, Pelletier [Pel06] measured the graving of a graphite target under a plasma torch with argon and oxygen. He observed that the graving rate was divided by 2.5 when he extinguished the plasma. As the graphite has a high reactivity at the temperature used in the study (1600 K-1800 K, diffusion limited oxidation), this indicates that a higher quantity of oxygen arrives at the graphite surface when the plasma is ignited. This could be due to the higher gas velocity or to the higher gas temperature.

II.2.5. The role of the silicon surface area

Nakamura et al. [NBS04] varied the distance between the plasma torch tip and the silicon surface. They observed a dimple with a free silicon surface and the silicon around was covered by a silica layer. The size of the dimple changed when the distance between the plasma torch tip and the silicon surface was varied. They calculated the surface area of the dimple and plotted the deboronization rate versus this surface area. This plot shows a linear relation between the surface area of the dimple and the deboronization rate. However the change of the distance between the plasma torch and the silicon modifies not only the surface area of the dimple but also the gas temperature and the gas velocity at the silicon surface.

The graving experiments of [Pel06],[DPB09] showed that the graving and thus the oxygen flux arriving at the graphite surface are not uniform. The oxygen flux decreased with the distance from the axis of the torch. This indicates that the deboronization is smaller at a high distance from the axis of the torch. An increase of the surface area of the silicon melt above the diameter where the deboronization rate is high is thus probably inefficient.

II.2.6. The role of the mass of the silicon melt

The half-life time $T_{0,5}$ of the boron concentration in the silicon melt is proportional to the mass of the silicon melt. Alemany et al. [ALD03] found the same boron concentration in the exhaust gases when using a 3 kg crucible and when using a 10 kg crucible (Figure II-7).

Nakamura et al. [NBS04] found that the deboronization rate is inversely proportional to the mass of silicon melt when they used the same plasma for a 0.6 kg melt and a 2.4 kg melt (Figure II-6). The half life divided by the mass $T_{0,5}$/m is therefore independant of the silicon mass and a good indicator for the productivity of the installation.

II.2.7. The role of stirring

Degoulange [Deg08] found that the temperature of the silicon surface below the plasma is higher without stirring than with stirring. He also found that the stirring may be important to transport the boron to the surface

Nakamura et al. [NBS04], on the contrary, found that an additional stirring had in his setup no influence on the deboronization rate. However, because of the high velocity of the gas flow provided by an arc torch (this strong jet is responsible for the „dimple"), there should always be a sufficient stirring in their facility.

II.2.8. Conclusion on the empirical relation ships

The empirical relationships show that the purification rate in the term of $T_{0,5}$/m is maximum when the concentration of water vapor or oxygen is close to the limit of the formation of a silica layer and when hydrogen is used instead of argon as carrier gas. However the operation of a plasma torch typically needs argon.

In plasma torches a higher gas flow leads only to a higher purification rate when the power is increased at the same time. A higher silicon temperature reduces the purification rate. However, this reduction may be compensated or even overcompensated by a higher oxygen concentration that can then be used without the formation of the silica layer. The silicon surface area should be adapted to the gas flow.

The dependence on the oxygen and the limitation due to a silica layer was further investigated by a literature survey about silicon oxidation (part II.4) and the dependence on hydrogen was studied using thermodynamic calculations (part II.5). The discussion in part II.7 suggests that a silica aerosol plays an important role. This hypothesis will be confronted to the experiments in chapter VII.

II.3. Oxidation of silicon

The oxidation of silicon with an oxidizing gas (H_2O) plays an important role in the purification process. Some papers have already studied the oxidation of solid and liquid silicon. There exist two different oxidation regimes. In the so called passive oxidation regime an oxide layer limits the oxygen flux to the silicon surface. In the active oxidation regime the diffusion of oxygen in the gas boundary layer limits the oxygen flux to the silicon surface. The coexistance of the two oxides SiO or SiO_2 makes the active oxidation complexe. There are different models describing the diffusion and chemical reactions in the active oxidation regime. The models predict the conditions for the transition to the passive oxidation regime. However the conditions that are predicted by the different models for the transition are different. All models use the assumption of a laminar boundary layer with a constant temperature. They use the simplified model with separation of diffusion and convection and one thickness of the boundary layer for all species. These models are presented and compared in the following.

II.3.1. Wagner's model

Wagner [Wag58] proposes a simple model to describe the transition from active oxidation to passive oxidation. For the active oxidation he assumes that the reactions at the

interface are very fast and no reactions take place in the gas phase. The oxidation is thus limited by the diffusion of the molecular oxygen O_2 across the boundary layer.

He assumes that the reactions are very fast so that the species at the surface are in chemical equilibrium. This implies that nearly all the oxygen is in the form of SiO and that the O_2 concentration is close to zero at the surface. The boundary layer consists only of a neutral gas, dioxygen and SiO.

Figure II-10 shows the concentration profiles of the active oxidation model of Wagner. The concentration of SiO at the silicon surface is more than twice as high as the gas bulk concentration of O_2 because the diffusion coefficient of SiO is by a factor 0.64 [RRA01] smaller than the diffusion coefficient of O_2. The flow of silicon atoms across the boundary layer is therefore equal to the flow of SiO and twice the flow of oxygen (Equation (II-12)). The oxygen flow can be calculated using the diffusion coefficient D_{O_2}, the oxygen partial pressure in the bulk $p^0_{O_2}$, the ideal gas constant R and the thickness of the boundary layer δ_{O_2} (Equation (II-13)).

$$j_{Si} = j_{SiO} = 2 \times j_{O_2} \qquad \textbf{(II-12)}$$

$$j_{O_2} = \frac{p^0_{O_2} D_{O_2}}{\delta_{O_2} RT} \qquad \textbf{(II-13)}$$

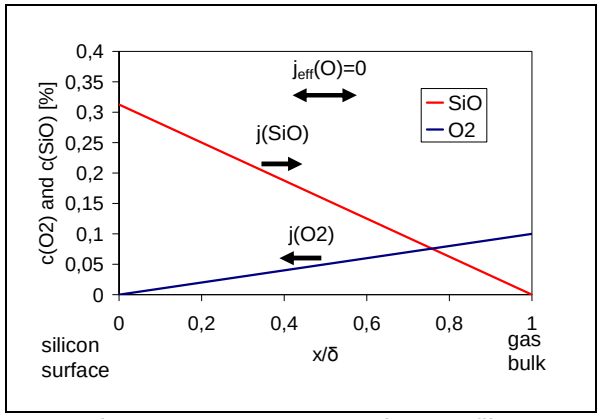

Figure II-10 Concentration profiles calculated with the active oxidation model of Wagner [Wag58]
Bulk concentration of O_2 = 0.1%

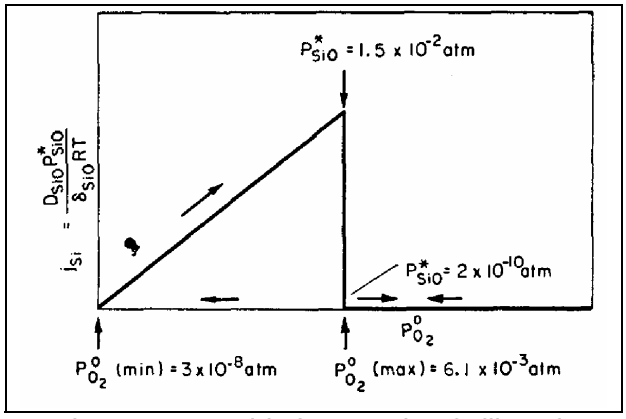

Figure II-11 Oxidation rate j_{Si} of silicon in oxygen-helium mixtures of constant total pressure at 1410 °C as a function of oxygen partial pressure $p^0_{O_2}$ [Wag58]

When the oxygen concentration in the bulk is increased, the concentration of SiO at the silicon surface increases proportionally. When the SiO concentration reaches the equilibrium partial pressure of the reaction $2SiO \leftrightarrow Si + SiO_2$ a silica layer gets formed (passive oxidation). This silica layer hinders the reaction between the oxygen and the silicon and the oxidation rate drops radically (see Figure II-11). The bulk oxygen concentration must be reduced to a very low value to remove the silica layer. Once the silica layer is removed, the oxygen concentration can be increased again to obtain a higher oxidation rate. In Figure II-11 one can see this hysteresis behaviour of the oxidation rate. A similar behaviour was also observed in the purification process.

II.3.2. Turkdogan's model

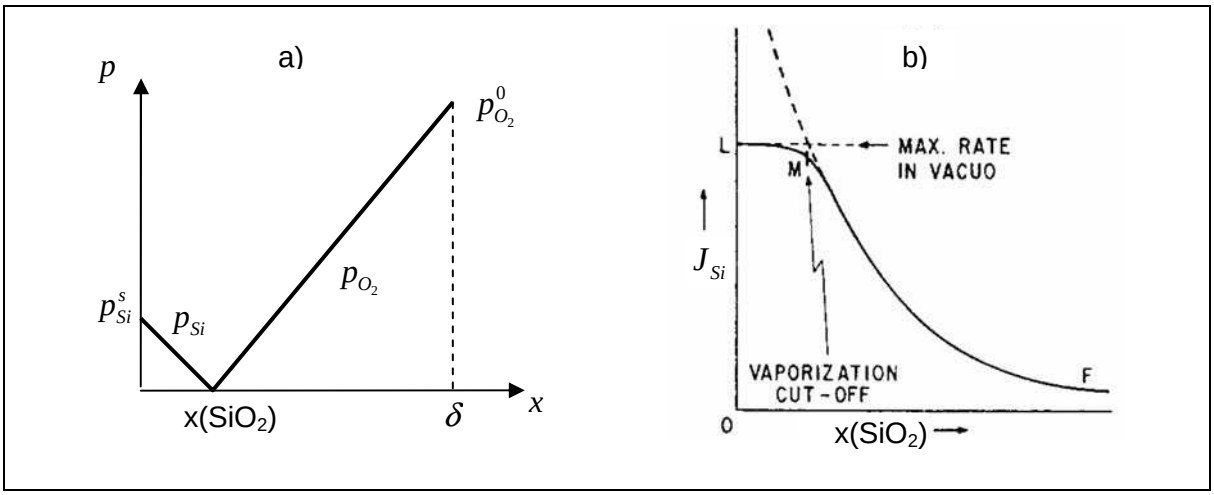

Figure II-12 a) Partial pressure profiles in Turkdogans [TGD63] counter flux model of metal vapour and oxygen an SiO_2 aerosol is formed at x(SiO_2)
b) dependence of the silicon flux on the distance x(SiO_2)

Turkdogan et al. [TGD63] suggest a counter flux model for the oxidation of the silicon. The oxygen and the silicon diffuse towards the point x(SiO_2) where they react to SiO_2 which forms an aerosol and is evacuated by the gas flow. At the silicon surface the partial pressure of silicon is p^s_{Si} and at the distance δ, which is the thickness of the boundary layer, the partial pressure of oxygen is equal to the partial pressure of oxygen in the bulk $p^0_{O_2}$ (Figure II-12 a). At x(SiO_2) the partial pressure of silicon and oxygen is very small compared to p^s_{Si} and $p^0_{O_2}$ respectively. The maximum flux of silicon is equal to the evaporation rate of silicon in vacuum, which is given by the Langmuir equation of evaporation (II-14) (Figure II-12 b) . Below the maximum flux the silicon flux is equal to the oxygen flux. Above the maximum flux a silica layer is formed and the silicon flux drops radically, similar to Wagner's model. While the formation of the silica layer in Wagner's model depends only on the oxygen partial pressure in the bulk, it depends in Turkdogan's model only on the oxygen flux to the surface. In Turkdogan's model the silica layer appears at a lower oxygen partial pressure, when the velocity is higher and thus the boundary layer is thinner. Measurements on iron and other metals confirmed this conclusion.

$$J^{\max}_{Si} = \frac{p^s_{Si}}{\sqrt{2\pi RTM_{Si}}} \qquad \text{(II-14)}$$

$M_{Si} = 28 g/mol$ is the molar mass of silicon.

II.3.3. Ratto's model

Ratto et al. [RRA01] proposed a model of the oxidation of the silicon, which is taking into account the reaction between Si and O_2 in the gas phase. The species taken into account are Si, SiO, SiO_2 and O_2. They assumed that the reactions in the gas phase are very fast so that the system is everywhere in chemical equilibrium. The formation of SiO_2 aerosol is taken into account by a sink term, which means that similar to Turkdogan's model the transport of the aerosol is not taken into account. The model does not predict the formation of a silica layer but it shows that active oxidation is possbile for oxygen concentrations higher than the maximum concentrations predicted by Wagner's model. Below a oxygen pressures of

0.01 Pa Ratto's model gives the same result as Wagner's model. The main transport is due to silicon and oxygen, similar to Turkdogan's model.

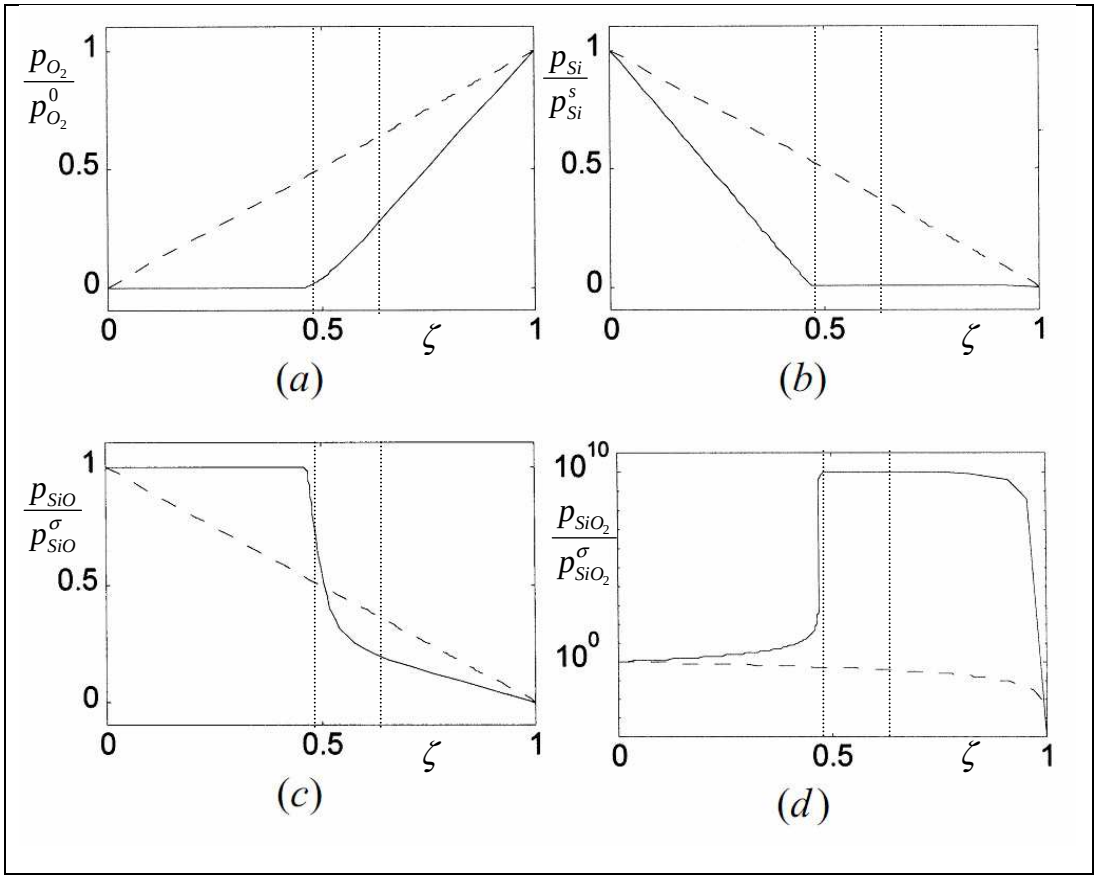

Figure II-13 Pressure profiles vs ζ. T=1750K, $p^0_{O_2} = 0.1Pa$. Solid lines = instaneous reactions. Dashed curves = no reaction, vertical dashed lines: heterogeneous layer with aerosol formation [RRA01]

(a) $p_{O_2} / p^0_{O_2}$; (b) p_{Si} / p^s_{Si}; (c) p_{SiO} / p^σ_{SiO}; (d) Semilog-y $p_{SiO_2} / p^\sigma_{SiO_2}$

p_{O_2}, p_{Si}, p_{SiO} partial pressure of O_2, Si, SiO

$p^0_{O_2}$ partial pressure of O_2 in the gas bulk

p^s_{Si} saturation partial pressure of Si

p^σ_{SiO}, $p^\sigma_{SiO_2}$ partial pressure of SiO, SiO_2 at the metal surface

ζ dimensionless spatial coordinate with origin at the interface and perpendicular to it

[RRA01] calculated the pressure profiles with a partial pressure of 0.1 Pa in the bulk gas as shown in Figure II-13. The profiles consist of three different layers. ζ is an dimensionless number that defines the position in the boundary layer. The silicon surface is at $\zeta = 0$. $\zeta = 1$ is the distance where the concentrations are equal to the concentrations in the bulk gas.

At ζ <0.49 they obtained a homogenous layer of reducing atmosphere (high Si partial pressure).

At 0.63< ζ they obtained a homogenous layer of oxidizing atmosphere (high O_2 partial pressure).

At 0.49< ζ <0.63 their model gives an heterogenous layer. In this heterogeneous layer O_2 and Si react to SiO_2. SiO_2 is at saturation vapour pressure and therefore condenses to an aerosol

The graphs a and b in Figure II-13 show the partial pressure of Si and O_2 respectively. Their profiles are very similar to Turkdogan's model with a small difference in the heterogenous layer 0.49< ζ <0.63. The constant concentration gradient of silicon and oxygen show that the transport of these species is not influenced by reactions from the other species.

The pressure profiles that are presented in Figure II-13 have been calculated for a oxygen partial pressure of 0.1 Pa in the gas bulk. This is much lower than 1000 Pa which would correspond to the typical atomic oxygen concentration in the gas blowing purification process.

We want to analyze how the pressure profiles change when we increase the partial pressure of oxygen from 0.1 Pa to 1000 Pa. The position of the heterogeneous layer is given by the diffusion rate of the silicon and the oxygen. The silicon partial pressure above the surface remains the same whereas the oxygen partial pressure is increased by a factor 10000. Thus, the heterogeneous layer moves very close to the silicon surface.

We approximate the thickness of the homogenous layer above the silicon surface (reducing atmosphere) using the oxygen flux density $j_o = 0.002 kg \times m^{-2} \times s^{-1}$ from the numerical model of Pelletier et al. [PDT10]. We assume that the silicon molar flux is half of the molar flux of atomic oxygen so that SiO_2 can be formed (II-15). We assume that silicon is only transported by diffusion from the silicon surface, where it is at the equilibrium pressure, towards the limit of the homogeneous boundary layer, where the partial pressure of silicon is zero. We use the vapor pressure and diffusion coefficient from [RRA01].

$$J_{Si} = 0.5 J_o = 0.06 mol / m^2 / s^1 \qquad \textbf{(II-15)}$$

$$\delta_1 = \frac{D_{Si} \Delta C}{J_{Si}} = \frac{D_{Si} p_{Si}^S}{J_{Si} \times RT} = \frac{0.00035 \times 0.1}{0.06 \times 8.31 \times 1750} m = 40 nm \qquad \textbf{(II-16)}$$

The calculated thickness of 40 nm (II-16) is smaller than the mean free path of molecules in air at ambient pressure and 1750 K which is approximately 380 nm [Jen88]. This indicates that a two layer model with a heterogeneous layer at the silicon surface and homogenous layer above may be sufficient for the description of the boundary layer.

This model does not take into account the transport of the SiO_2 aerosol which should diffuse towards the gaseous bulk (where it is evacuated) or towards the surface (where it is reduced). The diffusion towards the surface may modify the heterogeneous layer. The formation and reduction of the aerosol may lead to high aerosol concentration gradients with a significant mass flux, especially at high oxygen concentrations.

II.3.4. Comparison of the different models to measurements

All in all, the three models [Wag58], [TGD63] and [RRA01] give a boundary layer where the dioxygen concentration decreases from the bulk to the surface (or to the edge of the heterogeneous layer), with a gradient related to the oxygen flux by Fick's law. The oxygen is evacuated back under the form of SiO [Wag58] or it is removed at the point where it condensates in the form of SiO_2 as aerosol in the gas [TGD63],[RRA01].

In all models the silicon flux that is oxidized is proportional to the oxygen flux that arrives at the surface. However in [Wag58] the silicon flux is twice the oxygen flux while the silicon flux is equal to the oxygen flux in [TGD63] and [RRA01].

There is a fundamental difference for the transition between the active and passive oxidation regime. In [Wag58] the transition is independent of the oxygen flux and depends

only on the oxygen concentration and the temperature dependent formation of SiO. In [TGD63] the transition is independent of the oxygen concentration and depends only on the oxygen flux and the temperature dependant desorption of Si. [RRA01] does only show that active oxidation is possible at higher oxygen pressures than those predicted by [Wag58] but does not predict the limit between active and passive oxidation.

	Wagner [Wag58] $p_{O_2}[mbar]$	Turkdogan [TGD63] $J_O[mol/m^2/s^1]$
Condition for transition from active to passive oxidation at 1750 K, $p_{Si}^S = 0.1Pa$ [RRA01]	5.5	4.10^{-3}
Typical conditions in plasma refining in our group [PDT10]	10	0.12
Predicted oxidation regime	Passive	Passive

Table II-1 Comparison between the conditions for the transition to passive oxidation of the different models to the conditions in our group.

Table II-1 shows the comparison between the conditions for the transition to passive oxidation predicted by the model and the typical conditions in the plasma gas blowing purification process. The maximum oxygen partial pressure of the Wagner model has been taken from [Deg08] and the maximum oxygen flux density has been calculated with the Langmuir equation. Both models (Turkdogan and Wagner) predict that the oxidation should be in the passive oxidation regime although the process works in the active oxidation regime. This shows that the two models can not be used to predict the transition to passive oxidation in the plasma gas blowing process.

Both [Wag58] and [TGD63] predict a strong temperature dependence of the maximum oxygen partial pressure as we can see in Figure II-14, which shows the logarithm of the maximum partial pressure of oxygen against 1/T. As said before, in [TGD63] the transition from active to passive oxidation is independent of the concentration so that the curve in Figure II-14 is valid for the estimated boundary layer thickness and may be higher or lower for a respectively thicker or thinner boundary layer. The slope of the curves is the formation enthalpy of SiO for Wagner's model and the sublimination enthalpy of Si for Turkdogan's model.

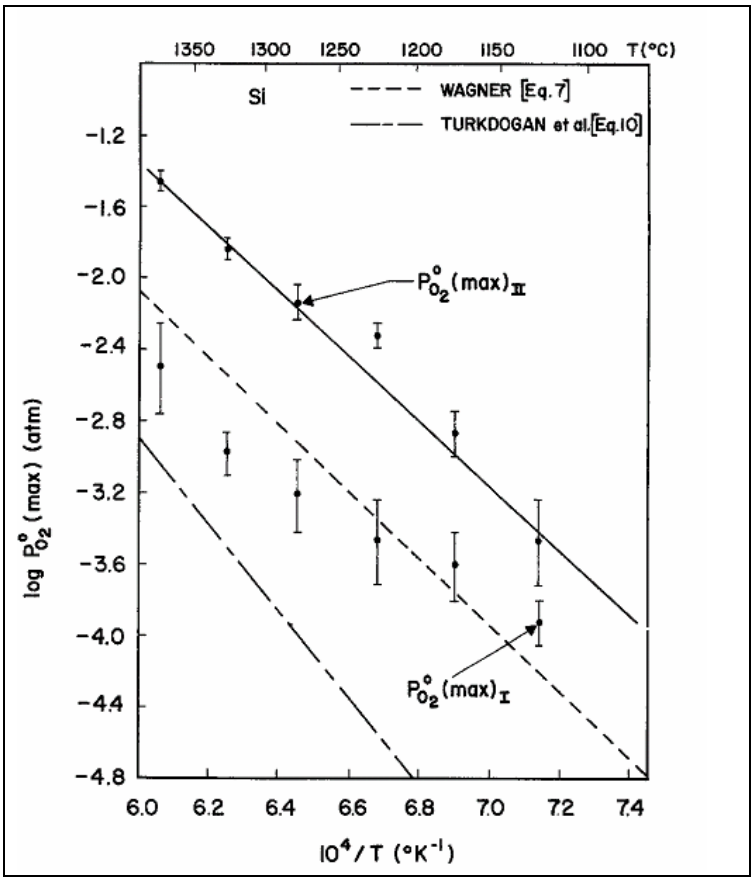

Figure II-14 Measured temperature dependence of the maximum partial oxygen pressure and the predictions of Wagner's model and Turkdogan's model [HG76]

Hinze and Graham [HG76] measured the temperature dependence of the active passive oxidation transition on solid silicon. They found that the transition took place in two steps. At a pressure $p_{O_2}^0(\max)_I$ silica whiskers form on the surface, but the active oxidation continues. At $p_{O_2}^0(\max)_{II}$ a silica layer is formed so that the oxidation changes from active to passive oxidation. The slope of $p_{O_2}^0(\max)_{II}$ in Figure II-14 is equal to the slope of Wagner's model, which indicates that the formation of SiO is the limiting phenomenon at the active passive oxidation transition. The formation of silica whiskers however show that a part of the oxygen reacts with the SiO before arriving on the silicon surface. The results of Hinze and Graham may agree with a two layer model similar to Ratto's model with the inclusion of the transport properties of the aerosol as discussed above.

On liquid silicon these whiskers can probably not form because they can not stick on the liquid silicon. Naess et al. [NTO12] observed active oxidation in a ladle at oxygen pressures that were higher than the maximum pressure for active oxidation predicted by Wagner's model. They explained this by the heterogeneous layer of Ratto's model.

Naess et al [NYZ12] studied experimentally the active oxidation of silicon. They measured the mass loss of a silicon melt in a tube with a flow of an argon-oxygen mixture.

They compared the mass loss at different oxygen partial pressures and to simulated oxygen fluxes using CFD. They used the assumption $J_{Si} = J_{SiO} = 2J_{O_2}$ and obtained a good agreement between the measured mass loss and the simulated oxygen flux, which indicates that the SiO is oxidized to SiO_2 outside the boundary layer. The precision of the measured mass loss is, however, not sufficient to show that SiO_2 is formed outside the boundary layer.

In the experiment they obtained amorphous, spherical SiO_2 particles with an average diameter of ~60nm and rather uniform size at the reactor walls. This shows that the SiO_2 particles may have been formed via the liquid state of SiO_2. They attributed this to the strongly exothermic nature of the reaction (II-17)

$$2SiO(g) + O_2(g) \rightarrow 2SiO_2(s) \quad (\Delta H = -773\ kJ/mol \text{ at } 1500℃) \qquad \textbf{(II-17)}$$

They suggest that gaseous SiO_2 is formed that condenses on the liquid particles. The high enthalpy of vaporization of SiO_2 ($\Delta H_{vap}(SiO_2) = -528\ kJ/mol$ at 2950℃) heats the liquid particles during condensation and maintain them so above the melting temperature. As the difference between the melting point and the boiling point of silica is less than 200 K the evacuation of heat from the aerosol particle may limit the condensation.

Hinze and Graham suggested that the SiO reacts with oxygen that is adsorbed on the surface of the SiO_2 whiskers according to reaction (II-18)

$$SiO(g) + O(ads) \rightarrow SiO_2(s) \qquad \textbf{(II-18)}$$

This strongly exothermic surface reaction may also explain the formation of the liquid SiO_2 droplets observed by Naess et al. If the evacuation of heat limits the condensation it makes no difference whether reaction (II-17) or (II-18) takes place.

II.3.5. Conclusion on the different models

The experimental results found in literature suggest that the oxygen diffuses to the surface of the silicon and reacts there to SiO(g) which reacts elsewhere to SiO_2(l/s). However it is not sure whether SiO_2(l/s) is formed in the boundary layer (fast reactions, in chemical equilibrium) as proposed by [RRA01] or rather outside the boundary layer (slow reactions, out of chemical equilibrium) [Wag58]. It would be of great scientific interest to determine whether the reaction $2SiO(g) + O_2(g) \rightarrow 2SiO_2(s)$ is in chemical equilibrium or to determine the deviation from chemical equilibrium.

In the case of slow chemical reactions, the deviation from chemical equilibrium may be different when the oxidizing gas is water vapor instead of oxygen. The reaction (II-17) needs a trimolecular collision so that it may be slower than the reaction (II-19) which needs only a bimolecular collision.

$$SiO(g) + H_2O(g) \rightarrow SiO_2(g) + H_2(g) \qquad \textbf{(II-19)}$$

The atomic oxygen of the plasma may react even faster due to its high reactivity (II-20)

$$SiO(g) + O(g) \rightarrow SiO_2(g) \qquad \textbf{(II-20)}$$

Even if the reactions in the gas phase are fast nucleation and condensation may be slow so that the concentration of SiO_2(s/l) may be out of chemical equilibrium.

If the chemical reactions in the gas phase are in equilibrium, the model of [RRA01] describes well the boundary layer but the transport of the aerosol should be included. If the chemical reactions are far from equilibrium, the model of [Wag58] would describe well the boundary layer. The formation of the aerosol in the boundary layer may significantly influence the purification process as we will discuss in more details later.

II.4. Thermodynamic calculations of the B/Si ratio at the silicon surface

When the chemical reactions are very fast, which is likely for a metal surface at high temperature, the concentration of different species reach locally their thermodynamic equilibrium at every instant in the process. This means that the local reaction rates of all reactions are always equal to the local reaction rates of their inverse reactions. We do not know the kinetics of the chemical reactions at the surface but we compare in the next chapter

the results of the thermodynamic calculations to experimental results and show in this way that the surface reactions are probably in chemical equilibrium.

At equilibrium, the system has minimized its Gibbs free energy and the concentrations can be calculated without the knowledge of the reactions that take place. The commercial program FactSage [FAC] can be used to calculate the concentrations at chemical equilibrium. FactSage includes a database of the most common chemical species and their Gibbs free energies. For a given mix of several elements and a given temperature and pressure it can calculate the quantity of each chemical compound by minimizing the Gibbs free energy of the system. The results can be represented as partial pressures or as quantity in mole. As the partial pressure is proportional to the molar fraction in the gas phase, the two representations are equivalent.

One of the consequences of this local chemical equilibrium at the surface is that the concentration of the oxidizing species (mainly H_2O) is very low in the gas phase at the surface. This is due to the strong ratio of the partial pressures $p_{SiO} / p_{H_2O} \approx 1000$, when there is an excess of silicon, and to the limitation of p_{SiO} due to the formation of SiO_2. The oxidation of the silicon is thus limited by the quantity of water vapor that arrives on the surface and not by the evacuation of the silicon oxide.

The chemical equilibrium between the vapour pressures in the gas phase and the concentrations in the liquid phase is important for the understanding of the mass transfer from the liquid to the gas phase. The total mole fractions of the elements oxygen, hydrogen and argon in the gas at the surface are similar to the mole fractions that are blown onto the surface as long as the diffusion coefficient of the reactants are similar to the diffusion coefficients of the products. The small diffusion coefficient of a SiO_2 aerosol that may be formed in the boundary layer can lead to a higher oxygen concentration at the surface of the silicon melt than in the bulk gas as we show later.

Using the same atomic concentrations as in the bulk gas, and a large excess of moles from the condensed phase, the concentrations of boron and silicon compounds at the surface at chemical equilibrium can be calculated. The ratio between the sum of all the concentrations of gaseous Si compounds and the sum of all the concentrations of all gaseous B compounds would be equal to the [B]/[Si] ratio in the exhaust gases, if the diffusion coefficient of all compounds were similar.

Degoulange [Deg08] and Nordstrand et al. [NT12] calculated the partial pressure of the volatile boron and silicon species at the silicon surface at chemical equilibrium using FactSage [FAC]. Figure II-15 shows the partial pressures of the major species at the silicon surface calculated by Nordstrand. Their calculation was done for 200 g of silicon with 10 ppma of boron and 810 L of moist hydrogen (3.2 vol pct H_2O). The molar quantity of silicon was chosen high enough to ensure a large excess of liquid phase species so that the liquid boron concentration is not modified by a different [B]/[Si] ratio in the gas phase.

The results show that:

- Nearly all hydrogen is in the form of H_2. This is because the compounds of hydrogen with the major species Si have a rather high Gibbs free energy.
- Nearly all oxygen is in the form of SiO. SiO has a very low Gibbs free energy (lower than that of H_2O). The silicon can thus reduce the water.
- The main gaseous species containing silicon is SiO and the main gaseous species containing boron is HBO. The other species have much lower concentrations so that the [B]/[Si] ratio in the gas phase is very close to the [HBO]/[SiO] ratio in the gas phase.
- The partial pressure of the gaseous boron species (mainly HBO) decreases with temperature. This is probably because the molecule HBO has a lower entropy

than the smaller molecule SiO. An increase of the temperature shifts thus the equilibrium between these two molecules towards SiO.

- The [B]/[Si] ratio in the gas phase which is similar to the [HBO]/[SiO] ratio (between 10^{-5} and 10^{-4}) is similar to the [B]/[Si] ratio in the liquid silicon (10 ppma). (This is modified by a new formation enthalpy of HBO, see further down)

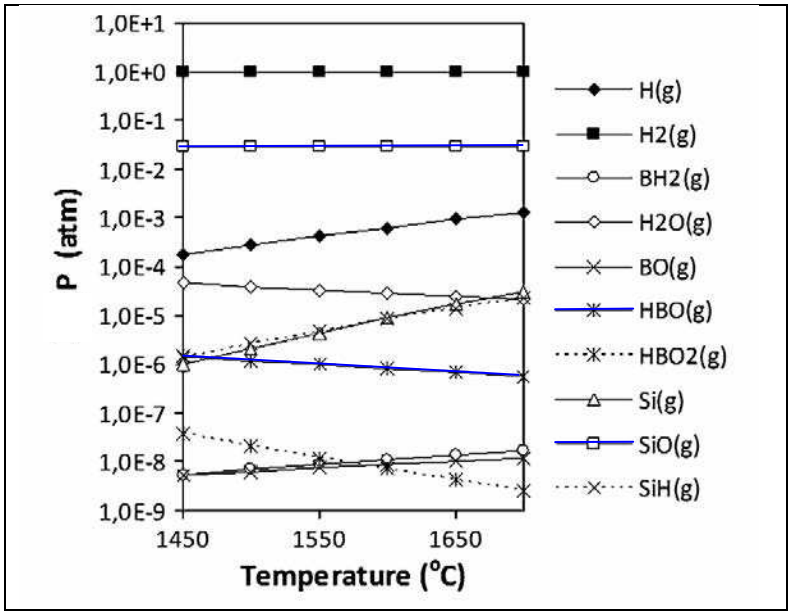

Figure II-15 Graphical representation of FactSage calculations of partial pressure of gaseous species vs temperature in the H_2-3.2 vol pct H_2O-Si-B system ([B]/[Si] ratio 10 ppma) [NT12]

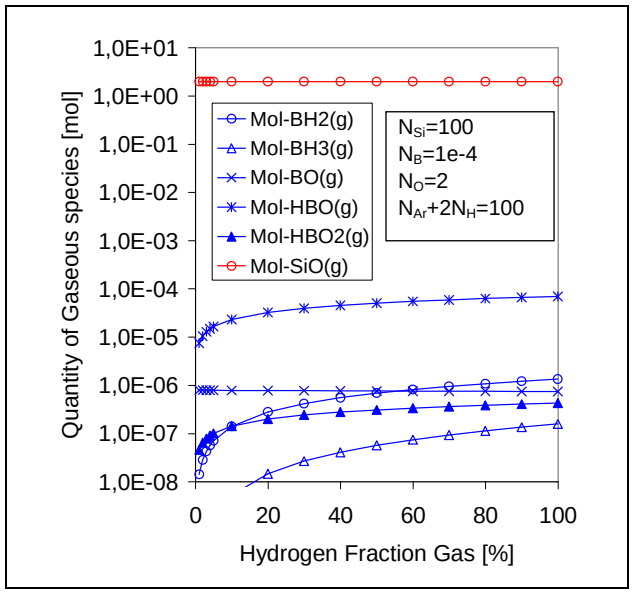

Figure II-16 Graphical representation of FactSage calculations of quantity of gaseous species vs hydrogen fraction in the H-Ar-O-Si-B system ([B]/[Si] ratio 10 ppma), T=1600 ℃

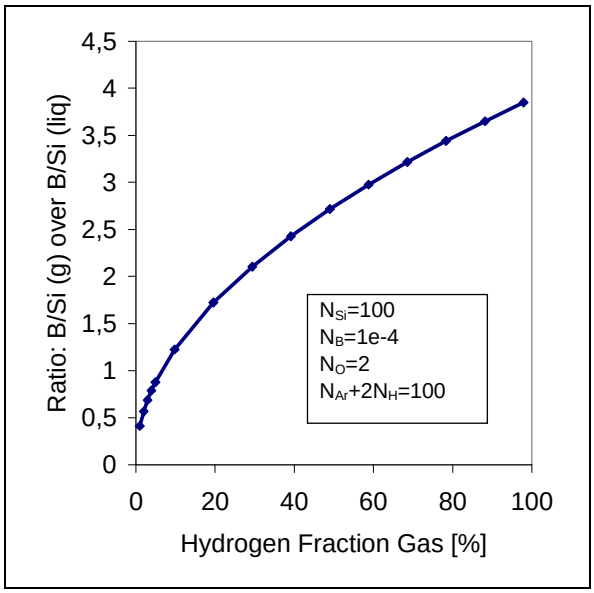

Figure II-17 The enrichement factor $R = \frac{[B(g)]}{[Si(g)]}\left(\frac{[B(l)]}{[Si(l)]}\right)^{-1}$ *vs the hydrogen fraction in the gas.*

Figure II-16 shows our results of FactSage calculations for different hydrogen concentrations. The calculations were done with 100 mol of silicon, 0.01 mol of boron (10 ppma), 1 mol of O_2 and 100 mol of Ar-H_2 mix with different Ar/H_2 ratios at 1600 ℃. We show only the major silicon and boron species. We ignore other species and boron and silicon species with lower concentrations. We verified that our results reproduces the results of Nordstrand represented in Figure II-15: At 96.8% H_2 and 1600 ℃ the ratio [HBO]/[SiO] is approximately $2.7 \cdot 10^{-5}$ in the calculation of Nordstrand and $3.5 \cdot 10^{-5}$ in our calculation. The database SiUP (Silicon Ultra Pure) that we used is thus equivalent to the database of [NT12] who used a priori the JANAF tables [JAN98]. We conclude this from a paper of the same group [TAN12]. The [HBO]/[SiO] ratio in our calculation is probably slightly higher because we used a higher activity of the boron: a=3.45 in our calculation and a=1 in [NT12]. One can see that the concentration of HBO increases with the hydrogen fraction, while the concentration of SiO remains constant. The Figure II-17 shows the enrichement factor R which is the ratio between the [B'(g)]/[Si'(g)] ratio in the gas phase and the [B(l)]/[Si(l)] ratio in the liquid phase (II-21). The total boron concentration in the gas phase [B'(g)] has been obtained by summing over all gaseous boron compounds (II-22) and is similar to the concentration of [HBO(g)]. The total silicon concentration in the gas phase [Si'(g)] has been obtained in the same manner and is similar to the concentration of [SiO(g)].

Enrichement Ratio: $$R = \frac{[B'(g)]}{[Si'(g)]}\left(\frac{[B(l)]}{[Si(l)]}\right)^{-1} \quad \textbf{(II-21)}$$

$$[B'(g)] = [HBO(g)] + [BO(g)] + [BH_2(g)] + [HBO_2(g)] + [BH_3(g)] \approx [HBO(g)] \quad \textbf{(II-22)}$$

This enrichement factor of the gas is smaller than one at low hydrogen fractions. This means that we should mainly remove the silicon from the Si/B mixture. However new chemical data give higher values as we will show later.

The strong increase of the enrichment factor with the hydrogen fraction explains why hydrogen improves the boron removal rate. The [B]/[Si] ratio in the gas phase is proportional to the sqare root of the hydrogen fraction. (The [B]/[Si] ratio in the liquid phase is constant).

This can be explained by the chemical equilibrium between the species SiO and HBO given by the reaction (II-23). The equilibrium constant of this reaction is given by equation (II-24). We combine equation (II-24) and (II-21) and obtain thus equation (II-25). Equation (II-25) shows that the enrichement factor R is proportional to the square root of the concentration of hydrogen, which is in turn proportional to the hydrogen fraction in the gas. As the concentration of SiO is independant of the hydrogen concentration, the concentration of HBO is proportional to square root of the hydrogen fraction in the gas. The concentration of HBO is also proportional to the [B(l)]/[Si(l)] ratio in the liquid phase, which explains the exponential decay of the boron concentration during purification

$$SiO(g) + B(l) + 0.5H_2(g) \leftrightarrow Si(l) + HBO(g) \quad \textbf{(II-23)}$$

$$K = \frac{[Si(l)][HBO(g)]}{[SiO(g)][B(l)][H_2(g)]^{0.5}} \quad \textbf{(II-24)}$$

$$R = K \times [H_2(g)]^{0.5} \quad \textbf{(II-25)}$$

II.4.1. Modification due to new formation enthalpy of HBO

The thermodynamic data used for the calculations in Figure II-15, Figure II-16 and Figure II-20 are probably not exact. Tang et al. [TAT12] found a formation enthalpy of HBO that was 31.1 kJ/mol lower than that used in the calculation and a formation entropy 0.3 J/mol/K higher. We can estimate the influence of this difference on the equilibrium by analyzing the equilibrium constant of the reaction that connects the two products of the global reactions SiO and HBO (II-26). In equation (II-27) we calculate the modification of the difference of the Gibbs energy of the reaction. ΔG^* is the value calculated with the new data, while ΔG is the value calculated with the old data. We see that at 1750 K the new ΔG^* is 31.6 kJ/mol/K smaller than the old ΔG.

$$SiO(g) + B(l) + 0.5H_2(g) \leftrightarrow Si(l) + HBO(g) \quad \textbf{(II-26)}$$

$$\Delta G^* = \Delta H^* - T\Delta S^* = \Delta G - 31.1kJ/mol - T\,0.3J/mol/K$$
$$\Delta G^*(1750K) = \Delta G - 31.6kJ/mol/K \quad \textbf{(II-27)}$$

The equilibrium constant K of the reaction (II-26) is given by equation (II-28)

$$K = \exp\left(\frac{-\Delta G}{RT}\right) = \frac{[Si(l)][HBO(g)]}{[SiO(g)][B(l)][H_2]^{0.5}} \quad \textbf{(II-28)}$$

$$K^*(1750K) = \exp\left(\frac{-\Delta G + 31.6kJ/mol}{RT}\right) = K\exp\left(\frac{31.6kJ/mol}{R \times 1750K}\right) = 8.8K \quad \textbf{(II-29)}$$

In equation(II-29) we compare the equilibrium constant K^* calculated with the new ΔG^* to the equilibrium constant K calculated with the old ΔG. The new equilibrium constant K^* is 8.8 times higher than the old equilibrium constant K. The enrichment factor R should be 8.8 times higher when the new data is used instead of the old data. While with the old data purification would have only been possible at a high hydrogen concentration, the new data show that it is also possible at lower concentrations. This modified data will be used in chapter VII to analyze our purification results.

II.5. Discussion of the chemical equilibrium

We use the measurements of Nordstrand et al. [NT12], Baba et al. [BHY95] and Imler et al. [IHL11] to compare them to chemical equilibrium calculations. Figure II-18 shows the dependence of the purification rate on the temperature. In the same graph we show the partial pressure of HBO in chemical equilibrium (taken from [NT12]). The very similar relative

variation of the purification rate and the partial pressure of HBO indicate that chemical reactions are in equilibrium at the interface, both with plasma [BHY95], [IHL11] and without plasma [NT12]. If the Boron purification rate was limited by chemical reactions, the increase of the temperature should lead to an increase of the purification rate because chemical reactions are typically faster at higher temperature (Arrhenius law). Furthermore, the diffusion coefficients in the gas phase increases with the temperature as $T^{1.5}$ (Chapman-Enskog theory), so that the variation of the diffusion fluxes remains small in the temperature range of the experiments.

We compare the measurement with different hydrogen fractions of [NT12] to chemical equilibrium. Figure II-19 shows the dependence of the purification rate from [NT12] on the hydrogen fraction in the gas and the partial pressure of HBO in chemical equilibrium, calculated before. The very similar curves of the purification rate and the partial pressure of HBO indicate that the chemical reactions are in equilibrium at the interface. It is very unlikely that the rate of the global reaction (II-30) is proportional to the square root of the hydrogen fraction as observed in the measurements.

The variation of the purification rate in dependence of the hydrogen fraction with plasma shown in Figure II-8 is however very different. This may be due to the influence of hydrogen on the velocity of the gas jet and thus the mass transfer. The study presented in Figure II-8 also used different setups so that there may also be other reasons for the difference to chemical equilibrium.

$$B(l) + H_2O(g) \rightarrow HBO(g) + 0.5H_2(g) \qquad \textbf{(II-30)}$$

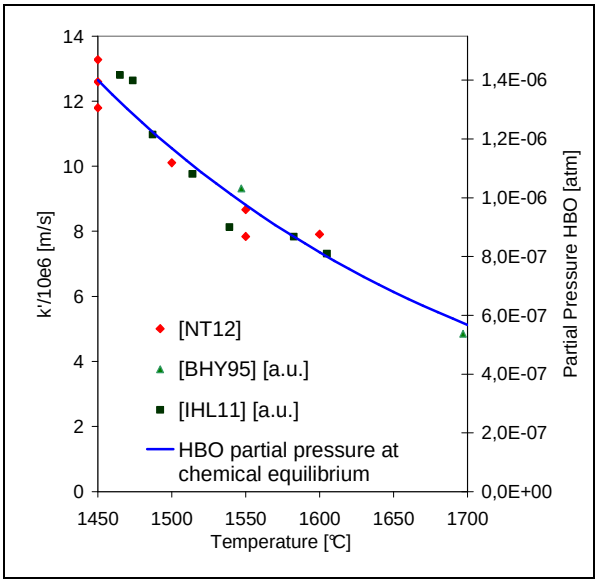

Figure II-18 The dependence of the partial pressure of HBO at chemical equilibrium and of the measured purification rate on the temperature. [NT12] without plasma, [BHY95] and [IHL11] with plasma

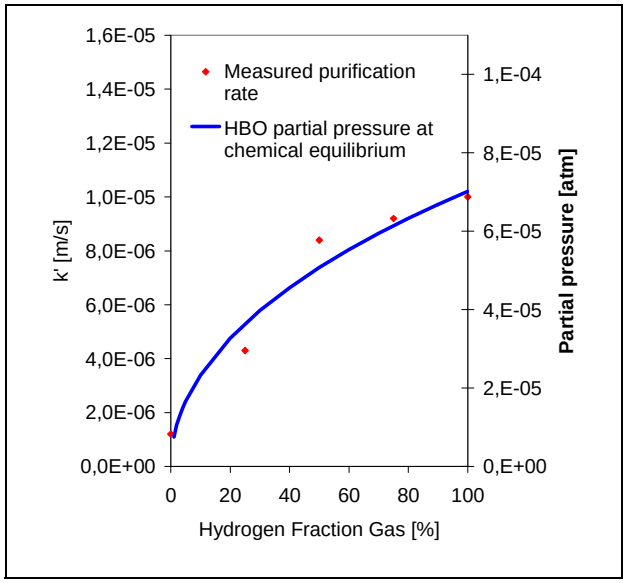

Figure II-19 The dependance of the partial pressure of HBO at chemical equilibrium and the measured purification rate [NT12] on the hydrogen fraction in the gas (without plasma)

Several authors ([NBS04], [Deg08], [NT12]) suggest that the chemical reactions are the rate limiting step. However, the strong influence of the hydrogen concentration and the temperature on the deboronization rate, which has been observed by different experimental studies, coincides with the thermodynamic calculation and is therefore in contradiction with this hypothesis.

We can thus conclude that the chemical reactions at the surface are probably at chemical equilibrium. As the chemical reactions at the surface are in equilibrium we can

assume that the reaction rates of the global reactions (II-31) and (II-32) and their inverse reactions are sufficiently fast so that they are not rate limiting.

$$Si + H_2O \rightarrow SiO + H_2 \quad \textbf{(II-31)}$$

$$B + H_2O \rightarrow HBO + 0.5H_2 \quad \textbf{(II-32)}$$

As the chemical reactions are in equilibrium the mass transfers of H_2O to the surface remains as rate limiting step.

II.5.1. Discussion of the role of radicals

In a process with plasma, the oxygen and hydrogen arrive partly in the form of radicals O and H at the silicon surface. While the radicals could have a big influence if the reaction between H_2O and boron was slow this is not the case if the reaction and the inverse reaction are fast. We can assume that the radicals that arrive at the silicon surface react immediately due to their high reactivity. As the reaction velocities are high the reaction products react also very fast so that system comes to the chemical equilibrium. It should thus not make a difference whether the oxygen and hydrogen arrive as radicals or whether they arrive in the form of H_2 and H_2O. The radicals that were believed to be important for the process are thus probably not important.

II.6. Chemical equilibrium in the boundary layer and SiO_2 formation

The evacuation of the reaction products does not play a role as long as the chemical reactions are rate limiting. However for chemical reactions in equilibrium the evacuation of the reactions products becomes important. For this reason we study the chemical equilibrium in the boundary layer.

At the silicon surface there is an excess of silicon so that all oxygen reacts to SiO. As there is an excess of silicon, the SiO_2 that is eventually created is reduced to SiO (if equilibrium conditions are reached and below a maximum partial pressure of SiO). Similar to the silicon oxidation model of Ratto that was described above, almost the whole boundary layer is oxidizing so that there is an excess of oxygen in the form of water vapour.

In the boundary layer, the absence of silicon in excess, changes significantly the concentrations in chemical equilibium as we can see in Figure II-20. The calculation of Figure II-20 was done using FactSage with 88 mol Ar, 4 mol H_2, 1 mol O_2, 0.1 mol Si and 10^{-4} mol B ([B]/[Si] ratio 1000 ppma, as sometimes reached in the exhaust gases of our facility). The small silicon and boron concentration should be representative at a point close to the bulk gas.

We show only the major species of boron and silicon in this graph and ignored species that have a much lower concentration.

- The major silicon specie at the silicon temperature (~1600℃±150℃) is the solid species SiO_2 which should condense to an aerosol. In hotter zones of the gas flow (when created by a plasma torch), the solid SiO_2 is reduced to gaseous SiO.
- The major boron specie is the gaseous BHO_2. In colder zones of the gas flow (when a cold gas is blown, or near cold walls), we get H_3BO_3.
- All silicon is oxidized
- All boron is oxidized

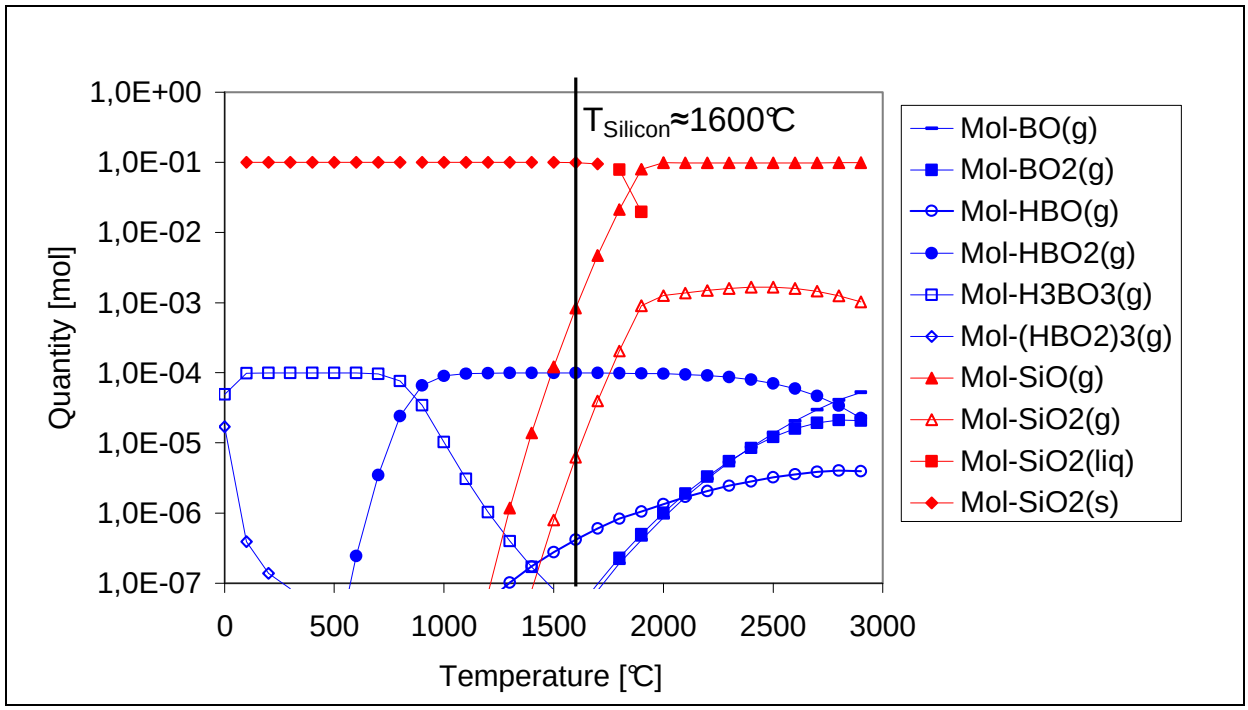

Figure II-20 Graphical representation of FactSage calculations of the amount of most important silicon and boron species vs temperature with a total amount of 88 mol Ar, 4 mol H_2, 1 mol O_2, 0.1 mol Si and 1e-4 mol B ([B]/[Si] ratio 1000 ppm)

As mentioned in part II.5 the [B]/[Si] ratio calculated at chemical equilibrium is about 10 times higher than the [B]/[Si] ratio in the liquid silicon. Looking at the thermodynamic calculation in the boundary layer we see that at the silicon temperature nearly all silicon is in the form of solid SiO_2, which should form an aerosol (as proposed by [RRA01]). This formation of a SiO_2 aerosol may modify the evacuation of the reaction products. As the diffusion of an aerosol is weaker than the diffusion of the gas H_2O, the total oxygen concentration at the surface may be higher than in the bulk gas. The weak diffusion of the aerosol may explain why the measured B/Si flux ratio that is evacuated is be higher than the [B]/[Si] concentration ratio at the surface (see chapter VII). In the following paragraph we study the formation of an aerosol in the boundary layer in more detail.

II.6.1. Aerosol formation in the boundary layer

Silica fumes are typically produced when an oxidizing gas is blown on liquid silicon. While this silica aerosol is probably formed in the boundary layer when the blown gas is cold, this is not so evident, when the hot gas (~9000 ℃) fro m the plasma is blown onto the silicon surface: in this case, the temperature increases rapidly with the distance from the silicon, which is unfavourable for the oxidation of SiO.

The equilibrium of the reaction $SiO(g) + H_2O(g) \leftrightarrow SiO_2(s) + H_2(g)$ is influenced by the concentration of hydrogen and the temperature. Figure II-21 shows the quantity of SiO_2 at chemical equilibrium in a system with 2 mol of SiO_2 and 96 mol Ar-H_2 mix in dependence of the hydrogen fraction for different temperatures. One can see that both hydrogen concentration and temperature play a role in the reduction of the SiO_2. Above 2500 ℃ no SiO_2 is present while below 1700 ℃ nearly all silicon is in the form of SiO_2. Between these two temperatures the hydrogen fraction influences the quantity of SiO_2. For a typical hydrogen fraction of 5 % most silicon is in the form of SiO_2 up to 2100 ℃.

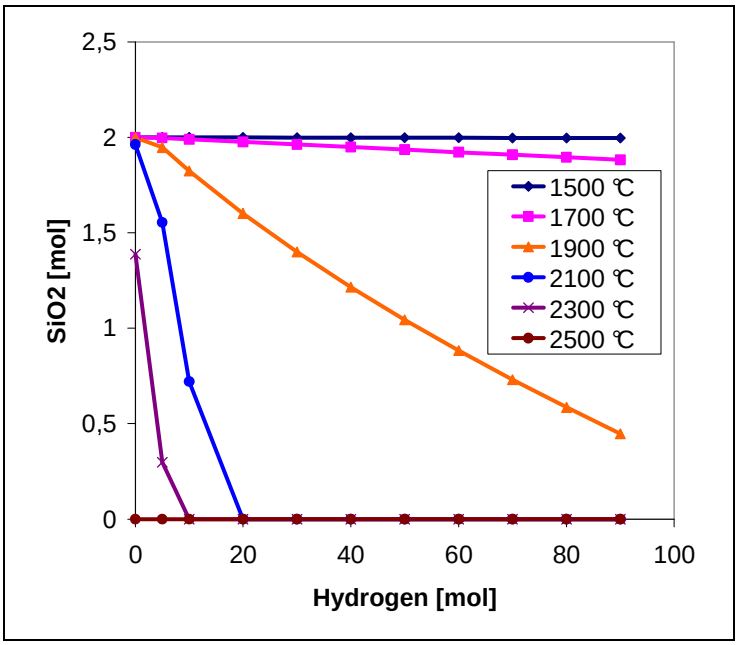

Figure II-21 Graphical representation of FactSage calculations of the amount of SiO_2 in a system with 2 mol Si, 3.5 mol O_2, 96-A mol Ar and A mol H_2 A varies from 0 to 90

Figure II-22 shows the temperature map and the mole fraction map of atomic oxygen with parameters that are typical for plasma gas blowing purification experiments. The parameters are presented in the same Figure. The black lines indicate the position of the concentration profile and temperature profile that are shown in Figure II-23. The data was simulated by S. Nosari during his internship, using a model similar to the model presented in [PDT10]. A concentration of 0 for oxygen species is defined as boundary condition at the silicon surface. This corresponds to a high reactivity of the silicon surface. The profiles were taken at distance of 20 mm from the centre of the crucible which is in the same axis as the plasma torch.

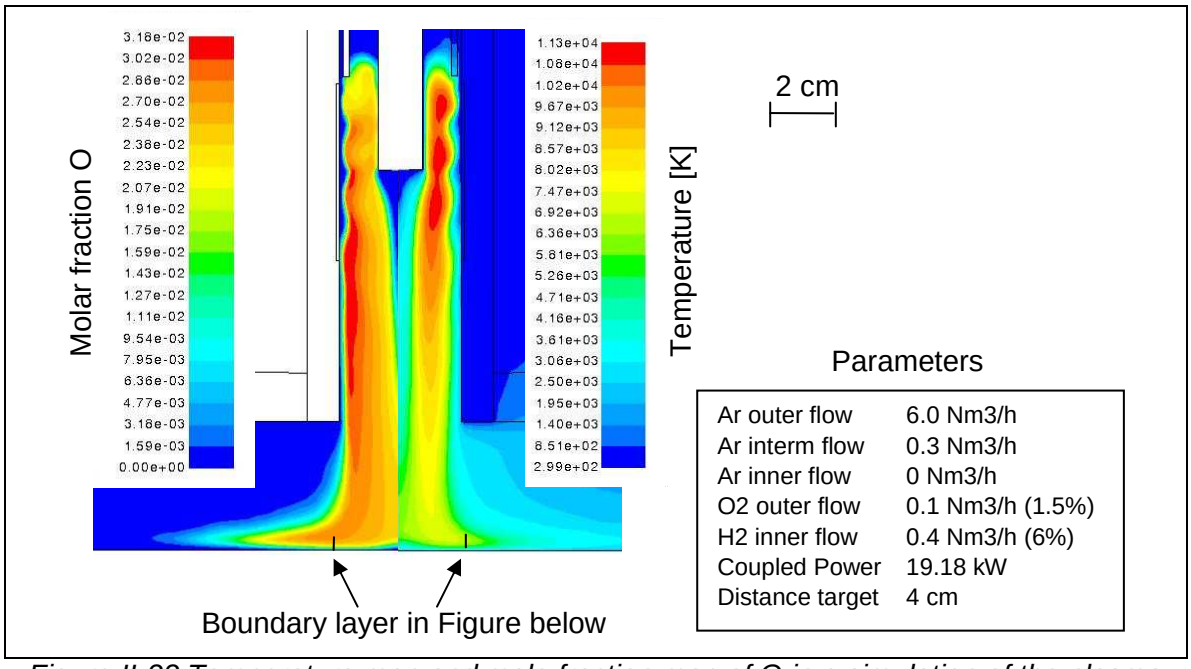

Figure II-22 Temperature map and mole fraction map of O in a simulation of the plasma gas blowing process

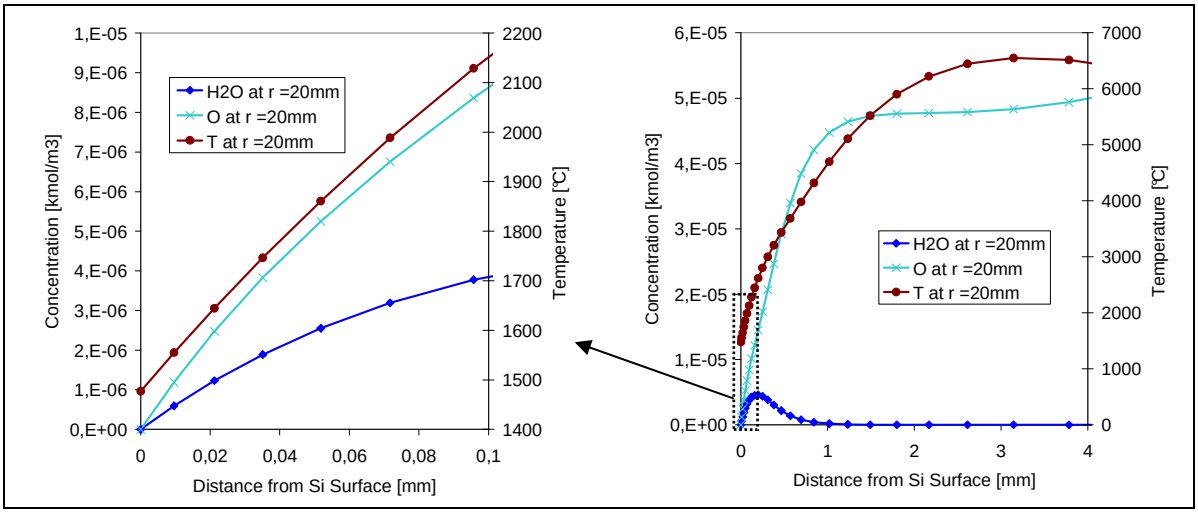

Figure II-23 The concentration and temperature profiles in the boundary layer of the plasma gas blowing process calculated with a numerical simulation

One can see that the thickness of the O boundary layer is about 1 mm and the thickness of the temperature boundary layer is about 2 mm. At a distance of 0.1 mm the temperature is higher than 2100 °C. The silica aerosol can thus on ly be formed in the thin layer of 0.1 mm.

We want to estimate if these 0.1 mm are thick enough to modify the mass transfer of the silicon. We use equation (II-10) to calculate the thickness of an aerosol boundary layer from the boundary layer of the oxygen boundary layer . We use a diffusion coefficient for the aerosol[i] of 0.0013 cm^2/s and a typical diffusion coefficient of a gas [Cus97] of 0.2 cm^2/s at 25 °C. The boundary layer of such an aerosol would thus be 20 % of the oxygen boundary

[i] Rudyak et al. [RDB09] measured a diffusion coefficient of an aerosol with Pt nanoparticles with a mean arithmetic diameter of 6.3 nm in nitrogen at 25°C to 0.0013 cm^2/s.

layer and thus be 200 µm thick (equation (II-33)). As the thickness of the layer, where the chemical equilibrium predicts an aerosol, is half of the thickness of the calculated boundary layer, this layer with aerosol may impact strongly the diffusion of silicon.

$$\delta_{aerosol} = \left(\frac{D_{aerosol}}{D_O} \right)^{\frac{1}{3}} \delta_O = 0.2 \times \delta_O \approx 200 \mu m \qquad \textbf{(II-33)}$$

For the average mass transfer coefficient k (m*s^{-1}) Cussler [Cus97] gives a formula that is proportional to the power to 2/3 of the diffusion coefficient. As the mass transfer rate $\dot{n}$ (mol.s^{-1}) of silicon is about half of the mass transfer rate of oxygen atoms, the total oxygen concentration at the surface increases with a lower mass transfer coefficient $k_{aerosol}$ of the silicon oxide (equation (II-35)). Equation (II-35) is equal for the mol number of SiO_2 aerosol particles and for the mol number of SiO_2.

$$k_{aerosol} = \left(\frac{D_{aerosol}}{D_{gaz}} \right)^{\frac{2}{3}} k_{gaz} = 0.16 \times k_{gaz} \qquad \textbf{(II-34)}$$

$$\Delta c_{aerosol} = \frac{j_{aerosol}}{k_{aerosol}} \qquad \textbf{(II-35)}$$

$$\Delta c_{SiO_2} = \frac{j_{SiO_2}}{k_{SiO_2}} \approx 6 \times \frac{j_{O_2}}{k_{O_2}} = 6 \times \Delta c_{O_2} \qquad \textbf{(II-36)}$$

j (mol.m^{-2}.s^{-1}) is the mass flux density

Δc (mol.m^{-3}) is the driving force concentration difference

If the aerosol would not dissociate at 0.1 mm it should lead to a six times higher total oxygen concentration (mainly SiO or SiO_2) at the silicon surface (II-36). A six times higher total oxygen concentration at the surface would mean that the evacuation of boron is six times faster. This approximation shows that the formation of an aerosol can significantly modify the rate of the purification process. Experimental results with plasma show an enrichment factor that is about ten times higher than the value calculated at chemical equilibrium (See chapter VII) and thus suggest that the slow diffusion of aerosol modifies the evacuated [B]/[Si] ratio. Another experiment that indicates an important role of the aerosol is the comparison between the oxidation of boron and silicon with oxygen from the silica plates of the crucible on the one hand and oxygen from the plasma on the other hand. The [B]/[Si] ratio is about ten times higher with the oxygen from the plasma (See chapter VII).

The size of the aerosol particles have a big influence on the diffusion coefficient and thus on the silicon oxide concentration at the surface. Quantitative predictions are therefore impossible with such a simplified model. However quantitative predictions of the evacuated [B]/[Si] ratio would be very important for the improvement of the. Therefore it is important to develop a numerical model that can simulate the role the formation of a SiO_2 aerosol on the evacuated [B]/[Si] ratio. Such a model should include the phenomenon nucleation, condensation, coagulation and diffusion of the aerosol and the flow regime. If the nucleation is very slow, supersaturation may occur so that the aerosol does not form. For the validation of the model experiments with well known flow conditions should be done. A model that takes into account nucleation, condensation and coagulation of the aerosol is difficult to handle. A first approximation could use a constant diffusion coefficient for the aerosol that is calculated from the size distribution of the particles that can be filtered from the exhaust gases. The size distribution can be measured with a scanning electron microscope [NTO12]. Such a model may be precise if the layer, where the aerosol particles grow, is thin compared to the diffusion boundary layer of the aerosol particles.

II.7. Conclusion

In this chapter we presented the mass transfer system and analyzed that the chemical reactions at the silicon surface are probably very fast so that they are not rate limiting. The mass transfer in the liquid is in general not rate limiting either due to inductive stirring or due to stirring by the gas flow. As the reactions are in chemical equilibrium the [B]/[Si] ratio in the gas phase can be calculated with programs that minimize the Gibbs free energy. The formation of a SiO_2 aerosol may modify the [B]/[Si] ratio that is evacuated from the surface due to the higher diffusion of gaseous HBO_2 compared to the solid or liquid SiO_2 aerosol. While the evacuated [B]/[Si] ratio depends probably on the chemical equilibrium and on characteristics of the SiO_2 aerosol, the total quantity of silicon that is oxidized and evacuated depends on the quantity of water vapour that arrives at the surface. If the oxidized silicon is not well evacuated from the surface an oxide layer forms which hinders the purification. In the following chapters we develop a method that allows characterizing the plasma of the purification process. We then use the results from the characterization to validate a computational fluid dynamic (CFD) model that can be used to better understand the purification process. In chapter VII purification experiments are compared to the theory developed in this chapter.

III. Spectroscopic techniques for the characterization of the plasma

III.1. Introduction

We have seen in chapter II that the characterization of the post-discharge zone is important for the understanding of the process. In this chapter we present the spectroscopic techniques that we used to characterize the plasma. First we look at the chemistry in the plasma and find that the gas temperature, the gas composition and the flow velocity are the parameters that are necessary to fully characterize the plasma. We then present the methods that we used to measure the temperature and the concentration ratios [H]/[Ar] and [O]/[Ar]. We present the line broadening mechanisms instrumental broadening, Stark broadening and Doppler broadening. The Stark broadening was used to measure the electron density and thus validate the temperature measurement. The simulation of the line profile is necessary to simplify the measurement of temperature and concentration ratios with a spectrometer with photomultiplier tube. The knowledge of the line profile allows us to calculate the total emissivity of a line from the spectral emissivity at the central wavelength.

III.2. Selection of the method

The objective of this study is to characterize the plasma torch. While for cold plasma torches the productivity of reactive species is an important parameter, this is not the case for a thermal plasma torch. Thermal plasma torches are close to chemical equilibrium because the reaction rates at high temperature and high pressure are high. This means that the concentration of each species is given by concentration of the elements and the temperature. In the post-discharge zone of an inductively coupled plasma, which is the zone that interacts with the silicon the temperature gradients are relatively low so that deviations from chemical equilibrium are small.

Figure III-1 shows the equilibrium concentration of the major species in a gas with the elements Ar, O and H. One can see in Figure III-1 that between 4000 K and 10000 K more than 90% of the oxygen and hydrogen atoms are in the form of atomic oxygen (O) and atomic hydrogen (H). From 4000 K to 2500 K the concentrations of O and H decrease while the concentrations of the molecules H_2O and H_2 increase. Below 2500 K more than 90% of oxygen and hydrogen are in form of the two molecules H_2O and H_2. OH has its highest concentration at 3200 K but even there its concentration is lower than those of O, H, H_2 and H_2O.

III.2.1. Chemical equilibrium of a Ar, H_2, O_2 plasma

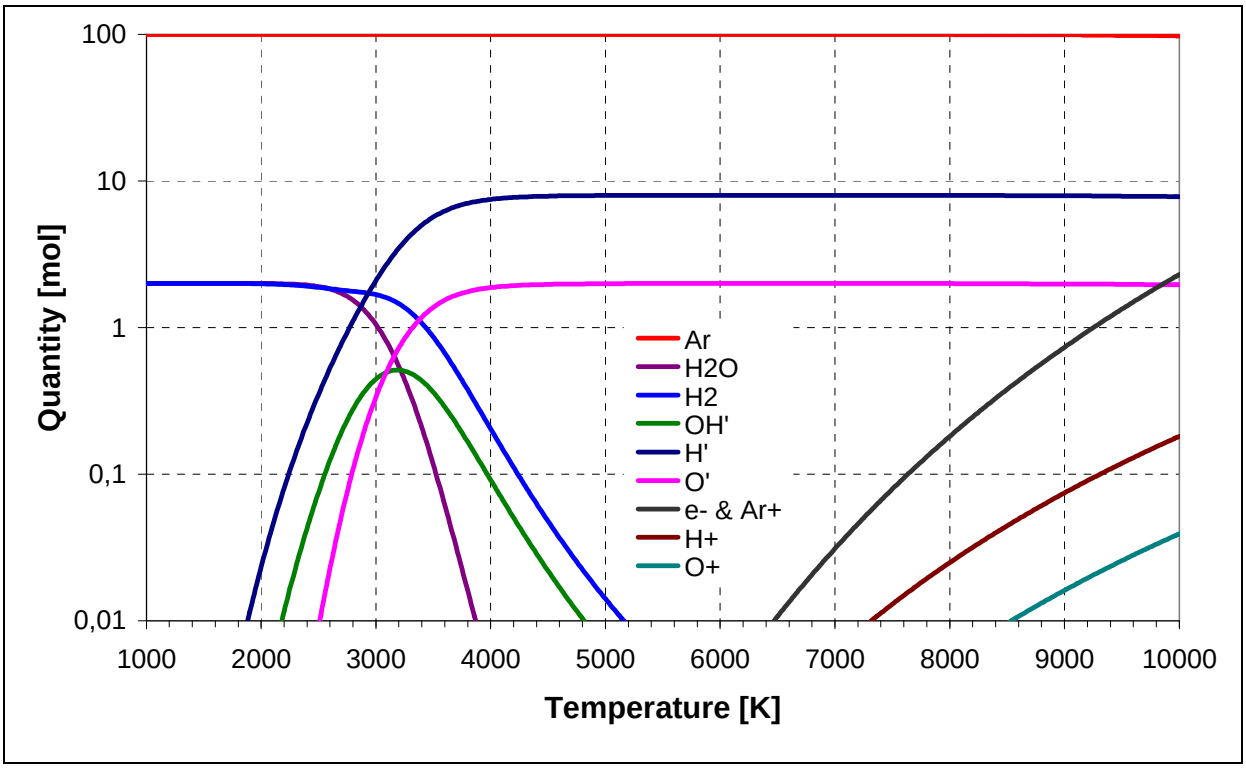

Figure III-1 Equilibrium concentrations. Calculation done with 100 mol Ar + 4 mol H_2 + 1 mol O_2

III.2.2. Deviations from chemical equilibrium in thermal plasma

Watanabe et al [WAS07] and Pelletier [Pel06] compared CFD models of inductively coupled plasma with and without chemical equilibrium. The small differences between the results with chemical equilibrium and the results without chemical equilibrium suggest that the plasma is close to chemical equilibrium. The analysis of the models also permitted to identify zones where deviations from chemical equilibrium occur. [WAS07] found higher concentrations of ions at the edge of the plasma in the induction zone when using a two temperature non-chemical equilibrium model. This model takes into account that the electrons have a higher temperature than the heavy particles because they absorb more energy from the electromagnetic field and because the energy transfer between heavy particles and electrons is small due to the big mass difference. [Pel06] found that deviations from chemical equilibrium occur in the boundary layer above the liquid silicon due to the strong temperature gradient. In his model the gas temperature above the boundary layer is between 4000 K and 8000 K, while the surface of the silicon is at 1680 K. The concentration of atomic oxygen at the surface is higher than in chemical equilibrium because it diffuses across the boundary layer. When we started this study it seemed that this deviation from equilibrium plays an important role. To our knowledge it is impossible to measure directly the flux of oxygen atoms to the surface. The best method that we found to determine the flux of radicals to the surface was to characterize precisely the post-discharge zone and to test so a numerical model similar to that of [Pel06] that can predict the flux of radicals towards the surface. In chapter II we showed that radicals do not play an important role. However the mass transfer of reactants to the surface is still important and needs a numerical model.

III.2.3. Different methods for the characterization of the post-discharge zone

As the parameters of the post discharge zone should have an important impact on the purification efficiency, this zone has to be investigated in details. The literature presented in the paragraph above indicates that this zone is close to chemical equilibrium so that we do not need to characterize the deviations from chemical equilibrium. The three parameters that are needed to fully describe the post discharge zone are the gas composition, the gas temperature and the flow velocity. As the measured temperature was between 6000 K and 10000 K, nearly all oxygen and hydrogen are in the atomic form. So the measurement of the ratios [O]/[Ar] and [H]/[Ar] is sufficient to determine the composition of the gas.

One method that can be used to characterize such a plasma is the enthalpy probe coupled to a mass spectrometer [Bou01] [Col11] [RSB95]. The enthalpy probe Figure III-2 a) is installed in the plasma. One can measure the gas composition and the enthalpy of a gas flow extracted with the enthalpy probe. The measurement of the pressure allows to calculate the velocity. The method can thus measure the temperature, the gas composition and the flow velocity of the gas. An inconvenience is that it is intrusive. In addition, the measurement with the enthalpy probe is slow and one can measure only one point at a time.

Two photon absorption laser induced fluorescence spectroscopy (TaLIF Figure III-2 b) can be used to measure concentration profiles of atomic oxygen and atomic hydrogen [BMB02] [NSG05]. In this method ground state atoms are excited by the absorption of two photons from the laser to a high level. The excited atoms then go to an intermediate level by the emission of a photon which is then measured perpendicular to the laser beam. The optical setup that measures the light can be focalized to different positions in the laser beam so that a high spatial resolution is possible. For absolute concentration measurements the setup can be calibrated with a known concentration of noble gas. At high temperatures the collisional quenching make the signal difficult to analyze because a big part of the excited atoms go to another level by collisional quenching instead of the emission of a photon. To our knowledge this method has not been applied for temperatures higher than 4000 K [BMB02]. It is thus not sure whether this method can precisely measure the concentrations at temperatures of about 10000 K and the method needs a very intense tunable laser with heavy maintenance and high costs. For these reasons we did not chose this method.

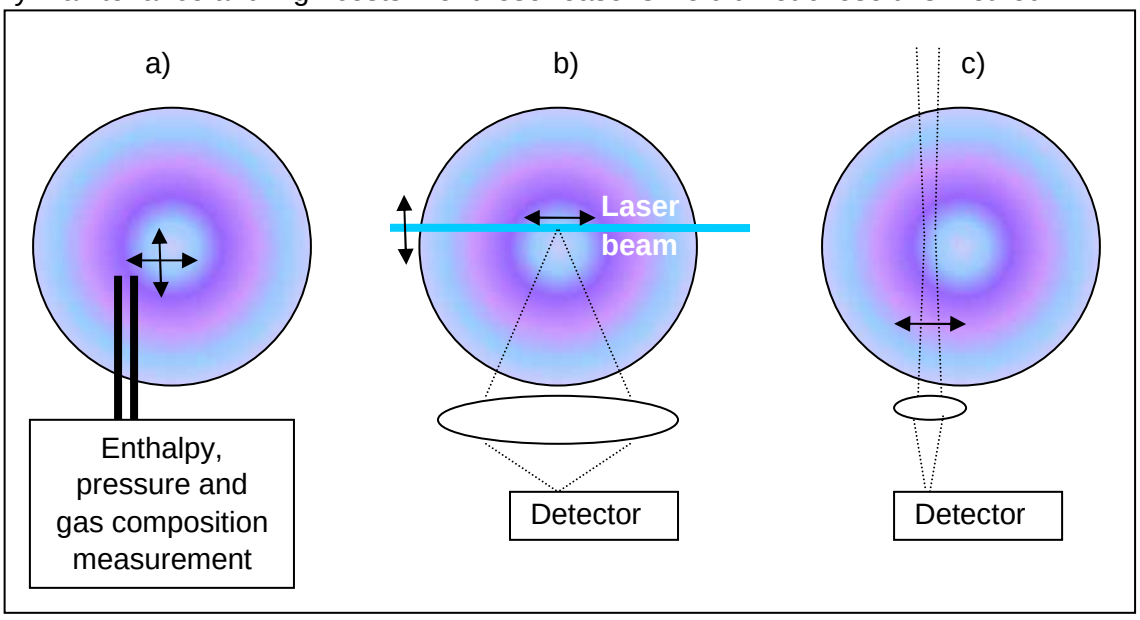

Figure III-2 Different methods for the characterization of a plasma
a) enthalpy probe, b) TaLIF c) emission spectroscopy

Atomic emission spectroscopy (AES Figure III-2 c) using Abel inversion is often used to measure temperature, electron densities and excited level densities, but only very few authors used it to measure total concentrations of an element. Kornblum et al. [KG77] and Buchner et al. [BFH97] used AES to measure the atomic density of Cu and Fe. Both used Abel inversion and line intensity ratios for the measurement of the temperature. Kornblum used the absolute intensity of a Fe line to calculate the total density of Fe and Buchner used the intensity ratio between a Cu line and an Ar line to calculate the total density of Cu.

Benmansour [Ben03] measured an Ar line, a Si line and a ionized Si line to determine the Si fraction in an inductively coupled plasma torch.

As one can measure only the light that comes out of the plasma the local emissivity can only be reconstructed with Abel inversion when the plasma is axially symmetric. The method works only for plasmas in local thermal equilibrium. We chose this method because it is easier to implement and allows sufficiently precise measurements of the gas composition in the temperature range of the studied plasma (6000 K-10000 K). In the following chapters we present the spectroscopic theory that we applied for the measurements.

III.3. Emissivity of atomic lines

Quantum mechanics requires that the electrons, which are bound to the nucleus, have defined energy levels. At the temperature T= 0 K the electrons are all in the lowest energy level. The atoms are in the ground state. At high temperature, collisions provide energy to the electrons so that they can get to higher energy levels. An atom in which the electrons are not only in the lowest energy levels is in an excited state. An atom in an excited energy state u can make a spontaneous transition to a lower energy state by emission of a photon, which takes the energy difference. Since the energies are discrete the wavelength is also discrete and the photons can be found in the spectrum as a spectral line. The probability of this transition is A_{ul} and the total emissivity of the transition is given by equation (III-1). A complete list of all symbols is given at the end of this chapter.

$$\varepsilon_{line} = \int_{line} \varepsilon(\lambda) d\lambda = n_u \times A_{ul} \frac{hc}{4\pi\lambda} \tag{III-1}$$

The emissivity is proportional to the concentration of the atoms in an excited state n_u.

When the concentration of the different energy states follow a Boltzmann distribution, the concentration of the atoms n_u in the excited state u with the energy E_u and the degeneracy g_u is given by equation (III-2), where $[X]$ is the total concentration of an element X. The partition function (III-3) is needed for normalization so that the sum of the concentrations of all energy states is equal to the concentration of the element.

Boltzmann distribution (discrete):

$$n_u = \frac{[X] \times g_u \times e^{-E_u / k_B T}}{Z(T)} \tag{III-2}$$

Partition function: $Z(T) = \sum_i g_i \times e^{-E_i / k_B T}$ (III-3)

The Boltzmann distribution is only valid in local thermal equilibrium. The validity of local thermal equilibrium and deviations from it are discussed in appendix A.

We obtain the emissivity from equations (III-1) and (III-2). It depends on two physical parameters:

- the concentration of the element
- the temperature of the plasma

$$\varepsilon_{line} = \frac{[X] \times g_u \times e^{-E_u / k_B T}}{Z(T)} \times A_{ul} \frac{hc}{4\pi\lambda} \qquad \text{(III-4)}$$

If we do not know the temperature we cannot calculate the concentration. Since we know the concentration of argon (its mole fraction is close to 100 %) we can measure the temperature using the emissivity of an argon line and the ideal gas law. Once we have measured the temperature, we can calculate the concentrations of other elements from the emissivity of a line of the element. The formulas are presented further down.

The transition probability A_{ul}, the Energy E_u, the wavelength λ and the degeneracy g_u are tabulated for many atomic lines on the website of the National Institute of Standards and Technology [nis]

III.3.1. The partition function

The partition function Z(T) normalizes the distribution so that the sum of the concentrations of all energy states is equal to the total concentration of the element. For the calculation of the partition function we need to know the energy states with a low energy. Table III-1 shows the summands of the partition function of oxygen at 10000 K as a sample calculation. The higher energy states above 10 eV have little influence on the partition function.

g_i	5	3	1	5	1
E_i [eV]	0	0,0196224	0,0281416	1,967364	4,189746
$g_i \times \exp(-E_i/(k_B * 10\,000K)$	5,00	2,93	0,97	0,51	0,01

Table III-1 Partition function of oxygen at 10000 K

$$Z(T = 10\,000K) = \sum_i g_i \times exp(-E_i/(k_B * 10\,000K)) = 5.00 + 2.93 + 0.97 + 0.51 + 0.01 = 9.42$$

The partition function of oxygen (see Figure III-3) is about 9 at 6000 K and varies with temperature. The energies of the first excited states of argon (11.5 eV) and hydrogen (10.2 eV) are very high compared to the highest temperature (10000 K ≡ 0.86 eV) in our plasma, so that the partition function for these two elements is approximately equal to the degeneracy of the ground state ($Z_{Ar} \approx g_{0,Ar} = 1, Z_H \approx g_{0,H} = 2$). This is because the number of atoms in an excited state is very small compared to the number of atoms in the ground state. Even at 10000K the partition functions of these two elements is very close to the degeneracy of the ground state: $Z_{Ar}(10000K) < 1.001$, $Z_H(10000K) < 2.001$

As the calculation of the partition function of oxygen costs calculation time we used two different methods to obtain the value of the partition function. In the first measurements we calculated the partition function of oxygen for several temperatures as shown in Figure III-3 and fitted a straight line. For the data processing we then used the straight line to calculate the partition function from the measured temperature. Later we calculated the partition function in 50 K steps and interpolated the value during the data processing.

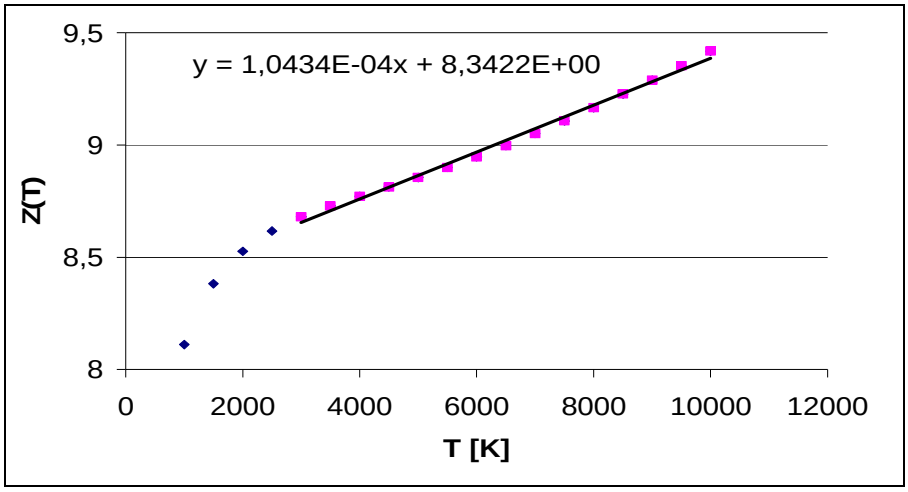

Figure III-3 Dependence of the partition function of oxygen on the temperature, $Z_{Ar} \approx g_{0,Ar} = 1$, $Z_H \approx g_{0,H} = 2$

III.4. Measurement of the temperature

There are several techniques that can be used to measure the temperature with optical emission spectroscopy. The intensity ratio method and the Boltzmann plot method use the intensity ratio of two or several lines. For these methods a relative calibration of the spectrometer is necessary. The absolute line intensity method needs an absolute calibration of the optical system.

III.4.1. Boltzmann plot

We rearrange equation (III-4) and obtain equation (III-5)

$$k_B \cdot \ln\left(\frac{4\pi\lambda}{hc}\frac{Z(T)\cdot\varepsilon_{line}}{g_u A_{ul}[X]}\right) = -E_u / T \qquad \text{(III-5)}$$

Equation (III-5) can be simplified by combining the constants in one new constant and obtain thus equation (III-6).

$$k_B \cdot \ln\left(\frac{\lambda\varepsilon_{line}}{g_u A_{ul}}\right) = -E_u / T + const. \qquad \text{(III-6)}$$

As we can see in equation (III-6), we can plot $k_B \cdot \ln\left(\frac{\lambda\varepsilon_{line}}{g_u A_{ul}}\right)$ against E_u to get $-\frac{1}{T}$ as slope. We can use so the emissivity of several lines and calculate the temperature with a linear regression. The difficulty of the method is to find lines with big energy differences in order to reduce the error from the measurement of the emissivity and the transition probabilities. The bigger the energy difference the smaller the impact on the slope. When the wavelengths of the two lines are far apart a relative calibration is necessary. Otherwise the wavelength dependant response of the optical setup would cause errors on the emissivity ratios.

III.4.2. Intensity ratio

The intensity ratio method is similar to the Boltzmann plot method but it uses only two lines. The temperature can thus be calculated without linear regression. Equation (III-4) can be used to calculate the emissivity of two different lines of the same element. Equation (III-7)

is obtained by dividing these two emissivities. We can rearrange equation (III-7) and obtain (III-8).

$$\frac{\varepsilon_{line,1}}{\varepsilon_{line,2}} = \frac{g_{u,1}A_{ul,1}\exp(-E_{u,1}/k_BT)}{g_{u,2}A_{ul,2}\exp(-E_{u,2}/k_BT)}\frac{\lambda_2}{\lambda_1} \quad \text{(III-7)}$$

$$T = \frac{E_{u,2}-E_{u,1}}{k_B \ln\left(\frac{g_{u,2}A_{ul,2}}{g_{u,1}A_{ul,1}}\frac{\lambda_1}{\lambda_2}\frac{\varepsilon_{line,1}}{\varepsilon_{line,2}}\right)} \quad \text{(III-8)}$$

III.4.3. Absolute line intensity method

While the absolute line intensity method needs an absolute calibration it has the advantage that an error on the intensity measurement has a smaller impact on the temperature evaluation. This can be explained by the fact that the absolute line intensity method is correspond to a Boltzmann plot between the ground state and one excited state. The energy difference is with 14.5 eV much higher than the maximum energy difference between two Ar lines 2.7eV.

Equation (III-4) can be rearranged to equation (III-9).

$$k_BT = \frac{-E_u}{\ln\left(\frac{Z(T)}{g_u[Ar]}\frac{\varepsilon_{line}4\pi\lambda}{A_{ul}hc}\right)} \quad \text{(III-9)}$$

The concentration of the other gases is very small compared to the concentration of argon whose molar fraction is between 70 and 100%. The concentration of argon atoms is therefore approximately equal to the total concentration of particles which depends on the temperature and can be calculated with the ideal gas law:

$$[Ar](T) = \frac{p}{k_BT} \quad \text{(III-10)}$$

The partition function is well approximated by $Z(T)=1$, as described above.

The total concentration $[Ar](T)$ depends on T. For the calculation of the temperature we have to estimate an initial temperature T_1 and then calculate T_2 using T_1. Then we calculate the next temperature T_{j+1} using the previous one T_j until it converges.

$$k_BT_{j+1} = \frac{-E_u}{\ln\left(\frac{1}{g_u[Ar](T_j)}\frac{\varepsilon_{line}4\pi\lambda}{A_{ul}hc}\right)} \quad \text{(III-11)}$$

The absolute line intensity method is a method that is often applied and has been compared to other measurements. Cao et al [CG95] compared the temperature measurement of absolute line intensity, boltzmann plot, hydrogen stark broadening and enthalpy probe in a DC plasma torch. He observed a good agreement above a minimum electron concentration of $1.3\text{x}10^{16}$ cm^{-3}. Chen et al [CHP94] and Pfender et al. [PFS91] observed that the absolute line intensity method gives a higher temperature than the enthalpy probe. They identified the diffusion of electrons due to the large temperature gradient and the entrainment of the cold air as reason for this difference. Mullen et al. [MNL88] compared the absolute line intensity method to the stark broadening method in an ICP and found a good agreement. Deviations were due to the underpopulation of the ground state as discussed in the appendix A. Regt et al. [RGM96] compared stark broadening, absolute line intensity and Thomson scattering and found a good agreement between the three methods. The comparison between the different methods found in literature shows that

the absolute line intensity method is an accurate method to measure the temperature. We therefore selected this method for the temperature measurements presented in this study.

III.5. Measurement of the concentration

Two methods for the measurement of the concentration can be used:

1) Using the total emissivity of a line: In local thermal equilibrium the total emissivity ε_{line} of a spectral line, which is emitted during a transition, depends on the concentration of the atoms and the temperature. If we know the temperature, we can calculate the total concentration of the atoms. Equation (III-4) can be rearranged to (III-12) which permits to calculate the absolute concentration of an element [X] from the absolute emissivity of an atomic line.

$$[X] = \frac{\varepsilon_{line} \cdot Z(T)}{A_{ul} \cdot g_u \cdot e^{-E_u / k_B T}} \cdot \frac{4\pi\lambda}{hc} \qquad \text{(III-12)}$$

2) Using the ratio between two lines:

We divide equation (III-12) for oxygen by the equation (III-12) for argon and obtain thus equation (III-13). With equation (III-13) we can calculate the concentration ratio [O]/[Ar] with the temperature and the ratio between the emissivity of an oxygen line and the emissivity of an argon line.

$$\frac{[O]}{[Ar]} = \frac{\varepsilon_{line,O}}{\varepsilon_{line,Ar}} \cdot \frac{\lambda_O \cdot g_{u,Ar} A_{ul,Ar}}{\lambda_{Ar} \cdot g_{u,O} A_{ul,O}} \cdot \frac{Z_O(T)}{Z_{Ar}(T)} \cdot \exp\left(\frac{E_{u,O} - E_{u,Ar}}{k_B T}\right) \qquad \text{(III-13)}$$

For multiplets (several lines with a similar wavelength and a similar energy) we can replace the factor $g_u A_{ul}$ in equation (III-13) by a sum $\sum_{multiplet} g_u A_{ul}$ and obtain thus equation (III-14).

$$\frac{[O]}{[Ar]} = \frac{\varepsilon_{line,O}}{\varepsilon_{line,Ar}} \cdot \frac{\lambda_O}{\lambda_{Ar}} \cdot \frac{g_{u,Ar} A_{ul,Ar}}{\sum_{multiplet} g_{u,O} A_{ul,O}} \cdot \frac{Z_O(T)}{Z_{Ar}(T)} \cdot \exp\left(\frac{E_{u,O} - E_{u,Ar}}{k_B T}\right) \qquad \text{(III-14)}$$

With the ratios [O]/[Ar] and [H]/[Ar] and the ideal gas law the total concentration can be calculated. In order to study the mixing of the elements and for the validation of a model the ratios [O]/[Ar] and [H]/[Ar] are sufficient. We therefore present in this manuscript the ratios [O]/[Ar] and [H]/[Ar] calculated with the two lines method.

III.6. The selection of the lines

CCD				PM
Low [O]/Ar	High [O]/Ar	Low [H]/Ar	High [H]/Ar	All
O 645.6 nm	O 645.6 nm	H 410.2 nm	H 410.2 nm	O 436.8 nm, H 486.1 nm
Ar 638.5 nm	Ar 641.6 nm	Ar 416.4 nm	Ar 415.9 nm	Ar 420.0 nm, 415.9 nm

Table III-2 The different sets of lines used for the concentration measurement (PM: Photomultiplier, CCD: CCD camera), Details in Table III-3

The atomic lines that we selected for the measurements are presented in Table III-2. With the spectrometer with photomultiplier tube we used always the same lines. With the spectrometer with CCD we used different lines for high and low [O]/[Ar] and [H]/[Ar]

The lines had to fit several criteria.

- The emission coefficient must be much higher than the emission coefficient of the continuum at the same wavelength. Otherwise the signal to noise ratio is too low. The noise is proportional to the square root of the total emissivity, while the signal is proportional to the difference between the total emissivity and the emissivity of the continuum.
- The emission coefficient must be lower than that of self-absorbed lines. Otherwise absorption would cause systematic errors. The comparison between the temperature measurement of an intense and a less intense line can show whether absorption causes errors.
- Interference with other atomic lines or molecular bands must be avoided. By looking at the tables of the atomic lines one can identify whether a line interferes with another line. Molecular bands can be detected during the measurement, as they are very intense at the edge of the plasma and less intense in the centre.

We used two different spectrometers in this study (see chapter IV). One spectrometer was equipped with a photomultiplier tube and one spectrometer was equipped with a CCD camera. The CCD camera has the advantage, that it can measure two atomic lines at the same time so that variations of the temperature have less influence on the measurement of the concentration ratio. The simultaneous measurement of two lines adds some additional criteria:

- The two lines used for the concentration measurement must have similar intensities because otherwise the signal of the less intense line would be too low.
- The two lines must be in the spectral bandwidth of the CCD so that they can be measured at the same time. At the same time one should use the smallest possible spectral bandwidth (grating with high groove density), so that the line is wider on the CCD and the dynamic of the total line intensity is higher.

For the measurement with the photomultiplier tube we used the argon lines at 420.0 nm and 415.9 nm, the oxygen multiplet at 436.8 nm and the hydrogen multiplet H-Beta at 486.1 nm.

As the intensity is proportional to the concentration, different argon lines with different emission coefficients were used for the measurements of low concentration ratios and high concentration ratios. We chose the oxygen mutliplet at 645.6 nm together with the argon line at 638.5 nm for low concentration ratios [O]/[Ar] and with the argon line at 641.6 nm for high concentration ratios [O]/[Ar]. We chose the hydrogen multiplet H-Delta at 410.2 nm together with the argon line at 416.4 nm for low concentration ratios [H]/[Ar] and with the argon line at 415.9 nm for high concentration ratios [H]/[Ar].

Table III-3 shows the data that is necessary for the calculation of the temperature and the concentration.

	λ [nm]	E_u [eV]	A_{ul} [s^{-1}]	$\frac{\Delta A_{ul}}{A_{ul}}$	g_u	$g_u A_{ul}$ [s^{-1}]	configurations	$\sum_{multiplet} g_u A_{ul}$ [s^{-1}]
Ar	415,859	14,5289126	1,40E+06	25%	5	7,00E+06	$5p_2$-$4s_2$	7,00E+06
Ar	416,418	14,5249124	2,88E+05	25%	3	8,64E+05	$5p_2$-$4s_1$	8,64E+05
Ar	420,068	14,4990527	9,67E+05	25%	7	6,77E+06	$5p_3$-$4s_2$	6,77E+06
Ar	638,472	14,8483681	4,21E+05	25%	3	1,26E+06	$6s_1$-$4p_1$	1,26E+06
Ar	641,631	14,8388101	1,16E+06	25%	5	5,80E+06	$6s_2$-$4p_1$	5,80E+06
H	410,170	13,2207023	4,29E+06	0.3%	4	1,72E+07	$6d_{3/2}$-$2p_{1/2}$	7,01E+07
	410,170	13,2207008	2,45E+05	0.3%	2	4,90E+05	$6s_{1/2}$-$2p_{1/2}$	
	410,171	13,2207023	2,86E+06	0.3%	4	1,14E+07	$6p_{3/2}$-$2s_{1/2}$	
	410,171	13,2207006	2,86E+06	0.3%	2	5,72E+06	$6p_{1/2}$-$2s_{1/2}$	
	410,176	13,2207023	5,15E+06	0.3%	6	3,09E+07	$6d_{5/2}$-$2p_{3/2}$	
	410,176	13,2207008	8,57E+05	0.3%	4	3,43E+06	$6d_{3/2}$-$2p_{3/2}$	
	410,177	13,2207008	4,90E+05	0.3%	2	9,80E+05	$6s_{1/2}$-$2p_{3/2}$	
H	486,128	12,7485375	1,72E+07	0.3%	4	6,87E+07	$4d_{3/2}$-$2p_{1/2}$	2,70E+08
	486,129	12,7485324	8,59E+05	0.3%	2	1,72E+06	$4s_{1/2}$-$2s_{1/2}$	
	486,129	12,7485375	9,67E+06	0.3%	4	3,87E+07	$4p_{3/2}$-$2s_{1/2}$	
	486,130	12,7485319	9,67E+06	0.3%	2	1,93E+07	$4p_{1/2}$-$2s_{1/2}$	
	486,136	12,7485394	2,06E+07	0.3%	6	1,24E+08	$4d_{5/2}$-$2p_{3/2}$	
	486,137	12,7485324	1,72E+06	0.3%	2	3,44E+06	$4s_{1/2}$-$2p_{3/2}$	
	486,137	12,7485375	3,44E+06	0.3%	4	1,37E+07	$4d_{3/2}$-$2p_{3/2}$	
O	436,819	12,358906	7,56E+05	10%	1	7,56E+05	$4p_0$-$3s_1$	6.83E+06
	436,824	12,358874	7,59E+05	10%	5	3,80E+06	$4p_2$-$3s_1$	
	436,826	12,358864	7,58E+05	10%	3	2,27E+06	$4p_1$-$3s_1$	
O	645,360	12,6608561	1,65E+06	18%	5	8,25E+06	$5s_2$-$3p_1$	4,13E+07
	645,444	12,6608561	2,75E+06	18%	5	1,38E+07	$5s_2$-$3p_2$	
	645,598	12,6608561	3,85E+06	18%	5	1,93E+07	$5s_2$-$3p_3$	

Table III-3 The data of the lines that were used in this study (Source [nis])

III.7. Calculation of the electron density using the Saha equation

In the paragraphs above we have presented the formula and the data that is necessary for the calculation of the temperature and the concentration ratios O/Ar and H/Ar from the measured emissivity of the lines. The calculation of the electron density can be used on the one hand to simulate the line profile with the theory of line broadening that is presented later. On the other hand the electron density measured with the line broadening can be compared to the calculated electron density and thus validate the temperature measurement.

In local thermal equilibrium the concentrations of ions, electrons and neutral atoms are in equilibrium. The Saha ionization equation (III-15) gives the ratio between two consecutive ionization stages with an ionization energy χ_Z (eV).

Z counts the ionization stages

n_0 (m-3) is the neutral atom density, n_1 (m-3) the singly ionized atom density and so on

n_e (m-3) is the electron density

$Z_Z(T)$ is the partition function of the ionization stage Z.

$$\frac{n_{Z+1}n_e}{n_Z} = 2\frac{Z_{Z+1}(T)}{Z_Z(T)}\frac{(2\pi m_e k_B T)^{3/2}}{h^3} exp\left(\frac{-\chi_Z}{k_B T}\right) \quad \text{(III-15)}$$

$$n_e \approx \sqrt{n_{tot} 2\frac{Z_{ion}(T)}{Z_{atom}(T)}\frac{(2\pi m_e k_B T)^{3/2}}{h^3}\exp\left(\frac{-\chi_1}{k_B T}\right)} \quad \text{(III-16)}$$

For argon at atmospheric pressure and 10000 K we can use the following assumptions:

- small degree of ionization $n_0 = n_{tot}$
- insignificant concentrations of multiply ionized ions $n_{z>1} = 0$
- quasineutrality $n_e = n_1$.

With these assumptions, the equation can be simplified to equation (III-16). The total density of particles n_{tot} (m^{-3}) can be calculated with the ideal gas law. χ_1 is the ionization energy of the ground state atom, which is 15.76 eV for Argon. When different elements with different ionization energies are in the plasma equation (III-16) is not valid because the electrons that are liberated by one element modify the equilibrium of the other elements. We assume that the number of electrons liberated by hydrogen and oxygen in our plasma is small compared to the number of electrons liberated by argon so that the equilibrium between argon atoms, argon ions and electrons is not modified and equation (III-16) remains valid. The ratio between the partition function of the ions and that of the ground state atoms is $Z_{ion}(T)/Z_{atom}(T) = 5.6$ at 10000 K and varies little with temperature. (5.59 at 9000 K and 5.63 at 10000 K.

At high electron densities the Debye shielding reduces the ionization energy. The Debye shielding describes the phenomenon that the electrons are attracted by the ions and thus shield their electric field. As the electrons are close to the ions they are at lower potential than when they where far from the ions. The ionization energy, which is the energy difference between a bound electron and an electron close to an ion, is thus lower. The reduction of the ionization energy $\Delta\chi$ (eV) can be calculated with equation (III-17). The Debye radius ρ_D (m) is given by equation (III-18).

$$\Delta\chi = \frac{e^2}{4\pi\varepsilon_0\rho_D} \quad \text{(III-17)}$$

$$\rho_D = \frac{\varepsilon_0 k_B T}{2e^2 n_e} \quad \text{(III-18)}$$

Without the Debye shielding the electron density would be in pure Argon at 10000K $n_e = 1.51\times10^{16}\,cm^{-3}$. At this electron density we can calculate the Debye radius $\rho_D = 39nm$ and the reduction of the ionization energy $\Delta\chi = 0.038eV$. The real electron density is thus $n_e = 1.55\times10^{16}\,cm^{-3}$. The neglecting of the Debye shielding would thus induce only a small error of 3% on the electron density. Figure III-4 shows the electron density calculated with the Saha-equation (III-16) taking into account the Debye shielding.

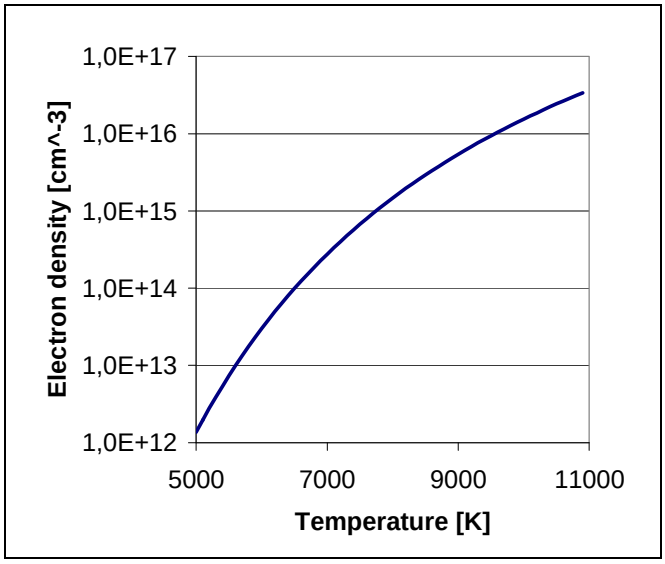

Figure III-4 Plot of the electron density calculated with the Saha-Equation for an Argon plasma

III.8. The broadening mechanisms

The knowledge of the different broadening mechanisms is necessary for two different measurements

For the measurement of the electron density using the line broadening we need to know the different sources of line broadening and the relation between line broadening and the electron density.

For the measurement of the [O]/[Ar] ratio or the [H]/[Ar] ratio with the monochromator with the photomultiplier tube the simulation of the line broadening is necessary to calculate the total emissivity of the line from the emissivity at the central wavelength.

The most important broadening mechanisms in plasma are Doppler broadening and Stark broadening. These broadening mechanisms are stronger for the hydrogen lines, than for the argon and oxygen lines. The monochromator adds instrumental broadening to the line profile. We show that instrumental broadening is the only significant broadening mechanism for the measurement of the argon and oxygen lines, while Doppler broadening and Stark broadening are significant for the hydrogen line.

III.8.1. Instrumental broadening

The instrumental broadening is very important for the simulation of spectra or for the measurement of line widths. It is often determined from the linear dispersion and the slit width. Another approach is to measure the broadening of a spectral line emitted from a low pressure discharge lamp. In such a source, especially in hollow cathode lamps, the Stark broadening is negligible and the Doppler broadening, due to the low gas temperature, is very weak so that the measured profile is very close to the spread function of the monochromator. Here we present a detailed simulation of the spread function of the monochromator. The formula were taken from the paper of Trassy et al. [TT98]

Simulating the spread function of the monochromator

The spread function of an ideal monochromator would be a dirac function so that the measured spectrum would be equal to the real spectrum. But a real monochromator adds instrumental broadening to the real spectrum.

Figure III-5 shows the sketch of a monochromator of the Czerny-Turner type. The light that enters through the entry slit is reflected by the convex mirror a) towards the grating b). The distance between the mirror and the entry slit is equal to the focal length of the mirror so that the light is reflected parallel and illuminates the whole grating. The grating reflects the light towards the second mirror c) which images the light on the CCD or on the exit slit. The angle at which the light is reflected depends on the wavelength and on the angle of the grating. The light is thus separated. In Figure III-5 the blue lines represent the light with a slightly lower wavelength and the red lines represent the light with a slightly higher wavelength. The signal on the CCD represents thus the signal of different wavelengths. In order to measure a spectrum with a photomultiplier tube, one has to turn the grating stepwise and measure the signal after each step.

For monochromators with a photomultiplier tube one uses generally spherical mirrors. Using curved slits one can thus obtain a high spectral resolution. When using CCD camera best performance can be obtained with an imaging spectrometer. The imaging spectrometer has toroidal mirrors so that the focal plane is flat and the spectral and spatial resolution is high all over the CCD. The toroidal mirrors have a different focal length in the axis that is perpendicular to the entry slit than in the axis that is parallel to the entry slit.

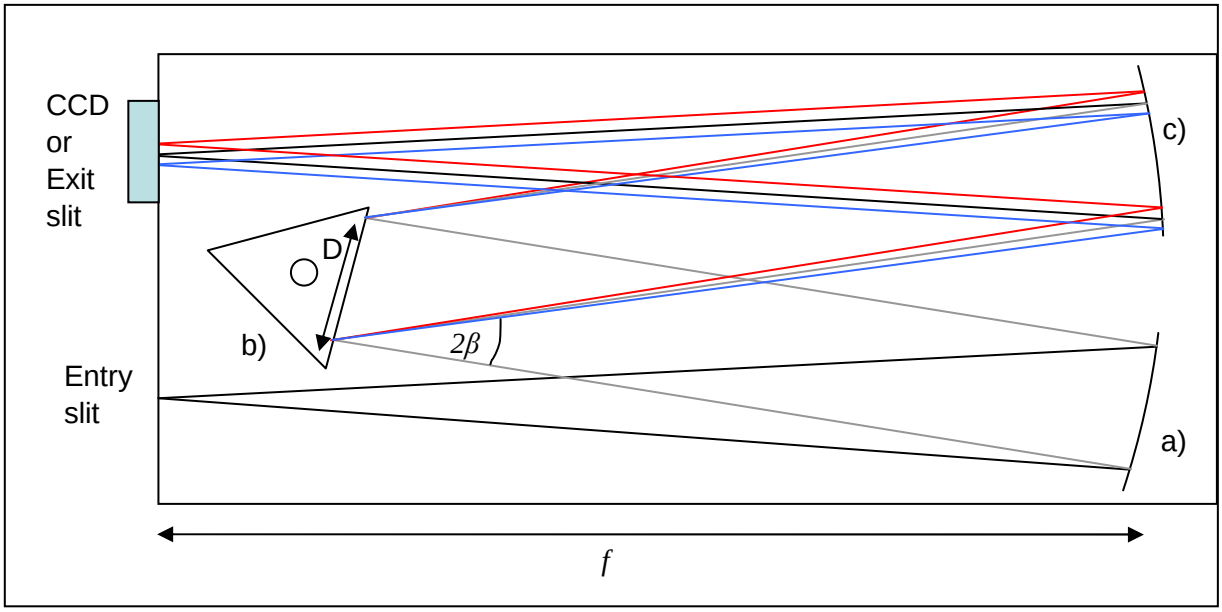

Figure III-5 Scheme of the monochromator of the type Czerny-Turner
a) convex mirrors, b) Grating, c) convex mirror

The measured spectrum is then the convolution of the real spectrum and the spread function of the monochromator. The spread function is determined by the broadening of the grating, the slits and the optical aberrations. The broadening due to optical aberrations is very small and is difficult to take into account because it is very sensitive to the alignment of the slits, the mirrors and the grating. An example for the calculation of the aberrations can be found in the paper of Gil [GS83]. For the simulation of the spread function we calculate therefore only the broadening due to the slits and the broadening due to the grating.

Calculating the dispersion of the monochromator

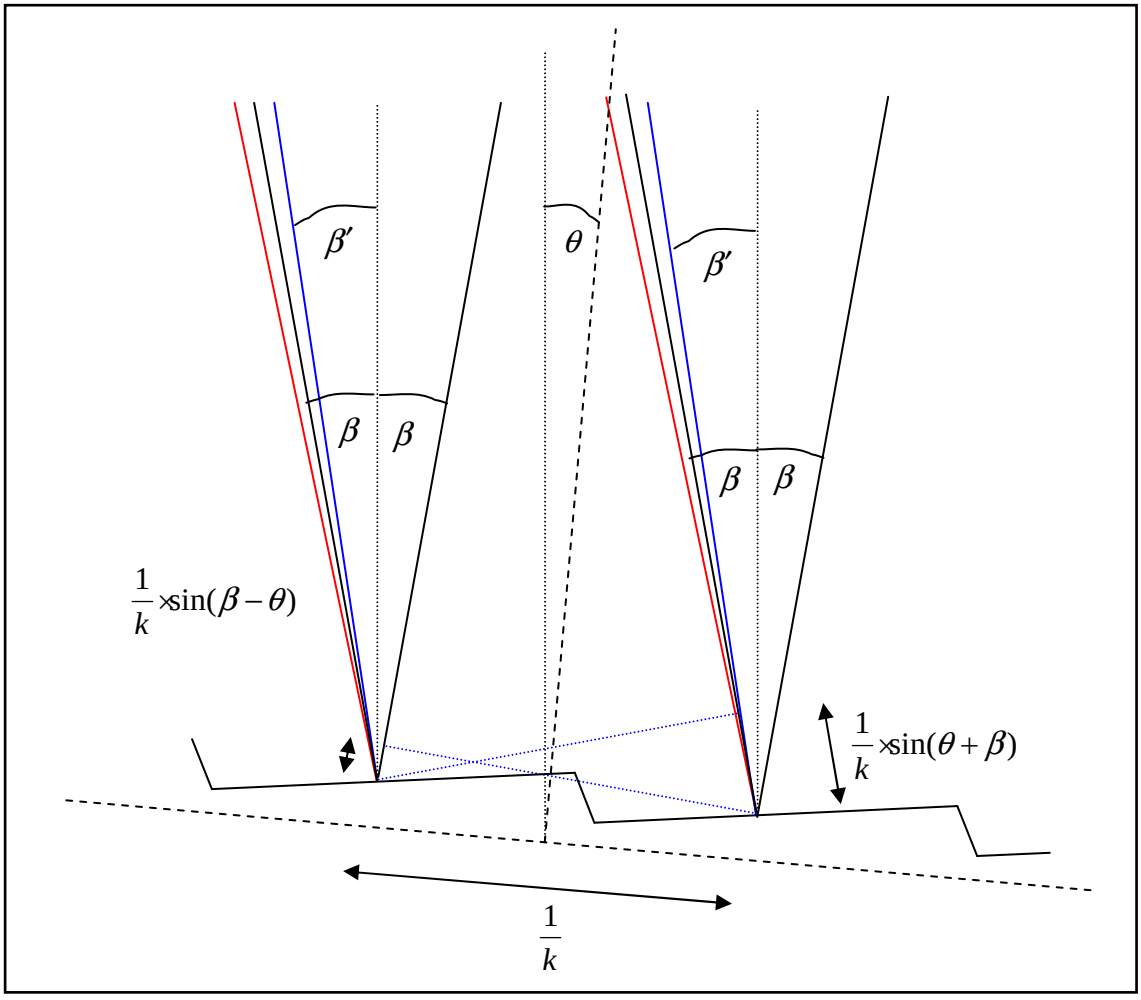

Figure III-6 Scheme of the path difference between two lines of the grating

Figure III-6 shows how the grating reflects the light. The path difference between the light that is reflected by two adjacent grooves is given by equation (III-19). k is the groove density, θ is the angle of the grating and 2β is the inclusion angle of the grating as shown in Figure III-5. Only when the path difference given by equation (III-19) is a multiple of the wavelength the light interference is constructive. For all other wavelengths the light interference is destructive. Equation (III-19) can be used to calculate the angle of the grating for a given wavelength.

$$\Delta x = \frac{1}{k} \times (\sin(\theta + \beta) - \sin(\theta - \beta)) = n\lambda \qquad \text{(III-19)}$$

For the blue line in Figure III-5 the path difference is slightly different (Equation (III-20))

$$\Delta x = \frac{1}{k} \times (\sin(\theta + \beta') - \sin(\theta - \beta)) = n\lambda \qquad \text{(III-20)}$$

The derivation of the wavelength with respect to the angle β' is then

$$\frac{d\lambda}{d\beta'} = \frac{1}{kn}\cos(\theta + \beta') \qquad \text{(III-21)}$$

By using the relation $d\beta'/dx = 1/f$ we obtain thus the dispersion on the CCD (Equation (III-22))

$$\frac{d\lambda}{dx} = \frac{1}{knf}\cos(\theta + \beta') \approx \frac{1}{knf}\cos(\theta + \beta) \qquad \text{(III-22)}$$

We use equation (III-19) and equation (III-22) to calculate the dispersion of the monochromator Acton SP2756.(f=750 mm, k=1800 mm^{-1}, β=6.49°) at a wavelength of λ=415 nm. We obtain θ=22.1° for the angle of the grating and $d\lambda / dx = 6.505 \times 10^{-7}$ for the dispersion . The measured dispersion between two atomic lines is 0.4% lower.

The spread function of the slits

The spread functions of the slits are rectangular. The width of the rectangles in the wavelength space is given by the product of the dispersion and the width of the slits. However the dispersion for the entry slit is different than for the exit slit so that we obtain equation (III-23) and (III-24) for the width of the spread function of the entry slit and the exit slit respectively. Δx_{entry} and Δx_{exit} are the slit widths. For a monochromator with a CCD camera the width of the exit slit is replaced by the width of a pixel of the CCD.

$$\Delta\lambda = \frac{d\lambda}{dx_{entry}}\Delta x_{entry} = \frac{\cos(\theta - \beta)}{knf}\Delta x_{entry} \qquad \text{(III-23)}$$

$$\Delta\lambda = \frac{d\lambda}{dx_{entry}}\Delta x_{exit} = \frac{\cos(\theta + \beta)}{knf}\Delta x_{exit} \qquad \text{(III-24)}$$

The spread function of the grating

The spread function of the grating is due to the interference of the light from the different grooves of the grating. At the center wavelength all grooves interfere constructively and the amplitude of the light is the sum of all amplitudes and therefore maximum. At a wavelength near to the center wavelength there is a small phase shift between the amplitude from the different grooves so that the amplitude is only a fraction of the maximum amplitude. Far from the center wavelength the phase shift is so big that the interference is destructive and the amplitude is close to zero.

$$I(\Delta\lambda) = I_0 \frac{\sin^2\left(\pi \times N \times \Delta\lambda / \lambda_0\right)}{\left(N \times \Delta\lambda / \lambda_0\right)^2} \quad \text{with } \Delta\lambda = \lambda - \lambda_0 \qquad \text{(III-25)}$$

Equation (III-25) gives the spread function of the grating. Its width depends only on the number of grooves of the grating N . In general for a monochromator the groove density k and the width of the grating D are given so that the number of grooves can be calculated with $N = k \cdot D$. When only small part of the grating is illuminated the number of grooves is reduced so that the spread function gets wider. Figure III-7 shows the spread function of a grating.

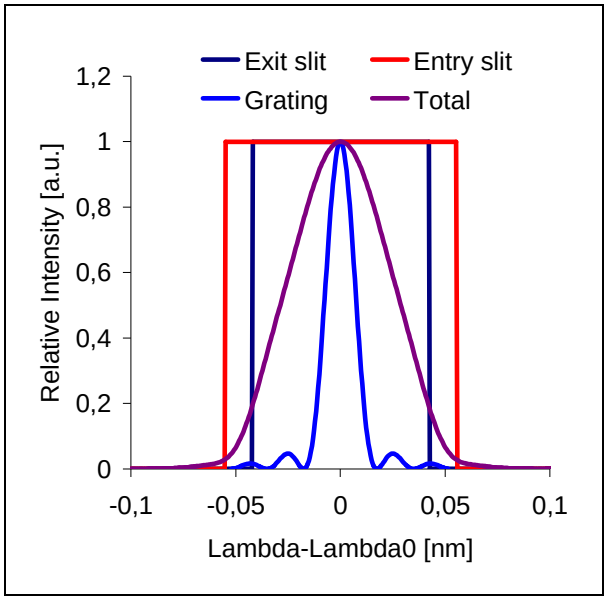

Figure III-7 Simulated spread function of the HR 640 using: f=640 mm, Slit widths= 90 µm, k=2400 mm^{-1}, D=10 mm, λ=420 nm, β=13.2°

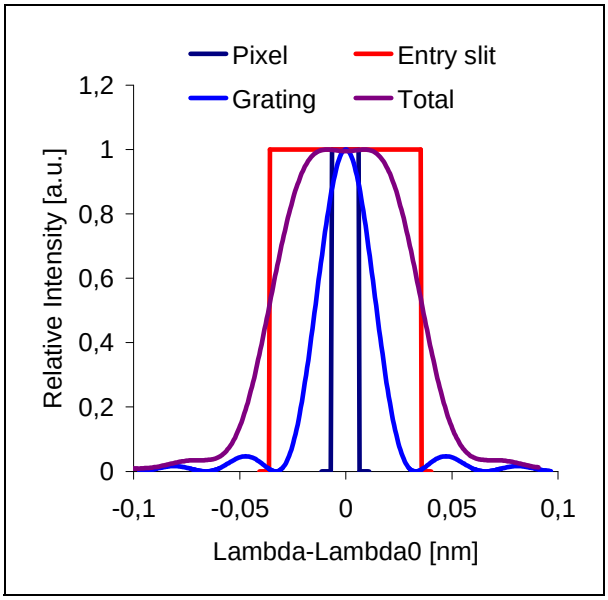

Figure III-8 Simulated spread function of the SP2756 using: f=750 mm, Pixel width = 20 µm, Entry slit width= 90 µm, k=1800 mm^{-1}, D=7 mm, λ=415 nm, β=6.49°

III.8.2. The spread function of the Jobin Yvon HR 640

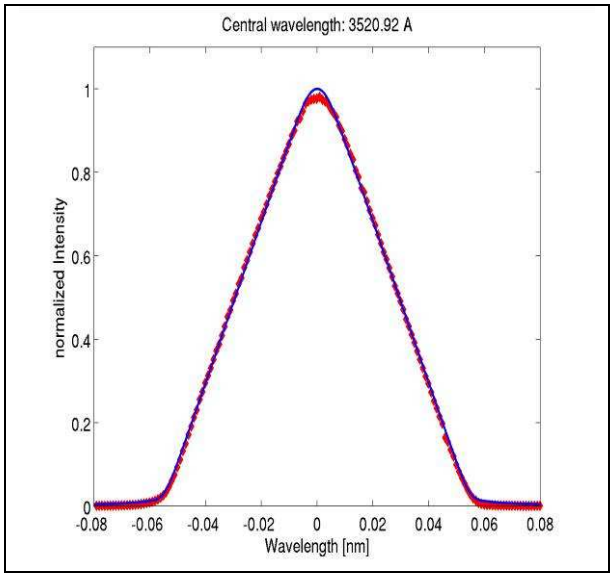

Figure III-9 Measured and simulated spectra at 352.1 nm f=640 mm, Slit widths= 90 µm, k=2400 mm^{-1}, D=10 mm, β=13.2°

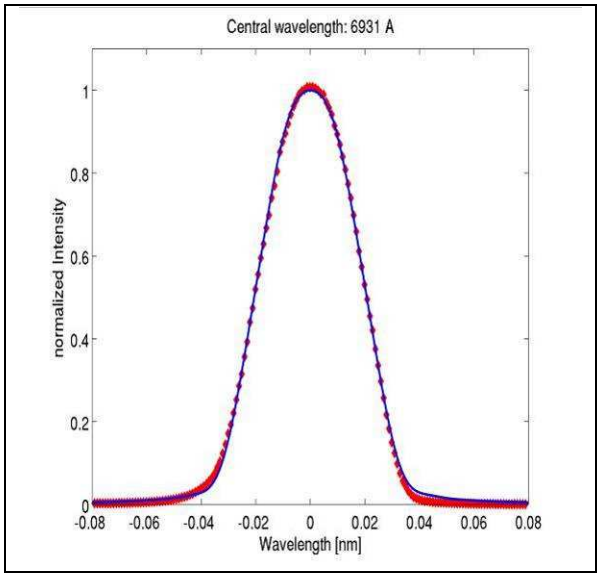

Figure III-10 Measured and simulated spectra at 693.1 nm f=640 mm, Slit widths= 90 µm, k=2400 mm^{-1}, D=10 mm, β=13.2°

Figure III-7 shows the simulated spread function of the monochromator Jobin Yvon HR 640 which is the convolution of the spread functions of the grating, the entry slit and the exit slit. The spread function of the entry slit is slightly wider than the spread function of the exit slit due to the different dispersion. Both slits were set to 100 µm in the experiment with the Jobin Yvon monochromator. As the simulated spread function with a slit of 100 µm was slightly larger than the measured spread function, we concluded that the real slit width was only 90 µm and used therefore 90 µm for the simulation of the spread function. We opened

the monochromator and observed that only a part of the grating was illuminated. We took this into account by simulating the spectra with a grating width of D=10 mm instead of D=106 mm (the full width of the grating). For the validation of the simulated spectra we measured several lines of different hollow cathode lamps. Hollow cathode lamps are known to have very small line broadening. Figure III-9 and Figure III-10 show the simulated and the measured line profiles. They are very similar and validate thus the simulation. The FWHM (full width at half maximum) of the spread function is about 0.05 nm.

III.8.3. The spread function of the Acton SP2756

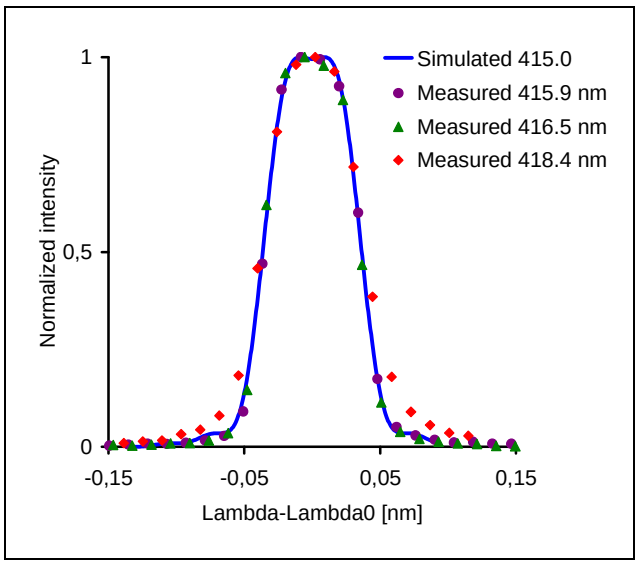

Figure III-11 Measured and simulated spectra at 415 nm, f=750 mm, k=1800 mm^{-1}, Pixel width = 20 µm, Entry slit width= 90 µm, D=7 mm, λ=415 nm, β=6.49°

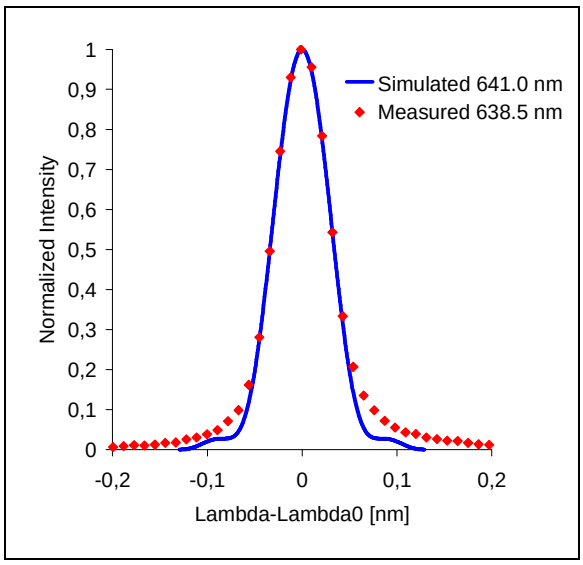

Figure III-12 Measured and simulated spectra at 641 nm, f=750 mm, k=1800 mm^{-1}, Pixel width = 20 µm, Entry slit width= 90 µm, D=7 mm, λ=415 nm, β=6.49°

Figure III-8 shows the simulated spread function of the monochromator Acton SP2756. The total spread function is the convolution of the spread functions of the grating, the entry slit and the pixel of the CCD camera. The diaphragm at the lens reduce the numerical aperture of the measured light to $2mm/350mm = 0.0057$ in the direction perpendicular to the grooves of the grating so that only a small part of the grating is illuminated (see Figure III-5). By multiplying the numerical aperture with the focal length of the monochromator we find that only a width of $D = 4.3mm$ of the grating are illuminated. The diffraction at the entry slit adds $f \sin^{-1}(\lambda / \Delta x_{entry}) = 0.3mm$ to the width of the grating that is illuminated. The comparison to experiments however showed that best coincidence could be obtained using $D = 7mm$ for the width of the grating that is illuminated. Figure III-11 and Figure III-12 show the comparison between measured Ar line profiles and the simulated spread functions of the monochromator. The measured profiles and the simulated spread function are almost identical. This validates the simulation method. The Ar lines where measured in the inductively coupled plasma in the zone where the measured temperature was around 8000 K. Small deviations between the measured spectra and the simulated spread functions can be due to the Stark broadening and the Doppler broadening. The FWHM of the spread function is about 0.07 nm.

III.8.4. Doppler broadening

The Doppler broadening is due to the velocity of the atoms. It is significant for the hydrogen atom and not for others because the hydrogen atom is very light and therefore at the same transitional temperature it moves much faster than other atoms. At 10000 K the thermal velocity of hydrogen is 13000 m/s while it is 3200 m/s for oxygen and only 2000 m/s for Argon. The thermal velocity is the most probable value for speed of the Maxwell distribution and given by equation (III-26)

$$v_{th} = \sqrt{\frac{2k_B T}{m}} \tag{III-26}$$

The Doppler broadening gives the line a Gaussian shape. Equation (III-27) gives a Gaussian profile. $\Delta\lambda$ is the FWHM and can be calculated with equation (III-28).

$$I(\lambda) = \exp(-\frac{(\lambda-\lambda_0)^2}{(\Delta\lambda)^2}\ln 2) \tag{III-27}$$

$$\Delta\lambda_D = 2\lambda_0\sqrt{\frac{2k_B T \ln 2}{m_H c^2}} \tag{III-28}$$

$k_B = 8.61734 \times 10^{-5} eV/K$

$m_H = 938.27 \mathrm{M}eV/c^2$

At a temperature of 7500 K the FWHM of the Doppler broadening of the hydrogen H-Beta line (486 nm) is $\Delta\lambda_D(7500K) = 0.0302\ nm$ and only $\Delta\lambda_D(7500K) = 0.0042\ nm$ for the argon line at 420 nm. The FWHM of the Doppler broadening of the hydrogen line has the same magnitude than the instrumental broadening. The line broadening of the argon line is much smaller and should thus not modify the line profile. The FWHM of the Doppler broadening is proportional to the square root of the temperature.

III.8.5. Stark broadening

The Stark broadening is due to collisions between the excited atoms and the free electrons and ions of the plasma. The charge of the free electrons and ions modify the electric field around the nucleus and modify thus the energy level of the bound electron. The energy difference of the transition is thus also modified and therefore the wavelength of the emitted light. Some emitted photons have smaller wavelength while others have a higher wavelength. The energy distribution of the photons is a Lorentz distribution. The measured atomic line has therefore a Lorentzian profile given by equation (III-29).

The Stark broadening is stronger for the hydrogen lines than for other lines, because the charge of the nucleus is very small and its electric field is therefore more sensitive to the fields of the free electrons and ions in the plasma.

$$I(\lambda) = \frac{1}{1+\frac{8(\lambda-\lambda_0)^2}{(\Delta\lambda)^2}} \tag{III-29}$$

$\Delta\lambda$ is the FWHM

Griem gives in the book “Plasma Spectroscopy” on page 305 [Gri64] a semi-empirical formula to calculate the electron density from the Stark broadening of the hydrogen Ballmer lines. (Equation (III-30)). The constant $C(n_e, T)$ (Å$^{-3/2}$ cm^{-3}) is tabulated for different electron densities and temperatures in the same book. Table III-4 shows Griem’s constant for the H-Beta line (486 nm) and the H-Delta line (410 nm). The constant varies only little with temperature and electron density. Griem does not give the constant for electron densities

lower than 10^{14} cm^{-3}. However at such low electron densities the Stark broadening is very small.

We rearrange equation (III-30) and obtain equation (III-31).

$$n_e = C(n_e, T) \times \Delta\lambda^{3/2} \quad \text{(III-30)}$$

$$\Delta\lambda = \left(\frac{n_e}{C(n_e, T)} \right)^{3/2} \quad \text{(III-31)}$$

The line width is proportional to the electron density to the power of 3/2. As the electron density increases strongly with the temperature (see above Calculation of the electron density using the Saha-equation) the stark broadening also increases strongly with the temperature.

	n_e		
	10^{14} cm^{-3}	10^{15} cm^{-3}	10^{16} cm^{-3}
H-Delta T=10 000 K	1.36E+14	1,18E+14	1,04E+14
H-Beta T=5 000 K	3,84E+14	3,68E+14	3,44E+14
H-Beta T=10 000 K	3,80E+14	3,58E+14	3,30E+14

Table III-4 Dependance of Griem's constant C [$Å^{-3/2}$ cm^{-3}] on the electron density n_e and temperature [Gri64]

The Stark broadening of the hydrogen H-Beta line (486 nm) at 7500 K (n_e=6.7*$10^{-20}$$m^{-3}$) is $\Delta\lambda_S(7500K) = 0.17\ nm$. At 7500 K the Stark broadening of the H-Beta line is much larger than the Doppler broadening and instrumental broadening.

III.8.6. Other broadening mechanisms

Natural line broadening is due to the energy-time uncertainty principle $\Delta E \cdot \Delta t \geq h$. The shorter the life-times of the upper and the lower excited state of a transition the larger is the natural line width. Griem [Gri64] gives an expression for the natural line width

$$\Delta\lambda = \frac{\lambda^2}{c} \left(\sum_i A_{ui} + \sum_j A_{lj} \right)$$

We calculate the natural line width of the argon line at 420.1 nm and find 1e-6 nm. This is much smaller than the instrumental broadening and should thus not modify the line shape.

Van der Waals broadening is due to the dipole interaction of an excited atom with the induced dipole of a ground state atom. Griem gives the formulas for the calculation of the van der Waals broadening which are very complex so that we don't present them here. Konjevic [KK97] applied the formulas to calculate a van der Waals width of 0.004 nm for an argon line at a temperature of T = 7000 K and atmospheric pressure. We can therefore conclude that van der Waals broadening is much smaller than instrumental broadening.

III.9. Measurement of the electron density using line broadening of hydrogen lines

We want to measure the electron density in order to test if the ions and excited states are in equilibrium and to validate the temperature measurement. The measurement of the line broadening of hydrogen Ballmer lines is a method that is often used to measure the electron density in a plasma. The hydrogen lines are used because the Stark broadening of these lines is stronger than for other lines (See Figure III-13). There are four hydrogen lines in the visible range (H-Alpha at 656 nm, H-Beta at 486 nm, H-Gamma at 434 nm, H-Delta at 410 nm). The line broadening of the H-Beta line and the H-Delta line varies less with temperature (less than 5% between 10000 K and 20000 K) than the line broadening of the H-

Alpha line and the H-Gamma line (up to 30% between 10000 K and 20000 K) [Gri64]. The H-Alpha lien is very intense so that it is often self absorbed and therefore rarely used for the measurement of the electron density. Typically the H-Beta line is used for the measurement of the electron density because it is more intense than the H-Delta line. In our study we used the H-Delta line because it is next to argon lines with similar intensities so that we can measure the temperature with the same spectrum using the absolute line intensity method.

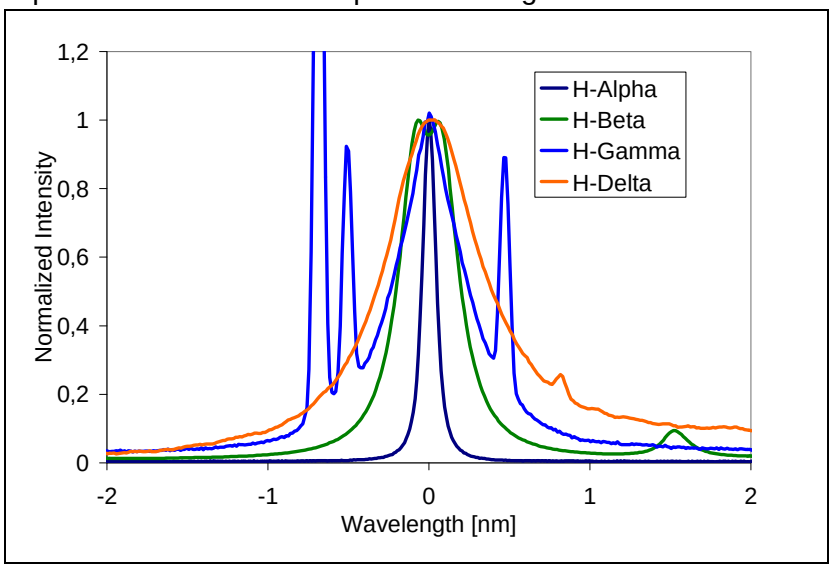

Figure III-13 Measured line profiles of the hydrogen lines

III.9.1. H-Delta line

The stark broadening of the hydrogen lines depends essentially on the electron density and varies only little with temperature. Therefore the measurement of the stark broadening can be used to determine the electron density. For measuring the stark broadening the other broadening mechanisms need to be considered. Especially at low electron densities other Doppler and instrumental broadening are important. A simple method to determine the stark width is by extracting the Lorentzian part from a Voigt profile using equation (III-32) [Mil87].

$$\Delta\lambda_V = \sqrt{\left(\frac{\Delta\lambda_L}{2}\right)^2 + \Delta\lambda_G^2} + \frac{\Delta\lambda_L}{2} \qquad \text{(III-32)}$$

$$\Delta\lambda_L = \frac{\Delta\lambda_V^2 - \Delta\lambda_G^2}{\Delta\lambda_V} \qquad \text{(III-33)}$$

$\Delta\lambda_V$ is the FWHM of the line which has a Voigt profile and $\Delta\lambda_L$ is the FWHM of the Lorentzian part. $\Delta\lambda_G$ is the FWHM of the Gaussian part due to the Doppler broadening and the instrumental broadening. By rearranging equation (III-32) we obtain the equation (III-33) which allows us to calculate the Lorentzian part from the Voigt profile. The instrumental broadening can be approximated with a Gaussian profile so that the FWHM of the Gaussian part can be calculated with equation (III-34). $\Delta\lambda_M$ is the FWHM of the instrumental broadening and $\Delta\lambda_D$ is the FWHM of the Doppler broadening.

$$\Delta\lambda_G = \sqrt{\Delta\lambda_M^2 + \Delta\lambda_D^2} \qquad \text{(III-34)}$$

.

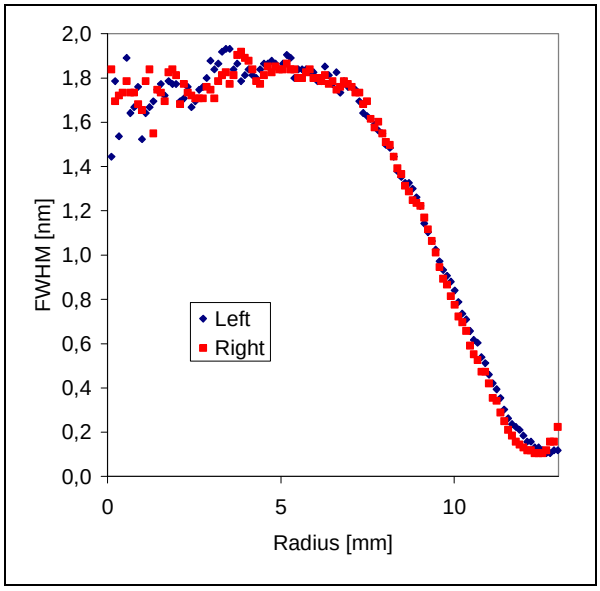

Figure III-14 Radial profile of the FWHM of the H-Delta line

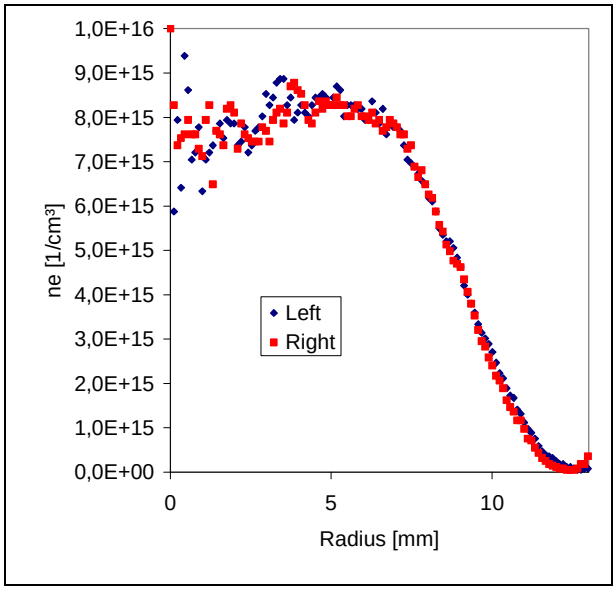

Figure III-15 Radial profile of the electron density measured from the line broadening of the H-Delta line

For the measurement of the electron density we use the radial profile of the FWHM of the H-Delta line as shown in Figure III-14. The measurement of the FWHM is described in chapter IV. We use the measured temperature to calculate the Doppler broadening and use $\Delta\lambda_M = 0.07nm$ for the instrumental broadening (Acton SP2756). Using equation (III-34) and (III-33) we obtain the Lorentzian FWHM due to the Stark broadening. We use equation (III-30) with the constant Griem's C at $n_e=10^{16}$ cm^{-3} and T=10000 K to calculate a first electron density which is then used to find a better constant using the interpolation between the three values of H-delta in Table III-4. The interpolated constant is then used to calculate the electron density using again equation (III-30).

The error on the measured electron density is mainly due to assumption of that the Lorentzian FWHM can be extracted from the totale FWHM with equation (III-32). We estimate the error on the Stark FWHM to $\Delta\lambda_M = 0.025nm$ which is about a fourth of the FWHM of instrumental and Doppler broadening. A measured electron density of $n_e=1\cdot10^{15}$ cm^{-3} has an accuracy of 9 % and a electron density of $n_e=8\cdot10^{15}$ cm^{-3} has an accuracy of 2 %. Other error sources may be an error on Griem's constant that we can not evaluate.

We will therefore use the measurement of the line broadening of the H-Beta line which is more often used an thus better known to validate the measurement with the H-Delta line in chapter VI.

III.9.2. H-Beta line

As the line broadening measurement is a standard method for the measurement of the electron density in plasma, the theoretic line profile of the H-beta line has been studied many times ([WKH75], [KWH93], [GC96], [GGC03]). Gigosos et al. [GGC03] give an extensive tabulation of line widths for wide ranges of electron density, temperature and reduced mass. They also give a formula for the FWHM of the H-Beta line (Equation (III-35)).

Gigosos Formula [GGC03]: $$FWHM = 4.800nm \times \left(\frac{n_e}{10^{23} m^{-3}}\right)^{0.68116} \quad \text{(III-35)}$$

Zikic [ZGI02] developed a program to simulate the line profile in dependency of the reduced mass of the emitter perturber pair, the electron temperature, the ion temperature

and the electron density. For the application of this simulation we assume local thermal equilibrium and use therefore the same temperature for the ions and for the electrons and we calculate the electron density with the Saha equation. The reduced mass of the hydrogen atom with the argon ion as perturber is 0.98u.

In Figure III-16 we compare the FWHM of Griems formula (III-30) to the FWHM of Gigosos fromula (III-35) and the line width of the simulated line profiles at local thermal equilibrium using the program of Zikic. The electron density of Gigosos and Zikic is slightly lower, which is probably due to the better simulation the ion dynamics. Gigosos's formula agrees very well with the simulation that we run with the program of Zikic. This shows that the Gigosos's formula is well adapted to the conditions in our plasma.

We estimate just as for the H-delta line the error on the measurement. A measured electron density of $n_e=1\cdot10^{15}$ cm^{-3} has an accuracy of 25 % and an electron density of $n_e=8\cdot10^{15}$ cm^{-3} has an accuracy of 6 %.

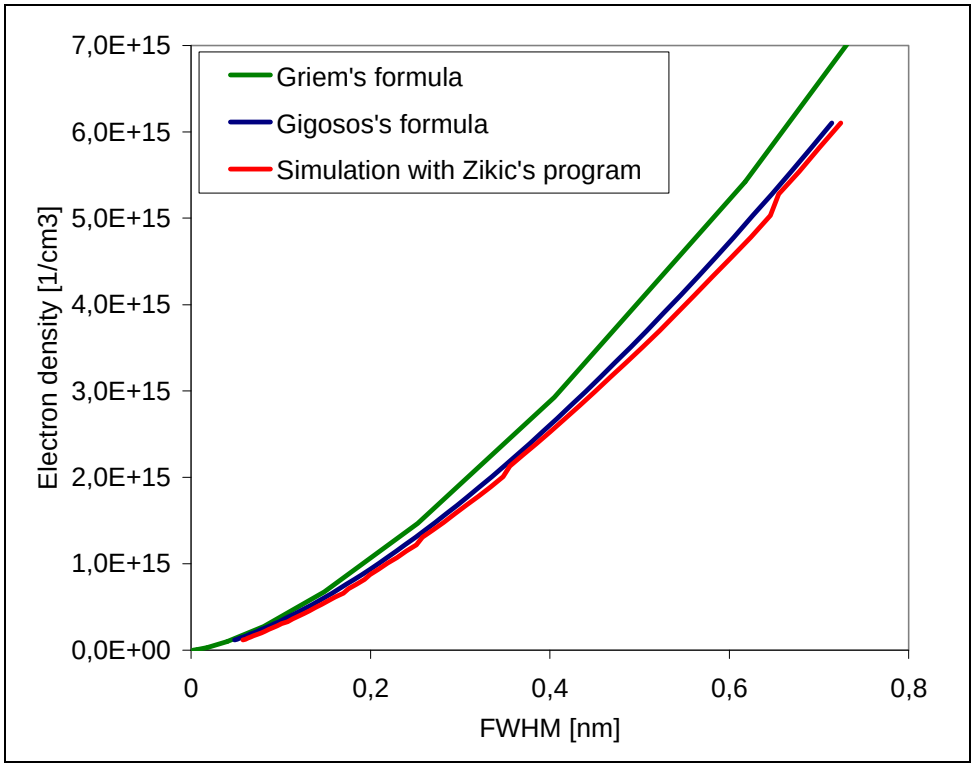

Figure III-16 Electron density vs FWHM for Griems formula (III-30), Gigosos formula (III-35) and for the simulation with the program of Zikic [ZGI02]

III.10. Line profile simulation

With a spectrometer with photomultiplier tube the measurement of the total emissivity of a line is not straight forward. One can only measure the spectral emissivity at one wavelength at a time. The spectral emissivity $\varepsilon(\lambda_0)$ (W/m3/nm) of a line can be written as product of the total emissivity of a line ε_{line} (W/m3) and line profile function $P(\lambda)$ (nm-1) as shown in equation (III-34).

We need therefore to know the line profile function $P(\lambda)$ in order to calculate the total emissivity of a line ε_{line} from the spectral emissivity at the central wavelength $\varepsilon(\lambda_0)$ as shown on equation (III-30). We can simulate the line profile function $P(\lambda)$.

$$\varepsilon(\lambda) = \varepsilon_{line} \times P(\lambda) \text{ with } \int_{line} P(\lambda) d\lambda = 1 \quad \text{(III-36)}$$

$$\varepsilon_{line} = \frac{\varepsilon(\lambda_0)}{P(\lambda_0)} \quad \text{(III-37)}$$

The shape of the line profile is the convolution of the three broadening mechanisms discussed above. The three profiles are shown in Figure III-17.

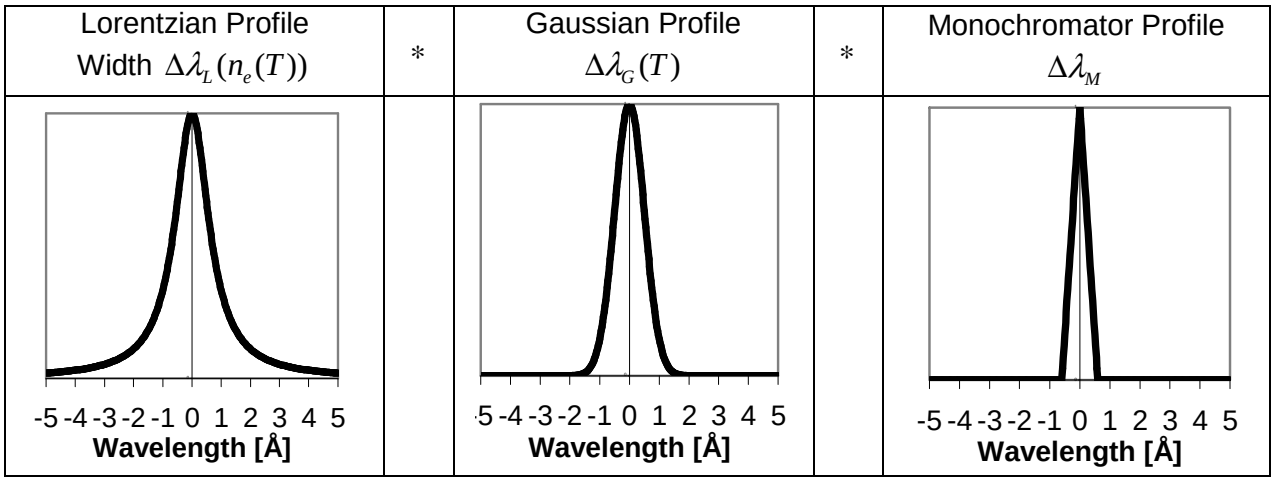

Figure III-17 Convolution of the different profiles

First we want to measure whether the Doppler broadening and Stark broadening are high compared to the instrumental broadening. We therefore measured the wavelength profile of the light that is coming from the centre of a plasma, that is at about 7500 K. As Doppler broadening and Stark broadening increase with the temperature they are strongest in centre of the plasma where the temperature is highest. Figure III-18 shows the normalized intensity profile for the four lines that were used for the measurement with the monochromator with photomultiplier and the spread function of the monochromator.

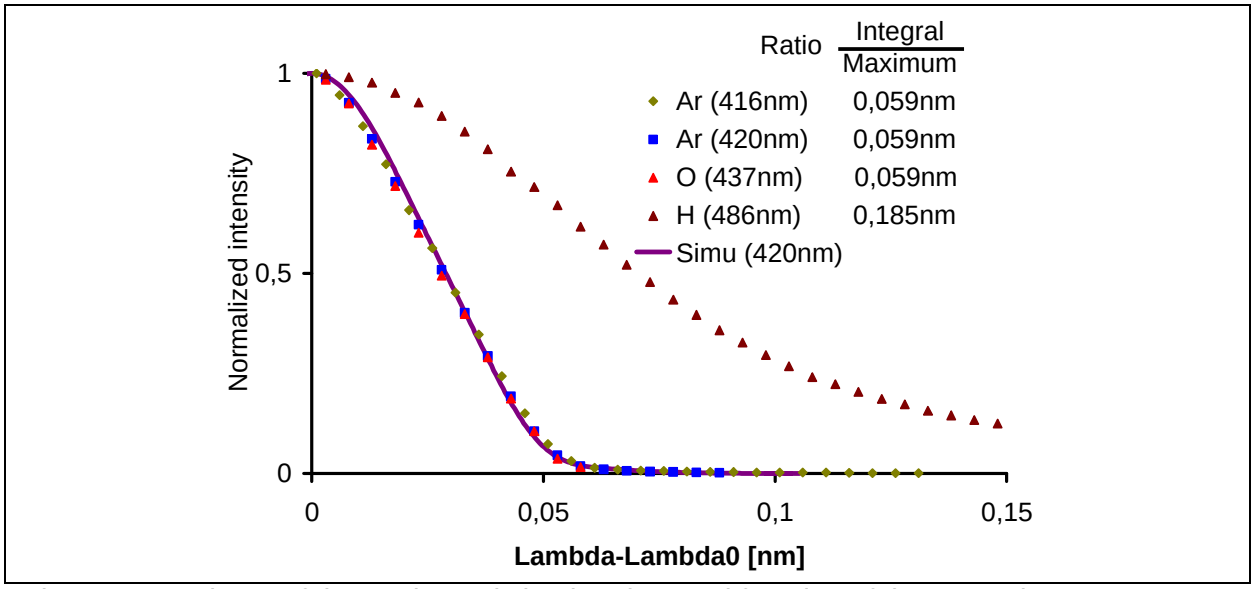

Figure III-18 Shape of the peaks and simulated spread function of the monochromator HR640 (slit width: 90 µm, f=640 mm, k=2400 mm^{-1}, D=10 mm, λ=420 nm, β=13.2°)

The oxygen peak and the two argon peaks have the same shape as the spread function of the monochromator, which means, that Doppler broadening and Stark broadening are

negligible. As these broadening mechanisms are negligible in the centre with the highest temperature, they are also negligible in the whole plasma. The line profile function $P(\lambda)$ is thus equal to the spread function of the monochromator multiplied by a normalization factor (so that the area under the curve is 1). We can thus use the spread function $P(\lambda_0)$ to calculate the total emissivity of the line ε_{line} from the emissivity at the central wavelength $\varepsilon(\lambda_0)$.

The shape of the hydrogen peak is very different from the shape of the spread function of the monochromator. This shows that Stark broadening and Doppler broadening are significant. For this reason we study the line broadening of the H-Beta line in order to be able simulate the line profile function.

III.10.1. Simulation of the Stark width of the H-beta line

As discussed above, the Stark broadening of the H-Beta line depends primarily on the electron density which can be calculated with the Saha-equation when the plasma is in local thermal equilibrium. In one direction the measurement of the Stark broadening can be used to measure the electron density and test thus the assumption of LTE. In the other direction the assumption of LTE permits to calculate the electron density (as described above) and calculate thus the Stark broadening.

We use equation (III-31) for the calculation of the Stark width.

Griem does not give the constant for electron densities smaller then 10^{14} cm^{-3}. The reason for this is probably the fact that the effect of Stark broadening is very small at low electron densities. We use a polynomial interpolation of the constant for H-Beta (see Table III-4) versus the logarithm of the electron density to obtain a value for the constant at every electron density (see Figure III-19). For electron densities smaller than 10^{14} cm^{-3} this is not very precise but since the Stark broadening is very small it does not have any effect on the concentration ratio measurements.

We use a linear interpolation between the constant at the two temperatures 5000 K and 10000 K.

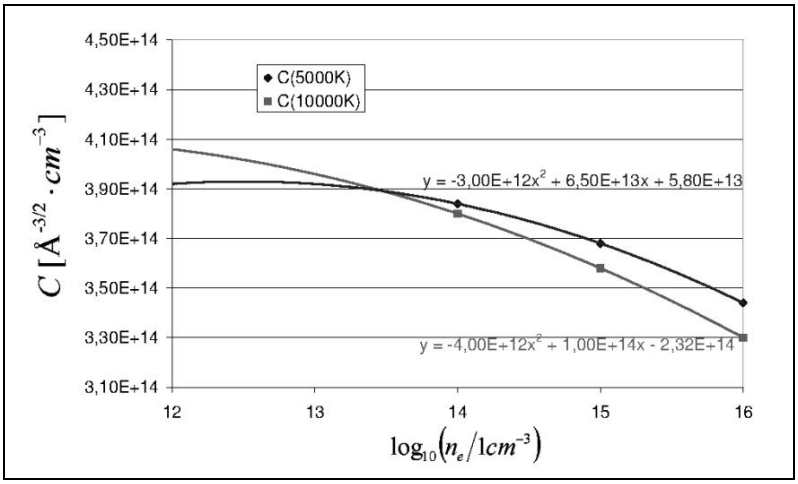

Figure III-19 Plot of Griem's constant vs electron density with interpolation

With the help of Griem's constant we can calculate the Stark broadening for different electron densities and hence for different temperatures. Since Griem's formula is semi-empirical and the estimation of the thermal equilibrium is not verified, an experimental validation is necessary. This will be discussed in appendix B.

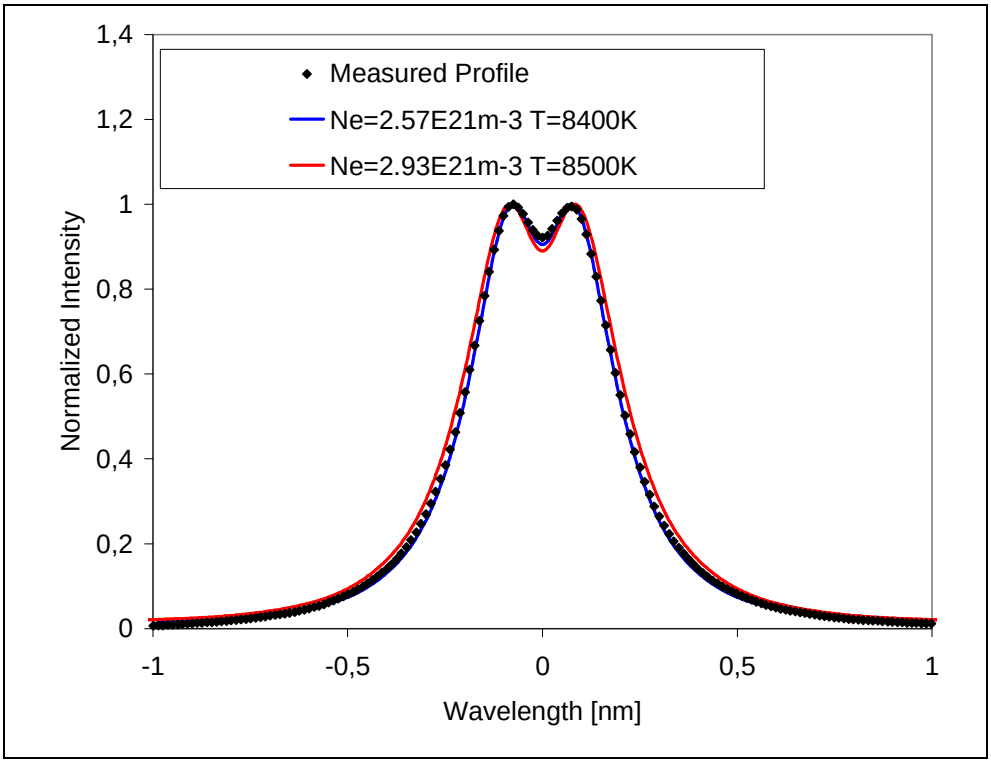

Figure III-20 Measured and simulated line profile of the H-Beta line, Acton SP2756, slit width 70 µm

While the Stark broadening of the H-Beta line gives Lorentzian shape at electron densities below $5x10^{20}$ m^{-3} this is not the case at higher electron densities as shown in Figure III-20. While the edge of the line has still a Lorentzian shape there is a dip in the centre. This dip is due to the ion-dynamics. Figure III-20 shows simulated profiles at two different temperatures and a measured profile. The Stark profiles calculated with the Zikic's program have been convoluted with a Doppler profile at 8500 K and the spread function of the monochromator Acton SP2756 at 486 nm with a slit width of 70 µm. The two simulated profiles are very close to the measured profile, which shows that it should be possible to simulate the ratio between the total emissivity and the emissivity at the central wavelength at electron densities of about $3x10^{21}$ m^{-3}.

However the verification of the simulation that we performed here would have been difficult with a monochromator without CCD detector. Therefore we did not apply the simulation with Zikic's program for the concentration ratio measurement [H]/[Ar] with the monochromator with photomultiplier tube. For measurements of the concentration ratio [H]/[Ar] above an electron density of $5X10^{20}$ m^{-3} (T~7500 K) we used the optical setup with a CCD camera.

The multiplet of the H-beta line:

The H-Beta line corresponds to the transition from the energy level n=4 to n=2 of the hydrogen atom. Figure III-21 shows the corresponding energy levels and the transitions between them.

In the energy level n=4 the angular momentum of the electron has the quantum number l = 0, 1, 2 or 3 (s, p, d or f). The total angular momentum, which is the sum of the spin and the angular momentum of the electron, can have the quantum number j=|l+s| or j=|l-s|. Therefore the possible configurations are $4s_{1/2}$, $4p_{1/2}$, $4p_{3/2}$, $4d_{3/2}$, $4d_{5/2}$, $4f_{5/2}$, $4f_{7/2}$.

In the energy level n=2 the angular momentum has the quantum number l = 0 or 1 (s or p) and the possible configurations are therefore $2s_{1/2}$, $2p_{1/2}$, $2p_{3/2}$. Due to the fine structure resulting from spin-orbit coupling, states with a larger total angular momentum have a higher energy. The difference between the energy states $s_{1/2}$ and $p_{1/2}$ is due to the Lamb-shift. These energy differences are approximately 10^{-4} times smaller than the energy difference between the state n=4 and n=2 so that the relative difference between the wavelengths of the lines of the multiplet is very small. All the lines are also split by the hyperfine interaction that results from interaction with the spin of the proton. This effect is too small to be relevant here.

Due to the selection rule for electric dipole radiation ΔI=±1 only the states 4p can make transitions to the 2s state and only the states 4s and 4d states can make transitions to the 2p state. Therefore there are seven possible transitions as shown in Figure III-21.

In Figure III-22 we show the factor $g_u A_{ul}$, which is proportional to the intensity (see equation (III-4)), for the seven different lines of the multiplet of H-Beta.

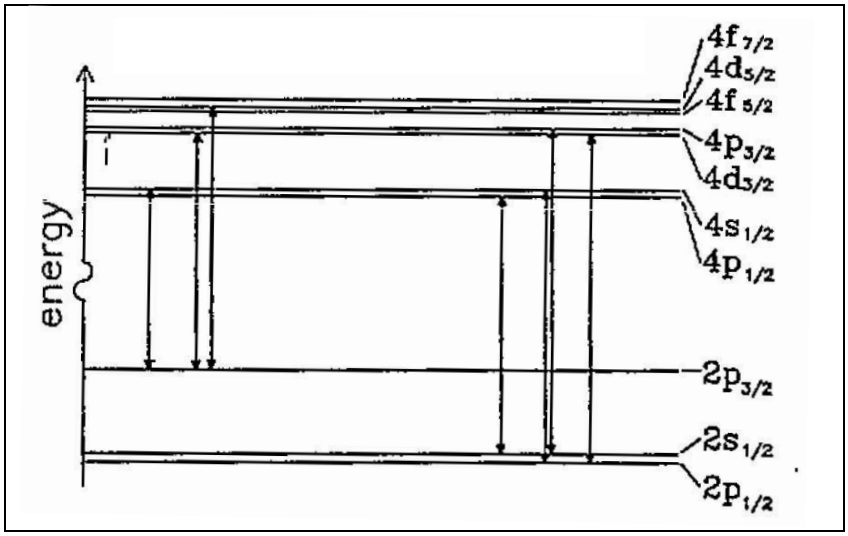

Figure III-21 Energy level scheme of H-Beta (source[HKP93])

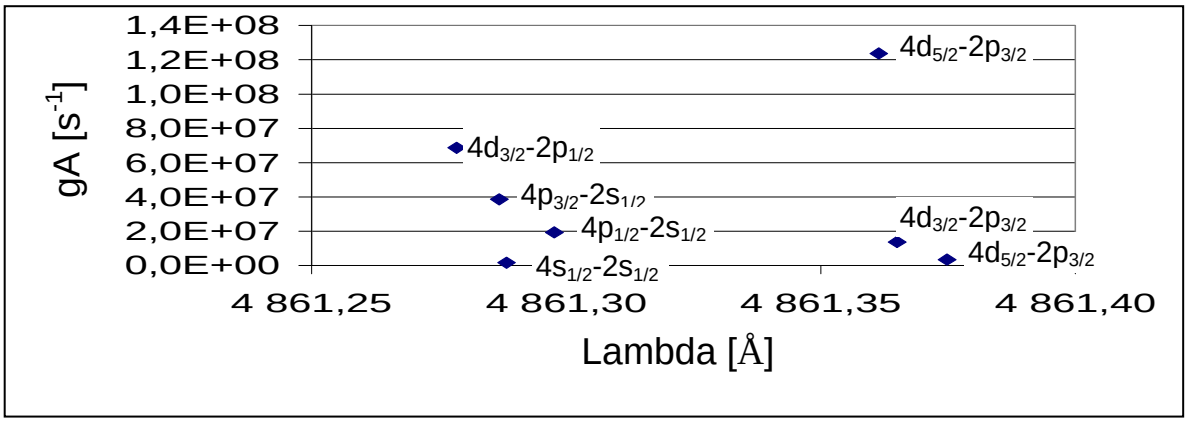

Figure III-22 The intensity of the different lines of the multiplet H-Beta

The difference between the smallest wavelength and the longest wavelength of the multiplet is about 0.01 nm. This adds an additional broadening to the line profile of H-Beta line which is in reality the sum of seven line profiles. This broadening is only significant when the Stark broadening is small. For the simulation of the line profile we took this into account. We simulated the seven line profiles of the multiplet and summed their profiles. For the

measurement of the electron density we did not take into account the broadening due to the wavelength difference between the lines of the multiplet.

III.11. Measurement of the electron density using the continuum emissivity

The radiation of the continuum is mainly due to the photo-recombination of ions and electrons. Equation (III-38) gives the emissivity of the continuum which depends on the wavelength, the temperature and the electron density [Hof78]. The sum extends over all ionic states of interest of the same atom.

The Bremsstrahlung due to collisions plays only a role at high electron densities and at infrared wavelengths [WKT91]. Equation (III-38) can be simplified to equation (III-39) using the assumption of a weakly ionized plasma. We calculated the partition function Z_1 of the singly ionized argon atom which is 5.6 at 10000 K and varies very little with temperature. The statistical weight of the ground state of the ions g_0^1 divided by the partition function of the ion is then 0.71. The equation (III-38) is in esu-units and has to be multiplied by $(4\pi\varepsilon_0)^{-3}$ to express it in SI-Units. The constant in equation (III-39) is then $C_1 = 1.63\times10^{-43} Wm^4 K^{0.5} sr^{-1}$ [BVM11].

$$\varepsilon_c(\lambda,T) = \frac{8e^6}{3c^2\lambda^2}\sqrt{\frac{2\pi}{2m_e^3 k_B T}} n_e \left(1-\exp\left(\frac{-hc}{\lambda k_B T}\right)\right)\times\sum_r \frac{g_0^r}{Z_r} n_r \times z_r^2 \xi^r(\lambda,T) \qquad \text{(III-38)}$$

$$\varepsilon_c(\lambda,T) = \frac{C_1}{\lambda^2}\frac{n_e^2}{\sqrt{T}}\left(1-\exp\left(\frac{-hc}{\lambda k_B T}\right)\right)\times 0.71\times\xi^1(\lambda,T) \qquad \text{(III-39)}$$

$$n_e = \sqrt{\frac{\varepsilon_c(\lambda,T)}{\xi^1(\lambda,T)}\sqrt{T}\,\frac{\lambda^2}{0.71\times C_1}\left(1-\exp\left(\frac{-hc}{\lambda k_B T}\right)\right)^{-1}} \qquad \text{(III-40)}$$

The Biberman factors $\xi_{c,Ar}(\lambda,T)$ for argon and oxygen plasma have been taken from papers of Hofsaess [Hof78] [Hof79] and are presented in Table III-5 for 410 nm and 640 nm. These two wavelengths are close to the lines that were used for the concentration measurement.

	410 nm	640 nm
$\xi_{c,Ar}$ 6000 K	1.28	2.00
$\xi_{c,Ar}$ 10000 K	1.48	1.85
$\xi_{c,O}$ 10000 K	0.46	0.65

Table III-5 The Biberman factors for argon plasma [Hof78], [Hof79]

The Biberman factors for oxygen are lower than the Biberman factors of Argon. A high oxygen concentration may therefore falsify the electron density calculated with the Biberman factors for argon.

III.12. Concentration measurement of the OH-radical

The calculation of the emissivity of molecules is complex. We thus simulated the emissivity of OH for different temperature with the program Specair [Lau02] which is available on the internet. The spectroscopic model used for the simulation of the OH spectrum is described in [LLK99]. The program includes a convolution with a spread function (in Specair it is called “slit function”). We used a triangular spread function with a base width of 0.12 nm. We compared the shape of the measured OH spectrum to the simulated spectrum at 5500 K (Figure III-23). The spectrum is very similar, especially between 3061 Å and 3067 Å. The differences could be due to the fact that the measured light is integrated over regions with different temperatures, but it could also be due to the simulated spectrum being imprecise. As the spectrum is very similar, we can use the measured spectral emissivity at an arbitrary wavelength and divide it by the simulated spectrum with a known concentration and thus obtain the concentration. For the measurement we chose the wavelength 3064 Å, because the maximum can easily be found in the spectrum.

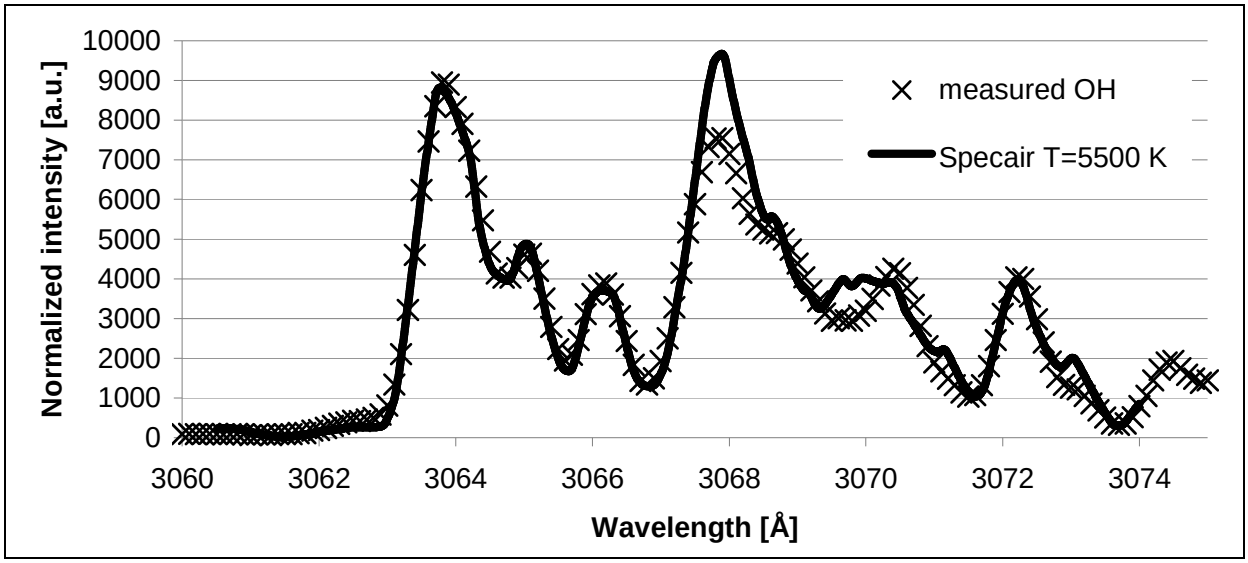

Figure III-23 Comparison of simulation and measurement of the OH spectrum

III.13. Abel inversion

In the paragraphs above we described how we can measure different parameters with the local emissivity. However with emission spectroscopy we can not measure directly the local emissivity because the light that comes out of the plasma is always the integral of the emissivity along a path across the plasma. The Abel inversion can be used for axially symmetric light sources to reconstruct the local emissivity from an intensity profile.

III.13.1. Theory

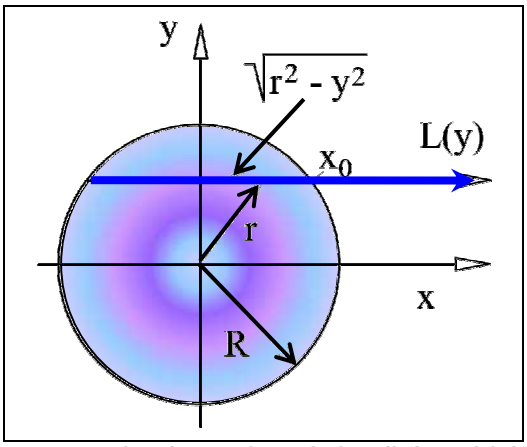

Figure III-24 Abel inversion
The circle stands for the plasma
The blue arrow stands for the observation chord

We measure the intensity of the light which comes from the plasma with the optical setup, which is described in chapter IV. This setup allows us to measure the light that is emitted into one direction along a thin observation chord that crosses the plasma (see Figure III-24). The intensity is the integral of the different local emissivities along this chord. We measure the intensity $L_\lambda(y)$ for different distances y to the centre of the axially symmetric plasma. We can then write for this intensity profile:

$$L_\lambda(y) = \int_{-x_0}^{x_0} \varepsilon_\lambda(x,y)dx = 2\int_0^{x_0} \varepsilon_\lambda(x,y)dx \qquad \text{(III-41)}$$

x is the direction of observation and x_0 the point where the chord leaves the plasma.

We use $x = \sqrt{r^2 - y^2}$ and $x_0 = \sqrt{R^2 - y^2}$ and thus obtain from (III-41) a relation between the lateral profile of the intensity $L_\lambda(y)$ and the radial profile of the emissivity $\varepsilon_\lambda(r)$.

$$L_\lambda(y) = 2\int_r^R \varepsilon_\lambda(r)\frac{rdr}{\sqrt{r^2 - y^2}} \qquad \text{(III-42)}$$

The Abel inversion (III-43) ([NO60]) is the inversion of equation (III-42). It allows us to calculate the radial emissivity profile from the lateral intensity profile.

$$\varepsilon_\lambda(r) = -\frac{1}{\pi}\int_r^R \frac{dL_\lambda(y)}{dy}\frac{dy}{\sqrt{y^2 - r^2}} \qquad \text{(III-43)}$$

There are different algorithms to calculate the integral of the Abel inversion for a finite number of elements. In our study we applied the method from Nestor and Olsen's studies [NO60]. The algorithm is explained in Appendix B. An elaborated study on the confidence intervals of the Abel inversion can be found in [CH06]. With the local emissivity one can calculate the temperature and the concentrations with the above-mentioned formulas (III-11) and (III-14).

III.13.2. Testing the Abel logarithm with a test function

In order to test the Abel algorithm the test function (III-44) with the known Abel inversion (III-45) was used [BPH96].

$$L(y) = \sqrt{1-y^2} \times (1 - 2.5 \times y^2) + 1.5 \times y^4 \times \ln\left(\frac{1+\sqrt{1-y^2}}{y}\right) \qquad 0 \le y \le 1 \qquad \text{(III-44)}$$

$$\varepsilon(r) = 1 - 3r^2 + 2r^3 \qquad 0 \le r \le 1 \tag{III-45}$$

In order to get test function with zero emissivity in the centre as it is the case in some measured profiles we subtract the test function (III-45) with 100 data points from the same function with 200 data points and obtain thus the new test function for the radial emissivity as shown in Figure III-26. We do the same procedure for the test function (III-44) and thus obtain the test function for the lateral intensity as shown in Figure III-25. The function in Figure III-26 is the Abel inversion of the function in the Figure III-25 because the Abel inversion of the sum of two profiles is equal to the sum of the Abel inversions of two profiles. We chose the amplitude so that it is close to the measured amplitude.

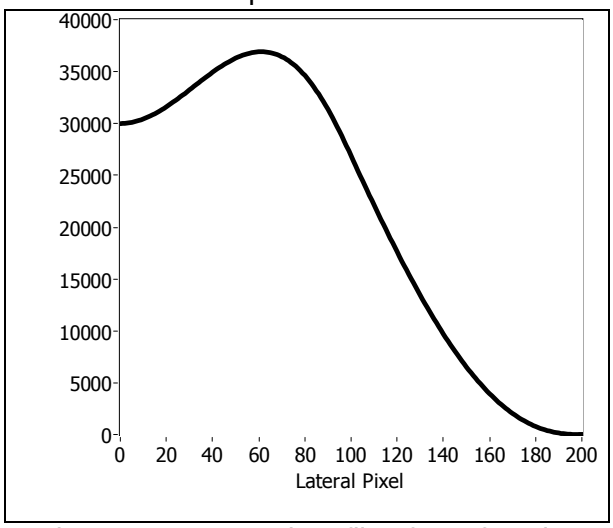

Figure III-25 Lateral profile of test function

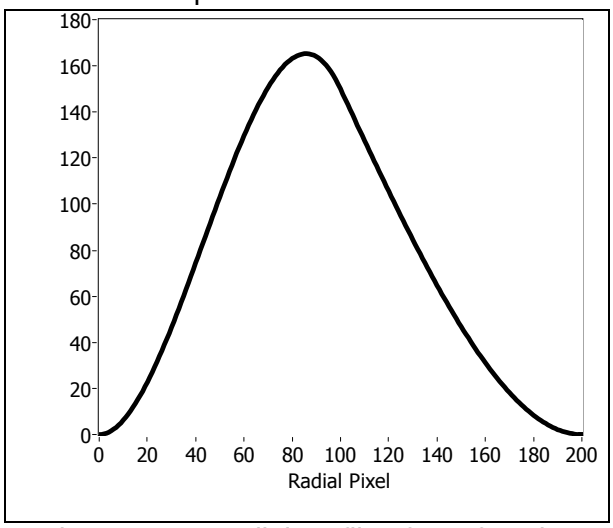

Figure III-26 Radial profile of test function

Figure III-28 shows the theoretical radial profile of Figure III-26 and the profile of Figure III-25 inverted by the Abel algorithm. The two profiles are so identical that no difference can be seen. Figure III-29 shows the relative error between the theoretical profile and the profile inverted by the Abel algorithm. The relative error is very small, with an exception for the very low emissivity in the center which shows that the used Abel algorithm is precise for this profile.

III.13.3. Testing the influence of noise and smoothing on the Abel inversion

As the Abel inversion uses the derivative of the signal it is very sensible to noise. We therefore simulate the noise in order to study the impact on the measurement. The amplitude of the shot noise of the camera is equal to the square root of the signal. While shot noise follows a Poisson distribution we simplified it by a uniform distribution with an amplitude that is the square root of the amplitude of the signal. Figure III-27 shows the lateral profile with and without the added shot noise. The shot noise is so small that the difference between the two profiles can hardly be identified. The Abel inversion amplifies the shot noise so that in Figure III-28 we can clearly see the difference between the Abel inversion of the signal without noise and the signal with noise.

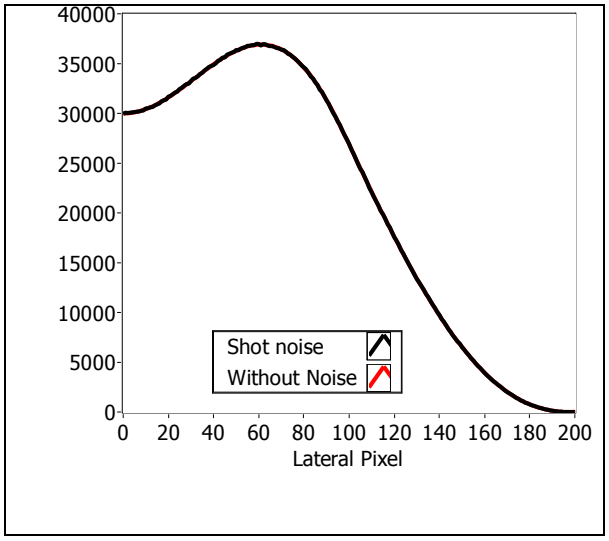

Figure III-27 Lateral profile of test function with added shot noise

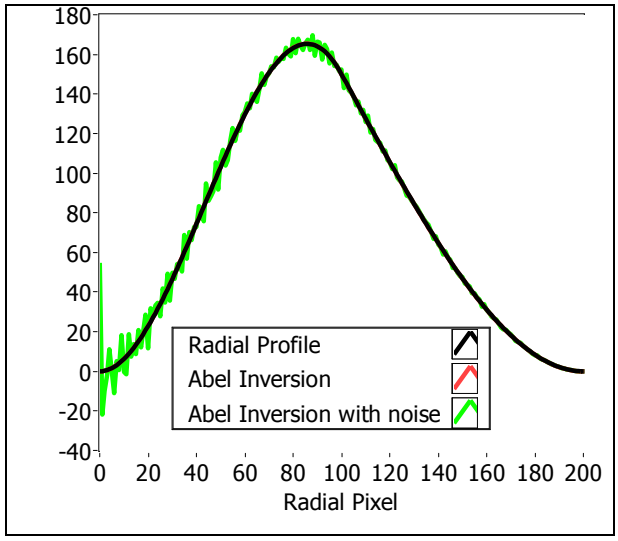

Figure III-28 Abel inversion of test function and test function with added shot noise

In order to reduce the shot noise a polynomial smoothing with the order 2 and a length of 11 data points was applied. In order to quantify the noise, 1000 simulations where run and the mean relative error on the Abel inversion is calculated. The relative error is the absolute difference between the calculated profile and the theoretical profile divided by the theoretical profile. Figure III-29 shows the mean relative error on the Abel inversion. One can see that the error is much higher with the noise than without the noise. The smoothing reduces the noise significantly.

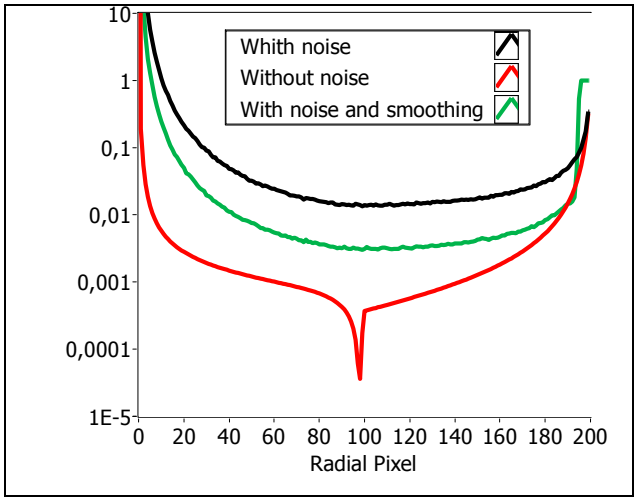

Figure III-29 Relative error on Abel inversion

III.14. Conclusion

We presented several spectroscopic techniques and chose the optical emission spectroscopy. The developed methods are based on the assumption of local thermal equilibrium and of symmetry of the plasma.

The measurement of the absolute emissivity of an Argon line can be used to calculate the temperature. The measurement of the emissivity ratio can be used to calculate the concentration ratios [H]/[Ar] and [O]/[Ar]. Line broadening plays an important role for emissivity measurements with a monochromator with photomultiplier tube that can only measure one spectral emissivity at a time. We showed that we can precisely simulate the

spread function of the two monochromators that we used in this study. Stark broadening can be used to measure the electron density and thus validate the assumptions of local thermal equilibrium and the temperature measurement.

The Abel inversion can be used calculate the radial emissivity (W/m^3) from a lateral intensity profile (W/m^2). We tested the Abel inversion algorithm with a test function and showed that the Abel inversion amplifies the noise on the lateral intensity profile. Polynomial smoothing can be used to reduce the noise.

In the following chapter IV we present the experimental facilities that are used for the generation of the plasma and for the measurement of the emissivity. In chapter V we present the spectroscopic measurements.

List of symbols

$[X]$ (m^{-3})	Concentration of the element X
A_{ul} (s^{-1})	Transition probability of the line between the excited states u (upper) and l (lower)
$c = 299792458\,\mathrm{m}\times\mathrm{s}^{-1}$	Speed of light
$C(n_e,T)$ (Å$^{-3/2}$ cm^{-3})	Griem's constant for Stark broadening
D (mm)	Width of the grating of the monochromator
$e = -1.602176565\times10^{-19}\,\mathrm{C}$	Electron charge
E_u (eV)	Energy of the excited state u (upper)
f (m)	Focal length
g_u	Degeneracy of the excited state u (upper)
$h = 1.054571726\times10^{-34}\,J\times s$	Planck constant
k (mm^{-1})	Groove density of the grating of the monochromator
$k_B = 8.61734\times10^{-5}\,eV\times K^{-1}$	Boltzmann constant
$L_\lambda(y)$ (W.m^{-2}.nm^{-1})	Spectral intensity of the light that exits the plasma at the position y
$m_e = 0.510998928\,\mathrm{MeV}\times c^{-2}$	Electron mass
$m_H = 938.27\,\mathrm{MeV}\times c^{-2}$	Hydrogen atom mass
n	Diffraction order
N	Number of grooves on the grating of the monochromator
n_e (m^{-3})	Electron density
n_{tot} (m^{-3})	Total particle density (Atoms, electrons, ions)
n_u (m^{-3})	Density of atoms in the excited state u (upper)
p (Pa)	Pressure
$P(\lambda)$ nm^{-1}	Line profile function
r (mm)	Radial coordinate for the position in the plasma
R (mm)	Radius of the plasma
T (K)	Temperature
v_{th} (m.s^{-1})	Thermal velocity of the atoms

y (mm)	Coordinate for the lateral position
$Z(T)$	Partition function
β (°)	Half inclusion angle of the grating of the monochromator
$\varepsilon_0 = 8.8541878176 \times 10^{-12} F \times m^{-1}$	Permittivity of the vacuum
ε_{line} (W.m^{-3})	Total line emissivity
$\varepsilon(\lambda), \varepsilon_\lambda$ (W.m^{-3}.nm^{-1})	Spectral emissivity
θ (°)	Angle of the orientation of the grating of the monochromator
λ (nm)	Wavelength
$\Delta\lambda$ (nm)	Full width at half maximum (FWHM)
$\xi_{c,O}$	Biberman factor
ρ_D (nm)	Debye length
$\Delta\chi$ (eV)	Reduction of the ionization energy
χ_Z (eV)	Ionization energy of the ionization stage Z

IV. Experimental Facilities

Before describing the experimental setup it is helpful to understand how an inductively coupled plasma torch works.

IV.1. How does an inductively coupled plasma (ICP) torch work?

An inductively coupled plasma torch consists basically of a gas flow and an induction coil which is installed around the gas flow (Figure IV.1 on the left). The induction coil creates an oscillating electromagnetic field and thus supplies energy to the plasma. The induction coil is connected in parallel to a capacitance and this LC-circuit oscillates at its resonance frequency. The LC-circuit is connected to the generator which supplies energy. We examine in more detail the energy transfer from the induction coil to the plasma:

The oscillating electric current in the induction coil induces a homogeneous oscillating magnetic field parallel to the axis of the induction coil and the plasma (Equation (IV-1), Figure IV.1 on the left). The oscillating magnetic field then induces an electric field which is tangential to the axis of the induction coil (Equation (IV-2), Figure IV.1 on the right,)

$$\nabla \times \vec{B} = \mu_0 \ \vec{j} + \mu_0 \varepsilon_0 d\vec{E} / dt \qquad \text{(IV-1)}$$

$$\nabla \times \vec{E} = -d\vec{B} / dt \qquad \text{(IV-2)}$$

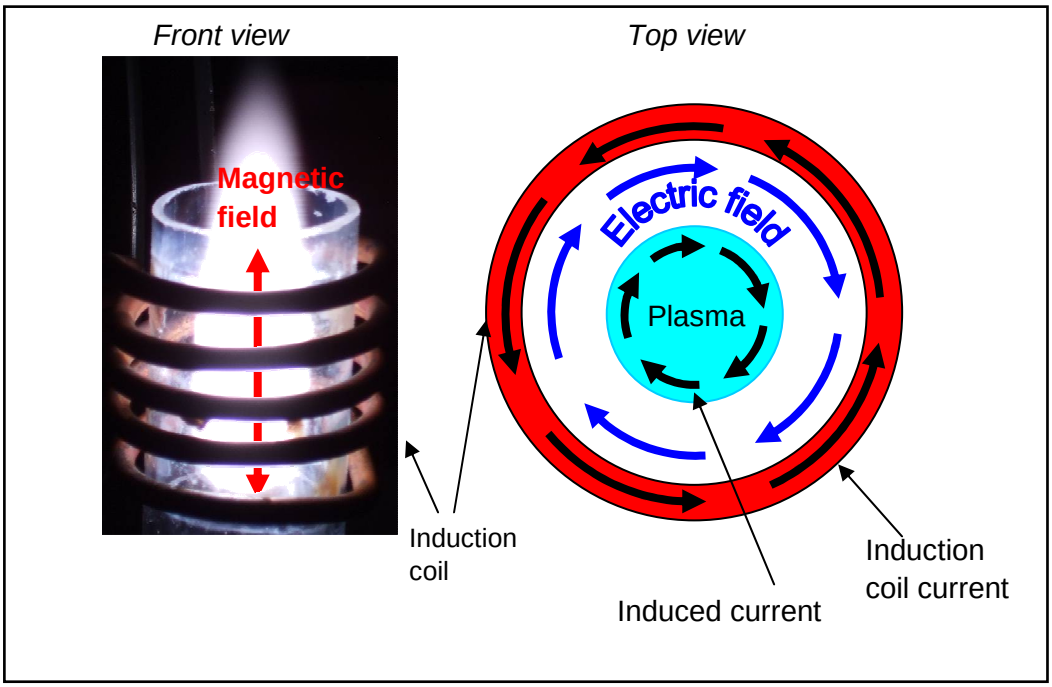

Figure IV.1 Electromagnetic fields in an inductively coupled plasma torch

This electric field then supplies energy to the electrons. The collision frequency of the electrons is much higher than the frequency of the electric field so that the power absorption of the electrons is similar to the power absorption in a constant electric field.

As the electric field accelerates a large number of electrons it creates a macroscopic current in the plasma which shields the electromagnetic field. The electromagnetic field in the interior of the plasma is therefore close to zero. The induced current flows in the opposite direction of the current in the induction coil in accordance to Lenz's law. An induced current has always a magnetic field that opposes the original change of magnetic flux. The magnitude of the depth to which the electromagnetic field penetrates into the plasma can be estimated with the formula for the skin depth (Equation (IV-3)). We use a typical generator

frequency of $f = 40MHz$ and the conductivity of Argon at thermal equilibrium at 7000 K $\sigma(7000K) \approx 400AV^{-1}m^{-1}$. (Calculated with T&TWinner [TTW]).

$$\delta = \sqrt{\frac{2}{2\pi f\ \mu\sigma}} = 4mm \quad \text{with} \quad \mu = 4\pi \times 10^{-7}\ \frac{V \rangle S}{A \times m} \tag{IV-3}$$

The calculated skin depth is only an approximation. The conductivity of the plasma increases strongly with the temperature because the electron concentration increases. At the edge of the plasma the temperature gradient is very high so that the conductivity gradient is also very large.

IV.2. The geometry of the plasma torches

In this study we used two different plasma torches. One plasma torch that is typically operated at 2 kW which will be denominated small torch and a second plasma torch that is typically operated at 40 kW that will be denominated big torch.

Both torches (Figure IV.3. and Figure IV.2) consist of three concentric tubes. (Outer tube, intermediate tube and inner tube). While the small torch has no active cooling the big torch has water cooling for the inner tube and the outer tube.

The outer tube isolates the plasma from the induction coil. The intermediate tube ends below the induction coil. The cross section between the intermediate tube and the outer tube is very small so that a gas flow with a high velocity can be injected between them. This outer flow confines the plasma and reduces the heat flow from the plasma to the outer tube and protects thus the outer tube from melting. The cold gas from the outer flow, which surrounds the plasma, has a very small conductivity and does not absorb power from the electromagnetic field. The hot gas of the plasma has a high conductivity and absorbs the power. Between the two gas flows the absorption of energy and the heat convection and diffusion are in equilibrium (see chapter VI). Torches without an intermediate tube need to be operated with higher gas flow rates to protect the outer tube and have thus a higher gas consumption. The outer flow is very important for the small torch without active cooling because a high heat flow from the plasma would melt the outer tube. The big torch is less sensitive to the high heat flow because the outer tube is water cooled.

The intermediate flow that is injected between the inner tube (injector) and the intermediate tube protects the intermediate tube from the heat of the plasma. When the intermediate flow is to low the plasma comes close to the intermediate tube which may melt.

The inner tube has the role to inject substances in the centre of the plasma without modifying the induction zone at the edge of the plasma. The injection of a water aerosol as it is done in chemical analysis would disturb the coupling if it would reach the induction zone.

IV.2.1. The small torch

The geometry of the small torch is shown in Figure IV.3. As described above, the inductively coupled plasma torches consist of three concentric tubes. The small torch has two quartz tubes and the injector tube is made of alumina. A photo of the small torch is shown in Figure IV.1

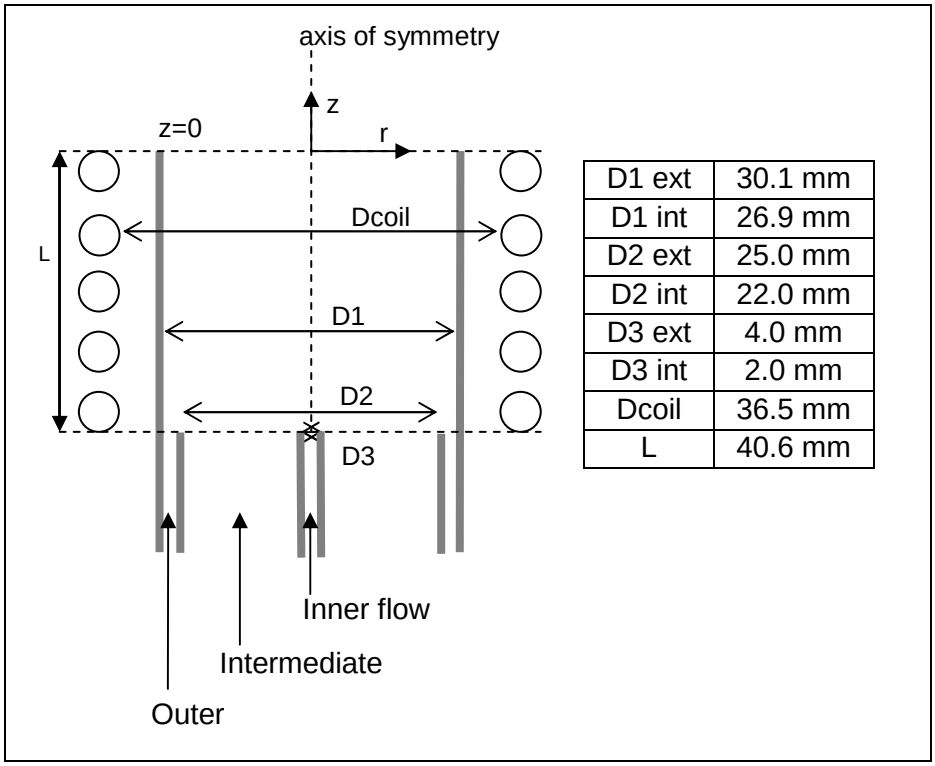

D1 ext	30.1 mm
D1 int	26.9 mm
D2 ext	25.0 mm
D2 int	22.0 mm
D3 ext	4.0 mm
D3 int	2.0 mm
Dcoil	36.5 mm
L	40.6 mm

Figure IV.3 Geometry of the small plasma torch

IV.2.2. The big torch

The geometry of the big torch is presented in Figure IV.4. The outer tube (orange) and the injector (blue) are water cooled copper tubes that can absorb higher heat fluxes than the quartz and alumina tubes of the small torch. The outer tube is divided into eight segments so that it does not shield the electromagnetic field. The intermediate tube (red) is a quartz tube. The big plasma torch is installed upside down on a reaction chamber. The outlet of the torch is at the top of the reaction chamber.

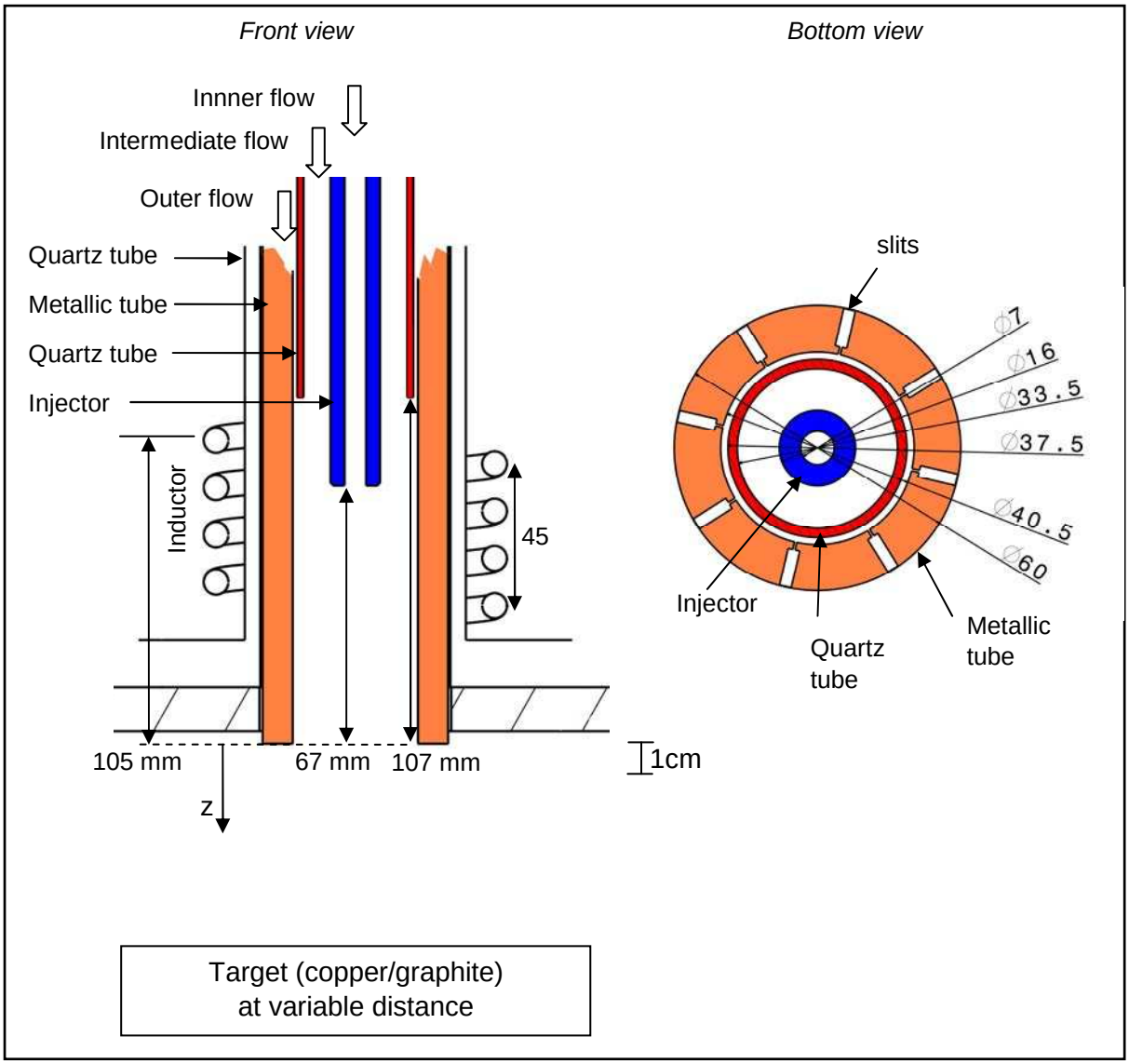

Figure IV.4 Geometry of the big plasma torch

IV.3. The RF generators

Our radio frequency (RF) generators work with a direct current. The alternating current from the power grid is transformed to a high voltage and then rectified. For the operation of the plasma torches, the voltage of the direct current is maintained constant. The direct current is measured in order to measure the power that is coupled into the plasma. In the measurements we give also the plate power, which is the power of the DC current. We assume that the power coupled into the plasma is proportional to the power of the DC current.

The high frequency alternating current is then created from the direct current using one or two triodes. The triode consists of a heated cathode, a grid and an anode in a low pressure chamber (Figure IV.5). The electrons form a cloud around the heated cathode and are attracted to the positively charged anode. When the grid is not charged the electrons flow from the cathode through the grid to the anode without interaction with the grid and the characteristics of the triode are similar to those of a resistor. When the grid is negatively charged the electrons are repulsed so that the current is reduced. When the grid is positively charged the electrons are accelerated and the current is increased.

In order to obtain an alternating current from the direct current the generator needs an oscillating circuit. The oscillating circuit is connected to the grid of the triode so that output voltage is fed back. The feedback loop acts so that the current increases when the voltage of

the circuit is maximal. In this way the triode supplies energy to the oscillating circuit at its resonance frequency.

IV.3.1. The power generator for the small torch

For the small 2 kW plasma torch we used a 40 MHz generator designed by RC DURR. It uses a tuned line oscillator which is described by Trassy [TM84] and Abdallah [ADJ76]. The oscillating circuit is formed by the anode lines which are a quarter wave length long (Figure IV.6). The frequency is therefore $f = c/(4l)$ (Figure IV.6). The LC-circuit couples to the plasma. When the plasma changes its shape or conductivity it causes a change of the impedance of the LC-circuit. The coupling lines play the role of an impedance matching system which minimizes power reflection of the LC-circuit.

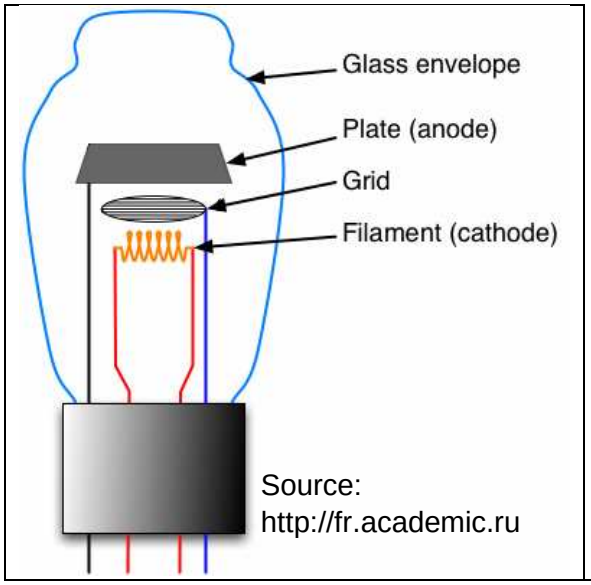

Figure IV.5 Triode

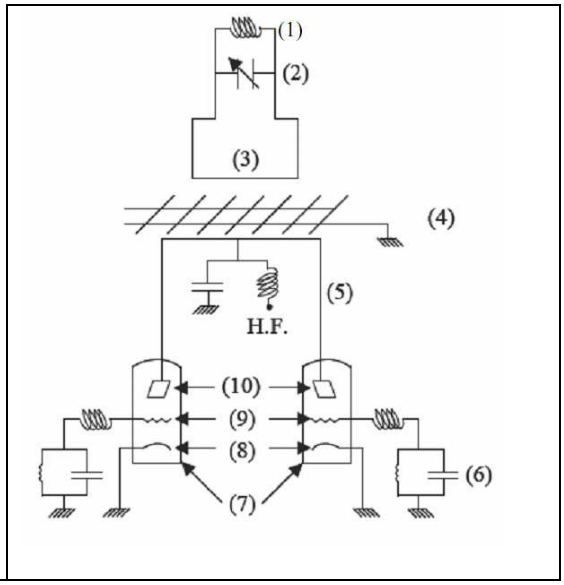

Figure IV.6 Tuned line generator
(1) inductor, (2) adjustable capacity
(3) coupling lines
(4) grid that screens the electric field
(5) Anode lines, (6) feedback circuit
(7) triodes, (8) Anode plates
(9) Grids, (10) Cathodes
[Ikh10]

IV.3.2. The power generator for the big torch

The generator of the big torch is of the type Collpits (Figure IV.7). The oscillating LC-circuit is formed by the capacitor and the induction coil on the right. The exact operation is rather complicated and has been well studied by Ernst. [Ern96]. We give here a simplified explanation for the working principle. During less than half of the period, when the top of the capacitor is negatively charged the feedback circuit charges the grid of the triode positively so that the triode becomes conductor. The short current peak that flows through the triode every period is separated by the choke coil and the link capacitor into a direct current and a radio frequency current. The radio frequency current flows towards the oscillating circuit and supplies it thus with energy. The frequency here is determined by the capacitor and the induction coil. $f = 1/(2\pi\sqrt{LC})$ and in our case is between 3.1 and 3.2 MHz depending on the impedance of the plasma.

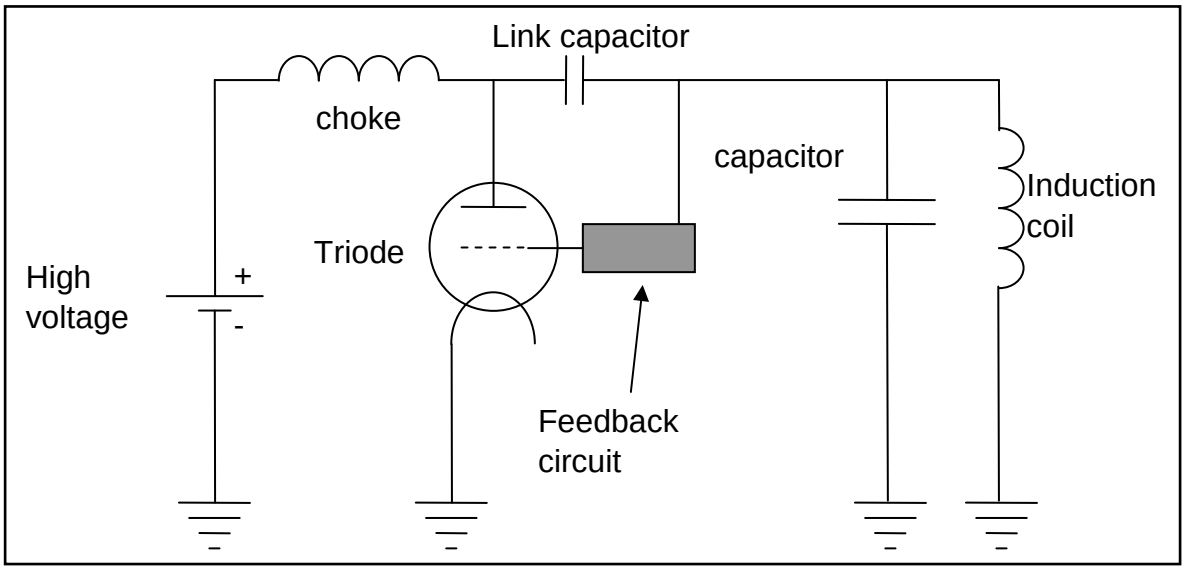

Figure IV.7 Generator of the type collpits

IV.3.3. The efficiency of the power generators

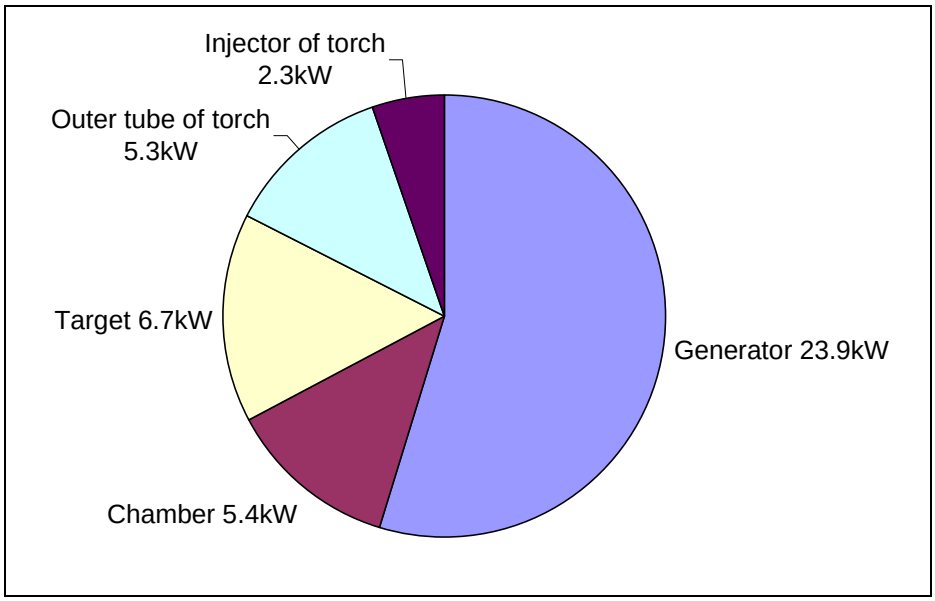

Figure IV.8 Power balance measured on the temperature difference of the coolant water for a DC power of 44.2 kW, Sum: 43.7 kW

The energy efficiency, the ratio between the power coupled into the plasma and the DC power is not known very precisely. However this factor is very important for the CFD model where the energy coupled to the plasma is set as a basic condition.

Lacombe [LDT08] reports an efficiency of 70 % for the power generator. We measured the power received by the different elements of the installation of the big torch by measuring the temperature difference and the flow rate of the coolant water. For this the plasma was operated during 30 min with the same parameters so that the power measured by the coolant flow has the time to stabilize. Especially the reaction chamber has a high thermal inertia so that the power stabilizes only after several minutes.

Figure IV.8 shows the results of this measurement. The heating power of the triode of 4.3 kW has yet been subtracted from the measured power of the coolant water of the generator (29.5 kW). The power evacuated by the gas flow was estimated to 0.2 kW using the temperature of the gas at the outlet of approximately 150°C. The power evacuated by the gas flow has been added to the power received by the chamber (5.2 kW).

The power received by the elements that are heated by the plasma (the torch, the chamber and the target) is only 45% of the DC power. As the outer tube also heated by the induced current, the efficiency is probably lower than 45%. 55% of the DC power remains in the generator. Benmansour [Ben03] found an efficiency between 38 % and 44 % for a 20 kW torch. This confirms our measurement.

The triode is probably the element that causes the major part of these losses. The power losses in the inductor are included in the measured power of the generator as they are on the same coolant circuit.

The sum of the power measured with the coolant water is slightly lower than the DC power. This difference may be due to the inaccuracy of the measurement of the DC power, due to heating of the generator from the rectifier or due to the inaccuracy of the power measurement of the coolant water.

IV.4. The flow controllers

Two different flow controllers were used in the experiments. For the spectroscopic experiments with the small torch and the purification experiments with the big torch rotameters were used to measure the flow. For the spectroscopic measurements with the big torch we used mass flow controllers.

IV.4.1. Rotameter

The flow controllers are mounted with a rotameter. With the rotameter the user can measure the flow rate and hence adjust the flow rate to a desired value. The rotameter consists of a float in a glass tube with a section that increases from the bottom to the top (see Figure IV.9.) The position of the float is determined by the equilibrium of the forces buoyancy, gravity and the flow forces. While the first two forces are constant, the latter changes with the flow rate and the position of the float. When the flow increases the float is pushed to a higher position until the flow force is the same as before. The user can read the position of the float which is approximately proportional to the flow rate. There are three different ways to calculate the flow rate from the position of the float.

- The easiest and least precise way is to divide the position by the length of the tube and multiply the result with by maximal flow rate that is given for the tube with the float.
- A more precise way is the use of calibration curves that are furnished by the manufacturer.
- The most precise way is to calibrate the flow meters regularly.

For the measurements on the small torch we always used the first method. For the purification experiments with the big torch, we calibrated the flow meters once.

We measured the flow rate with a 500 ml cup that was filled with water and placed upside down in a reservoir (Figure IV.10 right). We measured then the time it took to fill up the cup with the gas. We divided the volume of the cup by the measured time and obtained in this way the flow rate. We made several measurements for each flow meter and fitted than a second order polynomial (Figure IV.10). For high flow rates we used instead of the cup a jerry can whose volume was measured to be 27.3 l.

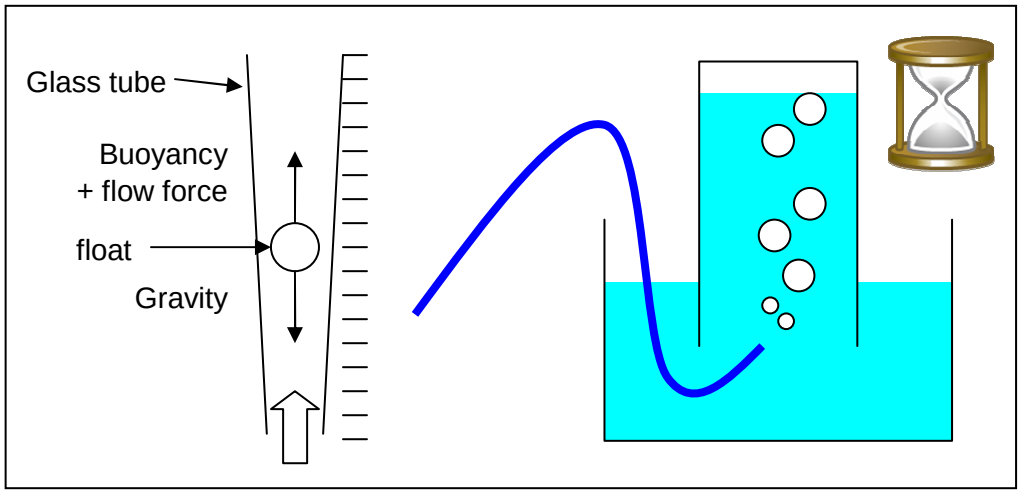

Figure IV.9 Setup flow controller test

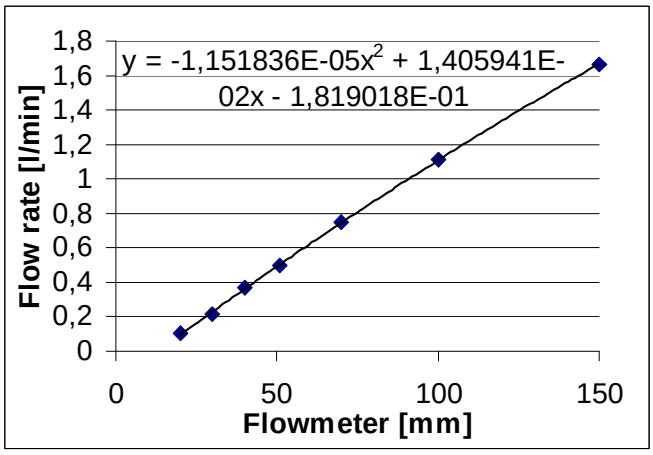

Figure IV.10 Calibration of the flow controller
The squares are the measured points and the curve is the fit

The mass flow rate which is interesting for our measurement depends on the value given by the flow meter and on the pressure. In [efu] a formula for the mass flow rate of a rotameter is deduced:

$$Q = C\overline{A}_b(z)\sqrt{\frac{2g\rho\left(\frac{V_f(\rho_f-\rho)}{A_f}-\rho h_f\right)}{\left[1-\left(\frac{\overline{A}_b(z)}{A_a(z)}\right)^2\right]}} \qquad \text{(IV-4)}$$

The cross section area of the tube $A_a(z)$ below the float and the cross section area of the space between the float and the tube $\overline{A}_b(z)$ are functions of the height *z*. The geometry (height h_f, cross section area A_f, volume V_f) and the density ρ_f of the float determine also the flow rate. In our case the density of the float ρ_f is about 1000 times higher than the density of the fluid ρ. With $V_f / A \approx h_f$ we can simplify equation (IV-4) to

$$Q = C\bar{A}_b(z)\sqrt{\frac{2g\rho\frac{V_f\rho_f}{A_f}}{\left[1-\left(\frac{\bar{A}_b(z)}{A_a(z)}\right)^2\right]}} \qquad \text{(IV-5)}$$

We can see that the mass flow is proportional to the square root of the density of the fluid $Q \mu \sqrt{\rho}$ and therefore also to the pressure in the rotameter $Q \mu \sqrt{p}$. The pressure of the inner flow and the outer flow are both equal to the atmospheric pressure. Due to the pressure drop in the torch the pressure of the coolant flow increases up to 2.1 bar at a flow rate of 6.5 m^3/h. We have to multiply the value from the calibration with the square root of the ratio between the pressure in the rotameter and the atmospheric pressure $\sqrt{p/p_{atm}}$. At high gas flows the expanding gas is cooled down. As no ice was observed at the bottle we can estimate that the temperature remained above 0 °C and temperature variations thus below 20 K. Temperature variations of 20 K may cause a variation of 3.4% as shown in equation (IV-6).

$$\frac{\Delta Q}{Q} = \left|\frac{dQ}{dT}\right|\frac{\Delta T}{Q} = 0.5\times\frac{\Delta T}{T} = 0.5\times\frac{20K}{293K} = 3.4\% \qquad \text{(IV-6)}$$

IV.4.2. Mass flow controller

The mass flow controllers used for the spectroscopic measurements on the big torch are from the Brooks SLAMf series. Figure IV.11 shows the working principle of such a mass flow controller. For the measurement of the flow rate the flow is divided into a flow 'A' that passes through the flow sensor and a flow 'B' that passes through a restrictor. The pressure difference between the point upstream of the restrictor and the point downstream is proportional to the total flow rate 'A'+ 'B'.

The flow sensor consists of a thin tube with a heater and two temperature sensors next to the heater. The heater heats the gas with a constant power. When the flow rate is zero the two temperature sensors next to the heater measure the same temperature. When gas flows through the flow sensor heat is carried from the heater to the downstream temperature sensor so that this temperature sensor measures a higher temperature than the upstream temperature sensor. This temperature difference $\Delta T = T_2 - T_1$ between the two sensors is proportional to the gas mass flow. The relation between the gas mass flow m $[kg/s]$ and the temperature difference ΔT is given by equation (IV-7).

$$\Delta T = A \times P \times C_P \times m \qquad \text{(IV-7)}$$

Where

A $[s^2K^2/kJ^2]$ Constant of proportionality

P $[kJ/s]$ Heater power

C_p $[kJ/kg/K]$ specific heat of the gas at constant pressure

The electronics creates a signal that is proportional to the measured temperature difference. A calibration is necessary so that the electronics can transform the signal into a mass flow. The calibration curve is different for different gases because the specific heat is different. With calibration the accuracy of the mass flow controller is 1%. A desired value can be set for the mass flow. The valve adapts then the gas flow until the flow sensor measures the desired value. The desired value is set in the unit sm^3/h (1sm^3/h = 1 m^3/h at 0 °C and 101.325 kPa).

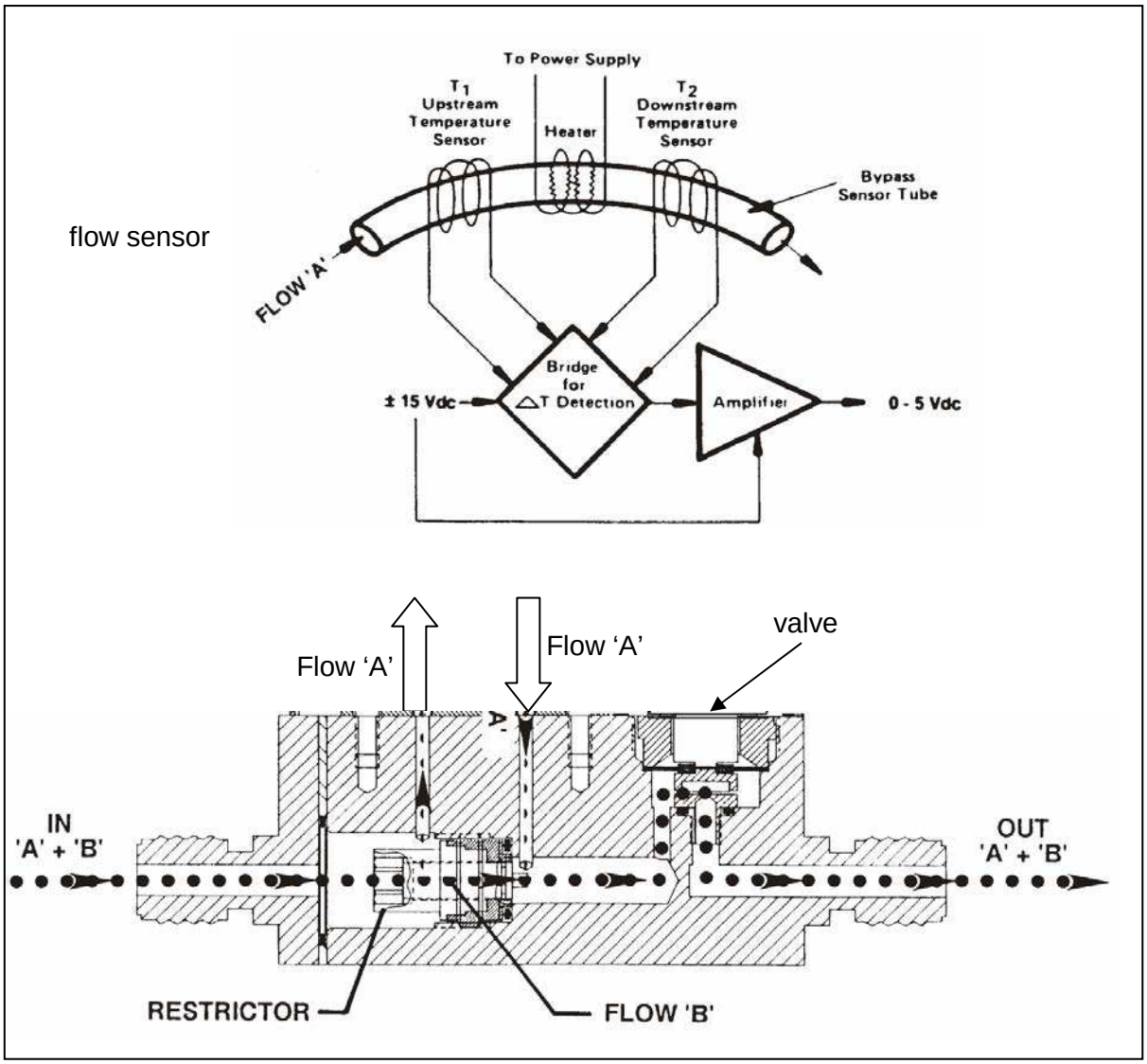

Figure IV.11 Working principle of the Brooks mass flow controller

IV.5. The nebulizer

We used a nebulizer of the type Meinhard (Figure IV.12 left) to inject water into the plasma. It consists of a nozzle with a gas flow and a small tube for the liquid. The liquid is sucked into the high velocity argon jet and turned into an aerosol. In our experimental setup the nebulizer is assembled with a Scott spray chamber (Figure IV.12 right), which removes the biggest droplets from the aerosol. A peristaltic pump was used to supply the liquid to the nebulizer.

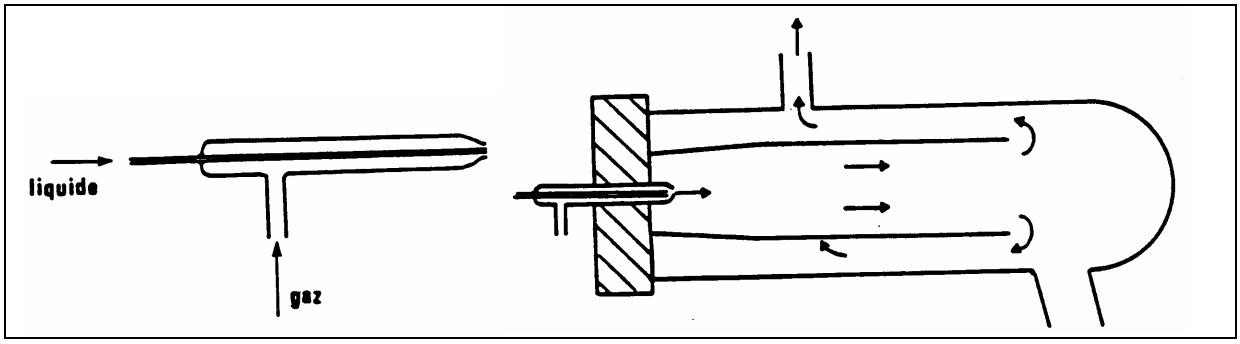

Figure IV.12 Nebulizer of type Meinhard (left) and assembled with a Scott spray chamber (right). Source [TM84]

IV.6. The optical setups

Two different optical setups were used in this study. For the measurements on the small plasma torch (~2 kW) a monochromator (Jobin-Yvon HR640) with a photomultiplier was used to test the method. The measurements on the big plasma torch were then done with an imaging monochromator (Acton SP2756) with a CCD camera. Table IV-1 compares the two monochromators and the optical setups

IV.6.1. Optical setup with Jobin-Yvon HR640 (with photomultiplier)

The first measurements were done with the optical setup that is shown in Figure IV.13. The light emitted by the plasma is reflected by a turning mirror towards the monochromator. A lens focuses the light onto the entry slit of the monochromator. Since the width of the entry slit is very small (100 µm * 2 mm) only the light which is coming from a chord, with the cross section of the image of the entry slit, can enter the spectrometer. This is important for the Abel inversion which is described in chapter III.

The spectrometer consists of a monochromator HR640 Jobin Yvon and a photomultiplier. The current from the photomultiplier is amplified and flows then to a box that counts the photons. The box sends a number of hits to the computer for the data acquisition. The number of hits per second is proportional to the intensity at the wavelength of the monochromator. The computer controls the turning mirror, the monochromator and the acquisition time. The turning mirror turns step by step and after each step the computer measures the intensity and obtains thus a lateral intensity profile. The measured number of hits per second is proportional to the spectral intensity at the wavelength at which the monochromator is set. The important details of the setup are given in Table IV-1.

	a) Jobin-Yvon	b) Acton
Monochromators		
Focal length	640 mm	750 mm
Half inclusion angle of grating	13.2°	6.49°
Grating size w x h	106 x 101 mm	68 x 68 mm
Groves	2400 mm^{-1}	1800 mm^{-1}
Slits	Straight	Straight
Entry slit width	100 µm	100 µm
Exit slit width	100 µm	none
Monochromator mirrors	Spherical	Toroidal
Detector	Photomultiplier tube	CCD camera Pixis-400B (1340*400 pixel, 20 µm, 16 bit)
External Optics		
Focal length of the lens	220 mm	300 mm
Lens	(Quartz)	Achromatic (N-BaK4/N-SF10)
External Mirror	Turning mirror, Step width 0.05° Repeatability <0.02°	Two motorized mirrors
	Figure IV.13	Figure IV.14

Table IV-1 Two optical setups, a) With Monochromator Jobin-Yvon HR640, b) With Acton SP2756

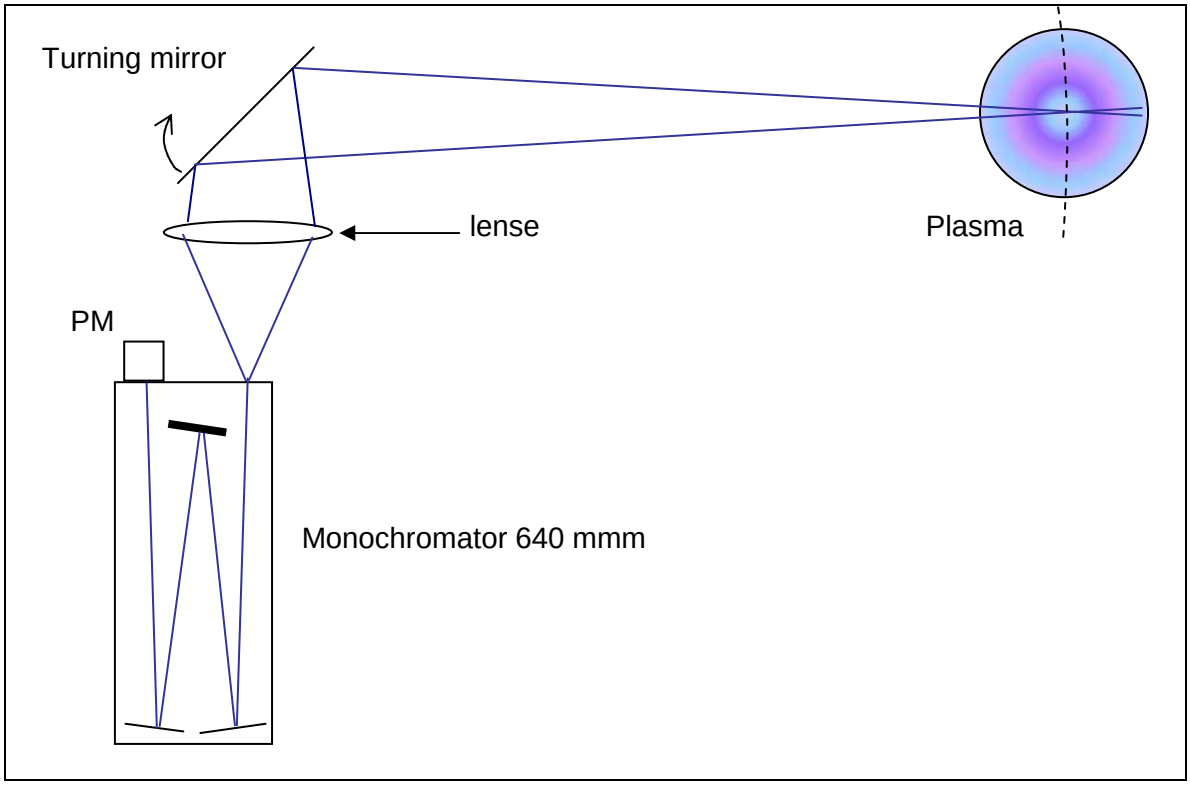

Figure IV.13 First optical setup with Jobin-Yvon monochromator used for measurements on the small plasma torch (~2 kW)

IV.6.2. Optical setup with Acton SP2756 (with CCD camera)

The first optical setup described above, had the inconvenience that the measurements were very slow and that temporal variations of the plasma had a big influence on the concentration measurement, because the two lines necessary for the concentration measurement could not be measured at the same time.

The light of the plasma (blue cylinder in Figure IV.14) goes through the window of the reaction chamber. Two mirrors reflect the light towards a lens (Focal length 300 mm) which focalizes the image on the entrance slit of the monochromator Acton SP2756 (See Table IV-1). A vertical rectangular diaphragm of 2x10 mm was installed next to the lens in order to reduce the intensity. The height of 10 mm was chosen to minimize the impacts of slit diffraction (of the diaphragm) and spherical aberrations.

The two mirrors are mounted on motorized linear stages so that the field of observation can be positioned in two directions. The lens is moved simultaneously so that the image of the plasma remains focalized. The variation of the magnification between 5.9 and 5.6 is taken into account during the data processing.

The two mirrors turn the image by 90° so that the image of the vertical plasma is horizontal. The vertical entry slit of the monochromator measures thus a horizontal profile of the plasma. The vertical dimension of the CCD is used for the spatial resolution and the horizontal dimension of the CCD is used for the spectral resolution. Each horizontal line of the CCD camera measures the spectrum of a different point of the plasma. The vertical lines of the CCD can thus be Abel inverted to find the local emissivity at the respective wavelength. It is thus possible to measure the radial emissivity of an argon line and a hydrogen or oxygen line in one 2D spectrum. This reduces significantly the error due to variations of the temperature between two measurements when the two lines are not measured at the same time.

Before the measurement the optical system is calibrated with a tungsten lamp for absolute intensity measurements. In order to use the full dynamic range of the camera, the

acquisition time is adapted between 0.05 s and 5 s after each measurement, so that the signal remains high without saturating the camera. The measurement and the real time data processing take from 2 to 7 seconds per spectrum depending on the acquisition time. It takes so about five minutes to measure a 2D concentration ratio map and a 2D temperature map with 90 horizontal lines. The monochromator and the CCD camera are controlled with LabView using the DLL of Winspec. The same LabView program controls also the motorized linear stages and can so do automatic measurements of 2D temperature and concentration ratio maps.

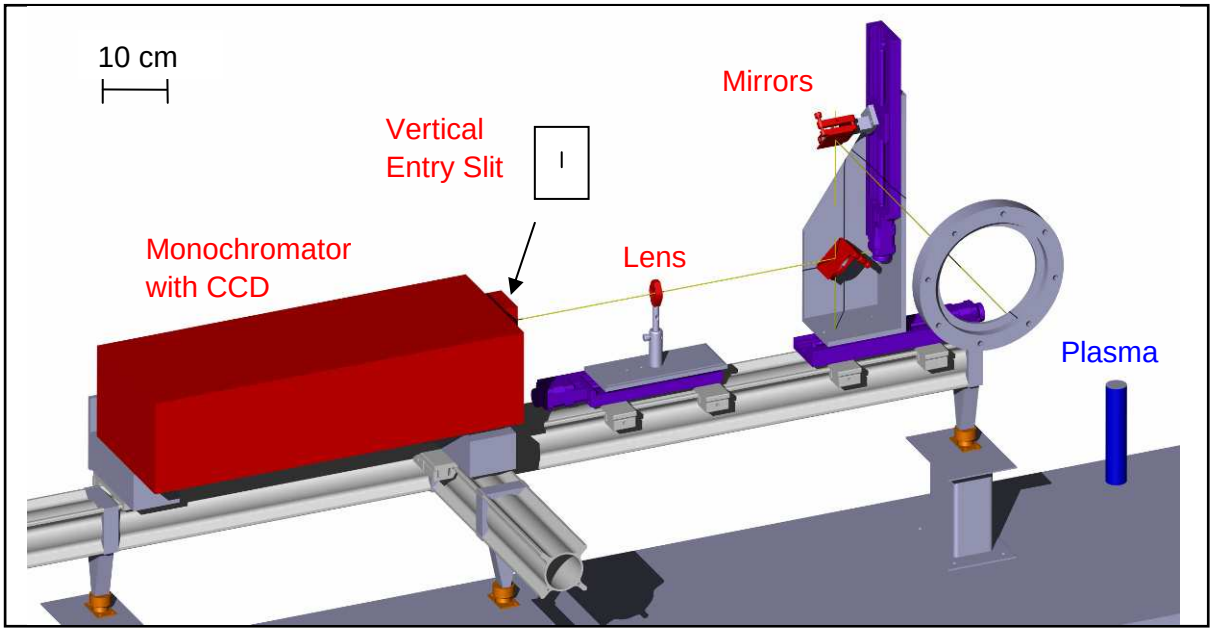

Figure IV.14 Second optical setup with Acton imaging monochromator with CCD camera detector used for measurements on the big plasma torch (~40kW)

IV.7. Error sources

IV.7.1. The non uniformity of the entrance slit

As the entrance slit is very thin, small irregularities on the blades of the slit have a big impact on the response. We measured the vertical response profile by measuring the light from a white computer screen. One motor was moving during the measurement so that the irregularities due to the pixels of the computer screen were reduced. Figure IV.15 shows the vertical response profiles for different slit widths. One can see that at a slit width of 20 µm the irregularities have a much bigger impact than at a slit width of 100 µm. We can deduce from the vertical transfer profiles that the size of the irregularities is about 20 µm.

A larger slit width has thus the advantage that the irregularities have a smaller impact. At the same time it reduces the vertical resolution. At a slit width of 100 µm the vertical resolution of the plasma is 0.6 mm. We chose therefore a slit width of 100 µm to have high vertical resolution and a small impact of the irregularities on the entrance slit. The spectrum is divided by the vertical response profile in order to remove the irregularities.

Another criterion that may define the slit width is the spectral resolution. A small slit width gives a higher spectral resolution so that two close lines can be separated. A large slit width gives a smaller spectral resolution but as the line is spread over more pixels it can be measured with a higher dynamic.

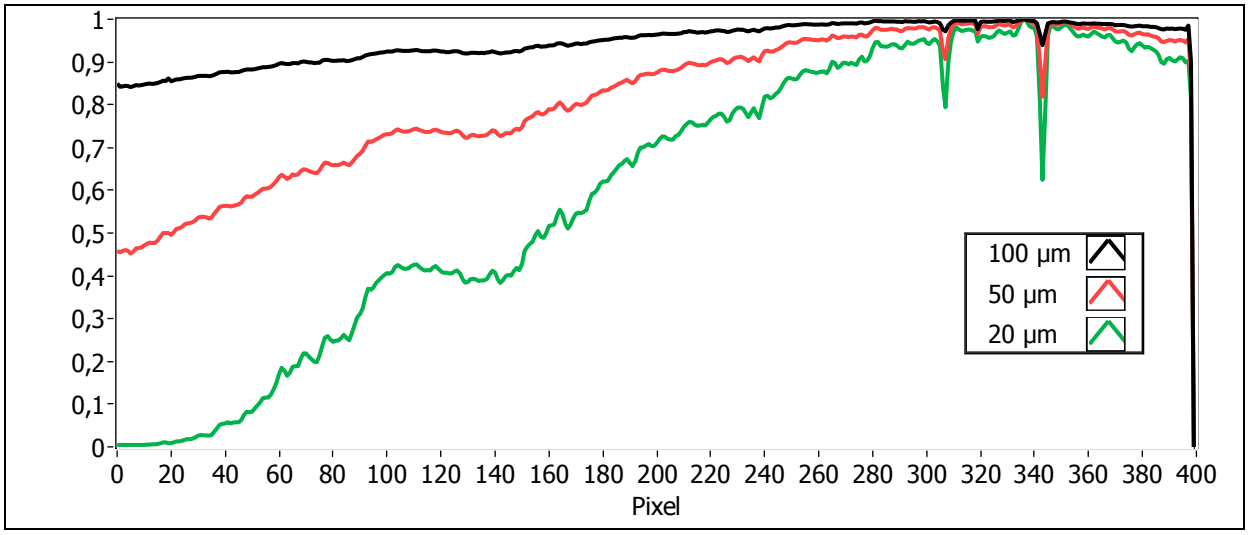

Figure IV.15 Vertical response profile for different slit widths.

IV.7.2. Flat field correction

At small wavelengths (<500 nm) the response of the CCD camera is not homogenous. For the measurement of the flat field we illuminated the entry slit with a torch and measured a 2D spectrum at 415 nm. We divided each vertical line of the 2D spectrum by its mean value and then we divided each horizontal line by its mean value. We obtain thus the pattern that is shown in Figure IV.16. One can see larger and smaller responses compared to the mean response. This effect occurs at small wavelengths and must therefore be considered for the measurement of the hydrogen line at 410.2 nm, while it is negligible at 640 nm for the measurement of the oxygen line. This pattern is a default of the CCD caused by the thinning process at the CCD fabrication. The spread of the different responses is only about 3% and can therefore hardly be seen in the raw spectrum (see Figure IV.20) but the Abel inversion amplifies the error so that it has a big impact on the concentration measurement. There are also some spots which are caused by dust particles on the camera. As the different responses are a linear effect one can divide the measured raw spectrum with the flat field spectrum of Figure IV.16 to reduce the impact of the different responses.

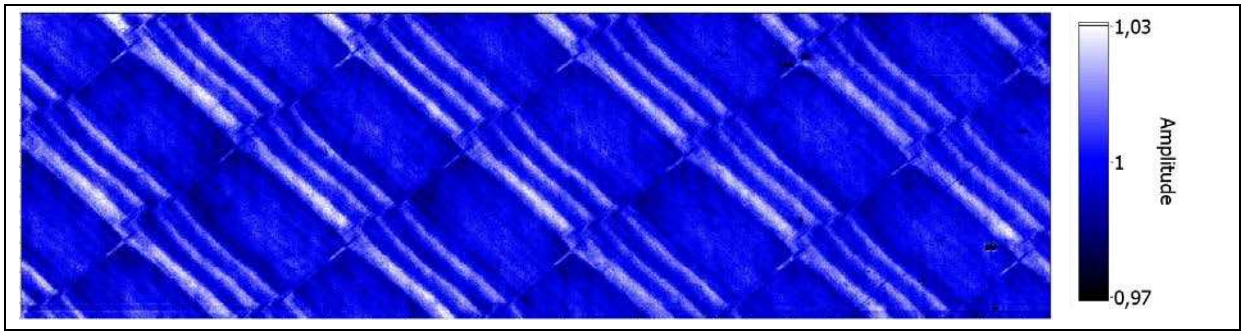

Figure IV.16 Relative response of the CCD to uniform illumination at 415nm.

The influence of the flat field correction on the measurement

In Figure IV.17 one can see the influence of the flat field correction on the measurement of a homogenous concentration profile of hydrogen. First the measured spectra were directly used to calculate the concentration ratio (see (a) in Figure IV.17). Then the same spectra were divided by the flat field of Figure IV.16 before the calculation of the concentration (see (b) in Figure IV.17). While in (a) some vertical lines appear they are not visible anymore in

(b). The vertical lines in (a) are thus caused by the non-uniform response of the CCD and can be corrected by the flat field correction.

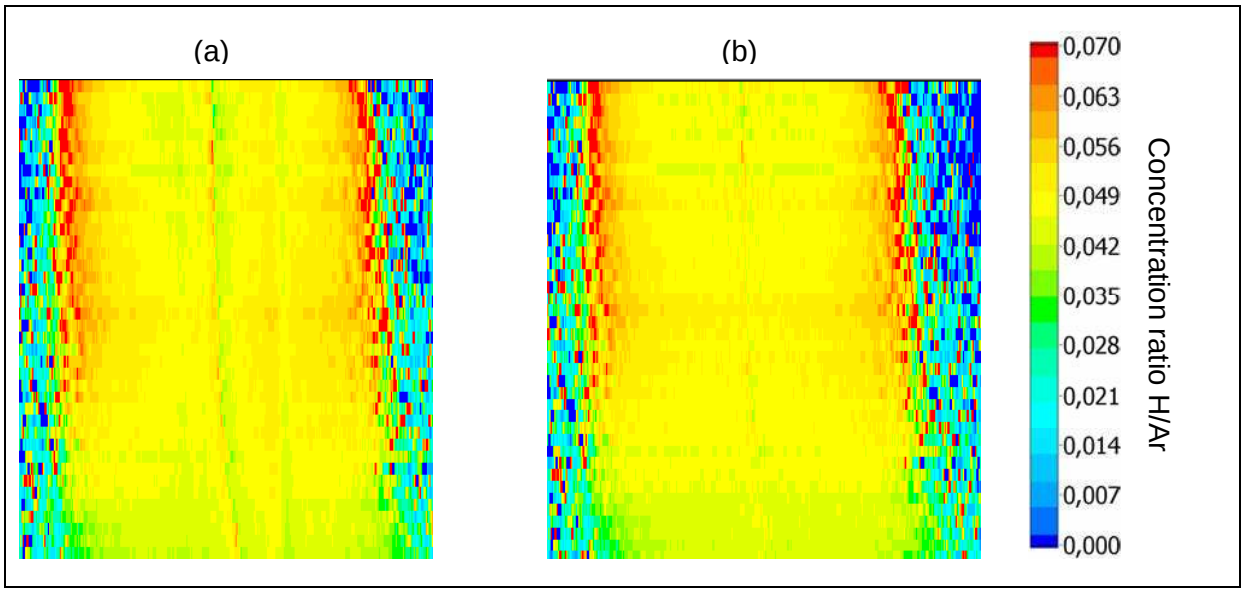

Figure IV.17 Concentration measurement H/Ar (a) without and (b) with flat field correction. in (b) the same raw spectra as in (a) were divided by the flat field of Figure IV.16

IV.7.3. Straylight

After the first measurements with the first setup stray light was identified as an error source. The stray light came from scratches and dirt on the mirror and on the lens and from the backside of the reaction chamber. In order to reduce the stray light the mirror and the lens were replaced by new ones and a black graphite felt was installed at the back side from the chamber. The graphite felt was treated with an oxy fuel torch in order to obtain a very low reflectivity. For this the oxy fuel torch was operated with an fuel rich mixture and the carbon black from the combustion was deposited on the graphite. Figure IV-18 shows two different temperature profiles. One of them was measured before the reduction of the stray light and the other was measured after the reduction of stray light. Before the reduction of stray light the measured intensity remains high at the edge of the plasma. After the reduction of the stray light the intensity goes very close to zero. Figure IV-19 shows the measured temperature profiles before and after the reduction of the stray light. Before the reduction of the stray light the measured temperature gradient decreases at the edge of the plasma. As the temperature around the plasma is much lower than 7500 K, it is clear that this decrease is not real but due to the stray light. After the stray light reduction the measured temperature gradient remains constant at the edge of the plasma. At a radius of 17 mm one can see a sharp transition between measured values that seem realistic and measured values that are strongly influenced by noise. The difference between the highest measured temperature and the lowest measured temperature could be increased from 1500 K to 3000 K.

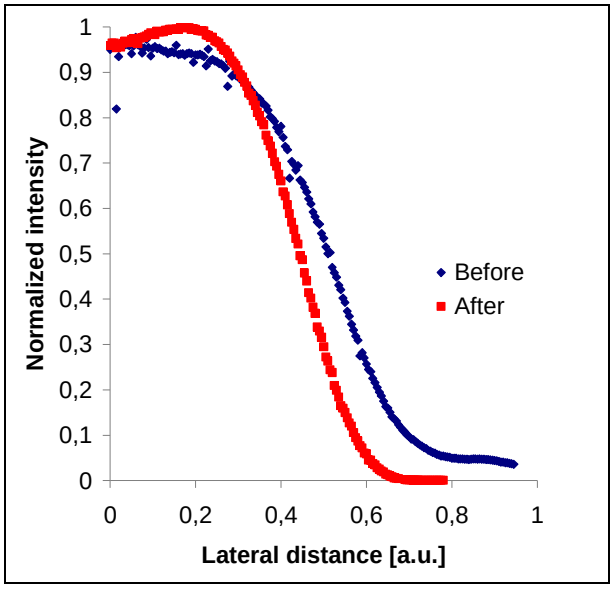

Figure IV-18 Intensity profile before and after stray light reduction

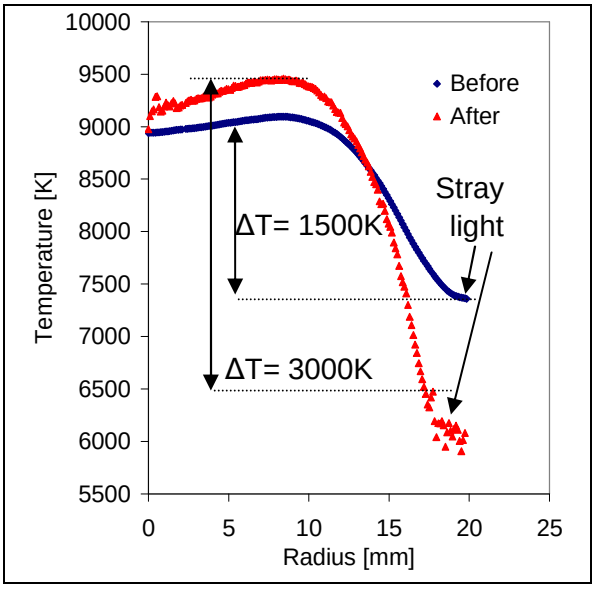

Figure IV-19 Temperature profile before and after stray light reduction

IV.8. Data processing

The monochromator, the CCD camera and the motorized linear stage are controlled by a homemade labview program. The same program calculated the concentration ratio and temperature profiles after each acquisition of a spectrum using the formula that have been described in chapter III. Here we describe briefly the data processing.

Figure IV.20 shows the two dimensional raw spectrum as acquired by the CCD camera. This spectrum is used to measure the temperature profile and the concentration ratio [H]/[Ar]. The spectrum is flat field corrected in order to remove diagonal fringes caused by the CCD. In order to obtain the absolute intensity, the spectrum is divided by the measured spectrum of the calibration lamp and multiplied by the intensity of the calibration lamp.

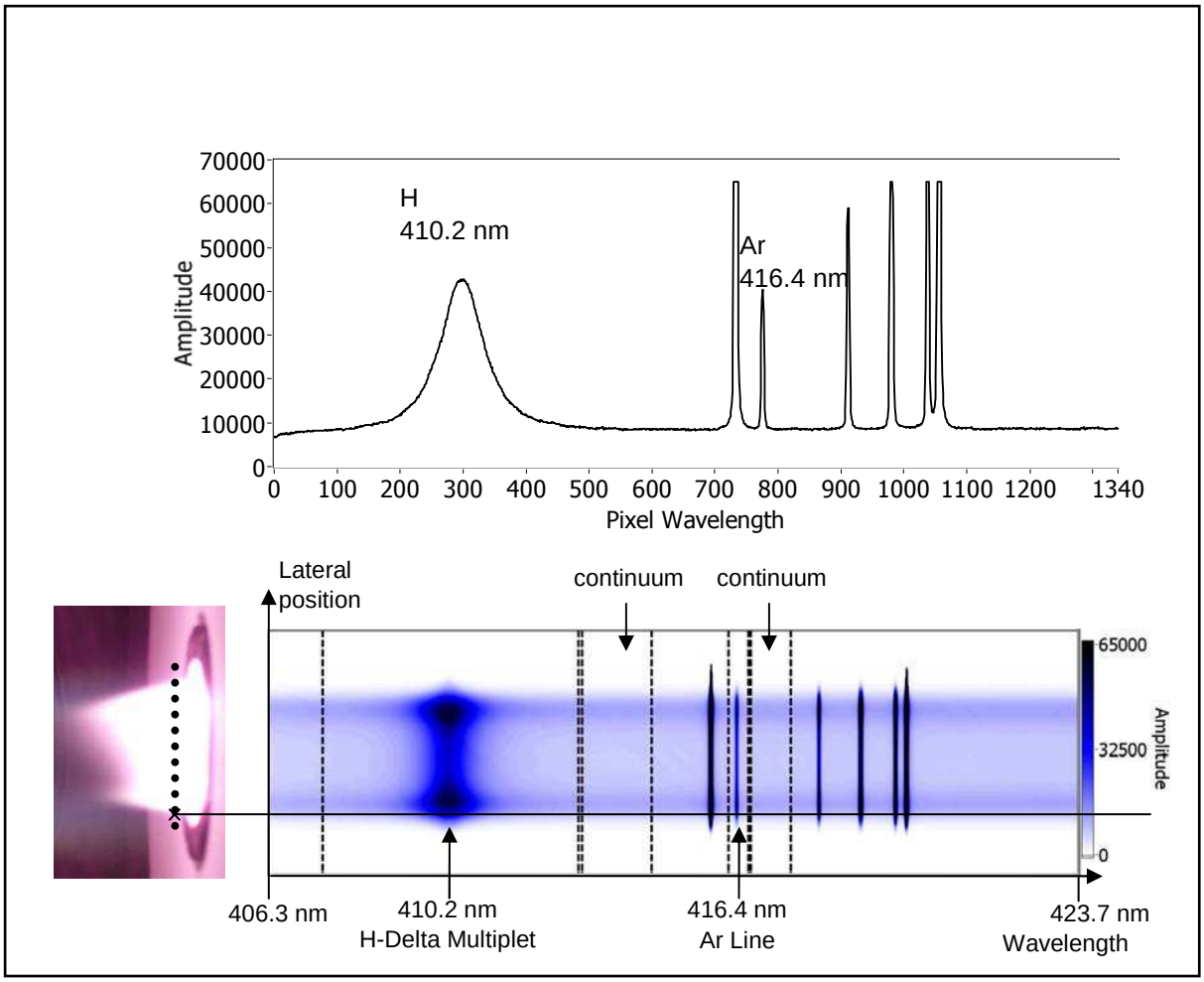

Figure IV.20 Two dimensional spectrum used for the measurement of the concentration ratio [H]/[Ar] and the temperature.

The vertical dashed lines in Figure IV.20 indicate the regions, which are integrated into the wavelength direction in order to obtain the lateral intensity profiles of the hydrogen line, the argon line and the continuum next to each line. The integration between the two dashed lines gives the integration over the width of the line so that the total emissivity is obtained. The lateral profile of the hydrogen line and the argon line are shown in Figure IV.21a. The continuum is not yet subtracted. All four lateral profiles are smoothed using a polynomial fit of the order 2 and a length of 11 points in order to remove the shot noise which would be amplified by the Abel inversion (see chapter III). Then the profiles are cut in the centre into two half profiles, which are then Abel inverted in order to obtain the radial emissivity profile (Figure IV.21b). At the edge and in the centre the emissivity is very low so that the signal to noise ratio is small. At the edge the signal to noise ratio is too small when emissivity is below 0.2% of the maximal emissivity so that these values are cut off. In the centre the noise is higher due to the Abel inversion. Here the limit where the values are cut off is chosen manually. The measurement is thus limited to the hot zone of the plasma where the emissivity is high.

The emissivity profiles of the continuum are then subtracted from the emissivity profiles of the hydrogen line and the argon line respectively. The local emissivity is then used to calculate the temperature (Figure IV.21c) and the concentration ratio (Figure IV.21d).

One can see in Figure IV.21c that at the edge of the plasma the noise on the temperature measurement is small down to 2500 K below the maximum temperature which corresponds

to 0.2 % of the maximum emissivity, the limit for the cut-off. The noise on the temperature measurement and on the concentration measurement is small between the two cut-off limits. The measurement is done from the outlet to 90 mm further down every 1 mm. In the result we present the left and the right part of the plasma to show the symmetry of the plasma. The measurement for oxygen is equivalent with the corresponding lines.

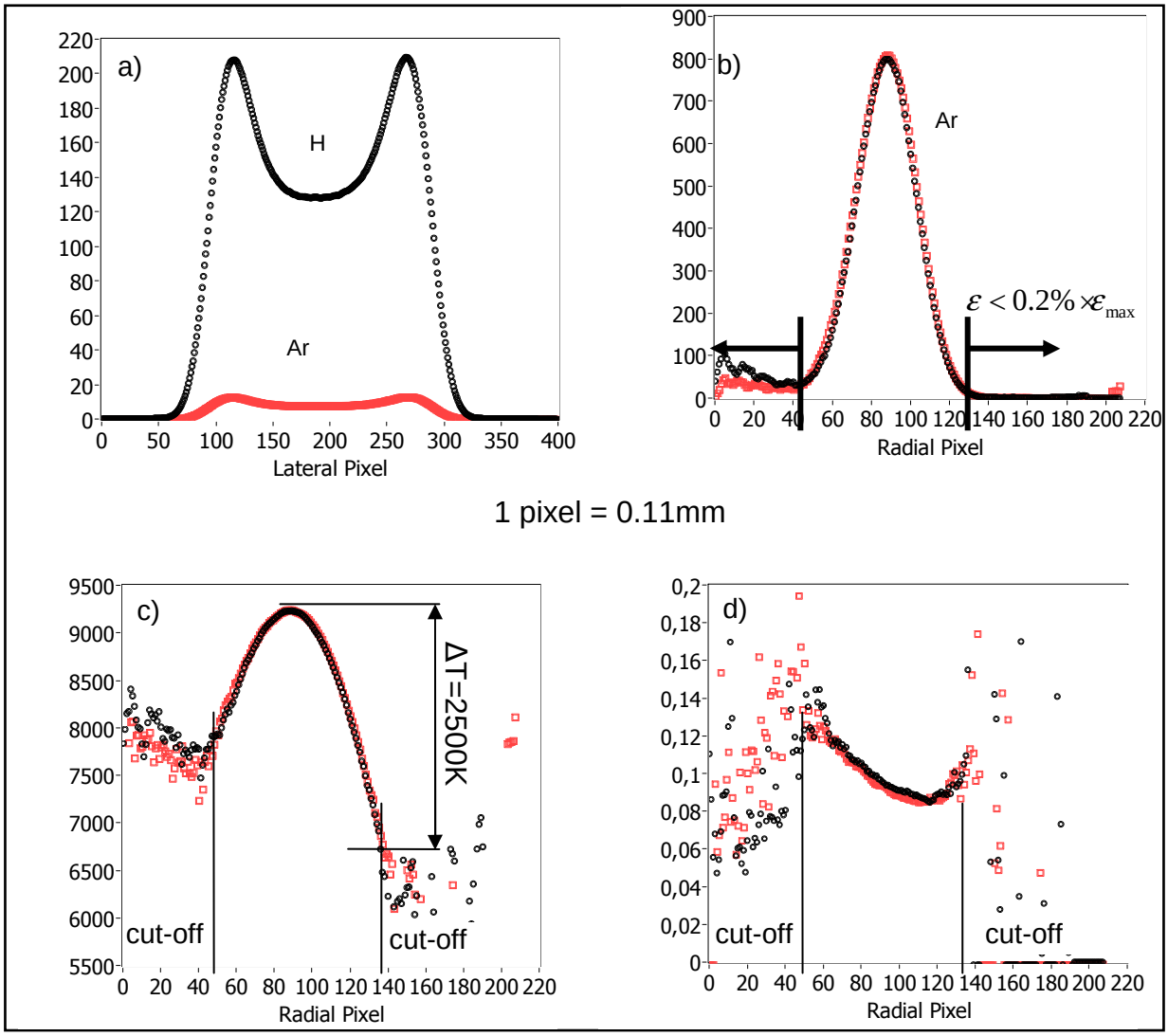

Figure IV.21 The profiles of the data processing (1 pixel correspond to 1 mm of the plasma)
a) Lateral Profiles
b) Abel inversion of Ar line (left and right)
c) Temperature profile (left and right)
d) Concentration ratio profile (left and right)

IV.9. Measurement of the FWHM of a line

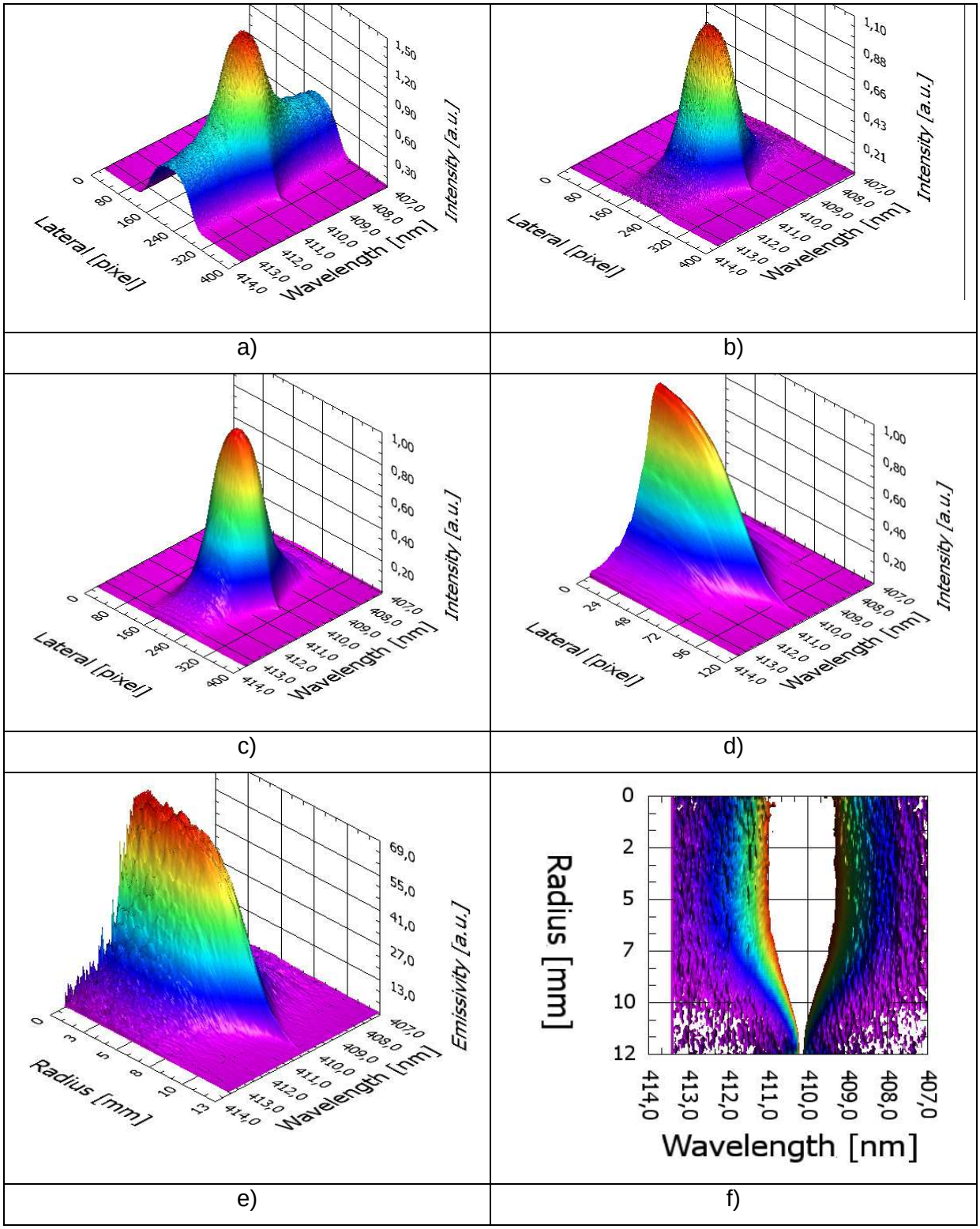

Figure IV-22 Data treatment for the measurement of the FWHM of the H-Delta line
a) The spectrum after flat field correction
b) The spectrum after the subtraction of the continuum
c) The spectrum after polynomial smoothing
d) The half spectrum
e) The Abel inverted spectrum
f) The Abel inverted spectrum divided by the maximum of each radius and cut at 0.5

Figure IV-22 shows the data treatment for the measurement of the FWHM of the H-Delta line.

- In a) we can see the measured spectrum which has yet been flat field corrected. In a first step the emissivity of the continuum is removed. For this the emissivity of the continuum is measured next to the line and then subtracted from the spectrum.
- b) shows the spectrum after the removal of the continuum. In a next step polynomial smoothing with the order 2 and a length of 11 data points is applied first in the wavelength direction and then in the lateral direction.
- The smoothed spectrum is shown in c).
- Then the spectrum is cut in the center. d) shows the half profile.
- The two half profiles are then Abel inverted. e) shows the Abel inverted spectrum. One can clearly see that the little noise of spectrum d) is amplified.
- Then the spectrum is divided by the maximum and cut at 0.5 as one can see in f). The width of the white space in the centre is the FWHM of the line.
- g) shows the radial profile of the FWHM. We can see that at higher radii the FWHM is much smaller than in the center.

IV.10. Data processing for optical setup with photomultiplier tube

The calculation of the temperature and the concentration ratio profile O/Ar using the measurements of the first optical setup with photomultiplier tube is very similar to the calculation using the measurements of the second optical setup with the CCD camera. The difference is that with the first optical setup only the spectral emissivity at the center wavelength of the line was measured and that this emissivity had to be multiplied with the constant ratio between the total emissivity and the emissivity at the center wavelength. With the local emissivity we can calculate the local temperature and the local concentration ratio O/Ar as described in Figure IV-23.

For the hydrogen line the ratio between the total emissivity and the emissivity at the central wavelength depends on the temperature. Therefore we need to calculate the temperature first and can then use the simulated ratio (as described in chapter III) to calculate the total emissivity. With the total emissivity we can calculated the concentration ratio H/Ar in the same manner as the concentration ratio O/Ar using the data of the hydrogen multiplet instead.

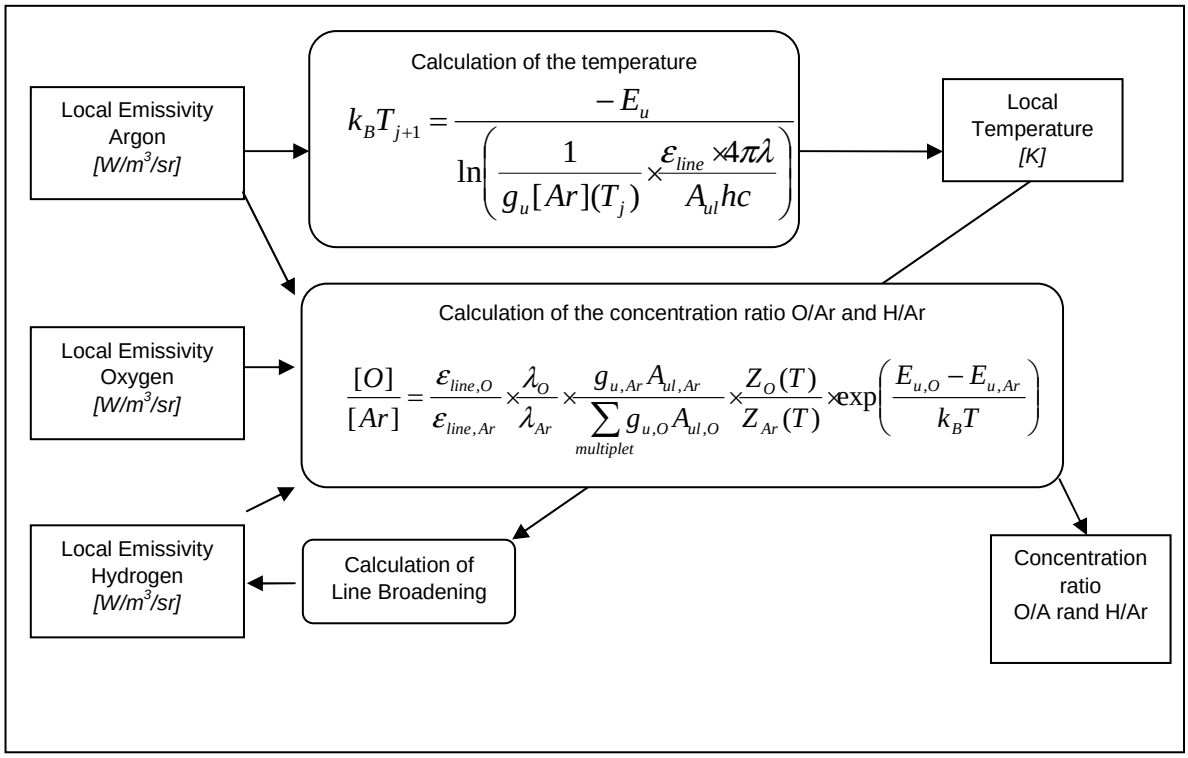

Figure IV-23 Methodology: Calculation of temperature and relative concentrations. The formula are described in chapter III

IV.11. Calibration of the optical setup

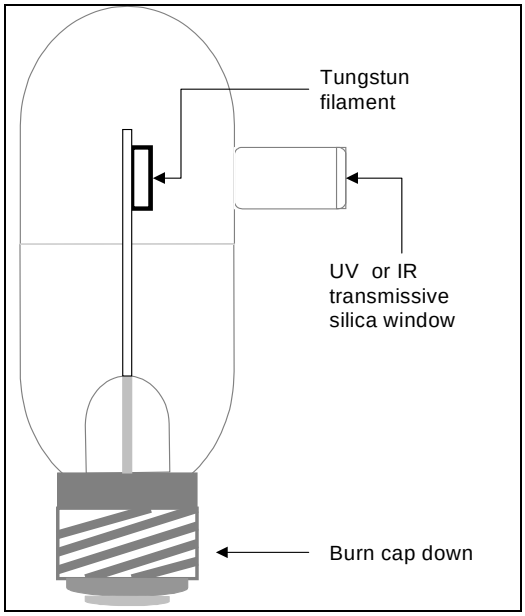

Figure IV.24 Tungsten ribbon secondary standard source with silica window Source: [TC99]

For the calibration of the optical setup, we replaced the plasma torch by a calibration lamp. The tungsten lamp, which we used has a special silica window which is transparent for UV and IR (see Figure IV.24). The lamp was tested by the "Laboratoire National d'Essais", which measured a temperature of 2330±4 K when the lamps was operated 14.30±0.10 A. We verified the temperature with a two-color pyrometer and obtained a similar precision on the temperature. The spectral radiance $I(\lambda,T)[W \times m^{-2} \times nm^{-1} \times sr^{-1}]$ of the tungsten ribbon is given by equation (IV-8). The error on the spectral radiance due to the temperature inaccuracy is about 4%.

$$I(\lambda,T)=\varepsilon(\lambda,T)\times\frac{2hc}{\lambda^5}\frac{1}{\exp\left(\frac{hc}{\lambda kT}\right)-1} \qquad \text{(IV-8)}$$

De Vos [Vos54] measured the emissivity $\varepsilon(\lambda,T)$ of a tungsten ribbon over a wide spectral range for different temperatures. Pon [PH84] fitted polynoms to the emissivity measured by De Vos. We used the polynoms from Pon to calculate the spectral radiance at 2330 K. The calculated spectral radiance was then multiplied by 0.92 [BBS71] to take into account the reflection losses at the quartz window of the tungsten lamp. We estimate an accuracy of 10 % for the spectral radiance of the tungsten lamp.

The image of the tungsten filament must be focused on the entry slit of the spectrometer. The measurements on the small torch were performed with a quartz lens that was not achromatic. Therefore the image of the lamp was not focused at all wavelengths which may induce an error on the calibration.

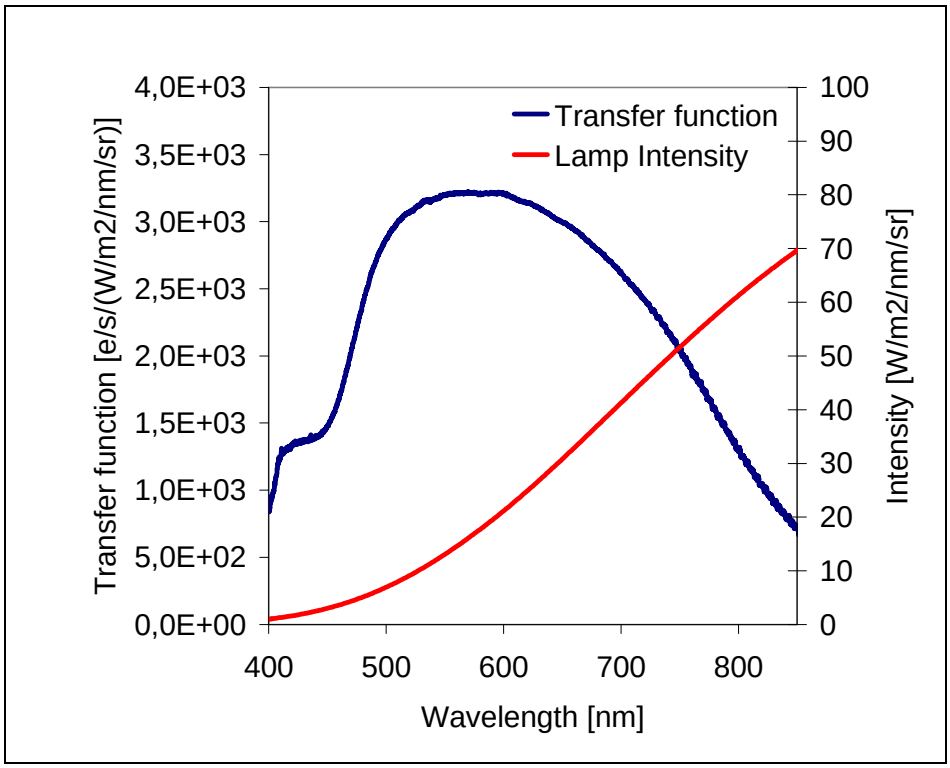

Figure IV.25 The transfer function of the Acton SP2756 with the 1800 mm^{-1} grating

Once the lamp was focused we measured the number of hits per second as a function of the wavelength. We divide the number of hits per second by the spectral radiance and find thus the transfer function of the optical setup. The transfer function varies with the wavelength as shown in Figure IV.25. The variation is on the one hand due to the variation of the sensitivity of the CCD camera and on the other hand due to the variation of the light collecting of the grating which turns when the wavelength is modified. Below 400 nm the absorption of the lens and the window of the reactor chamber becomes significant. The measured spectra (unit: e/s) needs to be divided by the transfer function to obtain the absolute intensity spectra (unit: $W/m^2/nm/sr$).

At the wavelength of the OH-radical (310 nm) the spectral radiance of the lamp is very low and stray light in the monochromator becomes important. At this wavelength the calibration is therefore not accurate.

IV.12. Conclusion

We have presented in this chapter the setup used for the spectroscopic measurements. We described the two plasma torches that were used and their RF generators. We measured the energy efficiency between the generator and the plasma. The energy efficiency is an important parameter for the CFD model. The flow controllers were presented and their precision was analyzed. We presented the two optical setups that were used. For the setup with CCD camera, the measured spectrum must be corrected for the non-uniformity of the entrance slit of the monochromator and for the non-uniformity of the response of the CCD capmera. We showed data processing that is used to calculate the radial temperature profile and the radial concentration ratio profile from a 2D spectrum of the CCD camera. We identified stray light as an error source and explained how the stray light could be reduced. We explained how we calibrated the optical setups with a calibration lamp.

V. Spectroscopic measurements

This chapter presents the spectroscopic measurements that have been performed. The first measurements have the objective to validate the measurement method. The method is based on the assumptions of local thermal equilibrium and symmetry. We did thus several measurements to test the assumption of local thermal equilibrium. Then several temperature and concentration ratio measurements are compared to the results of a CFD model in order to test the latter. The comparison shows that the k-ω-SST turbulence model gives better results than the k-ε turbulence model that we applied before. At the end several measurements show the dependence of the torch temperature and concentration distributions on several parameters.

Figure V-1 shows the superposition of an image of a typical plasma with the temperature and the concentration ratio measurement. The figure shows schematically how the spectroscopic measurement can make the invisible properties visible. Reflections from the opposite window that can be observed in the image do not perturb the spectroscopic measurements which were done with a black canvas behind the plasma.

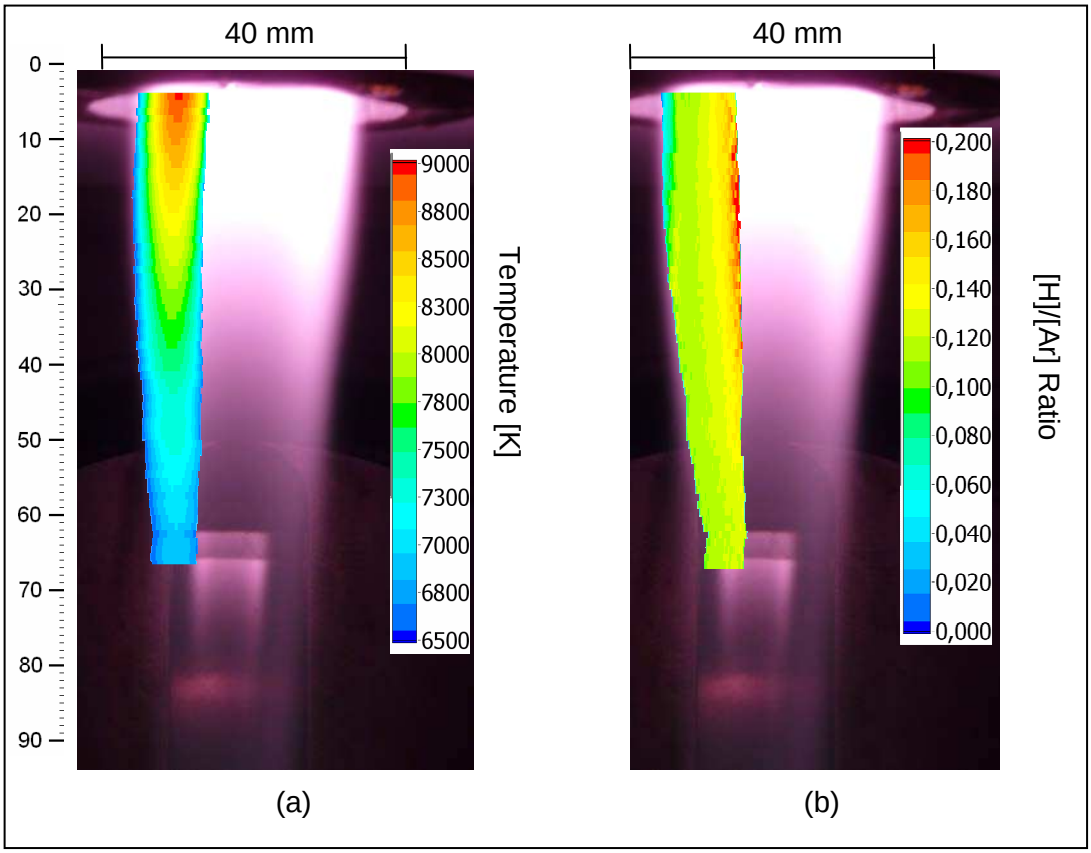

Figure V-1 Superposition of an image of the plasma with (a) temperature and (b) concentration ratio measurement

V.1. Experiments for the validation of the method

We do several measurements to validate the assumption of local thermal equilibrium. The first validation measurements were done with the first optical setup and the small torch (generator power 2 kW, see Chapter VI). These experiments could be done with the equipment that was yet available at the laboratory. The measurements with the first optical setup validate partly method and show the limits of this setup. Measurements with the new

optical setup that are presented later allowed examining more precisely error sources like fluctuations and discuss the assumption of local thermal equilibrium.

V.1.1. Measurement of the concentration ratios [H]/[Ar], [O]/[Ar] and [OH]/[Ar]

We measured the concentration ratios [H]/[Ar], [O]/[Ar] and [OH]/[Ar] in the small torch. We injected water which permits the creation of the three measured reactive species without the risks related to the use of hydrogen gas. We used a nebulizer for the injection of water. However the nebulizer does not permit to control precisely the water flow because a part of the water droplets deposit in the nebulizer. The measured water flow rate is thus not precise enough to be compared to the measured concentration ratios. Figure V-2 shows the measured concentration ratio profiles. The flow rates and power are presented in the figures. The error bars indicate the difference between the concentrations calculated from the left half profile and that calculated from the right half profile. The marks are at the mean values. The small error bars show that the plasma is very symmetric and thus that the Abel inversion is accurate. The small error bars also show that there is little noise on the measurement. Near the centre of the plasma the noise is more important because the Abel inversion is less precise in the centre.

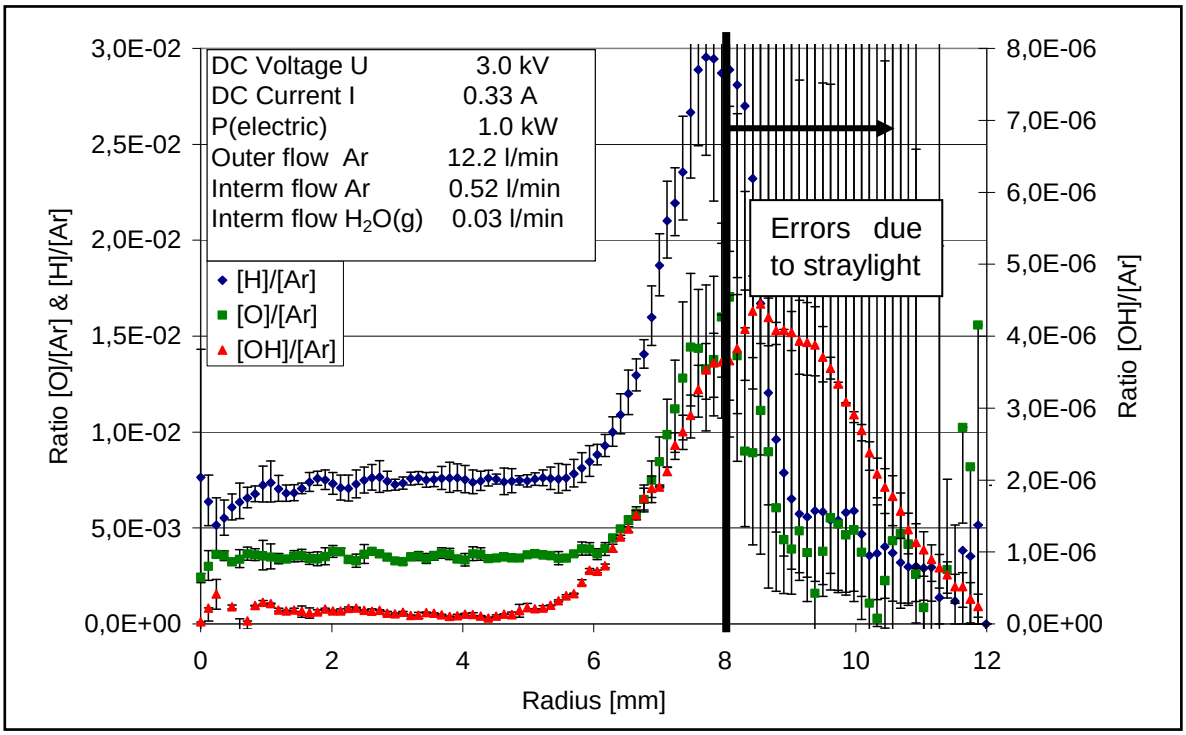

Figure V-2 : Concentration ratio profile of hydrogen, oxygen and the OH-radical

The profiles of the concentration ratios [O]/[Ar] and [H]/[Ar] are very flat for radii less than about 6 mm. This indicates that hydrogen and oxygen are well diluted. The measurements of oxygen and hydrogen are precise up to a radius of 8.5 mm. For higher radii the stray light is more intense than the intensity from the plasma. Sources of stray light are the mirror and the black canvas behind the plasma.

The concentration of hydrogen is approximately twice as high as the concentration of oxygen (we injected H_2O). It thus indicates that the line profile simulation of the hydrogen line is accurate and that the population of the excited states of the hydrogen line and the oxygen

line are in equilibrium with their respective ground state. A validation of the line profile simulation can be found in appendix B.

The concentrations of oxygen and hydrogen increase at the edge of the plasma. This may be due to a physical effect that increases the concentration of oxygen and hydrogen at the edge of the plasma or due to an effect that perturbs the measurement. Physical effects may be the demixing in the high temperature gradient in the induction zone or dilution with ambient air that contains some water vapor. An effect that perturbs the measurement is the change of volume of the plasma.

As the lines are not measured at the same time the volume of the plasma can change between the measurements of two lines. We observed this when we measured the profiles of an argon line twice. Due to the high emissivity gradient at the edge of the plasma a small increase of the width of the plasma can cause large errors at the edge of the plasma. When the plasma becomes wider between the measurement of the argon line and the oxygen line, the measured [O]/[Ar] ratio at the edge of the plasma is higher than the real [O]/[Ar] ratio. Therefore this optical setup can not measure accurately the [O]/[Ar] ratio and the [H]/[Ar] ratio at the edge of the plasma. An optical setup that measures simultaneously an oxygen (or hydrogen) line and an argon line is much less sensible to variation of the width of the plasma.

The concentration of the OH-radical (Figure V-2) is very small at the centre of the plasma. This corresponds to chemical equilibrium at this temperature. At a radius of about 5 mm the plasma temperature decreases and therefore the concentration of OH increases. Since the profile was not very symmetric, we have large error bars at a radius of 8 mm. The maximum in the plot is at 8.5 mm but this is very likely to be wrong because the temperature at larger radial positions is not well known and the concentrations are therefore calculated with an overestimated temperature. In reality the concentrations should be higher. Since we cannot measure the temperature below 5800 K, we cannot measure the concentration of the OH-radical at lower temperatures.

At the radius 7 mm the measured [OH]/[Ar] ratio is 1.9×10^{-6}. We compare this to the [OH]/[Ar] ratio at chemical equilibrium with the measured [O]/[Ar] (0.0085) and [H]/[Ar] ratio (0.019) and the measured temperature (6400 K). The chemical equilibrium was calculated with TTWinner [ttw]. At chemical equilibrium the [OH]/[Ar] ratio is 1.2×10^{-6}. This indicates that the magnitude of the measurement of the OH radical is correct.

Since the concentration of the OH-radical is very low at high temperatures it does not modify the composition of the plasma. For this reason we did not continue this measurement.

V.1.2. Comparing the temperature measurements with two different Ar lines

We measured the temperature with two different Ar lines (415.9 nm and 420.1 nm) in order to test whether the populations of their excited states are in equilibrium. The experimental parameters are the same as in the measurement of Figure V-2.

Figure V-3 shows the measured temperature profiles. There is only a small difference between the two temperature profiles, which could be caused by variations of the temperature and by the uncertainty on the transition probabilities, which is about 25%. This uncertainty is also represented by the error bars. The result shows that the populations of the two lines are in equilibrium.

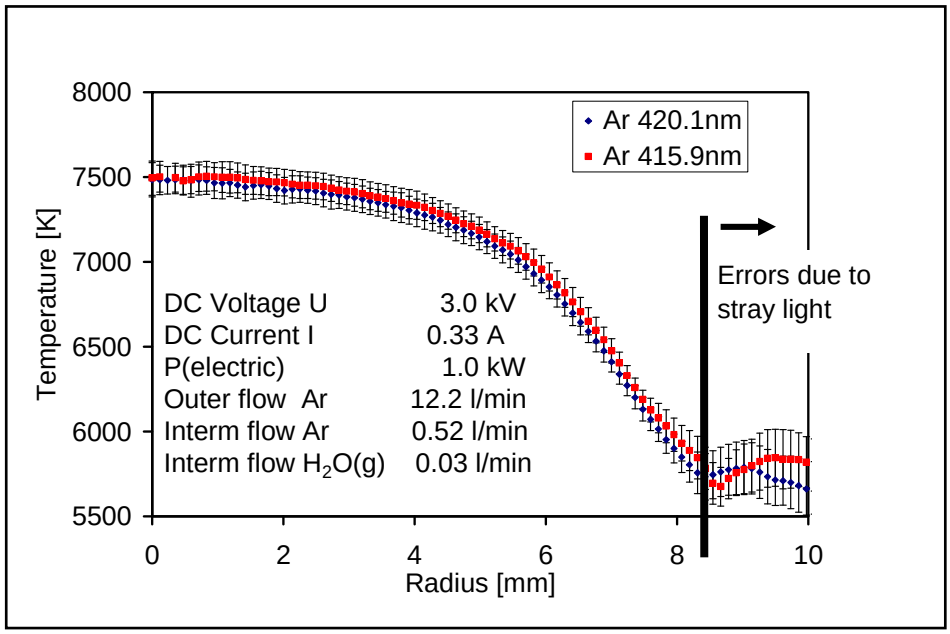

Figure V-3: Temperature profiles measured with two different argon lines

The temperature measurement is accurate up to a radius of 8.5 mm. At a radius of 8.5 mm the intensity of the lateral profile is only 1 % of the maximum intensity. At larger radii the intensity of stray light is higher than the intensity of the light coming from the plasma. The difference between the temperature calculated from the left half profile and the right half profile has been included into error bars. This error is small compared to the error due to the transition probabilities.

V.1.3. Measurement of the electron density

In this chapter we want to measure the electron density in order to validate the assumption of local thermal equilibrium. In local thermal equilibrium the electron density depends only on the gas temperature and the gas composition. The comparison of the measured electron density and the electron density calculated with the measured temperature can thus validate the assumption of local thermal equilibrium. For the measurement of the electron density we compare the continuum intensity method and the Stark broadening of H-Delta and H-Beta. The methods are described in chapter III. The experimental parameters for the measurements that are used for the validation are presented in Table V-1.

The electron densities are calculated with the Saha-equation using the temperature measured with the absolute line intensity method. Figure V-4 shows a temperature profile and the calculated electron densities.

As the electron density increases exponentially with the temperature the radial profiles have not the same shape. A small relative variation of the temperature leads to a high relative variation of the electron density. The electron density varies between 1.0×10^{15} cm^{-3} and $1.5 \times 10^{16} cm^{-3}$ in the observed temperature range (7600 K - 10000 K).

	0302H	0302F	0828R
Argon (outer flow) [Nm^3/h]	6.0	6.0	6.0
Argon (intermediate flow) [Nm^3/h]	0.3	0.3	0.0
Argon (inner flow) [Nm^3/h]	0.0	0.1	0.0
Hydrogen (inner flow) [Nm^3/h]	0.4	0.0	0.2
Plate Voltage U_{DC} [kV]	7.0	7.0	7.6
Current I_{DC} [A]	6.0	6.3	5.8
DC Power $U_{DC} * I_{DC}$ [kW]	41.8	43.8	44.0
Distance to target [mm]	193	193	40

Table V-1: Experimental parameters, electron density measurement

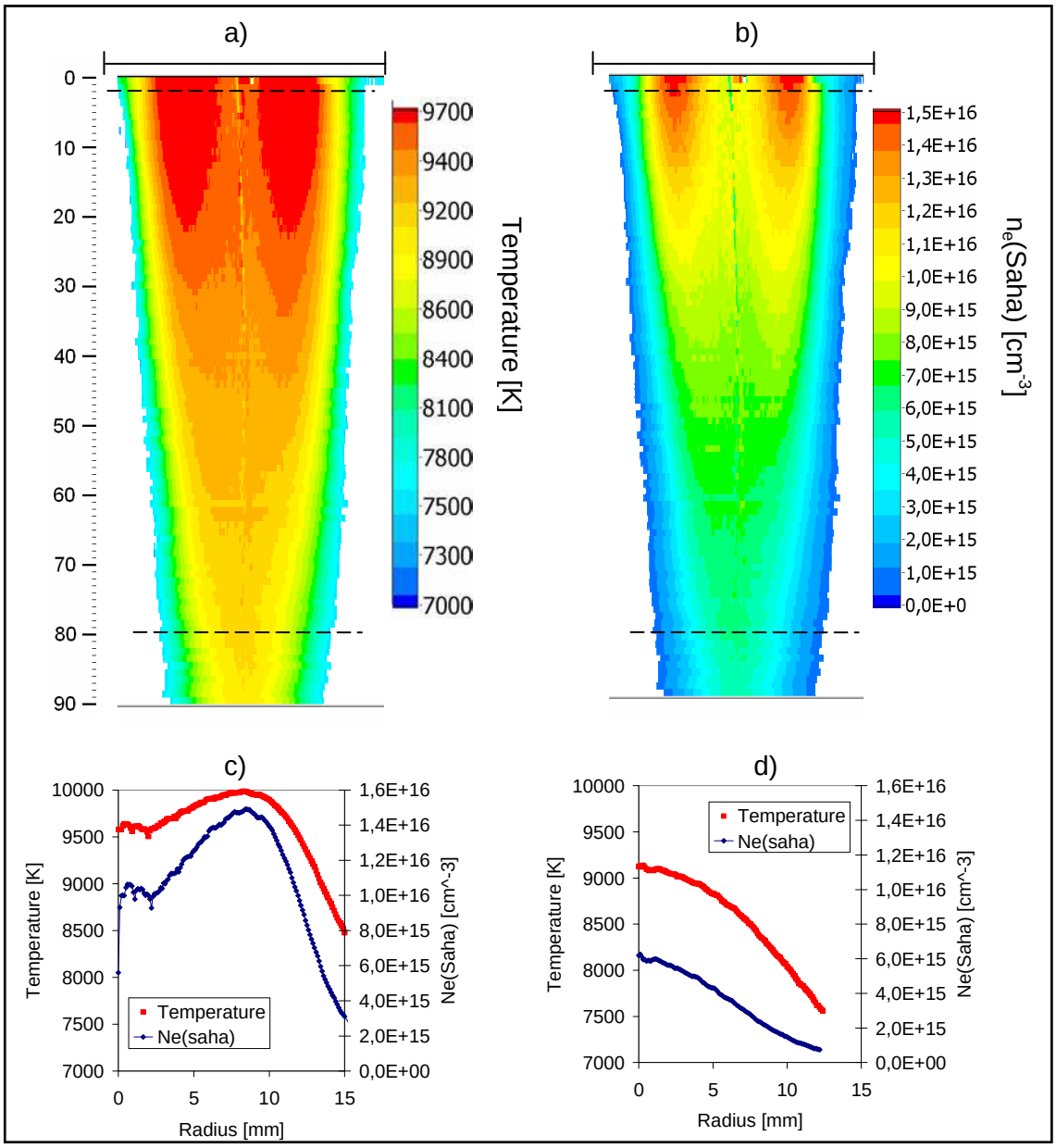

Figure V-4 a) Measured temperature map
b) electron density map calculated with the Saha equation using the temperature from a)
c) and d) Radial profile of temperature and electron density at z = 3 mm and z = 80 mm respectively, Parameters 0302F

Figure V-5 shows the electron density measured with the Stark broadening of the H-Delta line and the emissivity of the continuum. Both methods have been described in chapter III. The electron densities have been divided by the electron density calculated with the Saha-equation for argon. Differences between the two electron densities can thus be observed more easily. The ratio between the electron density measured with line broadening of the H-delta line and the electron density calculated with the Saha-equation and is between 0.7 and 1.0 and rather constant over the whole measured range (Figure V-5 a)).

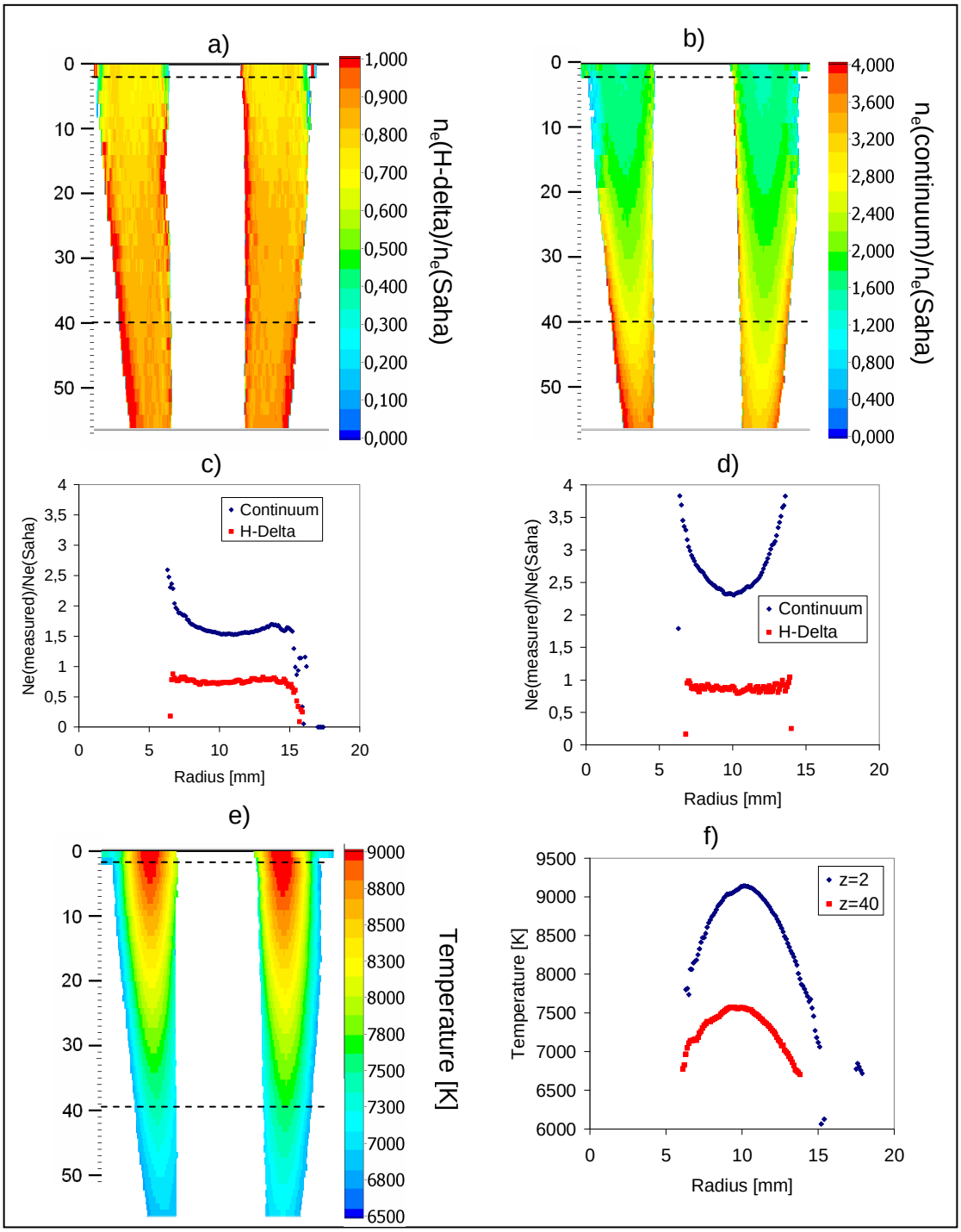

Figure V-5 Comparison between the electron density measured with the continuum and the electron density measured with the H-Delta line
a) 2D map of the ratio between the electron density measured with the H-delta line and the electron density calculated with the Saha-equation
b) 2D map of the ratio between the electron density measured with the continuum and the electron density calculated with the Saha-equation
c) Radial profile of a) and b) at z=2 mm
d) Radial profile of a) and b) at z=40 mm
e) 2D map of the temperature
f) Radial profiles of e) at z=2 mm and z=40 mm
Parameters 0302H

The ratio between the electron density measured with the continuum emissivity and the electron density calculated with the Saha-equation is 1.5 in the low temperature region and up to 4 in the high temperature region. We can not explain this temperature dependant variation, especially as the method depends only little on the temperature. As the H-Delta line broadening gives good results we conclude that the method using the continuum emissivity is not adapted for the measurement of the electron density in these conditions.

The electron density measured with the H-delta line broadening however fits very well with electron density calculated from Saha's equation using the measured temperature. This shows that the electron density is in equilibrium with the population of the excited states. The good coincidence between the measured electron density and the calculated electron density is however not a good indicator for deviations from LTE as they occure in partial LTE (pLTE see Appendix A). A plasma in partial local thermal equilibrium can have underpopulation of a factor b=0.1 of the ground state which leads to a small difference of about 10 % between the calculated and the measured electron density. The result of the electron density measurement will be discussed in more detail later together with the concentration measurement.

We want to compare the measurement of the electron density with the H-delta line to the measurement of the electron density with the H-beta line, which is more often used for the measurement of the electron density. Figure V-6 shows the electron density measured with the H-delta line and the electron density with the H-beta line. The results show that the two electron densities are nearly identical and thus validate the measurement of the electron density with the H-delta line. Small differences are probably due to a variation of the plasma between the two measurements. There no argon lines with similar intensity next to the H-Beta line so that the electron density measurement with the H-Beta line can not be compared directly to the absolute line intensity method.

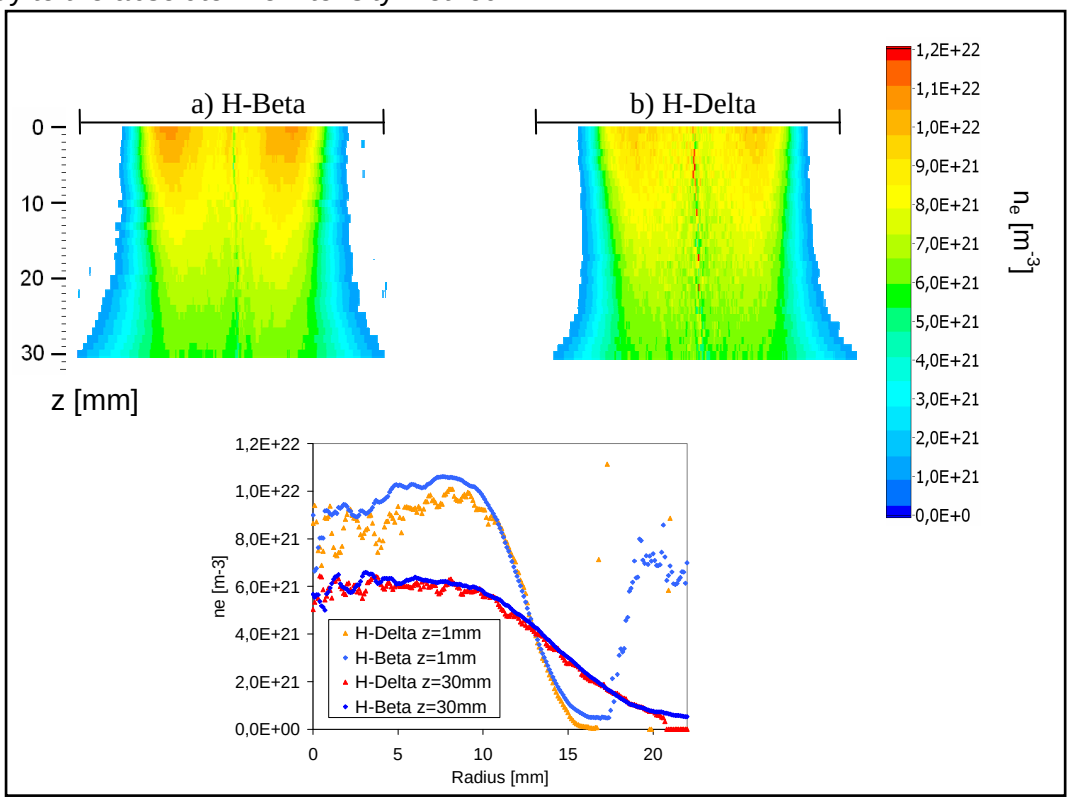

Figure V-6 Comparison between the electron density measured with a) the H-Beta line and b) the H-Delta line

V.1.4. Validation of the concentration measurement

In this experiment we inject a homogeneous Ar-O_2 or Ar-H_2 mix in the outer and intermediate flow so that we should obtain a uniform concentration ratio in the plasma. The plasma parameters are shown in Table V-2

	a) 0214B	b) 0214G	c) 0214M
Mixture (outer flow) [Nm^3/h]	5.6	5.6	6.6
Mixture (intermediate flow) [Nm^3/h]	0.5	0.5	0.5
Argon [Nm^3/h]	6.0	6.0	6.0
Hydrogen [Nm^3/h]	0.12	0.0	0.0
Oxygen [Nm^3/h]	0.0	0.12	1.1
[O_2]/[Ar] or [H_2]/[Ar] ratio	**0.02**	**0.02**	**0.18**
Plate Voltage U_{DC} [kV]	7.0	7.1	7.1
Current I_{DC} [A]	2.9	5.4	2.7
Frequency [MHz]	3.110	3.158	3.111
DC Power $U_{DC} * I_{DC}$ [kW]	21	38	19
Distance to target [mm]	193	193	193

Table V-2: Experimental parameters, validation of the concentration measurement

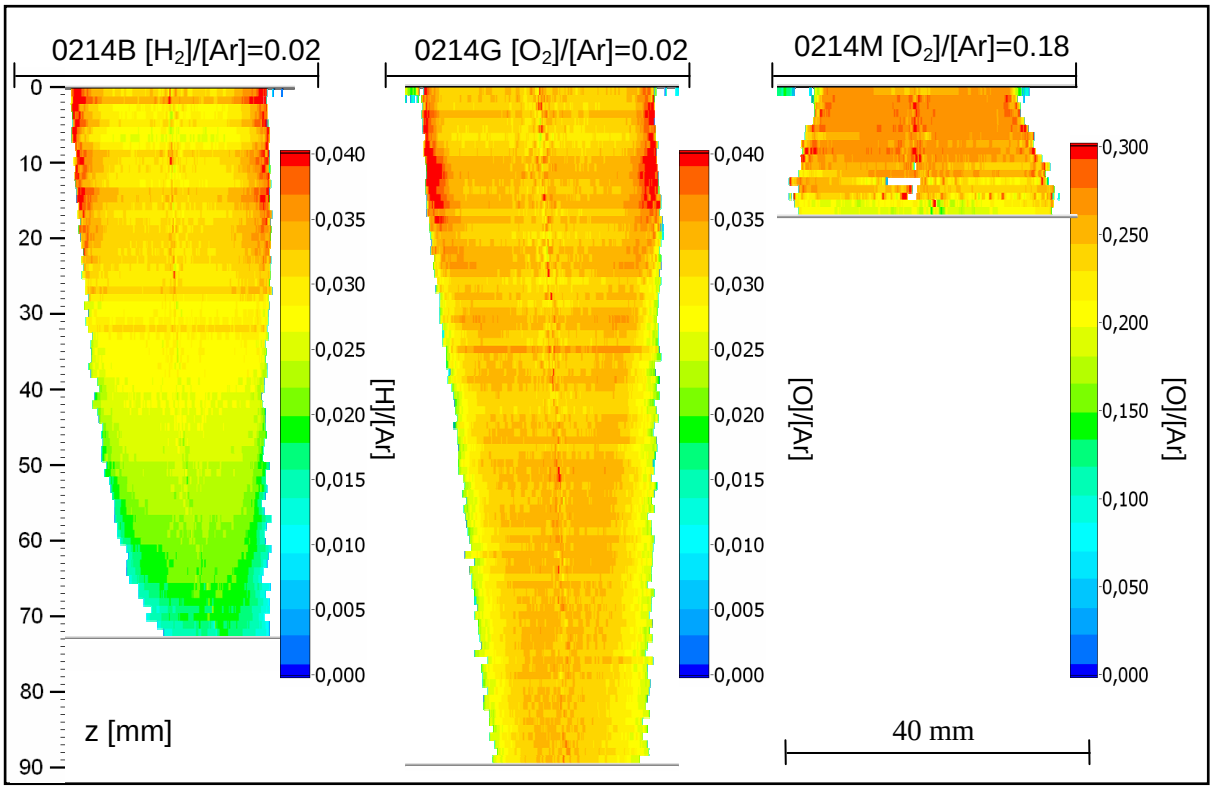

Figure V-7 : Measured maps of the concentration ratio [O]/[Ar] and [H]/[Ar] with injection of a homogenous mix of 0214B [H_2]/[Ar]=0.02, 0214G [O_2]/[Ar]=0.02 and 0214M [O_2]/[Ar]=0.18

Figure V-7 shows the measured concentration profiles for the injections of different homogenous Ar-H_2 and Ar-O_2 mixes. The different sizes of the plasma are mainly due to the different properties of the mixtures, which modify the coupling. This can be seen in the different values of the measured current I_{DC} that are shown in Table V-2. The plate voltage

was maintained constant so that a lower current leads to a lower induced power. The coupling efficiency is studied in more detail in chapter VI.

All three graphs in Figure V-7 show that the measured concentration ratio is almost homogenous and a little lower than the injected (atomic) ratio. The remaining small deviations are, on the one hand, a higher concentration of atomic species at the edge of the plasma in the upper part (0-20 mm from the outlet of the torch). On the other hand, a lower concentration is obtained in the lower part (30-90 mm from the outlet), especially at the edge of the hot zone. In the concentration ratio map a) in Figure V-7 the measured ratio in the lower zone from a distance of 40 mm to the lower end, is much lower than the injected concentration.

V.2. Discussion of the deviations

Figure V-8 shows the ratio between the electron density measured with the line broadening of the H-Delta line and the electron density calculated from the measured temperature using the Saha-equation. The same figure shows the ratio between the measured [H]/[Ar] ratio and the injected [H]/[Ar] ratio. One can clearly see that in at the edge in the lower part both graphs show a perturbation which is probably due to fluctuations of the plasma. At the upper edge the measured concentration is higher which is probably due to demixing. In the other zones the concentration is slightly lower than the injected concentration and the measured electron density is slightly lower than calculated electron density. This deviation may be due to an error of the calibration or due to the inaccuracy of the transition probability of the argon line. We will discuss each deviation in more detail

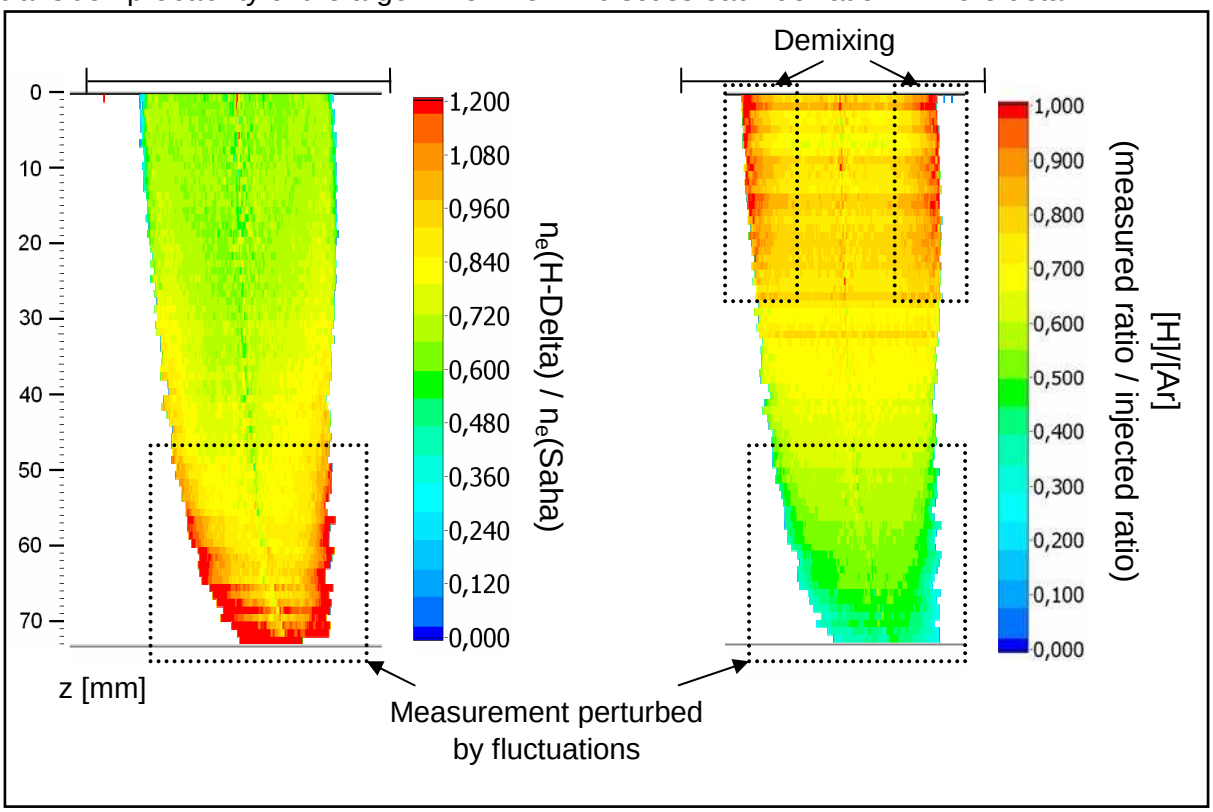

Figure V-8 Ratio between the electron density measured with the line broadening of the H-Delta line and the electron density calculated with the Saha equation on the left. Ratio between the measured [H]/[Ar] ratio and the injected [H]/[Ar] ratio on the right. Parameters 0214B [H_2]/[Ar]=0.02.

V.2.1. Fluctuations at the lower edge of the plasma

Fluctuations cause probably a difference between the measured electron density and the calculated electron density at the lower edge of the plasma. The absolute line intensity method measures a temperature that is below the maximum temperature when the plasma fluctuates. The line broadening measures an electron density that is close to the maximum electron density because the colder gas emits less light and has thus only little influence on the line width. The fluctuations cause therefore a higher ratio between the two electron densities as they can be seen in the measurement (Figure V-8).

The ratio between the emissivity of two lines is also close to the ratio at the maximum temperature. When fluctuations perturb the measurement a lower measured temperature is used to calculate the concentration ratio. One obtains a lower concentration than the real concentration as it can be observed in the measurement of Figure V-8. We use the simulation of the emissivity of an oscillating temperature to analyze how the fluctuations perturb the concentration measurement. We simulate the emissivity of a sinusoidal oscillation of the temperature around a mean temperature of 8000 K. Figure V-9 shows the oscillating temperature with an amplitude of 1000 K and the normalized simulated emissivities of the Ar line (upper level: 14.53 eV) and the H line (upper level: 13.22 eV). We then used the mean emissivity of the two lines to calculate the temperature and the concentration ratio. This corresponds to the measured temperature and concentration ratio because we also measure a mean emissivity with the spectrometer. Figure V-10 shows the dependence of the measured concentration and the measured temperature on the amplitude of the oscillation. Without fluctuations (amplitude = 0) the measured temperature and concentration are equal to the real temperature and the real concentration. When the amplitude is 2000 K, the measured temperature is 1200 K above the mean temperature and the measured concentration is about 9% lower than the real concentration.

For the measurement of the [O]/[Ar] ratio this effect is even stronger, because the energy difference between the upper level of the two lines is 2.3 eV and thus higher than for the [H]/[Ar] ratio (1.3 eV). The same oscillation would therefore lead to a measured oxygen concentration that is 15 % lower than the real concentration and can thus explain the lower concentration that we measured at the lower edge of b) in Figure V-7. However the plasma was much more stable with oxygen than with hydrogen so that the perturbations due to fluctuations are lower.

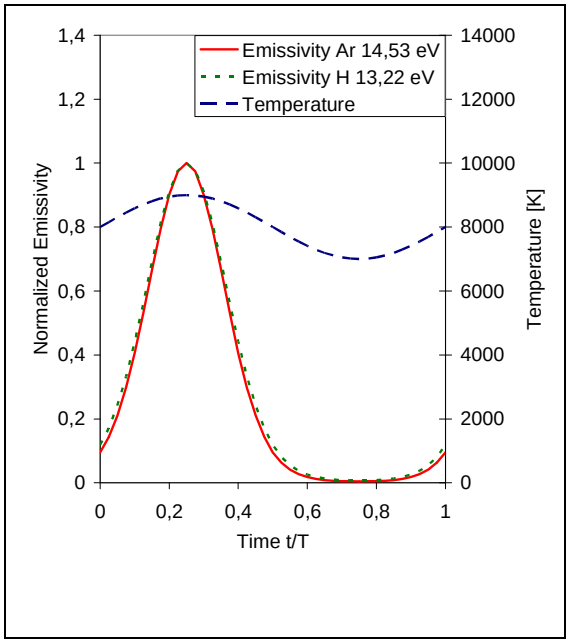

Figure V-9 Oscillating temperature and simulated emissivity of Ar and H vs time Mean temperature: 8000 K Amplitude: 1000 K

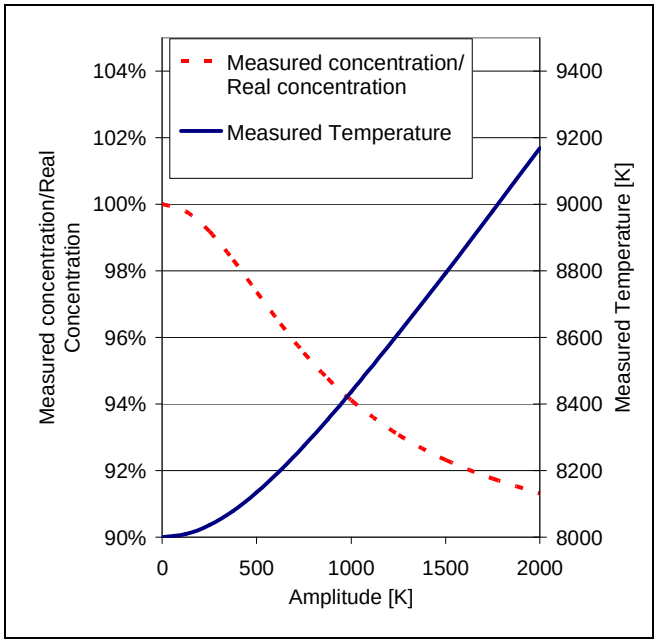

Figure V-10 Dependence of the measured concentration ratio [H]/[Ar] and the measured temperature on the amplitude of the temperature oscillation

V.2.2. Calibration and transition probability

An error on the calibration and an error on the transition probability of the argon line have the same impact on the temperature measurement.

The error on the lamp was estimated to 10 %. The accuracy of the transition probabilities of the argon lines is 25 %. The accuracy on the upper level density is thus better than 35 %. This corresponds to an accuracy on the temperature of about 200 K at a temperature of 9000 K.

In the centre of the measurement presented in Figure V-8 fluctuations are negligible. In this zone the ratio between the electron densities is about 0.7. The temperature is about 9500 K. The factor 0.7 corresponds to an error of 300 K on the temperature and is thus higher than the accuracy of the measurement. However the post-discharge zone is a recombining plasma so that the electron density should be rather higher than at thermal equilibrium. We can thus not explain the lower measured electron density. The real temperature is probably between the value measured with the absolute line intensity method and the value measured with the electron density.

With the equation (V-1) we can calculate that the measured [H]/[Ar] ratio is 4 % lower than the real ratio, when the measured temperature is 200 K higher than the real temperature. Thus even a high error on the absolute calibration (here 35 %) gives only a small error on the measurement of the concentration ratio.

A 25 % higher transition probability of the argon line would make the measured concentration ratio 25 % lower than the real ratio (equation (V-2)). The accuracy of the transition probability of the hydrogen lines is very high (< 0.3 %).

$$\frac{measured\ ratio}{real\ ratio} = \exp\left(\frac{E_{Ar,u} - E_{H,u}}{k_B} \times \left(\frac{1}{9000K} - \frac{1}{8800K}\right)\right) = 0.96 \qquad \text{(V-1)}$$

With $E_{Ar,u} - E_{H,u} = 1.3eV$

$$\frac{measured\ ratio}{real\ ratio} \approx 1 + \frac{\Delta A_{Ar}}{A_{Ar}} = 1 \pm 25\% \qquad \text{(V-2)}$$

V.2.3. Demixing

Demixing in the induction zone may be the reason for the higher measured concentration ratio at the upper edges. Demixing would not cause a measurement error but a real higher concentration ratio at the edge of the plasma. In the induction zone the temperature gradient is very high. Demixing due to mol fraction gradients of molecules and atoms may occur due to the dissociation reaction [Mur97]. We take as example an Ar-H_2 mix. For equal diffusion coefficients of Ar, H and H_2 the diffusion fluxes of Ar, H and H_2 are equilibrated when the mass fraction of H below the dissociation temperature is equal to the mass fraction of H_2 above the dissociation temperature. For a higher diffusion coefficient of H the diffusion fluxes are equilibrated when the mass fraction of H in the hot zone is smaller than the mass fraction of H_2 in the colder zone.

Thus, the mass fraction of H can be lower inside the plasma than outside in the cold gas due to demixing in the high temperature gradient in the induction zone. In the post-discharge zone the temperature gradient is much smaller so that H can diffuse from the higher mass fraction at the edge to the centre.

Figure V-11 shows the radial electro density (calculated from T) and the concentration ratio profiles of the measurements with a homogenous mix of a) [H_2]/[Ar] and b) [O_2]/[Ar]. Both the [H]/[Ar] ratio profile and the [O]/[Ar] ratio profile increase at the edge. The [H]/[Ar] ratio profile is flat up to a radius of 7 mm and the [O]/[Ar] ratio profile is flat up to a radius of 12 mm. This is probably because the plasma with oxygen is larger and because hydrogen has a higher diffusion coefficient.

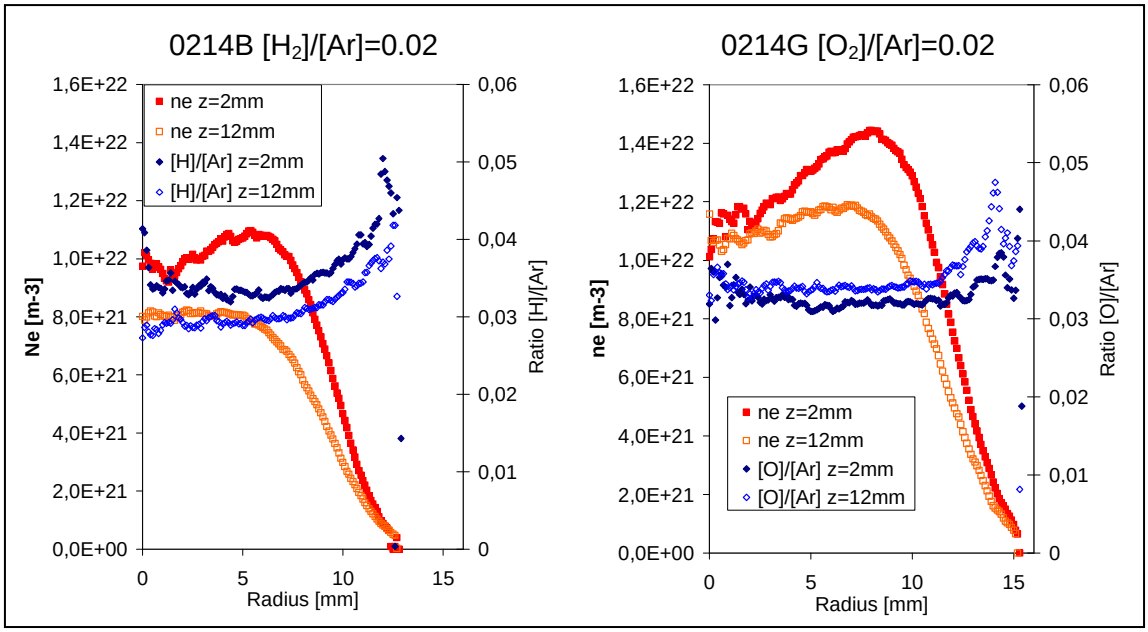

Figure V-11 Radial temperature profiles and concentration ratio profiles at z=2mm and z=12mm below the outlet of the torch.

V.2.4. Discussion of deviations due to pLTE

The measurement method that we apply is based on LTE. In pLTE the electrons and excited species are not in equilibrium with the ground state (see Appendix A). The overpopulation factor of the ground state may be different for the different elements and therefore induce an error in the measurement. The strong temperature gradient at the edge

of the plasma just below the outlet may reduce the overpopulation factor due to the ambipolar diffusion of ions and electrons [Gri64]. In such a case we would expect variation of the measured concentration that is strongly correlated to the electron density gradient. In Figure V-11 we can not observe a strong correlation between the electron density gradient and the measured concentration ratio. The higher concentration ratio is thus rather due to demixing than due to an error induced by pLTE. A collisional radiative model [HH85] could be used to evaluate if the electron impact de-excitation of the excited states to the ground state is fast enough to attain equilibrium.

Besides the ambipolar diffusion of electrons and ions the radiative cooling may also cause an underpopulation of the ground state (see Appendix A). Figure V-11 shows the temperature map and the concentration ratio [O]/[Ar] map of the measurement b) with a homogenous $[O_2]/[Ar]$ mix. The higher concentration ratio at the upper edge and the slightly lower concentration ratio at the lower edge can be attributed to demixing and fluctuations. The very uniform measured concentration ratio in the centre over a wide temperature range (8000 K – 9700 K) indicates that radiative cooling does not perturb the measurement. If radiative cooling would cause an underpopulation of the ground state we would expect a temperature dependence of this effect. Thus the measured concentration ratio should be different for different zones. We conclude that the underpopulation of the ground state is small and hence does thus not perturb the measurement.

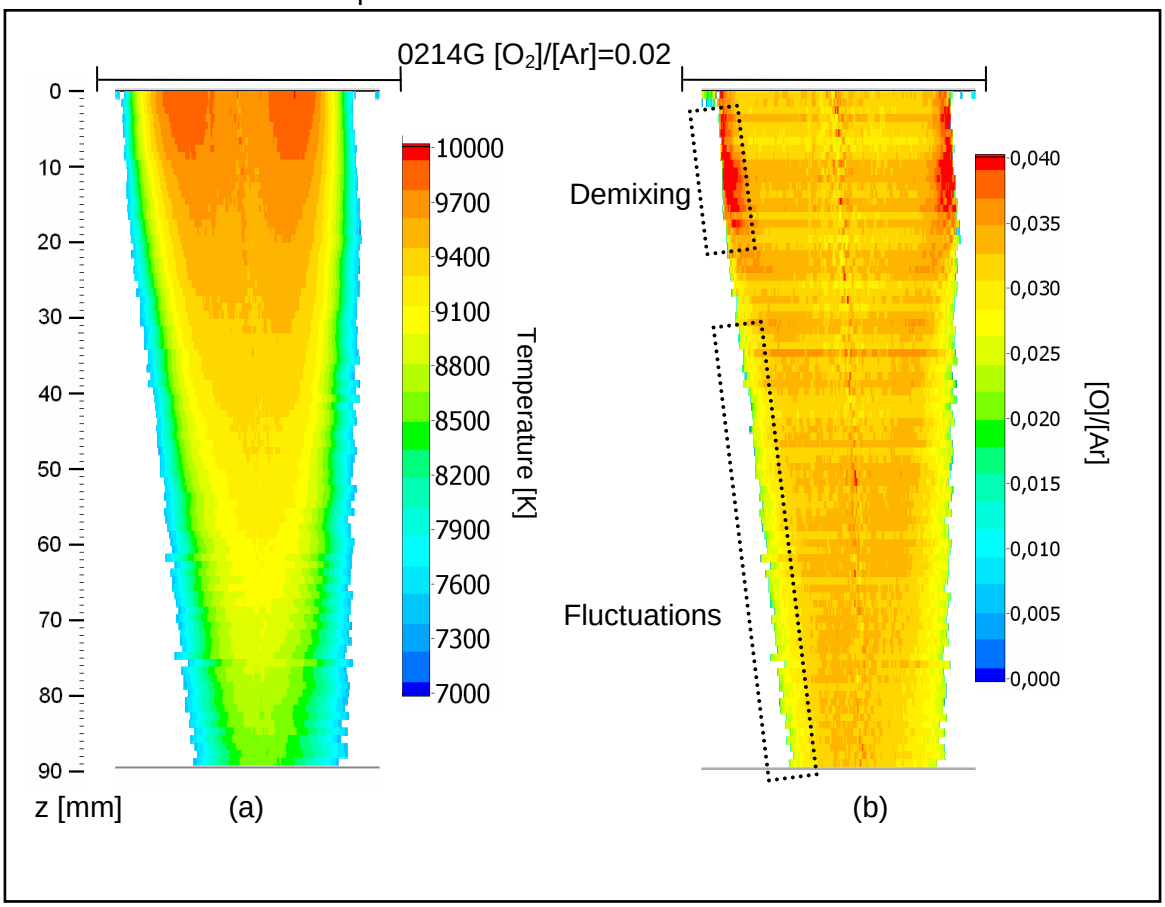

Figure V-12 Measured maps of the temperature (a) and the concentration ratio [O]/[Ar] (b). Parameters: b) $[O_2]/[Ar]=0.02$

V.2.5. Symmetry

Deviations from symmetry may also induce errors on the measurement. In the measurements above we presented the left profile and the right profile. As the left and the right profile give the same results we can conclude that the plasma is very symmetric in the

plane of the measurement. We observed that in the plane that is perpendicular to the plane of the measurement, the plasma is also symmetric. We can thus assume that the deviations from symmetry do not induce significant errors.

V.2.6. Conclusion

The validation measurements have shown that the two basic assumptions for our measurement (LTE and symmetry) are correct. However the comparison of the measured electron density is 30% lower than the electron density calculated from the measured temperature. We can not explain this difference. The accuracy of the temperature measurement is about 300 K which is the difference between the temperature calculated from the electron density and the measured temperature.

The measurements of homogenous Ar-O_2 and Ar-H_2 mixes have shown that the ground state population is also in equilibrium with the excited states populations.

The absolute accuracy of the concentration ratio is about 25 %. Higher concentrations at the upper edge of the plasma indicate that demixing takes place in the induction zone. We can thus not test if a concentration ratio measurement with a higher precision is possible. The error on relative variations is much lower. However fluctuations may significantly perturb the measurement at the edge of the plasma. We can thus use the measurement method to validate the model and to do a parametric study.

V.3. Validation of the CFD model

One of the objectives of the spectroscopic study is to test and to improve a computational fluid dynamics (CFD) model developed in our research group. In this chapter we will describe how the comparison helped to improve the model.

Figure V-13 shows the comparison between a measurement and the result of the model using k-ε as turbulent closure. One can see that the temperature fits very well at the outlet of the torch but then the temperature of the model decreases rapidly. At a distance of 40 mm from the outlet of the torch the temperature of the model is below 7000 K while it is still above 9000 K in the measurement. The difference can be explained by an overestimation of the turbulent diffusion in the model. An overestimation of the turbulent diffusion increases the diffusion of thermal energy and cools the plasma down. For this reason we chose to use the k-ω-SST model for turbulence, which seems to be better suited for cases where the density varies a lot. The following chapter will show the comparison between the model and the experimental results for different parameters that are presented in Table V-3. For the comparison we show the radial temperature and concentration profiles of the two different models and the measurement at different distances from the outlet of the torch.

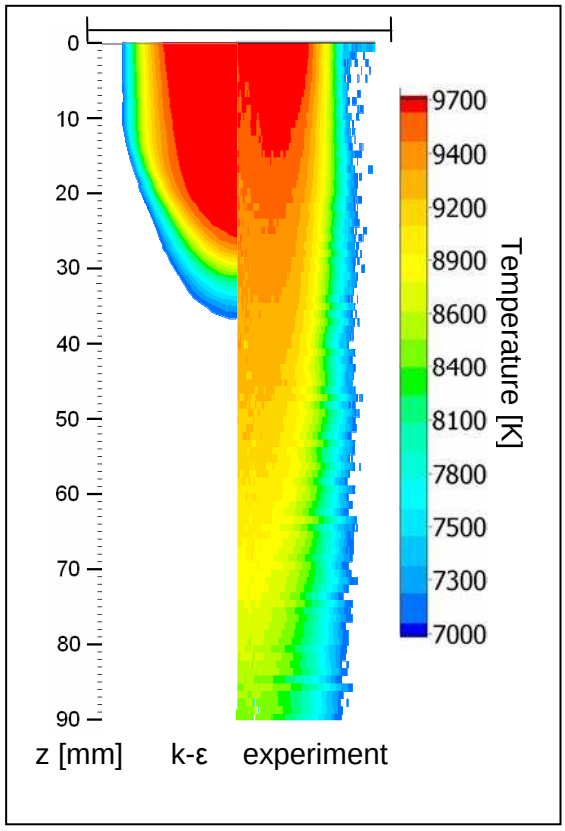

Figure V-13 Temperature map of the measured temperature (right) and the temperature of the model using k-ε (left). Experimental conditions 1402_h

	1402_h	1402 f	1402 m	0302 i	0828 h
Argon (outer flow) [Nm^3/h]	5.5	5.5	5.5	6.0	6.0
Argon (intermediate flow) [Nm^3/h]	0.5	0.5	0.5	0.3	0.3
Argon (inner flow) [Nm^3/h]	0.0	0.0	0.0	0.0	0.0
Hydrogen (inner flow) [Nm^3/h]	0.0	0.0	0.0	1.0	0.4
Oxygen (outer flow) [Nm^3/h]	0.22	0.06	1.01	0.0	0.1
Oxygen (intermediate flow) [Nm^3/h]	0.02	0.01	0.09	0.0	0.0
Total Oxygen / Argon	0.040	0.012	0.18	0.0	0.016
Plate Voltage U_{DC} [kV]	7.0	7.0	7.1	7.0	7.1
Current I_{DC} [A]	5.2	5.6	2.7	6.1	5.9
DC Power U_{DC} * I_{DC} [kW]	37	40	19	42	42
Coupled Power (model) [kW]	18.4	20.0	9.6	21.2	19.2
Distance Outlet-Target [mm]	193	193	193	193	40

Table V-3 Plasma parameters, comparison model and measurement

V.3.1. Comparison of the temperature

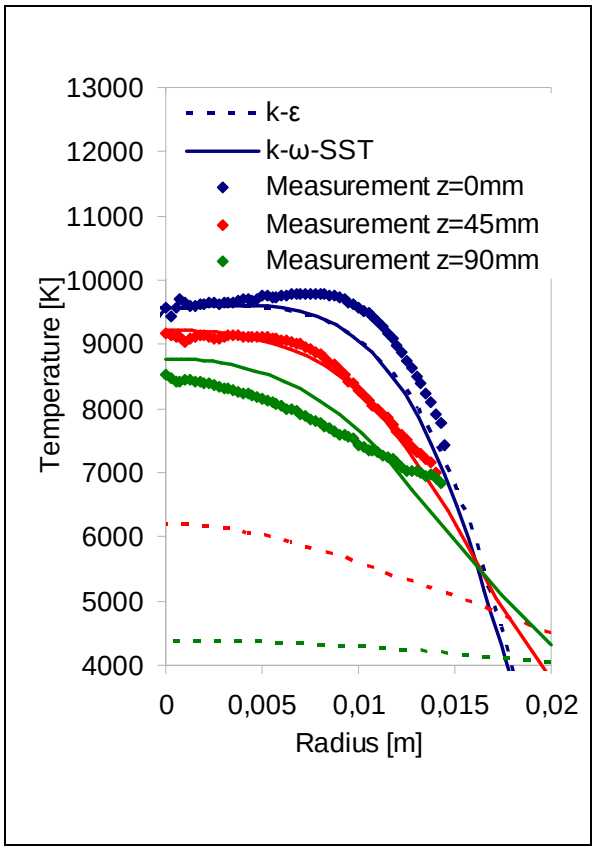

Figure V-14 Radial profiles of the measured temperature, the temperature simulated with the k-ω-SST model and with the k-ε model. Experimental parameters: 1402_f

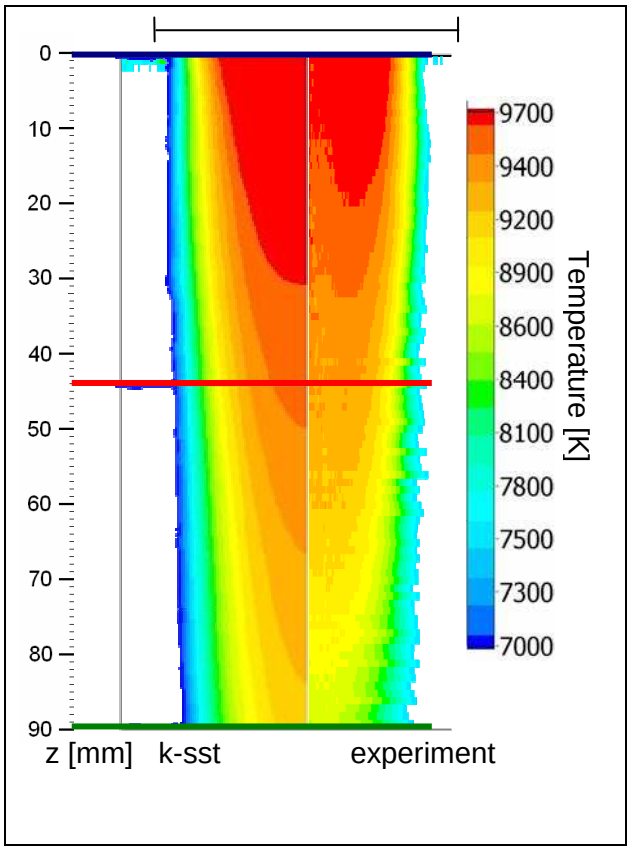

Figure V-15 Map of the measured temperature (right) and the simulated temperature using k-ω-SST (left). Experimental parameters: 1402_f

Figure V-14 and Figure V-15 show the measured and the simulated temperatures of a plasma with a homogenous argon-oxygen mix. (parameters 1402_f of Table V-3). As for the measurement above, the temperature in the k-ε model decreases too fast. The temperature of the k-ω-SST model is very similar to the measurement at a distance of z=45 mm from the outlet but slightly lower at the outlet (z=0 mm) and slightly higher at z=90 mm. This difference shows that the heat diffusion in the model is weaker than in the measurement. This can be due to slight underestimation of the thermal diffusion in the model or due to a higher flow velocity in the model.

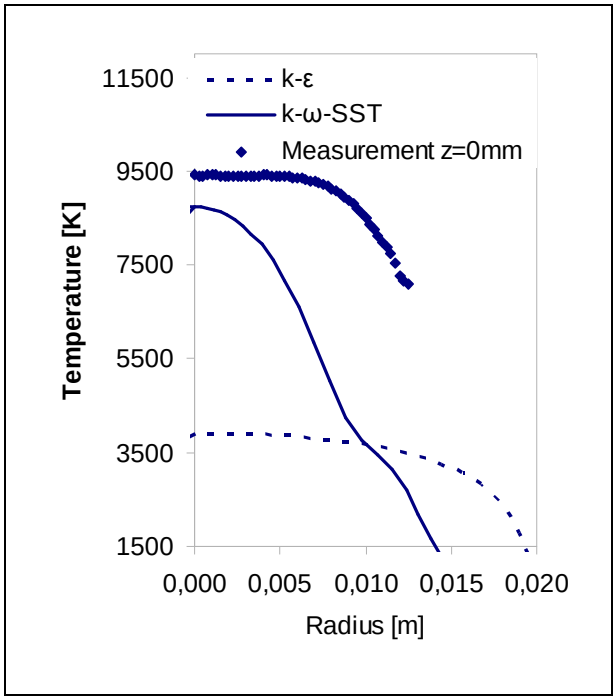

Figure V-16 Radial profiles of the measured temperature, the temperature simulated with the k-ω-SST model and with the k-ε model. Experimental parameters: 1402_m

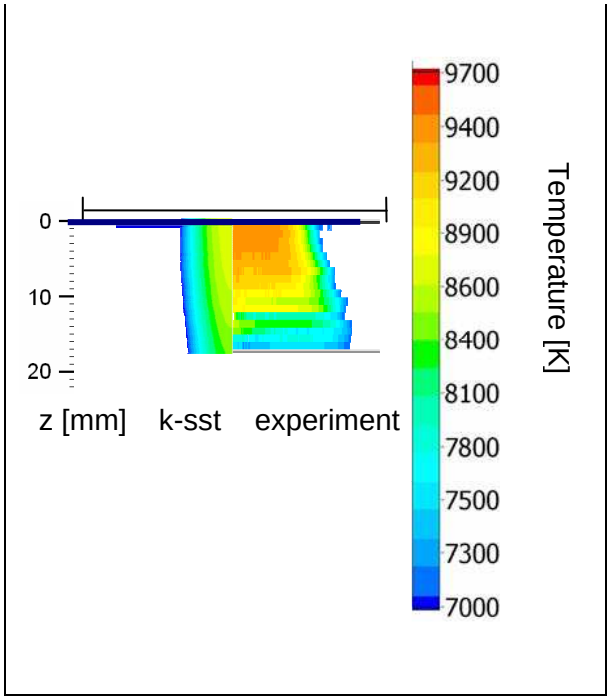

Figure V-17 Map of the measured temperature (right) and the simulated temperature using k-ω-SST (left). Experimental parameters: 1402_m

Figure V-16 and Figure V-17 show the temperature of a plasma with a homogenous Ar-O_2 mix at low power (parameters 1402_m of Table V-3). The measurements show a plasma with a diameter that increases with the distance from the outlet and cools then very fast.

The temperature of the k-ε model is much colder. The plasma of the k-ω-SST model is thinner than the measured plasma. The model did not converge well so that fluctuations remained strong. These fluctuations are of numerical nature because a steady state model was used. The simulated temperature profile is thus only the temperature of one instant of the numerical fluctuations. A plasma that has numerical fluctuations can hardly be compared to a real plasma.

This “tulip” shaped plasma of the measurement may be due to the recirculation of the hot plasma gas due to its lower density (due to the buoyancy). If this is the case we can estimate the velocity using a kinetic energy balance. We calculate the velocity of a 9000 K hot gas jet that dives 2 cm into 500 K cold gas. The energy balance (V-3) is the balance between the kinetic energy at the outlet of the torch and the energy due to the buoyancy of the hot gas that has a lower density. We find thus a velocity of 2.7 m/s. This velocity is much slower than the velocity calculated by the model which was 40 m/s. It is thus unlikely that the buoyancy causes the short length of the plasma.

$$\frac{\rho_{9000K}}{2} v^2 = \left(\rho_{500K} - \rho_{9000K}\right) gh \qquad \text{(V-3)}$$

$$v = \sqrt{\frac{\rho_{500K} - \rho_{9000K}}{\rho_{9000K}} 2gh} \approx \sqrt{\frac{9000K}{500K} 2gh} = 2.7\, m.s^{-1} \qquad \text{(V-4)}$$

The low measured current indicates that the plasma is in the low coupling mode where the plasma is only below the injector.

Another explanation for the short plasma is the transition to a turbulent flow. A turbulent flow has a diameter that increases and turbulences may rapidly cool the plasma. The swirl of the gas may play an important role for the transition to a turbulent flow. Nuntadusit et al.

[NWB12] observed that in water a jet with swirl becomes earlier turbulent than a jet without swirl.

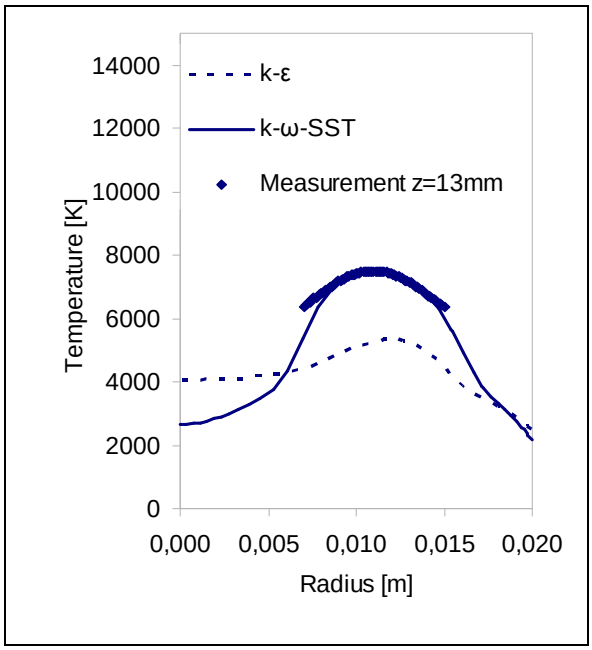

Figure V-18 Radial profiles of the measured temperature, the temperature simulated with the k-ω-SST model and with the k-ε model. Experimental parameters: 0302_i

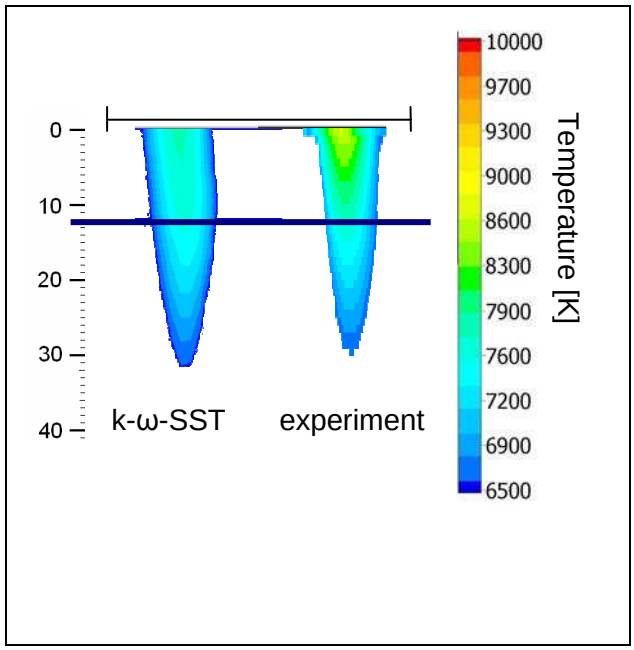

Figure V-19 Map of the measured temperature (right) and the simulated temperature using k-ω-SST (left). Experimental parameters: 0302_i

Figure V-18 and Figure V-19 show the measured and the simulated temperatures of a plasma with a large hydrogen flow rate in the inner flow (parameters 0302_i of Table V-3). The k-ω-SST model describes again much better the measured plasma than the k-ε model. The simulated temperature (k-ω-SST) and the measured temperature are high at the edge and much colder in the centre. The plasma has the shape of a tube with colder gas in the centre. At the outlet the simulated temperature is slightly lower than the measured temperature. At 13 mm below the outlet, the measured temperature profile and the simulated temperature profile are nearly identical.

Figure V-20 and Figure V-21show the measured and the simulated temperatures of a plasma with parameter similar to purification experiments with hydrogen in the inner flow and oxygen in the outer flow and a graphite target at 40 mm (parameters 0828_h of Table V-3). The simulated temperature (k-ω-SST) and the measured temperature are similar to those of the measurement presented before. This time the measured temperature is significantly higher than simulate temperature, especially at the edge of the plasma.

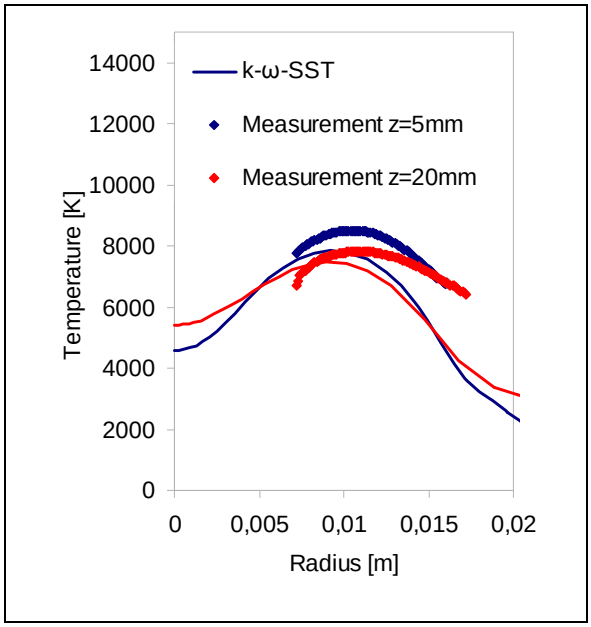

Figure V-20 Radial profiles of the measured temperature, the temperature simulated with the k-ω-SST model and with the k-ε model. Experimental parameters: 0828_h

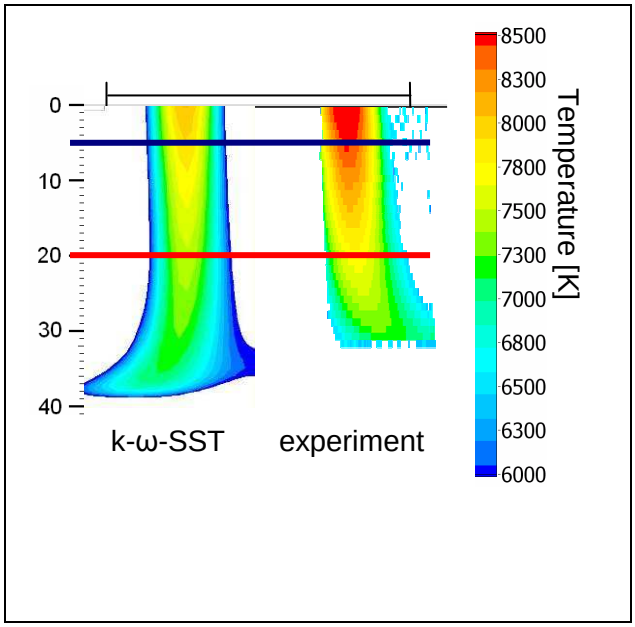

Figure V-21 Map of the measured temperature (right) and the simulated temperature using k-ω-SST (left). Experimental parameters: 0828_h

V.3.2. Comparison of the concentration ratios

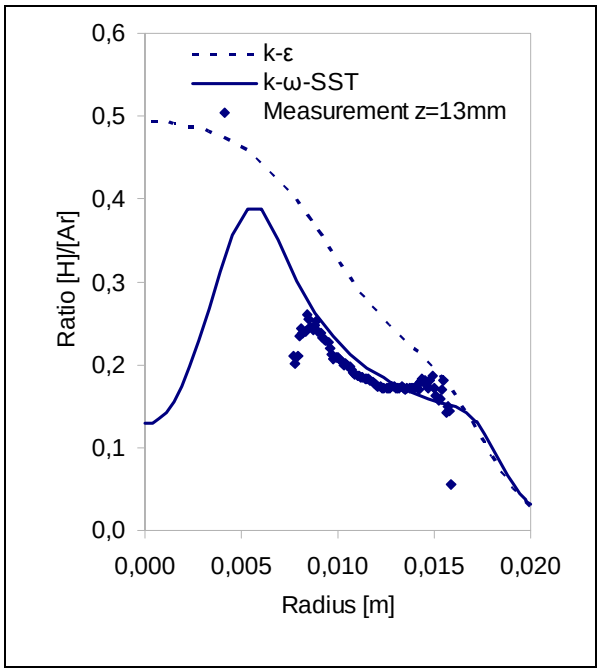

Figure V-22 Radial profiles of the measured concentration ratio [H]/[Ar], the ratio simulated with the k-ω-SST model and with the k-ε model. Experimental parameters: 0302_i

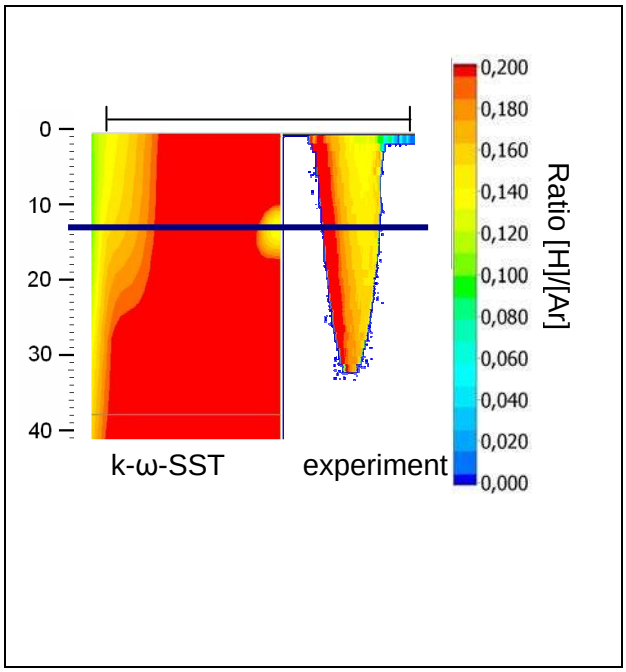

Figure V-23 Map of the measured concentration ratio [H]/[Ar] (right) and the ratio simulated with the k-ω-SST model (left). Experimental parameters: 0302_i

Figure V-22 and Figure V-23 show the measured and the simulated concentration ratios [H]/[Ar] for the measurement with a large hydrogen flow in the inner flow (parameters 0302_i of Table V-3). Both in the measurement and in the model one can observe a concentration

gradient of H in the radial direction. The concentration ratio [H]/[Ar] increases in the flow direction. This is surely due to the diffusion of the hydrogen from the centre along the concentration gradient.

At 13 mm below the outlet the measured concentration ratio profile and the simulated concentration profiles coincide very well.

At 20 mm below the outlet the increase of the concentration ratio in the flow direction is stronger in the model than in the measurement. This may be attributed to the numerical fluctuations that have yet been observed in the simulation at low power (Figure V-17).

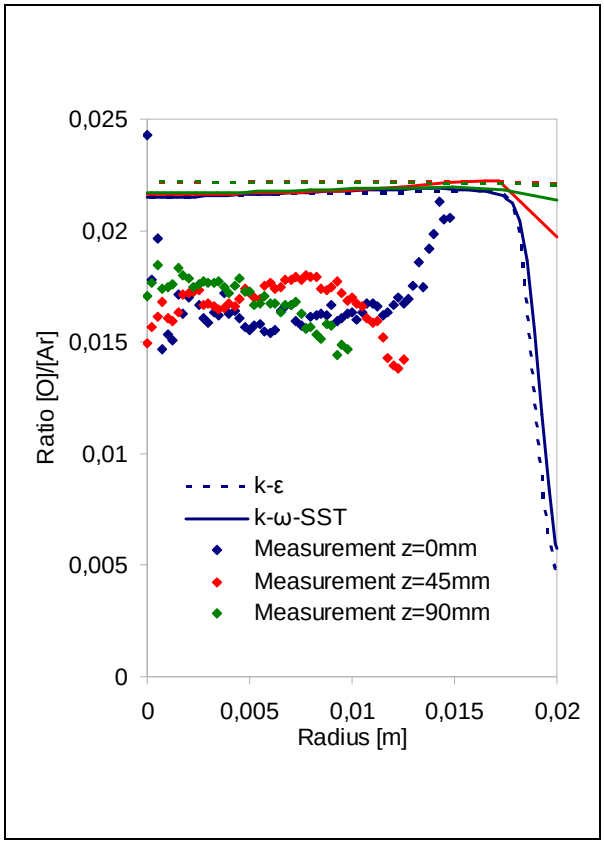

Figure V-24 Radial profiles of the measured concentration ratio [O]/[Ar], the ratio simulated with the k-ω-SST model and with the k-ε model. Experimental parameters: 1402_f

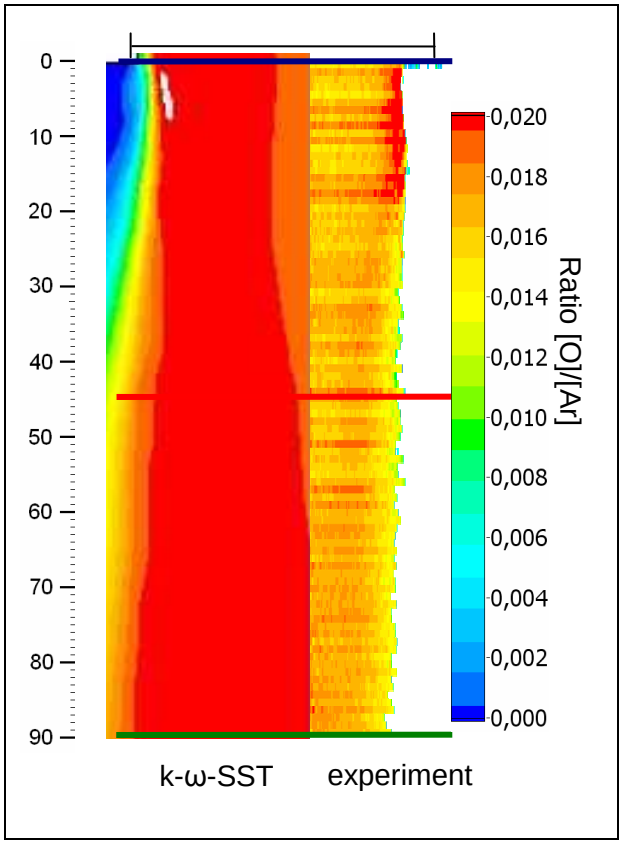

Figure V-25 Map of the measured concentration ratio [O]/[Ar] (right) and the ratio simulated with the k-ω-SST model (left). Experimental parameters: 1402_f

Figure V-24 and Figure V-25 show the measured and the simulated concentration ratio profile for the measurement with a homogenous argon oxygen mix (parameters 1402_f of Table V-3). In the model the concentration ratio is uniform and approximately equal to the injected ratio of 0.023. In the measurement the injected concentration was only 0.020. This explains partly why the measured concentration ratio is lower than the concentration ratio in the model. Demixing or the limited accuracy of the measurement can explain the remaining difference. The higher concentration at the edge below the outlet of the torch that we attributed to the demixing effect can not be observed in the model. This may be due to physical effects in the induction zone that are not taken into account in the model.

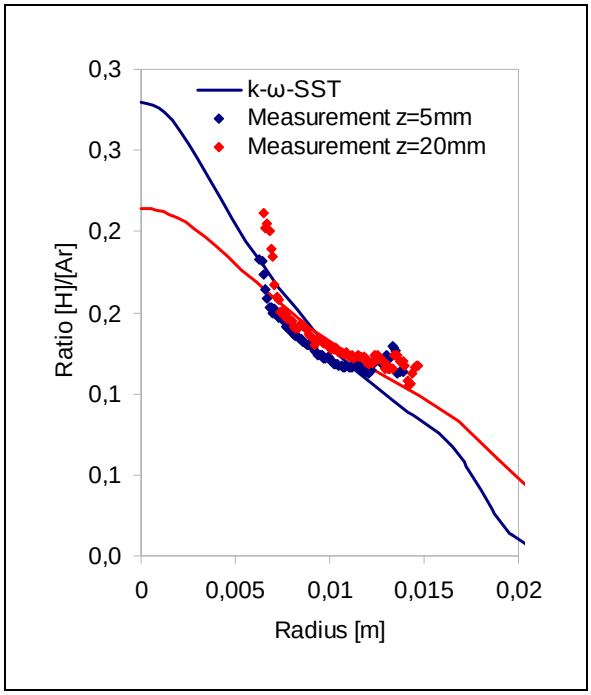

Figure V-26 Radial concentration ratio profiles [H]/[Ar] of the measured ratio, the k-ω-SST model and the k-ε model. Experimental parameters: 0828_h

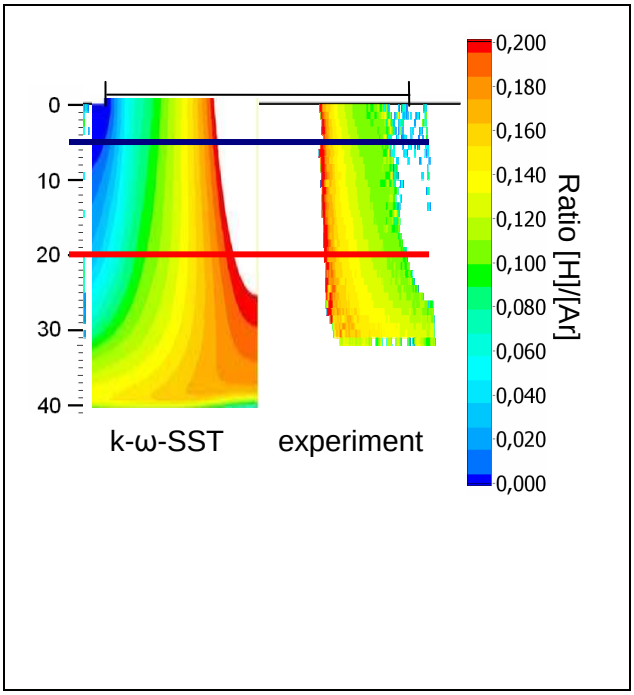

Figure V-27 Concentration ratio map [H]/[Ar] of the measured ratio(right) and the ratio of the model using k-ω-SST (left). Experimental parameters: 0828_h

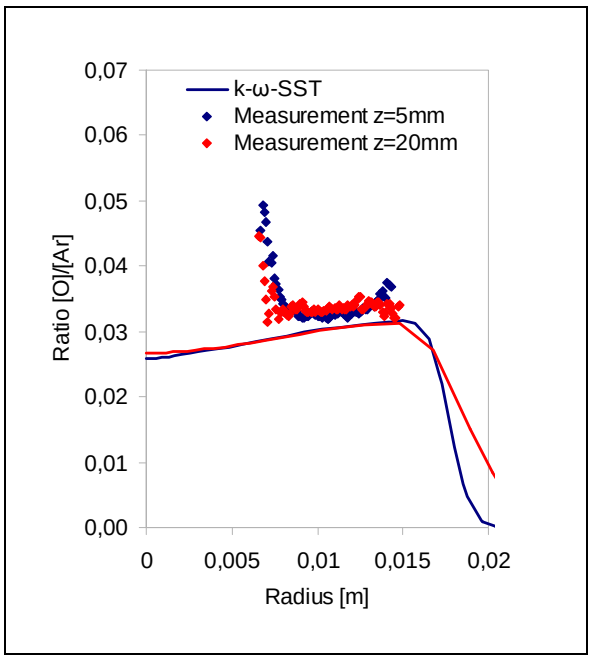

Figure V-28 Radial concentration ratio profiles [H]/[Ar] of the measured ratio, the k-ω-SST model and the k-ε model. Experimental parameters: 0828_h

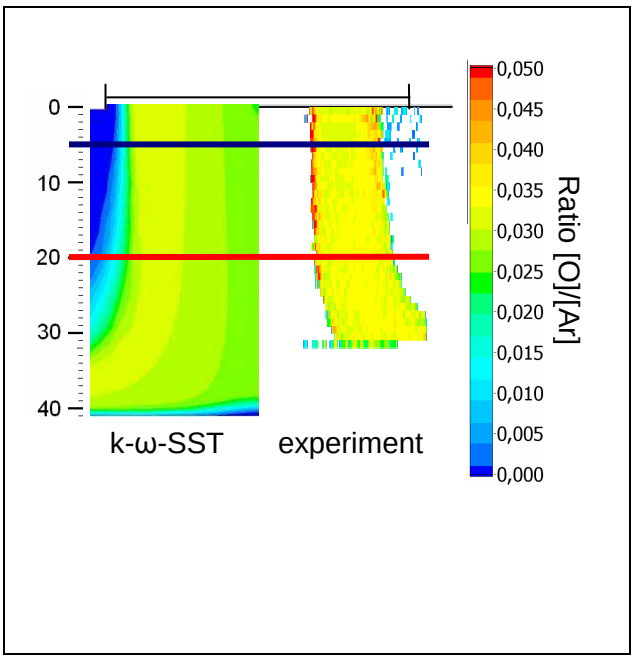

Figure V-29 Concentration ratio map [O]/[Ar] of the measured ratio(right) and the ratio of the model using k-ω-SST (left). Experimental parameters: 0828_h

Figure V-26, Figure V-27, Figure V-28 and Figure V-29 show the measured and the simulated [H]/[Ar] and [O]/[Ar] ratios for parameters similar to purification experiments with hydrogen in the inner flow and oxygen in the outer flow and a graphite target at 40 mm

(parameters 0828_h of Table V-3). The simulated profiles are very close to the measured profiles. The strong increase of the [O]/[Ar] ratio and the [H]/[Ar] ratio next in the centre is probably caused by fluctuations. Otherwise the simulated concentration profiles are very close to the measured concentration profiles. This result shows that the model can well simulate the mixing of the gases and thus probably also the mass the mass transfer to the surface.

V.3.3. Conclusion

The model and the measurement agree very well for plasma parameters that are similar to the parameters that are used in the purification process. For parameters with the real plasma in the low coupling mode the simulated plasma fluctuates strongly. The same fluctuations are small for the parameters that are used during purification. This shows that the model can be well used to analyze the flux of the reactive species towards the silicon surface. The flux of reactive species depends strongly on the velocity of the plasma which has not been measured. However, the good coincidence of the measured and simulated temperature indicates that the velocity of the simulated plasma is close to the real velocity.

For parametric studies to explore new geometries the numerical fluctuations may cause problems. As the model is steady-state the fluctuations are not physical. A transient model could be used to simulate the physical fluctuations. A transient model would thus better describe a real plasma where fluctuations can also be observed (see chapter VI).

V.4. Parametric study

We perform several measurements in order to study the influence of the different parameters on the concentration and temperature distribution in the plasma. Two of the parametric measurements (V.4.5 and V.4.6) are compared to parametric purification experiments in chapter VII.

V.4.1 Comparison of two different injection geometries

The objective is to test whether one gets a more homogenous [O]/[Ar] concentration ratio profile when injecting oxygen in the inner flow or in the outer flow. The injection of oxygen into the intermediate flow could not be tested because it extinguished the plasma.

V.4.2 The influence of the nature of the gas in the inner flow

The objective is to observe the effect of the nature of the gas in the inner flow on the temperature in the plasma and to observe the gas geometry effects on the mixing efficiency of O and H.

V.4.3 The influence of the nature of the gas in the outer flow

Three different Ar-O_2 mixes are injected in the outer flow while the intermediate flow and the inner flow are stopped so that the oxygen fraction is uniform in the whole torch.

V.4.4 The influence of a graphite target

The temperature and concentration profiles are measured once with the copper target at 193 mm distance from the outlet and once with a graphite target at 38 mm distance.

V.4.5 The influence of the power

The temperature and concentration profiles are measured for different plasma powers.

V.4.6 The influence of the oxygen and hydrogen flow rate

The temperature and concentration profiles are measured for different flow rates of oxygen in the outer flow and hydrogen in the inner flow.

V.4.1. Comparison of two different injection geometries

Figure V-30 shows the concentration ratio maps with the injection of oxygen in the inner flow (Figure V-30a) and with injection of oxygen in the outer flow (Figure V-30b). The argon inner flow is large so that the injection of oxygen in the inner flow does not modify the temperature. (parameters : Table V-4)

One can see that when oxygen is injected in the outer flow it is very well mixed with the argon. Only in the upper part in the center the concentration is a little lower due to pure argon in the intermediate flow and the inner flow. When oxygen is injected into the inner flow, it is not yet mixed at the outlet of the torch. The concentration is high in the center and low at the edge. With the distance the gases get more and more mixed so that at 60 mm below the outlet of the torch the concentration is similar to the case where oxygen is injected in the outer flow. But still the concentration at the edge is lower than in the centre. This shows that it is better to inject oxygen in the outer flow in order to obtain a homogenous oxygen concentration in the plasma.

	a)	b)
Argon (outer flow) [Nm^3/h]	6.0	6.0
Argon (intermediate flow) [Nm^3/h]	0.3	0.3
Argon (inner flow) [Nm^3/h]	1.0	1.0
Oxygen (outer flow) [Nm^3/h]	0	0.3
Oxygen (inner flow) [Nm^3/h]	0.3	0
Plate Voltage U_{DC} [kV]	7.0	7.0
Current I_{DC} [A]	6.4	5.4
Frequency [MHz]	3.135	3.130
DC Power $U_{DC} * I_{DC}$ [kW]	45	38
[O]/[Ar]	0.08	0.08

Table V-4 Plasma parameters, two different injection modes

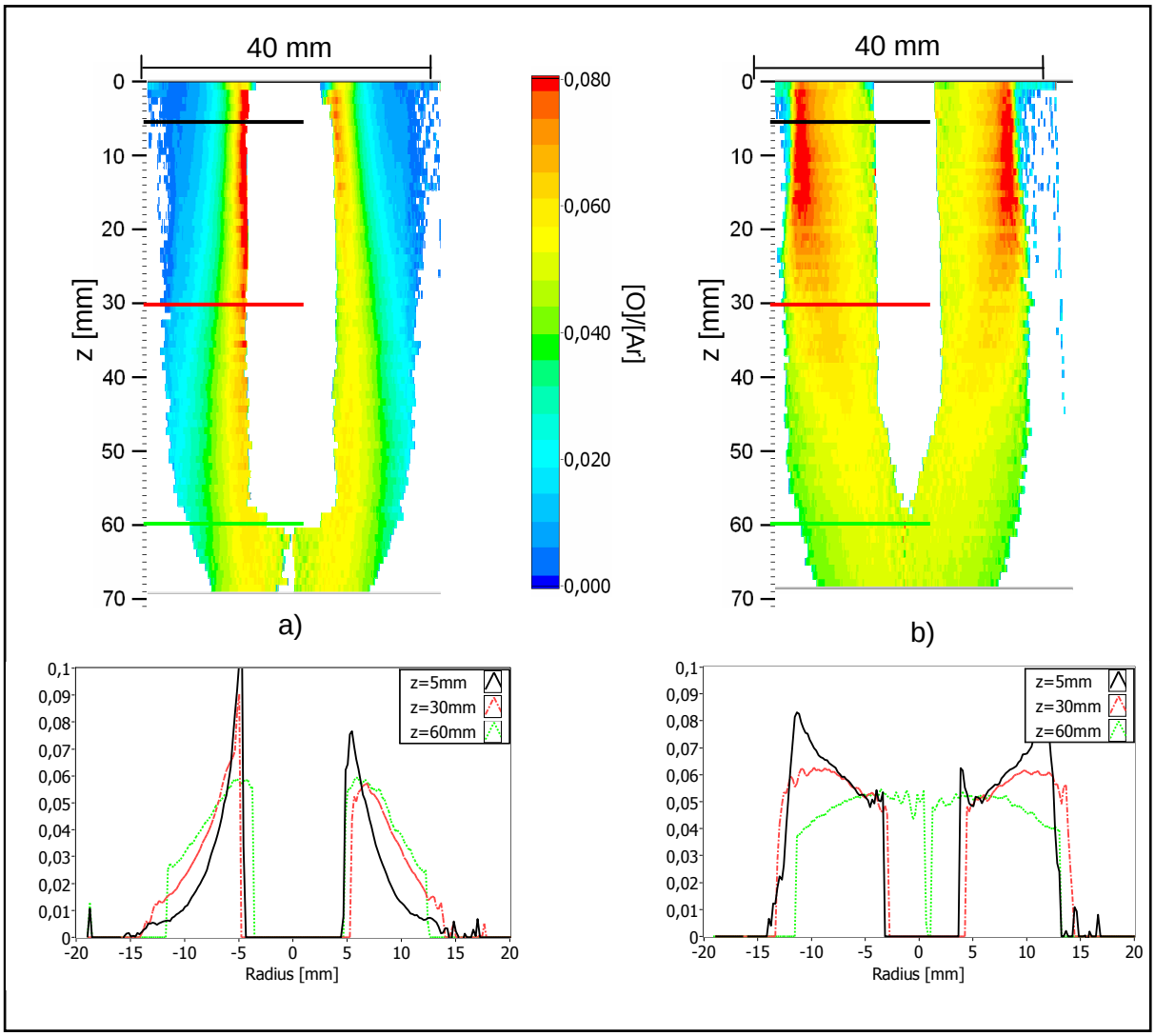

Figure V-30 Measured concentration ratio maps [O]/[Ar] for the injection of O_2 in a) the inner flow and b) the outer flow.

V.4.2. The influence of the nature of the gas in the inner flow

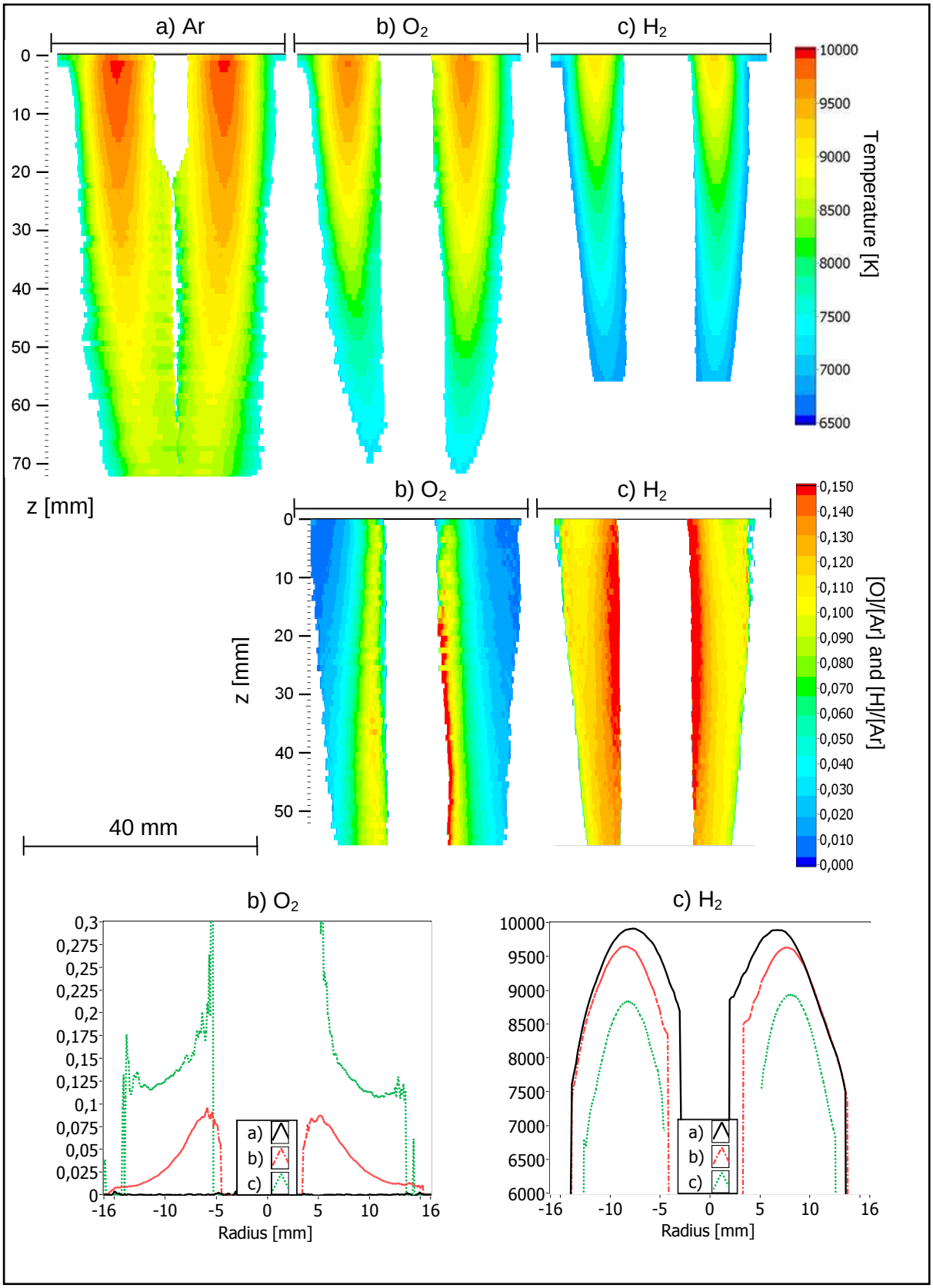

Figure V-31 Measured temperature maps for a) Ar, b) O_2 and c) H_2 injected in the inner flow. Corresponding [O]/[Ar] and [H]/[Ar] measured concentration ratios are presented below. Concentration ratio and temperature profiles at the altitude z=5mm are detailed below

	a)	b)	c)
Argon (outer flow) [Nm^3/h]	6.0	6.0	6.0
Argon (intermediate flow) [Nm^3/h]	0.3	0.3	0.3
Argon (inner flow) [Nm^3/h]	**0.4**	0.0	0.0
Oxygen (inner flow) [Nm^3/h]	0.0	**0.4**	0.0
Hydrogen (inner flow) [Nm^3/h]	0.0	0.0	**0.4**
Plate Voltage U_{DC} [kV]	7.0	7.0	7.0
Current I_{DC} [A]	6.4	6.4	6.4
Frequency [MHz]	3,133	3,133	3,133

Table V-5 Plasma parameters, the influence of the nature of the gas on the temperature and the mixing

Figure V-31 shows the temperature maps and the concentration ratio maps for the injection of three different gases (Ar, O_2, H_2) in the inner flow (parameters : Table V-5). One can see that the three different gases in the inner flow have different impacts on the temperature profiles. The plasma with oxygen is cooler than the plasma with argon only and the plasma with hydrogen is even cooler. This is due to the energy absorption of the dissociation of the molecular gases. In the concentration profiles one can see that hydrogen diffuses much better than oxygen. As hydrogen increases the thermal conductivity of the plasma, this can also explain why it cools the plasma even more down than oxygen. The molar enthalpy of hydrogen and oxygen is similar [Mek93] so that the temperature difference can only be explained by the higher thermal conductivity of hydrogen. When comparing the concentration ratio map [O]/[Ar] to the concentration ratio map [H]/[Ar], one can see that the contour lines of the [O]/[Ar] ratio diverge in the direction of the flow while the contour lines of [H]/[Ar] diverge in the upper part and converge in the lower part. This shows that the concentration of hydrogen in the centre decreases so that the concentration at a given distance also decreases.

V.4.3. The influence of the nature of the gas in the outer flow

Figure V-32 shows the temperature profiles for the injection of three different Ar-O_2 mixes in the outer flow. The intermediate flow and the inner flow are stopped. When the oxygen concentration is increased, the coupling efficiency decreases (see chapter VI). We increased the voltage in order to maintain the DC power and thus the power coupled to the plasma constant. The temperature in the centre is very similar for all three measurements. As the temperature in the centre cools down similarly in the three measurements, the velocity is probably similar.

The diameter of the plasma decreases with the oxygen fraction. At 9000 K a argon-2.5% oxygen mix has a 5 % higher enthalpy than pure argon and a argon-9.4% oxygen mix has a 19% higher enthalpy [ttw]. As the plasma with the higher oxygen fraction has a smaller diameter the total enthalpy flow is probably similar. This should be the case as the power that is coupled into the plasma is approximately the same.

	a)	b)	c)
Argon (outer flow) [Nm^3/h]	6.0	6.0	6.0
Argon (intermediate flow) [Nm^3/h]	0.0	0.0	0.0
Argon (inner flow) [Nm^3/h]	0.0	0.0	0.0
Oxygen (outer flow) [Nm^3/h]	0.0	0.15	0.62
Oxygen fraction	0%	2.5%	9.4%
Plate Voltage U_{DC} [kV]	6.0	6.4	6.7
Current I_{DC} [A]	5.2	5.0	4.8
DC Power [kW]	32.6	32.3	32.5
Distance GraphiteTarget [mm]	38	38	38

Table V-6 Plasma parameters, the influence of an argon-oxygen mix in the outer flow on the temperature

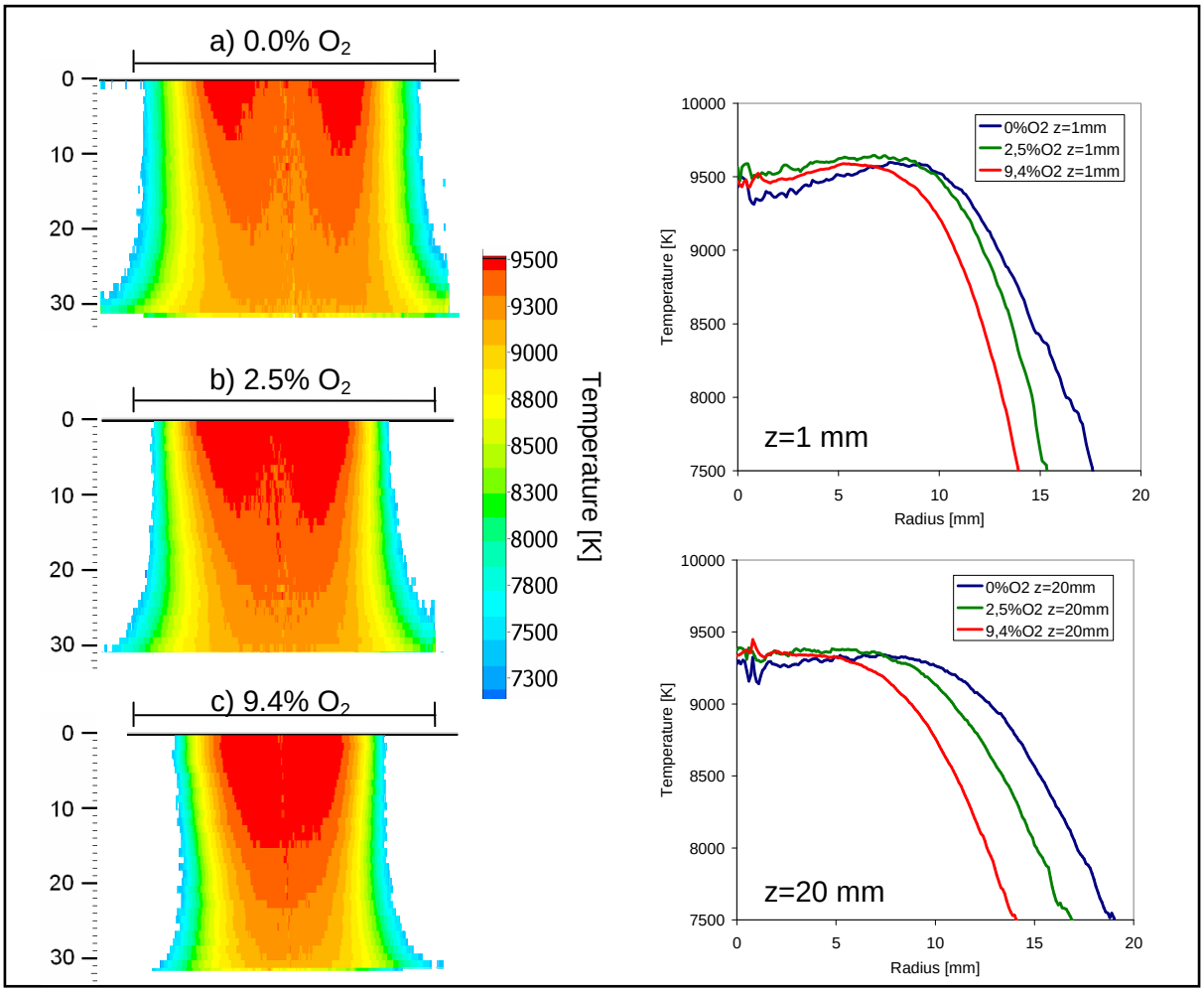

Figure V-32 : Temperature profiles for different Ar-O_2 mixes injected in the outer flow

V.4.4. The influence of a graphite target

	a)	b)
Argon (outer flow) [Nm^3/h]	6.0	6.0
Argon (intermediate flow) [Nm^3/h]	0.3	0.3
Argon (inner flow) [Nm^3/h]	0.0	0.0
Oxygen (outer flow) [Nm^3/h]	0.1	0.1
Hydrogen (inner flow) [Nm^3/h]	0.4	0.4
Plate Voltage U_{DC} [kV]	7.2	7.1
Current I_{DC} [A]	6.1	5.9
DC Power [kW]	43.9	41.7
Distance Target [mm]	193	38
Material of Target	Cupper	Graphite

Table V-7 Plasma parameters, the influence of a graphite target on the temperature and concentration profiles

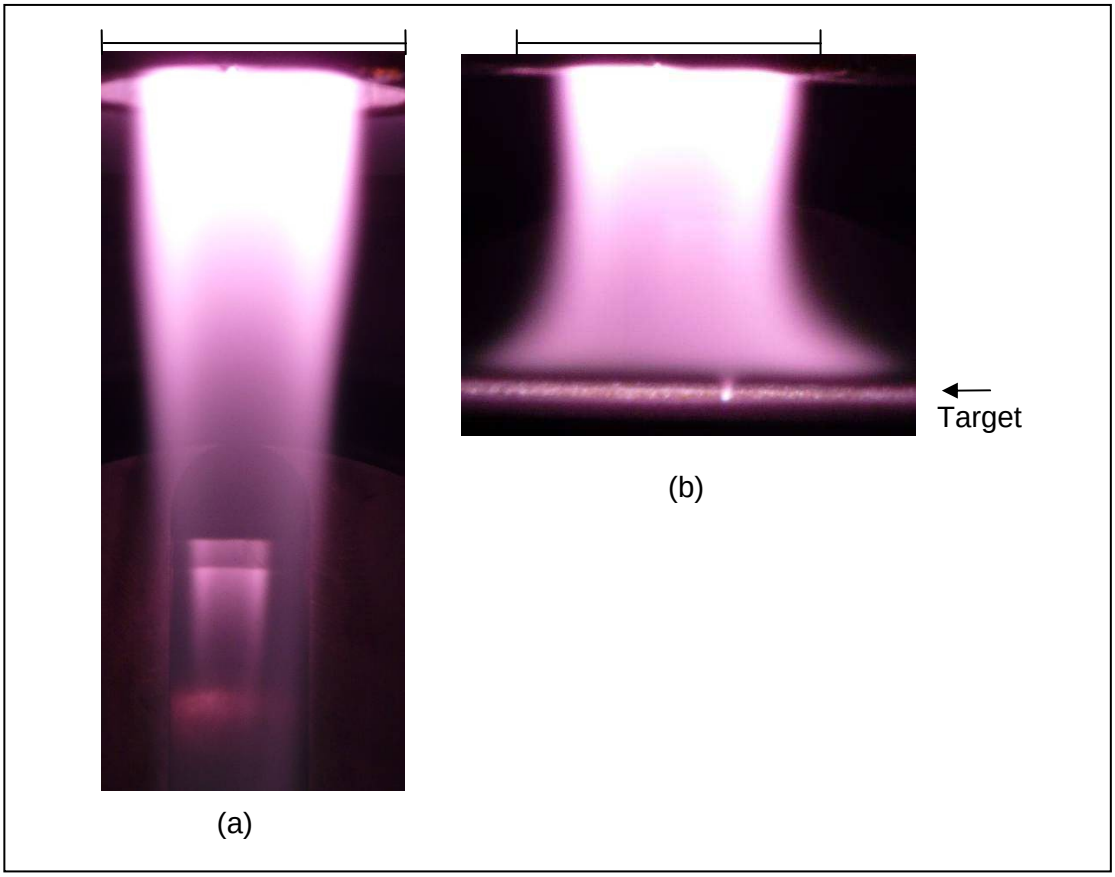

Figure V-33 : Photo of the plasma with target at a distance of (a) 193 mm and (b) 38 mm from the outlet of the torch

Figure V-34 shows the measured temperature and concentration ratio profiles for two different distances of the target (parameters : Table V-7). In one measurement the target is at a distance of z=193 mm to the outlet of the torch and in the other measurement the target is at a distance of z=38 mm to the outlet of the torch. Between z=0 mm and z=20 mm the profiles are nearly identical. The concentration of oxygen is slightly higher in the measurement with the target in the upper position. We can not explain this difference. The temperature is slightly higher in the measurement with the target in the lower position

because the DC power was 2.2 kW higher. Below z=20 mm the gas flow diverges in the measurement with the target in the upper position.

Figure V-33 shows the photos of the plasma for two different distances of the target. On the photo with the target in the lower position one can see the reflection of the plasma in the window at the opposite side of the chamber. On the photo with the target in the upper position one can see a small arc at the surface of the target. This shows that an electric current flow between the target and the plasma. The distance between the luminous zone of the plasma in the photo and the target is about 2 mm. From the comparison to measurements we can estimate that the luminous zone is above approximately 6000 K.

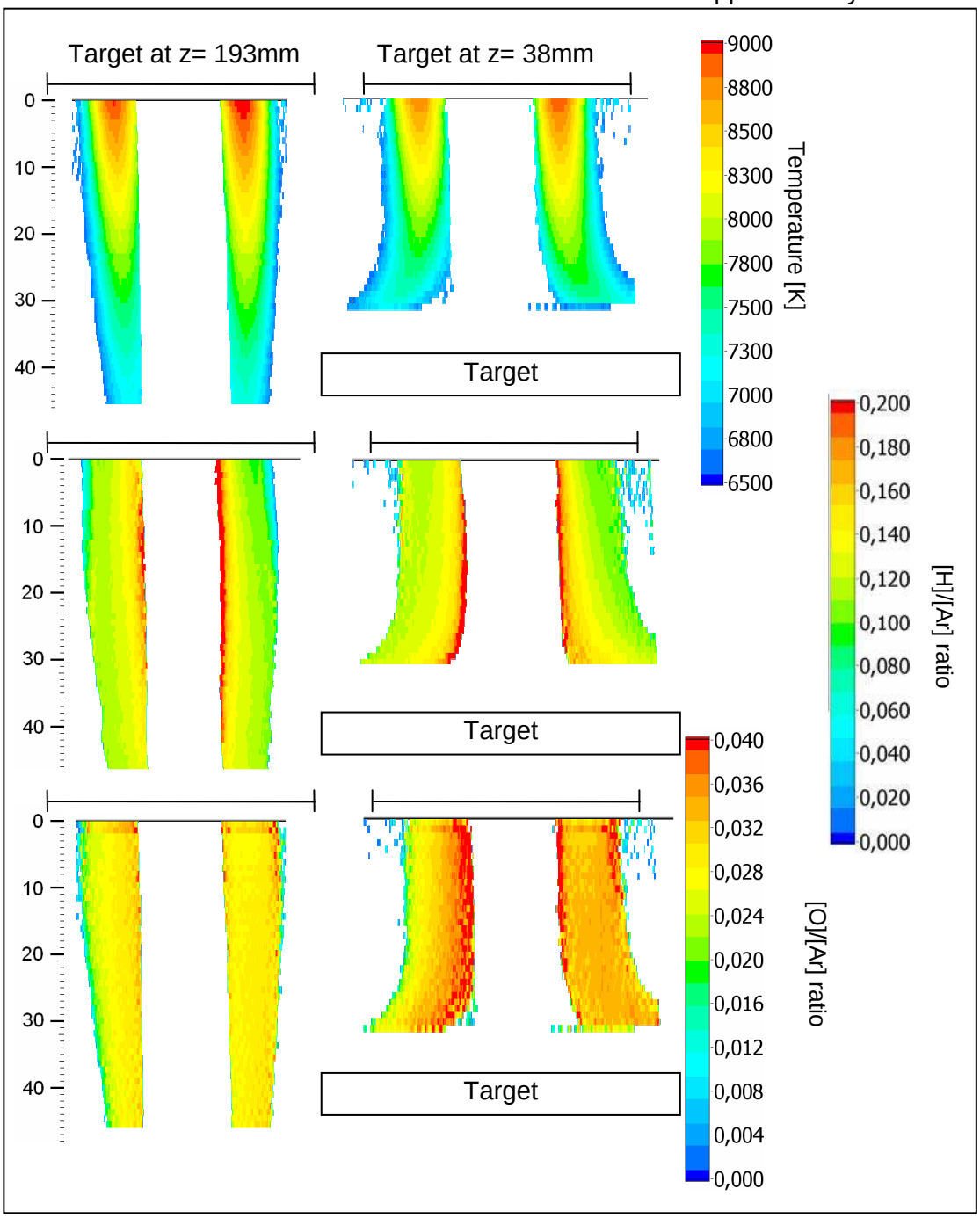

Figure V-34 : Temperature profiles and concentration ratio profile for two different distances of the target

V.4.5. The influence of the power

	a)	b)	c)
Argon (outer flow) [Nm^3/h]	6.8	6.8	6.8
Argon (intermediate flow) [Nm^3/h]	0.35	0.35	0.35
Argon (inner flow) [Nm^3/h]	0.14	0.14	0.14
Oxygen (outer flow) [Nm^3/h]	0.07	0.07	0.07
Hydrogen (inner flow) [Nm^3/h]	0.27	0.27	0.27
Plate Voltage U_{DC} [kV]	7.0	6.2	5.4
Current I_{DC} [A]	5.9	4.9	3.8
DC Power [kW]	41.4	30.5	20.7
Distance GraphiteTarget [mm]	38	38	38

Table V-8 Plasma parameters, the influence of the power on the temperature and concentration profiles

Figure V-36 shows the temperature profiles and the concentration profiles for different plasma powers (parameters : Table V-8). The temperature decreases with decreasing power from 9000 K at 41 kW to 6000 K at 21 kW. At 21 kW the plasma is asymmetric and one side it is more intense, probably due to the current between the plasma and the target. This can be seen in the photo in Figure V-35. Therefore the measurement at 20 kW is not very accurate. The concentration profiles are very similar besides the perturbed measurement at 20 kW. At 30 kW the measured concentration ratios [O]/[Ar] and [H]/[Ar] are slightly higher than at 41 kW. The slightly higher hydrogen concentration at 30 kW may be explained by a faster diffusion or a slower gas velocity. The slightly higher oxygen concentration may be due to less demixing. At 30 kW the diameter of the plasma is slightly smaller and also the cold channel in the centre is smaller. We performed a parametric purification experiment with the same parameters. This experiment is presented in chapter VII. In the measurements here we can mainly observe a decrease of the gas temperature. We do not observe a significant change of the concentration distribution but the measurement at 21 kW is strongly perturbed so that we can not be sure that the concentration distribution is the same than at 30 kW.

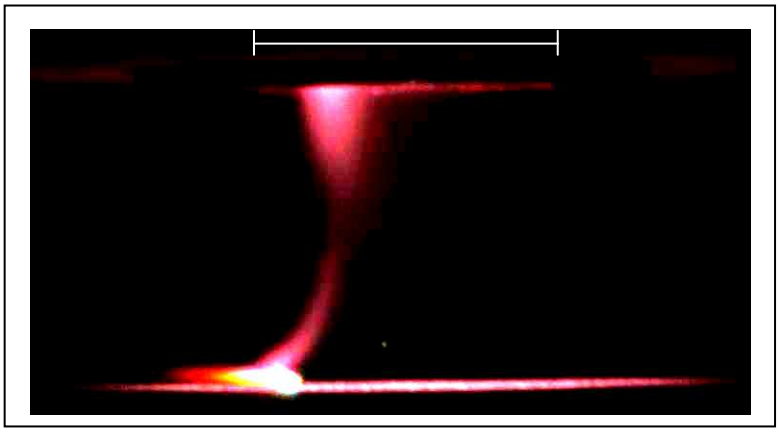

Figure V-35 : Photo of the plasma at 21 kW

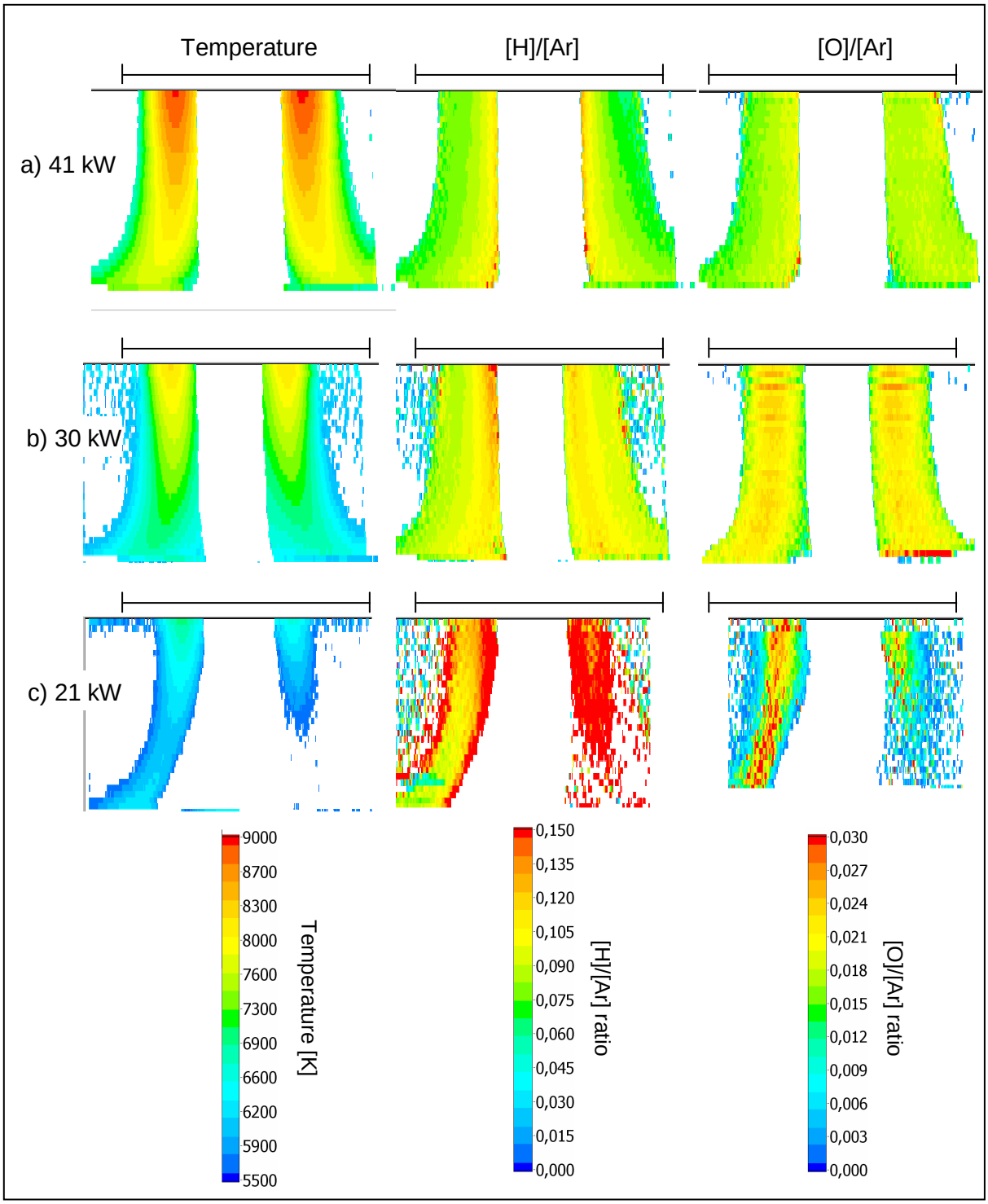

Figure V-36 : The temperature and concentration ratio profiles for different powers a) 41 kW, b) 30 kW and c) 21 kW

V.4.6. The influence of the oxygen and hydrogen flow rate

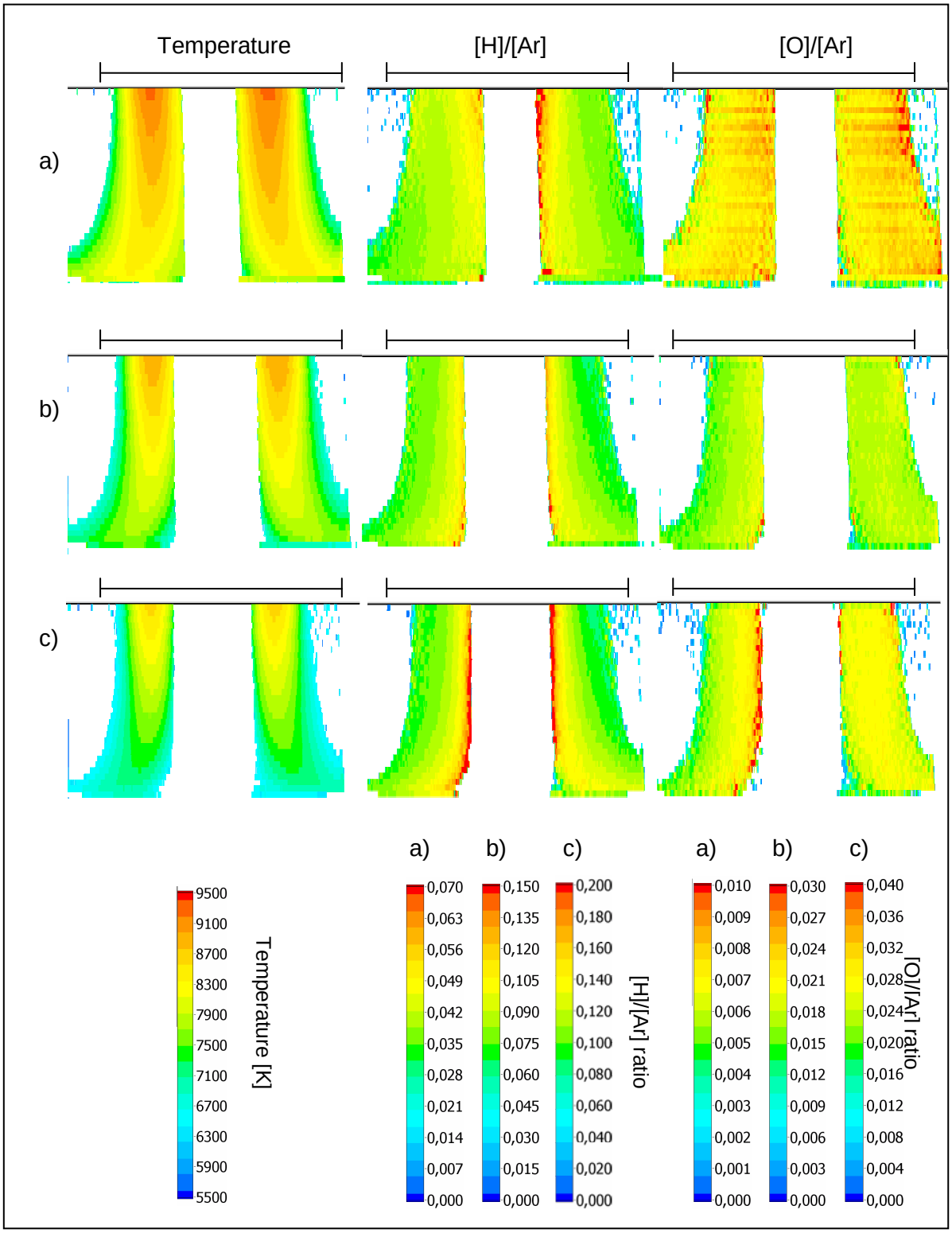

Figure V-37 : The temperature and concentration ratio profiles for different injected concentrations a) 0.4% O_2, 1.6% H_2, b) 0.9% O_2, 3.5% H_2 and c) 1.4% O_2, 5.0% H_2

	a)	b)	c)
Argon (outer flow) [Nm^3/h]	6.8	6.8	6.8
Argon (intermediate flow) [Nm^3/h]	0.35	0.35	0.35
Argon (inner flow) [Nm^3/h]	0.14	0.14	0.14
Oxygen (outer flow) [Nm^3/h]	0.03	0.07	0.11
Hydrogen (inner flow) [Nm^3/h]	0.12	0.27	0.39
Oxygen fraction	0.4%	0.9%	1.4%
Hydrogen fraction	1.6%	3.5%	5.0%
Plate Voltage U_{DC} [kV]	6.8	7.0	7.0
Current I_{DC} [A]	5.8	5.9	5.8
DC Power [kW]	39.7	41.4	40.7
Distance GraphiteTarget [mm]	38	38	38

Table V-9 Plasma parameters, the influence of oxygen and hydrogen on the temperature and concentration profiles

Figure V-36 shows the temperature profiles and the concentration profiles for the injection of different flow rates of oxygen in the outer flow and hydrogen in the inner flow (parameters : Table V-9). The hydrogen flow is about 4 times higher than the oxygen flow. The results show that the diameter of the plasma decreases and the diameter of the cold channel increase from a) to b). From b) to c) the diameter of the plasma decreases further while the diameter of the cold channel remains constant. The temperature of the plasma decreases when the concentrations of oxygen and hydrogen are increased. The [O]/[Ar] ratio and the [H]/[Ar] ratio in the plasma increase linearly with the injected concentration. In all three measurements the [O]/[Ar] ratio is uniform while the [H]/[Ar] ratio is higher in the centre. Similar to the injected oxygen and hydrogen flow rates, the measured [H]/[Ar] ratio is about four times higher than the measured [O]/[Ar] ratio.

The same parameters were used in a purification experiment that is presented in chapter VII. The spectroscopic measurement shows that the concentration distributions are approximately similar for the three measurements with a mean concentration that is proportional to the injected ratio. The variation of the concentration is thus the main difference that can modify the purification. The variation of the temperature and eventually the gas velocity may also modify the purification.

V.5. Parametric study on the small torch

In this study we measured the influence of different parameters on the temperature profile of the small torch. In this experiment the outer quartz tube was very long, so that ambient air cannot diffuse into the plasma. We measured the temperature profile 5 mm above the induction coil. We began the measurement with 8.5 l/min Ar in the outer flow, no flow in inner flow and intermediate flow and a voltage of 3500 V.

	a	b	c	d
Outer flow [l/min]	8.5	8.5	**6.6-13.1**	8.5
Intermediate flow [l/min]	0	0	0	**0.0-0.88**
Inner flow [l/min]	0	0	0	0
DC Voltage [V]	**3050-4000**	3500	3500	3500
DC Current [A]	0.38-0.44	~0.4	~0.4	~0.4
DC Power [W]	1160-1770	~1400	~1400	~1400
Oxygen concentration	0.0%	**0.0-0.5%**	0.0%	0.0%

Table V-10 Plasma parameters, parametric study on small torch

Then we changed

- the voltage (V.5.1)
- the concentration of oxygen (V.5.2)
- the outer flow rate (V.5.3)
- the intermediate flow rate (V.5.4)

The parameters are presented in Table V-10. The varied parameter is presented in the figures. Each time we measured the temperature profile so that we can see how it is influenced by the different parameters. The first measurement is in all diagrams. The reader can observe a small minimum at a radius of 1 mm in most of the plots which is due to a scratch on the quartz tube.

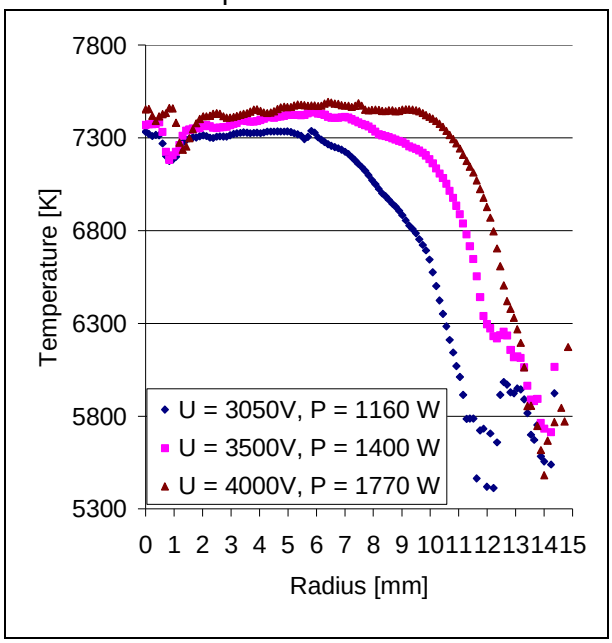

Figure V-38 Temperature profiles for different voltages V.5.1

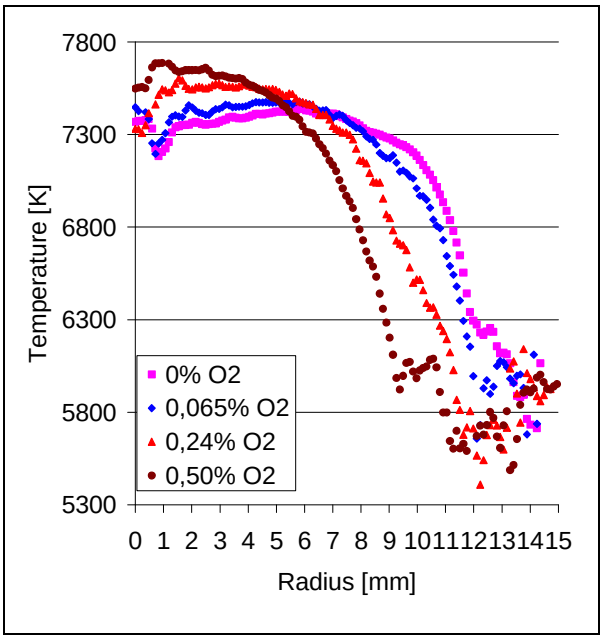

Figure V-39 Temperature profiles for different concentrations of oxygen V.5.2

V.5.1. The voltage

We observe in Figure V-38 that the voltage changes the width of the plasma. A higher voltage gives a larger width. The temperature in the centre changes very little. As the current increases with the voltage, the power (here U*I) increases faster than the voltage.

V.5.2. The concentration of oxygen

We observe in Figure V-39 that the concentration of oxygen has a large influence on the shape of the plasma. It changes the width and also the temperature in the centre. The higher the concentration of oxygen, the smaller is the width of the plasma and the higher is the temperature in the centre. This is due to an effect in the induction zone, where the absorption of energy from the electromagnetic field and the heat conduction are in equilibrium. This effect will be studied in more detail in chapter VI.

V.5.3. The outer flow rate

We observe in Figure V-40 that the outer flow cools the edge of the plasma. The higher the outer flow the smaller the width of the plasma. The temperature in the centre remains constant.

V.5.4. The intermediate flow rate

We observe in Figure V-41 that the intermediate flow does not change the temperature profile. The temperature without intermediate flow was not taken at the same time than the others. Eventually the power was slightly higher in this measurement, making the temperature profile slightly different to the others.

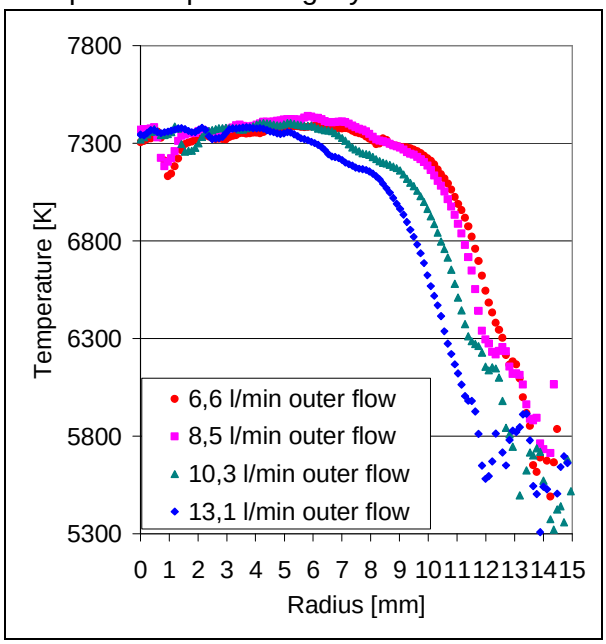

Figure V-40 Temperature profiles for different outer flows V.5.3

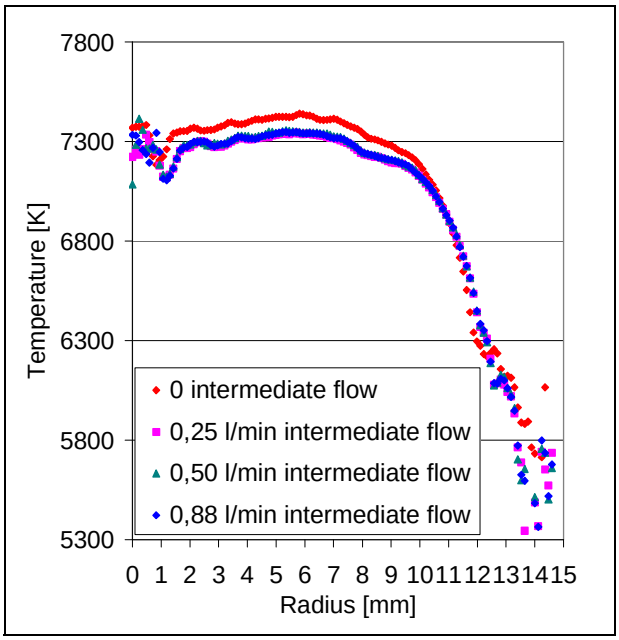

Figure V-41 Temperature profiles for different intermediate flow rates V.5.4

V.6. Conclusion

The validation measurements showed that the assumption of local thermal equilibrium is valid and that it is thus possible to measure the temperature and the concentration ratios [O]/[Ar] and [H]/[Ar] with the emissivity of atomic lines of the three elements. The temperature measurement of the method has a precision of ±300 K. The accuracy of the concentration ratio is mainly limited by the accuracy of the transition probability to about 25 %. Fluctuations of the plasma perturb the concentration ratio and temperature measurement at the edge of the plasma. The measured concentration ratio profiles indicate that demixing takes place in the induction zone. For this reason it was not possible to test whether concentration measurements with higher precision was possible.

We compared simulated and measured concentration ratio and temperature profiles. We found that the k-ε turbulence model that we used so far give results that are far from the real plasma. The k-ω-SST turbulence model gives better results that are very close to the measurements. As the simulated and the measured concentration and temperature distributions are similar we can assume that the model calculates also well the velocity. The parametric studies have shown that the plasma power has a significant influence on the plasma temperature. Hydrogen diffuses much better than oxygen and is well diluted in most cases. Oxygen diffuses only slowly to the exterior of the plasma when it is injected in the centre. In order to obtain a homogeneous concentration it is thus best to inject hydrogen in the inner flow and oxygen in the outer flow.

VI. Other measurements for the characterization of the plasma torch

In this chapter we present other measurement methods that were tested for the characterization of the plasma.

VI.1. The velocity measurement

We examined the oscillations of the plasma of the big torch with a high speed camera and got the idea to use these variations of the intensity to measure the flow velocity. The method is similar to the method that M.P. Planche used to measure the flow velocity of a DC plasma spray torch [PCF98]. A literature overview of velocity measurements in ICP torches can be found in the paper of Cicerone [CF89]. The different techniques are based on the dynamic pressure or on the time of flight of different tracers. The techniques based on the dynamic pressure are limited to zones where the probe can resist to the heat transfer from the plasma. Cicerone uses a method which is based on the emission of calcium which is injected into a small ICP torch for chemical analysis. Rahmane et al [RSB95] measured gas velocities between 60 m/s and 80 m/s at a distance of 23 mm below the outlet of the 25 kW torch at 33 kPa. The numerical model of Pelletier [Pel06] indicate velocities of 40 m/s below the outlet of the torch for the same parameters as studied here.

VI.1.1. Basic explanation

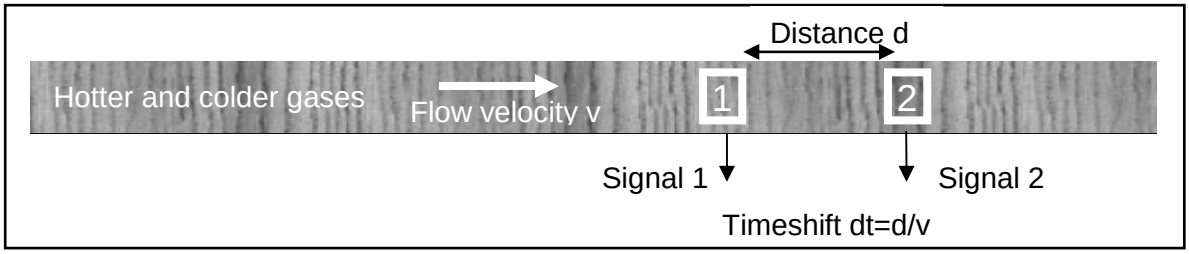

Figure VI.1 : Explanation of flow velocity measurements using temperature fluctuations

Our method is based on the time of flight of luminous fluctuations which are due thermal fluctuations. The hotter gas emits more light than the colder gas. When we measure the intensity at one point we can detect thus the thermal fluctuations (see Figure VI.1). These fluctuations move with the flow velocity. At a second point located further down in the flow we can measure the same fluctuations but they arrive delayed. This time shift is the time of flight from the first point to the second point. The signals of the intensity measurement at two points are thus time-staggered. The distance between the two points divided by the time shift gives us the flow velocity. One can calculate this time shift with the position of the maximum of the cross correlation of the two signal.

VI.1.2. Sources of fluctuations

We want to analyze the sources of the fluctuations that we use for the measurement

Kelvin-Helmholtz instability

In a shear layer between a high velocity zone and low velocity zone there is an instability of the Kelvin-Helmholtz type. This instability creates fluctuation. In some geometries these fluctuations are periodic. In this case the phenomenon is called vortex shedding. A famous example of vortex shedding is the Karman vortex street which is created by the flow over a body (Figure VI.2).

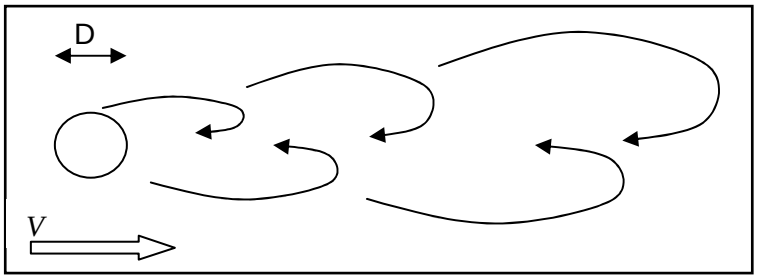

Figure VI.2 : Karman vortex street

The frequency f (Hz) of these oscillations can be evaluated with the Strouhal number St, where D (m) is the diameter and V (m.s^{-1}) is the velocity (Equation (VI-1))

$$St = \frac{fD}{V} \qquad \text{(VI-1)}$$

We also observed vortex shedding in our plasma torch. In Figure VI.3 we show the frames of a video taken with a high speed camera. In order to highlight the oscillations we subtracted the (temporal) mean signal from each frame. Red zones have a higher signal and blue zones a lower signal than the mean signal. The fluctuations are probably due to the shear layer between the high velocity of the plasma jet and the static gas in the reaction chamber. An overview of fluctuations of free jets is given by Han et al. [HG03]. They report Strouhal numbers between 0.25 and 0.5.

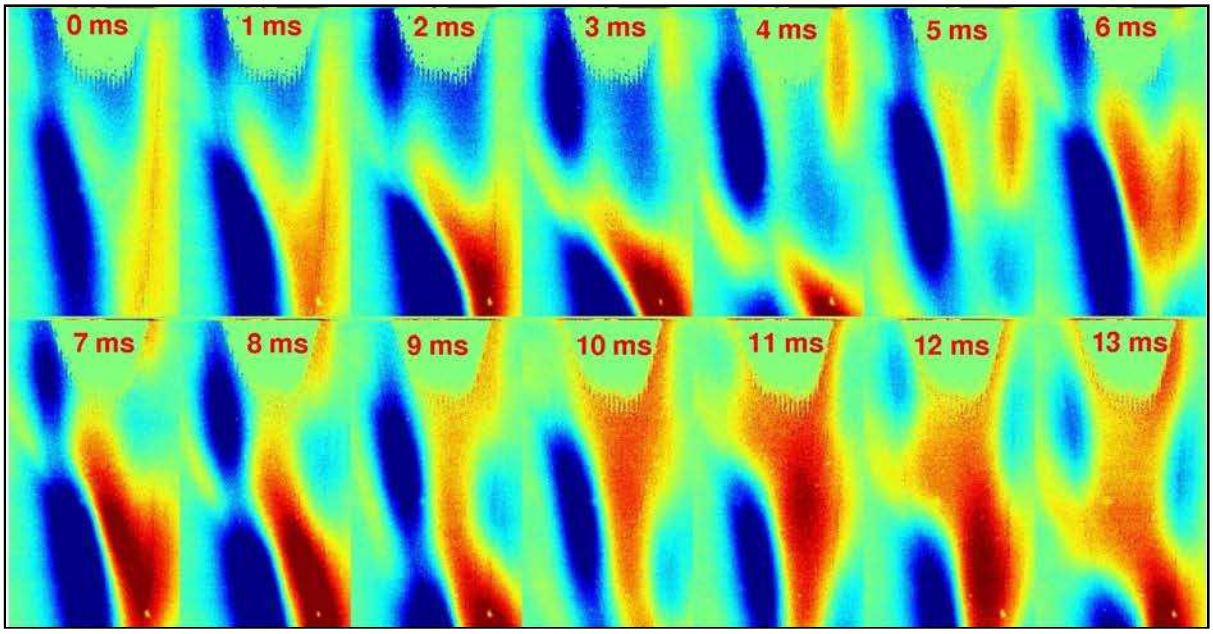

Figure VI.3 Vortex shedding of the plasma The (temporal) mean intensity has been subtracted from each frame. Shutter time: 59 µs Colors: green (0), red (stronger signal), blue (weaker signal)

Power-Supply

The power supply uses the electric current from the power grid. A rectifier converts the three phase alternating current to direct current. The rectifier lets pass always the highest voltage of the three phases and the three inversed phases as shown in Figure VI.4.

The rectified current (red) has therefore a small 300 Hz oscillation. The amplitude of the oscillating LC-circuit which injects the power into the plasma is proportional to the voltage of the direct current. We expect therefore an oscillation with 300 Hz on the temperature and the intensity of the plasma.

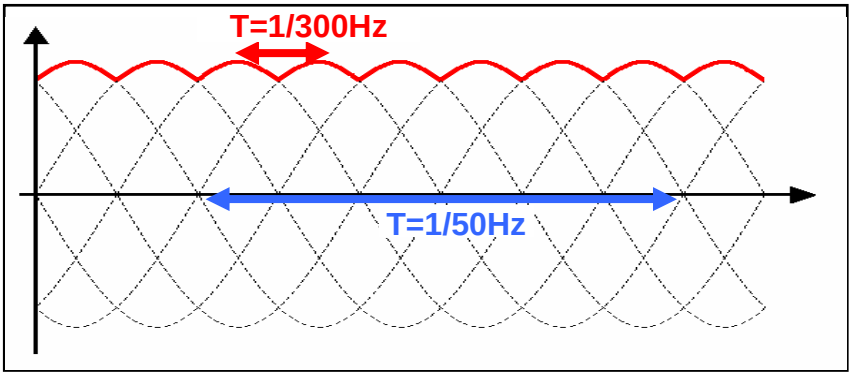

Figure VI.4 : Output voltage waveform of a three-phase full-wave rectifier

The spectrum of the fluctuations

We take a 500 frames high speed video of the plasma at a frame rate of 1000 per second. Then we calculate the frequency spectrum with the Fast Fourier Transformation (FFT) of an arbitrary point of the video (Figure VI.5). The maximum frequency of the spectrum (the Nyquist frequency) is thus 500Hz and the resolution is 250 points.

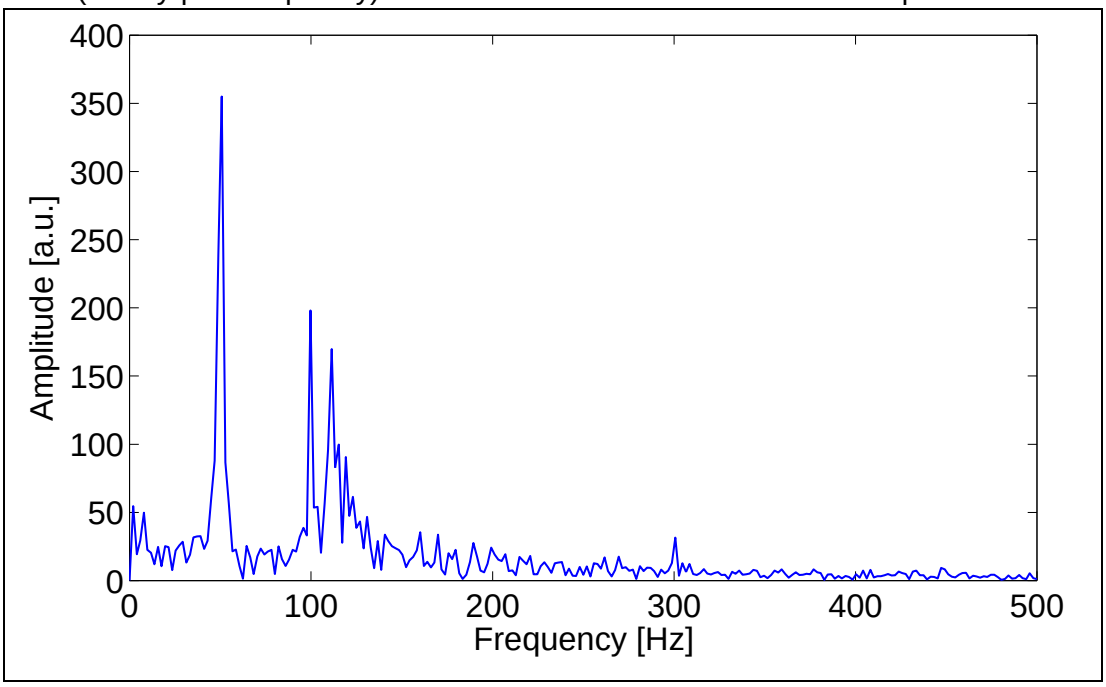

Figure VI.5 : Frequency spectrum at an arbitrary point of the video

We see in the frequency spectrum Figure VI.5 very narrow peaks at 50 Hz, 100 Hz and 300 Hz. As the peaks are very narrow and their frequencies are exactly at multitudes of 50 Hz we can assume that these fluctuations come from the power supply. The strong 50 Hz oscillation can be due to amplitude differences between the three phases. There is also a rather large peak at 110 Hz. This peak is probably due to vortex shedding. The vortex shedding that can be seen in Figure VI.3 has a period of about 5 ms (200 Hz). With a Strouhal number between 0.25 and 0.5 we thus obtain a velocity between 9 m/s and 35 m/s. These velocities are smaller than the velocities reported by Rahmane et al [RSB95]. This can be explained by the low density in the centre of the plasma. Therefore the slower flow with a higher density at the edge of the plasma may determine the frequency of the vortex shedding.

VI.1.3. Flow velocity measurement with a high speed camera

We take videos of 500 frames at a frame rate of 1 kHz and a shutter time of 10 µs. For the velocity calculation we take the signals of two points one above the other (white areas in Figure VI.6). In order to reduce the noise we took the sum of an area of 7*21 pixels. We can see in the Figure VI.6 some dark points which are due to dust particles on the CCD array of the camera. They have very little influence as they reduce only the absolute intensity which does not play a role in our measurement.

We measure the distance between the two areas by counting the pixels and dividing by the number of pixels per cm. For the calibration of the number of pixels per cm we take a video of a line gauge.

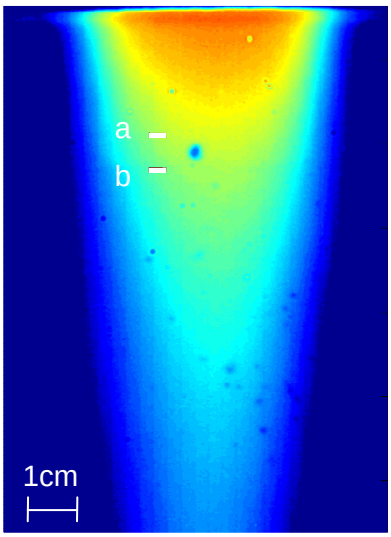

Figure VI.6 : Image of the plasma with representation of the two areas used for velocity measurement (mark a and b)

The two signals of the two areas (a and b) are shown in Figure VI.7. The green signal is from the area b (downstream). The intensity here is lower because the plasma is cooler. We can see that the variations of the two signals are very similar. We cannot see the time shift between the two signals because it is too small.

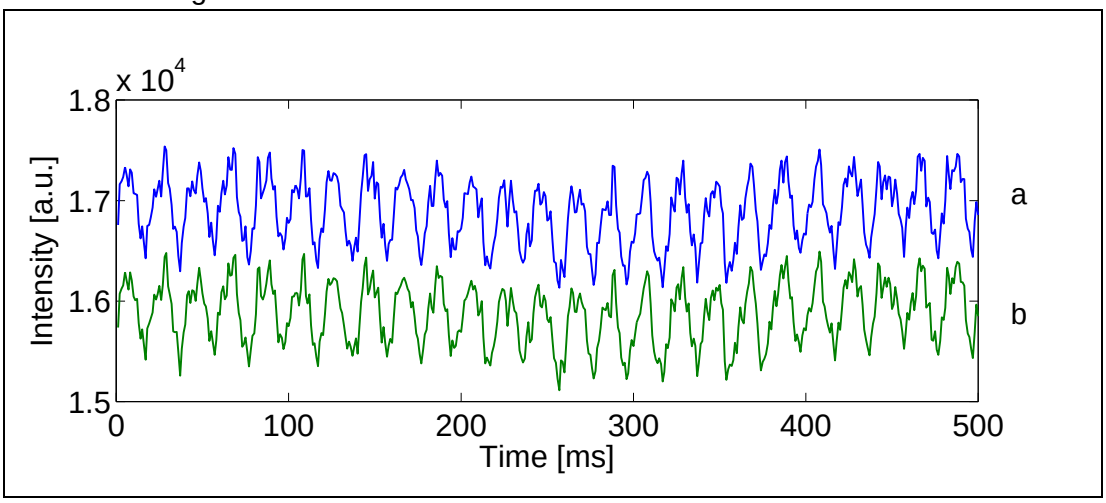

Figure VI.7 : Two signals from high speed movies

In order to calculate the time shift we subtract from each signal its mean value and then calculate the cross correlation between the two signal which is shown in Figure VI.8. For this purpose we use the matlab function “xcorr”.

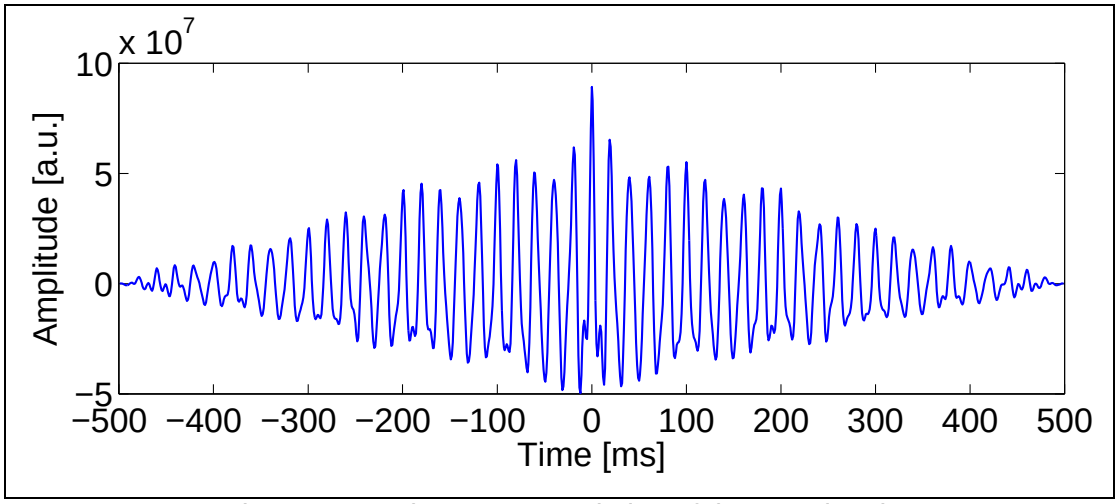

Figure VI.8 : The cross correlation of the two signals

The maximum in the middle of the cross correlation (Figure VI.8) is where the two signals coincide. The position of the maximum gives us thus the time shift between the two signals. The other maxima and minima can be explained by quasi-periodic oscillation of our signals (Figure VI.7) coming mainly from the generator (50 Hz). While all oscillations contribute to the peak in the centre of the correlation the quasi-periodic wave also gives maxima when the two signals are in phase or minima when they have a phase shift of 180 degree.

The temporal resolution of our signals is 1 kHz. The maximum of the correlation can therefore be calculated with a precision of 1 ms. We assume that the velocity of the plasma is 50 m/s so that the gases propagate about 5 cm in 1 ms. This distance is long compared to the size of the plasma. We need thus a higher precision on the measurement of the time of position of the maximum. We increase therefore artificially the resolution from 1 ms to 0.02 ms by interpolating the peak in the centre with the function “interp” of matlab (Figure VI.9). (the function “interp” performs low-pass interpolation by inserting zeros into the original sequence and then applying a special low-pass filter. (Source www.mathworks.com)). We can do this because there is very little statistical error in the cross correlation.

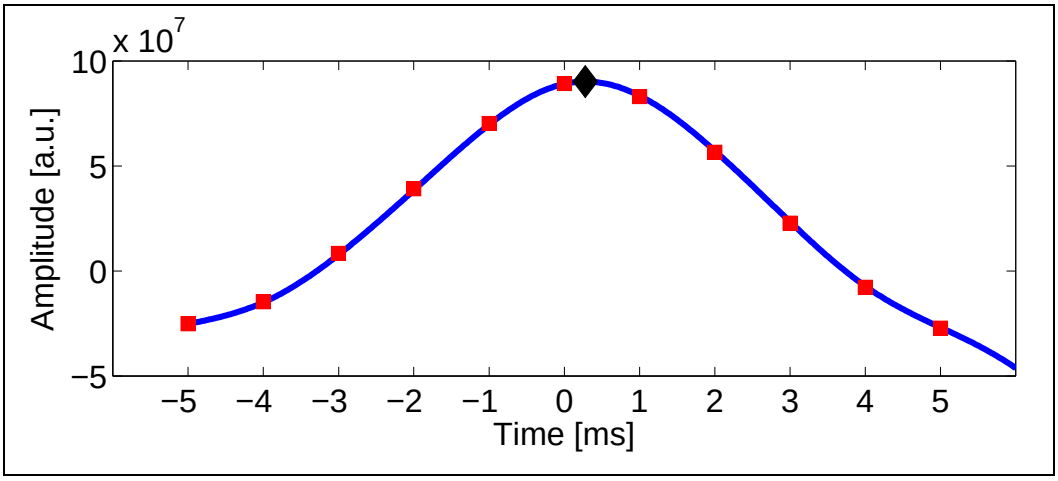

Figure VI.9 : Interpolation of the central maximum of the cross correlation (Red squares=data points, blue line=interpolation, black diamond=maximum)

We then move the point a of Figure VI.6 upstream and the point b downstream so that the centre between the points does not move. And repeat the method to calculate the time shift.

We calculate this way the time shift for 20 pairs of points with the same centre and plot it against the distance with the time shift on the x-axis (Figure VI.10)

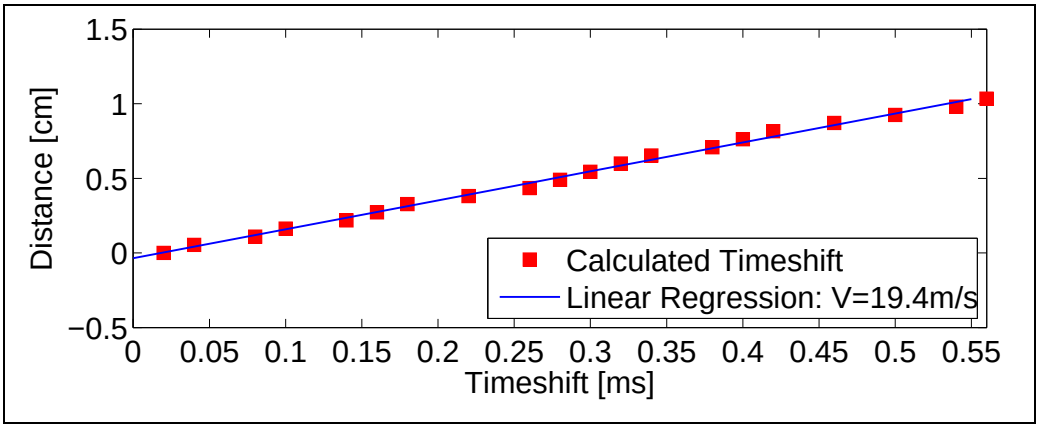

Figure VI.10 : Distance versus time shift of different points v=19.4m/s

The result is nearly linear, which shows us that there is little noise on the measurement. The interpolation method that we used to increase the precision does not create noise. We can now use linear regression to calculate the slope, which gives us directly the flow velocity.

The method is limited by the fact that we can only measure the intensity of the light coming out of the plasma. This light is always an integral over regions with different flow velocities and different emissivities. Figure VI.11 a) shows the spectroscopic measurement of the typical radial emissivity profile of an Argon line. The emissivity profile just below the outlet of the torch has a dip in the centre. The emissivity profile 60 mm further downstream has a high emissivity in the centre and a strong emissivity gradient towards the edge of the plasma. For such an emissivity profiles with a high emissivity gradient the intensity of a light beam that comes out of the plasma is mainly the integrated emissivity from the point that is closest to the centre of the plasma (red points in Figure VI.11). The autocorrelation of the light intensity is thus similar to the autocorrelation of the emissivity at the red point and gives thus the velocity at the red point.

For the emissivity profile with a dip just below the outlet the integration over regions with different flow velocities and similar emissivity does probably perturb the measurement at low radii. At higher radii the emissivity gradient is high so that the measurement method should work.

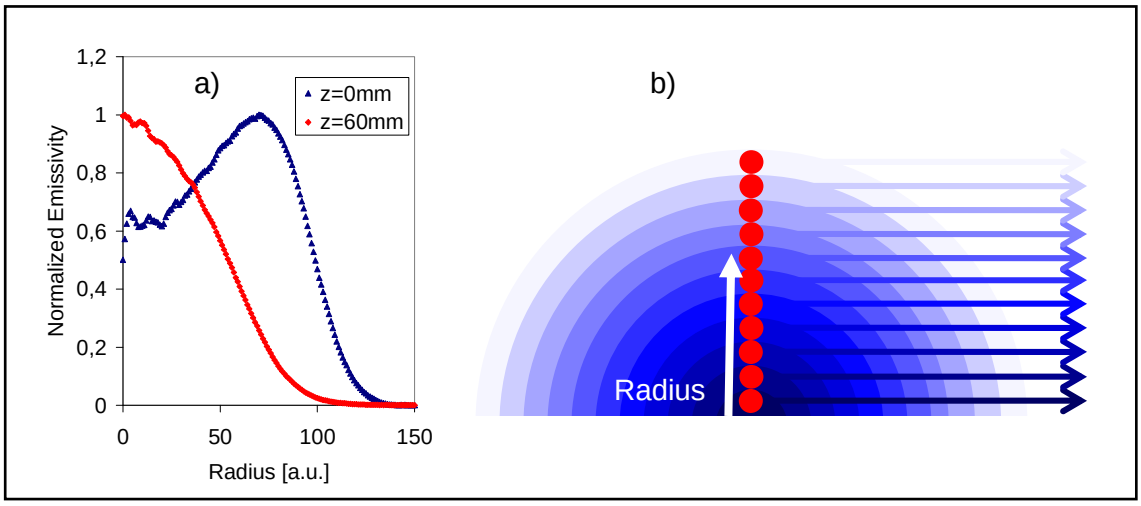

Figure VI.11 : a) Radial emissivity profiles of an argon line.
b) Schema to show that for a high emissivity gradient the intensity of the light beam coming out of the plasma is mainly from the zone (red point) which is closest to the centre (dark blue = high intensity/emissivity)

VI.1.4. Validation of the method

For the validation of the method we took videos with different experimental parameters. The setup of the gases is somewhat complex (Figure VI.12). It was planned for the validation of the concentration of oxygen. We measured the flow rate of pure argon which is going to the injector flow (1). Then we measured the flow rate of argon (2) and oxygen (3) before mixing them. The mix goes to the outer flow and over another flow meter (4) to the intermediate flow.

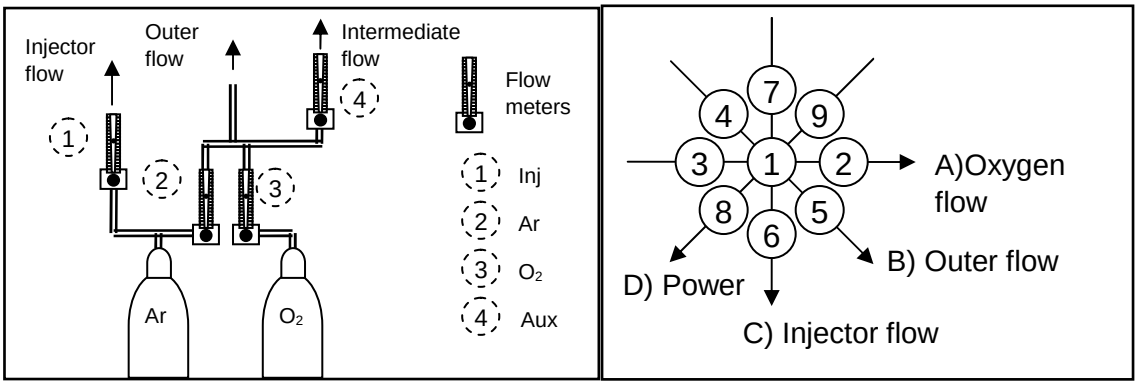

Figure VI.12: Schema of the gas flow measurement setup and chart of parameter variations

Voltage U [kV]	7.5
Current I [A]	3.3
P_{el} [kW]	24.8
Ar Inj (1) [l/min]	2.7
Ar Outer+Interm (2) [l/min]	83
O_2 Outer+Interm (3) [l/min]	1.4
Ar+O_2 Interm (4) [l/min]	4.7

Table VI-1: Experimental parameters "velocity measurements", central point (1)

As reference conditions we used the parameters shown in Table VI-1. From this central point ((1) in Figure VI.12), we changed the four main parameters:

A) the oxygen flow (2) and (3)

B) the outer flow (4) and (5)
C) the injector flow (6) and (7)
D) the power (8) and (9)

The experimental conditions are detailed in Figure VI.13 and Figure VI.14.

The current depends on the coupling coefficient between the plasma and the induction coil. The coupling coefficient changes a lot when the gas mixture and therefore the thermal conductivity changes. We varied the voltage in order to maintain the power constant.

The resulting velocity fields are presented in Figure VI.13 and Figure VI.14. The measured velocity profiles are similar. The difference between the velocity maps can not be clearly attributed to a change of the parameters and seem to be random. This differences show that especially in the zone, where the measured velocity is high, the measurement is not exact. The errors may be due to the integration of light across the plasma.

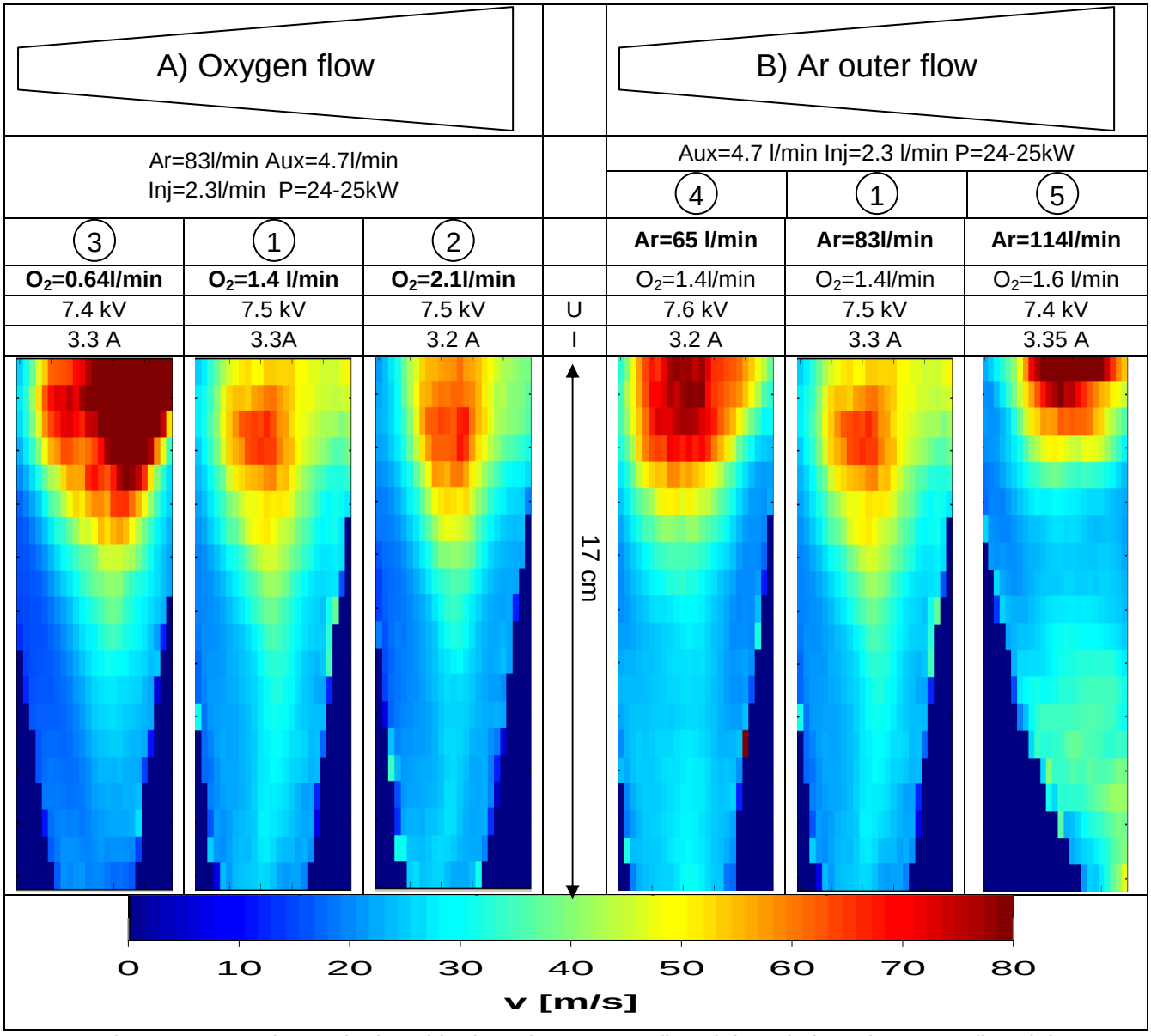

Figure VI.13 : Flow velocity with changing oxygen flow (A) and changing outer flow (B)

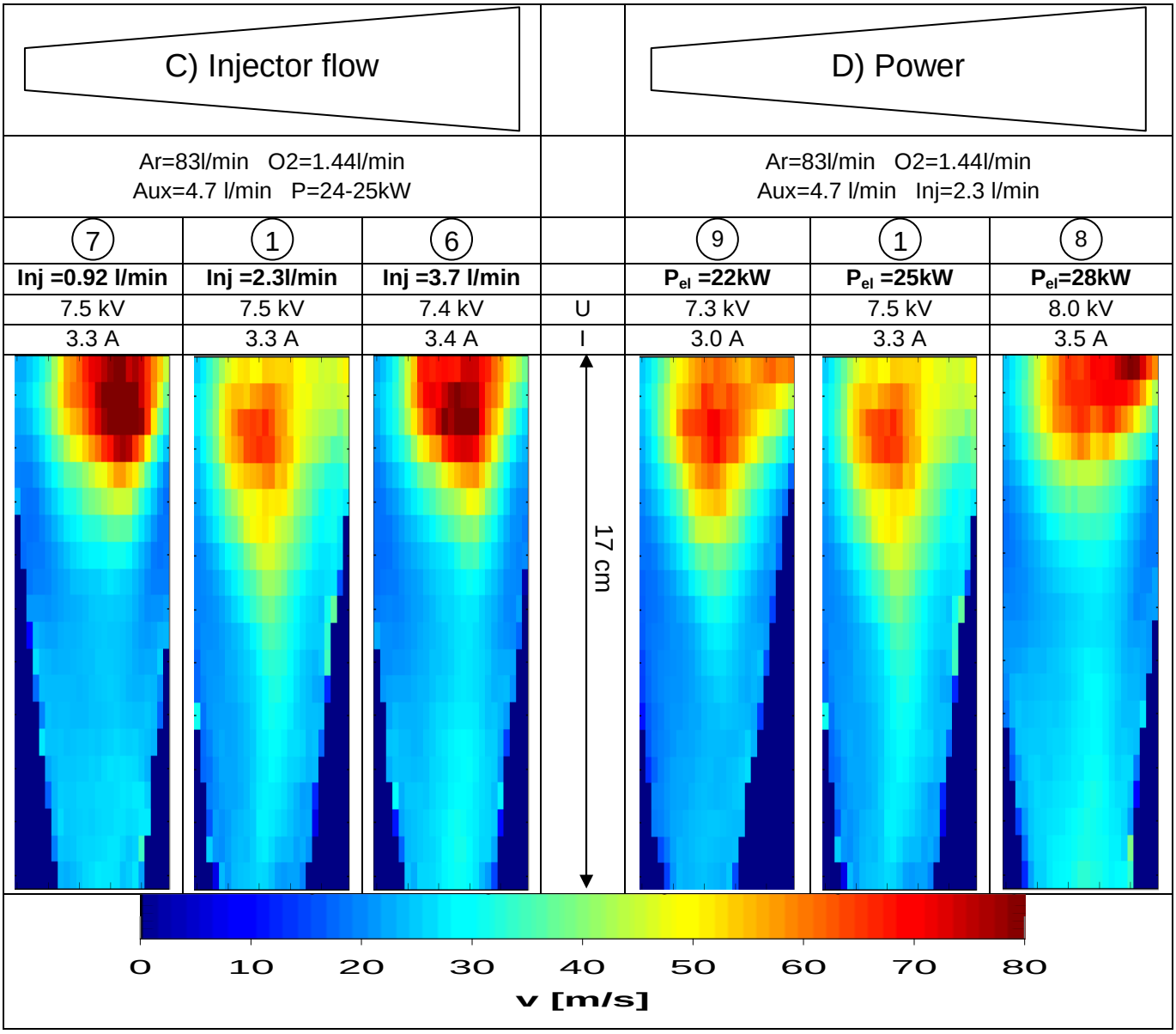

Figure VI.14 : Flow velocity with changing injector flow (C) and changing power (D)

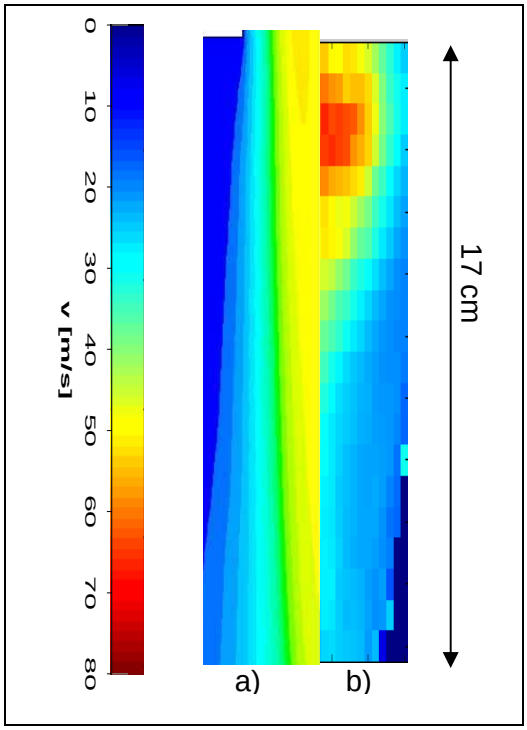

Figure VI.15 Comparison of simulated velocity map (a) and measured velocity map (b)

In Figure VI.15 we compare the measured velocity map with the parameters of Table VI-1 to a simulated velocity map with the parameters that are presented in Table VI-2. In the simulation the power is nearly twice as high as in the measurement so that only a qualitative comparison is possible.

Coupled Power [kW]	21.2
Power [kW]	42.4
H_2 Inj [l/min]	17
Ar Outer [l/min]	100
Ar Interm [l/min]	5

Table VI-2 Parameters of simulated velocity map

The high velocity zone (60 $m.s^{-1}$) that we measured below the outlet of the torch can not be seen in the simulated velocity profile. This also indicates that the measurement is not exact in this region. Further downstream, both the measurement and the model show a higher velocity in the centre and a lower velocity at the edge. The velocity in the model is higher. This may be due to the higher power in the model.

The errors on the measurement are too high to use the method to validate the velocity of the model. The enthalpy probe technique [RSB95] is probably better adapted to measure the velocity and to validate the model.

VI.2. The coupling

For the operation of an inductively coupled plasma torch a good coupling between the generator and the plasma is crucial. The objective of this chapter is to better understand the coupling between the inductor and the plasma. First we present an electric model for the coupling. Then we show that the coupling depends mainly on the size of the plasma. We analyze the gas properties that can modify the coupling and do measurements with different oxygen and hydrogen flows. We present measurements of the current and frequency for different operating conditions and use these measurements to validate the theory.

VI.2.1. Introduction

Commonly an air-cored transformer model is used to analyze macroscopic measurements of the induced power as shown in Figure VI.16 (a). The inductor L_0 is connected in parallel with the capacitor C to the generator. The inductor L_0 forms the primary circuit of the transformer. The plasma forms a single coil secondary (L_1, R_p inductance and resistance of the plasma). Figure VI.16 (b) shows the equivalent circuit of Figure VI.16 (a). The equivalent inductance L_{equ} and the equivalent resistance R_{equ} can be calculated from L_0, L_1 and R_p.

Fayoumi [FJ98] applied this model to obtain expressions that relate the macroscopic electrical properties L_{equ} and R_{equ} to the volume averaged microscopic plasma parameters, the electron density and the collision frequency of a cold plasma. He showed that in principle the measurement of L_{equ} and R_{equ} should allow to measure the microscopic parameters.

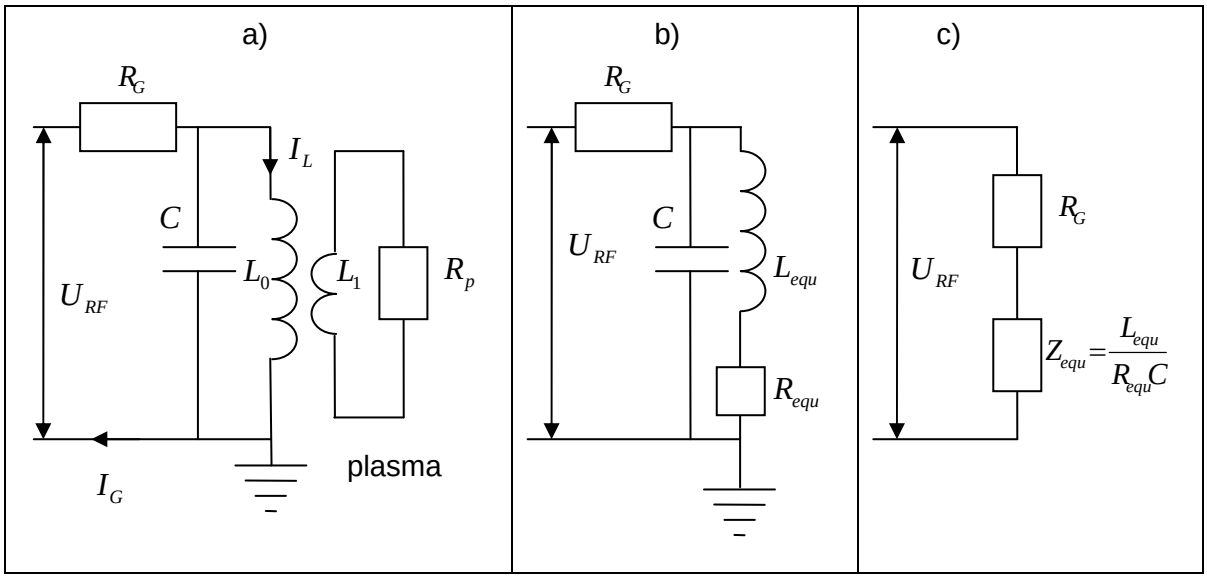

Figure VI.16 Equivalent circuits for the transformer model
R_G resistance of the generator, U_{RF} RF generator voltage , C capacitor, L_0 Inductor I_G generator current, I_L inductor current
a) Transformer model: Inductor as primary and plasma as secondary (L_0 inductance of the inductor, L_1, R_p inductance and resistance of plasma)
b) Equivalent circuit of a) R_{equ} and L_{equ} can be calculated from L_0, L_1, R_p
c) Equivalent circuit of b) at the resonance frequency of R_{equ}, L_{equ}, C

Fayoumi studied an inductively coupled plasma at low pressure (cold plasma). In a thermal plasma the microscopic plasma parameters are not uniform anymore and the electron density is higher. The higher electron density screens the magnetic field so that rather the volume of the plasma than the absolute value of the electron density defines the electrical parameters L_{equ} and R_{equ}.

J. Meyer implemented during his internship a model that can simulate the macroscopic electrical parameters L_{equ} and R_{equ} for our setup. We used the program Ophelie [GL88] that was developed in our laboratory. The program Ophelie can solve the equation (VI-2) and (VI-3) in an axisymmetric geometry. The program thus calculates the electrical parameters L_{equ} and R_{equ} for the inductor.

$$\nabla \times B = \mu_0 j \qquad \text{(VI-2)}$$

$$\nabla B = 0 \qquad \text{(VI-3)}$$

Figure VI.17 shows the geometry that we implemented in Ophelie. It takes into account the inductor, the segmented outer tube, the injector and a cylinder that represents the plasma. For the elements of the torch we used the conductivity of copper ($5x10^7$ S/m) and for the cylinder we used a conductivity of 6000 S/m (the conductivity of argon at 12500 K [ttw]). We calculated L_{equ} and R_{equ} for different external radii of the cylinder.

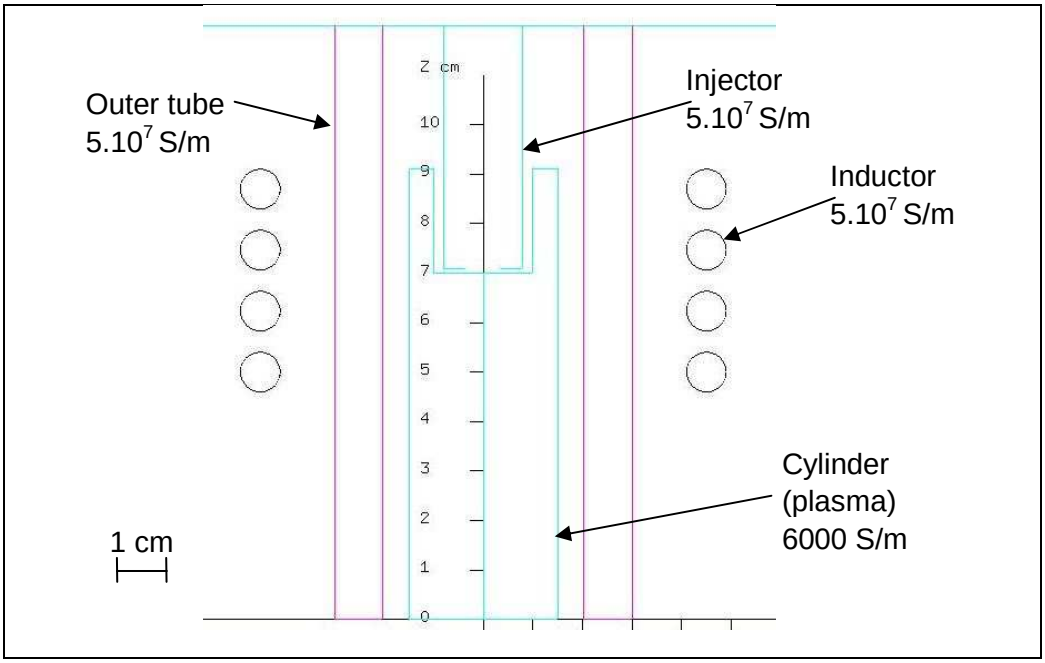

Figure VI.17 The geometry implemented in Ophelie for the simulation of the electrical parameters L_{equ} and R_{equ}

Figure VI.19 shows the simulated electrical parameters L_{equ} and R_{equ} of the inductor. The values at radius 0 were simulated without the cylinder that represents the plasma.

We tested if we can use the measured frequency to estimate the radius of the plasma. We assume that the generator oscillates at the resonance frequency of the tank circuit, which consists of the capacity and the inductor. The variation of the radius of the plasma, modifies the inductance of the inductor and thus the resonance frequency of the tank circuit. The resonance frequency of the tank circuit is given by equation (VI-4).

$$f_r = \frac{1}{2\pi}\sqrt{\frac{1}{L_{equ}C} - \frac{R_L^2}{L_{equ}^2}} \qquad \text{(VI-4)}$$

We use equation (VI-4) to calculate the resonance frequency using the values L_{equ} and R_{equ} without the cylinder (r=0 mm) (Figure VI.19) and the capacitance of 2 nF (capacitor of the tank circuit). We find a frequency of 2.8 MHz. We should measure a lower frequency because the connection between the inductor and the capacitor adds an inductance and reduces thus the resonance frequency. However the measured frequency is higher (f=3.109 MHz). We can thus deduce that the inductance calculated by Ophelie without charge is probably too high. The relative variation of the calculated inductance between the case without charge and with a cylinder of a radius of 15 mm is 3.7%. The relative variation between frequency without plasma and the highest measured frequency is only 0.9%. This corresponds to a variation of the inductance of 1.8%. Thus, even the relative variation of the calculated inductance is higher than the relative variation of the measured inductance.

The purpose of the simulation was to measure qualitatively the variation of the size of the plasma. As the calculated inductance and the measured inductance are very different we can measure only qualitatively variations of the size of the plasma.

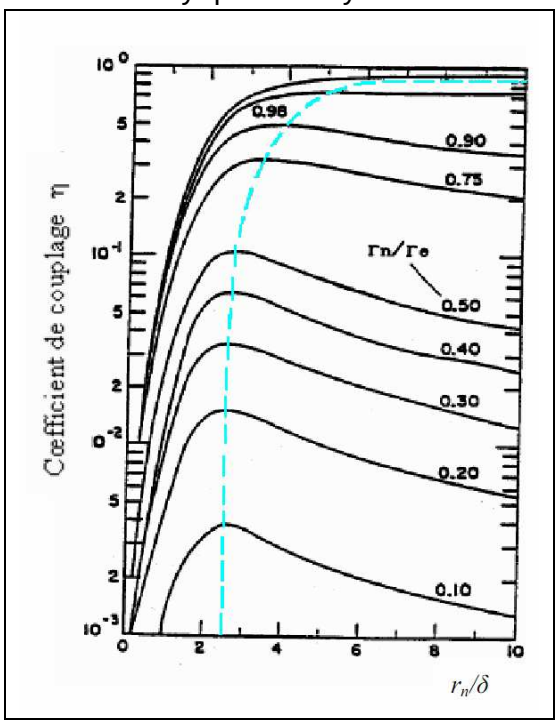

Figure VI.18 Dependence of the coupling coefficient η on the ratio r_n / δ for different radii r_n / r_e [Mek93]

r_n radius of the plasma

r_e radius of the inductor

δ skin depth

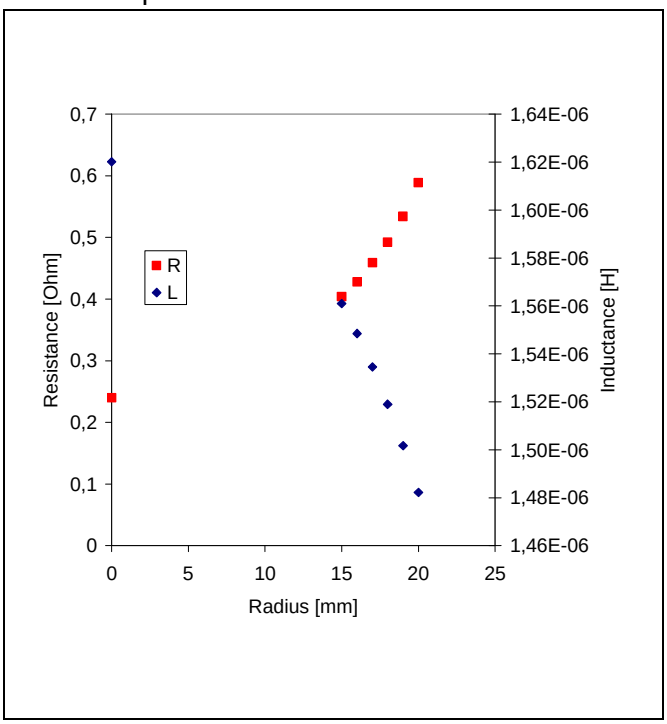

Figure VI.19 The simulated electrical parameters L_{equ} and R_{equ} in dependence of the radius.

The coupling coefficient η, is defined as the ratio between the active power P_0 (W), that is absorbed by the plasma and the reactive power P_e (W) of the magnetic field (VI-5).

$$\eta = \frac{P_0}{P_e} = \frac{R_{equ} I_L^2}{\omega L_{equ} I_L^2} = \frac{R_{equ}}{\omega L_{equ}} \qquad \text{(VI-5)}$$

Without energy absorption $\eta = 0\%$ the whole power of the induced magnetic field in the inductor would flow back to the oscillating circuit. At a coupling coefficient of 100 % no power

would flow back to the oscillating circuit so that an oscillation would be impossible. However the coupling coefficient is typically much lower than $\eta = 100\%$.

For a given setup the equivalent resistance R_{equ} is approximately proportional to the coupling coefficient η, because the inductance and thus the frequency vary only little (see Figure VI.19). Mékidèche [Mek93] calculated the coupling coefficient for cylinders in dependence of their radius and their conductivities. The results are presented in Figure VI.18. The figure shows the coupling coefficient versus plasma radius divided by the skin depth for the cylinders with different radii. The figure shows the following relations:

For a given radius the coupling is optimal when the skin depth δ (m) is between 20% and 40% of the radius of the plasma. The skin depth is given by equation (VI-6). In induction heating the frequency is in generally adapted to the conductivity of the material in order to obtain an optimal skin depth of about one third of the radius.

$$\delta = \left(\pi f \mu \sigma\right)^{-0.5} \tag{VI-6}$$

σ conductivity (S/m)

μ magnetic permeability (H/m)

f frequency (Hz)

For a conductivity of 6000 S/m and a frequency of 3 MHz the skin depth is 3.8 mm

For a radius that is four times larger than the skin depth the power that a cylinder absorbs is approximately proportional to its volume. The coupling coefficient is therefore approximately proportional to the square of the radius (see Figure VI.18, Figure VI.19).

The electrical parameters L_{equ} and R_{equ} play an important role for the adaptation of the impedance. The impedance of the tank circuit, which consists of the capacity and the inductor, needs to be adapted to the impedance of the generator. The generator operates due to the feedback circuit at the resonance frequency. At the resonance frequency the tank circuit can be simplified by the resistive impedance given by equation (VI-7) (see circuit Figure VI.16 c). Only when the impedance of the tank circuit is adapted, the generator can be operated at its maximum current and maximum voltage and thus at its maximum power.

$$Z_{equ} = \frac{L_{equ}}{R_{equ} C} \tag{VI-7}$$

When the impedance of the tank circuit is too big, the voltage attains the maximum voltage before the current.

When the impedance of the tank circuit is too small, the current attains the maximum current before the voltage.

When the impedance of the tank circuit is not adapted, the generator can thus not provide its maximum power. In order to obtain a higher impedance one can reduce the capacitance and vice versa one can increase the capacitance to reduce the impedance. In order to keep the resonance frequency constant it is possible to modify the inductance of the connection between the inductor and the capacitor (equation (VI-4)).

However when adapting the impedance one has to take into account the impedance at ignition. During ignition the plasma is operated with pure argon and one needs a high voltage (For more details, see paper in Appendix C). The generator is typically operated with a voltage that is controlled by a proportional-integral-derivative controller (PID controller). When the current exceeds the maximum current the generator stops. When the plasma is ignited the impedance of the tank circuit decreases abruptly and thus the current increases abruptly. The impedance of the tank circuit must thus be chosen so that the current after ignition remains below the maximum generator current. Otherwise ignition would not be possible because the generator would stop. However during normal operation the injection of

other gases than argon can reduce the coupling coefficient and thus increase the impedance. For the operation of a plasma with an argon-oxygen mix for example a higher capacitance is necessary to obtain the same impedance of the tank circuit as with pure argon. The capacitance should thus be adapted for normal operation and eventually reduced if the current at ignition is too high.

The coupling coefficient is important for the adaptation of the impedance and depends mainly on the volume of the plasma. Therefore, we examine the parameters that determine the volume of the plasma. Armstrong et al. [AR68] studied the energy balance in the induction zone. At an infinite small volume the power balance is equilibrated between the source of the inductive heating and the losses by radiation, diffusion and convection as shown in Figure VI.20. They obtained equation (VI-8) for the local power loss by diffusion and convection. This equation shows that the local power loss depends on the temperature gradient, the thermal conductivity K and the heat capacity ρC_p. The radius of the plasma is thus determined by the equilibration of the power losses and the power sources.

$$dP/dr = \frac{d}{dr}\left(2\pi r l\left[-K\frac{dT}{dr}\right]\right) + \rho C_p v(2\pi r)(T - T_{ambient}) \qquad \text{(VI-8)}$$

Molecular gases have a high heat capacity and a high thermal conductivity at the dissociation temperature (about 3000 K for hydrogen and oxygen) due to the dissociation reaction. The high thermal conductivity is due to diffusion of atoms to the colder zone, where they recombine and release energy and due to the diffusion of molecules to the hotter zone, where they dissociate and absorb energy.

Figure VI.22 shows the dependency of the thermal conductivity of different gas mixtures on the temperature. We can see that at about 3000 K the thermal conductivity of an argon-oxygen mixture is much higher than the conductivity of pure argon. At the same temperature the conductivity of the argon-hydrogen mixture is about five times higher than the conductivity of the argon-oxygen mixture.

Figure VI.21 shows the specific enthalpy of different gases. The specific enthalpy of the molecular gases is much higher than that of the atomic gases, because the enthalpy of the dissociation reaction is high compared to the enthalpy of the translational energy. While the specific enthalpy of hydrogen is about 13 times higher than that of oxygen, the molar enthalpy and thus the volumetric enthalpy are similar for the two gases. The difference in the specific enthalpy is due to the higher molar mass of oxygen. The molar enthalpy of hydrogen and oxygen are similar because the energy of the H-H bond (4.519 eV) is similar to that of the O-O bond (5.161 eV). As the molar enthalpies of oxygen and hydrogen are similar, the molar (and volumetric) heat capacites are also similar.

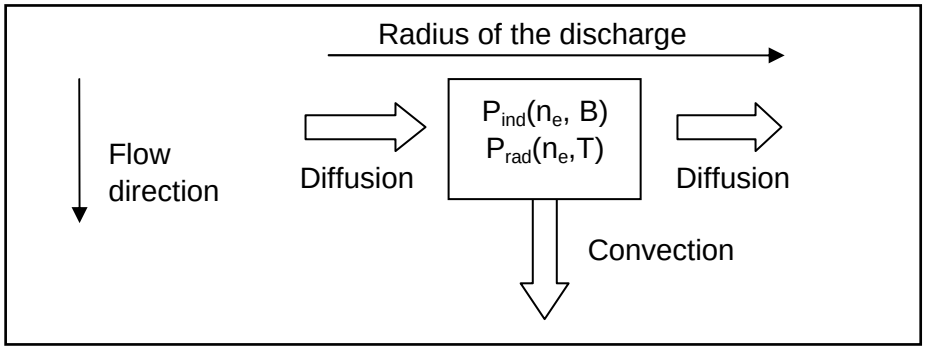

Figure VI.20 Local power balance in the induction zone
$P_{ind}(n_e,B)$ induced power (source)
$P_{rad}(n_e,T)$ radiated power (sink)

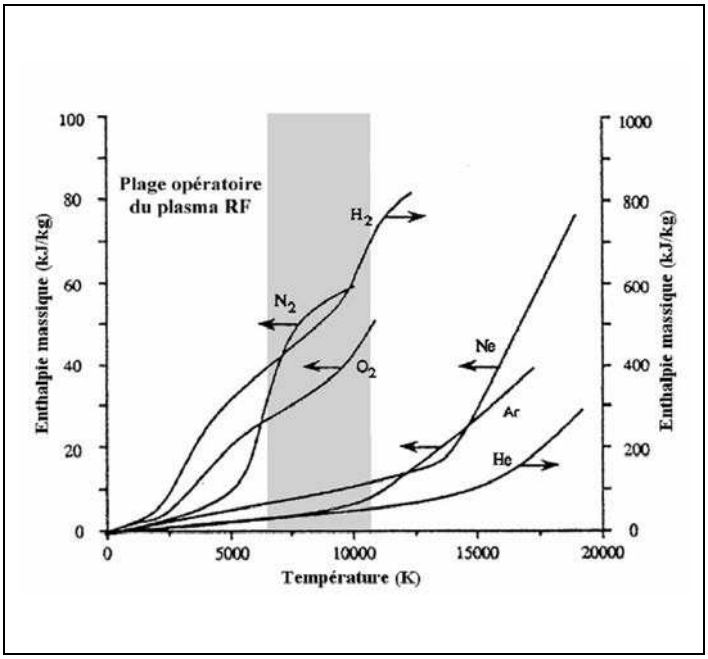

Figure VI.21 Dependence of the specific enthalpy of different gases on the temperature [BFP94]

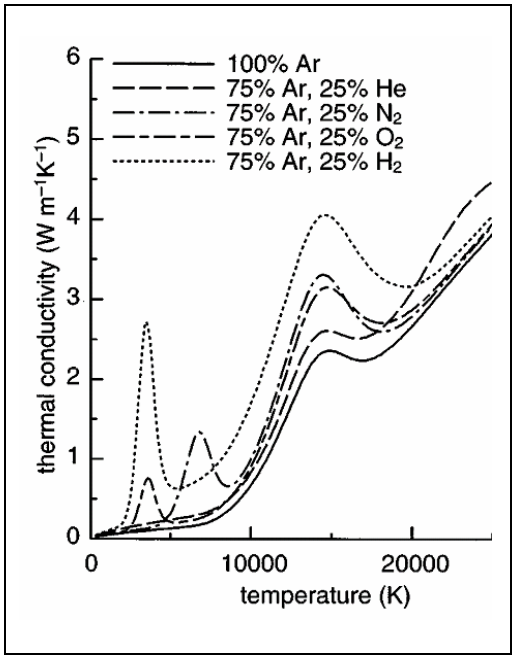

Figure VI.22 Dependence of thermal conductivity on temperature for argon and mixtures of 75% argon and 25% helium, nitrogen, oxygen and hydrogen by mole fraction [Mur96]

On the following pages we present measurements to analyze the dependence of the coupling coefficient on different parameters. We show that, when the inner tube is in a lower position (see Figure VI.23), a hysteresis effect exists with two different coupling efficiencies at exact the same experimental parameters.

We measure the direct current and the frequency of the generator. We assume that the RF current I_{RF} is proportional to the direct current and that the RF voltage U_{RF} is proportional to the plate voltage. The coupling coefficient is thus proportional to the ratio between the DC current and the plate voltage. The frequency indicates qualitatively the change of the volume of the plasma.

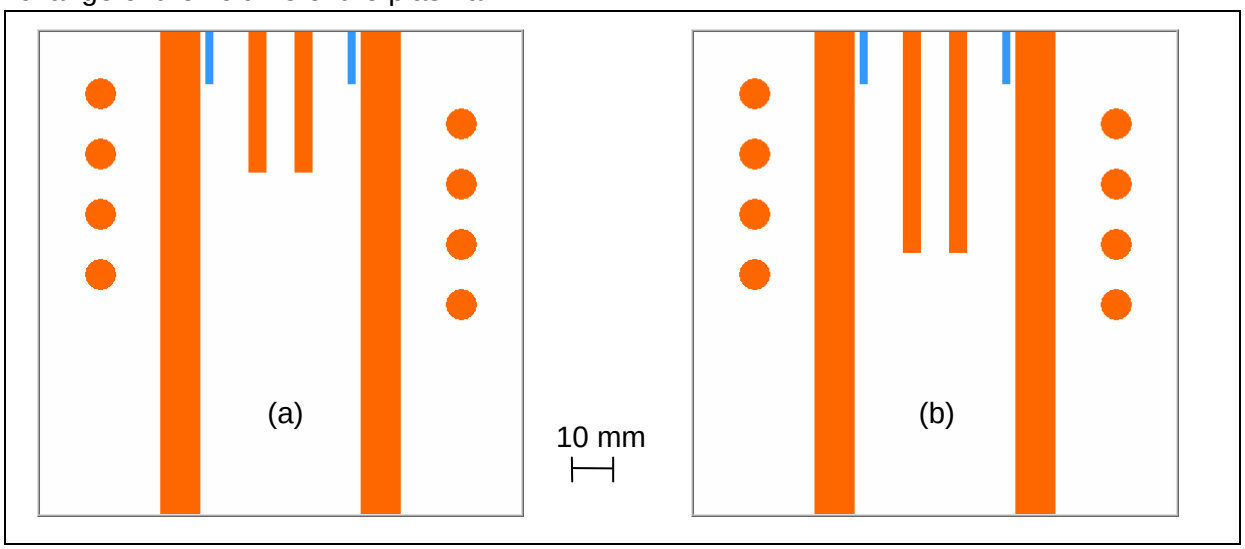

Figure VI.23 Two different geometries that were studied. (a) injector in upper position, (b) injector in lower position. The distance to the outlet were 85 mm and 65 mm respectively

VI.2.2. Dependence of the coupling on the voltage

While the gas flows were maintained constant, the voltage was reduced and then increased again. Figure VI.24 shows the dependence of the current and the frequency on the voltage for the two different geometries that are presented in Figure VI.23. When the injector is in the upper position (a), the current and the frequency increase linearly with the voltage. The increase of the frequency indicates an increase of the plasma volume. The current at 7.0 kV is three times higher than the current at 3.5 kV. This is consistent with the higher coupling coefficient at a bigger volume. If the coupling coefficient would remain constant, the current should be proportional to the voltage and thus increase by a factor two.

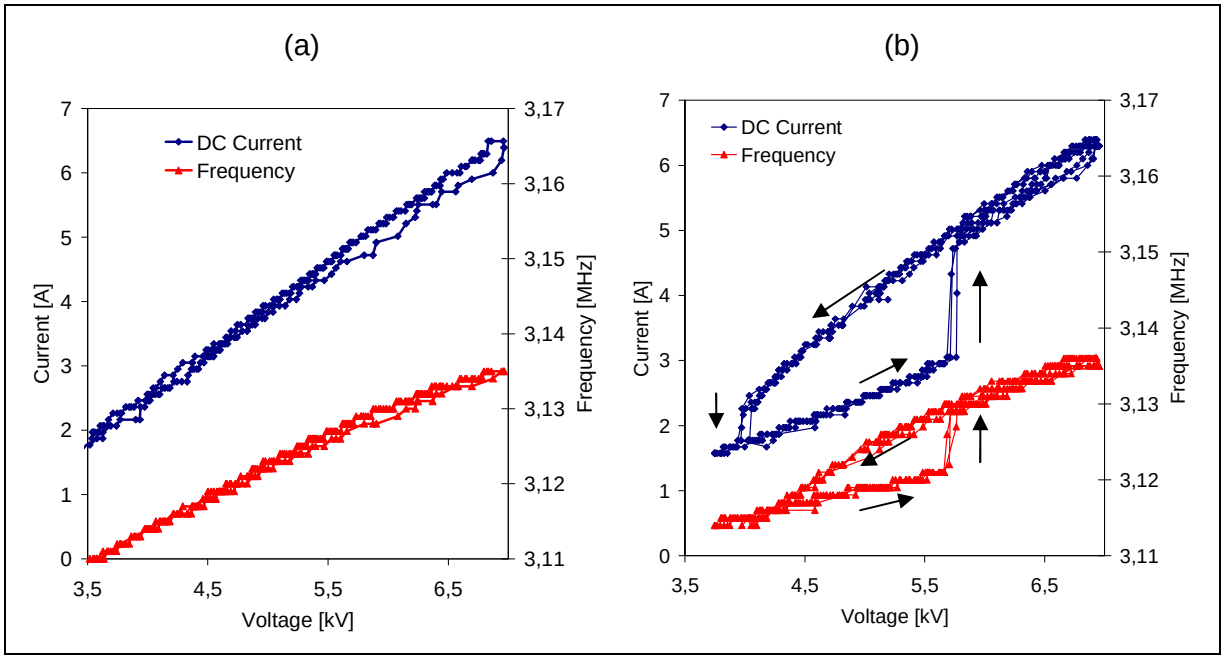

Figure VI.24 Dependence of current and frequency on the voltage,(a) injector in the upper position, (b) injector in the lower position, Ar outer flow 6.0 m^3/h, Ar intermediate flow 0.30 m^3/h

When the injector is in the lower position (b), the current and frequency show a hysteresis behaviour. There are two different coupling modes that we name high coupling mode (for the mode with a higher current) and low coupling mode (for the mode with a lower current). When the voltage is decreased we can observe a current drop at 4.0 kV. When the voltage is increased again the plasma remains in the low coupling mode so that at the same voltage the current is much lower than in the high coupling mode. At 5.8 kV the plasma jumps back to the high coupling mode which can be seen in a sharp rise of the current. The measurement was repeated three times and the two transitions occurred always at 4.0 kV and 5.8 kV. At 4.0 kV the frequency is equal for the two modes while it is lower for the low coupling mode at higher voltages. This shows that the volume of the plasma is smaller in the low coupling mode than in the high coupling mode. This explains partly why the low coupling mode has a lower current. At 4.0 kV the two modes have the same frequency. Here the difference could be due to different conductivities of the plasma that have the same inductance but a different resistance. The frequency and the current of the high coupling mode are identical to the frequency and the current in the setup with the injector in the upper position. This shows that the plasma is in the high coupling mode when the injector is in the upper position and that the coupling coefficient in the high coupling mode is not modified by the position of the injector.

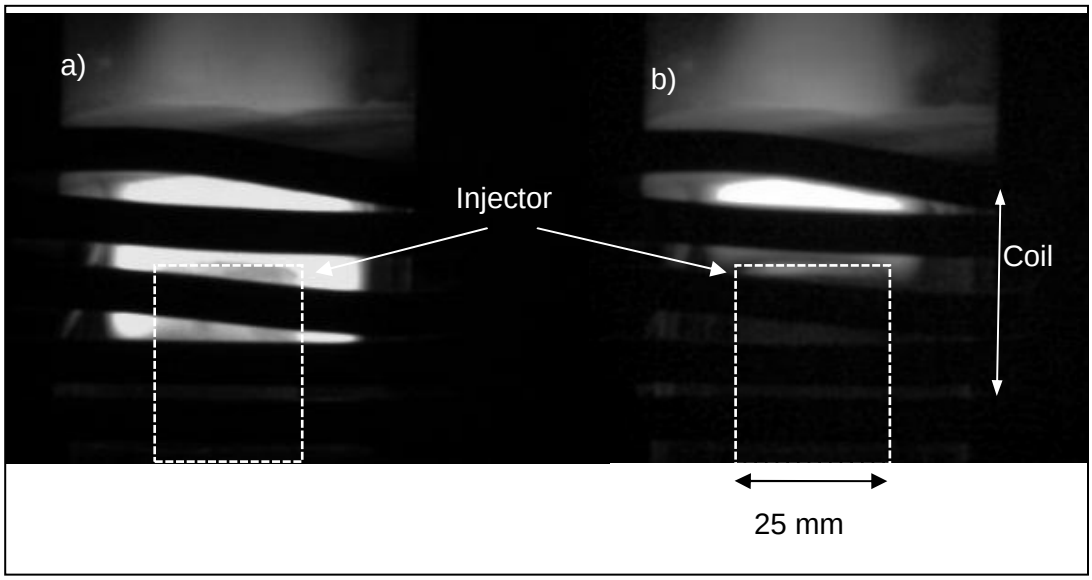

Figure VI.25 The two coupling modes at the same voltage and gas flows in the small torch a) high coupling mode, b) low coupling mode

The same hysteresis behaviour has also been observed in the small torch when a metallic injector with a diameter of 25 mm was placed so that it ends in the middle of the coil. Figure VI.25 shows pictures of the two modes in the small torch for the same experimental parameters. In the low coupling mode b) the plasma is only above the injector (post-injector zone) while in the high coupling mode a) the plasma is also around the injector.

We suggest the following explanation for the hysteresis behaviour. When the plasma is in the high coupling mode, the plasma around the injector is maintained by the RF field. When the RF field is decreased the plasma around the injector becomes thinner and thinner until the thermal losses are bigger than the induced power so that it disappears and only the plasma in the post-injector zone remains. When the RF field is increased again more and more power is induced in this post-injector zone. As the height of the plasma is smaller than in the high coupling mode, less power is induced and the diameter of the plasma is therefore also smaller. The plasma can not propagate around the injector because its diameter is too small. Only when the induced power is high enough, so that the diameter of the plasma is wider than the diameter of the injector, the plasma can propagate around the injector. When the plasma propagates around the injector more power is induced so that the size increases rapidly until it is stabilized in the high coupling mode.

VI.2.3. Dependence of the coupling on the intermediate oxygen and hydrogen flow rate

The same mode transition that was observed when the voltage was changed can also be observed when the intermediate oxygen flow is increased. Figure VI.26 shows the dependence of current and frequency on the intermediate oxygen flow. At the beginning the intermediate oxygen flow is low and the plasma is in the high coupling mode. Then the intermediate oxygen flow is increased and the current and frequency decrease slowly. At a flow rate of 0.08 m^3/h, the current and frequency decrease abruptly because the plasma jumps to the low coupling mode. After the mode transition the current and frequency are nearly constant. When the intermediate oxygen flow is decreased again the plasma remains in the low coupling mode until a flow rate of 0.01 m^3/h where it jumps back to the high coupling mode. Due to a small delay between the measurements of the frequency, the current and the flow rate, the jump of the frequency and the current are not at the same flow rate in the measurement.

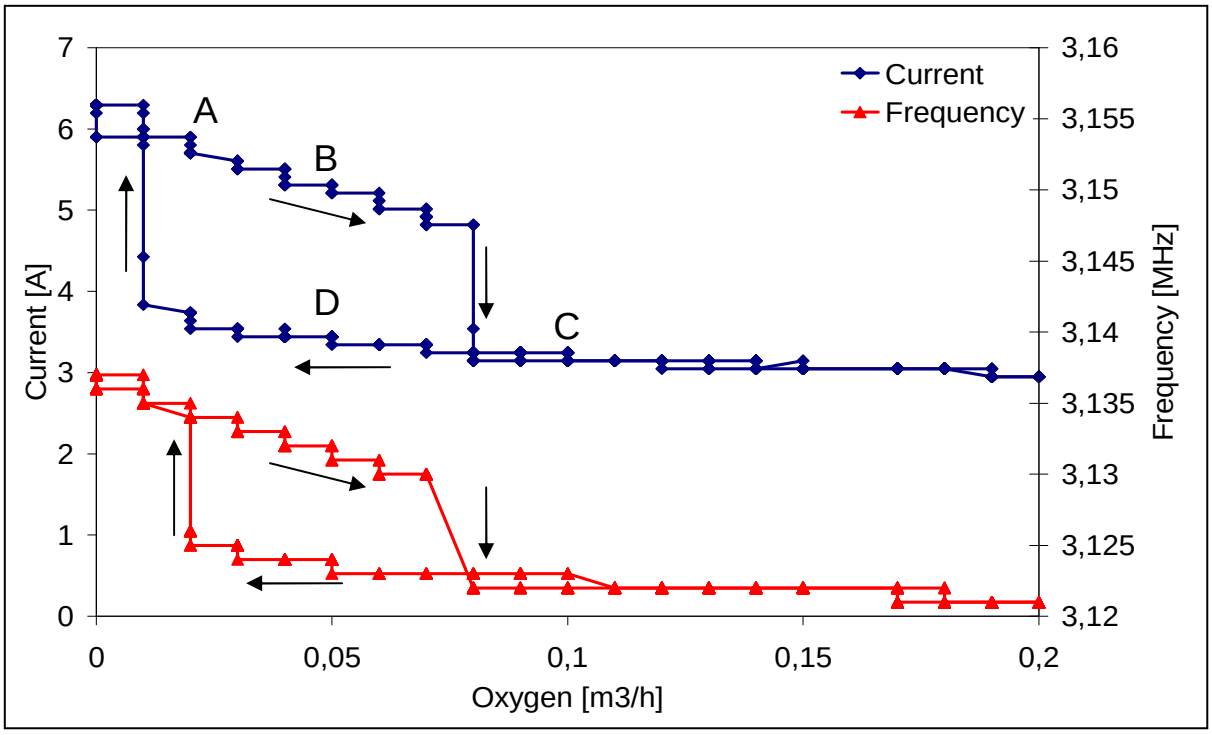

Figure VI.26 Dependence of current and frequency on the intermediate oxygen flow rate (Ar outer flow 6.0 m^3/h, Ar intermediate flow 0.5 m^3/h, DC Voltage 7.0 kV, injector in lower position)

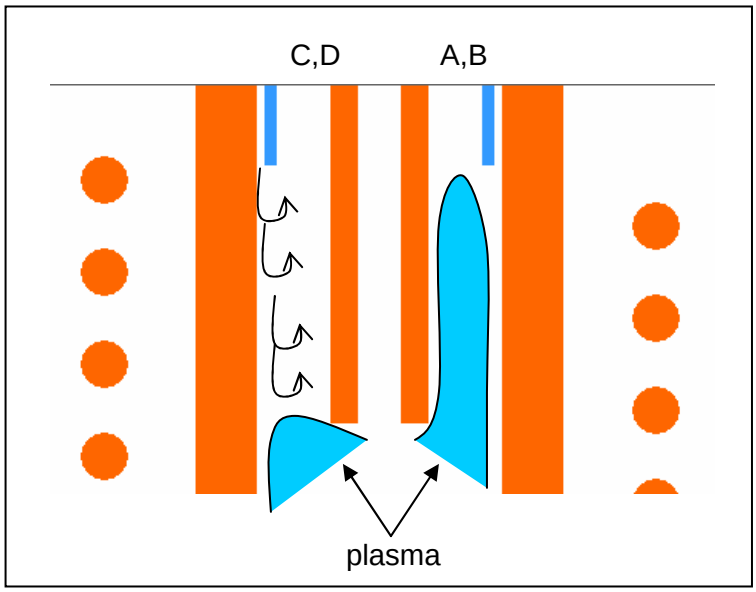

Figure VI.27 Turbulent mixing between outer flow and intermediate flow in the low coupling mode C,D and laminar flow in the high coupling mode A,B

Figure VI.28 shows the measured concentration and temperature profiles of the four points A, B, C and D of the hysteresis of Figure VI.26. The points B and D are measured at the same flow rate and same plate voltage. B is in the high coupling mode and D is in the low coupling mode. The temperature profile shows that the plasma in the low coupling mode D is slightly thinner and shorter than in the high coupling mode B. The concentration ratio profiles O/Ar are very different. While the O/Ar ratio is uniform in the low coupling mode D it is not uniform in the high coupling mode B. Below the outlet of the torch, the measured O/Ar ratio profile is very asymmetric in case B. However the measurement is not reliable because the

Abel inversion gives false results for asymmetric profiles, but it shows clearly that the O/Ar profile is not symmetric. The temperature profiles of A and C are very similar to those of B and D respectively. The concentration ratio profiles O/Ar of A and C are also very similar to those of B and D respectively but with a different mean concentration corresponding to the different oxygen flow rate.

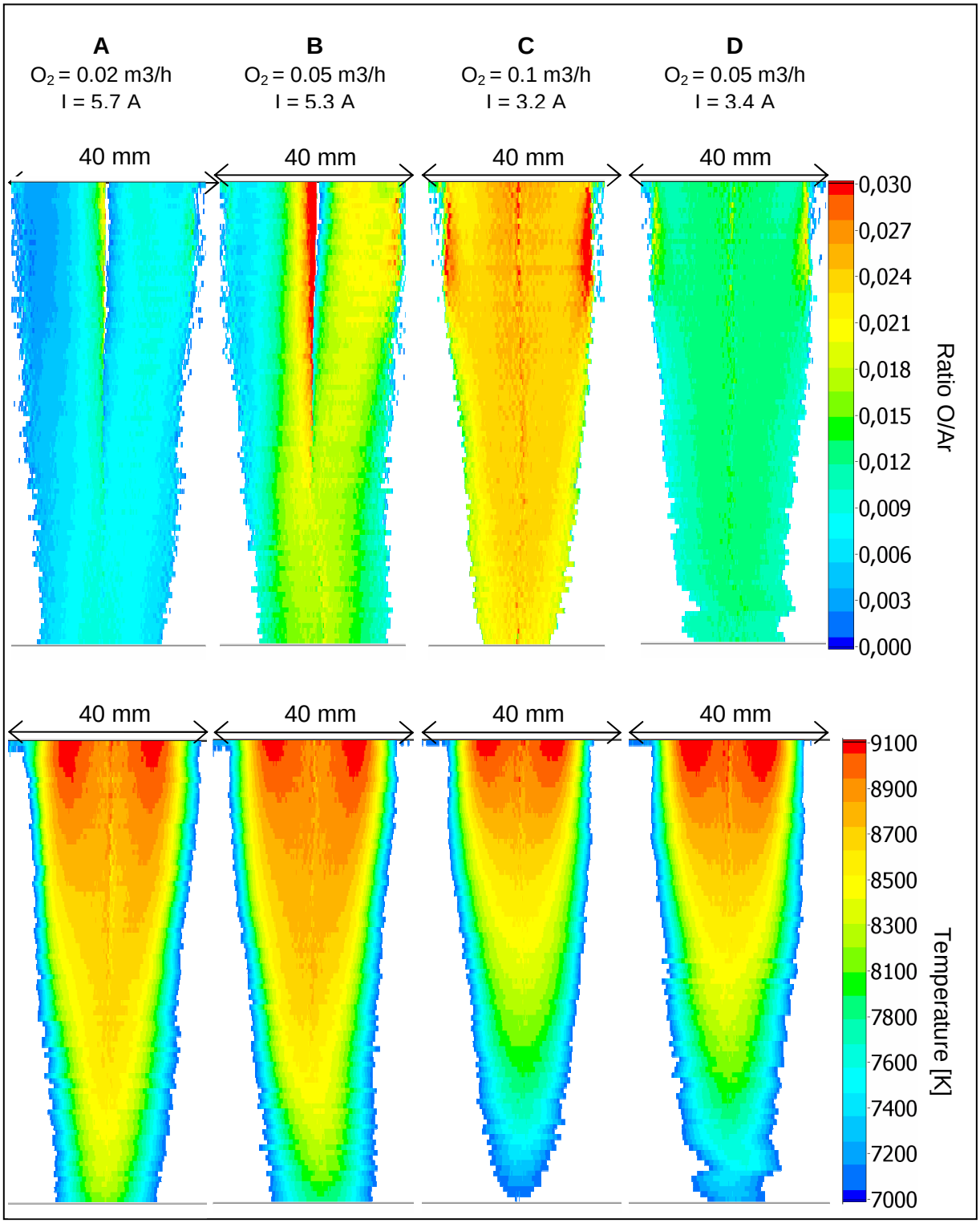

Figure VI.28 Radial atomic oxygen concentration profiles and temperature profiles for the different oxygen flows and different coupling modes of Figure VI.26.

The different O/Ar ratio distribution between the low coupling mode and the high coupling mode indicates that in the low coupling mode a turbulent flow mixes the intermediate flow with the other flow (see Figure VI.27). In the high coupling mode the mixing is less important. This can be explained by the high viscosity of the hot gases that establish a laminar flow with little mixing. At the lower end of the measurement, the O/Ar ratio is therefore higher in the high coupling mode B than in the low coupling mode D. The asymmetry in the high coupling mode can be due to a small asymmetry of the intermediate tube or due to the asymmetry of the magnetic field.

The triggering of the mode transition by the intermediate oxygen flow rate can be explained by the fact that the intermediate flow arrives directly on the plasma that surrounds the injector. The higher thermal conductivity and heat capacity of oxygen compared to argon, modifies the local power balance of Figure VI.20 and pushes thus the plasma towards the end of the injector.

Figure VI.29 shows the mode transition for the variation of the intermediate hydrogen flow. The hydrogen flow rate necessary for the jump to the low coupling mode is 0.02 m^3/h. The jump back to the high coupling mode has not been measured.

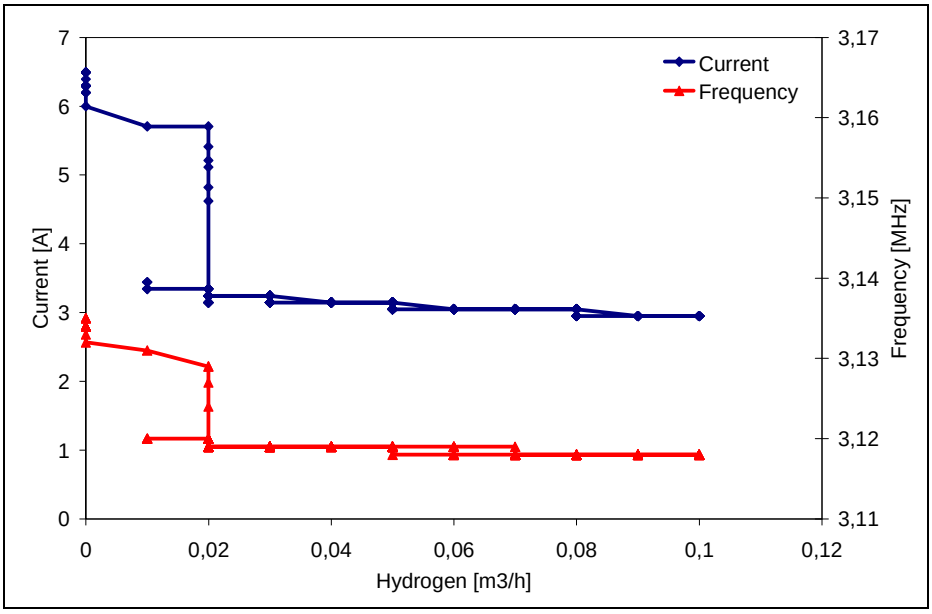

Figure VI.29 Dependence of current and frequency on the intermediate hydrogen flow rate (Ar outer flow 6.0 m^3/h, Ar intermediate flow 0.3 m^3/h, DC Voltage 7.0 kV, injector in lower position)

VI.2.4. Dependence of the coupling on the outer oxygen and hydrogen flow rate

Figure VI.30 shows the dependence of the current and the frequency on the outer oxygen flow rate. When the oxygen flow rate is increased the current and the frequency decrease first rapidly and then more and more slowly. The plasma remains in the high coupling mode. The decrease of the frequency indicates a decrease of the volume of the plasma.

Figure VI.31 shows the dependence of the current and the frequency on the outer hydrogen flow rate. The current and frequency decrease much faster than with the oxygen flow rate. At a hydrogen flow rate of 0.18 m^3/h the current and frequency (5.0 A, 3.126 MHz) are similar to the current and frequency at a oxygen flow rate of 1.1 m^3/h (five times higher concentration). At a hydrogen flow rate of 0.18 m^3/h the plasma jumps to the low coupling

mode. When the hydrogen flow rate is decreased the plasma jumps back to the high coupling mode at a hydrogen flow rate of 0.05 m^3/h.

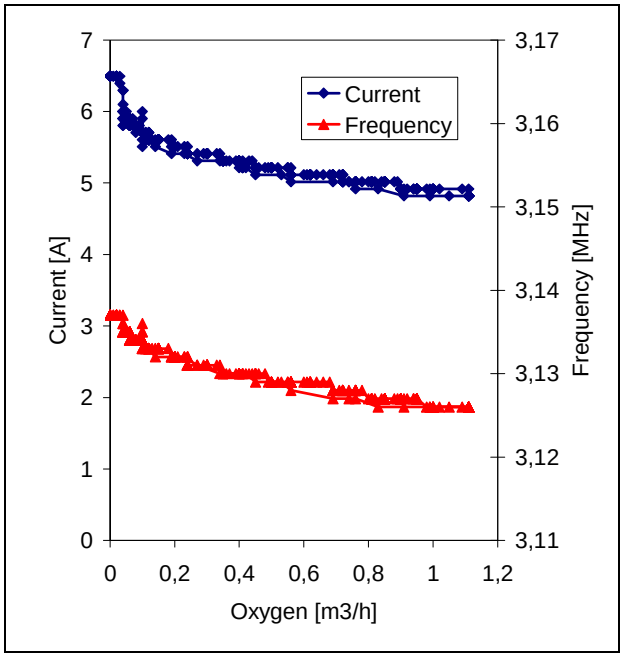

Figure VI.30 Dependence of current and frequency on the outer oxygen flow rate (Ar outer flow 6.0 m^3/h, Ar intermediate flow 0.3 m^3/h, DC Voltage 7.0 kV, injector in lower position)

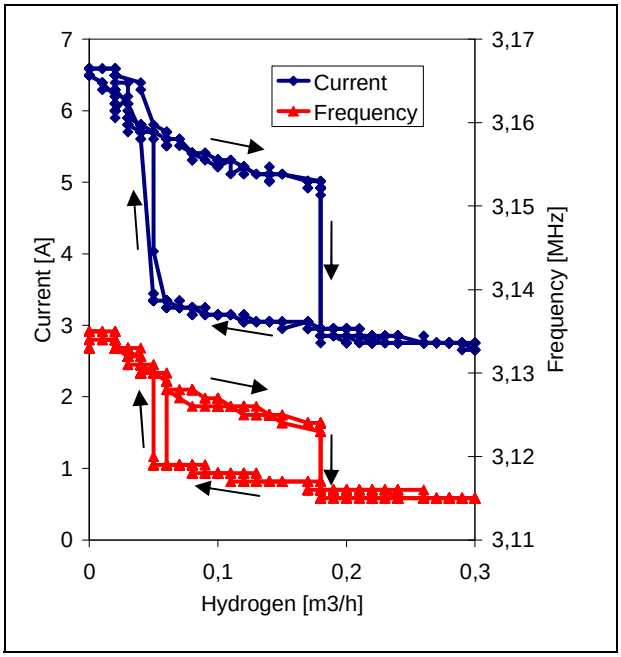

Figure VI.31 Dependence of current and frequency on the outer hydrogen flow rate (Ar outer flow 6.0 m^3/h, Ar intermediate flow 0.3 m^3/h, DC Voltage 7.0 kV, injector in lower position)

VI.2.5. Dependence of the coupling on the inner hydrogen flow rate

Figure VI.32 shows the dependence of the frequency and the current on the inner hydrogen flow. The current and the frequency are approximately constant.

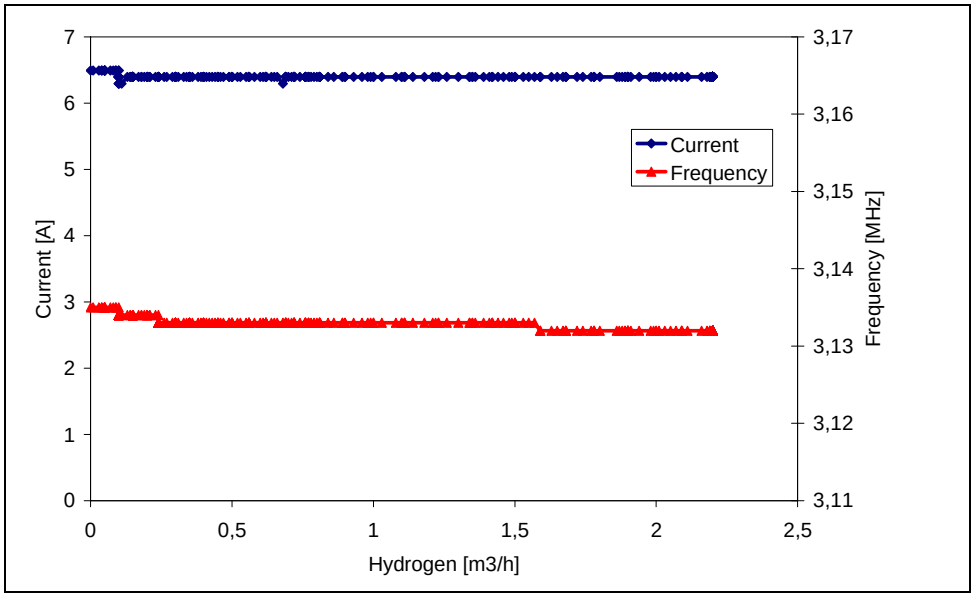

Figure VI.32 Dependence of current and frequency on the inner hydrogen flow rate (Ar outer flow 6.0 m^3/h, Ar intermediate flow 0.3 m^3/h, DC Voltage 7.0 kV, injector in lower position)

VI.2.6. Discussion of the influence of hydrogen and oxygen on the coupling

Even though the measurement of the frequency does not give quantitative information about the size of the plasma it still indicates that mainly the change of the size modifies the coupling coefficient.

The gases hydrogen and oxygen modify strongly the size of the plasma when they are mixed to the argon flow of the outer flow or intermediate flow. The biggest influence can be observed in the intermediate flow. This can be explained by the high thermal conductivity and the high heat capacity of the molecular gases. When they are injected into the intermediate flow or the outer flow, they modify the local energy balance (Figure VI.20). They reduce thus the volume of the plasma and reduce the coupling coefficient.

The influence of the hydrogen and oxygen in the injector flow is negligible. This shows that the gases injected in the injector do not modify the composition in the zone where the magnetic field induces the power. The increased hydrogen or oxygen concentration in the post-discharge zone does not modify the coupling. The injector flow allows thus to operate a plasma with high hydrogen concentration without problems with the coupling.

In the outer flow as well as in the intermediate flow hydrogen has a similar effect on the coupling as oxygen at an about five times lower flow rate (See Table VI-3). When hydrogen is injected in the intermediate flow the mode transition between high coupling mode and low coupling mode occurs at a five times lower flow rate than when oxygen is injected in the intermediate flow. The current and frequency at 0.18 m^3/h hydrogen in the outer flow is similar to those at 1.1 m^3/h oxygen in the outer flow.

This indicates that mainly the thermal conductivity of the gas mixtures modifies the coupling and thus the local power balance in the coupling zone. The conductivity of pure hydrogen at 3000 K is eight times higher than that of oxygen (See Table VI-3). The conductivity at this temperature is mainly due to the dissociation and recombination of molecules and atoms. The factor eight shows only qualitatively the different conductivities of the two gases. For the modification of the coupling the conductivity from 300 K up to the temperature of the plasma are probably important.

If the modified heat capacity of the gas mixture was the main reason for the modification of the coupling, hydrogen and oxygen would have the same impact, because their molar heat capacities are similar, and thus the same molar (or volume) flow rate should have the same effect.

	Oxygen	Hydrogen	Ratio
O_2/H_2 in intermediate flow: Mode transition	0.11 m^3/h	0.02 m^3/h	5.5
O_2/H_2 in outer flow: Current = 5.0 A	1.1 m^3/h	0.18 m^3/h	6.1
Conductivity at 3000 K [ttw]	0.87 W/m/K	6.78 W/m/K	8

Table VI-3 Comparison of the flow rate of oxygen and hydrogen that have the same impact on the coupling coefficient

VI.2.7. Conclusion on the coupling

In this chapter we have seen that it is important to maintain the coupling coefficient high so that the impedance of the tank circuit remains adapted to the generator. Otherwise the generator can not provide its full power. We showed that the coupling coefficient depends mainly on the size of the plasma which depends in turn on the thermal conductivity of the gases. Gases with a high thermal conductivity like hydrogen should thus be injected in the injector, where they do not modify the coupling. In the outer flow they would reduce the coupling coefficient and thus increase the impedance. In the intermediate flow pure argon should be injected because oxygen and hydrogen would strongly reduce the coupling

coefficient. The injection of oxygen in the outer flow modifies the coupling but the variation remains small enough so that it should allow an operation at the maximum power of the generator. In the measurements we observed a low coupling mode. In the low coupling mode the impedance of the tank circuit is very high so that the generator can provide only a fraction of the maximum power. One should take care not to operate the plasma torch in conditions where such a mode transition can occur because the mode jump would strongly modify the plasma.

VII. Measurements of the purification rate

VII.1. Introduction

In chapter II we examined the literature, and found that surface reactions seems to be at chemical equilibrium and to control the ratio between boron and silicon extraction, their (common) rate being controlled by some diffusion process in the gas. Considering that the enrichment factor of the gas was always higher than the ones calculated at chemical equilibrium, we suggested that the formation of a silicon aerosol may play a role.

In this chapter we confront this theory to the experiments that we did. In order to quantify the reaction products and the purification rate, we measured the relative concentration of boron and silicon in the exhaust gases. The boron concentration in the exhaust gases is proportional to the purification rate and to the boron concentration in the silicon. A long term purification (6h) was performed to validate the ICP signal by silicon samples that ware taken during the experiment. A second long term purification with doped electronic grade silicon evaluated the interaction between boron and other impurities in the silicon. We then performed several parametric measurements to evaluate the influence of different parameters on the purification rate. We measured the influence of the dissolved species by starting and stopping the oxygen and hydrogen flow. We examined under which conditions a silica layer gets formed with a cold gas jet with an argon-oxygen mix.

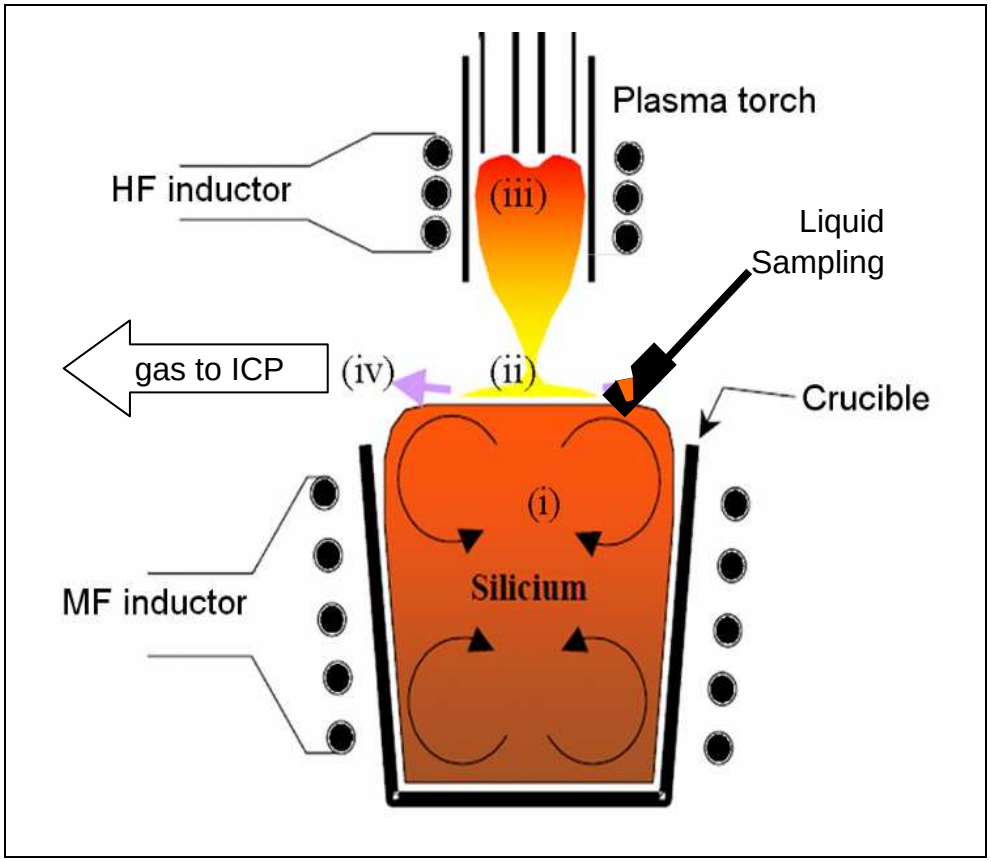

Figure VII-1 Schema of the purification process
Exhaust gas analysis by ICP and liquid sampling for concentration measurements of the silicon

VII.2. The setup for purification experiments

In Figure VII-1 a schematic diagram of the setup in our laboratory is shown. The boron is transported to the surface (i) by electromagnetic stirring. At the surface it reacts with the reactive species (ii) which are supplied by the gas flow that is heated by an inductively coupled plasma torch (iii). The volatile reaction products are then evacuated by the gas flow (iv).

VII.3. The crucible

For our experiments we used different setups for the crucible. Their properties are shown in Table VII-1. All setups consist of an inductor with five loops around the crucible that heats the silicon on the one hand and stirs it on the other hand. The electromagnetic field pushes the silicon to the center of crucible where it flows upwards or downwards. The induced current heats the silicon by Joule heating. The frequency of the electromagnetic field was chosen so that the skin depth of the electromagnetic field in the silicon melt is about one quarter of the radius of the crucible, which is optimal for the stirring. Delannoy et al. [DAL02] studied the stirring in the setup that we used and showed that the stirring is efficient so that the boron concentration at the surface is very close to the boron concentration of the bulk.

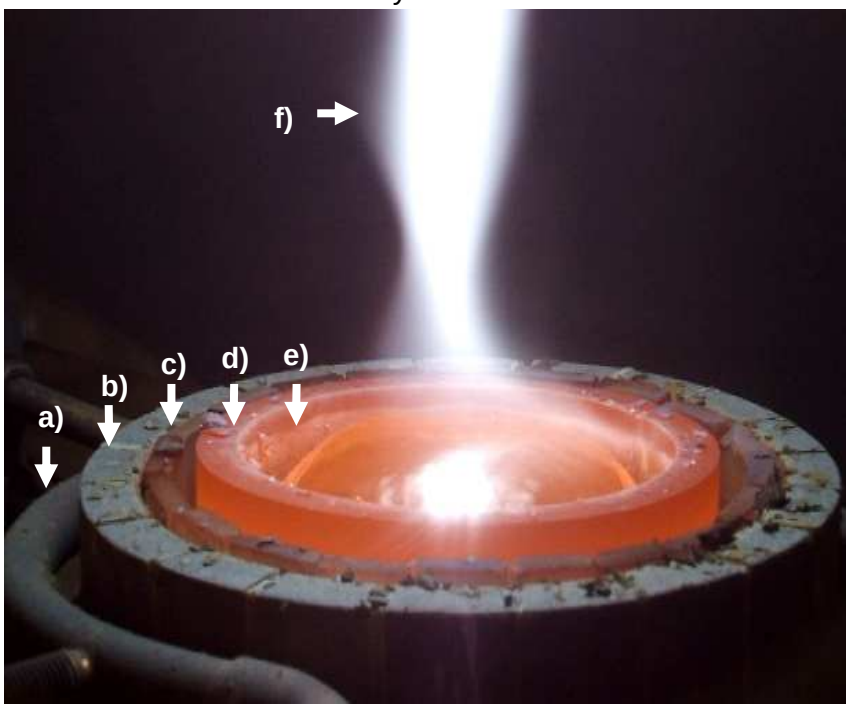

Figure VII-2 Image of the plasma purification process with crucible 3 a) inductor, b) segmented cold crucible, c) silica plates for thermal insulation, d) graphite crucible, e) silicon, f) plasma

	Crucible 1	Crucible 2	Crucible 3
Inner diameter	12 cm	17 cm	9 cm
Height	12 cm	15 cm	11 cm
Area	113 cm^2	227 cm^2	64 cm^2
Silicon mass	~3 kg	~8 kg	~2 kg
Frequency	~9 kHz	~7 kHz	~9 kHz
Material	Cold crucible (copper)	1.5 cm silica plates in cold crucible	Graphite crucible in cold crucible with silica plates around
Silicon Temperature	1410 ℃	Variable	Variable
	Plasma necessary for melting	Plasma necessary for melting	Melting without plasma possible
Pollution of the silicon	No	Yes	Yes

Table VII-1 Properties of the different crucibles used in the purification experiments

The outer container is a so called cold crucible. It consists of water cooled copper segments. As the crucible remains cold it does not pollute the silicon but evacuates a lot of heat. The cold crucible technology is typically used for the fusion of metals with high purity. The crucible is segmented so that it does not screen the electromagnetic field that is necessary for the heating and the stirring of the silicon.

Crucible 1 (cold crucible): When the crucible is used without thermal insulation inside, the silicon is maintained at its melting temperature. A thin solid silicon layer insulates the hot silicon melt from the cold crucible. The thickness of this solid silicon layer varies with the power induced in the silicon and maintains thus the silicon at its melting temperature.

Crucible 2: In this setup we added a 1.5 cm thick thermal insulation consisting of silica plates so that the temperature could be increased above the melting temperature of the silicon. However the silica plates may pollute the silicon and they dissolve oxygen in the silicon.

Crucible 3: In this setup (Figure VII-2) we added a graphite crucible into the cold crucible. The graphite crucible has the advantage that the silicon can be melted without the plasma. The graphite crucible may also pollute the silicon.

VII.3.1. Melting

For the melting of the silicon in the crucible 1 and 2 the plasma is necessary. The magnetic field can not couple to the solid silicon because it has a low conductivity and the grains are small. Magnetic fields couple efficiently when the skin depth is about a third of the radius of the object that is heated. In solid silicon the skin depths is large due to the low conductivity. In order to melt the silicon in the crucible the plasma blows the hot gases onto it. The hot gases melt some grains that form a small melt. This melt has a higher conductivity (and thus a smaller skin depth) and a bigger diameter than the grains. The magnetic field can thus couple to it and thus melt the remaining silicon grains. The graphite crucible has the advantage that the magnetic field can couple to the crucible and melt the silicon in it without plasma. An inconvenient of the graphite crucible is that it screens the magnetic field and reduces thus the stirring. However in the photo of Figure VII-1 we can see that the silicon surface has the shape of a dome. This comes from the magnetic pressure due to the strong

electromagnetic forces in the silicon. As the induction frequency is adapted for an optimal skin depth the high magnetic pressure indicates a strong stirring [DAL02].

During the melting we measure the frequency of the induction current of the crucible in order to follow the melting. The liquid silicon has a much higher conductivity than the solid silicon. The liquid silicon screens the electromagnetic field and reduces thus the inductance of the inductor. The inductor is connected in parallel with a capacitor to the power supply and forms thus an oscillating LC-circuit. The power supply adapts its frequency to the resonance frequency of this LC-circuit. A reduction of the inductance L leads to an increases of the resonance frequency of the LC-circuit (VII-1). As long as the frequency increases the silicon melts. When the increase of the frequency stops all silicon in the crucible has melted.

$$f = \frac{1}{2\pi\sqrt{LC}} \qquad \text{(VII-1)}$$

VII.3.2. Solidification

The measurement of the frequency is very important for the solidification. When the melt solidifies too fast, some liquid silicon can be trapped in the solid silicon. As the silicon expands when it solidifies (similar to water) this can break the crucible. In order to avoid the trapping of liquid silicon we heat the top of the melt with plasma. We regulate then the power of the crucible so that the melt solidifies slowly from the bottom to the top. We use the measurement of the frequency to measure qualitatively the velocity of solidification. On the contrary to the melting the frequency decreases during solidification. Figure VII-3 shows the crucible power and the frequency vs time during the solidification. The power was adapted so that the frequency has a constant slope. After the solidification the frequency was generally 500 Hz lower than before (for crucible 1 and 2). We regulate the power of the crucible so that the frequency has a constant slope of 500 Hz/h so that the solidification takes about one hour. When the directional solidification takes one hour, liquid silicon can not be trapped inside the solid silicon.

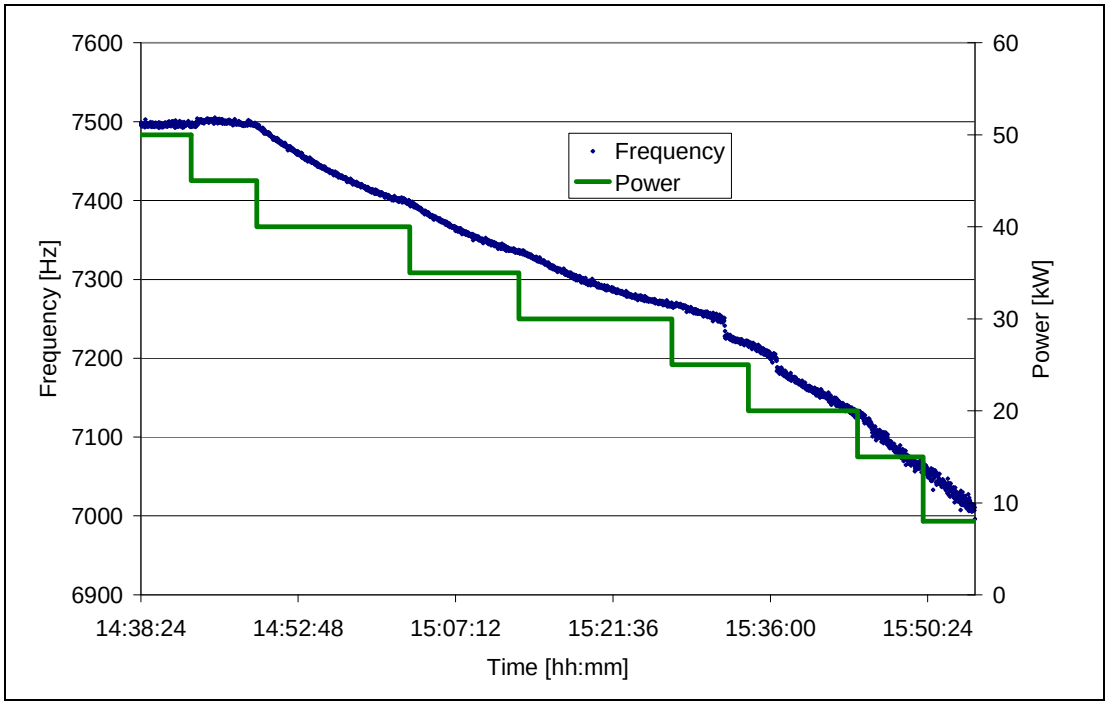

Figure VII-3 The power of the crucible and the frequency during solidification

VII.4. The analyzing of the exhaust gases

In the plasma gas blowing purification process the boron is volatilized and then evacuated by the gases. By measuring the concentration of boron in the exhaust gases we can thus analyze the purification efficiency. The boron concentration in the exhaust gas is proportional to the total boron flow that is extracted from the silicon when the gas flows remain constant. By comparing the boron concentration for different operation parameters one can thus compare directly their efficiency, assuming that the boron concentration of the melt remains constant. When the plasma is operated for a long time with the same parameters the boron flow and thus the boron concentration in the exhaust gases decrease proportionally to the boron concentration in the silicon melt. Such a measurement can be used to measure the half-life of the boron concentration in the melt.

The chemical analysis of solutions by ICP is a standard method which can measure quantitatively concentrations of most elements. The unknown solution is injected through a nebulizer into the plasma and the intensity of the atomic lines emitted by the plasma is measured with a spectrometer. Then a standard solution with known concentration is injected. From the known concentration and the ratio between the intensities one can obtain the concentration of the measured element in the unknown solution. We use the same ICP for the concentration measurement of the exhaust gases.

The analysis of gases by ICP is a method that is often applied in literature [TD95], [SM97], [CPR03]. In general it is applied to analyze the flue gases of combustion processes such as waste incineration or thermal power plants. For absolute concentration measurements the method needs a calibration. However in our study we measure only relative variations.

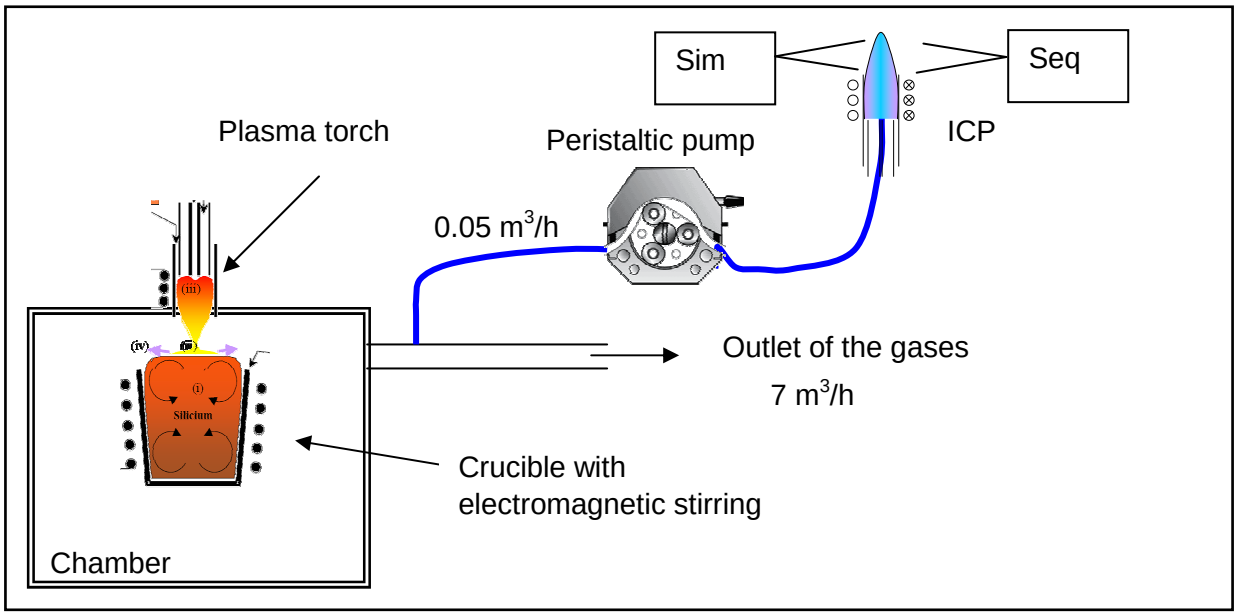

Figure VII-4 The analysis of the gases

In our setup we inject the gases from the outlet of the reaction chamber with a peristaltic pump into the injector flow of the ICP (see Figure VII-4). As the temperature and the gas flow in the ICP are constant the intensity of the lines (equation (VII-2)) depends only on the concentration $[X]$ of the injected elements. (see chapter III)

$$\varepsilon_{line} = \frac{[X] \times g_u \times e^{-E_u / k_B T}}{Z(T)} \times A_{ul} \frac{hc}{4\pi\lambda} = const \times [X] \qquad \text{(VII-2)}$$

We measure the intensity of a boron line and the intensity of a silicon line and can thus measure the relative variations of the quantities of boron and silicon that are volatilized. For the measurement of the line intensity it is necessary to first measure the intensity at the maximum of the line and then measure the continuum, which needs to be subtracted from the intensity at the maximum.

The ICP (Spectro analytical instrument) was equipped with two spectrometers that we name Sim (Simultaneous) and Seq (Sequential):

VII.4.1. The spectrometer Sim

The spectrometer Sim can measure several atomic lines simultaneously. It has several photomultipliers that are arranged so that each photomultiplier measures one line. For the wavelength calibration of this spectrometer one of the elements that can be detected by the photomultipliers needs to be injected into the plasma. We used the fume of the silicon to calibrate the spectrometer. During the automatic calibration procedure the spectrometer moves the entry slit to measure a line profile. An algorithm searches the maximum of the line profile and thus moves the entry slit to this position. When a measurement procedure is developed one has to measure a line profile. Then the position of the maximum of the peak and the position for the measurement of the continuum need to be defined. It is not sure whether the different photomultipliers have the same response so that the ratio between the signals of two different lines is proportional but not equal to the ratio of their intensities.

VII.4.2. The spectrometer Seq

The spectrometer Seq can measure the intensity at every wavelength in the bandwidth from 160 nm to 466 nm. It has several photomultipliers and several entry slits with optical fibers. The photomultipliers and entry slits are arranged so that each combination fiber-photomultiplier covers a different part of the total bandwidth. The photomultipliers are moved by a step motor so that the intensity at every wavelength in the total bandwidth can be measured. A more detailed description of the instrument can be found in [Pel06]. The wavelength of this spectrometer is calibrated on an argon line so that no extra elements need to be injected into the plasma. Similar to the spectrometer above, a line profile needs to be measured and the position of the maximum of the peak and the position for the measurement of the continuum must be defined. The ratio between the signals of two lines with similar wavelengths is equal to the ratio of their intensities. It is thus possible to measure the concentration ratio [B]/[Si] in the gas.

Element	λ	E_u	g_u	A_{ul}	Z (5000 K)	Z (8000 K)
B	249.772 nm	4.964 eV	2	1.68e8 s^{-1}	6.01	6.04
Si	251.611 nm	4.954 eV	5	1.68e8 s^{-1}	9.95	10.34

Table VII-2 The data of the boron line and silicon line used for the measurement of the exhaust gases [nis]

With equation (VII-2) and the data from Table VII-2 we can calculate the dependence of intensity ratio B/Si of the two atomic lines in dependence of the concentration ratio [B]/[Si]. We assume that the temperature of the ICP is between 5000 K and 8000 K [CCM01]. We find that the concentration ratio [B]/[Si] is then between 1.46 (5000 K) and 1.61 (8000 K) higher than the intensity ratio B/Si of the measured atomic lines. By multiplying the intensity ratio by a factor 1.53±0.08 we can thus calculate the concentration ratio.

VII.4.3. The method used, B(Sim) - Si(Seq)

For the parametric measurements we wanted to measure the relative dependence on the different parameters. For this it was more important to measure fast with little noise than to measure the absolute concentration ratio. For this reason we chose not to use the spectrometer Seq for the two lines. The applied method does therefore not allow to measure the enrichment factor.

In order to measure the boron line without noise, a high signal and a long acquisition time is needed. As the photomultipliers of the spectrometer Sim were not well adjusted we chose not to measure the two lines with this spectrometer, but only one of the two lines. We measured the boron line at 249.772 nm with the spectrometer Sim because this spectrometer has higher response than the spectrometer Seq. We measured simultaneously the silicon line at 251.611 nm with the spectrometer Seq.

We assume that the quantities of boron and silicon that arrive in the ICP are proportional to the quantities that are volatilized. When we change a parameter we can thus see directly if the purification efficiency gets better or worse. In order to compare different parameters we have to wait until the signal is stabilized.

During the measurements deposits are formed in the tube that brings the exhaust gas to the ICP. These deposits absorb the reaction products that we measure and thus the signal decreases. Once the signal is stabilized we use a high argon flow as a purge gas to remove these deposits in the tube. During this time the ICP measurement is incorrect and after cleaning the ICP signals are a somewhat higher. We use the ICP signals after the cleaning for the comparison of different parameters.

VII.5. Measurement of the enrichment factor

We use the signal ratio B/Si = $1.6 \cdot 10^{-3}$ (both lines measured by the Seq spectrometer) at the beginning of the experiment XXL33 done by Fourmond [Fou03] with the same experimental setup (see Figure VII-5). The parameters and results of this experiment are presented in Table VII-3. We calculate the concentration ratio [B]/[Si] with equation (VII-3).

$$\frac{[B(g)]}{[Si(g)]} = 1.53 \times \frac{\varepsilon_B}{\varepsilon_{Si}} = 1.53 \times 1.60 \times 10^{-3} = 2.45 \pm 0.13 \times 10^{-3} \qquad \text{(VII-3)}$$

The atomic concentration ratio in the silicon is $18 \cdot 10^{-6}$ (18 ppma). The concentration ratio in the gas [B]/[Si] is thus 136 times higher than in the liquid. As introduced in chapter II, we call this factor the enrichment factor R (VII-4).

$$R = \frac{[B(g)]}{[Si(g)]}\left(\frac{[B(l)]}{[Si(l)]}\right)^{-1} = \frac{2.45 \times 10^{3}}{18 \times 10^{-6}} = 136 \pm 7 \qquad \text{(VII-4)}$$

Argon flow	80 l/min
Oxygen flow	0.43 l/min 0.5%
Hydrogen flow	4.1 l/min 5%
Estimated silicon flux	0.73 mol/h
Plasma power	34 kW
Crucible power	82 kW
Silicon temperature	1410 ℃
Silicon mass	9.3 kg
Boron	18 ppma
$T_{0.5}$	150 min
$T_{0.5}$/m	16 min/kg
Crucible diameter	200 mm
Crucible	Cold crucible

Table VII-3 Parameters of the purification XXL33 of [Fou03]

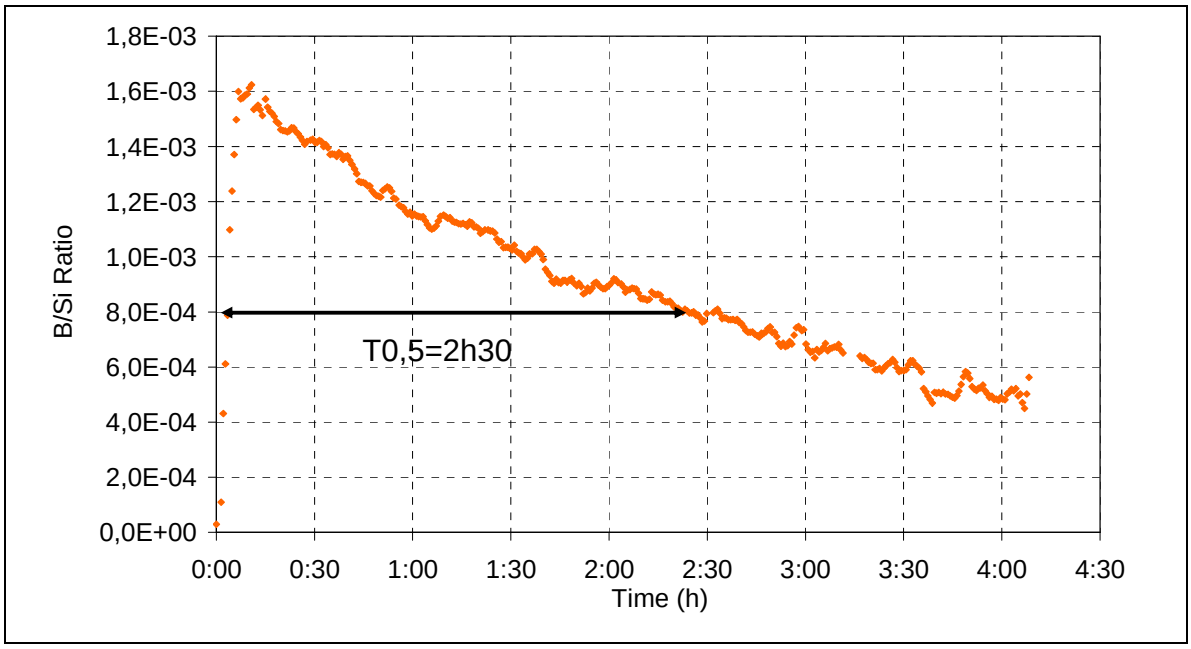

Figure VII-5 Results of the purification experiment XXL33 of [Fou03]

We can also estimate the enrichment factor with the half-life time $T_{0.5}$ using the assumption that the flux of silicon is half of the oxygen flux ($J_{Si} = J_{SiO_2} = 0.5 J_O = J_{O_2}$ (mol/m^2/s)). The derivatitive with respect to time of the boron concentration in the liquid silicon is proportional to the boron concentration (equation (VII-5), first order law). Due to mass conservation the derivative of the boron concentration is equal to the molar boron flow rate out of the silicon divided by the volume of the melt (equation (VII-5)). The molar flow rate of boron is proportional to the molar flow rate of silicon and the concentration ratio in the liquid (VII-6). The proportionality factor is the enrichment factor R multiplied with the [B(l)]/[Si(l)] ratio in the liquid silicon. We replace the product of the concentration and the volume by the mass divided by the molar mass, the silicon flux by the oxygen flux and the decay rate by the half-life and obtain thus equation (VII-7). We rearrange equation (VII-7) so that we find the expression for the enrichment factor (VII-8). We use the assumption that about 70% of the injected oxygen react with the silicon to calculate the effective oxygen flux $J_{O_2} A$. This oxidation efficiency comes from the simulation of a similar plasma gas flow [Let11] and

depends on the process design. Therefore, the molar oxidation rate of silicon is $J_{Si}A = 0.73 mol/h$. For the calculation of R we use the values of Table VII-3.

$$\frac{d[B(l)]}{dt} = K[B(l)] = J_B A \times V^{-1} \quad \text{(VII-5)}$$

$$K[B(l)] = R \times J_{Si} A \frac{[B(l)]}{[Si(l)]} V^{-1} \quad \text{(VII-6)}$$

$$\frac{\ln 2}{T_{0.5}} = R \times J_{O_2} A \frac{M_{Si}}{m} \quad \text{(VII-7)}$$

$$R = \frac{m \cdot \ln 2}{T_{0.5} \times M_{Si} \times J_{Si} A} = \frac{9.3 kg \cdot \ln 2}{150 \min \times 0.028 kg/mol \times 0.73 mol/h} = 126 \quad \text{(VII-8)}$$

$[B(l)],[Si(l)]$	Concentration of the Boron and Silicon in the liquid (mol/m^3)
K	Decay factor (s^{-1})
J_B	Boron flux (mol/m^2/s^1)
A	Surface area of the silicon (m^2)
$J_{O_2}A$	Effective molar flux of oxygen (mol/s)
V	Volume of the silicon load (m^3)
$T_{0.5}$	Half-life time of the boron concentration (min)
M_{Si}	Molar mass of silicon (kg/mol^1)
m	Mass of the silicon load (kg)
$R = \frac{[B(g)]}{[Si(g)]}\left(\frac{[B(l)]}{[Si(l)]}\right)^{-1}$	Enrichment factor

With this calculation we obtain an enrichment factor of 126 (VII-8). This value is very close to the measured enrichment factor of 136 and validates thus the measurement of the enrichment factor. The small difference may be explained by the inaccuracy of the oxidation efficiency of 70% (an oxidation efficiency of 65% could explain the difference).

Total flow	3 l/min
Argon fraction	96.8%
Water vapor fraction	3.2%
Water vapor flux	0.23 mol/h
Silicon temperature	1500 ℃
Silicon mass m	200 g
Purification time	4.5 h
k	$1.2 \cdot 10^{-6}$ m/s
$T_{0.5}$	235 min
$T_{0.5}$/m	470 min/kg
Crucible surface A	32.2 cm^2

Table VII-4 Parameters and results of a purification of [NT12]

We use the same formula to calculate the enrichment factor of the experiment at 96.8% Ar and 3.2% H_2O of the experiment of Nordstrand et al [NT12]. The formed fume in the

experiment was completely white[1]. This indicates that only SiO_2 was formed and no SiO. The maximum SiO_2 flux that may have been produced is half of the water vapor flow. We can thus calculate the lower limit for the enrichment factor which would be exact if all water vapor reacts.

We use equation (VII-9) with $\rho_{Si} = 2.56 g/cm^3$ to calculate the half-life time $T_{0.5}$. Then we use equation (VII-10) with the data of Table VII-4 to calculate the enrichment factor. We obtain an enrichment factor of 11. This enrichment factor gives only the lower limit. It may be higher if only a part of the water vapour reacts. A measurement of the enrichment factor without plasma should be done to determine the enrichment factor more exactly.

$$T_{0.5} = \frac{\ln 2}{K} = \frac{V \ln 2}{kA} = \frac{m \cdot \ln 2}{\rho_{Si} kA} = 234 \min \qquad \text{(VII-9)}$$

$$R = \frac{m \cdot \ln 2}{T_{0.5} \cdot M_{Si} \cdot 0.5 J_{H_2O} A} = \frac{0.2 kg \cdot \ln 2}{234 \min \cdot 0.028 kg/mol \cdot 0.5 \cdot 0.23 mol/h} = 11 \qquad \text{(VII-10)}$$

Nakamura et al. [NBS04] measured an enrichment factor of $R_{\exp} = 36$ at 2.5 % H_2O and 97.5 % Ar and at a silicon temperature between 1600 °C and 1700 °C.

VII.6. Comparison between the measured and the thermodynamic enrichment factors

We compare the measured and estimated enrichment factors to the enrichment factors at chemical equilibrium. The chemical equilibrium calculations (see chapter II) show, that the enrichment factor depends significantly on the temperature and on the hydrogen fraction. The oxygen fraction does not modify the enrichment factor because the equilibrium between the most important gaseous species SiO and HBO does not depend on the oxygen fraction.

We want to find the enrichment factor at chemical equilibrium at 1410 °C and 5 % hydrogen which are the parameters of [Fou03]. For this we use the enrichment factor calculated at 1600 °C and 5% hydrogen (0.88). We extrapolate to 1410 °C by using the temperature dependence of the HBO partial pressure (Multiplication by 1.9). Then we multiply by 8.8 to take into account the correction of the formation enthalpy of HBO (see chapter II). We obtain an enrichment factor of 15 at chemical equilibrium. We repeat the same extrapolation for the conditions of [NBS04] and [NT12] and present them in Table VII-5.

	H_2O+H_2 Fraction	Silicon Temperature	Plasma	$R_{\exp}$	R_{thermo}	$R_{\exp} / R_{thermo}$
[Fou03]	5 %	1410 °C	X	136	15	9
[NBS04]	2.5 %	1600-1700 °C	X	36	5.5	7
[NT12]	3.2 %	1500 °C		>11	6	>2

Table VII-5 Comparison between measured and thermodynamic enrichment factors (lower limit due to water vapour flow)*

The measured enrichment factors and those at chemical equilibrium are presented in Table VII-5. The two measured enrichment factor with plasma are significantly higher than the enrichment factor at chemical equilibrium. The lower limit for the enrichment factor measured without plasma is also higher than the enrichment factor at chemical equilibrium. This indicates that an effect modifies the enrichment of the gases. The relative dependence

[1] Personal communication from Dr Nordstrand 16.10.2012

of the purification rate on the temperature and the hydrogen concentration indicate that the surface is at chemical equilibrium. The effect that leads to a higher enrichment factor is thus probably a different evacuation of the reaction products. The slow diffusion of a SiO_2 aerosol may explain the higher evacuation of the boron species. The smaller enrichment factor (compared to chemical equilibrium) in the experiment without plasma may be explained by recirculations that enrich the bulk gas with the reaction products. When the bulk gas has a high silicon and boron concentration the concentration gradient is small so that a higher enrichment factor due to the slow diffusion of a SiO_2 aerosol is not possible. The small nozzle at high distance to the silicon surface is an evidence for this theory. However it should be validated with a large nozzle that is close to the silicon surface. It would be interesting to study the influence of the diameter of the nozzle and the distance to the silicon surface on the enrichment factor.

VII.7. Dependence of the Silicon loss on the enrichment factor

When the target boron concentration is very low, the loss of silicon may become important. The loss of silicon depends only on the enrichment factor R and the ratio between the initial and the final (target) boron concentration $[B(l)]_{initial}/[B(l)]_{target}$. The equation (VII-12) has been obtained from the equation (VII-11) and the equation (VII-6). It does not take into account that the loss of silicon should increase slightly the boron concentration in the melt. Thus, for high losses the formula underestimates the losses.

$$[B(l)]_{target} = [B(l)]_{initial} \exp(-K\Delta t) \quad \text{(VII-11)}$$

$$\frac{\Delta m_{Si}}{m_{Si}} = \frac{1}{R} \ln\left(\frac{[B(l)]_{initial}}{[B(l)]_{target}}\right) \quad \text{(VII-12)}$$

For the reduction of the boron concentration by a factor 20 the loss of silicon is only 3 % for an enrichment factor of 100 and it is 30 % for an enrichment factor of 10.

VII.8. Long time purification experiments

VII.8.1. Objectives

The long time purification has two objectives. On the one hand it allows comparing the exponential decay of the boron signal of the ICP to the exponential decay of the boron concentration in the silicon melt. The similar decay validates thus the ICP signal. On the other hand we compare two different silicon types. We compare the purification of metallurgical silicon to the purification of doped electronic grade silicon. We can thus test whether the other impurities that are contained in the metallurgical silicon interact with the boron and thus modify the deboronization rate.

VII.8.2. Method

Two purifications were carried out during about six hours each. The first was done with metallurgical grade silicon (with 25 ppmw of boron) and the second with electronic grade silicon that was doped with 25 ppmw of boron. The difference between the two results show whether the impurities other than boron that are at a much higher concentration in the metallurgical grade silicon have an impact on the deboronization rate. To validate the ICP signal a small silicon sample (~5 g) was taken from the crucible every 30 min. The silicon samples were sent to a partner laboratory for the measurement of the boron concentration by ICP. During the purification the relative boron and silicon concentrations are measured in the exhaust gases of the purification installation. We used the spectrosopic method with two

spectrometers that is described above. The ICP signal can thus not be used to measure the absolute concentration ratio [B]/[Si] in the exhaust gases.

Special care was taken to use the same parameters for the two purifications. Only the mass of silicon was slightly different. Table VII-6 shows the parameters used for the two purification experiments.

Ar Outer flow	6.8 Nm^3/h
Ar Intermediate flow	0.39 Nm^3/h
Ar Inner flow	0.14 Nm^3/h
Hydrogen (Inner flow)	0.31 Nm^3/h (4.2%)
Oxygen (Outer flow)	0.06 Nm^3/h (0.8%)
DC Power	38 kW
Frequency crucible	9 kHz
Mass of the silicon melt	3.2 kg (met) 2.9kg (el)
Purification time	6 h
Crucible	Crucible 1
Distance crucible torch	40mm

Table VII-6 The parameters of the two purifications

VII.8.3. Data processing

The boron signal measured by the ICP is proportional to the quantity of boron that leaves the reaction chamber, which is proportional to the boron concentration of the silicon melt. When the sample is taken the crucible is moved into a lower position and the line which goes to the ICP is cleaned with a strong argon flow. This has a large impacts on the boron signal and the silicon signal. As it has the same impact on the two signals the ratio between the two signal is much less perturbed.

Keeping process parameters constant we assume that the quantity of silicon that leaves the reaction chamber is constant so that we can use the ratio between the boron signal and the silicon signal to measure the evolution of the boron concentration of the silicon load. A linear regression on the logarithm of the ratio was used to calculate the half-life. The ICP signals measured during the sample-taking were disturbed and therefore removed. The points that were removed are the grey points in Figure VII-6. On the concentration of the silicon samples a linear regression was used. The statistical error of the linear regression was used to calculate the error on the half-life.

VII.8.4. Results

Metallurgical grade silicon

Figure VII-6 shows the signal ratio B/Si from the ICP and the concentration of the samples that were taken during the purification of the metallurgical grade silicon. We use logarithmic scaling for the y-axis to show that the concentration decreases exponentially. This can be seen by the fact that the signal ratio B/Si of the ICP and the boron concentration of the samples follow well a straight line. The linear regressions on the logarithm of the values give two half-lifes that are almost identical. This result shows that the ICP signal can be used to measure the half-life and that the signal of the ICP is a good indicator for the purification efficiency.

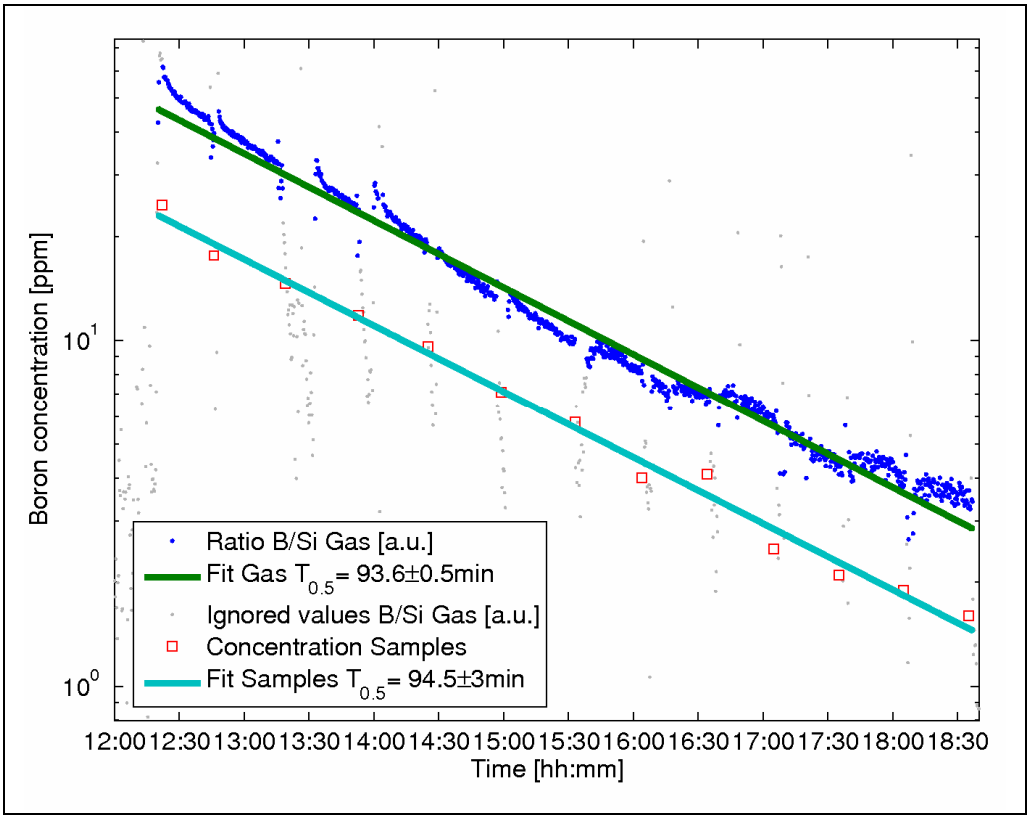

Figure VII-6 B/Si ratio of ICP the signal and the silicon samples during purification of metallurgical grade silicon

time	12:22	12:46	13:19	13:53	14:25	14:59	15:33	16:04	16:34	17:05	17:35	18:05	18:35
ppmw (boron)	24,6	17,6	14,6	11,8	9,6	7,1	5,8	4	4,1	2,5	2,1	1,9	1,6

Table VII-7 Concentration of the silicon samples (Purification of metallurgical grade silicon)

The half life of the boron concentration in the silicon melt is 94 min. Dividing this value by the mass of the silicon (3.2 kg) we find $T_{0.5}$/m = 29 min/kg. This is much slower than the 12 s/kg obtained by Nakamura [NBS04] with a 300 kg silicon load and a 650 kW arc torch. The purification rate of Nakamura is higher because of the higher hydrogen concentration (as shown by thermodynamics at the interface) power and the higher gas flows.

Doped electronic grade silicon

Figure VII-7 shows the signal ratio from the ICP and the concentration of the samples that were taken during the purification of the doped electronic grade silicon. The half-life is with 89 min a little smaller than those of the metallurgical grade silicon, but this is mostly due to the smaller mass of the silicon load. The half-life divided by the mass (2.9 kg) is $T_{0.5}$/m=31 min/kg and almost identical with that of the metallurgical grade silicon. The results show that the influence of the other impurities is negligible in the examined conditions.

In this measurement the statistical errror on the measurement is very small (0.1 min for the ICP and 1 min for the samples, see Figure VII-7). The difference between the half-life calculated from the samples and that calculated from the ICP signal is bigger than the statistical error. This shows that there is a small systematic error in one of the two measurements. It is possible that the slow clogging with the SiO_2 dust of the reaction chamber and the line which goes to the ICP causes a small systematic error on the ICP signal. However this error remains small so that it should not perturb the measurement.

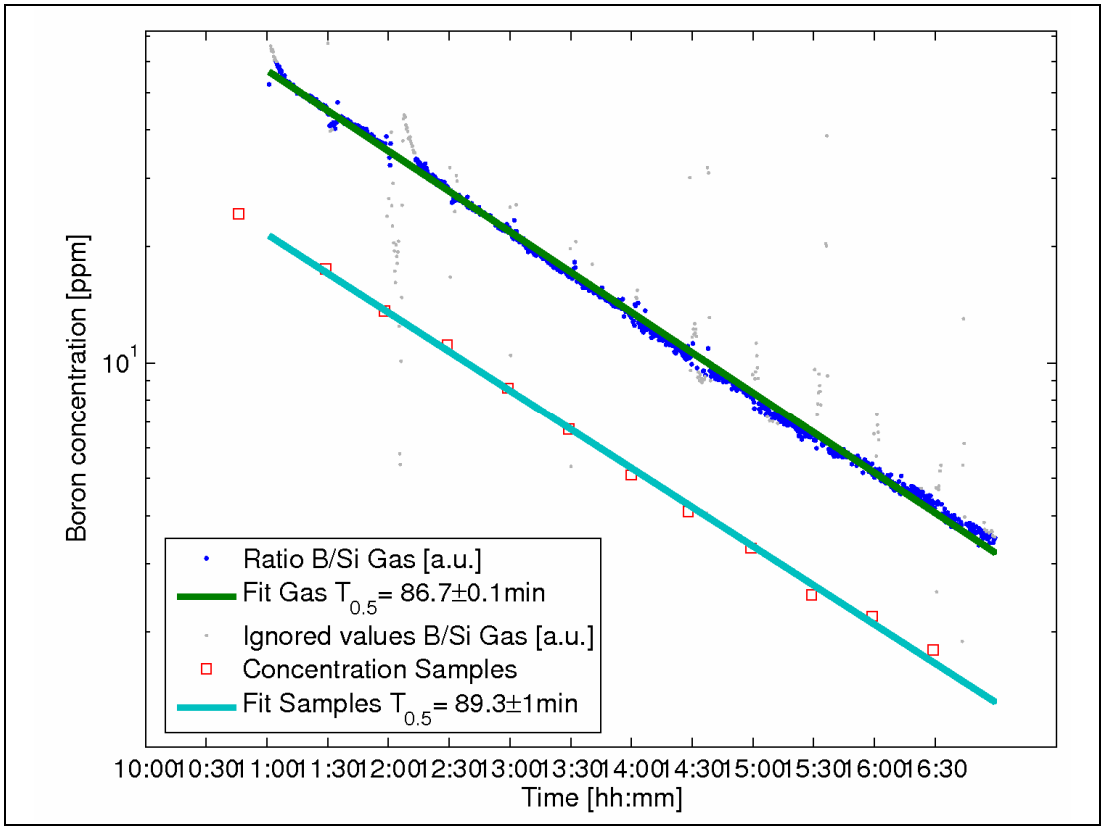

Figure VII-7 B/Si ratio of ICP the signal and the silicon samples during purification of doped electronic grade silicon

Temps	10:46	11:29	11:58	12:29	12:59	13:29	14:00	14:28	14:59	15:29	15:59	16:29
ppmw (bore)	24,3	17,5	13,6	11,1	8,6	6,7	5,1	4,1	3,3	2,5	2,2	1,8

Table VII-8 Concentration of the samples (Purification of doped electronic grade silicon)

Oxide layer

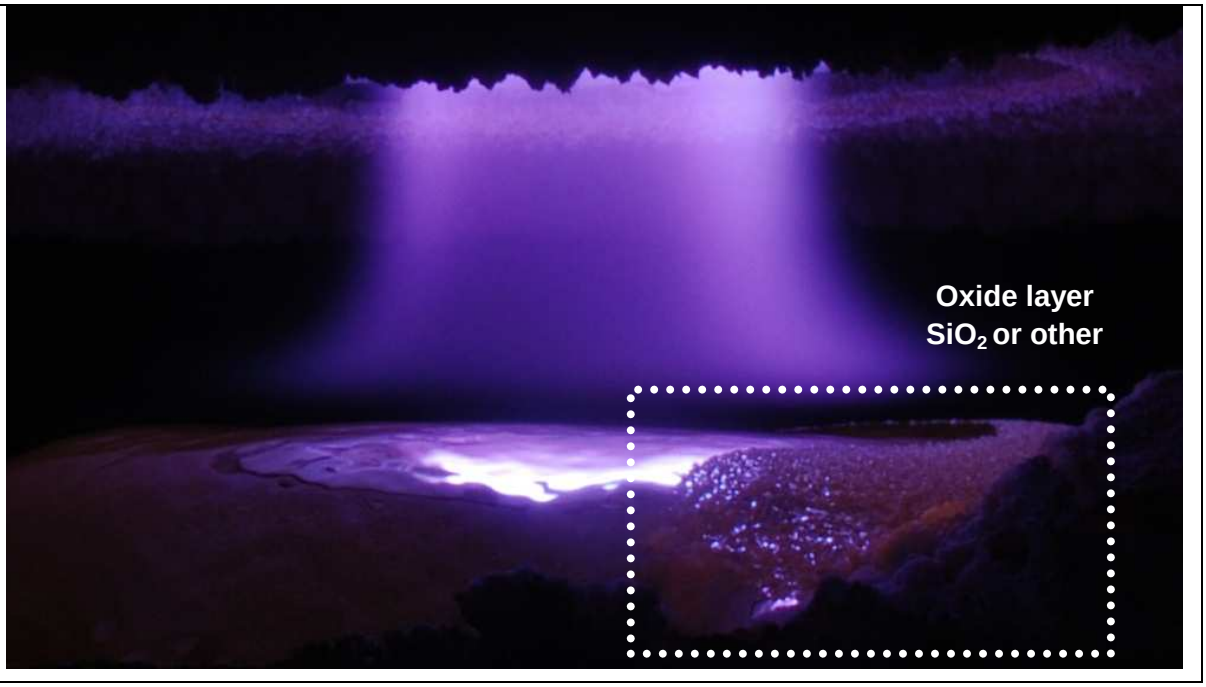

Figure VII-8 Oxide layer observed after 3 h purification of the metallurgical grade silicon

During the purification of the metallurgical grade silicon an oxide layer has been observed 3 h after the start of the purification and remained until the end. Figure VII-8 shows a photo of the purification with this oxide layer on the top. This layer has not been observed during the purification of electronic grade silicon. It is possible that impurities other than boron have caused this oxide layer but it may also be a random effect. The oxide layer was probably of silica and may have contained oxides of other impurities. If the oxide layer would have grown bigger it would have probably reduced the purification rate.

VII.9. Parametric study

The objective of this study is to find empirically the optimal parameters for purification. In a parametric study we examined the influence of the following parameters on the purification rate:

- the crucible power (VII.6.1)
- the plasma power (VII.6.2)
- the distance between torch and crucible (VII.6.3)
- the concentration of hydrogen separately (VII.6.4)
- the concentration of oxygen and hydrogen together (VII.6.5)
- abrupt variation of the O_2 and H_2 concentration (VII.6.6)

For this we varied each parameter separately around the central parameters. The parameters and their range of variation are shown in Table VII-9.

Paragraph	VII.6.1	VII.6.2	VII.6.3	VII.6.4	VII.6.5	VII.6.6
Outer flow Ar [Nm^3/h]	6.8	6.8	6.8	6.8	6.8	6.8
Intermediate flow Ar [Nm^3/h]	0.34	0.34	0.23	0.24	0.34	0.34
Inner flow Ar [Nm^3/h]	0.14	0.14	0.09	0.09	0.14	0.14
Outer flow O_2 [Nm^3/h]	0.07	0.07	0.06	0.06	**0.03-0.11**	**0.07**
O_2 fraction	0.93%	0.93%	0.8%	0.8%	**0.38%-1.42%**	**0.93%**
Inner flow H_2 [Nm^3/h]	0.27	0.27	0.31	**0.05-0.42**	**0.12-0.39**	**0.27**
H_2 fraction	3.7%	3.7%	4.3%	**0.7%-5.8%**	**1.8%-5.3%**	**3.7%**
Plasma power [kW]	35	**20-45**	32	32	35	35
Crucible power [kW]	**40-70**	60	75	55	60	60
Dist.Torch Crucible [mm]	40	40	**32-80**	40	40	40
Crucible	2	2	2	2	2	2

Table VII-9 The parameters for the parametric study

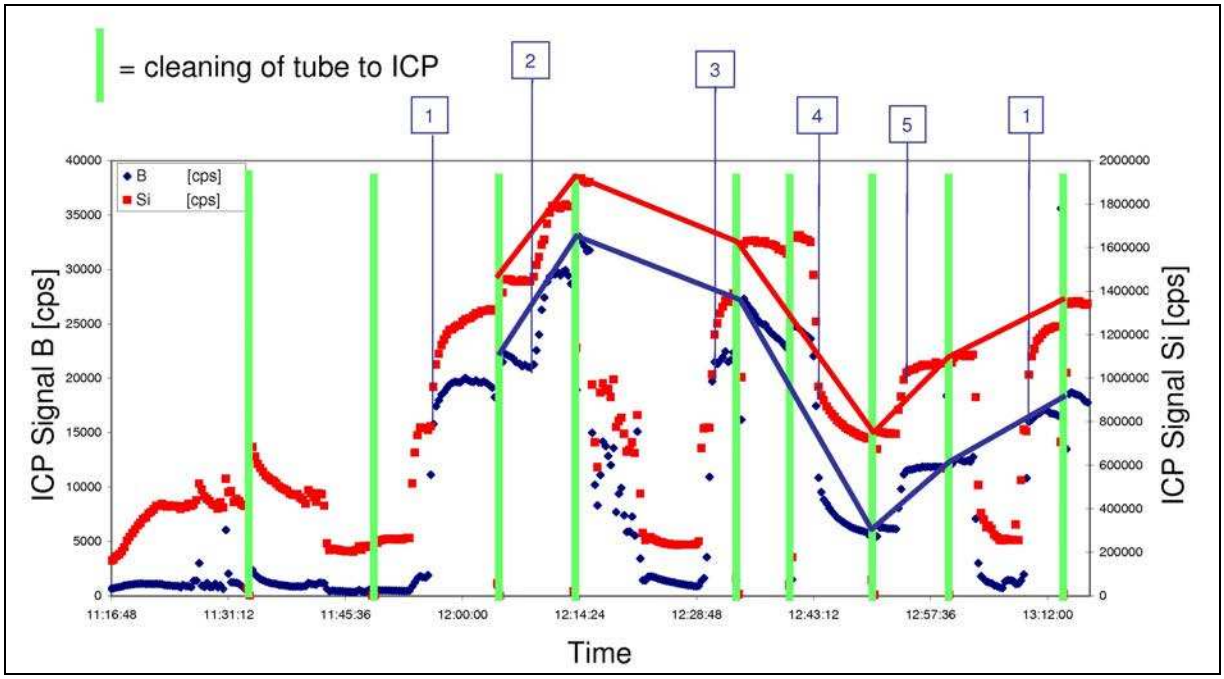

Figure VII-9 ICP Signal during parametric purification experiments. The dots are the raw data and the lines connect the points used for the comparison

We used the ICP signal to evaluate the efficiency which should be proportional to the Boron signal as long as the gas flows remain constant. Figure VII-9 shows the ICP signal of one of the parametric purification experiments (here VII.6.5 as example). The numbers show the time where the parameters have been changed. After the modification of a parameter we waited until the ICP signal of boron was constant. With a large argon flow we purged the tube, which brings the exhaust gases to the ICP. The green vertical lines show the purging of the tube. The purging leads to a strong increase of both the boron and the silicon signal.

In order to compare the signal for different parameter we use the ICP signal just after the purging of the tube. In Figure VII-9 these points are connected with lines.

VII.9.1. Influence of the power of the crucible

We changed the power of the crucible between 40 kW and 70 kW and measured the ICP signal in order to test how the purification is influenced by the power of the crucible.

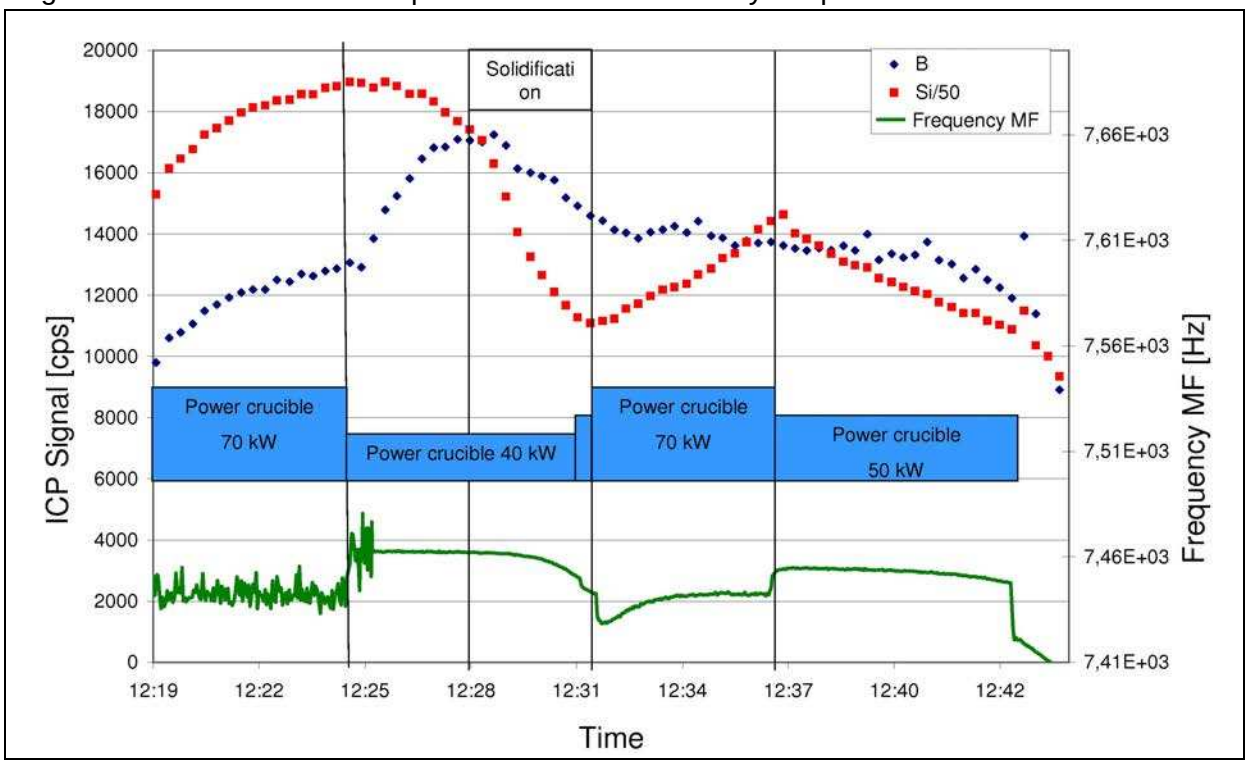

Figure VII-10 The ICP signal of boron and silicon in the exhaust gases, the crucible power and the frequency vs time.
The blue rectangles show the crucible power

Figure VII-10 shows the ICP signal of boron and silicon, the power of the crucible and the induction frequency of the crucible. We can see that the reduction of the crucible power at 12:25 causes a slow increase of the boron signal and thus increases the purification rate. Only three minutes later the boron signal decreases again. The increase of the silicon rate is probably due to a decrease of the silicon temperature. The reduced power also reduces stirring. A reduced stirring may reduce the purification rate which could be seen by a sharp decrease of the boron signal. This can not be observed in the measurement which thus shows that stirring at 40 kW is still very efficient.

The decrease of the temperature leads to solidification of some silicon from 12:28 to 12:31, which can be seen in the decrease of the induction frequency. At 12:31 the power is increased. And the increase of the frequency shows that the solidified silicon melts again.

The reduction of the oxygen flux from the silica plates of the crucible due to solidified silicon may explain the decrease of the ICP signal of silicon and boron at 12:28.

The results shows that stirring is very efficient and that the crucible power modifies the purification rate due to the modification of the silicon temperature. It shows that for constant plasma parameters the purification is faster when the silicon is colder. The optimal temperature would be just above the melting temperature. However at higher silicon temperature one can inject a higher oxygen concentration without forming a silica layer so that the reduced purification rate may be balanced. The formation of a silica layer will be presented further down in this chapter.

We studied in more detail the role of the temperature on the purification rate. For this we used a graphite crucible which was equipped with a thermocouple. We measured simultaneously the silicon temperature and the boron and silicon concentration in the exhaust gases. The parameters are shown in Table VII-10. Figure VII-11 shows the temperature and the relative variation of the B/Si ratio of the ICP signal vs time. The modification of the power is indicated in the same figure. An increase of the power leads to a strong increase of the temperature and vice versa. We use the data of Figure VII-11 and plot the B/Si ratio versus the temperature. Figure VII-12 shows the temperature dependence of the B/Si ratio together with the partial pressure of HBO. The partial pressure values of HBO ware taken from the chemical equilibrium calculation from [NT12] presented in chapter II. These values were calculated at a high hydrogen fraction but the temperature dependence of the HBO partial pressure at low hydrogen fractions should be the same.

Between 1500 K and 1700 K both curves decrease similarly. This shows that the temperature dependence of the purification rate agrees with the chemical equilibrium.

Plasma power [kW]	36
Distance Torch Crucible [mm]	40
Flow rate Ar [Nm^3/h]	7
O_2 fraction	1.0 %
H_2 fraction	4.0 %
Crucible power [kW]	**18-30**
Crucible	3

Table VII-10 Parameters for the measurement of the temperature dependence of the purification

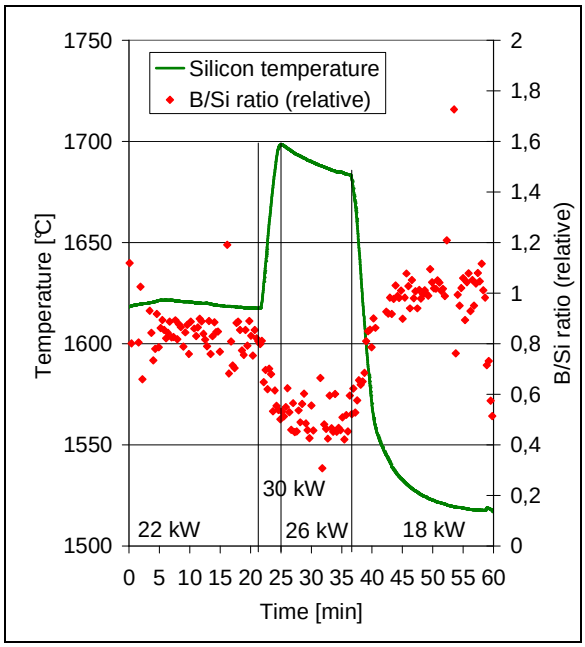

Figure VII-11 The change of the relative B/Si ratio (ICP) and the temperature with time. The changing crucible power is indicated above the time axis

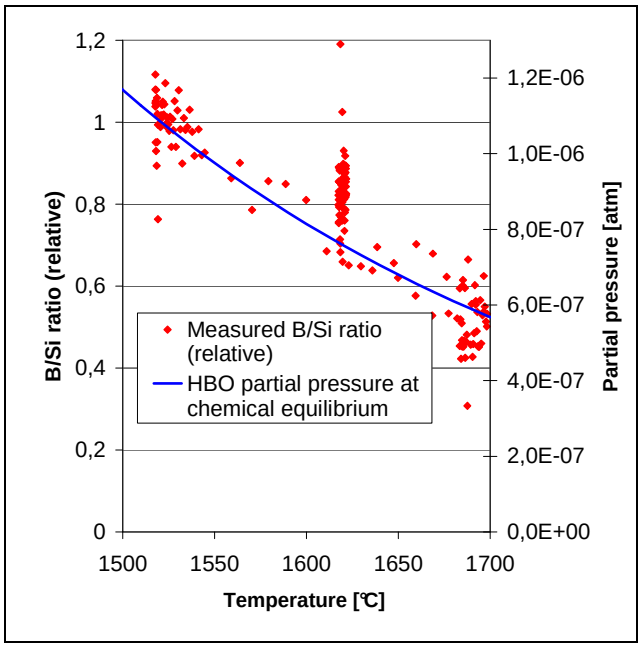

Figure VII-12 The dependence of the relative B/Si ratio of the ICP signal on the temperature and the HBO partial pressure at chemical equilibrium

VII.9.2. Influence of the plasma power

Figure VII-13 shows the raw data of the measurement of the ICP signal of boron and silicon for different plasma powers between 20 kW and 45 kW (DC power). We always

alternated between a point at high power and point at low power and waited until the signal stabilized. We can see in Figure VII-13 that when the plasma is operated at a high power (40 kW at 13:20 and 45 kW at 13:50) the boron signal decreases continuously. This is probably due to an increase of silicon temperature (as we observed in the measurement before). An increase of the temperature of the cooling water of the crucible confirms the slow variation of the silicon temperature. The purification rate at higher power may thus be higher if the silicon temperature was maintained constant.

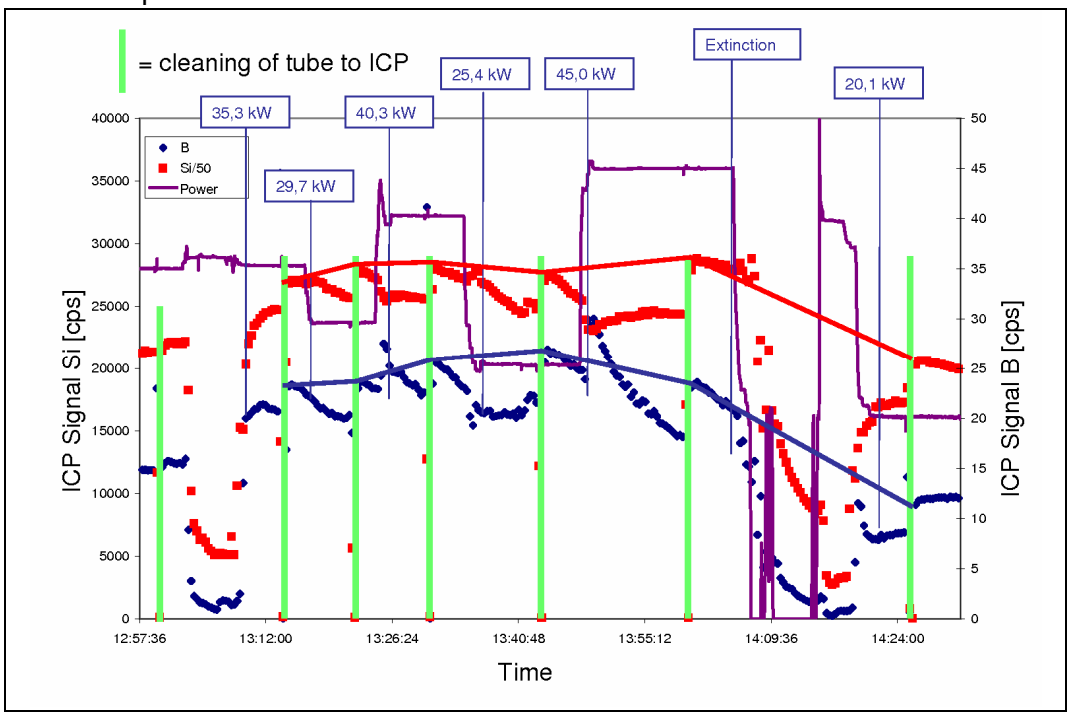

Figure VII-13 The dependence of the ICP signal of boron and silicon in the exhaust gases on the plasma power, raw data

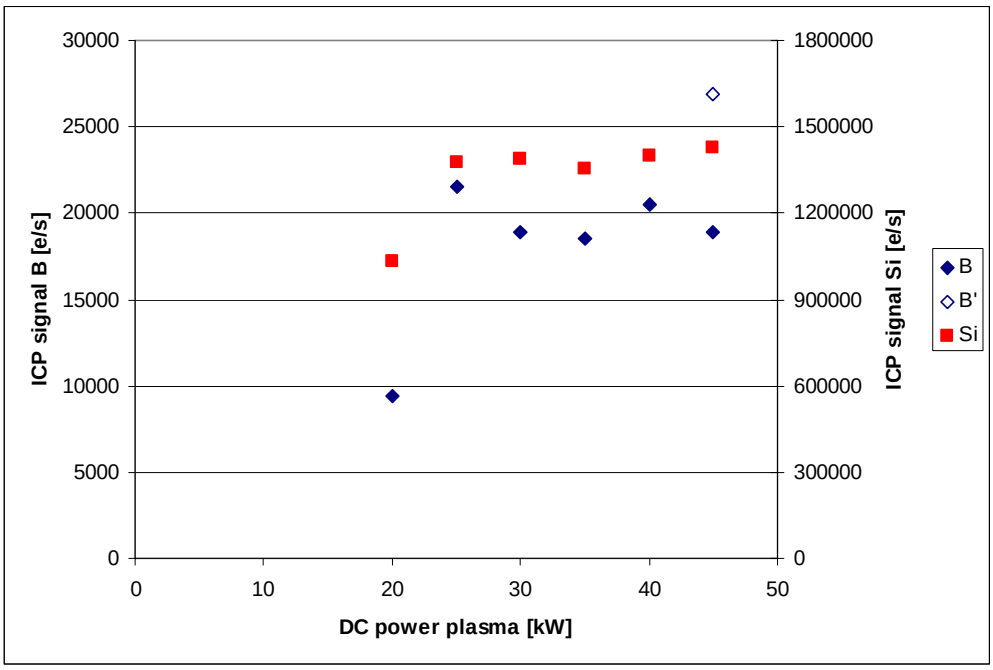

Figure VII-14 The dependence of the ICP signal of boron and silicon in the exhaust gases on the plasma power.

Figure VII-14 shows the signal after the gas purging. Between 25 kW and 45 kW the ICP signals of boron and silicon are constant. The purification remains thus also constant. However at 13:48 in Figure VII-13, when the power is increased from 25 kW to 45 kW, the boron signal increases by 25 %. This increase corresponds probably to an increase of the purification rate at a constant silicon temperature. This point is represented as B' in Figure VII-14.

The point at 20 kW however has a lower ICP signal for silicon and a significantly lower ICP signal for boron. We verified on the measured voltage and the measured current that the plasma is in the same coupling mode as at the other points (see chapter VI). The rather small difference on the silicon signal indicates that approximately the same amount of oxygen arrives at the surface. The extinction of the plasma right before the measurement of the point at 20 kW may have perturbed the measurement. However it seems that below a minimum power the purification rate decreases strongly. In order to consolidate this findings the measurement should be repeated with a cold crucible that maintains the silicon temperature constant and several repetitions of the same power.

The measurements of the temperature and the oxygen and hydrogen distribution for the same parameter have been presented in chapter V. At 20 kW the measured temperature was much lower than at 30 kW. This may explain the lower purification rate at 20 kW.

VII.9.3. The influence of the distance between the crucible and the torch

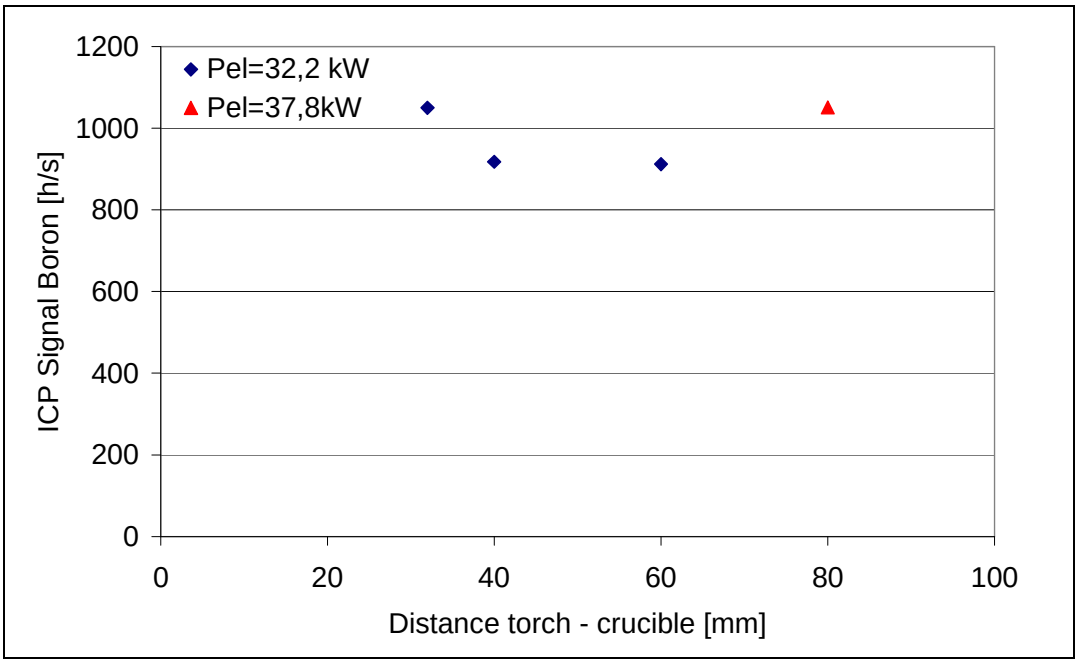

Figure VII-15 The dependence of the purification rate on the distance between the torch and the crucible

Figure VII-15 shows the dependence of the ICP signal of Boron and Silicon on the distance between the torch and the crucible. The point at 80 mm was measured with a higher plasma power. The difference between measured ICP signals is small. This shows that the influence of the distance is not significant in the observed range (30 mm - 80 mm).

VII.9.4. Influence of the hydrogen concentration separately

In this experiment we tested the influence of the hydrogen concentration separately. Figure VII-16 shows the result of the experiment. The point at 6% hydrogen was measured twice. The ICP signal of silicon is similar for all points. This shows that the hydrogen fraction does not modify the oxidization of the silicon. But it modifies significantly the oxidization of boron as we can see in the variation of the ICP signal of boron. The dependence of the B/Si ratio on the hydrogen fraction follows approximately a square root function and agrees thus with the calculations of the chemical equilibrium.

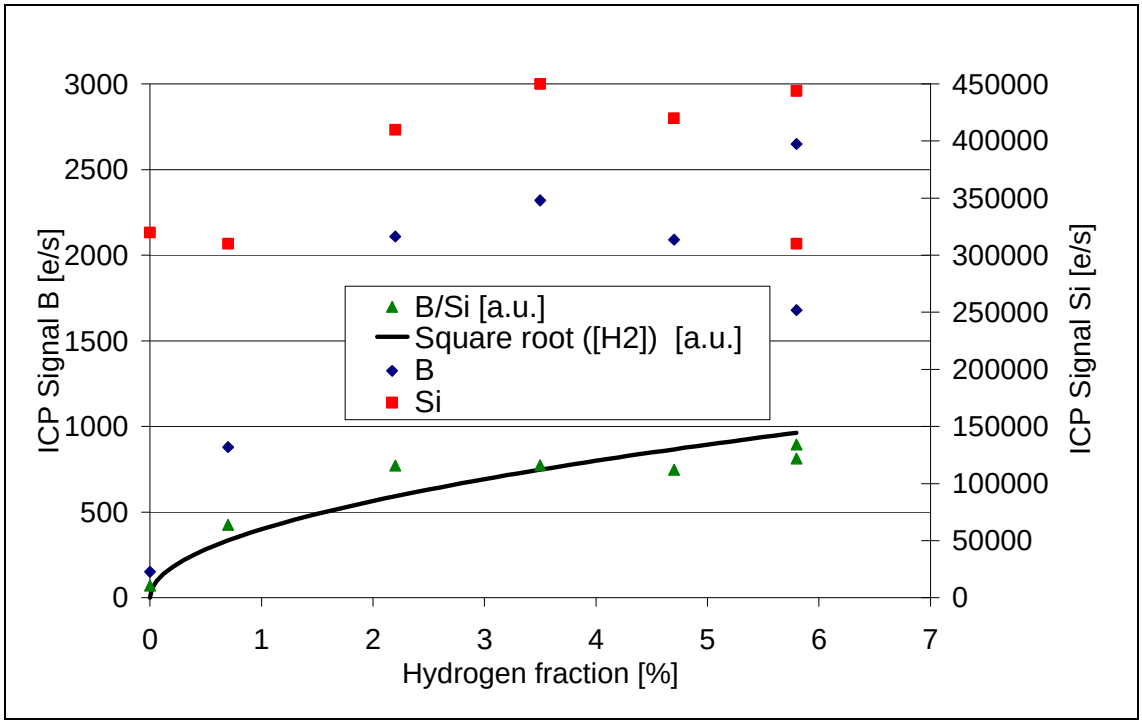

Figure VII-16 The dependence of the ICP signal of boron and silicon in the exhaust gases on hydrogen fraction, (Oxygen fraction: 0.8 %)

VII.9.5. Influence of the concentration of oxygen and hydrogen together

We changed the flow rates of oxygen and hydrogen simultaneously with a constant H_2/O_2 ratio of about 4 between oxygen and hydrogen.

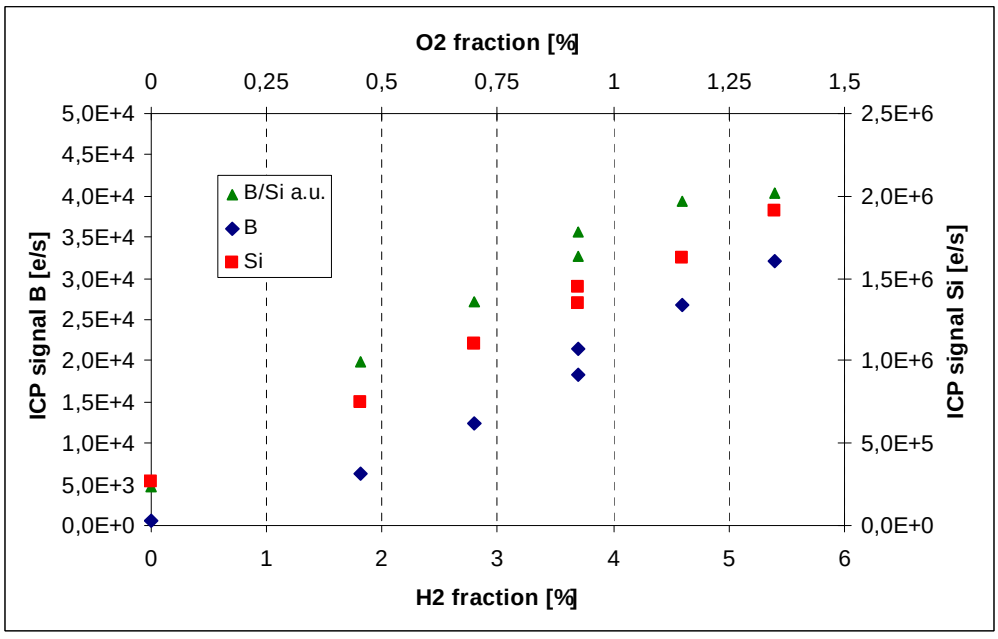

Figure VII-17 The dependence of the ICP signal of Silicon and Boron in the exhaust gases on the O_2 and H_2 fraction. The O_2 fraction is approximately one quarter of the H_2 fraction

Figure VII-17 shows the dependence of the ICP signal on the concentration of hydrogen and oxygen (which is ¼ of the hydrogen concentration). The ICP signal of silicon increases

linearly with the oxygen concentration with a small offset at 0 % oxygen. The offset is probably due to the oxygen flux from the silica plates that insulates the silicon from the cold crucible. The linearity shows that the oxidation of silicon is proportional to the quantity of oxygen that is injected into the plasma which is probably in turn proportional to the quantity of oxygen that arrives at the surface.

The more hydrogen and oxygen we inject the higher is the quantity of boron that is volatilized and hence the faster the purification of silicon proceeds. The point one at 3.7% hydrogen, which was measured twice, shows that we have a good repeatability. The two concentrations of silicon are similar while the signal of boron decreased because the silicon was purified in-between. The analysis of silicon samples showed that the boron concentration decreased by 19% between the two measurements.

In chapter V we presented measurements of the distribution of the temperature, the hydrogen and the oxygen in the plasma for the same parameters as presented here. We observed that the higher concentration of the reactive gases reduced the temperature in the plasma. This may also induce a variation of the purification rate.

VII.9.6. Measurement of the time response of the ICP signal to abrupt starting and stopping of the oxygen and hydrogen flow

The objective of this measurement was to find indications for the role of the in the silicon melt dissolved species, which may have an important role as suggested by Degoulange [Deg08]. As the concentrations of the dissolved species do not attain equilibrium instantly when the concentrations of the plasma are modified, we may use the response of the ICP signal to an abrupt starting or stopping of the oxygen and hydrogen flow, to separate the deboronization rate due to dissolved species and the deboronization rate due to surface reactions.

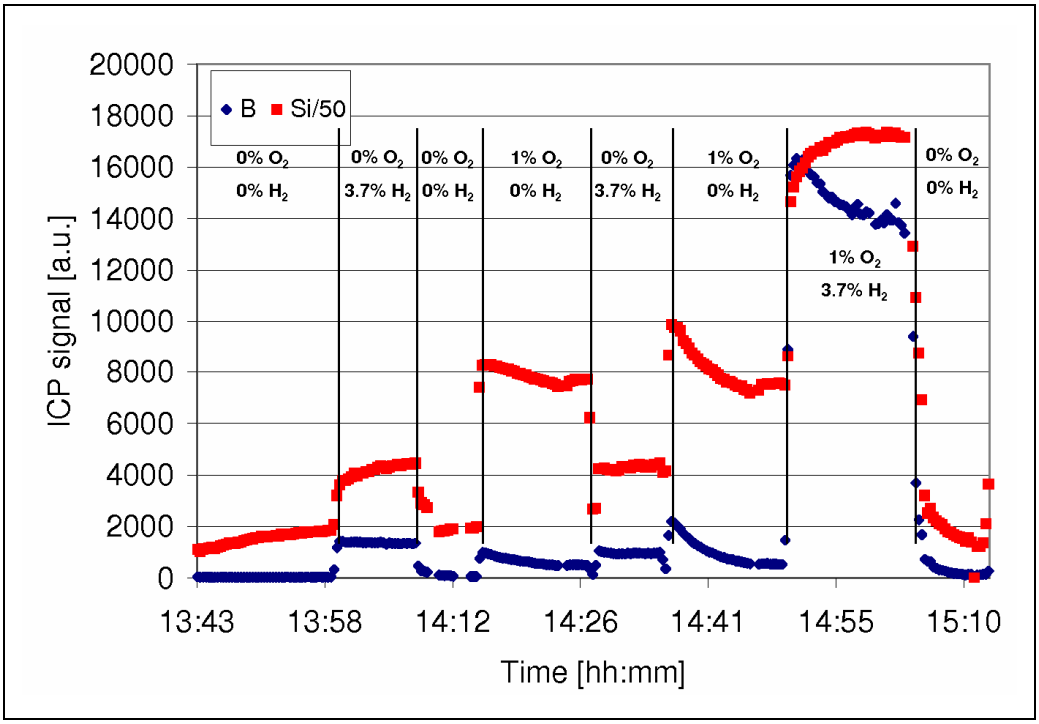

Figure VII-18 The time dependency of the ICP signal of boron and silicon the injection of oxygen and hydrogen were started and stopped abruptly

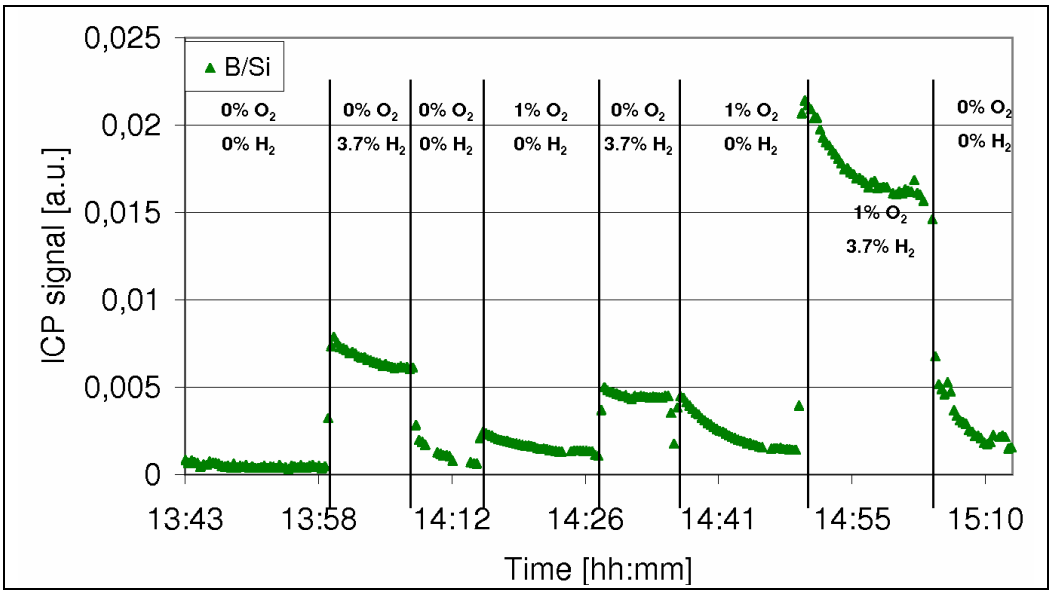

Figure VII-19 The time dependency of the B/Si ratio of the ICP signal the injection of oxygen and hydrogen were started and stopped abruptly

Figure VII-18 shows the ICP signal of boron and silicon during the measurement. Figure VII-19 shows the B/Si ratio. The vertical lines show the time when the oxygen and the hydrogen flows where started and stopped. The measured ICP signals that were perturbed by the purge of the tube, that brings the exhaust gases to the ICP, were removed.

During the measurement we observed that the shape of the plasma for the gas analyzing (ICP) was modified when hydrogen is started and stopped in the plasma for purification. This may explain why the silicon signal increases by a factor two when the hydrogen flow is started and decreases again by a factor two when the hydrogen flow is stopped.

Dissolved species

The ICP signal of silicon and boron react rapidly to the stopping and starting of the hydrogen and oxygen gas flows. In less than a minute the signals attain the new value. The ICP signal of boron is significantly higher when oxygen and hydrogen are injected at the same time than when they are injected one after another. This indicates that the dissolved species do not play an important role for the purification process.

However the role of dissolved hydrogen can be seen at 14:15 and 14:37 when oxygen is injected into the plasma after the hydrogen flow has been stopped. The boron signal decreases exponentially due the evaporation of dissolved hydrogen that evaporates slowly. The signal is higher at 14:37 than at 14:15 which is probably because the hydrogen flow was stopped just before and the hydrogen concentration in the silicon melt is thus higher at 14:37 than at 14:15.

The solulibility of hydrogen in silicon at 1800 K and 0.04 bar hydrogen is 1.4 l/kg [JLL11]. This high solulibility can explain the slow decrease of the boron signal after the stopping of the hydrogen flow. We use the exponential decrease from the higher signal to the offset at the lower signal to calculate the characteristic time due to the mass transfer in the silicon melt and find 3 min. Degoulange [Deg08] found a value of the same magnitude (7 min) for the evaporation of oxygen which has probably a smaller diffusion coefficient and a numerical model gave a value of 2 min [DAL02]. These results indicate that the mass transfer in the melt should not be rate limiting as long as the half life time is much longer than 3 min.

The dissolution of hydrogen in the silicon melt should not influence the process in normal conditions as the concentration of hydrogen saturates and thus the flow from the gas into the silicon is equal to the flow from the silicon to the gas.

Oxygen from the silica plates of the crucible can diffuse into the silicon so that the silicon is also oxidized when no oxygen is injected into the plasma. The vaporization of silicon is negligible due to the low vapor pressure. (0.1 Pa at 1700 K [Des86]). The silicon signal at 13:43 and at 14:10 in Figure VII-18 is thus due to the oxidation of silicon. The solubility of oxygen is about 4 ppm or 0.02 l/kg [NMM94] at 1700 K and increases with the temperature. The plasma was ignited at 13:42 and the temperature of the cooling water of the crucible show an increase of the temperature between 13:42 and 14:00. As the solubility of oxygen increases with the temperature, the evaporation rate of SiO increases also. The oxygen concentration in the silicon melt is probably saturated.

Chemical equilibrium

In chemical equilibrium the ratio between the partial pressure of HBO and the partial pressure of BO is $p_{HBO} / p_{BO} = 16$ at 4 % hydrogen at 1600 °C (old data, see chapter II). The partial pressure of the gaseous boron species is thus 16 times higher when 4 % hydrogen is in the gas, than when no hydrogen is in the gas. The partial pressure of BO is independent of the hydrogen concentration and the partial pressure of HBO is zero when no hydrogen is injected. The partial pressure of other gaseous boron species is much smaller. In the experimental results we can see a similar increase of the B/Si ratio of the ICP signal when hydrogen is injected (see Figure VII-19). At 13:58 the B/Si ratio increases by a factor 19 and at 14:49 the B/Si ratio increases by a factor 15. These factors agree with the ratio predicted by the chemical equilibrium calculations as shown in Table VII-11. For this comparison we used the old data for the formation enthalpy of HBO because when using the new data one needs also to modify the formation enthalpy of the other boron species.

chemical equilibrium	O_2	H_2	$p_{HBO} / p_{BO} = 16$
Measurement at 13:58	0%	0% → 3.7%	19
Measurement at 14:49	1%	0% → 3.7%	15

Table VII-11 Variation of the B/Si ratio when H_2 is injected

Evacuation of SiO vs SiO_2

Figure VII-20 shows a detail of Figure VII-18. At 14:15 oxygen was injected into the argon plasma. The silicon signal increased by a factor 4. The boron signal increased at the same time by a factor around 16. The B/Si ratio of the ICP signal increases thus by a factor 4. The chemical equilibrium calculation predicts that the ratio between the gaseous species of silicon and boron remains constant when the oxygen source is modified. The increase of the B/Si ratio may however be explained by the formation of an aerosol.

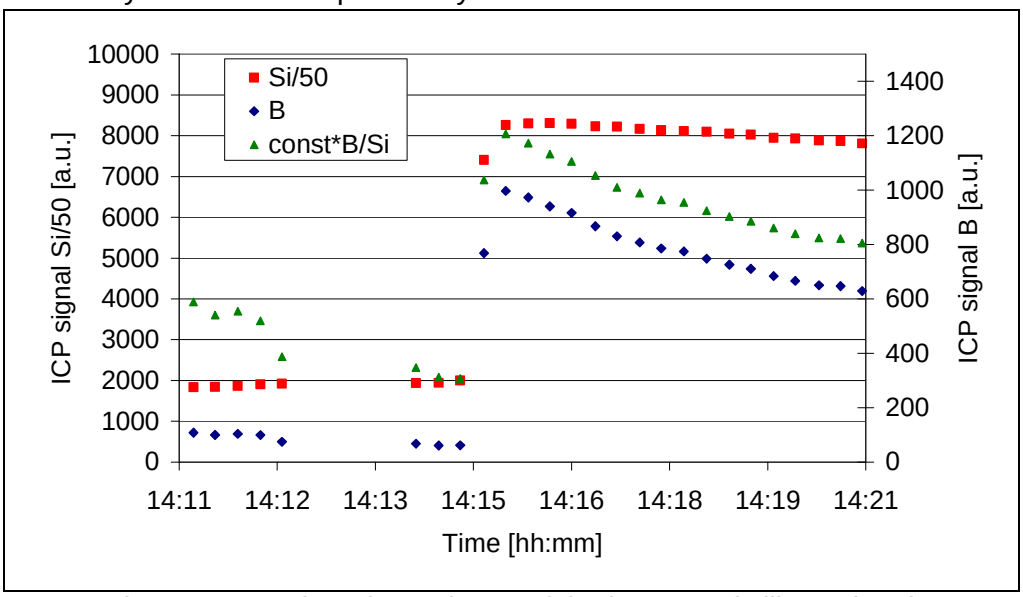

Figure VII-20 Time dependence of the boron and silicon signal.
At 14:15 1% of oxygen is added to the before pure argon plasma.

Before the injection of oxygen in the plasma the silicon and the boron were oxidized by the oxygen that diffused from the silica plates of the crucible into the silicon melt. We can assume that the silicon was oxidized to SiO because the atmosphere above the silicon is not oxidizing. The vapor pressure of silicon is about 0.1 Pa at 1700 K [Des86] so that the vaporization of silicon should be small compared to the vaporization of SiO.

When oxygen was injected into the plasma, the gas furnished supplementary oxygen to the silicon surface. We can assume that the silicon was oxidized to SiO_2 because the atmosphere above the silicon was oxidizing due to the oxygen from the plasma. The silicon signal is four times higher when oxygen is injected. As the SiO_2 flux is four times higher than the SiO flux before it contains eight times more oxygen. We can thus assume that the plasma transports seven times more oxygen to the surface than the silica plates.

The increase of the B/Si ratio when oxygen is injected into the plasma is probably due to the difference between the diffusion coefficient of gaseous SiO and the SiO_2 aerosol. As the SiO_2 aerosol has a smaller diffusion coefficient, the concentration of silicon oxide at the silicon surface is higher for the same oxygen mass transfer rate. As the concentration of silicon oxide is higher at the surface, the concentrations of HBO and BO are also higher. Thus for the same silicon oxidation rate more boron compounds are formed. HBO was probably formed because there was still dissolved hydrogen in the silicon melt. However it would be interesting to repeat this measurement with hydrogen in the gas flow.

VII.10. Formation of the silica layer

Chemical equilibrium calculation and experiments (at constant H_2/O_2 ratio) have shown that the deboronization rate is proportional to the oxygen concentration. But when the oxygen concentration is too high, a silica layer gets formed on the surface, which thus limits the oxygen concentration that can be used in the process. The formation of the silica layer is the transition from active to passive oxidation as it has been described in chapter II.

In this experiment we test the influence of the gas velocity and the silicon temperature on the formation of the silica layer. We did this experiment without plasma, because the gas velocities are easier to control without plasma.

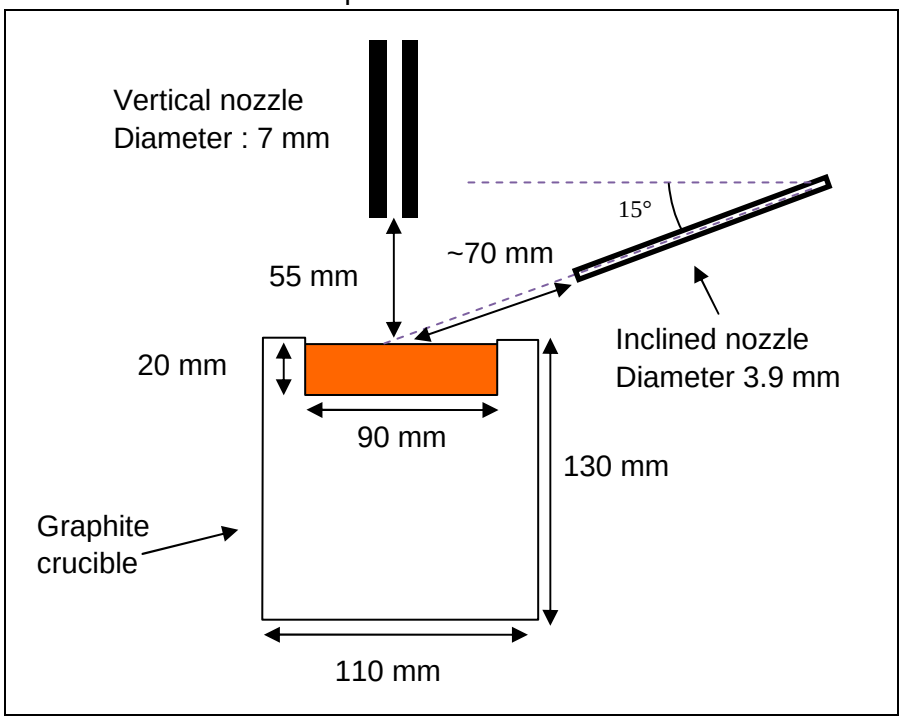

Figure VII-21 The geometry of the setup for the test of different parameters on the formation of the silica layer

Figure VII-21 shows the setup used for the experiment. The graphite crucible consists of a graphite block with a 20 mm deep cavity with silicon at the top. The shallow cavity avoids that the dilatation during solidification at the end of the experiment breaks the crucible. The graphite block is heated by induction. Due to the thermal inertia of the crucible it took about 20 min until the temperature of the silicon stabilized after a change of the induction power of the crucible. The temperature of the silicon was measured with a two color pyrometer. During the injection of oxygen the temperature measurement was perturbed by the fume in the reaction chamber. We did the measurement of the temperature thus before the injection of the oxygen and verified that the gas flow did not modify the temperature of the silicon.

We used two different injection modes. On the one hand we used a vertical nozzle with a diameter of 7 mm at a distance of 55 mm to the silicon surface and on the other hand we used an inclined nozzle with a diameter of 3.9 mm at a distance of about 70 mm to the silicon surface.

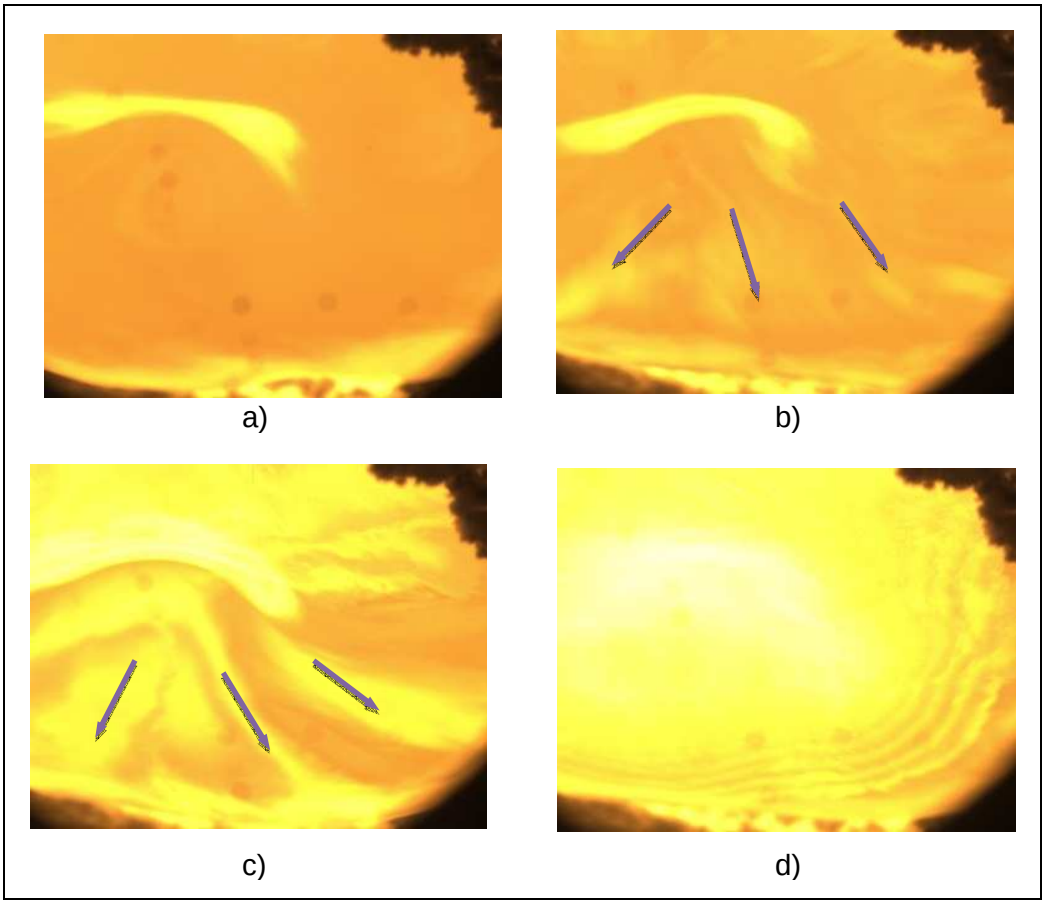

Figure VII-22 Photos of the growth of the silica layer:
The oxygen concentration is increased from a) to d), injection in vertical nozzle. Arrows indicate silica movement as seen on videos
a) the silicon surface is bare
b) and c) more and more silica is formed at the surface and evacuated
d) a silica layer covers the surface

We measured the minimum oxygen concentration at which the silica layer appears for different total gas flows and different silicon temperatures. For this purpose we increased the oxygen flow until we observed the silica layer and then we reduced the oxygen flow rapidly in order to avoid that the silica layer becomes thicker. When the silica layer becomes thicker it takes a long time to remove it. And before the silica layer is completely removed one cannot test the limit for the formation of the silica layer.

Figure VII-22 shows the growth of the silica layer, when an argon-oxygen mixture is injected into the vertical nozzle. At low oxygen concentration the silicon surface is bare (a). When the oxygen concentration is increased above a threshold, one can observe silica at the surface that is evacuated by the gas flow and the stirring of the silicon (b). When the oxygen concentration is further increased more and more silica can be observed (c) Above a second threshold a fixed silica layer rapidly grows from the edge of the surface to the centre and covers then the whole surface (d). The concentration of the first threshold is very close to the second threshold. In the following measurements we always measured the second threshold.

Interference fringes that can be observed in Figure VII-22 d) show that the thickness of the layer is probably some micrometers because the thickness of the layer varies by approximately 500 nm between two fringes.

VII.10.1. The influence of the silicon temperature

We measured the dependence of the threshold oxygen concentration for the silica layer formation on the silicon temperature. We injected of 1 m^3/h of Ar and increased the oxygen flow until the silica layer appeared.

Silicon temperature	1410 °C	1560 °C	1680 °C
Measured dioxygen fraction	3.6%	7.1 %	> 19%
Dioxygen fraction in Wagner model	0.55%	3.5%	15%
Enrichment factor R 5%H_2+Plasma	130	76	50
Normalized deboronization rate (=arb. const. * x_{O2} * R)	1.00	1.15	>2.03

Table VII-12 Dependence of the threshold dioxygen fraction for the formation of the silica layer on the temperature.

Table VII-12 shows the temperature dependence of the maximal dioxygen fraction that can be injected without the plasma. We can clearly see the strong increase of the threshold concentration with the temperature. At 1410 °C the silica layer forms at a dioxygen fraction of 3.6 % while at 1560 °C it forms only at 7.1 % and at 1677 °the oxide layer does not form up to 19 %, which was the limit of the flow meter.

While the oxygen fractions that can be injected increases, the enrichment factor decreases due to the chemical equilibrium (Table VII-12). We used the enrichment factor calculated above and extrapolated it to the different temperatures using the temperature dependence of the enrichment factor from chemical equilibrium. The purification rate should be proportional to the product of the enrichment factor and the oxygen fraction. At the maximum oxygen fraction the purification rate should thus be only slightly higher at 1560 °C than at 1410 °C while it should be more than twice as high at 1680 °C. This may indicate that higher oxygen mass concentration at high temperatures overcompensate the lower B/Si ratio.

We want to compare the measured maximum oxygen fractions to the Wagner theory. In the Wagner theory the solid silica layer forms, when the SiO is above a threshold partial pressure and decomposes in Si and SiO_2. The partial pressure of SiO is about two times the oxygen pressure of the gas phase.

Degoulange [Deg08] calculated the dependence of the threshold partial oxygen pressure on the temperature using FactSage. Figure VII-23 shows his result together with the measurement. The calculated threshold dioxygen partial pressure at 1560 °C is 35 kPa which corresponds to an dioxygen fraction of 3.5%. The measured value is 7.1% and thus twice as high. At 1420 °C the threshold oxygen fraction of the calculation however is 0.55% and thus significantly lower than the measured fraction of 3.6 % at 1410 °C. The difference between the measured and the calculated threshold oxygen fraction indicates that the oxidation can not be described by the Wagner model. Wagner model predicts an increase of the maximum partial pressure with temperature but it largely overestimates the relative variation (Factor 2 in measurement and Factor 7 in Wagner model between 1410°C and 1560°C).

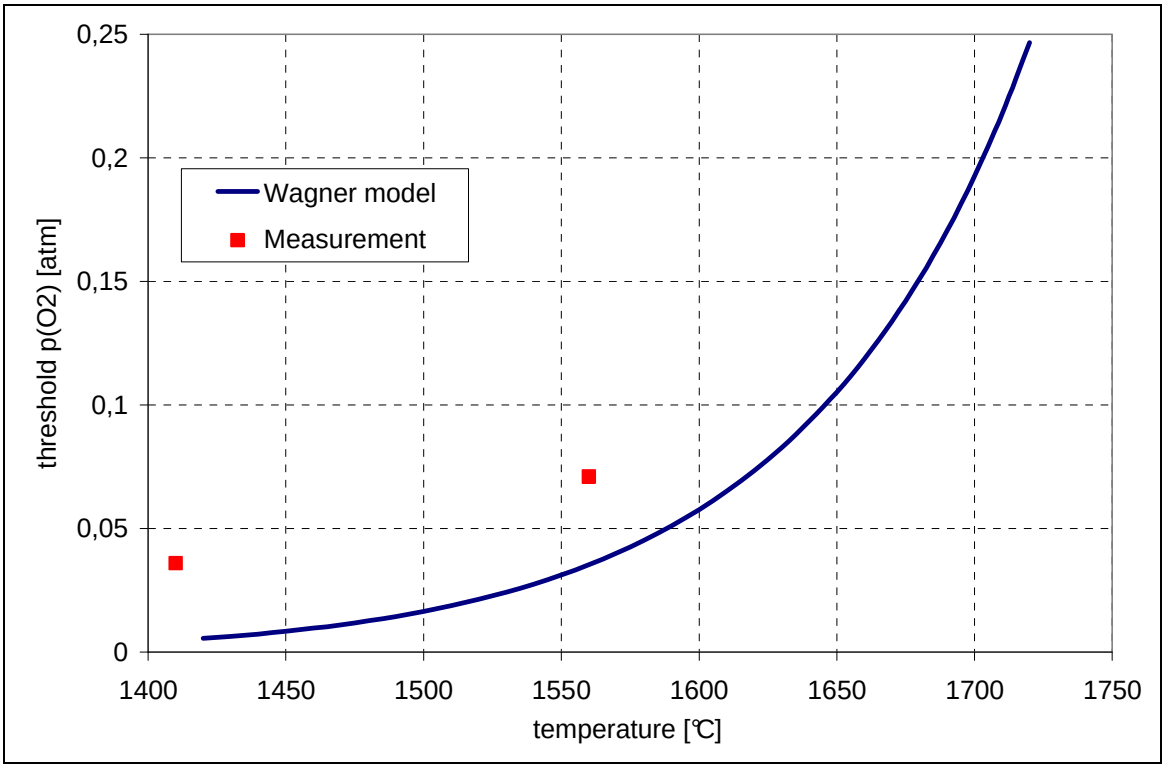

Figure VII-23 Threshold for the formation of the SiO_2 layer in dependence of the temperature.
Chemical equilibrium calculation for Wagner model: (700 Si + 1 Ar + <A> O_2) [Deg08]

VII.10.2. The influence of the gas velocity

We measured the threshold oxygen concentration for the formation of the silica layer in dependence of the gas velocity. We first set the argon flow and then increased the oxygen flow until the silica layer gets formed.

The results are presented in Table VII-13. The gas velocities are calculated with the total flow rate and the diameter of the nozzle. The measured threshold oxygen fraction decreases when the total flow rate increases. Figure VII-24 shows the threshold oxygen flow rate for the vertical nozzle and the inclined nozzle in dependence of the total flow rate. The oxygen flow rate increases with the total flow rate but they are not proportional. It is thus not sure whether the maximum mass transfer rate of oxygen towards silicon surface varies with the gas velocity.

At the same total flow rate the inclined nozzle has a higher threshold oxygen flow rate. This is not only due to the lower nozzle diameter which causes a higher velocity, because at the same velocity the threshold oxygen fraction for the inclined nozzle is more than twice the threshold for the vertical nozzle. The flow pattern, which depends on the angle of the jet and on the distance from the nozzle to the surface, should also play a role on the mass transfer properties of the boundary layer.

	Vertical Nozzle				Inclined Nozzle		
Total Flow rate [Nm^3/h]	1.3	2.3	3.8	6	1.2	2.2	3.5
Gas velocity [m/s]	9.1	16	27	44	26	48	78
Oxygen Flow rate [Nm^3/h]	0.089	0.14	0.18	0.23	0.16	0.2	0.23
Oxygen fraction	7.1%	6.2%	4.9%	3.9%	13%	9.1%	6.6%

Table VII-13 Dependence of the threshold oxygen fraction for the formation of the silica layer on the gas velocity.

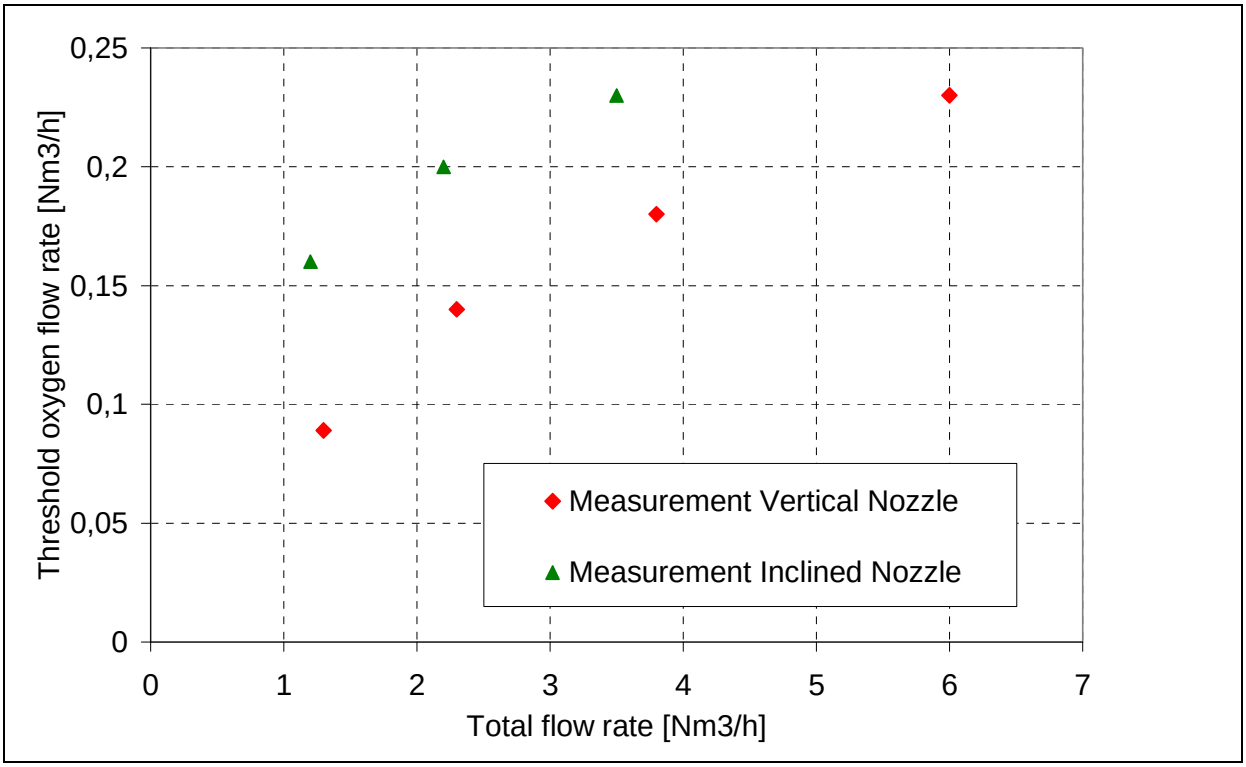

Figure VII-24 The dependence of the threshold oxygen flow rate on the total flow rate

VII.10.3. Discussion on the silica layer formation

The measurements have shown that the silica layer formation depends on the silicon temperature, the oxygen fraction and the gas velocity.

The measurements indicate that the higher maximum oxygen concentration at a higher silicon temperature can overcompensate the lower B/Si ratio. This issue was yet discussed in [FNP04] and [Deg08] but there is no exact experimental validation. The purification rate at different silicon temperatures at the limit of the silica layer formation should be thus verified experimentally.

The measurements are in contradiction with the Wagner model (chapter II) that predicts that the formation of the silica layer depends only on the oxygen fraction and the silicon temperature. It thus indicates that the Wagner model does not describe the oxidation in our conditions. The mass transfer rate from the gas to the surface and the mass transfer rate from surface to the gas have the same dependence on the gas velocity.

Turkdogans model predicts a dependence on the three parameters but we have seen in chapter II that it predicts a silica layer formation at much lower oxygen fluxes than in our setup. Eventually another reaction than the silicon evaporation in Turkdogans model is responsible for the silica layer formation. The reduction SiO_2 aerosol particles to SiO may be an example for a reaction that triggers the formation of the silica layer.

The oxidation of liquid silicon is thus a phenomenon that is not well understood so far. However this phenomenon has an important influence on the silicon purification. On the one hand it limits the silicon oxidation rate due to the formation of a silica layer. It thus also limits the boron removal rate which is proportional to the silicon oxidation rate. On the other hand the aerosol characteristics seem to modify the evacuated B/Si ratio and thus also the boron removal rate.

Therefore a theoretical understanding of the oxidation of liquid silicon is very important to find the optimal conditions for the silicon purification.

VII.11. Conclusion

We showed that the measurement of the ICP signal can measure accurately the purification rate with long term purification. The comparison of the purification of doped electronic grade silicon and the purification of metallurgical silicon showed that the interactions between boron and other impurities do not modify the purification rate. The parametric study allowed determining the parameters that have a significant influence on the purification rate. The silicon temperature, plasma power, hydrogen and oxygen concentration are parameters that have a significant influence on the purification rate. An experiment has shown that the oxidation due to dissolved oxygen from the crucible leads to a smaller B/Si ratio than the oxygen from the plasma. This indicates that the formation of a SiO_2 aerosol may be the reason why the measured B/Si ratio is higher than the chemical equilibrium B/Si ratio. By modifying the B/Si ratio, the SiO_2 aerosol also modifies the purification rate. The formation of the silica layer under a cold gas jet depends on the silicon temperature, the oxygen fraction and also on the gas velocity. This silica layer hinders the purification. It would be interesting to measure at which temperature the maximum purification rate can be obtained at the limit of the formation of the silica layer. A understanding of the silicon oxidation would be interesting both for the influence of the aerosol on the evacuation of the reaction products and for the maximum quantity of oxygen or water vapour that can be provided to the surface.

VIII. General conclusion

The objective of this study is a better understanding of the plasma refining process to reduce the boron content in silicon for solar cells. The process consists of a plasma torch that blows a mix of argon, oxygen and hydrogen at high temperature onto the surface of a silicon melt.

Processes based on segregation are not very efficient for the removal of boron due to its segregation coefficient close to one. Therefore there is a great interest for a boron removal process such as plasma refining. A combination of segregation and plasma refining may thus be an alternative to the Siemens process that is generally used for the purification of silicon (see chapter I). We identified that in order to make the process economically viable it is important to reduce the gas consumption and to scale up. Both could so far only done with empirical study because a fundamental understanding of the process is missing.

We present a simplified mass transfer model in chapter II. The boron as well as the silicon get oxidized by the water vapor. Convection, diffusion and chemical reactions determine thus the mass transfer and the purification rate. We give an overview on experimental results found in literature to identify the influence of different parameters on the purification rate. We examine the literature about the silicon oxidation which is the main reaction that takes place in the purification process. The silicon oxidation limits the water vapor flux that can be provided to the silicon surface because a silica layer gets formed when the water vapor flux is too high. We compare experimental results from literature to chemical equilibrium calculations and show that the chemical reactions at the surface are probably in equilibrium. This is in contradiction with most papers that suggest that the chemical reactions are the rate limiting step in the process. As the chemical reactions are at equilibrium the transfer of reactants to the surface and the evacuation of the reaction products remain as rate limiting steps. The formation of a silica aerosol may modify the evacuation of the silicon oxides. The gaseous boron compounds may diffuse stronger through the boundary layer than the silica aerosol particles. This theory can explain why the boron/silicon ratio found in exhaust gases is higher than that calculated at chemical equilibrium. The formation of a silica aerosol agrees with an oxidation model from literature and chemical equilibrium calculations. The total quantity of silicon that is oxidized is thus determined by the water vapor flux that arrives at the silicon surface. The boron flux that is evacuated from the silicon is determined by chemical equilibrium and probably also by characteristics of the silica aerosol.

For a better understanding of the process the characterization of the plasma torch is very important. In chapter III we discuss several methods for the characterization of the plasma. We identified the temperature, the concentration ratios O/Ar and H/Ar and the gas velocity as the parameters that are necessary to fully characterize the plasma. We compared several techniques and found that optical emission spectroscopy is best adapted for the measurement of the temperature and the O/Ar and H/Ar ratio in our plasma. For the measurement of the temperature we use the absolute line intensity method with Abel inversion. This method is often applied in literature. For the measurement of the concentration ratios we use the emissivity ratio between two lines. Such a method was rarely applied in literature and needs thus an experimental validation. We analyzed different line broadening mechanisms. The line broadening of the H-Beta and the H-Delta line can be

used to measure the electron density which gives us the possibility to validate the temperature measurement. Line broadening simulation is important when the spectral emissivity can be measured at only one wavelength at a time.

In chapter IV we present the experimental setups that were used for the spectroscopic measurements. We used two different plasma torches and two different optical setups. The first optical setup used a monochromator with photomultiplier tube and a rotating mirror. A second setup used a monochromator with a CCD camera and mirrors on translational stages. The second setup was especially developed for this application and allowed fast measurements of the whole post-discharge zone. We present the data processing that is used to obtain the radial temperature and concentration ratio profiles from a two dimensional spectrum using the theory presented in chapter III. In the same chapter we analyze several error sources. The stray light induces errors in the cold zone of the plasma. Interference fringes on the CCD camera and the non uniformity of the entrance slit have been taken corrected numerically so that they do not induce errors on the measurement.

In chapter V we present the spectroscopic measurements. Several measurements have been performed to test the validity and the precision of the method. The measurement of the electron density validated the temperature measurement but there is a difference of 300 K between the two methods. The injection of homogenous O_2/Ar and H_2/Ar mixtures showed that the concentration ratios O/Ar and H/Ar can be measured with an absolute accuracy of about 25% which is the accuracy of the transition probability of the argon lines. The measurements indicate that demixing occurs in the induction zone so that we do not know exactly the concentration in the validation experiments and can thus not validate the measurement more accurately. Fluctuations at the edge of the plasma induce errors on the concentration measurement in this zone. Once the measurement method was validated we used the characterizations to validate a computational fluid dynamics (CFD) model. The model was largely improved by using the k-ω-SST turbulent closure instead of the k-ε model that was used before. The model can be used to simulate the mass transfer towards the silicon surface. Several parametric measurements show the influence of different parameters on the concentration ratios and the temperature in the plasma.

In chapter VI we present other measurement methods that were developed for the characterization of the plasma. For the measurement of the flow velocity we filmed the fluctuations of the plasma with a high speed camera. However this method is not accurate enough to validate the velocity of the CFD model. We also analyzed the coupling between the plasma and the inductor. A good coupling is important to induce a high power into the plasma. We showed that oxygen and hydrogen reduce the coupling coefficient. We could show that the thermal conductivity is responsible for the reduction of the coupling coefficient and not the heat capacity. Hydrogen has a higher thermal conductivity so that it should be injected in the injector of the plasma torch where it does not influence the coupling. We also observed a hysteresis effect with two different modes at the same external parameters.

In chapter VII we perform measurements of the purification rate to test the theory that was developed in chapter II. The measured B/Si ratios in the exhaust gases are higher than at chemical equilibrium and indicate thus that boron is better evacuated from the surface than silicon. Two long time purifications showed that the interaction between other impurities and boron have no significant influence on the purification rate. A parametric study showed

the influence of different parameters on the purification rate. Equivalent to the literature experiments presented in chapter II we observe that the B/Si ratio in the exhaust gases depends on the silicon temperature and on the hydrogen fraction as predicted by chemical equilibrium (same relative dependence). We show that oxygen from the silica crucible and oxygen from the plasma lead to a different B/Si ratio. This is can be explained by the weak evacuation of the SiO_2 aerosol, thought to be also responsible for the measured B/Si ratio that is higher than the chemical equilibrium B/Si ratio. A study of the formation of the silica layer showed that the maximum oxygen concentration depends on the silicon temperature and on the flow velocity. The measured parameters for the formation of a silica layer do not agree with the existing models and show that there is a need for a better understanding of the oxidation of liquid silicon.

As we have shown that the radicals from the plasma probably are not necessary for the purification one should test whether similar efficiencies (gas & energy consumption) of the process can be obtained with a cold gas jet. For a fundamental understanding of both the plasma refining process and the cold gas blowing process a better understanding of the silicon oxidation is important. In a first step a numerical model such as that of Ratto [RRA01] with the addition of the aerosol diffusion may be developed. The diffusion coefficient may be obtained from the measured size of the aerosol particles. In a second step deviations from chemical equilibrium for example due to the slow aerosol condensation may be studied. The chemistry of boron may be added to such a model to better understand how the aerosol can modify the evacuated B/Si ratio. A simultaneous measurement of the aerosol particle size distribution and the enrichment factor with a cold gas jet may also give more information about the influence of the aerosol.

We have shown that the developed optical emission spectroscopy method can measure the temperature and concentration ratios. A concentration ratio measurement on a mixture of atomic gases (no demixing) may give more information on the precision of the method. The method may also be applied to characterize other processes that use inductively coupled plasma torches. Examples for other processes are spheroidization, nanosized powders synthesis, induction plasma spraying and waste treatment.

VIII.1. New concepts for the purification without plasma

The findings of the present study open the way for new concepts that may reduce significantly the costs of the process, but need yet to be validated. We present here concepts for the reactor that may facilitate the scale-up of the process.

VIII.1.1. Different jet geometries

The purification rate is proportional to the enrichment factor and the quantity of silicon that is oxidized which is equivalent to the quantity of water vapour that is furnished to the surface. The increase of the mass transfer of water vapour to the surface should thus increase the purification rate.

A way to increase the mass transfer at constant flow rate per surface area would be the use of a nozzle array. A first idea may be given by the paper from Martin [Mar77], who studied the heat and mass transfer of nozzle arrays as shown in Figure VIII.1 b) and c). For a given mean mass flow per surface area he found the optimal conditions for the nozzle

diameter (equation (VIII-1)) and the nozzle spacing (equation (VIII-2)) as function of the height H above the surface.

Nozzle diameter: $D = \frac{1}{5} H$ **(VIII-1)**

Nozzle spacing: $L = \frac{7}{5} H$ **(VIII-2)**

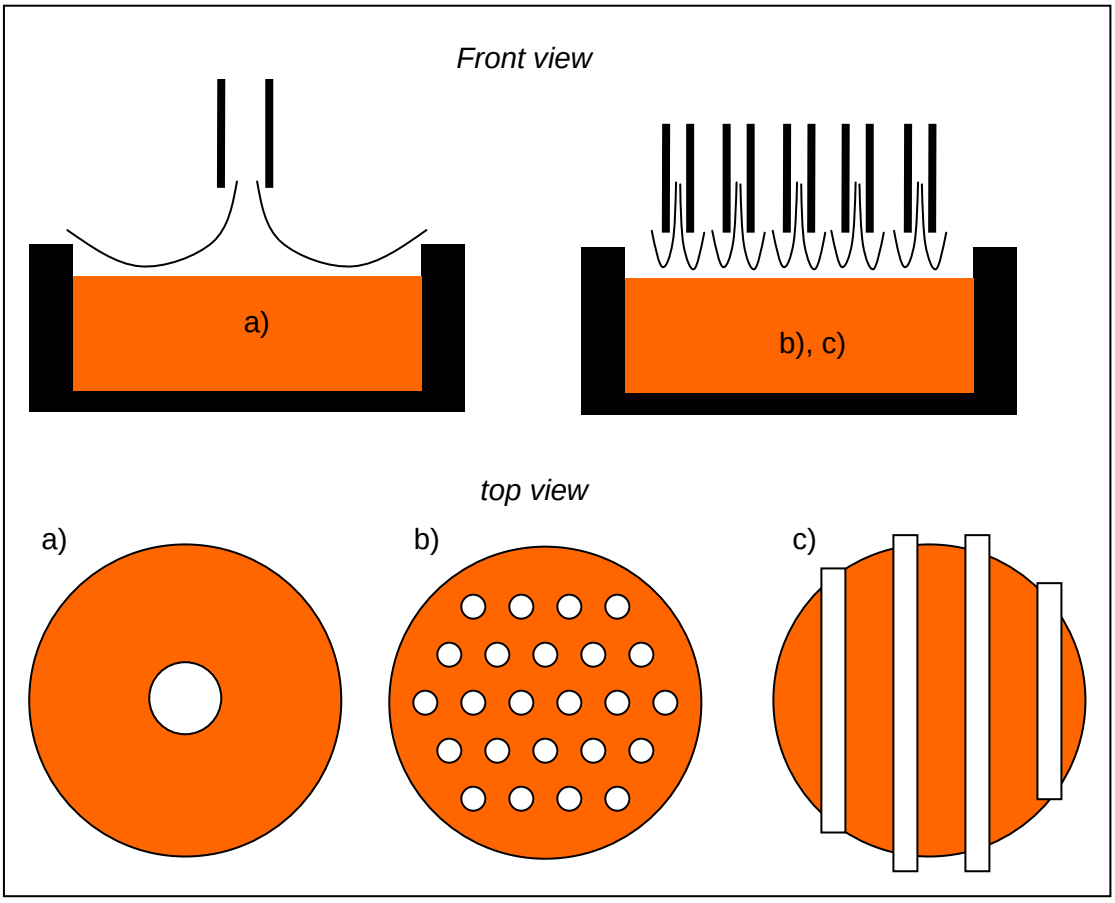

Figure VIII.1 New reactor designs a) single nozzle, b) multiple round nozzles c) multiple slot nozzles

At the optimal conditions the mean mass transfer is maximal. The optimal conditions are similar for slot nozzles (c) and round nozzles (d). The slot nozzles should be used when the impact velocity should not be too high. For the purification process a too high impact velocity leads probably to the ejection of silicon drops so that slot nozzles probably permit to obtain higher boron removal rates than round nozzles. When the nozzle diameter and the nozzle spacing are adapted, the mass transfer increases, when the height above the surface is reduced.

However it is not sure whether the formation of the silica layer limits the mass transfer of water vapour. This still needs to be validated. One needs also to validate whether recirculations reduce the enrichment factor.

VIII.1.2. Continuous purification of a thin silicon film

Reactors with a crucible with stirring have a limited silicon surface which may thus limit the flux of silicon that can be oxidized and thus the flux of boron that can be removed. A significant increase of the surface could be obtained by treating a thin silicon film on a substrate of silicon resistant material as suggested by the patent of Kurz et al. [KSG90]. The silicon film needs to be thin, so that diffusion homogenizes the boron concentration across the thickness of the silicon film. The substrate must have a high wettability and the velocity of the gas should not be too high, so that the film does not break up into drops. As silicon wets very well most of the materials the choice of the substrate is large. [KSG90] suggest ceramic, mixed ceramics, high density graphite or quartz glass. A difficult task is to assure that the thin film flows everywhere with the same velocity, otherwise pure silicon would be mixed with less pure silicon at the bottom. Another difficult task is probably to maintain the substrate at a uniform constant temperature. We suggest two thin film reactor geometries.

Counter flow reactor

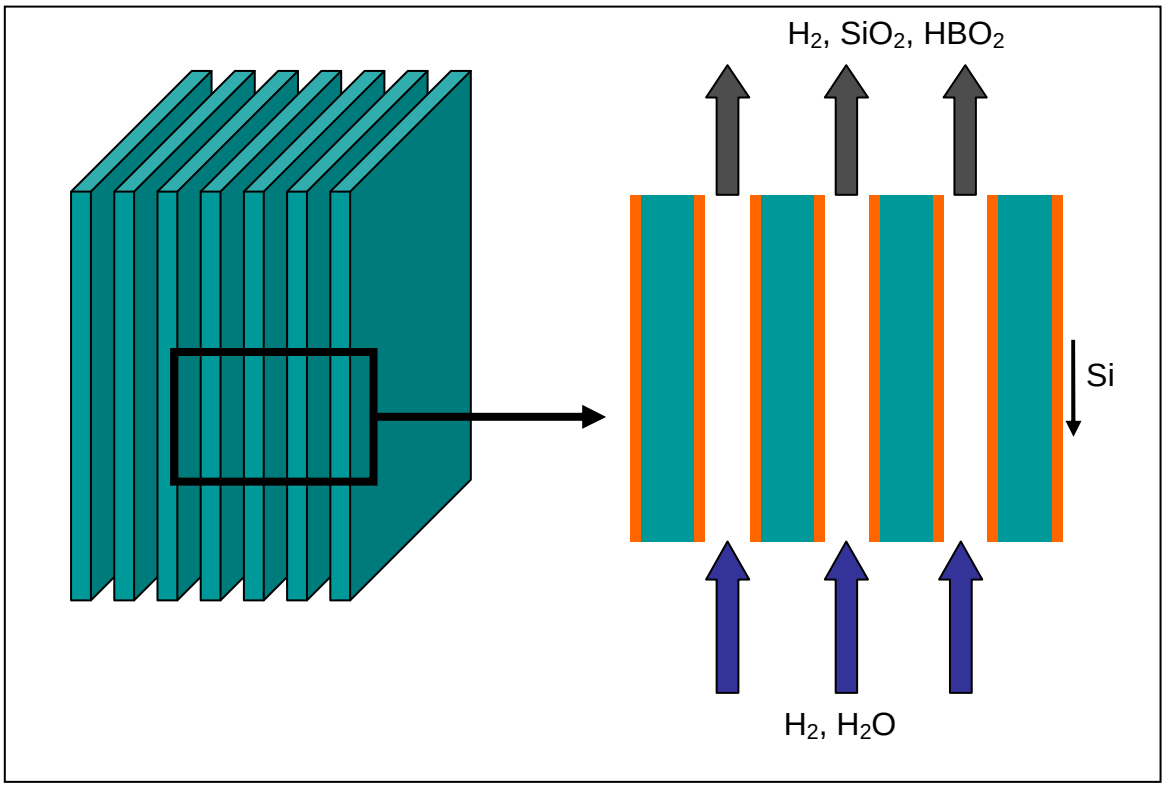

Figure VIII.2 New reactor design, purification of a thin silicon film in counter flow reactor

By assembling several plates one next to another as shown in Figure VIII.2, one can obtain a large silicon surface. The silicon film flows downwards while the gas flow goes upwards (counter flow reactor).

We want to compare the gas consumption per kg of purified silicon of such a setup to the gas consumption of the plasma refining process with a silicon melt. We assume that the silicon concentration in the exhaust gas is equal in the two processes. In this case the gas

consumption is inverse proportional to the mean [B(g)]/[Si(g)] ratio in the gas phase. The ratio [B(l)]/[Si(l)] is the boron concentration of the raw material. In the plasma refining process, the boron concentration in the gas decreases with the time. For a purification of a factor 16 the mean [B(g)]/[Si(g)] ratio is about one third of the [B(g)]/[Si(g)] ratio at the beginning. (VIII-3). For the counter flow process the gas consumption is independent of the degree of purification. The [B(g)]/[Si(g)] ratio is given by the chemical equilibrium if the mass transfer between liquid and gas is efficient (VIII-4).

$$mean\left(\frac{[B(g)]}{[Si(g)]}\right) = R_{\exp} \times \frac{[B(l)]}{[Si(l)]} \times \frac{1}{T \times \ln 16} \int_0^{T \times \ln 16} e^{-\frac{t}{T}} dt = 0.34 \times R_{\exp} \times \frac{[B(l)]}{[Si(l)]} \qquad \textbf{(VIII-3)}$$

$$\frac{[B(g)]}{[Si(g)]} = R_{chem\ equ} \frac{[B(l)]}{[Si(l)]} \qquad \textbf{(VIII-4)}$$

As the experimental enrichment factor is about six times higher than the enrichment factor at chemical equilibrium, the mean [B(g)]/[Si(g)] ratio with plasma is about twice as high as the counter flow reactor. The gas consumption is thus only half of the counter flow reactor. The further enrichment with boron in the counter flow reactor can thus not balance the higher experimental enrichment factor which is probably due to the slow diffusion of the SiO_2 aerosol. However we do not know whether the high enrichment factor that can be obtained with plasma may also be obtained with a cold gas jet. Eventually a counter flow reactor is more efficient than an array of gaz nozzles.

Thin film reactor with multiple nozzles

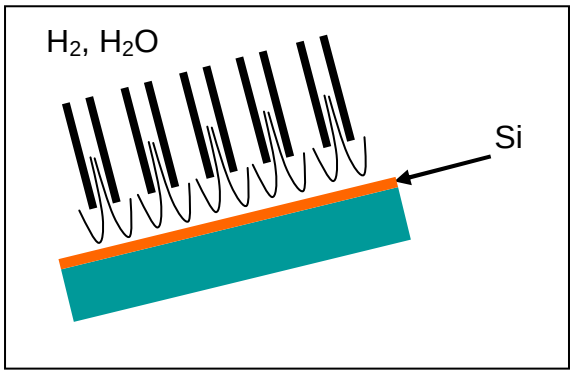

Figure VIII.3 New reactor design, purification of a thin silicon film with multiple nozzles

While the continuous treatment with a plasma torch is rather complicated due to the inhomogeneous mass transfer and the high heat transfer this may be simpler with a multiple nozzle array. Figure VIII.3 shows the schema of such a setup. The multiple nozzle array blows the hydrogen and water vapour onto the silicon surface.

In comparison to a reactor with gas nozzles above a silicon melt in a crucible, such a reactor may have a lower cost per surface area. The gas consumption per kg of purified silicon should be similar to the gas consumption of a reactor with a silicon melt.

A. Appendix A: About local thermal equilibrium

A.1. Local thermal equilibrium

For the plasma diagnostics that we use in this study the concept of local thermal equilibrium is very important. A good understanding of this concept is therefore crucial for the interpretation of the measurement results. We begin with the presentation of the processes that are important for the establishment of thermal equilibrium in a gas at about 10000 K at atmospheric pressure. Then we present the concept of complete thermal equilibrium as it is the best way to understand the energy distributions of the particles. After that we present the concepts of local thermal equilibrium (LTE) and partial local thermal equilibrium (pLTE).

A.1.1. The microscopic processes

We present the microscopic processes that take place in a gas at high temperature.

$$e + A \leftrightarrow A' + e'$$

Elastic collision

In an elastic collision two different or similar particles can exchange kinetic energy.

$$A(j) \leftrightarrow A(i) + h\upsilon .$$

Emission ↔ Absorption

An excited atom in an energy level *j* can make a spontaneous transition to a lower energy level *i* by emission of a photon. The inverse process is the excitation of the atom by absorption of a photon. The energy modes excitation and radiation can exchange energy through this process.

$$e + A(0) \leftrightarrow A(j) + e'$$

Inelastic collision

In an inelastic collision an electron loses kinetic energy when colliding with an atom while the atom gains excitation energy. For this process the kinetic energy of the electron must be higher than the difference between the two energy levels. In the inverse process the electron gains kinetic energy while the atom loses excitation energy.

$$\underline{e} + A(i) \leftrightarrow e' + A^{+}(j) + e''$$

Ionization ↔ Three body Recombination

An excited atom can be ionized by the collision with an electron. Ionization of ground state atoms is very rare because the ionization energy (15.75 eV for Ar) is very high compared to the mean kinetic energy of the electrons (1.3 eV at 10000 K). The inverse process is the three body recombination. The energy modes excitation, ionization and kinetic energy of the electrons can exchange energy through this process.

$$h\upsilon + A(i) \leftrightarrow A^{+}(j) + e$$

Photoionization ↔ Radiative recombination

Photoionization is the ionization of an excited atom with the absorption of a photon. The inverse process is the radiative recombination. The energy of the photons must be higher than the ionization energy for the excited state. The energy modes excitation, ionization and radiation can exchange energy through this process.

$$A + h\upsilon + e \leftrightarrow A + e'$$

Photoabsorption ↔ Bremsstrahlung

When an electron collides with a particle it is accelerated and emits Bremsstrahlung. The inverse process is Photoabsorption. The energy modes kinetic energy and radiation can exchange energy through this process.

A.1.2. Complete thermal equilibrium

When we put a gas into a cavity with constant wall temperatures T it tends to maximize its entropy according to the second law of thermodynamics. Once it has achieved the maximum entropy all microscopic processes that are described above are as frequent as their inverse processes and the gas is in complete thermal equilibrium. As all these processes are in detailed balance, the energy distributions of the particles remain constant and they depend on only two thermodynamic variables: the temperature T and the pressure p.

The energy distribution for distinguishable particles with the highest entropy for a fixed total energy is the Boltzmann distribution. The kinetic, the excitation and the ionization energy modes follow therefore Boltzmann distributions. The only difference between the three distributions is the state density which depends on the energy.

For the Boltzmann-distribution of the population of the energy levels the state density is the degeneracy g_j and $Z(T)$ is the normalization factor.

$$n_j = \frac{n_{tot} \cdot g_j \cdot e}{Z(T)} \exp\left(\frac{-E_j}{k_B T}\right) \tag{A-1}$$

The Maxwell-Boltzmann distribution for the velocity v of particles with a mass m has a state density which is homogeneous in momentum space. Therefore there is a factor v^2 (surface of a sphere in momentum space) and $\sqrt{2/\pi \cdot m^3/(k_B T)^3}$ is the normalization factor.

$$f(v)dv = \sqrt{\frac{2}{\pi}\left(\frac{m}{k_B T}\right)^3} v^2 \, exp\left(\frac{-mv^2}{2k_B T}\right) dv \tag{A-2}$$

The Saha ionization equation gives the ratio between two consecutive ionization stages with an ionization energy χ_Z. Z counts the ionization stages. n_0 is the neutral atom density, n_1 the singly ionized atom density and so on. n_e is the electron density. The Saha ionization equation is similar to the Boltzmann-distribution of the energy levels but one has to include the state density $(2\pi m_e k_B T)^{3/2}/h^3$ and the spin degeneracy 2 of the free electron. $Z_Z(T)$ is the partition function of the ionization stage Z.

$$\frac{n_{Z+1} n_e}{n_Z} = 2\frac{Z_{Z+1}(T)}{Z_Z(T)} \frac{(2\pi m_e k_B T)^{3/2}}{h^3} exp\left(\frac{-\chi_Z}{k_B T}\right) \tag{A-3}$$

For argon at atmospheric pressure and 10000 K we can use the assumptions of quasineutrality $n_e = n_1$, small degree of ionization $n_0 = n_{tot}$ and insignificant concentration of multiply ionized ions $n_{z>1} = 0$. In this case, the equation can be simplified to:

$$n_e^{Saha}(T) \approx \sqrt{n_{tot} 2\frac{Z_{ion}(T)}{Z_{atom}(T)} \frac{(2\pi m_e k_B T)^{3/2}}{h^3} \exp\left(\frac{-\chi_1}{k_B T}\right)} \tag{A-4}$$

The photons however do not follow a Boltzmann distribution because two photons with the same energy are not distinguishable. Planck's Law (A-5) which gives the distribution of the photons is based on Bose-Einstein statistics

$$I(\lambda)d\lambda = \frac{2hc^2}{\lambda^5} \frac{1}{e^{hc/(\lambda k_B T)} - 1} d\lambda \tag{A-5}$$

A.1.3. Local thermal equilibrium (LTE)

In a plasma the conditions for complete thermal equilibrium are practically impossible to fulfill. Temperature and density gradients are almost always present. For this reason, thermal equilibrium can only be defined locally. At each point the system increases its local entropy so that the local energy distributions approach the equilibrium distributions. Transport phenomena causes deviations from the maximal local entropy and therefore from the equilibrium distributions. In the case considered here, the deviations are mainly caused by the fact that photons can leave the system.

The term local thermal equilibrium (LTE) was first used to describe the plasma in the interior of the sun where the scale of the temperature gradient is small compared to the mean free path of material particles and photons. In this case it is possible to define regions in which the energy distributions of the particles are nearly the same as in complete thermal equilibrium; however, the density and temperature depend on the position in the plasma.

Later LTE was also used to describe laboratory plasmas where the mean free path of photons is very long but the mean free paths of material particles are still short compared to the scale of the temperature gradient. In this case photo ionization/radiative recombination and emission/absorption are no longer in equilibrium. The radiation transport reduces the number of ions and highly excited atoms. If the collision rates are sufficiently high the collisional processes elastic collision, super-elastic collision and ionization are still in detailed balance. This is the case in a collision dominated plasma. That means that the Saha-equilibrium for the ionization, the Maxwell-Boltzmann-Distribution for the material particle velocity and the Boltzmann-Distribution for the excited states remain valid and all distributions have the same temperature T at each coordinate. As the mean free path of the photons is very important for LTE on the one hand and the spectroscopic measurement on the other hand we examine the radiative transport equation.

A.1.4. Radiative transport equation:

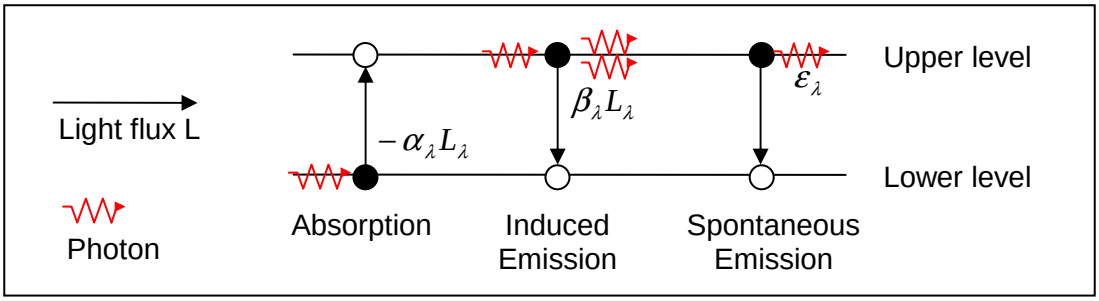

Figure A.1 Radiative sources and sink of an atomic line

The radiative transport equation is a continuity equation with the source terms spontaneous emission ε_λ and induced emission $\beta_\lambda L_\lambda$ and the sink term absorption $-\alpha_\lambda L_\lambda$ (see

Figure *A.1*). For a one dimensional system the equation (A-6) describes the radiative transport. The index λ stands for the wavelength dependence of the coefficients. In a three dimensional system one has to take into account the solid angle and the direction of a light beam.

$$\frac{dL_\lambda}{dx} = \varepsilon_\lambda - (\alpha_\lambda - \beta_\lambda)L_\lambda \qquad \text{(A-6)}$$

We replace the induced emission and the absorption by an effective absorption $\alpha'_\lambda = \alpha_\lambda - \beta_\lambda$:

$$\frac{1}{\alpha'_\lambda}\frac{dL_\lambda}{dx} = \frac{\varepsilon_\lambda}{\alpha'_\lambda} - L_\lambda \tag{A-7}$$

The homogeneous solution $dL^h_\lambda / dx = 0$ of the radiative transport equation is the ratio $\varepsilon_\lambda / \alpha'_\lambda$. It describes radiation in thermal equilibrium. For atomic line emission we can write:

$$\frac{\varepsilon_\lambda}{\alpha'_\lambda} = \frac{c^2}{4\pi\lambda^2}\frac{A_{ul}n_u}{B_{lu}n_l - B_{ul}n_u} = \frac{c^2}{4\pi\lambda^2}\frac{A_{ul}}{B_{ul}}\frac{n_u}{n_l - n_u} = \frac{2hc^2}{\lambda^5}\frac{n_u}{n_l - n_u} \tag{A-8}$$

We can replace the emission coefficients by the Einstein coefficients and use the relation $B_{ul} = B_{lu}$ and $A_{ul}/B_{ul} = 8\pi h/\lambda^3$. The indices u and l stand for the upper and lower energy level. When we use the Boltzmann distribution of the excited state which is valid in a collision dominated plasma we obtain the Blackbody radiation for the ratio $\varepsilon_\lambda / \alpha'_\lambda$.

$$\frac{\varepsilon_\lambda}{\alpha'_\lambda} = \frac{2hc^2}{\lambda^5}\frac{1}{e^{hc/(\lambda k_B T)} - 1} = B_\lambda \tag{A-9}$$

This relationship is known as Kirchhoff's law. It is valid when the radiation source is in thermal equilibrium. The link between the emission coefficient ε_λ and the effective absorption coefficient α'_λ assures that there is no net energy transport between two media at the same temperature, which is forbidden as a result of the second law of thermodynamics.

We can now look for the particular solution of the radiative transport equation:

$$\frac{1}{\alpha'_\lambda}\frac{dL^p_\lambda}{dx} = -L^p_\lambda \quad \rightarrow \quad L^p_\lambda = c' \times exp(-\alpha'_\lambda x)$$

The general solution, the sum of homogenous and particular solution is given by (A-9) where the constant c is defined by the boundary conditions. ($c = 1$ for $L_\lambda(0) = 0$)

$$L_\lambda(x) = L^h_\lambda + L^p_\lambda = B_\lambda(1 - c \times \exp(-\alpha'_\lambda x)) \tag{A-10}$$

The parameter $\int_x^{x+\Delta x} \alpha'_\lambda dx$ where Δx is the size of the medium is called the optical thickness. In an optically thin medium absorption is negligible while in an optically thick medium emission and absorption are in equilibrium and the intensity is given by the blackbody radiation spectrum. The mean free path of a photon is $1/\alpha'_\lambda$.

We want to calculate the mean free path of the photons of the atomic lines of argon. Therefore we use the emission coefficient and Kirchhoff's law.

The global emission coefficient of an atomic line is

$$\varepsilon_{line} = \int_{line} \varepsilon_\lambda d\lambda = \frac{n_{tot} \times g_u \times e^{-E_u/k_B T}}{Z(T)} \times A_{ul}\frac{hc}{4\pi\lambda} \tag{A-11}$$

The wavelength dependent emission coefficient depends on the line profile $P(\lambda)$ which depends on line broadening $\varepsilon_\lambda = P(\lambda) \times \varepsilon_{line}$.

$$\frac{1}{\alpha'_\lambda} = \frac{B_\lambda}{\varepsilon_\lambda} = \frac{B_\lambda}{P(\lambda) \times \varepsilon_{line}} \tag{A-12}$$

The atomic line has a high emissivity in the centre of the line and a low emissivity at the edge of the line. Therefore the photons at the centre wavelength have a shorter mean free path than the photons at the edge of the line.

In order to estimate the magnitude of the mean free path of a photon we use a very unrealistic rectangular line broadening with a width of 10^{-3}nm which is the width that has been calculated by Lacombe (page 63 [LAC08])

The mean free path of the photons is then

$$\frac{1}{\alpha'_\lambda} = \frac{B_\lambda \times 10^{-3} nm}{\varepsilon_{line}} = \frac{Z(T)}{n_{tot} \times g_u} \times \frac{8\pi}{A_{ul}} \frac{c}{\lambda^4} \frac{10^{-3} nm}{e^{-E_l / k_B T} - e^{-E_u / k_B T}} \tag{A-13}$$

In Table A-1 we show that all lines that correspond to transitions to the ground state have a very short mean free path (< 1 µm). We also show, using some typical lines as examples, that the mean free paths of lines corresponding to transitions to excited states can have all orders of magnitude between 0.1 µm and 10 m. Lines with long mean free paths have a small transition probability.

Lambda [nm]	A_{ul} [1/s]	E_l [eV]	E_u [eV]	g_u	Mean free path [m]	
					10000 K	8000 K
104.8	5.10E+08	0.00	11.83	3	5.63E-08	4.50E-08
86.7	3.13E+08	0.00	14.30	3	1.96E-07	1.57E-07
87.6	2.70E+08	0.00	14.15	3	2.18E-07	1.74E-07
106.7	1.19E+08	0.00	11.62	3	2.25E-07	1.80E-07
88.0	7.70E+07	0.00	14.09	3	7.51E-07	6.01E-07
87.0	3.50E+07	0.00	14.26	3	1.73E-06	1.38E-06
811.5	3.31E+07	11.55	13.08	7	8.24E-05	1.75E-03
965.8	5.43E+06	11.62	12.91	3	6.83E-04	1.46E-02
1300.8	8.90E+06	13.30	14.26	3	1.03E-03	3.49E-02
2397.3	3.60E+05	13.33	13.85	1	1.01E-02	3.30E-01
1146.8	369000	13.15	14.23	5	1.94E-02	6.37E-01
557.3	660000	13.09	15.32	7	1.00E-01	3.46E+00
594.9	150000	13.28	15.37	3	1.00E+00	3.62E+01
442.4	7300	11.72	14.52	3	1.04E+01	2.45E+02

Table A-1 Mean free path of some argon lines

Energy transport by radiation is very complicated to take into account in numerical modeling of the plasma that is examined here. Photons with very long mean free paths can be taken into account by treating them as energy sinks (they leave the plasma without interaction) and photons with very short mean free paths can be taken into account by a thermal diffusion coefficient. For the others one has to take into account details of emission and absorption. As the global absorption and emission coefficient and the line profile depend on the temperature a precise modeling is very complicated. Further information can be found in the thesis of Lacombe [LAC08].

For the spectroscopic measurement of the emissivity it is important to use atomic lines with very long mean free path. Otherwise absorption would cause errors. We use a taylor serie for the exponential of the solution of the radiative transport equation (A-9) and get equation (A-14)

$$L_\lambda(x) = B_\lambda(1-(1-\alpha'_\lambda x + (\alpha'_\lambda x)^2 ...)) \tag{A-14}$$

For $\alpha'_\lambda x < 0.01$ the quadratic term is 99% smaller than the linear term and can therefore be neglected. We find then for the intensity the equation (A-15) which depends only on the

emissivity. We can apply the criterion $\alpha'_\lambda x < 0.01$ to the ICP that we study which has a width of about 0.04 m and find thus a minimal mean free path of $1/\alpha'_\lambda > 4m$

$$L_\lambda(x) = B_\lambda \alpha'_\lambda x = \varepsilon_\lambda x \tag{A-15}$$

A.1.5. Departure from LTE

Departure from LTE is always due to energy transport. In an ICP at atmospheric pressure there are three transport modes that can affect LTE:

- Application of an electric field to supply energy
- Loss of energy by radiation
- Transport of energy by the ambipolar diffusion of electrons and ions due to high temperature gradients

The departure is important when reactions that are responsible for the equilibrium are too slow to distribute the energy uniformly. Reactions with a small energy transfer rate that can be out of equilibrium are on the one hand the collisions between electrons and heavy particles and on the other hand the collision induced excitation of atoms in the ground state together with its inverse reaction.

Two temperature for heavy particles and electrons

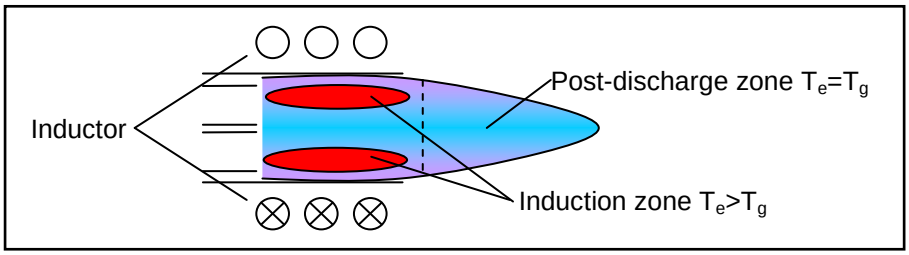

Figure A.2 Induction zone and post-discharge zone of an inductively coupled plasma (ICP)

The energy transfer between electrons and heavy particles by elastic collisions is not very efficient because of the small mass ratio. If either the electrons or the heavy particles lose or win energy, the energy balance between them is disturbed. The energy balance for electrons and for heavy particles is still maintained at different temperatures for each of them. So the Maxwell-Boltzmann velocity distribution is still valid but with a different temperature T_e for the electrons and T_g for the heavy particles. In inductively coupled plasma this phenomenon occurs in the induction zone, because nearly all the energy that is supplied by the electric field is absorbed by the electrons as their mass is much smaller than the mass of the ions. The difference between these two temperatures can be calculated with the formula given in the book “Plasma Diagnostics” [LR68] Chapter 3 page 147:

$$\frac{T_e - T_g}{T_e} = \frac{(\lambda eE)^2}{(\frac{3}{2}k_B T_e)^2}\frac{m}{4m_e} \tag{A-16}$$

λeE is the energy that each electron gains from the electric field between two collisions (λ mean free path of the electron) and $\frac{3}{2}k_B T_e$ is the average thermal energy of the electron. This departure from LTE is important in the induction zone where the induction coil induces a current in the plasma (See Figure A.2). We find the characteristic time for the establishment of kinetic equilibrium between electrons and heavy particles with a formula given in the same book:

$$\tau \approx \left(7.5 \times 10^{-7} (\chi_1 / k_B T)^{\frac{3}{2}} n_e \right)^{-1} \times \frac{m}{m_e} \text{ sec} \quad \text{(A-17)}$$

$\chi_1 = 15.75 eV$ is the ionization energy of argon and n_e is the electron density in cm^{-3} which can be calculated with the Saha ionization equation. We get for the characteristic time $2 \times 10^{-7} s$ at 10000 K. The flow time ($> 1cm / 100\, m/s = 10^{-4} s$) of the hot zone from the induction zone to the post-discharge zone is large compared to this characteristic time. In the post-discharge zone the kinetic temperature should be thus the same for electrons and heavy particles. This deviation should therefore not influence the measurements. Regt [RGM96] measured in a 1.2 kW ICP a heavy particle temperature of 3000-5000 K and an electron temperature that was 1000-2000 K higher 7 mm after the coil. This agrees with the characteristic time that is with 8×10^{-4} sec much higher than at 10000 K.

Partial LTE (pLTE)

In LTE the excited levels are in equilibrium with the neutral ground level (Boltzmann equilibrium (A-18),(A-20)) and with the ion ground level (Saha equilibrium (A-19), (A-21)). A frequently occurring deviation from LTE is partial LTE (pLTE). If a plasma is in pLTE the excited levels are in equilibrium with the ion ground level but the neutral ground level is not in equilibrium with those levels ((A-20) and (A-21) remain valid for i,j>1). This is probable, when the excited levels are close to the ionization energy and far from the ground level, as it is the case for Ar, O and H. The reaction rate of (A-18) is then much slower than the reaction rate of (A-19) because of the smaller energy gap.

$$X(1) + \underline{e} \leftrightarrow X(i) + e \quad \text{(A-18)}$$

$$X^+(1) + e + e \leftrightarrow X(i) + \underline{e} \quad \text{(A-19)}$$

$$\frac{n_i}{n_j} = \frac{g_i}{g_j} \exp\left(-\frac{E_i - E_j}{k_B T} \right) \quad \text{(A-20)}$$

$$\frac{n_e \times n_1^+}{n_i} = \frac{2 g_1^+}{g_i} \left(\frac{2\pi m_e k T}{h^2} \right)^{3/2} \exp\left(-\frac{\chi_1 - E_i}{kT} \right) \quad \text{(A-21)}$$

The disequilibrium can be caused by an electric field, radiative energy losses or ambipolar diffusion of ions and electrons. As the concentration of the ion ground level is much higher than the concentration of the excited levels the transport of excited levels does not cause deviations from LTE. (In LTE at 9000 K only 5 ppm of the Ar atoms are in an excited state while 6600 ppm of the atoms are ionized). In a recombining plasma the ion density is higher than in equilibrium, while in an ionizing plasma the ion density is lower than in equilibrium. Nowak [NMS88] measured the excitation temperature and the electron density and showed that the ICP is ionizing next to the induction zone and recombining in the post discharge zone. (Figure A.2). Due to energy losses the ion ground level and the excited levels are overpopulated in the post discharge zone.

Figure A.3 shows a simplified scheme for the energy exchange of a recombining plasma in pLTE. The kinetic energy of the electrons and the heavy particles is in equilibrium with the excited levels and the ion ground level. The system loses energy by radiation of the electrons (Bremsstrahlung) and of the excited levels. The electrons can transfer by collisions the energy between the heavy particles and the excited states so that they remain in equilibrium and cool down simultaneously. The transition from the excited state to the ground state,

however, is slow and forms therefore a bottleneck. The concentration of the ground state atoms is thus not in equilibrium with the concentration of the excited states and the ions.

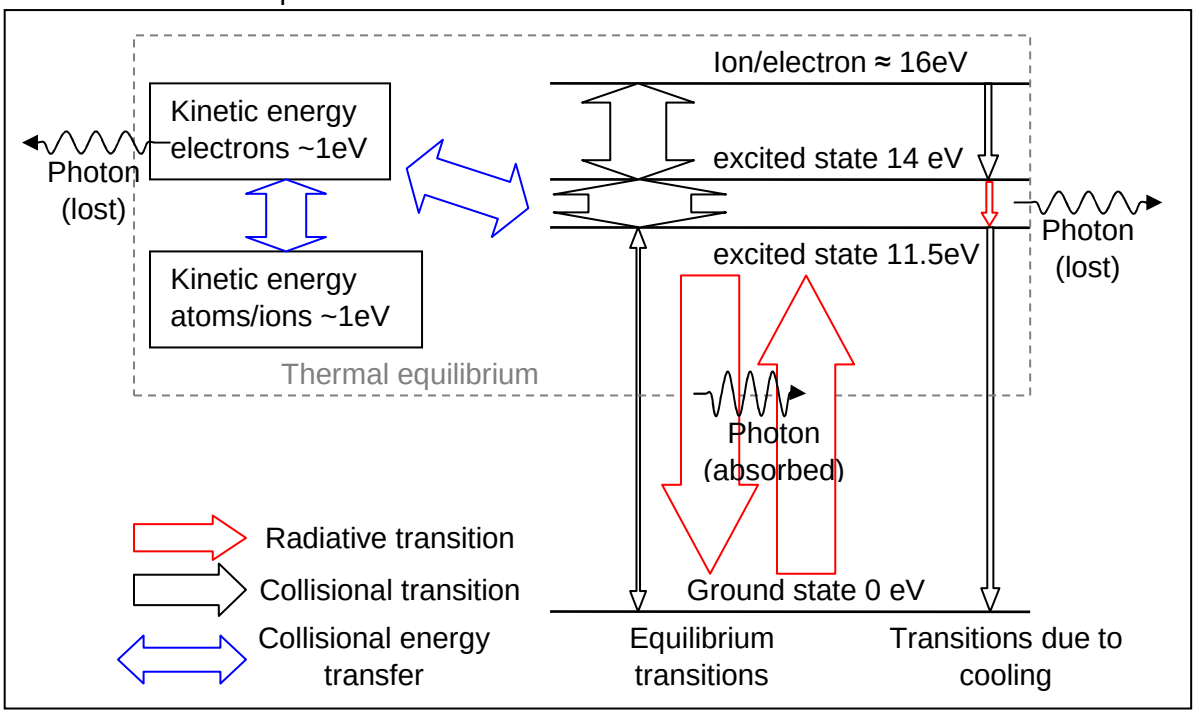

Figure A.3 Simplified scheme for the transitions of Ar plasma in pLTE

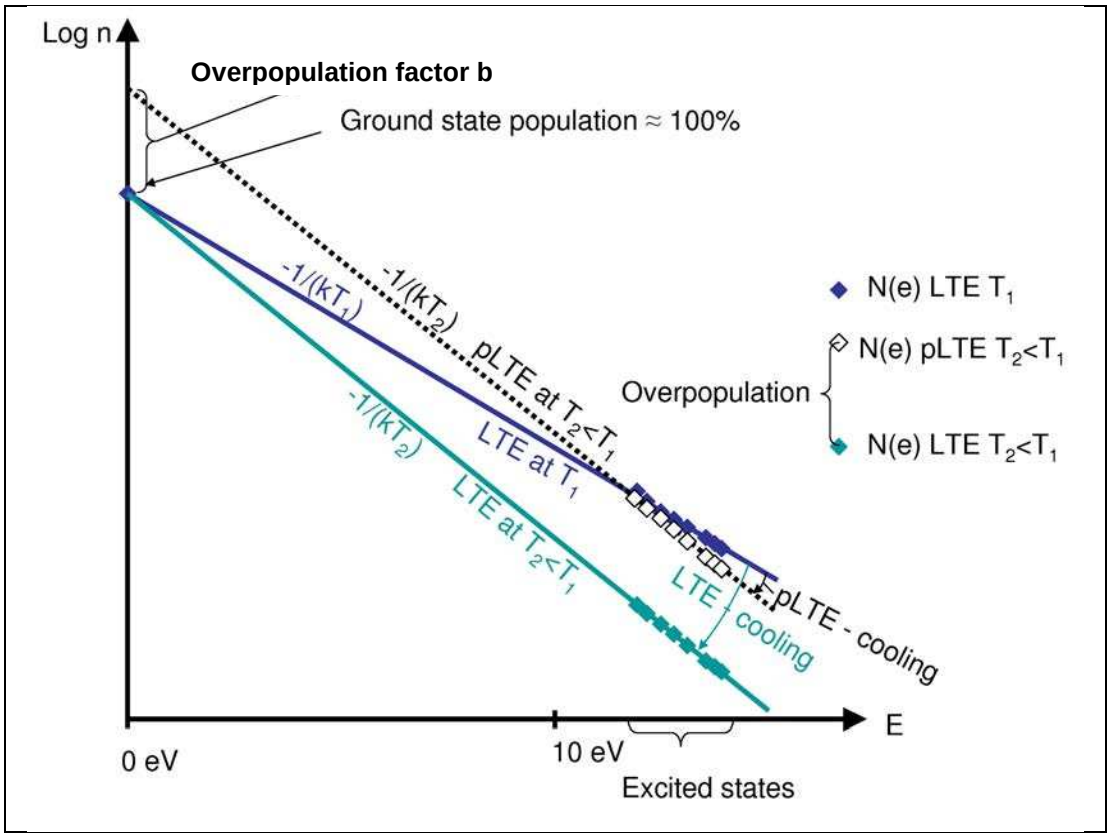

Figure A.4 Difference between slow (LTE) cooling and fast (pLTE) cooling

Although in typical atmospheric ICP conditions the neutral ground level concentration is almost the same for LTE and pLTE (close to 100%) it is more convenient to define one overpopulation factor b for the ground level, than to define two overpopulation factors for the

excited levels and the ions. (Recombining plasma $b<1$, Ionizing plasma $b>1$, LTE $b=1$) The Boltzmann equilibrium of LTE (A-20) remains valid for i>1 in pLTE but it must be modified for the neutral ground level (A-22). The overpopulation of the excited levels is then given by $1/b$ (A-23) and the overpopulation of the ion ground level by $1/\sqrt{b}$ (A-24).

Figure A.4 shows the Boltzmann plot of a plasma in LTE at a temperature T_1 that cools down to a temperature T_2. When the plasma cools down slowly the balance between the ground state atoms and the excited atoms is maintained and the plasma remains in LTE. The new boltzmann plot is similar to the first with a different slope. When the plasma cools down rapidly the reaction between the ground state and the excited states can not follow so that the concentrations are not balanced anymore. The slope of the Boltzmann plot is the same than in LTE but it does not cross the ground state concentration which does not vary because it is close to 100%. The excited states and the ion ground level are overpopulated compared to the LTE at the temperature T_2.

$$\frac{n_i}{n_1}=\frac{1}{b}\times\frac{g_i}{g_1}\exp\left(-\frac{E_i-0}{k_BT}\right) \qquad \text{(A-22)}$$

$$n_i=\frac{g_i}{b}\times\frac{1}{Z_{pLTE}(T)}\exp\left(-\frac{E_i}{k_BT}\right) \qquad \text{(A-23)}$$

$$n_1^+(T)=\frac{1}{\sqrt{b}}n_1^{+,Saha}(T) \qquad \text{(A-24)}$$

n_1	atom in the neutral ground level
n_i	atom in the excited level i
n_1^+	singly ionized atom in the ground level
χ_1	ionization energy
e	electron
$\underline{e}$	electron with high kinetic energy
b	overpopulation factor of the ground level

$$Z_{pLTE}(T)=g_1+\sum_{i>1}\frac{g_i}{b}\times\exp\left(-\frac{E_i}{k_BT}\right)$$

The deviation of the ion density from equilibrium of different elements is different depending on the equilibrium ion density and the reaction rates between the ion ground level and the neutral ground level. Therefore the overpopulation factor b is different for different elements and may therefore induce an error on measurements that use LTE.

As the measured concentration ratio is proportional to the concentration ratio of the excited levels, the relative error induced by the overpopulation is b_{Ar}/b_O-1 for the [O]/[Ar] ratio and b_{Ar}/b_H-1 for the [H]/[Ar] ratio.

In order to give an estimation for the overpopulation factor we refer to Nowak [NMS88] who showed with measurements of excited states populations and electron densities that the overpopulation factor b_{Ar} is between 0.1 in recombining regions and 10 in ionizing regions of an ICP similar to the small ICP used in this study. A detailed study of the influence of the recombination on the overpopulation factors can be obtained with a collisional-radiative model. Hasegawa [HH85] developed a collisional-radiative but he did not calculate the level

densities for an recombining plasma that is optically thick for the resonance lines, as it is the case in the plasma that have been studied here.

Equation (A-25) shows that at an excited state at 14.5 eV has the same population at 9000 K with $b = 1$, at 8013 K with $b = 0.1$ and at 10264 K with $b = 10$. As our temperature measurement is based on the population of an excited state, the error that can be induced by an overpopulation factor $b = 10$ or $b = 0.1$ is about 1000 K.

$$\frac{g_i}{1} \times \exp\left(-\frac{14.5eV}{k_B 9000K}\right) \approx \frac{g_i}{0.1} \times \exp\left(-\frac{14.5eV}{k_B 8013K}\right) \approx \frac{g_i}{10} \times \exp\left(-\frac{14.5eV}{k_B 10264K}\right) \quad \text{(A-25)}$$

The electron density is in equilibrium with the excited states and thus not a good indicator to determine whether the ground state is overpopulated or not. A recombining plasma at 8013 K with $b = 0.1$ has only a 13% lower electron density than a LTE plasma at 9000 K ($b = 1$).

$$n_1^+(8013K, b = 0.1) = \frac{1}{\sqrt{0.1}} n_1^{+,Saha}(8013K) \approx 0.87 \times n_1^{+,Saha}(9000K) \quad \text{(A-26)}$$

B. Appendix B: Experimental validation of the Stark width

As presented in chapter III we measure only the emissivity at the central wavelength of a line when we use the monochromator equipped with a photomultiplier tube. The total emissivity of the argon and oxygen lines can be obtained by multiplying the measured emissivity with a constant factor. The total emissivity of the hydrogen line can be obtained by multiplying the measured emissivity with a temperature dependant factor that can be calculated with the theory of the line broadening. On the following pages we present a method to validate the simulated line profiles.

For this we measure the lateral intensity profile at several wavelengths next to the central wavelength of the H-Beta line at 486 nm and use Abel inversion to obtain the radial emissivity profile. At each radial position we fit then a simulated profile and can obtain thus the Lorentzian width that is due to Stark broadening. For the simulation of the Doppler width we need the temperature which we measured with an argon line.

B.1. The wavelength profile

First we measured the temperature profile with an argon line as described in Chapter III. In the next step we measured the wavelength profile of the H-Beta line at the centre of the plasma (blue graph in Figure B-1). The centre of the peak in Figure B-1 is about 0.3 Å higher than the theoretical wavelength of the hydrogen multiplet (4861.3 Å). This small difference is due to an imperfect calibration of the monochromator, and the theoretical profiles have been shifted of a constant value to account for this default. We chose seven wavelengths for which we measured the lateral profiles and calculated the radial profiles with the Abel inversion. The red squares in Figure B-1 show these seven wavelengths.

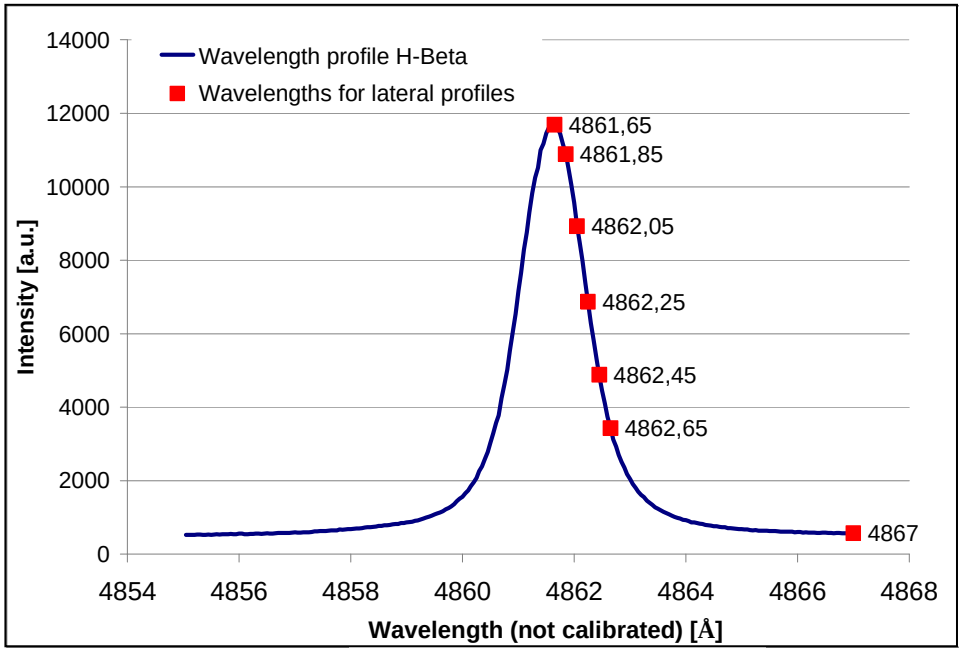

Figure B-1 Measured Wavelength profile of the H-Beta line

We obtain for each radial position the emissivity of the seven different wavelengths (Figure B-2). We use these seven emissivities and the temperature measured with an argon line, to fit a theoretical line profile for hydrogen as described below. From the fitted function

we obtain the Stark width, which is strongly dependant on the electron density in the plasma. We do this fit for all radii and thus obtain separately the Stark width and the temperature across the plasma.

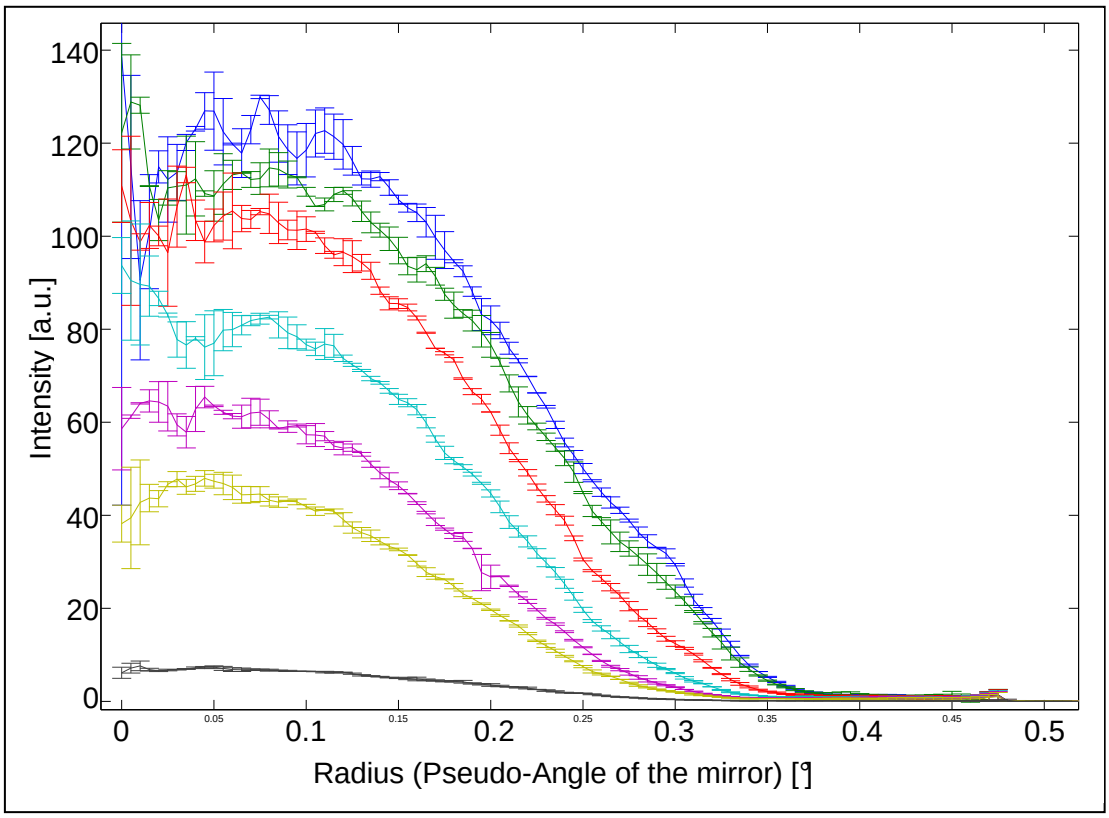

Figure B-2 Radial profiles of the different wavelengths (red squares in Figure B-1)

B.2. Fit of the line profile

We have measured a line profile at each radial position with seven different wavelengths. We do fit a simulated line profile to this measured wavelength profiles to obtain the Lorentzian width. First we describe the method for the simulation of the line profile.

From chapter III we know that the emission profile has the shape of a Voigt function. An analytical expression for the Voigt function, being the convolution of a Lorentz function and a Gauss function, does not exist. The three functions are defined by equations (B-1), (B-2) and (B-3). Where $\Delta\lambda_G$ is the half width at half maximum (HWHM) of the Gauss function and $\Delta\lambda_L$ is the HWHM of the Lorentz function

Lorentz function $$P_L(\lambda) = \frac{\sqrt{2}}{\pi \times \Delta\lambda_L} \frac{1}{1 + \frac{2(\lambda - \lambda_0)^2}{(\Delta\lambda_L)^2}} \quad \text{(B-1)}$$

Gauss function $$P_G(\lambda) = \frac{\sqrt{\ln 2}}{\sqrt{\pi}\Delta\lambda_G} exp\left(-\frac{(\lambda - \lambda_0)^2}{(\Delta\lambda_G)^2} \times \ln 2 \right) \quad \text{(B-2)}$$

Voigt function $$P_V(\lambda) = \int_{-\infty}^{\infty} P_G(\lambda - t) \times P_L(t) dt \quad \text{(B-3)}$$

Since the convolution needs a lot of computing time it is inconvenient for a fitting algorithm. We used thus a different method to calculate the Voigt function, using the real part of the complex error function, which can be calculated fast.

The complex error function is defined to be (Abramowitz [AS65], Chapter 7):

$$\omega(z) = \frac{i}{\pi}\int_{-\infty}^{\infty}\frac{e^{-t^2}}{z-t}dt \qquad \text{(B-4)}$$

At the end of this chapter we show that the Voigt function (equation (B-3)) is equal to the real part of the complex error function:

$$P_V(\lambda) = \frac{Re[\omega(z)]}{\Delta\lambda_G\sqrt{\pi/ln\,2}} \qquad \text{(B-5)}$$

with $z = \dfrac{(\lambda-\lambda_0)+i\Delta\lambda_L/\sqrt{2}}{\Delta\lambda_G/\sqrt{ln\,2}}$.

Qualitatively we can see that the numerator in the integral of the complex error function is similar to the Gauss function and the denominator is similar to the Lorentz function, so that this is plausible.

For the calculation of the complex error function, we used an algorithm written by D. Holmgren which is printed in at the end of this chapter. We compared the Voigt function calculated with the complex error function to the Voigt function calculated by convolution for different parameters. We observed identical profiles and validated thus the method using the complex error function.

The monochromator adds instrumental broadening to the line profile. For the measurement we used a width of 100 µm for the entry and the exit slit of the monochromator. The spread function of the monochromator Jobin Yvon HR640 is in these conditions very similar to a triangular profile with a width of 1.2 Å, which we used for the spread function.

The simulated profile is then the convolution of the three profiles in Figure B-3. The convoluted profile needs to be multiplied by the intensity of the peak and the continuum radiation must be added to it. As discussed before the first convolution has been replaced by the method using the complex error function, whereas the convolution of the Voigt function by the monochromator profile is calculated by numerical integration.

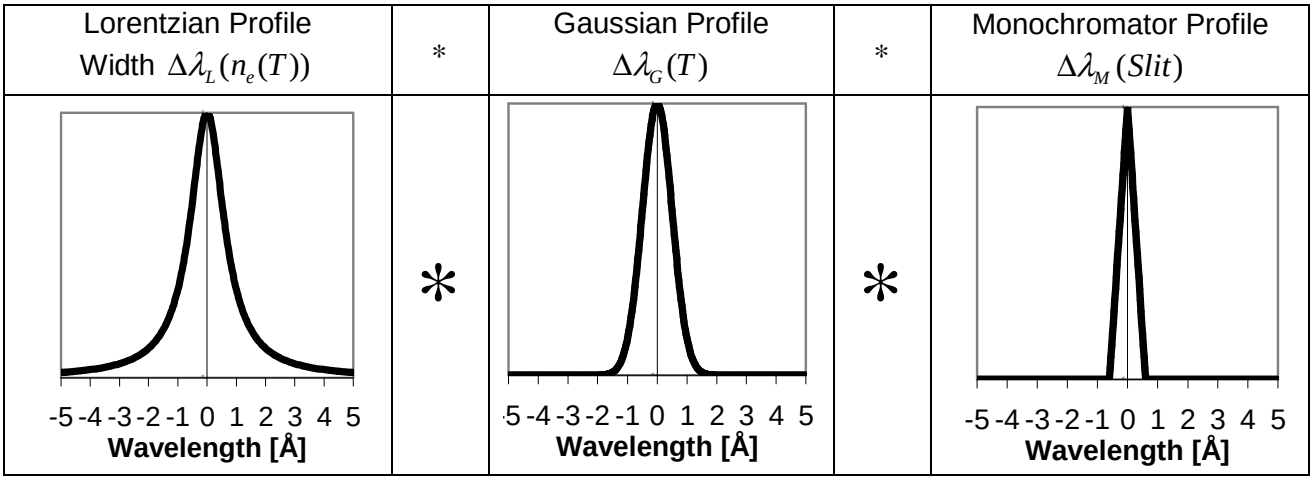

Figure B-3 Convolution of the different profiles

The shape of the simulated profile finally depends on five parameters:

- the width of the Stark broadening → Lorentz width $\Delta\lambda_L(n_e(T))$
- the width of the Doppler broadening → Gauss width $\Delta\lambda_G(T)$
- the intensity of the peak
- the intensity of the continuum
- the width of the monochromator profile

Two of these parameters are known and don't have to be fitted: we know the Gauss width of the Voigt profile because we measured the temperature, and we also know the profile of the monochromator. The unknown parameters are the intensity of the continuum, the peak intensity and the Lorentz width of the Voigt profile. We therefore fit the three unknown parameters with an iterative process, as indicated in Figure B-4. We simulate a profile at each iteration, calculating a Voigt profile that is convoluted with the monochromator profile and added to the background intensity. Then the simulated profile is compared to the measured profile with the least squares method. The function fminsearch of matlab continues to iterate until it finds a global minimum for the three parameters that are fitted. Figure B-5 shows the fitted line profile at the centre of the plasma together with the experimental emissivity values (points) deduced from Abel inversion of the measured lateral intensity distributions.

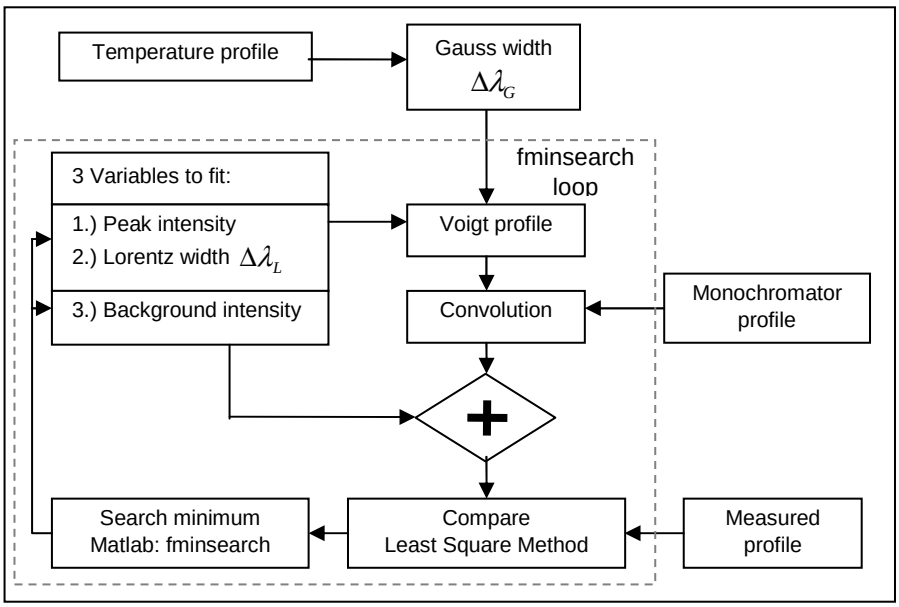

Figure B-4 Methodology for fitting the peak

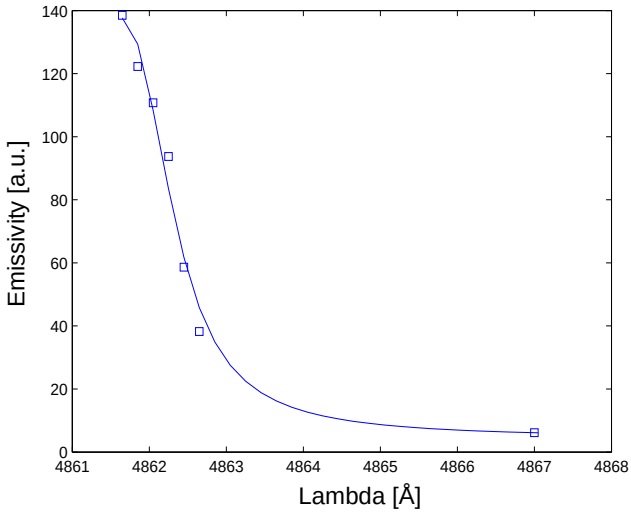

Figure B-5 Measured points at radius 0 with the fitted peak

B.3. Comparison of calculated and measured Stark width

As explained in chapter III, the Stark width of hydrogen lines depends principally on the electron density of the plasma, which should be related to the temperature by the Saha equation at local thermal equilibrium (LTE). Figure B-6 shows a comparison of the measured Stark width (from the method explained above) to the Stark width calculated at LTE from the local measured temperature (see chapter III). Both curves use data measured at the outlet of the small torch with the experimental parameters of Table B-1.

The calculated Stark width at LTE is higher than the measured values, so that it seems that the electron density at the outlet of our torch is 2.5 times lower than its LTE value. However as the measurement was done in the post-discharge region the electron density should be rather higher than in LTE. The difference could be explained by an error of the temperature measurement. If the measured temperature was 500 K lower the measured Stark width would fit the calculated Stark width. However such an error on the temperature measurement would mean that the measured emissivity is 7 times higher than the real emissivity. We did not further investigate where this difference comes from. We used the 2.5 times lower electron density for the line profile simulation for the hydrogen concentration ratio measurement.

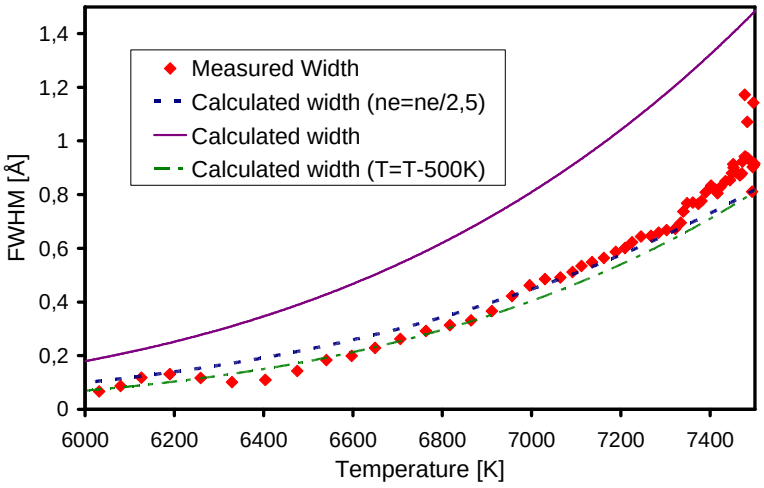

Figure B-6 Calculated and measured Stark broadening versus temperature

DC Voltage U	3.0 kV
DC Current I	0.33 A
P(electric)	1.0 kW
Outer flow Ar	12.2 l/min
Intermediate flow Ar	0.52 l/min
Intermediate flow $H_2O(g)$	~0.03 l/min

Table B-1 Parameters for the validation of the line profile simulation

B.4. The Voigt function

The Gauss function is

$$P_G(\lambda) = \frac{\sqrt{ln\,2}}{\sqrt{\pi}\Delta\lambda_G} exp\left(-\frac{(\lambda-\lambda_0)^2}{(\Delta\lambda_G)^2}\times ln\,2\right) \quad \text{(B-6)}$$

The Lorentz function is

$$P_L(\lambda) = \frac{\sqrt{2}}{\pi\times\Delta\lambda_L}\frac{1}{1+\frac{2(\lambda-\lambda_0)^2}{(\Delta\lambda_L)^2}} \quad \text{(B-7)}$$

The Voigt function is the convolution of the Gauss function and the Lorentz function:

$$P_V(\lambda) = \int_{-\infty}^{\infty} P_G(\lambda - t')\times P_L(t')dt' \quad \text{(B-8)}$$

We use (B-6),(B-7) and (B-8) and obtain

$$P_V(\lambda) = \frac{\sqrt{2}}{\pi\times\Delta\lambda_L}\frac{\sqrt{ln\,2}}{\sqrt{\pi}\Delta\lambda_G}\int_{-\infty}^{\infty}\frac{exp\left(-\frac{(\lambda-t'-\lambda_0)^2}{(\Delta\lambda_G)^2}\times ln\,2\right)}{1+\frac{2(t'-\lambda_0)^2}{(\Delta\lambda_L)^2}}dt' \quad \text{(B-9)}$$

We make the following replacements:

$\Delta\lambda_G = \sigma\sqrt{2\times ln\,2}$; $\Delta\lambda_L = \gamma\sqrt{2}$; $\lambda = x + 2\lambda_0$; $t' = t + \lambda_0$

and obtain the following expression for the Voigt function $P_V(\lambda)$:

$$P_V(\lambda) = \frac{1}{\pi\sqrt{2\pi}}\times\frac{1}{\gamma\sigma}\int_{-\infty}^{\infty}\frac{exp\left(-\frac{(x-t)^2}{2\sigma^2}\right)}{1+\frac{t^2}{\gamma^2}}dt \quad \text{(B-10)}$$

We want to show that the Voigt function can be written as the real part of the complex error function $\omega(z) = \frac{i}{\pi}\int_{-\infty}^{\infty}\frac{e^{-t'^2}}{z-t'}dt'$ with $z = \frac{x+i\gamma}{\sigma\sqrt{2}}$. We replace the real part of the complex error function by the sum of the complex error function and its complex conjugate

$$P_V(\lambda) = \frac{Re[\omega(z)]}{\sigma\sqrt{2\pi}} = \frac{\omega(z)+\omega^*(z)}{2\sigma\sqrt{2\pi}} = \frac{1}{2\sigma\sqrt{2\pi}}\left(\frac{1}{\pi}\int_{-\infty}^{\infty}\frac{i(z-t')^*\times e^{-t'^2}}{(z-t')(z-t')^*}dt' + \frac{1}{\pi}\int_{-\infty}^{\infty}\frac{(i(z-t')^*)^* e^{-t'^2}}{(z-t')(z-t')^*}dt'\right)$$

$$P_V(\lambda) = \frac{1}{2\sigma\pi\sqrt{2\pi}}\int_{-\infty}^{\infty}\frac{(iz^* - iz)\times e^{-t'^2}}{zz^* - t'z^* - t'z + t'^2}dt'$$

Then we let $z = \frac{x+i\gamma}{\sigma\sqrt{2}}$

and obtain $P_V(\lambda) = \frac{1}{2\sigma\pi\sqrt{2\pi}}\int_{-\infty}^{\infty}\frac{\frac{2\gamma}{\sigma\sqrt{2}}\times e^{-t'^2}}{\frac{x^2+\gamma^2}{2\sigma^2} - t'\frac{2x}{\sigma\sqrt{2}} + t'^2}dt'$

We replace $t' = \frac{x-t}{\sigma\sqrt{2}}$ and $dt' = \frac{-dt}{\sigma\sqrt{2}}$, and obtain

$$P_V(\lambda) = \frac{1}{\sigma\pi\sqrt{2\pi}} \int_{-\infty}^{\infty} \frac{\frac{\gamma}{\sigma\sqrt{2}} \times exp\left(-\frac{(x-t)^2}{2\sigma^2}\right)}{\frac{x^2+\gamma^2}{2\sigma^2} - \frac{(x-t)}{\sqrt{2}\sigma}\frac{2x}{\sigma\sqrt{2}} + \frac{(x-t)^2}{2\sigma^2}} \frac{dt}{\sqrt{2}\sigma}$$

$$P_V(\lambda) = \frac{1}{\sigma\pi\sqrt{2\pi}} \int_{-\infty}^{\infty} \frac{\gamma exp\left(-\frac{(x-t)^2}{2\sigma^2}\right)}{x^2+\gamma^2-2x^2+2xt+x^2-2xt+t^2} dt$$

$$P_V(\lambda) = \frac{1}{\pi\sqrt{2\pi}} \frac{1}{\gamma\sigma} \int_{-\infty}^{\infty} \frac{exp\left(-\frac{(x-t)^2}{2\sigma^2}\right)}{1+\frac{t^2}{\gamma^2}} dt \qquad \text{(B-11)}$$

The equation (B-11) is the same as equation (B-10). We have thus shown that the Voigt function can be written as the real part of the complex error function.

B.4.1. Implementation of the complex error function in matlab

For the calculation of the complex error function we use the matlab file written by D. Holmgren:

```
% Function to evaluate complex error function for any
% z = x + i*y.  This uses Hui's rational approximation.
% Real part is Voigt function, imaginary part is dispersion
% (ie., complex index of refraction).  Works for both scalars
% and vectors.  Have not yet made function applicable to whole
% z-plane.
% by D. Holmgren, July 23 95.
function f = cerf(z)
% coefficients of rational approximation...
      a0 = 37.24429446739879 + 0*i;
      a1 = 57.90331938807185 + 0*i;
      a2 = 43.16280063072749 + 0*i;
      a3 = 18.64649990312317 + 0*i;
      a4 = 4.67506018267650 + 0*i;
      a5 = 0.56418958297228 + 0*i;
      b0 = 37.2442945086 + 0*i;
      b1 = 99.9290005933 + 0*i;
      b2 = 118.6763981260 + 0*i;
      b3 = 80.6459493922 + 0*i;
      b4 = 33.5501020941 + 0*i;
      b5 = 8.2863279156 + 0*i;
% evaluate complex error function...
      x = real(z); y = imag(z); nl = length(x);
% z is a scalar...
      if nl == 1,
      zh = y - i*x;
      f=(((((a5*zh+a4)*zh+a3)*zh+a2)*zh+a1)*zh+a0)/…
((((((zh+b5)*zh+b4)*zh+b3)*zh+b2)*zh+b1)*zh+b0);
      end
% z is a vector...
            if nl ~= 1,
      zh = y - i.*x;
      f=(((((a5 .*zh+a4).*zh+a3).*zh+a2).*zh+a1).*zh+a0)./…
((((((zh+b5).*zh+b4).*zh+b3).*zh+b2).*zh+b1).*zh+b0);
      end
end
```

B.5. Abel inversion

This Chapter is rewritten from the paper of Nestor and Olsen [NO60]

$$\varepsilon(r) = -\frac{1}{\pi}\int_r^R \frac{dL(y)}{dy}\frac{dy}{\sqrt{y^2 - r^2}} \tag{B-12}$$

We want to numerical algorithm to solve the equation (B-12) for a discrete function. We replace in equation (B-12) $r^2 = v$ and $y^2 = u$ and obtain thus

$$\varepsilon(r(v)) = -\frac{1}{\pi}\int_v^{R^2} \frac{dL'(u)}{du}\frac{du}{\sqrt{u - v}} \tag{B-13}$$

For the discretization we divide the integral into sub-integrals with an equal width $\Delta y = a$. We assume that $L(u)$ is a linear function of u in each zone.

$$\varepsilon(ak) = -\frac{1}{\pi}\sum_{n=k}^{N-1} \left.\frac{dL'(u)}{du}\right|_{u=(an)^2} \int_{(an)^2}^{[a(n+1)]^2} \frac{du}{\sqrt{u - (ak)^2}} \tag{B-14}$$

Where

$$\left.\frac{dL'(u)}{du}\right|_{u=(an)^2} = \frac{L'([a(n+1)]^2) - L'([an]^2)}{a^2[(n+1)^2 - n^2]}$$

After performing the indicated integration in equation (B-14) and transforming back to original coordinates, we obtain

$$\varepsilon_\lambda(ak) = -\frac{2}{\pi a}\sum_{n=k}^{N-1} A_{k,n}[L(a[n+1]) - L(an)] \tag{B-15}$$

Where

$$A_{k,n} = \frac{\sqrt{(n+1)^2 - k^2} - \sqrt{n^2 - k^2}}{2n+1}$$

B.5.1. Matlab implementation

We used the following implementation in matlab. The vector “lat” contains the lateral intensity profile and calculated radial emissivity profile is written in the vector “EPS”. The radial emissivity must be divided afterwards by the distance between two points of the lateral profile.

```
function EPS=Abel(lat)
    [m]=size(lat);
    for i=1:m
        EPS(i,1)=0;
        AKN=0;
        AKNm=0;
        k=i-1;
        for j=i:m
            n=j-1;
            AKN=(sqrt((n+1)*(n+1)-k*k)-sqrt(n*n-k*k))/(2*n+1);
            EPS(i,1)=EPS(i,1)+(AKNm-AKN)*L(j);
            AKNm=AKN;
        end
        EPS(i,1)=-EPS(i,1)*2/pi;
    end
end
```

Plasma Sources Sci. Technol. **21** (2012) 045011 (7pp) doi:10.1088/0963-0252/21/4/045011

E–H mode transition of a high-power inductively coupled plasma torch at atmospheric pressure with a metallic confinement tube

Jochen Altenberend, Guy Chichignoud and Yves Delannoy

SIMAP, 1130 rue de la Piscine, BP 75, F-38402 St Martin d'Heres Cedex, France

E-mail: jochen.altenberend@simap.grenoble-inp.fr

Received 1 December 2011, in final form 21 May 2012
Published 31 July 2012
Online at stacks.iop.org/PSST/21/045011

Abstract
Inductively coupled plasma torches need high ignition voltages for the E–H mode transition and are therefore difficult to operate. In order to reduce the ignition voltage of an RF plasma torch with a metallic confinement tube the E–H mode transition was studied. A Tesla coil was used to create a spark discharge and the E–H mode transition of the plasma was then filmed using a high-speed camera. The electrical potential of the metallic confinement tube was measured using a high-voltage probe. It was found that an arc between the grounded injector and the metallic confinement tube is maintained by the electric field (E-mode). The transition to H-mode occurred at high magnetic fields when the arc formed a loop. The ignition voltage could be reduced by connecting the metallic confinement tube with a capacitor to the RF generator.

(Some figures may appear in colour only in the online journal)

Thermal plasma torches have replaced flames in many material processes as high-temperature enthalpy sources (i.e. powder spheroidization, cutting, welding, waste treatment). Thermal plasma torches can be arc torches or inductively coupled plasma torches. Inductively coupled plasma torches have the advantage of high purity because the energy is induced by a magnetic field so that the plasma is not in contact with an electrode as is the case in arc torches. Low-power inductively coupled plasma torches (2 kW), used for chemical analysis, are generally confined by a quartz tube. At higher values of power (40 kW–1 MW) the confinement needs a cooling system that absorbs and evacuates the radiation power of the plasma without screening the magnetic field. This can be achieved using a water-cooled ceramic confinement [1] or a segmented water-cooled metallic confinement tube [2]. While ceramic confinement has better energy efficiency due to its low electrical conductivity, metallic confinement has the advantage of good resistance to high heat fluxes and mechanic shocks. Plasma torches with a metallic confinement tube are used, for example, for the purification of silicon for solar cells [3] and for Earth re-entry simulations [4]. In the case of purification of silicon the metallic confinement tube was chosen to reduce the risk of water falling onto the silicon, which would cause an explosion.

During the ignition of an inductively coupled plasma a mode transition takes place. The gas first breaks down in a capacitive discharge (E-mode) and turns, when the electromagnetic field is high enough, into the H-mode. Several papers deal with this E–H mode transition in low-pressure plasmas from 0.1 to 10 Pa. Cunge *et al* explain the mechanisms of the E–H mode transition well [5]. In the E-mode, the plasma is powered mainly by the electric field and has a low electron density. In the H-mode, the plasma absorbs more power, and is powered mainly by the magnetic field and has a higher electron density. In low-pressure plasmas in the E-mode, the power absorption and power losses are both nearly proportional to the electron density and the electric field. Above a threshold electromagnetic field the power absorption is higher than the power losses so that the electron density increases strongly until the power losses and absorption are again equilibrated in the H-mode.

Some atmospheric-pressure torches can be ignited at low pressures, but an ignition at atmospheric pressure is cheaper because it does not need expensive vacuum technology. In their

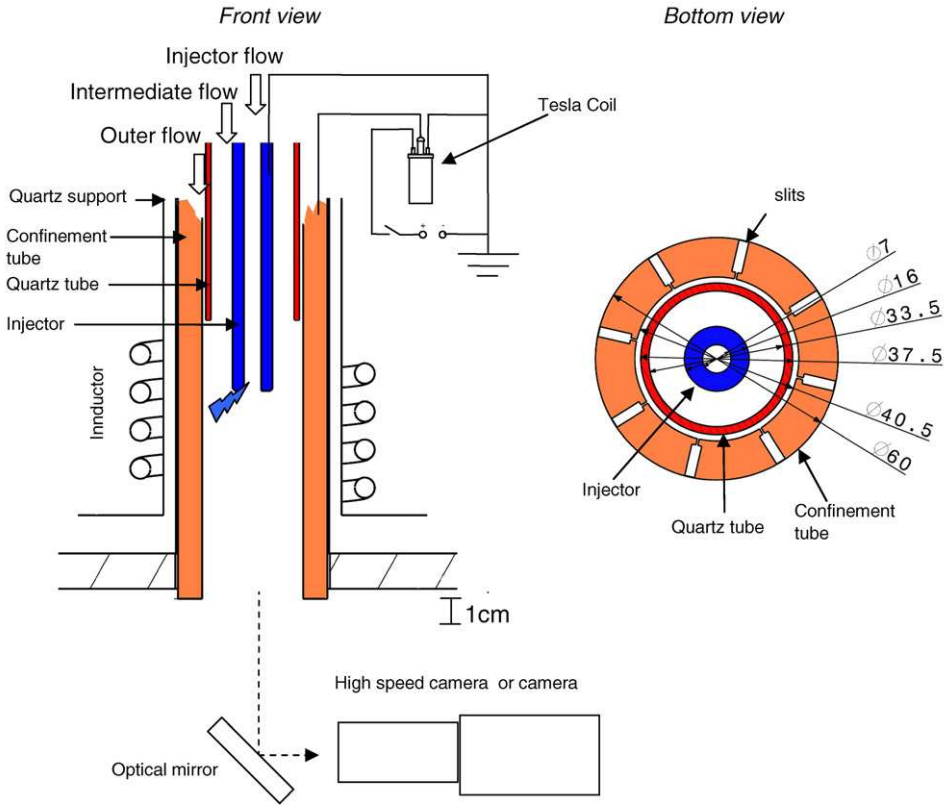

Figure 1. Geometry of the experimental setup.

book Laroche and Orfeuil present several techniques for the ignition of atmospheric-pressure torches [6]. The E–H mode transition at high pressures is different from the E–H mode transition at low pressures because the E-mode is not diffuse and therefore a higher electromagnetic field is necessary for the mode transition. A high electromagnetic field requires a high generator voltage. The high generator voltage makes operation difficult because it can cause arcing or very high power absorption after ignition.

Using high-efficiency solid-state power supplies for the operation of plasma torches requires handling the ignition with a low generator voltage. Such power supplies have a higher energy efficiency than tube-type oscillator power supplies, but are limited in frequency (typically <1 MHz) and voltage (typically <1 kV). So far complex auxiliary systems have been necessary for ignition at atmospheric pressure with solid-state power supplies. For example, the company Tekna proposes a multi-coil induction torch with a second generator for ignition [9].

Razzak *et al* studied the mode transition at atmospheric pressure in a 20 kW plasma torch with a quartz confinement [7, 8]. We assume that this mode transition can be generalized to any torch with electrically insulating confinement while it is different in an electrically conducting confinement, as shown in this paper.

The purpose of this paper is to study the E–H mode transition in a plasma torch with a segmented metallic confinement tube and to find a method that can reduce the minimum voltage necessary for the E–H mode transition. The findings may help one to replace plasma process systems with expensive vacuum technology with cheaper systems without vacuum technology and to replace tube-type oscillator power supplies with high-efficiency solid-state power supplies.

1. Experiment

The experimental setup is shown in figure 1. The plasma torch consisted of a segmented metallic confinement tube, an auxiliary quartz tube and a metallic injector. The slits between the segments avoided currents that would screen the magnetic field. The confinement tube and the injector were water cooled. An inductor with four turns induced a current in the plasma. The inductor L_1 was connected in parallel with a high voltage capacitance ($C_1 = 2.5$ nF) to the RF power generator of type Collpitts (Hüttinger, 60 kW, figure 2). The inductor L_1 and the capacitor C_1 acted as a tank circuit with a resonance frequency of 2.6 MHz. A plate voltage U_{dc} between 0 and 8.0 kV was applied to the triode. The voltage of the grid of the triode oscillated with the tank circuit. Therefore, the current of the triode also oscillated with the tank circuit. The link capacitor and the choke separated the RF current and the direct current. The RF current I_{RF} flowed to the tank circuit and the direct current (plate current) I_{dc} flowed to the high-voltage source, where it was measured. The plate voltage U_{dc} was generated by a voltage transformer and a rectifier. A proportional–integral–derivative (PID) controller regulated the thyristors at the low-voltage entry of the generator to maintain the plate voltage constant at the desired value. A galvanic isolation and a Fluke NetDAQ were used to measure the plate voltage U_{dc} and the direct current I_{dc} of the generator. An optical mirror inclined

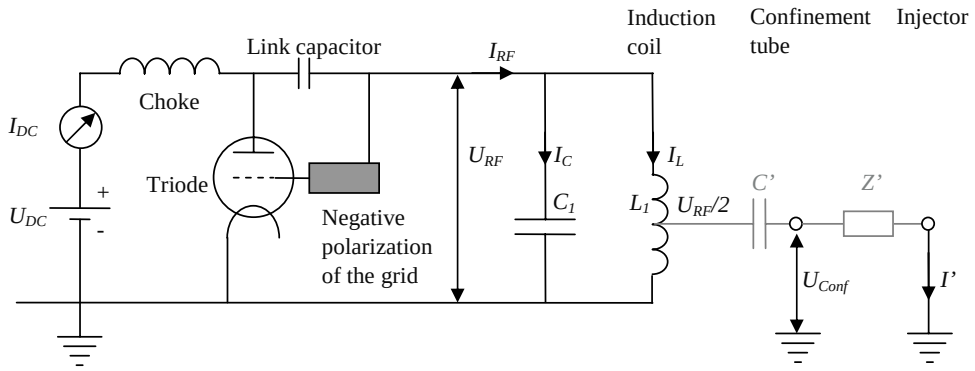

Figure 2. Circuit diagram of the power supply and the equivalent circuit for the plasma torch (grey).

at 45° was used to observe the plasma. Pictures of the E-mode were taken with a camera (Nikon D80, ISO 1600, aperture 7.1, exposure time 250 μs). The E–H mode transition was filmed with a high-speed camera (AOS X-motion, objective: sigma 150 mm, 1 : 2.8, aperture: 32, shutter time: 200 μs, frame rate: 1000 Hz). The outer flow was set to be 50 l min^{-1}, the intermediate flow to be 6.5 l min^{-1} and the inner flow to be 2.3 l min^{-1}. All flows were pure argon. The outer flow was injected with a swirl. The injector was connected to the ground. In order to film the E–H mode transition the plate voltage U_{dc} was set to be 7.5 kV. Then a short high-voltage peak ($\Delta t = 0.2$ ms, $U = 4$ kV) was applied to the floating confinement tube using a Tesla coil, similar to those in automobiles, in order to create an electric field higher than the breakdown field between the confinement tube and the injector. When the high-voltage peak was applied, the gas broke down in the E-mode, which was maintained by the RF electric field. The voltage from the Tesla coil was zero when the E–H mode transition took place.

The voltage of the confinement tube U_{Conf} and the generator RF voltage U_{RF} were measured using a high voltage probe (Tektronix P6015A) and an oscilloscope (Tektronix TDS 220).

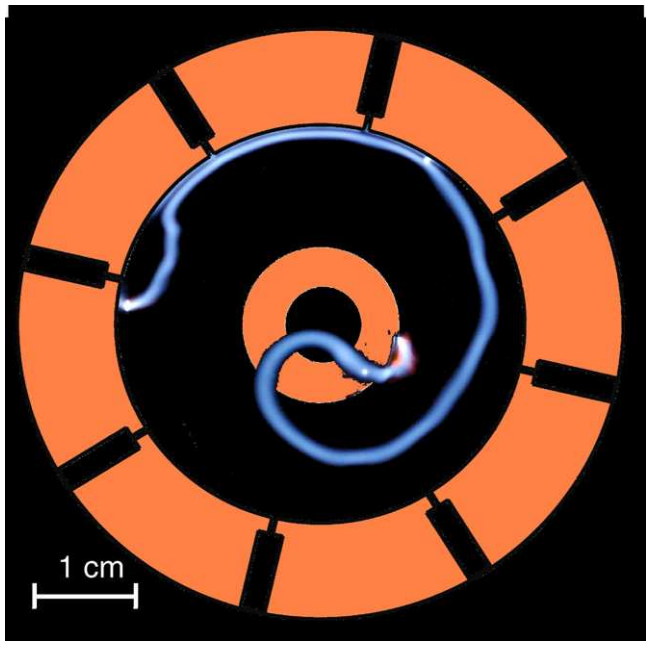

Figure 3. Picture of the E-mode (superposed with the image of the torch).

2. Results and discussion

2.1. The E–H mode transition

We observed that the high voltage of the Tesla coil created an arc between the confinement tube and the injector. The arc was then maintained by the electric field (figure 3). The time between the ignition of the arc (E-mode) and the transition to the inductive plasma (H-mode) varied from a tenth of a second up to several seconds. Comparing several videos of the ignition showed that the transition from E-mode to H-mode always follows the same mechanism, as shown in figure 4. The arc has a spiral shape between the injector and the confinement tube. We observe that the arc turns around the injector while the arc feet remain fixed. Between (*g*) and (*h*) in figure 4 a connection between the inner turn and the outer turn of the arc occurs. This short-circuited loop acts as a transformer secondary with the inductor being the primary. The intensity of the plasma then grows very fast until it stabilizes in the H-mode. This E–H mode transition is very different from the E–H mode transition in torches with quartz confinement observed and studied by Razzak [8]. The plasma in the E-mode in the torch with quartz confinement consists of several axial and tangential filaments on the surface of the quartz confinement. During the E–H mode transition one tangential filament grows in intensity and forms the H-mode. As the metallic confinement tube has a high electrical conductivity it cancels the axial and tangential electric fields on the surface of the confinement tube. Therefore, the filaments, as they can be observed in quartz confinement, cannot exist in metallic confinement. In low-pressure torches the E-mode is a diffuse discharge that occupies the whole volume in the inductor [5]. Its geometry is similar to the H-mode but it has a lower electron density.

We measure the increase in the plate voltage U_{dc} and the dc current I_{dc} when the arc is ignited (figure 5). Since the voltage is controlled at a fixed value the voltage increase may be a measurement error. The increase in the current is probably due to the small power absorption in the E-mode. During the transition to H-mode the current increases strongly because of

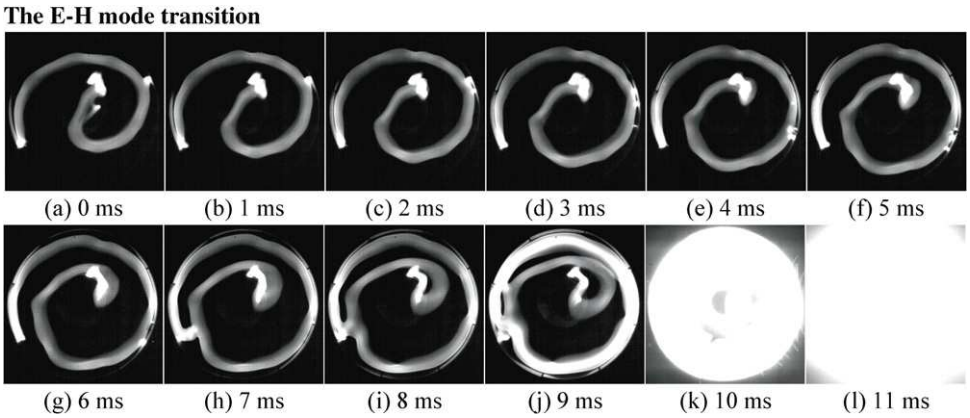

Figure 4. Transition from E-mode to H-mode ($U_{dc} = 7.5\,kV$).

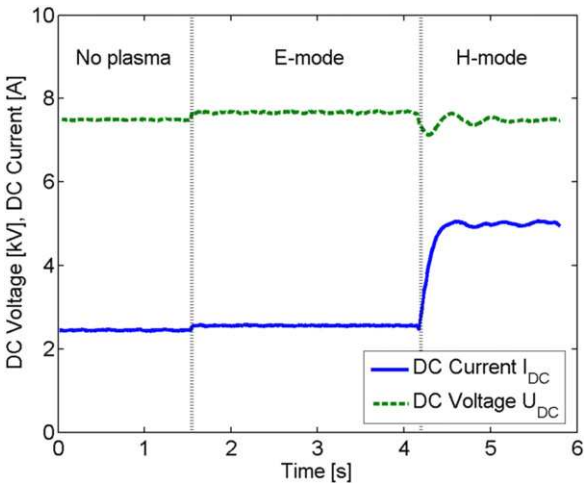

Figure 5. The dc voltage and dc current during ignition.

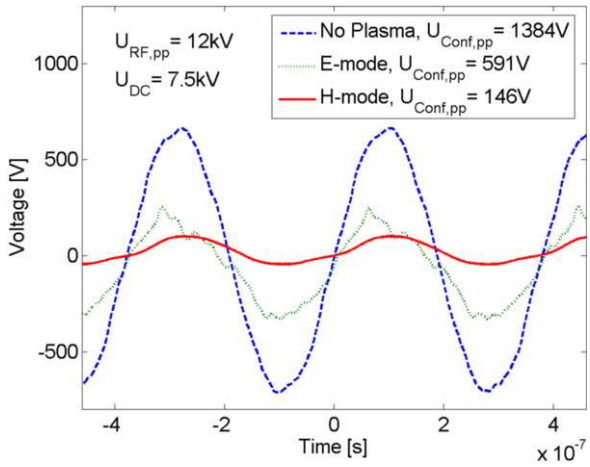

Figure 6. Voltage of the confinement tube U_{conf} for three modes occurring during the plasma ignition.

the power absorption of the plasma. The high current induces a reduction in the plate voltage, which is rapidly cancelled by the PID controller. This is the reason for the oscillation of the voltage. We can see in figure 5 that the current and therefore the power absorption in the H-mode are very high compared with the E-mode.

In our configuration a plate voltage U_{dc} of 5.5 kV is necessary to maintain the E-mode and by increasing the voltage the transition to H-mode occurs at a plate voltage U_{dc} of 7.5 kV. The arc is maintained by the electric field between the confinement tube with a floating potential and the injector which is connected to the ground. The oscillating potential of the confinement tube U_{Conf}, which is shown in figure 6, loses its sinusoidal form when the arc is ignited. This can not only be due to the electrical properties of the arc but also to parasite inductances and capacitances. The mean potential of the inductor is half the voltage of the RF generator U_{RF} due to symmetry. The inductor together with the confinement tube forms a capacitor C', whereas the space between the confinement tube and the injector has an impedance Z', as shown in the equivalent circuit of figure 2.

The potential of the confinement tube U_{Conf} is smaller when the arc is ignited because the arc reduces the impedance Z' between the confinement tube and the injector, which is connected to the ground. In the H-mode the potential of the confinement tube is even smaller because the impedance Z' is smaller due to the large volume and the high electron density of the plasma.

The formation of a closed loop does not always lead to an E–H mode transition. Figure 7 shows a spiral that evolves into a loop, which then disappears between (e) and (f), while the short straight connection between the confinement tube and the injector remains. This reconnection can also be seen in the oscillating potential of the confinement tube U_{Conf}, which increases when the arc becomes longer and drops when the arc reconnects (figure 8). The time between two reconnections is about 20 ms. In general, many reconnections occur before the E–H mode transition.

The formation of the spiral from a straight radial arc is probably due to the Lorentz force. The magnetic field is parallel to the axis of the torch and the arc current is perpendicular to the axis of the torch. The Lorentz force is then perpendicular to the arc and the axis of the torch, and can swirl the arc. However, the phase shift between the magnetic field and the arc current must be small.

From the equivalent circuit of figure 2, the inductor current can be approximated to $I_L = -I_C = -U_{RF} \mathrm{j} C_1 \omega$ because the

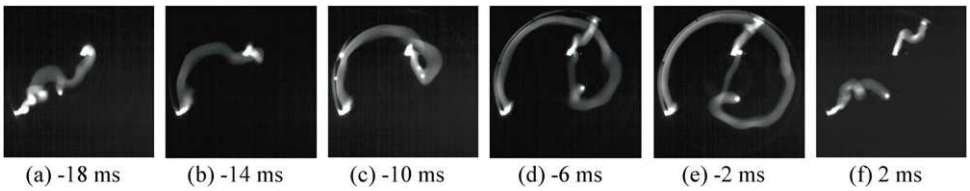

Figure 7. Reconnection: the arc forms a loop which disappears ($U_{dc} = 7.5\,kV$).

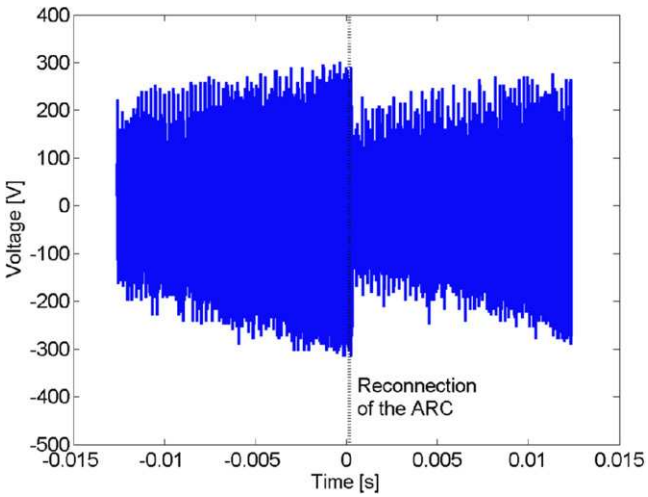

Figure 8. Effect of the reconnection on the voltage of the confinement tube U_{Conf}.

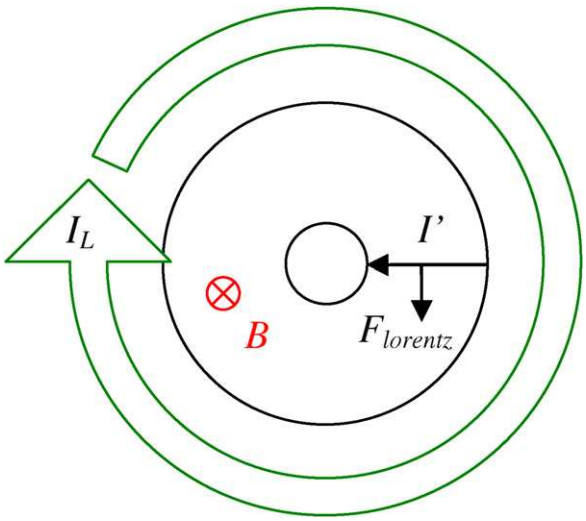

Figure 9. Direction of the Lorentz force seen from the top.

resonance circuit has a high quality factor ($I_{RF} \ll I_L$). The arc current can be approximated to $I' = (U_{RF}/2)\mathrm{j}C'\omega$ because $U_{Conf} \ll U_{RF}/2$ when the arc is ignited (figure 6). Therefore, the phase of the arc current I' (from the confinement tube to the injector) is opposite to the phase of the inductor current (from top to bottom). Figure 9 shows the direction of those currents seen from the top when $I' > 0$ and $I_L < 0$ (the inductor has the shape of a left-handed helix and the lower end is connected to the ground) and also the direction of the magnetic field (downwards) and the Lorentz force (clockwise).

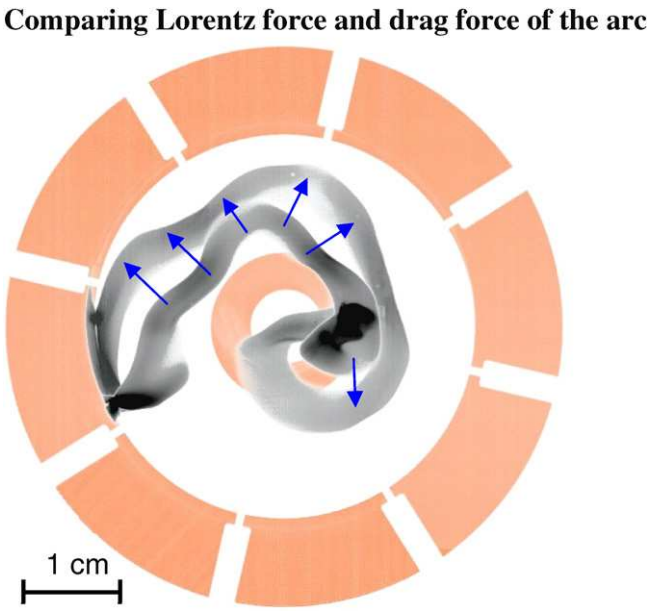

Figure 10. Superposition of two frames of the high-speed video ($\Delta t = 5\,ms$, E-mode, $U_{dc} = 7.5\,kV$).

In the diagram (top view) the Lorentz force turns clockwise as it does in the pictures taken with the camera (bottom view inverted by a mirror). Considering that the arc foot at the outer tube stays fixed, the direction of the Lorentz force explains the clockwise formation of a spiral, as seen in figures 4 and 7.

2.2. Comparing the Lorentz force and drag force of the arc

It would be possible to achieve a fundamental understanding of the arc movement by numerical modelling. Several papers use a qualitative model for the movement of the arc, which takes only the Lorentz force and the drag force into account [12–14]. We want to test whether this model describes well the movement of the arc and to validate an estimation for the arc current. In order to find the speed of the arc two frames with a time difference of 5 ms are superposed (figure 10). By comparing the length of the arrows in figure 10 with the diameter of the torch a speed of about $1\,m\,s^{-1}$ was calculated. The picture taken with the Nikon camera (figure 3), which has a better image sharpness than the videos, is used to measure the diameter of the arc to be about 2 mm. The drag force can be calculated assuming the arc to be an infinite solid cylinder. The drag coefficient of $C_D = 1.3$ was taken from [14]. The drag force is then $f_D = C_D \cdot \frac{1}{2}\rho u_0^2 d = 2 \times 10^{-3}\,N\,m^{-1}$.

We calculate the magnitude of the magnetic field with the approximation of an LC circuit with a high quality factor and

the formula for a long solenoid:

$$|I_L| = |U_{\mathrm{RF}}|C_1\omega$$

$$B = \mu_0 \frac{N}{l} I_L = \mu_0 \frac{N}{l} \cdot U_{\mathrm{RF}} C_1 \omega = \mu_0 \frac{4}{0.05m} 12\,\mathrm{kV} \cdot 2.5\,\mathrm{nF} \cdot 2.6\,\mathrm{MHz} \cdot 2\pi = 0.05\,\mathrm{T} \quad \text{(peak to peak)}.$$

In order to calculate the current of the arc we estimate the capacitance between the inductor and the confinement tube using the formula for a cylindrical capacitor:

$$C' = \frac{2\pi\varepsilon_0}{\ln(90\,\mathrm{mm}/60\,\mathrm{mm})} 0.05\,\mathrm{m} \approx 7\,\mathrm{pF},$$

$$I' = \frac{U_{\mathrm{RF}}}{2} \cdot C'\omega = 2\pi \cdot 2.6\,\mathrm{MHz} \cdot 7\,\mathrm{pF} \cdot 6\,\mathrm{kV} = 0.7\,\mathrm{A} \quad \text{(peak to peak)}.$$

The mean Lorentz force is then $f_{\mathrm{L}} = I \cdot B = \frac{1}{8} \cdot 0.7\,\mathrm{A} \cdot 0.05\,\mathrm{T} = 4 \times 10^{-3}\,\mathrm{N\,m^{-1}}$. The factor $\frac{1}{8}$ is necessary because the magnetic field and the current are peak-to-peak values.

The same order of magnitude is obtained for the Lorentz force f_{L} and the drag force f_{D} showing that this qualitative model is reasonable to describe the movement of the arc. It validates the order of magnitude of the arc current I'.

2.3. Reducing the ignition voltage

After studying the E–H mode transition two methods for reducing the minimum plate voltage U_{dc} for the E–H mode transition were tested. The objective is to increase the electron density of the arc so that the magnetic field can better couple to the closed loop so that the probability for the E–H mode transition is higher. For the first method, we used a capacitor C_2 to increase the arc current I' in the E-mode. The capacitor C_2 consisted of two copper plates with a capacitance of 40 pF and was connected to the upper point of the capacitor C_1, which has an oscillating potential U_{RF} (setup (*b*) in figure 11). Hull [10] patented a similar setup in 1988, but his objective was to reduce the generator voltage necessary for the breakdown of the gas and not the generator voltage for the E–H mode transition.

The classic setup (setup (*a*) in figure 11) needs a minimum plate voltage U_{dc} of 7.5 kV for the E–H mode transition. When the capacitor is connected (setup (*b*) in figure 11) this minimum voltage U_{dc} was significantly reduced to 6.0 kV. This shows the importance of the arc current I' from the confinement tube to the injector. A higher arc current I' produces a higher electron density and the magnetic field can therefore couple better. This finding can help one to develop plasma torch setups that can work with lower generator voltages. We also tested another setup with the capacitor C_2 connected to the floating injector and the confinement tube connected to the ground (setup (*c*) in figure 11). In this setup the Tesla coil was connected to the injector. Such a setup has the advantage that it does not need complicated electrical insulation between the metallic confinement and the reaction chamber at the outlet of the torch. In this setup the arc turned in the opposite direction and the minimum plate voltage U_{dc} for the E–H mode transition was 7.0 kV.

The second method that was tested was a Penning mixture of Ar and 0.03% acetylene [11]. The Penning mixture has

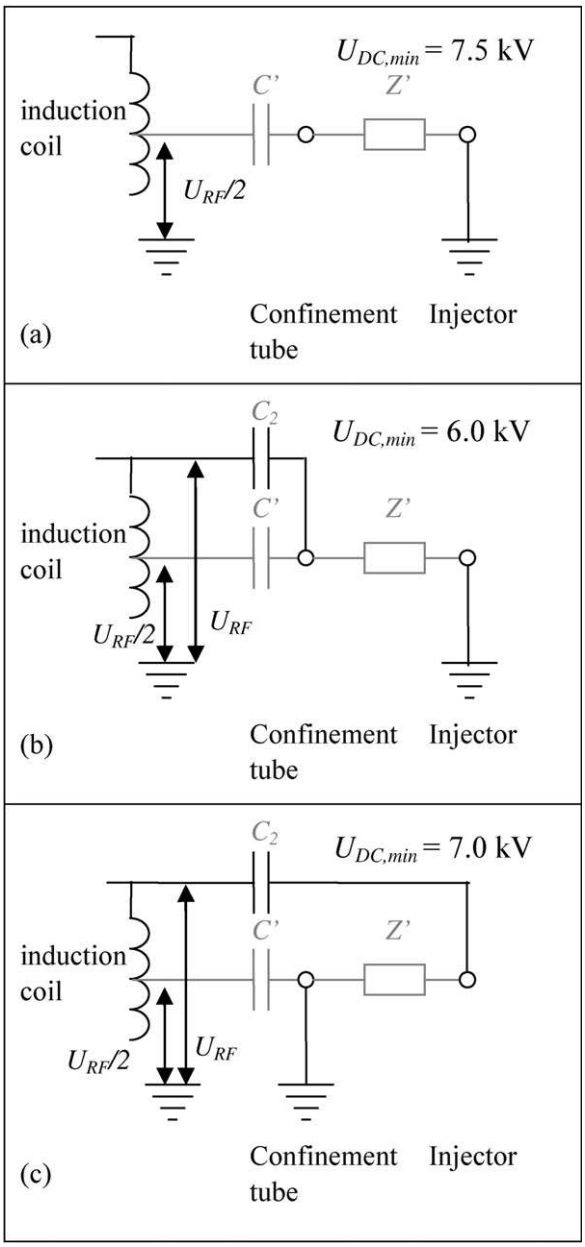

Figure 11. Equivalent circuit for different setups and the minimum plate voltage for the E–H mode transition $U_{\mathrm{dc,min}}$.

a very low breakdown voltage, but to our knowledge it has not yet been tested whether it reduces the minimum voltage necessary for the E–H mode transition. A negative effect of the Ar–acetylene mixture was observed. Up to a plate voltage of 8.0 kV, the limit of the generator, the plasma remained in the E-mode. While the Penning effect increases the electron density because metastable argon atoms ionize acetylene molecules other effects may reduce the electron density. For example, the recombination of an acetylene ion with an electron together with the decay of the resulting excited acetylene molecule. As the plate voltage necessary for the E–H mode transition is higher when using the Penning mixture, the effects that reduce the electron density are probably more important than the Penning effect.

3. Conclusion

The ignition of a 40 kW inductively coupled plasma torch with a metallic confinement tube was investigated. It was shown that in the E-mode an arc between the floating confinement tube and the grounded injector is maintained. During the E–H mode transition the arc forms a spiral and a connection between two turns forms a loop to which the magnetic field can couple. An argon–acetylene Penning mixture could not reduce the minimum generator voltage necessary for the E–H mode transition. Connecting the confinement tube with a 40 pF capacitor to the RF generator reduced the minimum plate voltage necessary for the E–H mode transition from 7.5 to 6.0 kV.

Acknowledgments

This work was financially supported by the OSEO as part of the project Solar Nano Crystal. The authors would like to express their sincere gratitude to G Cunge, R Ernst and C Trassy for interesting discussions.

References

[1] Jurewicz J and Boulos M 1993 High performance induction plasma torch with a water-cooled ceramic confinement tube *US Patent No* 5200595
[2] Hull D E 1984 Induction plasma tube *US Patent No* 4431901
[3] Alemany C, Trassy C, Pateyron B, Li K-I and Delannoy Y 2002 Refining of metallurgical-grade silicon by inductive plasma *Sol. Energy Mater. Sol. Cells* **72** 41–8. *EMRS 2001 Symposium E: Crystalline Silicon for Solar Cells*
[4] Bottin B, Chazot O, Carbonaro M, van der Haegen M and Paris S 1999 The VKI plasmatron characteristics and performance *RTO AVT Course on Measurement Techniques for High Temperature and Plasma Flows (Rhode-Saint-Genèse, Belgium, 25–29 October 1999)* ed J M Charbonnier and G S R Sarma, NATO-RTO EN-8
[5] Cunge G, Crowley B, Vender D and Turner M M 1999 Characterization of the e to h transition in a pulsed inductively coupled plasma discharge with internal coil geometry: bi-stability and hysteresis *Plasma Sources Sci. Technol.* **8** 576
[6] Laroche G and Orfeuil M 1991 *Les Plasmas dans L'industrie* (Paris-la-Défense: Electra)
[7] Razzak M A, Kondo K, Uesugi Y, Ohno N and Takamura S 2004 Transition from electrostatic-to-electromagnetic mode in a radio-frequency ar inductively coupled plasma in atmospheric pressure *J. Appl. Phys.* **95** 427–33
[8] Razzak M A, Takamura S and Uesugi Y 2005 Dynamics of E–H mode transition in high-pressure RF inductively coupled plasmas *IEEE Trans. Plasma Sci.* **33** 284–5
[9] Boulos M and Jurewicz J 2005 Multi-coil induction plasma torch for solid state power supply *US Patent No* 6919527
[10] Bieniewski T M and Hull D E 1988 Starter for inductively coupled plasma tube *US Patent No* 4766351
[11] Heylen A E D 1970 Maximization of argon-hydrocarbon penning mixtures *J. Phys. D: Appl. Phys.* **3** 789
[12] Harvey R L, Kuethe A M and Nicolai L M 1967 Model of an electric arc balanced magnetically in a gas flow *American Inst of Aeronautics and Astronautics, Aerospace Sciences Meeting 5th*, Paper 67-96
[13] Kalra C S, Gutsol A F and Fridman A A 2005 Gliding arc discharges as a source of intermediate plasma for methane partial oxidation *IEEE Trans. Plasma Sci.* **33** 32–41
[14] Gangoli S P, Gutsol A F and Fridman A A 2010 A non-equilibrium plasma source: magnetically stabilized gliding arc discharge: I. Design and diagnostics *Plasma Sources Sci. Technol.* **19** 065003

I. Introduction

La présente étude a pour objectif de mieux comprendre le procédé de raffinage en bore du silicium par plasma réactif. Avant de présenter le procédé lui-même, la technologie « standard » utilisée pour la purification est présentée. Cette technologie utilise le procédé Siemens. Nous présentons plusieurs technologies qui peuvent remplacer le processus de Siemens à moindre coût. Le procédé de raffinage par plasma peut éliminer le bore qui peut difficilement être éliminé par d'autres procédés. À la fin de ce chapitre, nous présentons la nécessité d'une compréhension fondamentale du processus de raffinage par plasma.

I.1. La technologie standard pour la production du silicium de qualité solaire

I.1.1. Production du silicium métallurgique

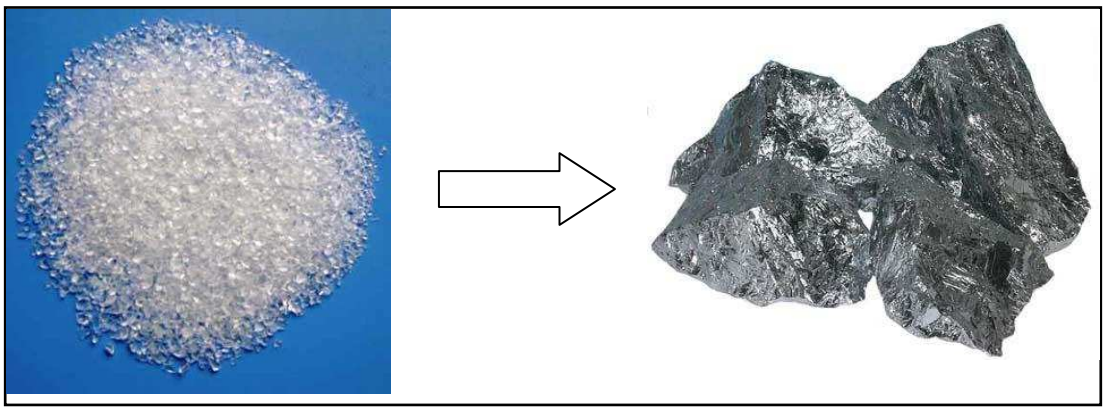

Figure I-1 Blocs de silice et silicium

Les matières premières pour la production de silicium sont le quartz et les réducteurs (charbon, coke, bois). Le quartz est un composé chimique constitué de deux éléments parmi les plus abondants sur terre, l'oxygène et le silicium. La plupart des sables contiennent une grande quantité de quartz, mais pour la production de silicium des pierres de silice pure sont utilisées. Les pierres de silice sont réduites par du charbon dans un four à arc électrique (Figure I-2). L'énergie fournie par le four est utilisé pour faire fondre le quartz de manière à pouvoir réagir avec les agents réducteurs.

La production d'une tonne de silicium nécessite [Dub90]:

- 2,5 tonnes de quartz
- 0,8 tonne de charbon de bois
- 0,2 tonne de coke
- 1,2 tonne de bois
- 0,1 tonne électrodes de graphite
- 11.000 kWh d'électricité

La réaction globale qui prend place dans le four de réduction est : $SiO_2 + 2C \rightarrow Si + 2CO$. Cette réaction globale est la somme des différentes réactions élémentaires qui ont lieu dans différentes zones du four de réduction. Une description détaillée peut être trouvée dans [STT98] Le silicium est coulé dans un creuset avec bullage d'air (raffinage par oxydation). L'oxygène de l'air réagit avec les éléments qui sont plus réactifs que le silicium, tels que l'aluminium et le calcium. Les oxydes forment une couche sur le silicium et peuvent ainsi être enlevés. Le silicium produit par le four a une forte concentration d'impuretés qui proviennent

du quartz et des réducteurs. Baluais et al. [BCD09] ont mesuré la concentration de plusieurs impuretés dans le silicium en sortie d'un four à arc électrique (tableau I-1). Les teneurs en impuretés varient selon les matières premières et un compromis doit être trouvé compte tenu de leur pureté, de leur coût et de leur disponibilité. En particulier, les teneurs en bore et phosphore de la matière première sont primordiales parce que la purification de ces éléments du silicium est coûteuse. En choisissant bien le quartz et les réducteurs la concentration en bore peut être réduite jusqu'à 7 ppm et la concentration en phosphore peut être réduite à 10 ppm [Deg08]. Les impuretés doivent être éliminées afin d'obtenir du silicium de grade solaire. Cela se fait habituellement avec le procédé Siemens

Fe	Ca	Al	Ti	B	P	C
2400 ppm	98 ppm	245 ppm	240 ppm	32 ppm	19 ppm	100 ppm

Tableau I-1 Concentration des impuretés dans le silicium métallurgique [BCD09]

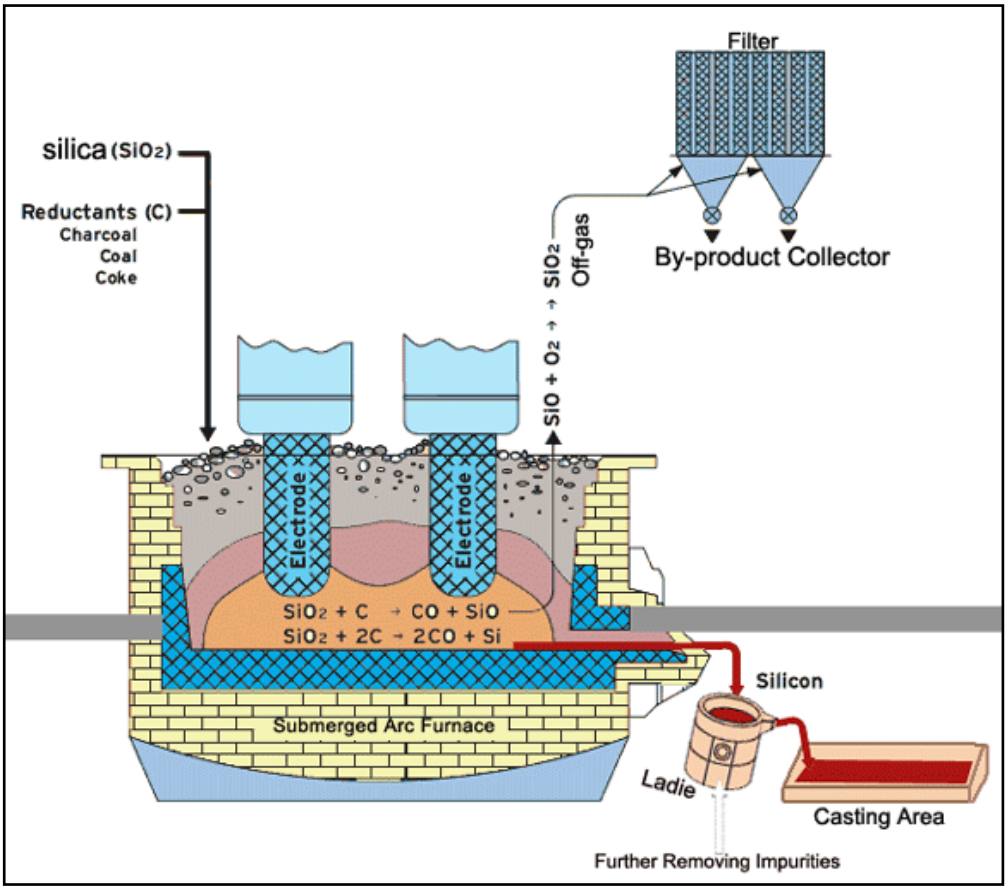

Figure I-2 Four de réduction

I.1.2. Purification par le procédé Siemens

Dans le procédé Siemens le silicium métallurgique réagit avec du chlorure d'hydrogène produisant ainsi le trichlorosilane.

$$Si + 3HCl \rightarrow SiHCl_3 + H_2$$

Le trichlorosilane est alors séparé des impuretés par distillation. Le trichlorosilane de haute pureté est alors réduit en silicium dans un réacteur CVD (Chemical Vapour Deposition)..

$$SiHCl_3 + H_2 \rightarrow Si + 3HCl$$

Pour la purification de 1 kg de silicium, la consommation d'énergie du procédé Siemens est de 110kWh d'électricité [AW07] et de 51 kWh de chaleur. Cela représente 30% de l'apport total en énergie primaire nécessaire pour la production d'une cellule solaire. Par conséquent de nouveaux procédés sont actuellement mis au point pour remplacer le procédé Siemens. Les coûts de production de silicium solaire du procédé Siemens est d'environ 50 € / kg [SSC10], et le silicium obtenu a seulement ~ 0,02 ppm d'impuretés. Un dopant peut être ajouté au silicium pour augmenter la conductivité (dopage), par exemple le bore pour obtenir du silicium de type p et le phosphore pour obtenir du silicium de type n.

I.2. La voie métallurgique

Le procédé Siemens pour la purification du silicium nécessite beaucoup d'énergie et il est ainsi couteux. Ce procédé a été développé pour fournir du silicium de haute pureté pour l'industrie des semiconducteurs. L'industrie solaire a besoin d'une pureté moins drastique, mais de volumes beaucoup plus grands, et donc un silicium moins cher est souhaité. Des procédés de purification alternatifs ont le potentiel de réduire le coût du silicium solaire. Dans le manuscrit en anglais nous présentons quelques technologies qui peuvent purifier le silicium et qui peuvent être adaptées pour l'industrie. Toutes les technologies sont basées sur ces trois phénomènes physiques:

- Ségrégation;
- Evacuation des impuretés, ou de leurs produits de réaction, due à une solubilité plus élevée dans une phase séparée ;
- Evacuation des impuretés volatiles ou des produits de réaction volatiles.

Ici nous allons présenter une combinaison de deux procédés qui peut réduire la concentration de tous les éléments.

I.2.1. Ségrégation

Quand un cristal de silicium croît, l'ajout d'un atome de silicium au réseau cristallin coûte moins d'énergie que l'ajout d'un atome d'impureté. Cet effet microscopique conduit à une plus faible concentration macroscopique de l'impureté dans le solide que dans le liquide en raison d'une plus grande solubilité de l'impureté dans le liquide. A l'équilibre le rapport entre les concentrations d'impureté entre le solide et le liquide est donné par le coefficient de ségrégation thermodynamique. Le Tableau I-2 montre des coefficients de ségrégation thermodynamiques pour différents éléments. Lorsque la solidification est assez lente, de sorte que le transport dans le silicium liquide homogénéise la concentration d'impuretés dans le liquide de façon efficace, le coefficient de ségrégation effectif est proche du coefficient de ségrégation thermodynamique. La solidification peut ainsi être utilisée pour purifier le silicium.

La ségrégation fonctionne bien pour les éléments avec des coefficients de ségrégation petits, tandis que ce n'est pas très efficace pour les éléments phosphore et bore qui ont des coefficients de ségrégation proches de un. La ségrégation peut être mise en œuvre dans un procédé de solidification dirigée.

Impuretés	Al	B	C	Ca	Cu	Fe	P	Ti
coefficient de ségrégation thermodynamique	2.10^{-3}	0.8	0.07	0.05	4.10^{-4}	8.10^{-6}	0.35	10^{-6}

Tableau I-2 Coefficients de ségrégation thermodynamique

Solidification dirigée

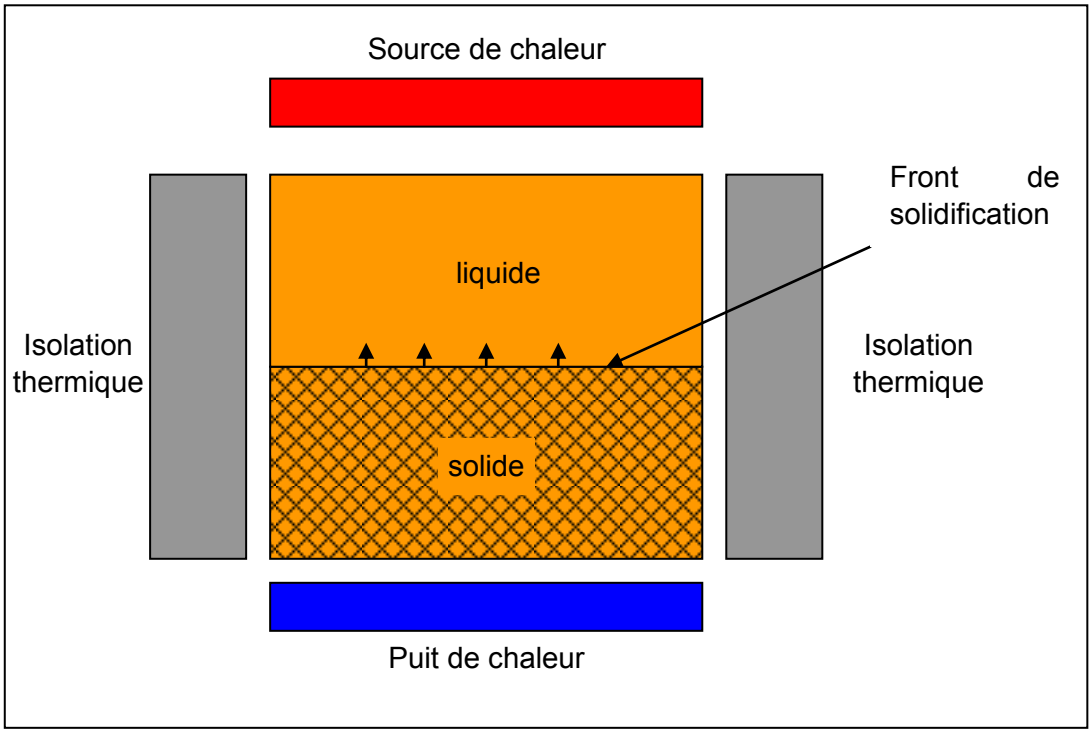

Figure I-3 Schéma d'un four pour la solidification dirigée

Au cours de la solidification dirigée le silicium est refroidi sur une face du creuset (en général le fond) et se solidifie dans une direction imposée, comme représenté sur la Figure I-3, ce qui permet d'utiliser la ségrégation pour concentrer les impuretés dans le dernier liquide. La vitesse de solidification est limitée par le transport des impuretés de l'interface solide-liquide vers la masse de liquide. Quand la diffusion est le seul mécanisme de transport, la solidification doit être lente pour éviter une concentration d'impuretés plus élevée au-dessus de l'interface solide-liquide. Le bullage d'air [And04], le brassage électromagnétique [LDZ12] et l'agitation mécanique peuvent être utilisés pour homogénéiser la concentration des impuretés dans le silicium liquide par convection. Ainsi, une plus grande vitesse de solidification peut être utilisée parce que la concentration à l'interface solide-liquide reste faible.

Après la solidification, les impuretés sont concentrées dans l'extrémité du lingot qui a solidifié en dernier. Cette extrémité est coupée afin d'obtenir un lingot avec une concentration moyenne qui est beaucoup plus faible que la concentration initiale. Sinon, la masse fondue de silicium peut être partiellement solidifiée de sorte que les impuretés sont concentrées dans le dernier liquide, qui est enlevé.

Dans des conditions idéales le profil de concentration après une solidification complète peut être calculée avec l'équation Scheil (I 1) [KF86], où k est le coefficient de ségrégation d'équilibre, C_0 est la concentration avant la solidification, x est la position dans le lingot et L est la longueur du lingot. Figure I-4 montre le résultat de l'équation de Scheil pour le phosphore et le bore avec différentes concentrations initiales.

$$C(x) = kC_0\left(1 - \frac{x}{L}\right)^{k-1} \qquad \textbf{(I-1)}$$

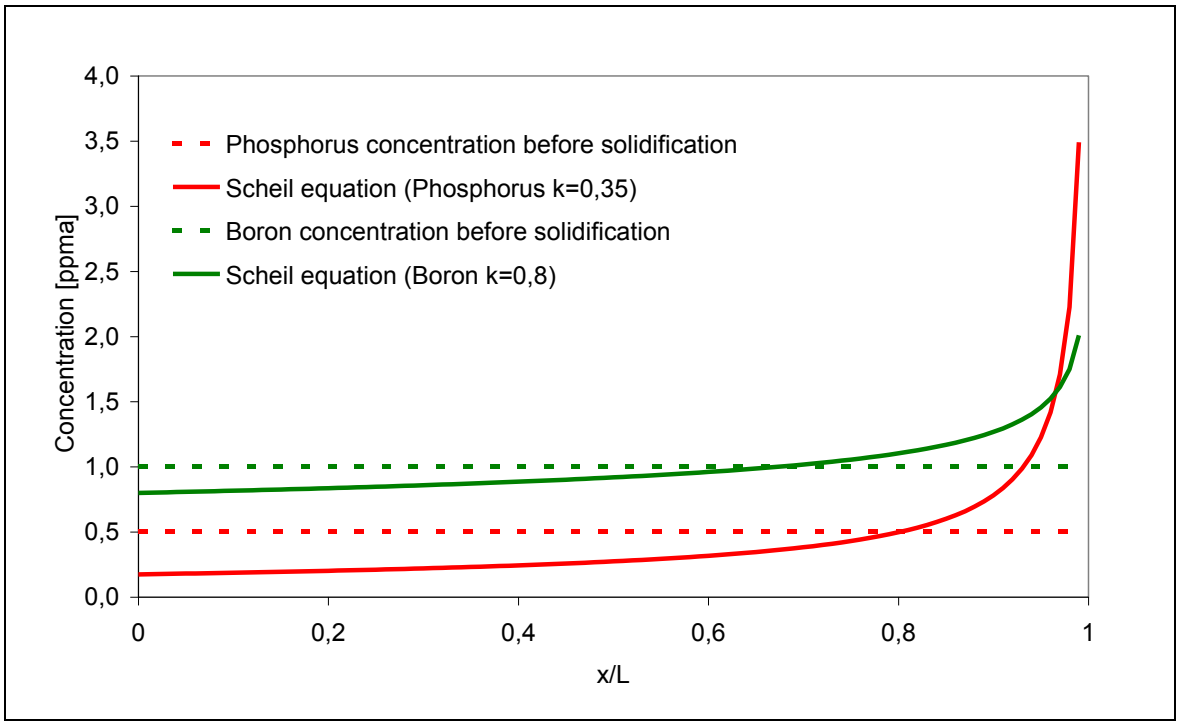

Figure I-4 Profil de concentration du bore et du phosphore après une solidification dirigée.

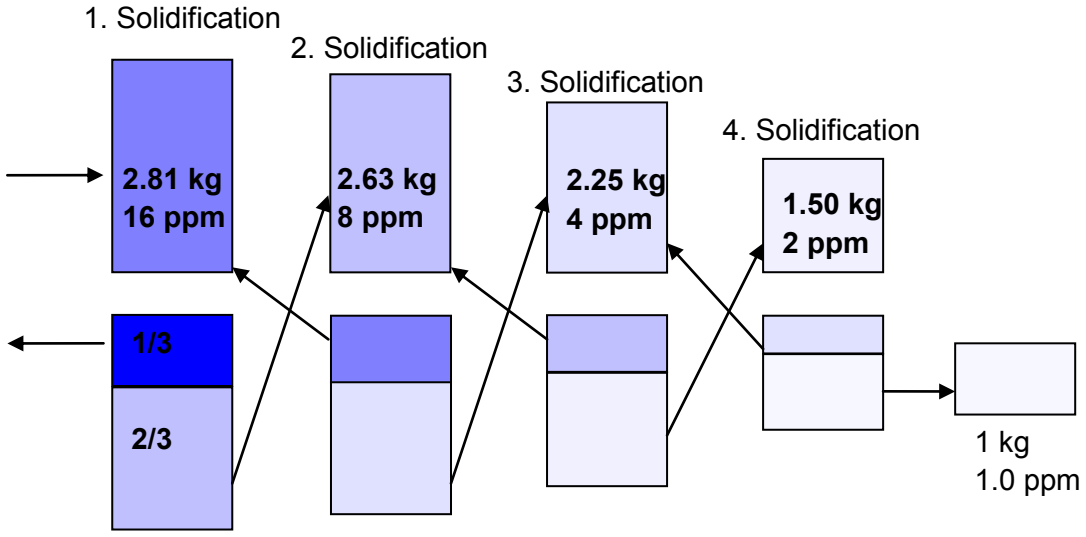

Figure I-5 Schéma pour un procédé de purification avec quatre solidifications dirigées (2/3 de la charge est solidifié et a ainsi la moitié de la concentration initiale en phosphore, le 1/3 qui reste liquide a deux fois la concentration initiale en phosphore et peut-être recyclé dans la solidification précédente.

Nous proposons un procédé avec plusieurs étapes de solidifications successives pour enlever le phosphore, dont le coefficient de ségrégation est proche de 1. Le choix du creuset est très important parce que les creusets qui ne polluent pas le silicium (typiquement en silice) sont très chers et ne peuvent pas être réutilisés. Les premières solidifications peuvent

être faites dans un creuset qui pollue le silicium mais seulement avec des éléments qui sont efficacement éliminés lors de la dernière solidification ou lors de la cristallisation. Il est important d'éviter la pollution avec des éléments qui ségrégent peu, surtout le phosphore.

I.2.2. Evacuation des impuretés volatiles ou des produits de réaction volatils.

Raffinage par plasma

Un plasma thermique avec de l'argon, de l'hydrogène et de l'oxygène (ou vapeur d'eau) est soufflé sur le silicium fondu. L'hydrogène et l'oxygène réagissent avec le bore et forment des produits volatils qui sont évacués par le flux de gaz.

La méthode a été appliquée par Morvan et al [MAC83]. Ils ont utilisé une petite torche à plasma inductive de 12 kW. Le flux de gaz contenait de l'argon avec 1% d'hydrogène et jusqu'à 0,2% d'oxygène. Depuis, le procédé a été amélioré en permanence. Une amélioration consiste en l'utilisation de brassage électromagnétique de la masse fondue de silicium de sorte que le bore est mieux transporté à la surface du bain [ATP02]. Une autre amélioration repose sur l'utilisation des torches à plasma de haute puissance jusqu'à 1,2 MW [NBS04] avec des flux de gaz élevés. Une purification rapide de grandes quantités de silicium a ainsi été rendue possible.

Il a pu être démontré que la purification est possible à l'échelle industrielle, mais les réactions chimiques au cœur du procédé sont encore mal comprises. Dans cette étude, nous cherchons à mieux comprendre ce procédé dans le but de l'améliorer. Pour cela nous caractérisons le plasma en utilisant la spectroscopie d'émission, puis nous analysons les interactions entre le plasma et le bain du silicium. Pour cette seconde étape nous utilisons un modèle simplifié de transfert de masse et nous calculons l'équilibre chimique à la surface du silicium avec le programme commercial Factsage.

I.3. Pureté visée

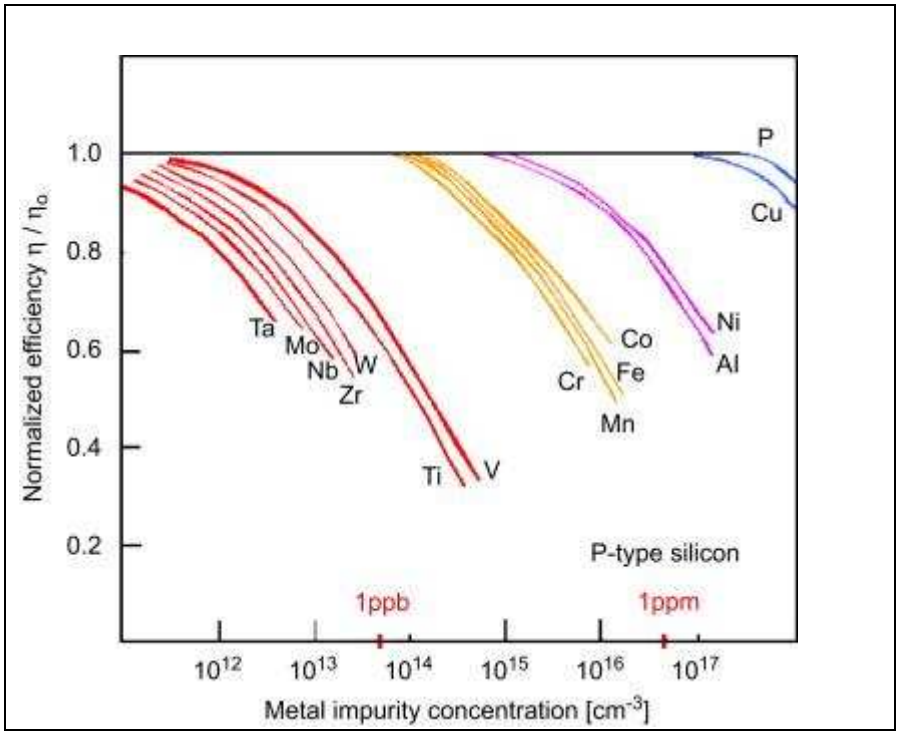

Figure I-6 Effet de la concentration des impuretés métallique (at/cm^{-3}) dans un monocristal sur l'efficacité normalisée d'une cellule solaire [Piz10],[DRH80]

Les impuretés peuvent réduire l'efficacité de la cellule solaire. En dessous d'une concentration maximale l'effet de l'impureté est négligeable, mais au-dessus de cette concentration, l'impureté dégrade de plus en plus le rendement des cellules solaires lorsque sa concentration croît. Les études sur un monocristal dopé ont montré que la concentration maximale acceptable est très différente pour les différents éléments (Figure I-6). L'effet des diffuseurs rapides peut être réduit par le gettering au cours du processus de fabrication de la cellule de telle sorte qu'une concentration plus élevée que l'indique la Figure I-6 peut être acceptable. Pendant le gettering les éléments diffusent à des emplacements où ils sont électriquement inactifs et n'ont donc pas d'influence sur le rendement de la cellule.

Le coût de la purification du silicium par la voie métallurgique augmente fortement avec le niveau de pureté souhaité. Par conséquence, il est possible d'obtenir un prix plus bas pour l'électricité (mesuré en $\$/W_c$ ou Dollar par Watt crête) avec une cellule solaire qui a une efficacité légèrement inférieure et en même temps un prix plus bas parce que le silicium est moins pur. Afin d'optimiser le niveau de pureté pour un bas prix de l'électricité il faut analyser le coût de l'ensemble du module. Powell et al [PWC12] ont estimé un coût de 0,23 $\$/W_c$ pour la charge de silicium et 1,29 $\$/W_c$ pour le module total. En utilisant un silicium de qualité inférieure avec qui coûte la moitié du prix et donnant un rendement de 9% (relatif) inférieur on obtient ainsi le même coût par watt crête ($\$/W_c$) pour la cellule solaire. Cela donne une idée quelle dégradation du rendement peut être acceptable pour réduire le coût du silicium.

Pour le silicium métallurgique la concentration de bore et de phosphore est cruciale, car ces éléments sont difficiles à enlever. Delannoy [Del11] suggère une concentration maximale de 0,5 ppm (en poids) de bore et 1,5 ppm de phosphore. Elkem [Elk12] annonce des concentrations inférieures à 0,2 ppm de bore et 0,62 ppm de phosphore. Dans les deux spécifications les concentrations atomiques sont similaires. Lorsque la concentration en donneurs est semblable à la concentration en accepteurs les deux se compensent et

augmentent la résistivité du silicium. Un tel silicium est appelé silicium compensé. Xiao et al. [XYX12] ont montré que l'efficacité d'une cellule solaire au silicium compensé avec moins de 5 ppm de bore est similaire à l'efficacité du silicium dopé classique. Toutefois, la formation de complexes de bore-oxygène peut réduire considérablement l'efficacité quand la concentration de bore est élevée. Cet effet se produit lors de l'exposition de la cellule solaire à la lumière et est donc appelé dégradation sous éclairement (LID pour Light Induced Degradation) [GKR11].

Au cours de la cristallisation le phosphore ségrége beaucoup plus que le bore. On obtient ainsi un rapport P / B plus élevé dans la partie supérieure du lingot de silicium que dans la partie inférieure. Avec 0,4 ppm de bore et 1,0 ppm de phosphore comme concentrations initiales, 88% du lingot est de type p après solidification et peut être utilisé pour la production de cellules solaires. La résistivité du lingot change également avec la concentration en phosphore. Avec le co-dopage de gallium on peut augmenter la résistivité et la fraction de silicium de type p [KWH10].

I.4. Conclusion

Nous avons présenté la technologie actuelle qui est généralement utilisée pour la production du silicium solaire. Ensuite, nous avons présenté une combinaison des procédés qui a le potentiel de produire du silicium avec une pureté inférieure à moindre coût que le procédé standard. La purification du silicium par plasma, qui fait partie de cette combinaison, peut efficacement réduire la concentration de bore dans le bain du silicium.

Quand une nouvelle configuration de purification par plasma est mise en œuvre (up-scaling), il est important d'adapter les différents paramètres afin d'obtenir le taux de purification le plus élevé possible. Il faut ainsi optimiser la température, la composition et la vitesse du plasma. Les paramètres qui peuvent être modifiés sont la puissance, les débits de gaz et de la géométrie de la torche à plasma. Jusqu'à présent, le procédé est mal compris. Les améliorations peuvent seulement être obtenues par des études empiriques. Avec une meilleure compréhension du procédé, il serait plus facile d'optimiser une installation.

L'objectif de cette étude est d'obtenir une meilleure compréhension du transfert de masse et des réactions qui jouent un rôle dans le processus. Pour cela nous avons d'abord analysé et amélioré un modèle de transfert de masse pour identifier les étapes limitantes du procédé (chapitre II). Un modèle numérique de mécanique des fluides a été élaboré au laboratoire par Mickael Majchrzak. Ce modèle simule le plasma et peut ainsi calculer le transfert de masse vers la surface de silicium. La validation de ce modèle par spectroscopie est le point le plus important de cette étude. Dans le chapitre III, nous présentons la théorie qui est nécessaire à la compréhension de la méthode spectroscopique. Dans le chapitre IV, nous présentons les installations expérimentales pour la mise en œuvre de la méthode. Dans le chapitre V, les résultats des mesures spectroscopiques sont présentés et comparés au modèle. Au chapitre VI, nous présentons des expériences de mesure des vitesses de gaz et des mesures du couplage électromagnétique dans la torche à plasma à couplage inductif. Dans le chapitre VII, nous présentons des tests paramétriques de l'efficacité de la purification.

II. Purification du silicium par plasma

Dans ce chapitre nous faisons un aperçu de la théorie et des mesures sur le procédé trouvées dans la littérature. Nous utilisons un modèle de transfert de masse simple pour trouver l'étape limitante du procédé (Figure II-1). Le transport du bore vers la surface n'est probablement pas l'étape limitante parce que le brassage est efficace. La littérature [NBS04] suggère que les réactions chimiques à la surface sont lentes et qu'elles sont ainsi limitantes.

Cependant notre hypothèse est que les réactions chimiques à la surface sont rapides et que les espèces sont en équilibre chimique à la surface. Avec un équilibre chimique à la surface l'évacuation des produits de réaction et le transport de l'oxydant vers la surface du silicium restent comme étapes limitantes. Dans ce chapitre nous démontrons la validité de l'équilibre chimique à la surface du silicium.

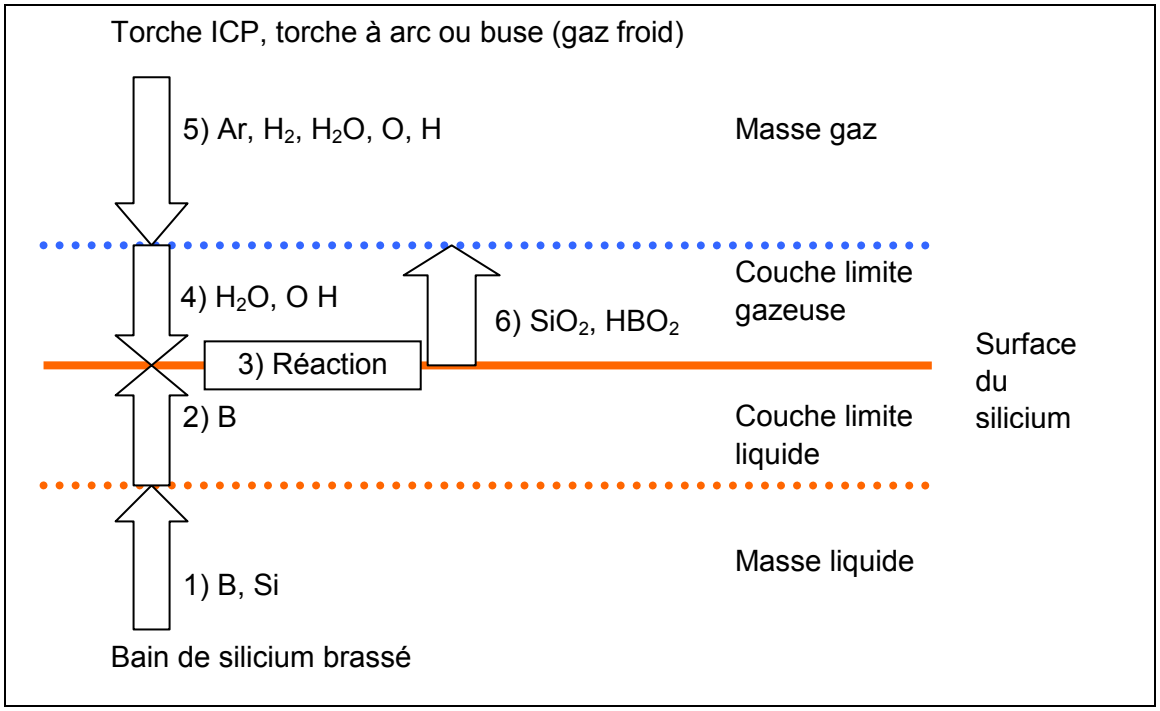

Figure II-1 Modèle de transfert de masse du procédé de purification
1) Convection du silicium et du bore
2) Diffusion du bore à travers une couche limite liquide
3) Réaction du silicium avec des oxydants
4) Diffusion des oxydants à travers une couche limite gazeuse
5) Convection d'argon, d'hydrogène et d'oxydants
6) Diffusion d'un aérosol de SiO_2 et de HBO_2 gazeux

La variation relative de la vitesse de purification mesurée avec la fraction d'hydrogène et la température est très similaire à la variation relative de la pression partielle d'HBO à l'équilibre chimique. (Figure II-2, Figure II-3). Ceci montre que les concentrations à la surface du silicium sont en équilibre chimique. Si les réactions étaient l'étape limitantes, la vitesse de purification devrait augmenter avec la température (loi d'Arrhenius). Dans les mesures trouvées dans la littérature on voit que la vitesse de purification décroit avec la température. Ainsi, les réactions chimiques ne peuvent pas être l'étape limitante.

Dans le chapitre II nous montrons aussi que l'atmosphère réductrice au dessus du silicium est très fine parce que la pression partielle de l'oxydant (O ou H_2O) dans le jet de gaz est beaucoup plus grande que la pression partielle du silicium à la surface. Comme l'atmosphère réductrice est très fine, c'est l'atmosphère oxydante qui devient importante pour l'évacuation des produits de réaction. En atmosphère oxydante le silicium est oxydé en silice qui forme un aérosol en dessous d'environ 2000°C pendant que le bore reste sous forme d'une espèce gazeuse (HBO_2). Le plasma a une température bien plus élevée (~8000K) mais à proximité de la surface du silicium la formation de silice est possible. Cependant on ne sait pas si cette formation (germination et croissance de germes) est suffisamment rapide pour que les concentrations soient à équilibre chimique. La formation de l'aérosol peut avoir un rôle important dans le procédé. La formation de l'aérosol peut expliquer pourquoi on

mesure un rapport B/Si plus élevé dans les gaz en sortie de réacteur que prédit par la

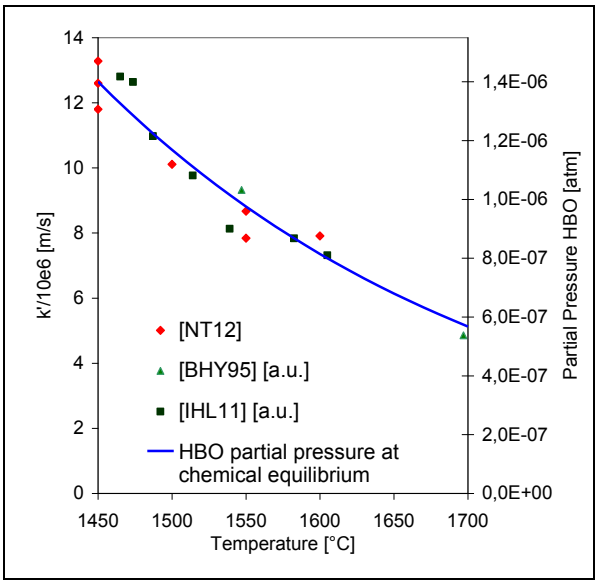

Figure II-2 Variation relative de la pression partielle d'HBO à l'équilibre chimique et de la vitesse de purification mesurée avec la température : [NT12] en jet de gaz froid, [BHY95] et [IHL11] avec un plasma

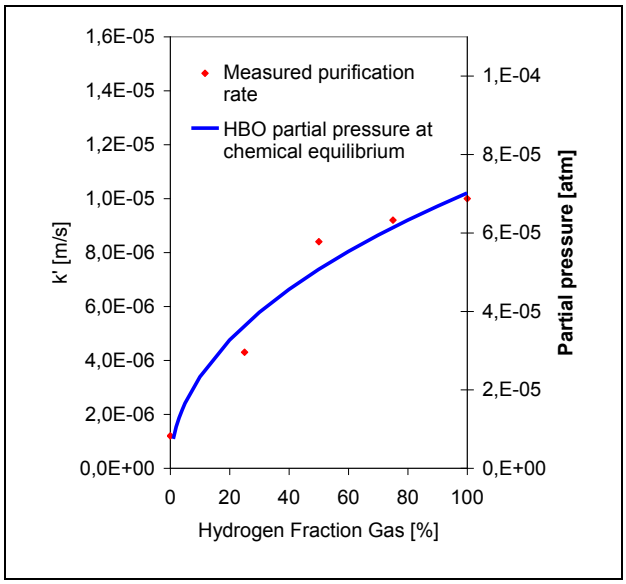

Figure II-3 Variation relative de la pression partielle d'HBO à l'équilibre chimique et de la vitesse de purification mesurée [NT12] avec la fraction d'hydrogène dans le gaz

III. Techniques spectroscopiques pour la caractérisation du plasma

Par un calcul d'équilibre chimique nous pouvons montrer que les éléments sont sous forme atomique (Ar, O, H) dans le plasma. Nous développons ainsi une méthode de caractérisation de la température et des rapports O/Ar et H/Ar.

Cette méthode est basée sur la spectroscopie d'émission. Nous utilisons l'émissivité des raies atomiques pour calculer la température et les rapports de concentration. L'émissivité d'une raie est donnée par la formule (III-1). L'émissivité d'une raie atomique dépend de la température, de la concentration de l'élément et de quelques constantes de la raie que l'on peut récupérer dans la base de données de spectres atomiques du NIST [nis].

$$\varepsilon_{\text{line}} = \frac{[\text{X}]\cdot g_u \cdot e^{-E_u/k_B T}}{Z(T)} \cdot A_{ul} \frac{hc}{4\pi\lambda} \qquad \text{(III-1)}$$

En mesurant l'émissivité d'une raie d'argon on peut calculer la température du plasma parce que sa concentration est connue (la fraction d'argon est proche de 100%). Avec le rapport des émissivités entre une raie d'hydrogène et une raie d'argon on peut ensuite calculer le rapport de concentration H/Ar. Le calcul du rapport O/Ar est équivalent.

Il faut prendre en compte quelques critères pour le choix des raies. Pour mesurer une seule raie il faut éviter les raies trop intenses qui peuvent être auto-absorbées. Il faut aussi éviter l'interférence de deux raies à la même longueur d'onde.

Pour mesurer deux raies en même temps il faut choisir deux raies avec des longueurs d'onde proches pour être dans la bande passante du spectromètre (le spectre doit être entièrement sur la caméra ccd du spectromètre). En plus les deux raies doivent avoir des intensités similaires, sinon la dynamique de la caméra CCD limite la mesure.

Les raies atomiques choisies sont présentées dans le Tableau III-1. Les premières mesures ont été faites avec un spectromètre équipé d' un photomultiplicateur (PM). Cet instrument peut mesurer seulement une raie atomique à la fois. Nous avons par la suite fait des mesures avec un spectromètre avec caméra CCD qui permet de mesurer plusieurs raies en même temps. Nous avons sélectionné des raies d'argon plus intenses pour des valeurs élevées de H/Ar ou O/Ar.

CCD				PM
Bas [O]/Ar	Haut [O]/Ar	Bas [H]/Ar	Haut [H]/Ar	Tout
O 645.6 nm	O 645.6 nm	H 410.2 nm	H 410.2 nm	O 436.8 nm, H 486.1 nm
Ar 638.5 nm	Ar 641.6 nm	Ar 416.4 nm	Ar 415.9 nm	Ar 420.0 nm, 415.9 nm

Tableau III-3 Les raies sélectionnées

III.1.1. La fonction de transfert des monochromateurs

Nous avons calculé les fonctions de transfert des deux monochromateurs utilisés dans notre étude (élargissement instrumental). Nous trouvons une bonne coïncidence entre la fonction de transfert simulée et la fonction de transfert mesurée. Cette comparaison valide la simulation de la fonction de transfert. La connaissance de la fonction de transfert et très importante pour la mesure de l'émissivité avec un monochromateur qui est équipé avec un photomultiplicateur. Le photomultiplicateur mesure seulement l'intensité à une longueur d'onde à la fois. Avec la connaissance de la fonction de transfert on peut calculer l'émissivité totale d'une raie à partir de l'émissivité spectrale à la longueur d'onde centrale de la raie.

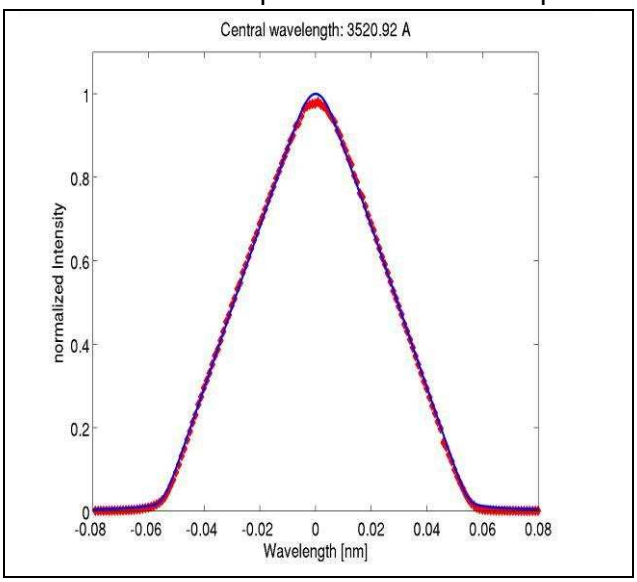

Figure III-1 Spectres mesuré et simulé à 352.1 nm
f=640 mm, Fente= 90 µm,
k=2400 mm^{-1}, D=10 mm, β=13.2°

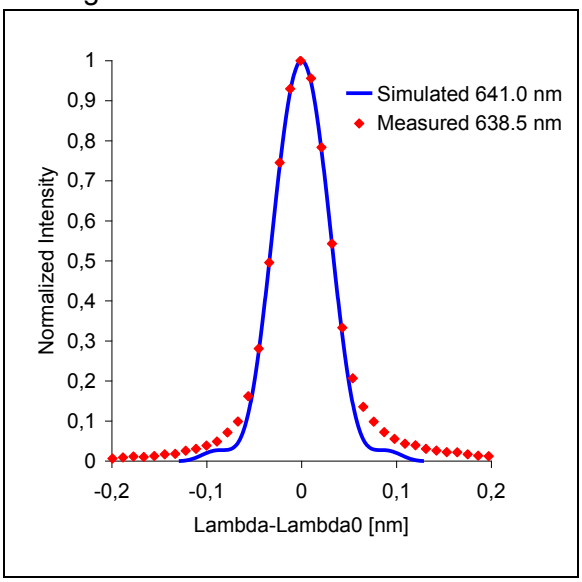

Figure III-2 Spectres mesuré et simulé à 641 nm, f=750 mm, k=1800 mm^{-1},
Pixel = 20 µm, Fente= 90 µm, D=7 mm,
λ=415 nm, β=6.49°

III.1.2. Elargissement Doppler et Stark

Pour le calcul de l'émissivité des raies d'hydrogène il faut prendre en plus en compte l'élargissement de la raie, alors que cet élargissement est petit pour les raies d'argon et d'oxygène par rapport à l'élargissement instrumental. L'élargissement des raies d'hydrogène est principalement dû aux effets Doppler et Stark. L'élargissement Doppler donne un profil Gaussien à la raie et l'élargissement Stark donne un profil Lorenzien. Le cumul des deux

élargissements donne une convolution du profil Gaussien et du profil Lorenzien. Cette convolution a le nom de fonction de Voigt. Le profil mesuré est une convolution de la fonction de Voigt de la raie et de la fonction de transfert du monochromateur (Figure III-3)

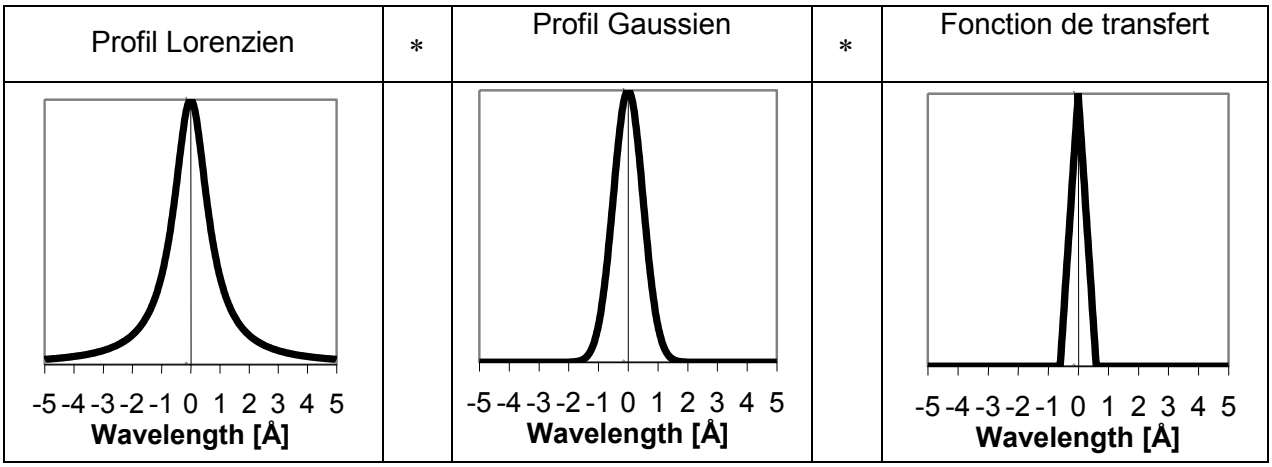

Figure III-3 Convolution des différents effets d'élargissement

III.1.3. Mesure de la densité électronique

Gigisos et al. [GGC03] donnent la formule (III-2) pour la relation entre la largeur à mi-hauteur (FWHM – Full width at half maximum) de la raie H-Beta. On peut ainsi calculer la densité électronique à partir de la largeur à mi-hauteur mesurée. Nous appliquons cette méthode à la raie H-Delta en utilisant une formule de Griem [Gri64]. La Figure *III-4* montre le profil radial de la largeur à mi-hauteur de la raie H-Delta mesuré dans le plasma. La Figure *III-5* montre le profil radial de la densité électronique calculé à partir du profil de la Figure *III-4*.

$$\mathrm{FWHM} = 4.800\mathrm{nm}\cdot\left(\frac{n_e}{10^{23}\mathrm{m}^{-3}}\right)^{0.68116} \qquad \text{(III-2)}$$

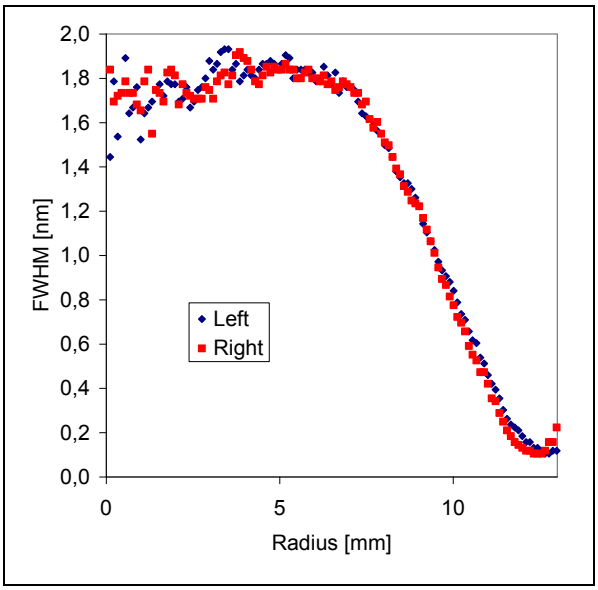

Figure III-4 Profil radial de la largeur à mi-hauteur de la raie H-Delta

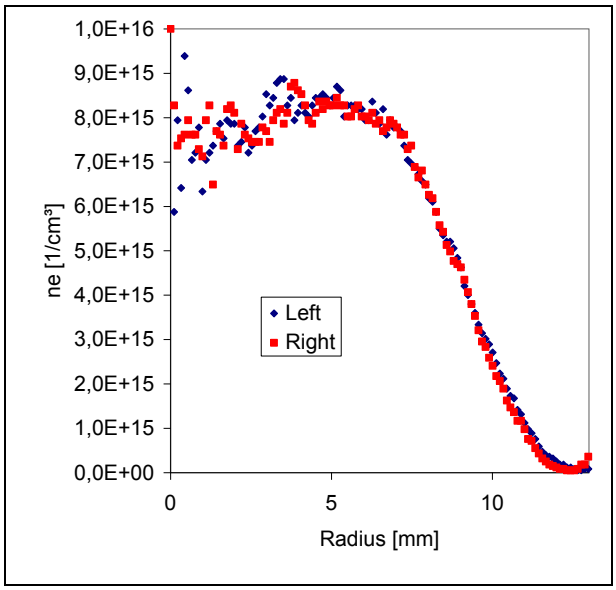

Figure III-5 Profil radial de la densité électronique calculé à partir de la largeur à mi-hauteur de la raie H-Delta

III.1.4. Inversion d'Abel

On mesure la lumière qui sort du plasma. Cette lumière est l'intégrale de l'émissivité à travers le plasma. On cherche à mesurer l'intensité d'une fine corde d'observation. Si on mesure cette intensité pour plusieurs positions y, on obtient un profil d'intensité. Un algorithme appelé inversion d'Abel peut être utilisé pour calculer l'émissivité à partir du profil d'intensité. Cet algorithme est seulement valable si les profils d'émissivité sont axisymétriques.

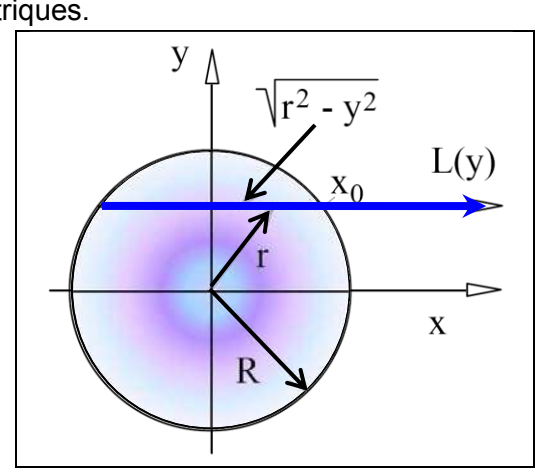

Figure III-6 Inversion d'Abel
Le cercle remplace le plasma
La flèche bleue indique la corde d'observation

La mesure de l'émissivité absolue d'une raie d'argon permet de calculer la température. La mesure du rapport d'intensité entre une raie d'argon et une raie d'hydrogène ou d'oxygène permet quant à elle de calculer les rapports de concentration [H]/[Ar] et [O]/[Ar]. L'élargissement spectral joue un rôle particulièrement important sur la précision des mesures de l'émissivité sur un monochromateur équipé d'un photomultiplicateur, ce dernier ne pouvant mesurer une émissivité spectrale à la fois. Nous avons pu démontrer que nous pouvions simuler précisément la fonction de dispersion des deux monochromateurs utilisés au cours de cette étude. L'élargissement Stark peut être utilisé pour mesurer la densité électronique et valider l'hypothèse de l'équilibre thermique local et ainsi valider les mesures de température.

L'inversion d'Abel peut être utilisée pour calculer l'émissivité radiale (W/m^3) à partir d'un profil latéral d'intensité (W/m^2). L'algorithme utilisé pour l'inversion d'Abel a été évalué avec une fonction de test, ce qui nous a permis de mettre en évidence que l'inversion d'Abel amplifie le bruit sur le profil latéral d'intensité. Un lissage polynomial peut cependant permettre de réduire ce bruit.

Dans le chapitre suivant IV nous présentons les moyens expérimentaux utilisés pour la génération du plasma et pour la mesure de l'émissivité. La chapitre V présente quant à lui les résultats des mesures spectroscopiques.

IV. Les dispositifs expérimentaux

IV.1. La torche à plasma

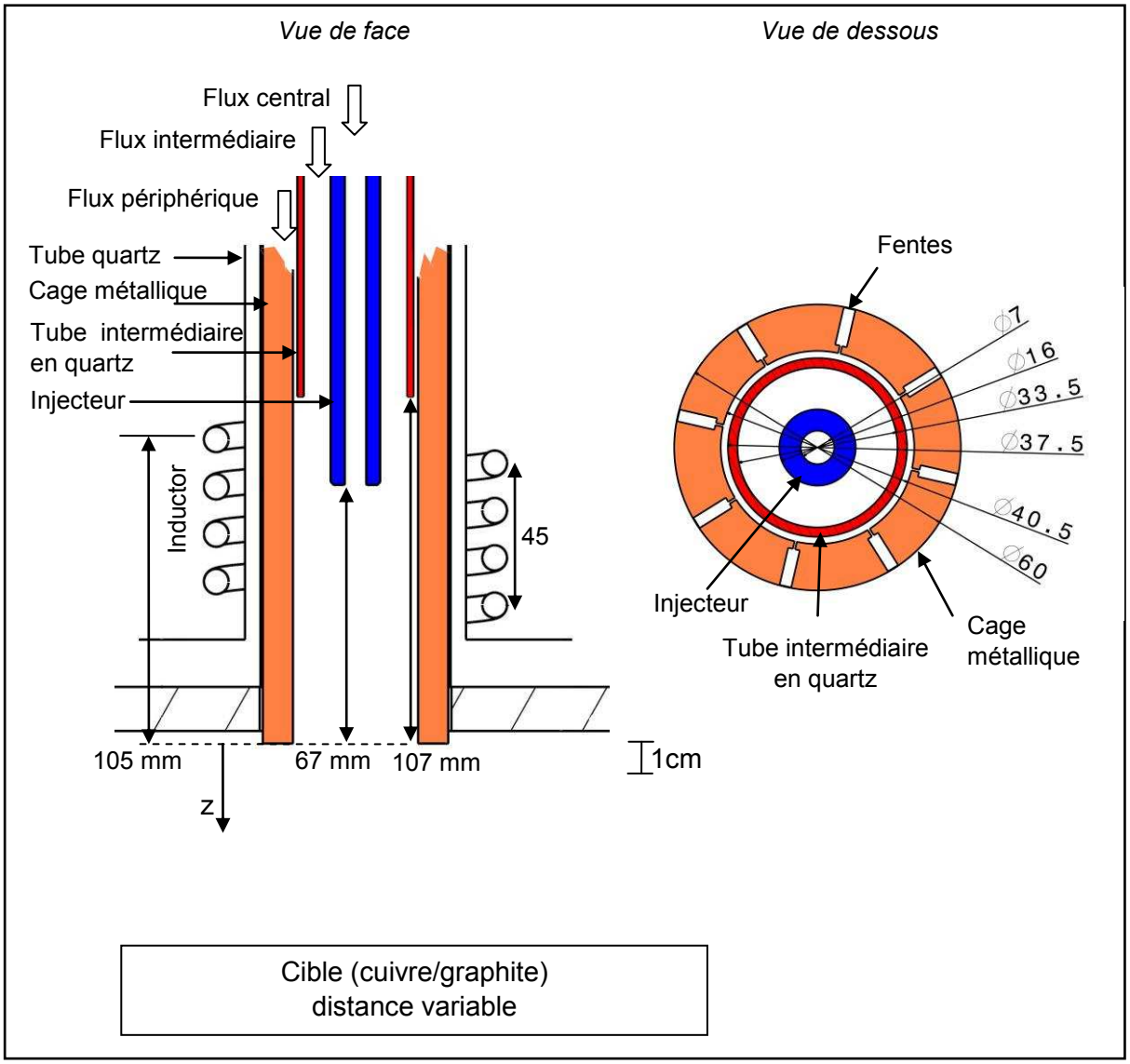

Figure IV.1 Géométrie de la torche à plasma

La torche à plasma consiste en trois tubes concentriques. Dans la petite section entre le tube extérieur et le tube intermédiaire un grand flux de gaz (flux périphérique ou outer flow) est injecté. Ce flux de gaz confine le plasma. Le flux de gaz du tube central (inner flow) est injecté à l'intérieur de plasma et ne modifie pas la composition du plasma dans les zones où le plasma couple avec le champ électromagnétique. L'hydrogène, qui modifie fortement le couplage quand il est injecté dans le flux périphérique, doit être injecté préférentiellement dans le flux central.

IV.2. Le système optique

La Figure IV.2 montre un dessin de l'installation optique utilisée pour les mesures spectroscopiques avec le monochromateur avec CCD. La lumière du plasma est réfléchie par deux miroirs en direction du monochromateur. Une lentille projette la lumière du plasma

sur la fente d'entrée du monochromateur. L'image est tournée par les deux miroirs de 90°. L'image du cylindre vertical (qui représente le plasma) est ainsi horizontale. La fente d'entrée verticale mesure une coupe horizontale du plasma. Comme les miroirs sont motorisés on peut faire un balayage vertical et cartographier tout le plasma. Un programme Labview est utilisé pour faire les mesures et le même programme fait aussi le traitement de données pour obtenir la carte de température et la carte des rapports de concentration O/Ar et H/Ar.

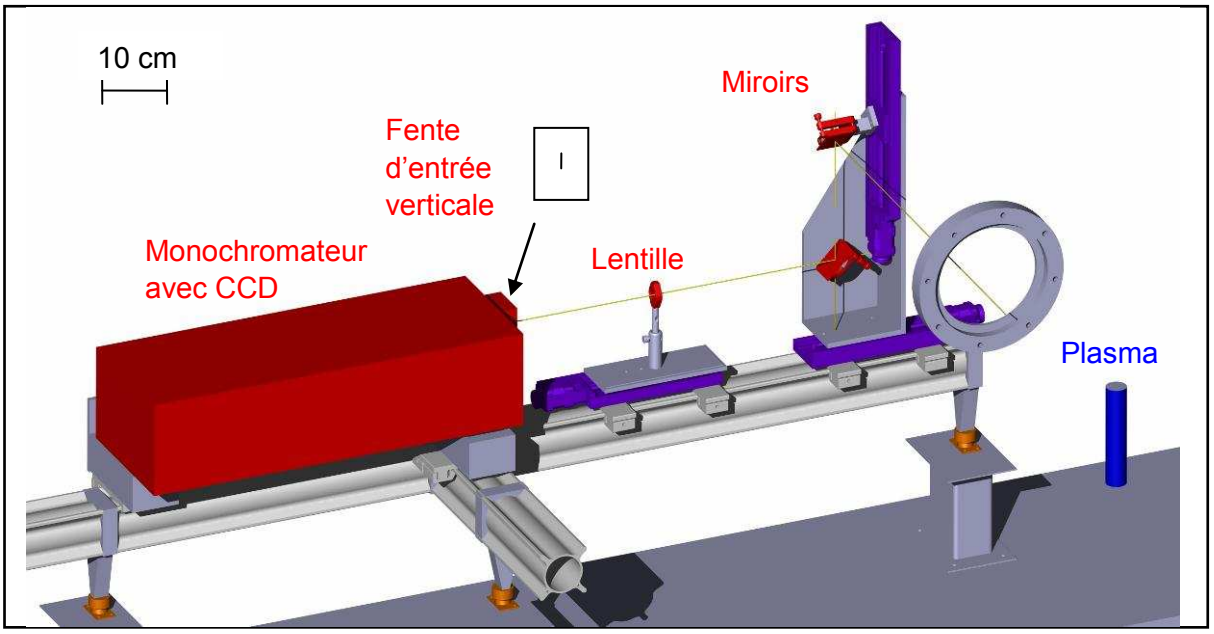

Figure IV.2 Le système optique pour les mesures avec monochromateur avec CCD

IV.3. Autres éléments du chapitre 4:

Nous présentons le générateur et nous présentons une mesure de l'efficacité de couplage entre le générateur et le plasma. L'efficacité du couplage est un paramètre qui est important pour le modèle numérique du plasma (CFD, computational fluid dynamics model). Les débitmètres sont présentés et nous analysons leur précision. Nous examinons le système optique. Les spectres mesurés doivent être corrigés pour annuler l'effet de la non-uniformité de la fente d'entrée et pour annuler l'effet de la non-uniformité de la réponse de la camera CCD. Nous présentons le traitement de données utilisé pour calculer des profils radiaux de température et de rapport de concentration à partir des spectres 2D de la caméra CCD. Nous identifions la lumière diffuse comme source d'erreur et nous expliquons comment on peut réduire la quantité de lumière diffuse. Nous expliquons comment nous calibrons le système optique avec une lampe de calibration. La calibration absolue permet de mesurer l'émissivité absolue à partir de laquelle on peut calculer la température.

V. Mesures spectroscopiques

V.1. Validation de la méthode

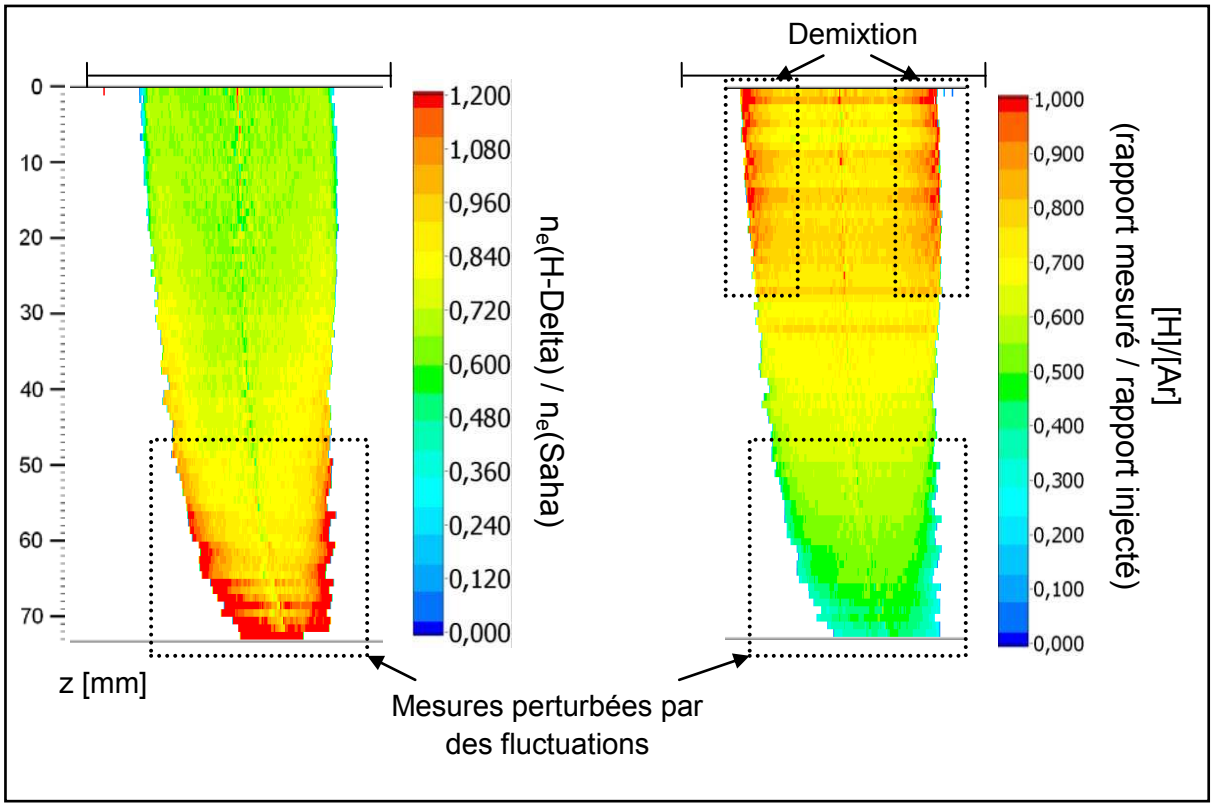

Figure V-1 Mesures de validation, mélange homogène de $[H_2]/[Ar]=0.02$
A gauche : Rapport entre la densité électronique mesuré avec l'élargissement de la raie H-Delta et la densité électronique calculé avec l'équation de Saha
A droite : Rapport entre le rapport H/Ar mesuré et le rapport H/Ar injecté.

Comme la méthode utilisée dans cette étude est peu appliquée dans la littérature nous faisons plusieurs expériences pour la valider. Des mesures de validation ont montré que le plasma est très proche de l'équilibre thermodynamique local ce qui est nécessaire pour la validation de la mesure de concentration et de température. La Figure V-1 montre un des résultats principaux des mesures de validation. La mesure de la densité électronique avec deux méthodes montre que dans la plus grande zone du plasma les deux méthodes mesurent la même valeur. Ceci montre que le plasma est en équilibre thermodynamique local. En bas les mesures sont perturbées par des fluctuations. Les fluctuations perturbent aussi la mesure du rapport de concentration H/Ar. En haut la mesure de la densité électronique n'est pas perturbée. La concentration plus élevée mesurée en haut au bord n'est donc probablement pas due à une perturbation mais plutôt due à la démixtion dans la zone de couplage. La démixtion est un effet qui pousse un gaz moléculaire dans un gradient de température autour de la température de dissociation vers la température froide parce que le molécules ont un coefficient de diffusion plus faible que les atomes.
En moyenne le rapport de concentration mesuré est proche au rapport de concentration injecté. Ceci valide la mesure du rapport de concentration. La différence d'environ 25% entre

le rapport mesuré et le rapport injecté est probablement dûe à l'imprécision de 25% sur la probabilité de transition de la raie d'Argon.
Le rapport moyen entre les deux mesures de la densité électronique qui est proche de l'unité indique que la précision sur la mesure de température est ±300 K

V.2. Comparaison modèle expérience

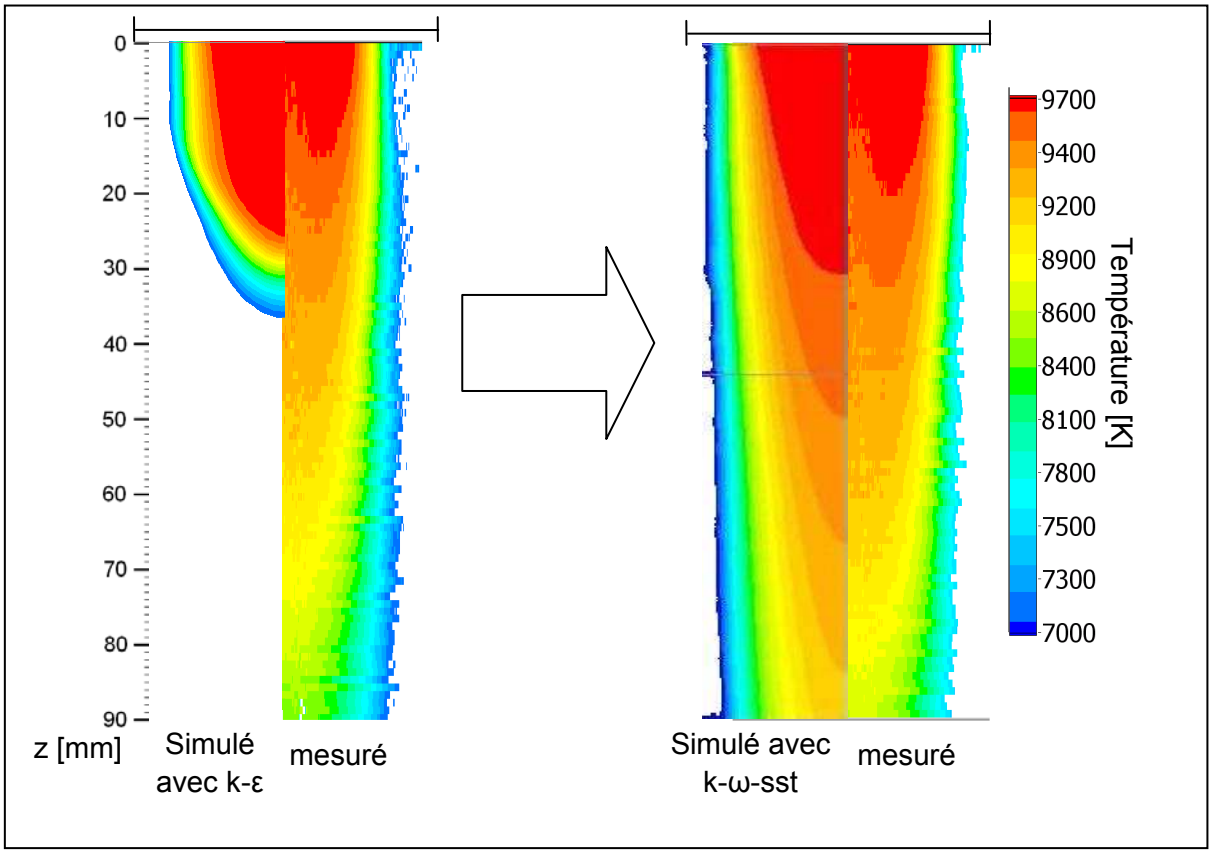

Figure V-2 Comparaison entre modèle et mesure avec les deux modèles de turbulence k-ε et k-ω-sst

La Figure V-2 montre la comparaison entre modèle et mesure. Le modèle k-ε était utilisé auparavant pour la simulation de la turbulence. Le plasma simulé refroidit plus rapidement que le plasma mesuré. Ceci est probablement dû à une surestimation de la diffusion turbulente dans le modèle k-ε. La diffusion turbulente plus élevée fait que la chaleur du plasma diffuse plus que dans le plasma réel. Pour cette raison nous avons remplacé le modèle de turbulence k-ε par le modèle k-ω-sst. On peut voir dans la Figure V-2 que la carte de température simulée avec ce modèle de turbulence est similaire à la carte de température mesurée. Cette comparaison, parmi d'autres, montre que le modèle peut précisément simuler le plasma.

V.3. Autres éléments du chapitre 5:

Des mesures paramétriques ont montré que la puissance plasma a un effet significatif sur la température du plasma. L'hydrogène diffuse plus que l'oxygène et il est en général bien dilué. L'oxygène ne diffuse que lentement vers l'extérieur du plasma quand on l'injecte au centre du plasma. Pour obtenir une concentration homogène il est préférable d'injecter l'oxygène à l'extérieur et l'hydrogène à l'intérieur.

VI. Autres mesures de caractérisation du plasma

VI.1. Mesures de vitesse

Nous avons testé une méthode de mesure de vitesse dans le plasma. Pour cela nous avons filmé le plasma avec une caméra rapide. Dans les films nous avons mesuré la propagation de fluctuations le long du plasma.

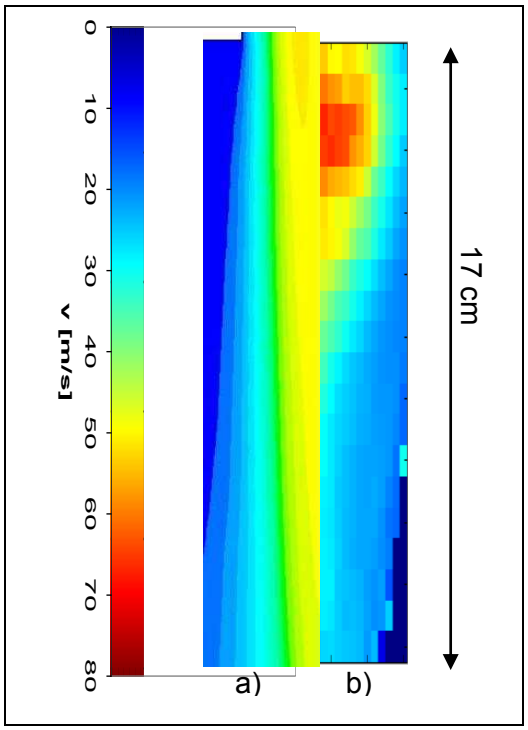

Figure VI.1 Comparaison entre une carte de vitesse simulée (a) et une carte de vitesse mesurée (b)

Dans la Figure VI.1 nous comparons une carte de vitesse mesurée à une carte de vitesse simulée. La zone à grande vitesse (60 m/s) que nous mesurons en-dessous de la sortie de la torche ne peut pas être observée dans la carte de vitesse simulée. Ceci indique que la mesure n'est pas exacte dans cette zone. L'erreur est probablement due à l'intégration de la lumière à travers le plasma. Plus en aval le modèle et la mesure indiquent une vitesse plus élevée au centre et plus basse au bord du plasma. La vitesse dans le modèle est plus élevée, ce qui peut être dû à une puissance plasma plus élevée dans le modèle.

Les erreurs de mesure sont trop grandes pour utiliser ces mesures pour la validation du modèle. La sonde enthalpique [RSB95] est probablement mieux adaptée pour mesurer la vitesse et pour valider le modèle.

VI.2. Le couplage

Le coefficient de couplage est un paramètre important pour l'utilisation de la torche à plasma. Si le coefficient de couplage est petit il faut utiliser une plus grande tension pour injecter la même puissance. Le coefficient de couplage détermine l'impédance du circuit oscillant (formé par le boitier de condensateurs et l'inducteur de la torche à plasma). En variant la valeur de la capacité on peut adapter l'impédance du circuit oscillant. Si l'impédance est adaptée on peut obtenir le courant maximal à la tension maximale. Si l'impédance n'est pas adaptée on peut seulement obtenir une partie de la puissance maximale du générateur.

Nous démontrons que le coefficient de couplage dépend surtout de la taille du plasma qui à son tour dépend de la conductivité thermique des gaz. Les gaz avec une grande conductivité thermique comme l'hydrogène devraient être injecté dans l'injecteur, ou ils ne modifient pas le couplage. Injecté dans le débit extérieur l'hydrogène réduirait le coefficient de couplage et augmenterait ainsi l'impédance. Le débit intermédiaire devrait être de l'argon pur parce que l'oxygène et l'hydrogène réduiraient fortement le coefficient de couplage. L'injection de l'oxygène modifie le couplage mais les variations restent suffisamment faibles pour permettre l'utilisation du plasma à la puissance maximale du générateur.

Pendant les mesures nous avons observé un mode à faible couplage. Dans ce mode à faible couplage l'impédance du circuit oscillant est élevée et réduit fortement la puissance maximale que le générateur peut fournir. Ce mode de faible couplage peut apparaitre dans les mêmes conditions de fonctionnement que le couplage normal (voir Figure VI.2 et Figure VI.3). Pour les procédés il est important d'employer la torche à plasma dans des conditions où la transition de mode ne peux pas apparaitre, car la transition du couplage normal vers le faible couplage modifie fortement les propriétés du plasma.

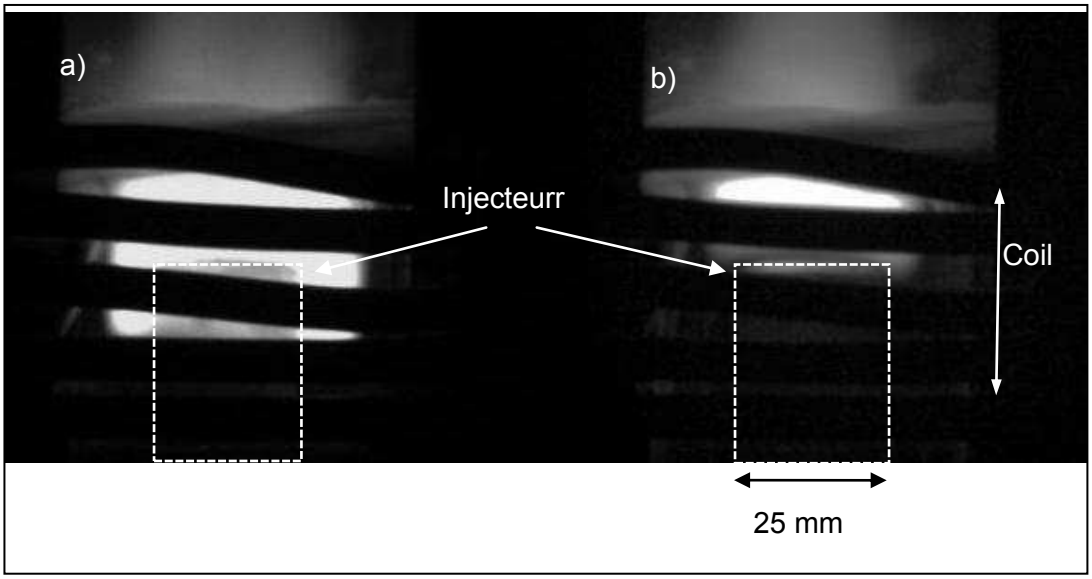

Figure VI.2 Le deux modes de couplage à la même tension et les mêmes débits de gaz dans une petite torche a) normale, b) bas couplage

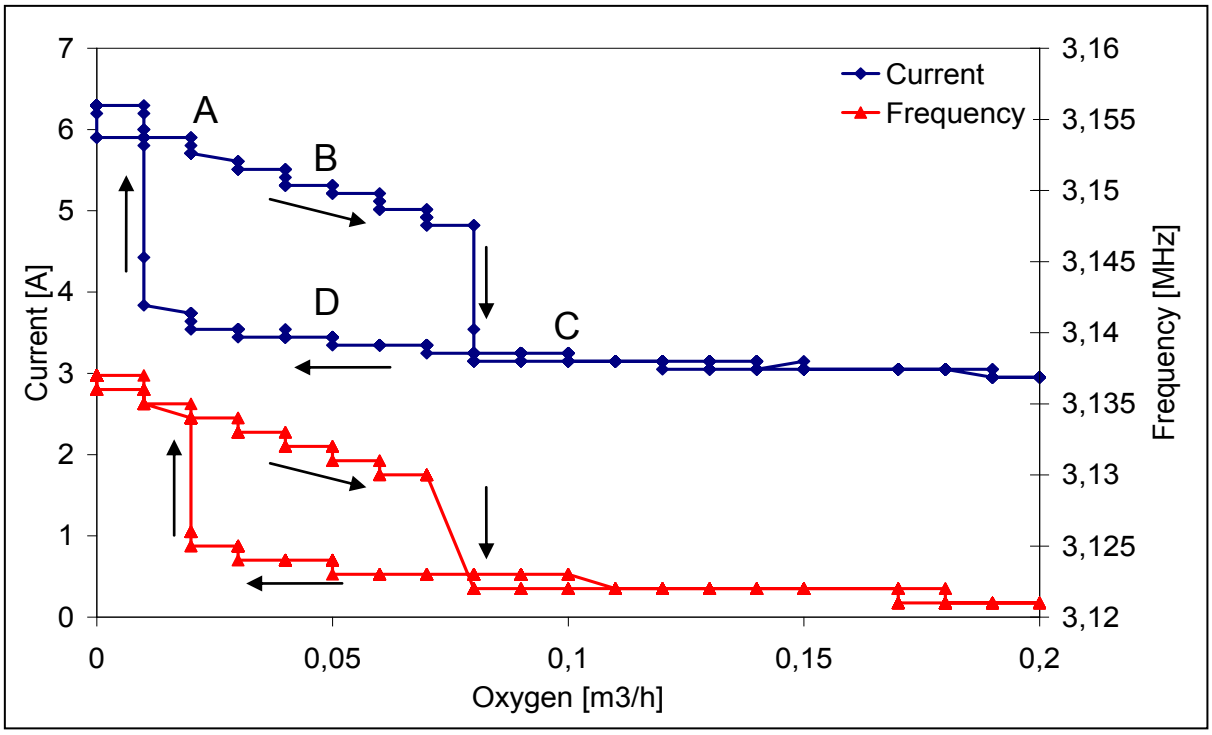

Figure VI.3 Variations du courant et de la fréquence avec le débit intermédiaire d'oxygène A+B couplage normal ; C+D faible couplage

VII. Mesure de la vitesse de purification

VII.1. Mesure du facteur d'enrichissement

	H_2O+H_2 Fraction	Température du silicium	Plasma	R_{exp}	R_{thermo}	R_{exp} / R_{thermo}
[Fou03]	5 %	1410 °C	X	136	15	9
[NBS04]	2.5 %	1600-1700 °C	X	36	5.5	7
[NT12]	3.2 %	1500 °C		>11*	6	>2

Tableau VII-1 Comparaison entre facteur d'enrichissement mesuré et facteur d'enrichissement thermodynamique (limite basse dû au flux de vapeur d'eau)*

Nous avons calculé le facteur d'enrichissement thermodynamique pour les conditions opératoires (fraction d'hydrogène et températures de silicium) correspondant à plusieurs mesures de la littérature ([NBS04], [NT12]) et de notre groupe [Fou03]. Les facteurs d'enrichissement sont présentés dans le tableau VII-1. Pour la mesure de [Fou03] nous avons mesuré le facteur d'enrichissement avec deux méthodes différentes. Nous avons utilisé d'un coté le rapport B/Si du signal ICP et la concentration du bore dans le silicium. D'un autre coté nous avons utilisé le temps de demi-vie de la concentration de bore dans le bain et le flux d'oxygène qui arrive à la surface. Avec les deux méthodes nous trouvons un facteur d'enrichissement similaire qui est bien plus élevé que le facteur d'enrichissement à l'équilibre chimique. Les mesures de [NBS04] montrent aussi un facteur d'enrichissement plus élevé qu'à l'équilibre chimique. La mesure de [NT12], par contre, est peu différente de

l'équilibre chimique. Le facteur d'enrichissement est probablement plus élevé dans [Fou03] et [NBS04] parce que le plasma modifie l'évacuation de l'aérosol de SiO_2.

VII.2. Vérification de la méthode de mesure

Une pompe péristaltique prélève un débit constant des gaz en sortie du réacteur. Ce gaz prélevé est envoyé dans un analyseur ICP commercial (Spectro). Dans le plasma de l'analyseur ICP les composé de silicium et de bore sont dissociés et excités. Le bore atomique et le silicium atomique émettent ainsi des photons avec la longueur d'onde des raies atomiques. L'émission de ces raies atomiques dépend de la concentration des éléments dans le gaz. Un spectromètre mesure l'intensité des raies atomiques. Ce signal est proportionnel à la concentration des éléments dans les gaz en sortie. La concentration de bore dans les gaz en sortie est proportionnelle à la vitesse de purification mais aussi à la concentration de bore dans le bain de silicium. Le signal de bore est ainsi aussi proportionnel à la vitesse de purification. La vitesse de purification est un paramètre crucial du procédé. Avec notre mesure nous pouvons faire varier des paramètres du plasma et mesurer comment la vitesse de purification varie. Nous pouvons ainsi mesurer la dépendance de la vitesse de purification en fonction de plusieurs paramètres.

Dans une première mesure nous mesurons la décroissance de la concentration du bore dans le silicium. Nous mesurons la décroissance sur le signal ICP en prenant le rapport B/Si et nous mesurons la décroissance de la concentration du bain avec des prélèvements du silicium liquide. Sur les deux mesures nous observons une décroissance exponentielle avec le même temps de demi-vie. Nous validons ainsi que la purification suit une cinétique de premier ordre et que le signal ICP mesure bien les concentrations des éléments.

VII.3. Interaction du bore avec autres impuretés

Nous avons mesuré le temps de demi-vie de la concentration de bore sur une charge de silicium électronique et avec les mêmes paramètres sur une charge de silicium métallurgique. Les deux temps de demi-vie divisés par la masse de silicium sont identiques. Cette observation montre que les autres impuretés n'ont pas un effet significatif sur la vitesse de purification. Les interactions entre les autres impuretés et le bore sont faibles.

VII.4. Etude paramétrique

Nous avons mesuré la vitesse de purification en faisant varier différents paramètres. Ici nous allons montrer une petite synthèse de l'influence de différents paramètres :

La puissance MF du creuset: La variation de la puissance creuset induit une variation lente du signal de bore. L'augmentation de la puissance creuset fait décroitre le signal de bore. La vitesse de purification est ainsi plus basse quand la puissance creuset est plus élevée. La puissance creuset fait varier le brassage d'une coté et la température de silicium de l'autre coté. Comme le signal de bore varie lentement la variation de la vitesse de purification est probablement due à la variation de la température du silicium. La variation du brassage est immédiate et devrait ainsi induire une variation abrupte du signal de bore. La diminution de la vitesse de purification avec l'augmentation de la température du silicium est en accord avec un équilibre chimique à la surface du silicium.

La puissance plasma : Dans la gamme de 25 kW à 45 kW nous observons seulement une petite variation du signal de bore. A 20 kW le signal de bore est beaucoup plus faible. La vitesse de purification est ainsi plus faible à 20 kW.

La distance entre creuset et torche : Le signal de bore varie seulement très peu entre la distance minimale (30 mm) et la distance maximale (80 mm). Dans la gamme explorée l'effet de la distance est donc pas significatif.

La concentration d'hydrogène : Le signal du silicium varie très peu avec la concentration d'hydrogène qui a été varié entre 0% et 6%. Le rapport de B/Si augmente avec la concentration d'hydrogène et varie approximativement avec la racine de la concentration d'hydrogène comme prédit par l'équilibre chimique à la surface du silicium

VII.5. L'aérosol

Nous avons fait une mesure qui donne du poids à l'hypothèse que la formation d'un aérosol est responsable pour le rapport B/Si plus élevé par rapport à l'équilibre chimique.

Dans cette mesure nous soufflons d'abord un plasma d'argon pur sur une charge de silicium dans un creuset en silice. Ensuite nous ajoutons 1% d'oxygène au plasma. L'atmosphère au-dessus du silicium est d'abord réductrice et ensuite oxydante. L'atmosphère oxydante peut faciliter la formation de l'aérosol parce que l'oxygène peut oxyder le SiO qui est formé à la surface du silicium.

La Figure VII-1 montre le signal de bore et du silicium et leur rapport pendant la mesure. Tout d'abord, avec un plasma d'argon pur, nous observons un signal de silicium. Ceci est probablement dû à l'oxydation du silicium par l'oxygène du creuset en silice. Quand l'oxygène est ajouté au plasma le signal de silicium augmente parce que le flux d'oxygène est plus élevé. Le rapport B/Si augmente aussi, bien que l'oxygène ne décale pas l'équilibre entre les produits HBO et SiO. L'augmentation du rapport B/Si es ainsi probablement due à une évacuation plus faible du SiO causée par la formation d'un aérosol de SiO_2 dans la couche limite qui est en atmosphère oxydante.

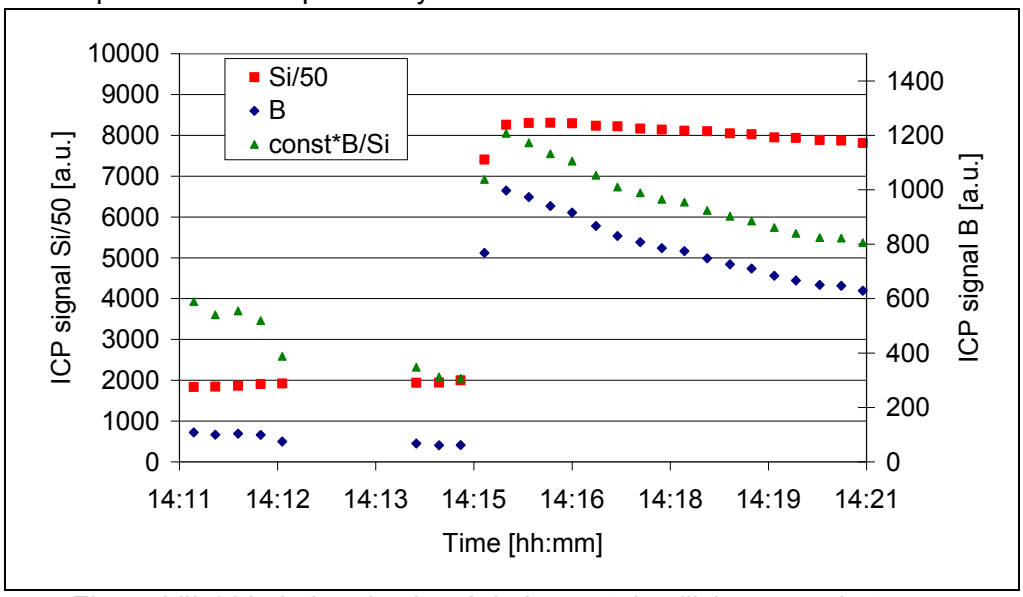

Figure VII-1 Variation du signal de bore et du silicium avec le temps. A 14:15 1% d'oxygène est ajouté au plasma d'argon

VII.6. Formation d'une couche de silice

La vitesse de purification est proportionnelle à la concentration d'oxygène dans le plasma. Au dessus d'un seuil une couche de silice se forme sur la surface de silicium. Cette couche forme une barrière entre le plasma et le silicium et réduit ainsi la vitesse de purification. Nous avons mesuré la concentration d'oxygène à partir de laquelle la couche de silice se forme pour différents températures de silicium et pour différents débits de gaz. Quand on augmente la température de silicium la concentration d'oxygène maximale (pour éviter la couche de silice) croit de façon exponentielle. Pour un débit plus élevé la concentration maximale est plus basse.

La vitesse de purification croît avec la concentration d'oxygène et décroit avec la température. Ainsi on ne peut pas dire exactement si la purification à une température de silicium plus élevée et une concentration d'oxygène maximale élevée est plus rapide qu'à une température plus basse.

VIII. Conclusion générale

Nous voulons souligner encore une fois les résultats importants de cette thèse. Avant ce travail on pensait que les réactions chimiques à la surface du silicium n'étaient pas en équilibre et que l'oxydation du bore constituait l'étape limitante. Dans ce travail nous avons proposé l'hypothèse que les réactions chimiques à la surface du silicium sont en équilibre et qu'ainsi le transport de l'oxygène vers la surface et l'évacuation des produits de réaction déterminent la vitesse de purification. La comparaison entre des mesures et des données de la littérature renforce cette hypothèse. Avec cette nouvelle théorie l'évacuation des produits de réaction devient importante. Nous avons ainsi analysé l'oxydation du silicium. La formation d'aérosol peut expliquer pourquoi le rapport B/Si mesuré est plus élevé que celui calculé par la thermodynamique.

Le résultat principal des mesures spectroscopique est l'amélioration d'un modèle numérique. Auparavant le modèle de turbulence k-ε a été utilisé mais les cartes de température simulées étaient très différentes des cartes de température mesurées. Nous avons ainsi remplacé le modèle k-ε par le modèle k-ω-sst. Avec le modèle k-ω-sst les cartes de température simulées étaient très similaires aux cartes de température mesurée. Nous pouvons ainsi conclure que le modèle simule bien le plasma et peut être utilisé pour trouver d'autres paramètres que la vitesse de purification.

Avec ces deux résultats nous nous approchons de l'objectif d'un modèle qui peut simuler la vitesse de purification. Avec un tel modèle on pourrait plus facilement optimiser le procédé.

References

[ALD03] C. Alemany, K-I Li, Y. Delannoy, B. Pateyron, P. Proulx, D. Morvan, C. Trassy, *Plasma refining of metallurgical silicon: thermodynamic and chemical aspects.* Progress in Plasma Processing of Materials 2003, P. Fauchais Ed. Begell House, NY (2003) pp 717-722

[AW07] MJ. Alsema, EA. de Wild-Scholten. Reduction of the environmental impacts in crystalline silicon module manufacturing. In *Proceedings of the 22nd European Photovoltaic Solar Energy Conference and Exhibition, Milan*, pp 829-836, 2007.

[And04] P Andre, Etude et optimisation du brassage par bullage du silicium liquide, Master Thesis, Grenoble INP, 2004

[Apo12] Apollon solar, private communication

[ADJ76] M. H. Abdallah, R. Diemiaszonek, J. Jarosz, J. M. Mermet, J. Robin and C. Trassy, Etude spectrométrique d'un plasma induit par haute fréquence, Partie 1: Performance Analytiques, *Analytica Chimica Acta,* Vol 84 pp 271-282, 1976

[AR68] D. R. Armstrong and W. E. Ranz, Design of inductively coupled plasma, *I&EC process design and development,* Vol. 7, No. 1, 1968

[AS65] M. Abramowitz and I.A. Stegun. *Handbook of Mathematical Functions, With Formulas, Graphs, and Mathematical Tables,*. Dover Publications Inc., new edition, June 1965.

[ATP02] C. Alemany, C. Trassy, B. Pateyron, K.I Li, Y Delannoy, Refining of metallurgical-grade silicon by inductive plasma, *Solar Energy Materials and Solar Cells,* 72, 1-4, pp 41-48, 2002

[BBS71] E. Beder, C. Bass and W. Shackleford, Transmissivity and Absorption of Fused Quartz Between 0.22 µm and 3.5 µm from Room Temperature to 1500℃," *Applied Optics* 10, pp 2263-2268, 1971

[BCD09] G. Baluais, Y. Caratini, Y. Delannoy, C. Trassy, High purity metallurgical silicon and method for preparing same, US patent No 7,858,063 B2, 2010

[Ben03] M. Benmansour, Developpement, contrôle et modélisation d'un procédé de projection de poudres de silicium par plasma rf – application aux couches minces photovoltaiques, PhD thesis Université Pierre et Marie Curie, 2003

[BFP94] M.Boulos, P.Fauchais and E.Pfender, Thermal plasmas fundamentals and applications, Vol 1, Plenum press, New York, 1994

[BFH97] P. Buchner, H. Ferfers, H. Schubert, and J. Uhlenbusch. Evaporation of copper powders in an inductively coupled thermal rf plasma-numerical modelling and spectroscopic measurements. *Plasma Sources Science and Technology*, 6:450–459, 1997.

[BHY95] H. Baba, K. Hanazawa, N. Yuge, Y. Sakaguchi, H. Terishima and F. Aratani, Metallurgical Purification for Production of Solar Grade Silicon from Metallic Grade Silicon, *13th European Photovoltaic Solar Energy Conference,* 1995, Nice

[BMB02] M. G. H. Boogaarts, S. Mazouffre, G. J. Brinkman, H. W. P. van der Heijden, P. Vankan, J. A. M. van der Mullen, D. C. Schram, and H. F. Dobele. Quantitative two-photon laser-induced fluorescence measurements of atomic hydrogen densities, temperatures, and velocities in an expanding thermal plasma. *Review of Scientific Instruments*, 73(1):73–86, 2002.

[Bou01] M. Boulos. Visualization and diagnostics of thermal plasma flows. *Journal of Visualization*, 4:19–28, 2001

[BPH96] M. J. Buie, J. T. P. Pender, J. P. Holloway, T. Vincent, P. L. G. Ventzek and M. L. Brake. Abel's inversion applied to experimental spectroscopic data with off axis peaks. *Journal of Quantitative Spectroscopy and Radiative Transfer*, 55:231–243, 1996.

[BVM11] W. Bussière, D. Vacher,S. Menecier and P. André, Comparative study of an argon plasma and an argon copper plasma produced by an ICP torch at atmospheric pressure based on spectroscopic methods, *Plasma Sources Science and Technology,* 20, pp 45004-45027, 2011

[BWK09] A. Bidiville, K. Wasmer, R. Kraft, C. Ballif, Diamond wire-sawn silicon wafers – from lab to the cell production, 24th European Photovoltaic Solar Energy Conference and Exhibition, 2009, Hamburg, Germany

[Car08] J.A. Carson, Solar Cell Research Progress, Nova Publishers, 2008

[CCM01] G.C.Y. Chan, W.T. Chan, X. Mao, R.E. Russo, Comparison of matrix effects in inductively coupled plasma using laser ablation and solution nebulization for dry and wet plasma conditions, *Spectrochilica Acta Part B: Atomic Spectroscopy,* V 56, I 8, pp 1375-1386, 2001

[CF89] M. T. Cicerone and P. B. Farnsworth. A simple, non-invasive method for the measurement of gas flow velocities in the inductively coupled plasma. *Spectrochimica Acta Part B: Atomic Spectroscopy*, 44(9):897–907, 1989.

[CG95] M. Cao, D.V. Gravelle, Investigation on the Departures from Thermodynamic Equilibrium in a DC Plasma Jet, International Symposium on Plasma Chemistry 12, p723

[CH06] G. C.-Y. Chan and G. M. Hieftje. Estimation of confidence intervals for radial emissivity and optimization of data treatment techniques in abel inversion. *Spectrochimica Acta Part B: Atomic Spectroscopy*, 61(1):31 – 41, 2006.

[CHP94] W. L. T. Chen, J. Heberlein and E. Pfender, Diagnostics of a Thermal Plasma Jet by Optical Emission Spectroscopy and Enthalpy Probe Measurements, *Plasma Chemisty and Plasma Processing,* Vol 14, No. 3, 1994

[Col11] V. Colombo. Validation of 3d modelling of an inductively coupled thermal plasma reactor through enthalpy probe measurements. In *ISPC 20*, 2011

[CPR03] P.J. Clarkson, D.J. Poole, C.K. Ryu, V.N. Sharifi, J. Swithenbank, Continuous measurement of metals in flue gas using ICP-OES, *Anal Bioanal Chem,* 377, pp 39-47, 2003

[Cus97] E.L. Cussler, Diffusion: Mass Transfer in Fluid Systems (2nd ed.). New York: Cambridge University Press, 1997

[DAL02] Y Delannoy, C. Alemany, K.-I. Li, P. Proulx, and C. Trassy. Plasma-refining process to provide solar-grade silicon. *Solar Energy Materials & Solar Cells*, 72:69–75, 2002.

[Deg08] J. Degoulange. *Purification et caractérisations physico-chimiques et électriques de silicium d'origine métallurgique destine à la conversion photovoltaique*. PhD thesis, Institut National Polytechnique de Grenoble, 2008.

[Del09] Y. Delannoy, Prospective sur la cinétique de purification plasma, Internal report, Octobre 2009

[Del11] Y. Delannoy, Purification of silicon for photovoltaic applications, *Journal of Crystal Growth*, In press, Available online 9 December 2011, ISSN 0022-0248, 10.1016/j.jcrysgro.2011.12.006. (http://www.sciencedirect.com/science/article/pii/S0022024811010256)

[Des86] P.D. Desai, Thermodynamic Properties of Iron and Silicon, *Journal of Physical and Chemical Reference Data,* V 14, I 3, pp 967-984, 1986

[DPB09] J. Degoulange, D. Pelletier, B. Bournonville, G. Chichignoud, Y. Delannoy, and C. Trassy. Experimental study of the effect of reactive gas injection geometry in atmospheric pressure inductive plasma torch on the chemical efficiency. *High Temperature Material Processes*, 13:220, 2009.

[DRH80] J.R. Davis, A. Rohatgi, R.H. Hopkins, P.D. Blais, P. Rai-Choudhury, J.R. McCormick, H.C. Mollenkopf, Impurities in silicon solar cells, *IEEE Transactions on Electron Devices,* 27, p. 4, 1980

[Dub90] J. C. Dubrous, F. ; Anglezio. Structure and behaviour of metallurgical silicon. In *Electric furnace conference proceedings*, p 241, 1990.

[efu] http://www.efunda.com/designstandards/sensors/flowmeters/flowmeter_va.cfm, 22.10.2012

[Elk12] A-K. Soiland, J.O. Odden, B. Sandberg, K. Friestad, J. Hakedal, E. Enebakk, S. Braathen, Solar silicon from metallurgical route by elkem solar – a viable alternative to virgin polysilicon, *6th International Workshop on Crystalline Silicon Solar Cells, CSSC 6, Aix les Bains,* 2012

[Ern96] R. Ernst, Analyse par méthode analytique du comportement d'un générateur à induction à triode haute fréquence pour torche à plasma inductif, *Journal de physique III France* Vol **6** pp. 1733-1758, 1996

[FAC] Thermfact/CRCT and GTT Technologies, www.factsage.com

[FJ98] I M El-Fayoumi and I R Jones, The electromagnetic basis of the transformer model for an inductively coupled RF plasma source, *Plasma sources science and technology* 7, pp 179-185, 1998

[FKM06] G. Flamant, V. Kurtcuoglu, J. Murray, A. Steinfeld, Purification of mettalurgical grade silicon by a solar process, *Solar Energy Materials & Solar Cells* 90 (2006) pp 2099-2106

[FNP04] E. Fourmond, C. Ndzogha, D. Pelletier, Y. Delannoy, C. Trassy, Refining of metallurgical silicon for crystalline solar cells, European Photovoltaic Solar Energy Conference 2004

[Fou03] E. Fourmond, Rapport d'avancement sur la purification par plasma du silicium UMG, Internal Report 03.09.2003

[GC96] M A Gigosos and V Cardenoso, New plasma diagnosis tables of hydrogen Stark broadening including ion dynamics *Journal of Physics B: Atomic Molecular and Optical Physics* 29 4795, 1996

[GGC03] M A Gigosos, M A Gonzalez and V Cardenoso,Computer simulated Balmer-alpha, -beta and -gamma Stark line profiles for non-equilibrium plasmas diagnostics, *Spectrochimica Acta B* 58 pp 1489—1504, 2003

[GKR11] J. Geilker, W. Kwapil, S. Rein, Light-induced degradation in compensated p- and n-type Czochralski silicon wafers, *Journal of applied physics,* 109, 053718, 2011

[GL88] A. Gagnoud and I. Leclercq, Electromagnetic Modelling of Induction Melting Devices in cold Crucibles, *IEEE Transactions on Magnetics*, 24, 1,pp 573-575, 1988

[GS83] M. A Gil and J. M Simon. Aberrations in plane grating spectrometers. Optica Acta: International Journal of Optics, 30(6):777 – 806, 1983

[Gri64] Hans R. Griem. *Plasma spectroscopy*. McGraw-Hill, 1964.

[HG76] J.W. Hinze and H.C. Graham, The active oxidation of Si and SiC in the viscous gas-flow regime, *Journal of electrochemical society,* Vol 123, 7, pp 1066-1073, 1976

[HG03] B. Han and R. J. Goldstein. Instantaneous energy separation in a free jet. part i. flow measurement and visualization. *International Journal of Heat and Mass Transfer*, 46(21):3975 – 3981, 2003.

[Hof78] D. Hofsaess, Emission continua of rare gas plasmas,*J. Quant. Spectrosc. Radiat. Transfer*, Vol 19, pp. 339-352, 1978

[Hof79] D. Hofsaess Photoionization cross sections calculated by the scaled Thomas-Fermi method (hv ≤ 50 eV), *Atomic Data and Nuclear Data Tables*, Volume 24, Issue 4, pp 285–321, 1979

[HH85] T. Hasegawa and H. Haraguchi. A collisional-radiative model including radiation trapping and transport phenomena for diagnostics of an inductively coupled argon plasma. *Spectrochimica Acta Part B: Atomic Spectroscopy*, 40(10-12):1505–1515, 1985.

[HKP93] H Hermann, J Kruse, A Piel, E W Weber, and V Helbig. Charged and neutral particle shift and broadening of resolved balmer- beta fine structure lines at low electron densities. *Plasma Sources Science and Technology*, 2(3):214, 1993.

[IHL11] W.R. Imler, R.E. Haun, R.A. Lampson, M. Charles and P. Meese, Efficacy of plasma arc treatment for the reduction of boron in the refining of solar-grade silicon, *37th IEEE Photovoltaic Specialists Conference (PVSC)*, pp 3435-3439,2011

[Ikh10] N. Ikhlef, Modelisation numérique d'une installation convertisseur-plasma d'induction en vue d'une commande optimale, PhD thesis, Université de Batna, 2010.

[IM96] T. Ikeda, M. Maeda, Elimination of Boron in Molten Silicon by Reactive Rotating Plasma Arc Melting. *Materials Transactions, JIM,* Vol. 37, No. 5 (1996) pp 983-987

[ITR11] International Technology Roadmap for Photovoltaics (ITRPV) Results 2011, Semi PV group, www.itrpv.net

[JAN98] M.W. Chase, NIST-JANAF Thermochemical Tables (Wood-bury, NY: NIST, 1998).

[JB10] M.D. Johnston, M. Barati, Distribution of impurity elements in slag-silicon equilibria for oxidative refining of metallurgical silicon for solar cell applications, *Solar Energy Materials & Solar Cells* 94, pp 2085-2090, 2010

[JB11] M.D. Johnston, M. Barati, Effect of slag basicity and oxygen potential on the distribution of boron and phosphorus between slag and silicon, *Journal of Non-Crystalline Solids* 357, pp 970-975, 2011

[Jen88] S. G. Jennings, The mean free path in air, *Journal of Aerosol Science*, 19, No. 2 pp 159-166, 1988

[JLL11] G. Jiang, Y. Li, Y. Liu, Calculation of hydrogen solubility in molten alloys, *Transactions Nonferrous Metals Society China* 21, pp 1130-1135, 2011

[JPV12] J. John, V. Prajapati, B. Vermang, A. Lorenz, C. Allebe, A. Rothschild, L. Tous, A. Urena, K. Baert and J. Poortmans, Evolutionary process development towards next generation crystalline silicon solar cells: a semiconductor process toolbox application, *EPJ Photovoltaics* 3, 35005, 2012

[KG77] G. R. Kornblum and L. De Galan. Spatial distribution of the temperature and the number densities of electrons and atomic and ionic species in an inductively coupled rf argon plasma. *Spectrochimica Acta Part B: Atomic Spectroscopy*, 32:71–96, 1977.

[KF86] W. Kurz, D. J. Fisher, Fundamentals of Solidifcation, 1986

[KJS02] Chandra P. Khattak, D. B. Joyce, and Frederick Schmid. A simple process to remove boron from metallurgical grade silicon. *Solar Energy Materials and Solar Cells*, 74(1-4):77–89, October 2002.

[KK97] R. Konjevic and N. Konjevic. On the use of hon-hydrogenic spectral line profiles for electron density diagnostics of inductively coupled plasmas. *Spectrochimica Acta Part B: Atomic Spectroscopy*, 52:2077–2084, 1997.

[KSG90] G. Kurz, I. Schwirtlich, K. Gebauer, Continuous process for refining silicon, US patent 4,900,532 1990

[KWH93] D E Kelleher, W L Wiese, V Helbig, R L Greene and D H Oza, Advances in plasma broadening of atomic hydrogen, Physica Scripta 75 T47, 1993

[KWH10] F. Kirscht, M. Walerysiak, M. Heuer, A. Jouini, K. Ounadjela, Method and system for controlling resisitivity in ingots made of compensated feedstock silicon, US patent 0258768 A1, 2010

[Lac08] J G Lacombe. Transferts radiatifs dans les plasmas thermiques. PhD thesis, L'Institut polytechnique de Grenoble, 2008.

[Lau02] C.O. Laux. Radiation and nonequilibrium collisional-radiative models. In *von Karman Institute Lecture Series 2002-07 Physico-Chemical Modeling of High Enthalpy and Plasma Flows, eds. D. Fletcher, J.-M. Charbonnier, G.S.R. Sarma, and T. Magin, Rhode-Saint-Genèse, Belgium*, 2002.

[LDT08] J G Lacombe, Y Delannoy, and C Trassy. The role of radiation in modelling of argon inductively coupled plasmas at atmospheric pressure. *Journal of Physics D: Applied Physics*, 41(16):165204, 2008.

[LDZ12] T. Liu, Z. Dong, Y. Zhao, J. Wang, T. Chen, H. Xie, J. Li, H. Ni, D. Huo, Purification of metallurgical silicon through directional solidification in large cold crucible, Journal of Crystal Growth, In press, Available online 2 July 2012, ISSN 0022-0248, 10.1016/j.jcrysgro.2012.06.037.

[Let11] S. Letout, Rapport sur les Simulations numérique de la Torche plasma Photosil: Apport des espèces à la surface du silicium liquide, Confidential internal report, December 2011

[LF10] L.M. Fraas, L.D. Partain, Solar Cells and their applications, 2010

[LFG10] J. Liu, Q. Falcoz, D. Gauthier, G. Flamant, C.Z. Zheng, Volatilization behavior of Cd and Zn based on continuous emission measurement of flue gas from laboratory-scale coal combustion, *Chemosphere,* 80, pp 241-247, 2010

[LLK99] D.A. Levin, C.O. Laux, C.H. Kruger, A general model for the spectral calculation of oh radiation in the ultraviolet, *Journal of Quantitative Spectroscopy and Radiative Transfer,* Vol. 61, No. 3, pp. 377-392, 1999

[LLY12] C.W. Lan, W.C. Lan, A. Yu, Y.M. Yang, W.C. Hsu, B. Hsu, A. Yang Development of high-quality multi-crystalline silicon for photovoltaic industry in taiwan, *6th International Workshop on Crystalline Silicon Solar Cells, CSSC 6, Aix les Bains,* 2012

[LR68] W. Lochte-Holtgreven and J. Richter. *Plasma diagnostics*. North-Holland Pub. Co., 1968.

[MAC83] D. Morvan, J. Amouroux, M. C. Charpin, and H. Lauvray. Elimination du bore dans le silicium par fusion de zone sous plasma inductif haute fréquence : rôle des plasmas réactifs et du laitier. caractérisation du silicium photovoltaïque. *Revue de Physique Appliquée*, 18(4):13, 1983.

[Mar77] H. Martin, Heat and Mass Transfer between Impinging Gas Jets and Solid Surfaces, *Advances in Heat Transfer* 13, pp 1-60, 1977

[Mek93] M. R. Mékidèche, Contribution à la modélistation numérique d'une torche à plasma d'induction, PhD theses, Université de Nantes, 1993

[Mey12] Meyer Burger, Manufacturer of wafering saws, www.meyerburger.ch

[MGS06] A. Müller, M. Ghosh, R. Sonnenschein, P. Woditsch, Silicon for photovoltaic applications, *Materials Science and Engineering: B,* 134 2-3, pp 257-262, 2006

[MMS96] T. Miki, K. Morita, and N. Sano. Thermodynamics of phosphorus in molten silicon. *Metallurgical and Materials Transactions B*, 27:937–941, 1996. 10.1007/s11663-996-0007-x.

[MNL88] J. A. M. van der Mullen, S. Nowak, A. C. A. P. van Lammeren, D. C. Schram and B. van der Sijde, *Spectrochimica Acta,* Vol 43B, Nos 4/5, pp. 317-324, 1988

[Mur96] A. B. Murphy, Demixing in free-burning arcs, *Physical Review E,* Vol 55 No. 6,1997

[Mur97] A. B. Murphy, Demixing in free-burning arcs, *Physical Review E,* V 5 No. 6, 1997

[NBS04] N. Nakamura, H. Baba, Y. Sakaguchi, S. Hiwasa and K. Yoshiei. Boron removal in molten silicon with steam added plasma melting method. *Journal of the Japan Institute of Metals*, 45(10):858–864, 2004.

[nis] Y. Ralchenko, A.E. Kramida, J. Reader and NIST ASD Team (2011). *NIST Atomic Spectra Database* (ver. 4.1.0), [Online]. Available: http://physics.nist.gov/asd [2012, June 21]. National Institute of Standards and Technology, Gaithersburg, MD.

[NMM94] T. Narushima, K. Matsuzawa, Y. Mukai, Y. Iguchi, Oxygen Solubility in Liquid Silicon, *Materials Transactions, JIM,* Vol 35 No.8 pp 522-528, 1994

[NMS88] S. Nowak, J. A. M. van der Mullen and D. C. Schram, Electron density and temperature determination in an ICP using a non-equilibrium concept, *Spectrochimica Acta Part B: Atomic Spectroscopy,* 43:1235-1245, 1988

[NO60] O. H. Nestor and H. N. Olsen. Numerical methods for reducing line and surface probe data. *SIAM Review*, 2(3):200–207, 1960.

[Nor12] E. Nordstrand, Removal of boron from silicon by moist hydrogen gas, *UMG – Silicon seminar at Hurtigruten*, Trondheim-Tromsø, Norway, 24.-26.April 2012

[NSG05] K. Niemi, V. Schulz von der Gathen, and H. F. Döbele. Absolute atomic oxygen density measurements by two-photon absorption laser-induced fluorescence spectroscopy in an rf-excited atmospheric pressure plasma jet. *Plasma Sources Science and Technology*, 14(2):375, 2005.

[NT12] E. F. Nordstrand and M. Tangstad. Removal of boron from silicon by moist hydrogen gas. *Metallurgical and Materials Transactions B*, pages 1–9, 2012.

[NTO12] M.K. Naess, G. Tranell, J.E. Olsen, N.E. Kamfjord, K.Tang, Mechanisms and Kinetcis of Liquid Silicon Oxidation During Industrial Refining, *Oxidation of Metals*, Vol 78, pp 239-251, 2012

[NWB12] C. Nuntadusit, M. Wae-hayee, A. Bunyajitradulya, S. Eiamsa-ard, Visualization of flow and heat transfer characteristics for swirling impinging jet, *Internation Communications in Heat and Mass Transfer*, V. 39, I 5, pp 640-648, 2012

[NYZ12] M.K. Naess, D.J. Young, J. Zhang, J.E. Olsen, G. Tranell, Active Oxidation of Liquid Silicon Experimental Investigation of Kinetics, *Oxidation of Metals,* Pre-print 2012, DOI: 10.1007/s11085-012-9312-8

[PCF98] M. P. Planche, J. F. Coudert, and P. Fauchais. Velocity measurements for arc jets produced by a DC plasma spray torch. *Plasma Chemistry and Plasma Processing*, 18(2):263–283, 1998.

[PDT10] D.Pelletier , Y.Delannoy, C.Trassy, Numerical study of the reactive species, *High temperature material processes* 14 pp 211-221, 2010

[Pel06] D. Pelletier. Modélisation de la cinétique chimique dans les plasmas inductifs - Application aux procédés. PhD thesis, INP Grenoble, 2006.

[PFC12] E. Pihan, G. Fortin, D. Camel, N. Plassat, D. Chavrier, J. Champliaud, S. Bailly, N. Enjalbert, A. Jouini, Recent developments on seeded growth in pilot and industrial size furnaces, *6th International Workshop on Crystalline Silicon Solar Cells, CSSC 6, Aix les Bains,* 2012

[PFS91] E. Pfender, J. Fincke and R. Spores, Entrainment of Cold Gas into Thermal Plasma Jets, *Plasma Chemistry and Plasma Processing,* Vol. 11, No. 4, 1991

[PH84] R. M. Pon and J. P. Hessler, Spectral emissivity of tungsten: analytic expressions for the 340-nm to 2.6-µm spectral region, *Applied Optics,* Vol. 23, No.7, 1984

[Piz10] S. Pizzini, Towards solar grade silicon: Challenges and benefits for low cost photovoltaics, *Solar Energy Materials & Solar Cells*, 94:1528-1533, 2010

[PSS07] D. Poole, V. Sharifi, J. Swithenbank, B. Argent, D. Ardelt, On-line detection of metal pollutant spikes in MSW incinerator flue gases prior to clean-up, *Waste Management,* 27, pp 519-532, 2007

[Pvi12] http://pvinsights.com, October 21, 2012

[PWC12] D.M. Powell, M.T. Winkler, H.J. Choi, C.B. Simmons, D. Berny Needleman and T. Buonassisi, Crystalline silicon photovoltaics: a cost analysis framework for determining technology pathways to reach baseload electricity costs, *Energy & Environmental Science,* 5, p 5874, 2012

[RBM07] S. Rousseau, M. Benmansour, D. Morvan, and J. Amouroux. Purification of mg silicon by thermal plasma process coupled to dc bias of the liquid bath. *Solar Energy Materials and Solar Cells*, Vol 91(20) pages 1906–1915, December 2007.

[RGH95] N. Rao, S. Girshick, J. Heberlein, P. McMurry, S. Jones, D. Hansen and B. Micheel, Nanoparticle Formation Using a Plasma Expansion Process, *Plasma Chemistry and Plasma Processing,* Vol. 15, No. 4, 1995

[RGM96] J.M. de Regt, F.P.J. de Groote, J.A.M. van der Mullen and D.C. Schram, Comparison of active and passive spectroscopic methods to investigate atmospheric inductively coupled plasmas, *Spectrochimica Acta Part B 51* pp 1371-1381, 1996

[RDB09] V.Y. Rudyak, S.N. Dubtsov, A.M. Baklanov, Measurement of the temperature dependent diffusion coefficient of nanoparticles in the range of 295 K to 600 K at atmospheric pressure, *Journal of Aerosol Science,* V 40, I 10, pp 833-843, 2009

[RSB95] M. Rahmane, G. Soucy, and M. I. Boulos. Diffusion phenomena of a cold gas in a thermal plasma stream. *Plasma Chemistry and Plasma Processing*, 16:S169–S189, 1995. 10.1007

[RRA01] M. Ratto, E. Ricci, E. Arato and P. Costa. Oxidation of Metals with Highly Reactive Vapors: Extenstion of Wagner Therory. *Metallurgical and Materials Transactions B*, Vol. 32, pages 903-911

[SGS90] I.C Santos, A.P Gonçalves, C.Silva Santos, M Almeida, M.H Afonso, M.Joaquina Cruz, Purification of metallurgical grade silicon by acid leaching, Hydrometallurgy, Volume 23, Issues 2–3, January 1990, Pages 237-246

[SGS04] S.M. Schnurre, J. Gröbner, R. Schmid-Fetzer, Thermodynamics and phase stability in the Si-O system, *Journal of Non-Crystalline Solids* 336, pp 1-25, 2004

[SKS92] K. Suzuki, T. Kumagai, N. Sano, Removal of Boron from Metallurgical-grade Silicon by Applying the Plasma Treatment. *ISIJ International,* Vol. 32 (1992), No. 5 pages 630-634

[SLK87] I. Schwirtlich, H. Lange and W. Kannchen, Process for refining silicon and silicon purified thereby, US patent 4,837,376 1987

[SM97] M.D. Seltzer, G.A. Meyer, Inductively coupled argon plasma continuous emissions monitor for hazardous air pollutant metals, *Environ Sci. Tenchnol.*, 31, pp 2665-2672, 1997

[SSC10] www.bernreuter.com, solar silicon conference 2010

[STT98] A. Schei, J. Kr.Tuset, H. Tveit, "Production of high silicon alloys", edition Tapir, (1998)

[SYM04] T. Shimpo, T. Yoshikawa, and K. Morita. Thermodynamic study of the effect of calcium on removal of phosphorus from silicon by acid leaching treatment. *Metallurgical and Materials Transactions B*, Vol 35, pages 277–284, 2004. 10.1007/s11663-004-0029-1.

[Tan12] K. Tang, The basic properties for UMG-SI processes and some examples, *UMG –Silicon seminar at Hurtigruten*, Trondheim-Tromsø, Norway, 24.-26.April 2012

[TAT12] K. Tang, S. Andersson, E. Nordstrand and M. Tangstad, Removal of Boron in Silicon by H2-H2O Gas Mixtures, JOM Journal of the Minerals, Metals and Materials Society, Vol 64, No. 8, pp952-956, 2012

[TC99] A Tazeem, Diagnostic spectroscopique d'un procede de depot de couche diamant assiste par plasma a pression atmospherique, PhD thesis, 1999

[TD95] C. Trassy, R. Diemiaszonek, On-line Analysis of Elemental Pollutants in Gaseous Effluents by Inductively Coupled Plasma Optical Emission Spectroscopy: Thermodynamic Aspects, *Journal of Analytical Atomic Spectrometry,* Vol 10, pp 661- 600, 1995

[TGD63] E.T. Turkdogan, P. Grieveson and L.S. Darken, Enhancement of diffusion-limited rates of vaporization of metals, *The Journal of Physical Chemistry*, Vol 67, No 8, pp 1647-1654,1963

[TL10] Y-D Tai, Y-C Lin, Recovery of silicon and silicon carbide powder from kerf loss slurry using particle phase-transfer method, US Patent 284885, 2010

[Tis06] S. Tisler, Deposition of Solid Particles from Aerosol Flow in Laminar Flat-Plate Boundary Layer, PhD thesis, Talinn university of technology, 2006.

[The56] H. C. Theuerer, Removal of boron from silicon by hydrogen water vapour treatment" Journal of Metals, 8 (AIME Trans. 206) p. 1316, 1956

[TM84] Christian Trassy and Jean-Michel Mermet. *Les applications analytiques des plasmas haute-fréquence*. Technique et documentation, 1984.

[TST09] M. Tangstad, J. Safarian, K. Tank, New solar grade silicon production processes, Version 3, Trondheim 2009

[TT98] C. Trassy, A. Tazeem, Simulation of atomic and ionic absorption and emission spectra for thermal plasma diagnostics: application to a volatilisation study in a plasma jet, *Spectrochimica Acta Part B: Atomic Spectroscopy*, Vol 54, Issues 3–4, pp 581-602, 1998

[TTW] T&twinner, a program for the calculation of chemical equilibrium constituition and transport properties. url: http://ttwinner.free.fr.

[TTY09] L. A. V. Teixeira, Y. Tokuda, T. Yoko and K. Morita, Behavior and State of Boron in CaO-SiO_2 Slags during Refining of Solar Grade Silicon

[Voo61] W. Voos, Production of pure silicon, U.S. Patent 2,972,521, 1961.

[Vos54] J. C. De Vos, A new determination of the emissivity of tungsten ribbon, *Physica XX,* pp 690-714, 1954

[Wag58] C. Wagner. Passivity during oxidation of silicon at elevated temperatures. *Journal of Applied Physics*, 29:1295–1297, 1958.

[WAS07] T. Watanabe, N. Atsuchi and M. Shigeta. Modeling of non-equilibrium argon-hydrogen induction plasmas under atmospheric pressure. *Thin Solid Films*, 515(9):4209 – 4216, 2007. SPSM 18

[WKH75] W. L. Wiese, D. E. Kelleher, and V. Helbig, Variations in Balmer-line Stark profiles with atom-ion reduced mass, Physical Review A 11, 1854–1864, 1975

[WKT91] A. T. M. Wilbers, G. M. W. Kroesen, C. J. Timmermans and D. C. Schram, The continuum emission of an arc plasma, *J. Quant. Spectrosc. Radiat. Transfer* Vol 45, No. 1, pp 1-10, 1991

[WLT08] T.Y. Wang, Y.C. Lin, C.Y. Tai, R. Sivakumar, D.K. Rai, C.W. Lan, A novel approach for recycling of kerf loss silicon from cutting slurry waste for solar cell applications, *Journal of Crystal Growth,* 310, pp 3403-3406, 2008

[WWT 02] K. Wegner, B. Walker, S. Tsantilis, S.E. Pratsinis, *Chemical Engineering Science,* 57, pp 1753-1762, 2002

[XYX12] C. Xiao, D. Yang, X. Yu, P. Wang, P. Chen, D. Que, Effect of dopant compensation on the performance of Czochralski silicon solar cells, *Solar Energy and Materials & Solar Cells,* 101, pp 102-106, 2012

[YAH01] N. Yuge, M. Abe, K. Hanazawa, H. Baba, N. Nakamura, Y. Kato, Y. Sakaguchi, S. Hiwasa, and F. Aratani. Purification of metallurgical-grade silicon up to solar grade. *Prog. Photovolt: Res. Appl.*, 9(3):203–209, 2001.

[YAM05] T. Yoshikawa, K. Arimura, and K. Morita. Boron removal by titanium addition in solidification refining of silicon with si-al melt. *Metallurgical and Materials Transactions B*, 36:837–842, 2005. 10.1007/s11663-005-0085-1.

[YBA93] N. Yuge, H. Baba, F. Aratini, Methode and apparatus for purifying silicon, US patent 5,182,091 1987

[YM09] T. Yoshikawa, K. Morita, Refining of silicon during its solidification from a Si-Al melt, *Journal of Crystal Growth* 311, pp 776-779, 2009

[ZGI02] R. Zikic, M.A. Gigosos, M. Ivkovic, M.A. Gonzalez, N. Konjevic, A program for the evaluation of electron number density from experimental hydrogen balmer line profiles, *Spectrochimica Acta Part B 57,* pp 987-998, 2002

Abstract
The plasma refining process studied in this work can efficiently remove boron from silicon. In combination with other processes one can purify silicon for solar cells at low costs. The hot gases from the thermal plasma torch are blown onto the surface of a silicon melt. However the chemistry at the silicon surface is so far poorly understood. For a better understanding of the process we do parametric measurements of the boron removal rate, we calculate the chemical equilibrium concentrations and we measure the temperature and radical concentrations in the plasma, using emission spectroscopy.
The comparison of boron removal rates from literature to calculated chemical equilibrium concentrations shows that the chemical reactions at the silicon surface are probably at chemical equilibrium. However, the boron to silicon ratio in the exhaust gases is higher than predicted by the chemical equilibrium calculations. This is probably due to the formation of a silica aerosol in the reactive boundary layer. The results of the parametric measurements of the boron removal rate agree also with this theory.
Several validation experiments showed that emission spectroscopy with Abel inversion can be used to measure the temperature and the concentration ratios O/Ar and H/Ar in the plasma. The spectroscopic results helped to improve significantly a numerical mode. The results also showed that hydrogen diffuses strongly in the plasma while oxygen diffuses much less.

Résumé
Le procédé de purification par plasma, étudié dans ce travail, peut efficacement enlever le bore du silicium. En combinaison avec d'autres procédés on peut ainsi purifier du silicium pour des cellules solaires à bas coûts. Cependant, la chimie à la surface du silicium est encore mal comprise. Pour une meilleure compréhension du procédé nous effectuons des mesures paramétriques de vitesse de purification, nous calculons l'équilibre chimique et nous mesurons la température et la concentration des radicaux dans le plasma, utilisant la spectroscopie d'émission.
La comparaison entre des vitesses de purification de la littérature et des concentrations à l'équilibre chimique calculé montre que les réactions chimiques à la surface du silicium sont probablement en équilibre. Cependant, le rapport entre le bore et le silicium dans les gaz en sortie du réacteur est plus élevé que prédit par les calculs de l'équilibre chimique. Ceci est probablement dû à la formation d'un aérosol de silice dans la couche limite réactive. Les résultats des mesures paramétriques de la vitesse de purification sont en accord avec cette théorie.
Plusieurs expériences de validation montrent que la spectroscopie d'émission peut être utilisé pour mesurer la température et les rapports de concentration O/Ar et H/Ar dans le plasma. Les résultats des mesures spectroscopiques ont aidé à améliorer de façon significative un modèle numérique. Les résultats ont montré que l'hydrogène diffuse fortement dans le plasma tandis que l'oxygène diffuse beaucoup moins.